



Universidad  
del País Vasco

Euskal Herriko  
Unibertsitatea

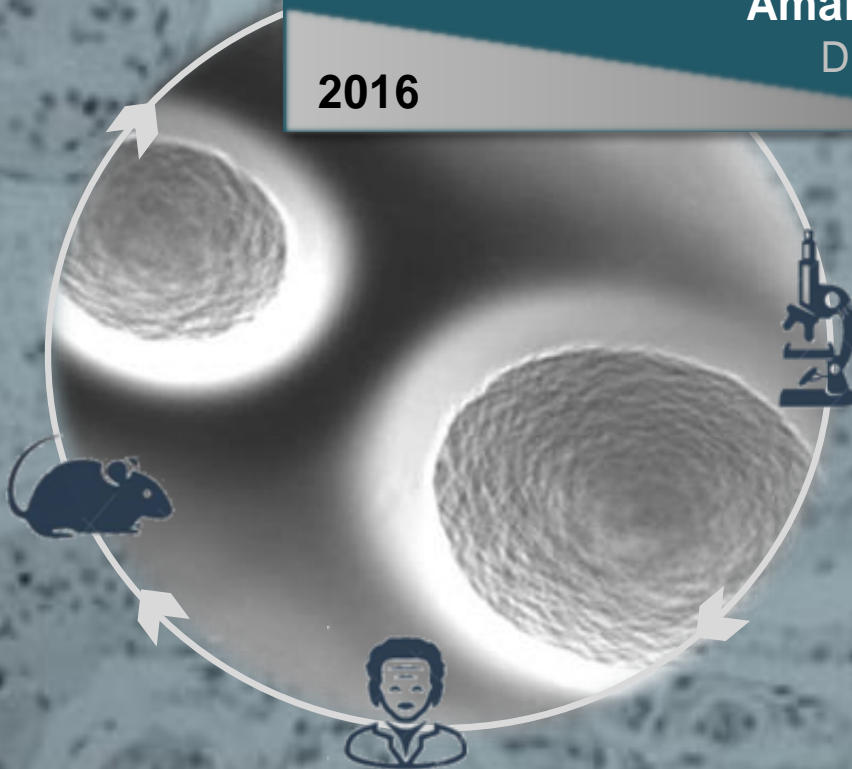
# *Metabolic Alterations in Prostate Cancer Pathogenesis*

Doctoral Thesis

**Amaia Arruabarrena-Aristorena**

Director: Arkaitz Carracedo Pérez

2016



# ***Metabolic Alterations in Prostate Cancer Pathogenesis***

*Doctoral Thesis*

*Report of the experimental work to apply for the grade of Doctor in Biological Sciences, into the Doctorate Programme of Molecular Biology and Biomedicine of the University of the Basque Country, The work herein has been performed by Amaia Arruabarrena Aristorena at the Center for Cooperative Research in Biosciences (CIC bioGUNE) under the mentorship of Dr. Arkaitz Carracedo Pérez.*

**Amaia Arruabarrena Aristorena**

**2016**

Supported by:







*"Lo que sabemos es una gota,  
lo que ignoramos un inmenso océano"*  
*(Isaac Newton)*

*Zuei aita ta ama,  
Zuri bruja,  
Zuri poxoki.*



---

<b>-Dox:</b> non-induced	<b>BAD:</b> Bcl-2-associated death promoter protein
<b>+ Dox:</b> induced with doxycycline	<b>BCAA:</b> Branched Chain Amino Acids
<b>µg:</b> microgram	<b>BCKA:</b> Branched Chain Ketoacids
<b>µM:</b> microMolar	<b>bHLH-LZ:</b> basic Helix-Loop-Helix-Leucine Zipper
<b>1,3-DAP:</b> 1,3-diaminopropane	<b>Bhmt:</b> Betaine-homocysteine S-methyltransferase
<b>1C:</b> one carbon	<b>BIOEF:</b> Basque biobank for research
<b>3PG:</b> 3-phosphoglycerate	<b>BPE:</b> Bovine Pituitary Extract
<b>4E-BP:</b> Eukaryotic Translation Initiation Factor 4E-binding Protein	<b>BPH:</b> Benign Prostatic Hyperplasia
<b>a.u.:</b> arbitrary units	<b>BRRS:</b> Bannayan-Riley-Ruvalcaba syndrome
<b>aa:</b> amino acid	<b>Cad:</b> Cadaverine
<b>AAALAC:</b> Association for Assessment and Accreditation of Laboratory Animal Care International	<b>CAD:</b> Carbamoyl-Phosphate Synthetase 2
<b>ABC:</b> Avidin/Biotin Complex	<b>CBS/Cbs:</b> Human/Murine Cystathionine β Synthase
<b>ABD:</b> ATP-binding cassette	<b>CDK-4:</b> Cyclin-dependent kinase 4
<b>ACF:</b> Aberrant Crypt Foci	<b>cDNA:</b> complementary DNA
<b>ACN:</b> Acetonitrile	<b>CEIC:</b> Clinical Research Ethics Committee
<b>AD:</b> Alzheimer's disease	<b>Chow:</b> regular diet
<b>AGC:</b> cAMP-dependent, cGMP-dependent and protein kinase C protein kinase family	<b>CHX:</b> Cyclohexamide
<b>AKT:</b> Protein Kinase B, PKB	<b>CI:</b> Confidence Interval
<b>AMD1/Amd1:</b> Human/Murine S-adenosylmethionine decarboxylase	<b>CID:</b> Collision Induced Dissociation
<b>Amp:</b> Ampicillin	<b>c-MYC:</b> Myc proto-oncogene protein
<b>AP:</b> Anterior Prostate	<b>Cre:</b> recombinase
<b>APAO:</b> Acetylpolyamine Oxidase	<b>CRPC:</b> Castration-Resistant Prostate Cancer
<b>APC:</b> Adenomatous Polyposis Coli	<b>CS:</b> Cowden syndrome
<b>AR:</b> Androgen Receptor	<b>Cth:</b> Murine Cystathionase
<b>Arg, R:</b> Arginine	<b>Cys:</b> Cysteine, C
<b>ATCC:</b> American Type Culture Collection	<b>CZ:</b> Central Zone
<b>Atg13:</b> Autophagy-related protein 13	<b>dcSAM:</b> decarboxylated S-adenosylmethionine
<b>ATG5:</b> Autophagy related 5 homolog	<b>DEPTOR:</b> DEP domain containing mTOR-interacting protein
<b>ATG7:</b> Autophagy related 7	<b>DFMO:</b> α-difluoromethylornithine
<b>ATM:</b> Ataxia telangiectasia mutated protein kinase	<b>DG:</b> Diglyceride
<b>ATP:</b> Adenosine Triphosphate	<b>DHS:</b> Deoxyhypusine Synthase
<b>AZ:</b> antizyme	<b>DLP:</b> Dorso-Lateral Prostate
<b>AZi:</b> antizyme inhibitor	

<b>DMSO:</b> Dimethyl Sulfoxide	<b>GEMM:</b> Genetic Engineered Mouse Model
<b>DNA:</b> Desoxyribonucleic Acid	<b>GlcNAc:</b> N-acetylglucosamine
<b>DOHH:</b> Deoxyhypusine Hydroxylase	<b>GLDC:</b> Glycine decarboxylase
<b>DRE:</b> Digital Rectal Examination	<b>Gln:</b> glutamine, Q
<b>DTT:</b> Dithiothreitol	<b>Glu:</b> Glutamate, E
<b>DU145<sup>MYC-AMD1-HA WT</sup>:</b> DU145 cells overexpressing AMD1 fused to HA and myctags	<b>Gly:</b> Glycine, G
<b>EGF 1-53:</b> Epidermal Growth Factor 1-53	<b>Gnmt<sup>-/-</sup>:</b> Whole body Gnmt knockout
<b>EGFR:</b> Epidermal Growth Factor Receptor	<b>GNMT/Gnmt:</b> Human/Murine Glycine N-methyltransferase
<b>eIF2<math>\alpha</math>:</b> eukaryotic translation initiation factor 2 complex	<b>Gnmt<sup>+/+</sup>:</b> Whole body Gnmt wild-type
<b>eIF4G:</b> eukaryotic Initiation Factor 4G	<b>GPCR:</b> G-protein-coupled receptor
<b>eIF5A:</b> eukaryotic translation initiation factor 5A	<b>GSK3:</b> Glycogen Synthase Kinase 3
<b>EMT:</b> Epithelial-Mesenchymal Transition	<b>H&amp;E:</b> Haematoxylin and Eosin
<b>ES:</b> Embryonic Stem	<b>h:</b> hour
<b>ETBF:</b> enterotoxigenic <i>Bacteroidesfragilis</i>	<b>H<sub>2</sub>O<sub>2</sub>:</b> Hydrogen Peroxide
<b>ETC:</b> Electron Transport Chain	<b>HBP:</b> Hexosamine Biosynthetic Pathway
<b>FA:</b> Formaldehyde	<b>HBS:</b> HEPES-Buffered Solution
<b>FAD:</b> Flavin Adenine Dinucleotide	<b>HCC:</b> Hepatocellular Carcinoma
<b>FAO:</b> Fatty Acid Oxidation	<b>HCys:</b> Homocysteine
<b>FAP:</b> Familial Adenomatous Polyposis	<b>HEPES:</b> 4-(2-hydroxyethyl)-1-piperazineethanesulfonic acid
<b>FAT:</b> FRAP (FKBP12–rapamycin-associated protein)-ATM (ataxia telangiectasia mutated)-TRRAP	<b>HGPIN:</b> High Grade Prostatic Intraepithelial Neoplasia
<b>FATC:</b> C terminus of FRAP-ATM-TRRAPcomplex	<b>HPLC:</b> High-Performance Liquid Chromatography
<b>FBS :</b> Fetal Bovine Serum	<b>H-Ras:</b> GTPase HRas
<b>FDR:</b> False Discovery Rate	<b>IARC:</b> International Agency for Research in Cancer
<b>FI-ToF-MS:</b> Flow Injection-Time-of-Flight Mass Spectrometry	<b>IGF-1R:</b> Insulin-like growth factor 1 receptor
<b>FKBP12:</b> Peptidyl-prolyl cis-trans isomerase FKBP12	<b>IHC:</b> Immunohistochemistry
<b>flox:</b> loxP recognition sequences	<b>Ile:</b> Isoleucine, I
<b>FOXO:</b> Forkhead Box Family of Transcription Factors	<b>INPP4B:</b> Inositol Polyphosphate 4-phosphatase type II
<b>FRAP:</b> Fluorescence recovery after photobleaching	<b>IPA:</b> Ingenuity Pathway Analysis
<b>FRB:</b> FKBP12-rapamycin binding	<b>IRES:</b> Internal Ribosome Entry Sites
	<b>IRS1:</b> Insulin Receptor Substrate 1
	<b>JNK:</b> c-Jun N-terminal kinase
	<b>KDa:</b> Kilodalton
	<b>KFSD:</b> Keratosis Follicularis Spinulosa Decalvans



---

<b>Kg:</b> kilogram	<b>NAD:</b> Nicotinamide Adenine Dinucleotide
<b>K<sub>m</sub>:</b> Michaelis constant	<b>FC:</b> Fold Change
<b>KRAS:</b> GTPase KRas	<b>NADPH:</b> Nicotinamide Adenine Dinucleotide Phosphate
<b>LBE:</b> LST8-bindingelement	<b>NAFLD:</b> Non-alcoholic fatty liver disease
<b>LC/MS:</b> Liquid Chromatography / Mass Spectrometry	<b>NCI:</b> National Cancer Institute
<b>LDD:</b> Lhermitte-Duclos disease	<b>NE:</b> Neuroendocrine
<b>Leu:</b> Leucine, L	<b>nM:</b> nano Molar
<b>m/z:</b> mass to charge ratio	<b>N-MYC:</b> N-myc proto-oncogene protein
<b>Mat2:</b> Methionine adenosyltransferase II	<b>NNMT:</b> Nicotinamide N-Methyltransferase
<b>MAX:</b> Protein max	<b>NP:</b> Nanoparticle
<b>MDM2:</b> Mouse Double Minute 2 homolog	<b>ODC1/Odc1:</b> Human/Murine Ornithine Decarboxylase 1
<b>Met Def:</b> methionine restricted	<b>OGT:</b> O-GlcNAc Tranferase
<b>Met:</b> methionine, M	<b>ORF:</b> Open Reading Frame
<b>MFA:</b> Metabolic Flux Analysis	<b>OXPPOS:</b> Oxidative Phosphorylation
<b>mg:</b> miligram	<b>p21<sup>Cip1/WAF1</sup>:</b> Cyclin-dependent kinase inhibitor 1
<b>MGBG:</b> methylglyoxal-bis (guanylylhydrazone)	<b>p27<sup>Kip1</sup>:</b> Cyclin-dependent kinase inhibitor p27
<b>MK:</b> MK2206	<b>p53:</b> Tumor protein p53
<b>mLST8:</b> mammalian lethal with sec-13 protein 8	<b>PA:</b> Polyamine
<b>mM:</b> milli Molar	<b>Paox:</b> Murine Peroxisomal N <sub>1</sub> -Acetyl-Spd/Spm Oxidase
<b>mm<sup>3</sup>:</b> cubic milimeters	<b>PB:</b> Probasin
<b>Mo:</b> Month	<b>PB-Cre:</b> Probasin-Cre
<b>Mock:</b> empty vector	<b>PC:</b> Phosphatidylcholine
<b>mRNA:</b> messenger RNA	<b>PCa:</b> Prostate Cancer
<b>MS/Ms:</b> Human/Murine Methionine Synthase	<b>PCR:</b> Polymerase Chain Reaction
<b>mSin1:</b> mammalian stress-activated map kinase-interacting protein 1	<b>PD:</b> Parkinson´s disease
<b>MTA:</b> Methylthioadenosine	<b>PDK1:</b> Phosphoinositide-dependent kinase 1
<b>MTD:</b> Maximum-Tolerated Dose	<b>PDs:</b> pharmacodynamics
<b>m-THF:</b> methyl-tetrahydrofolate	<b>PDTX:</b> Patient Derived Tumor Xenograft
<b>Mthfr:</b> Murine Methylenetetrahydrofolate reductase	<b>PE:</b> Phosphatidylethanolamine
<b>mTOR:</b> Mechanistic Target of Rapamycin	<b>PEG:</b> Polyethylene glycol
<b>mTORC1:</b> Mechanistic Target of Rapamycin Complex 1	<b>PEMT/Pemt:</b> Human/Murine Phosphatidyletanolamine N methyltransferase
<b>mTORC2:</b> Mechanistic Target of Rapamycin Complex 2	<b>PET:</b> Positron Emission Tomography

<b>PFA:</b> Paraformaldehyde	<b>PZ:</b> Peripheral Zone
<b>PH:</b> Pleckstrin-homology	<b>RAD001:</b> Everolimus
<b>PHTS:</b> PTEN hamartoma tumor syndromes	<b>RAFT:</b> rapamycin and FKBP12 target
<b>PI:</b> Propidium Iodide	<b>Rapa, R:</b> Rapamycin
<b>PI3K:</b> Phosphoinositide 3-kinase	<b>RAPTOR:</b> Regulatory-associated protein of mammalian Target Of Rapamycin
<b>PICS:</b> <i>Pten</i> -loss induced cellular senescence	<b>REDD1:</b> Damage-inducible transcript 4 protein (DDIT4)
<b>PIKK:</b> PI3K-related kinase	<b>RICTOR:</b> Rapamycin-insensitive Companion of mammalian Target Of Rapamycin
<b>PIN:</b> Prostatic Intraepithelial Neoplasia	<b>RIPA:</b> RadiolImmunoPrecipitation Assay buffer
<b>PIP<sub>2</sub>:</b> Phosphatidylinositol-4,5-bisphosphate, PI(4,5)P <sub>2</sub>	<b>RNA:</b> Ribonucleic Acid
<b>PIP<sub>3</sub>:</b> Phosphatidylinositol-3,4,5-trisphosphate, PI(3,4,5)P <sub>3</sub>	<b>ROS:</b> Reactive Oxygen Species
<b>PKC<math>\alpha</math>:</b> Protein Kinase C- $\alpha$	<b>RP:</b> Radical Prostatectomy
<b>PKR:</b> IFN-induced double-stranded RNA-dependent protein kinase	<b>RT:</b> Retention Time
<b>PKs:</b> pharmacokinetics	<b>RT:</b> Room Temperature
<b>PLP:</b> Pyridoxal Phosphate	<b>RTK:</b> Receptor Tyrosine Kinase
<b>PPAR<math>\gamma</math>:</b> Peroxisome Proliferator-activated Receptor gamma	<b>RT-QPCR:</b> Real Time-Quantitative-Polymerase Chain Reaction
<b>PPP:</b> Pentose Phosphate Pathway	<b>S6K:</b> Ribosomal Protein S6 Kinase
<b>PPRE:</b> PPAR response element	<b>SAH:</b> S-adenosylhomocysteine
<b>PRAS40:</b> Proline-Rich AKT Substrate 40 kDa	<b>Sahh:</b> Murine S-adenosylhomocysteine hydrolase
<b>PRE:</b> Polyamine-responsive element	<b>SAM:</b> S-adenosylmethionine
<b>proAMD1/proAmd1:</b> Human/Murine AMD1 proenzyme	<b>SAM486A:</b> (E)-2-(4-carbamimidoyl-2,3-dihydro-1H-inden-1-ylidene)hydrazinecarboximidamide dihydrochloride
<b>protor1/2:</b> protein observed with rictor 1 and 2	<b>Sardh:</b> Sarcosine dehydrogenase
<b>PSA:</b> Prostate-Specific Antigen	<b>SCD1:</b> stearyl-CoA desaturase 1
<b>PSVs:</b> polyamine-sequestering vesicles	<b>Ser:</b> Serine, S
<b><i>Pten</i><sup>+/-</sup>:</b> <i>Pten</i> heterozygosity, <i>Pten</i> heterozygousç	<b>SGK1:</b> Glucocorticoid-induced Protein Kinase 1
<b>PTEN<sup>C124S</sup>:</b> catalytically inactive PTEN	<b>SH2:</b> Src-homology 2
<b><i>Pten</i><sup>Hyl</sup>-:</b> hypomorphic <i>Pten</i> mutant	<b>SHIP1:</b> Src-homology 2 (SH2)-containing phosphatase 1
<b><i>Pten</i><sup>pc-/-</sup>:</b> <i>Pten</i> prostate-specific knockout	<b>SHIP2:</b> Src-homology 2 (SH2)-containing phosphatase 2
<b><i>Pten</i><sup>pc+/-</sup>:</b> <i>Pten</i> prostate-specific wild-type	<b>shRNA:</b> short-hairpin RNA
<b>PTEN<sup>WT</sup>:</b> PTEN wild-type	
<b>PTEN:</b> Phosphatase and tensin homolog	
<b>Put:</b> Putrescine	

<b>shSC:</b> short-hairpin Scramble	<b>UPLC-MS:</b> Ultra-high Performance Liquid-Chromatography coupled to Mass Spectrometry
<b>SLC:</b> solute carrier	<b>UPR:</b> Unfolded Protein Response
<b>Slc3a2:</b> Murine Solute Carrier Family 3 Member 2	<b>UTR:</b> Untranslated Region
<b>SMO:</b> Spermine Oxidase	<b>V:</b> Vehicle
<b>SN:</b> Supernatant	<b>Val:</b> Valine, V
<b>SNP:</b> Single-nucleotide Polymorphism	<b>VP:</b> Ventral Prostate
<b>Spd:</b> Spermidine, N-(3-aminopropyl)butane-1,4-diamine	<b>WHO:</b> World Health Organization
<b>SpdS:</b> Spermidine Synthase	<b>WT:</b> Wild-Type
<b>Spm:</b> Spermine, N,N'-bis(3-aminopropyl)butane-1,4-diamine	<b>XIC:</b> Extracted Ion Chromatogram
<b>SpmS:</b> Spermine Synthase	
<b>SRS:</b> Snyder-Robinson syndrome	
<b>SSAT1/Ssat1:</b> Human/Murine Spermidine/spermine N <sub>1</sub> -acetyltransferase	
<b>Std Er:</b> Standard Error	
<b>T:</b> Torin-1	
<b>TBS-T:</b> Tris-Buffered Saline solution containing Tween-20	
<b>TCA (solution):</b> Trichloroacetic acid	
<b>TCA:</b> Tricarboxylic Acid Cycle	
<b>TCEP:</b> tris(2-carboxyethyl)phosphine	
<b>TG:</b> Triglyceride	
<b>THF:</b> Tetrahydrofolate	
<b>Thr:</b> Threonine, T	
<b>TNM:</b> Tumor, Node, Metastasis	
<b>ToF-MS:</b> Time-of-Flight Mass Spectrometry	
<b>TRAMP:</b> transgenic adenocarcinoma of the mouse prostate	
<b>TRRAP:</b> Transformation/Transcription Domain Associated Protein	
<b>TSC2:</b> Tuberous Sclerosis 2 Protein	
<b>t-SSAT1:</b> truncated SSAT1	
<b>TURP:</b> Trans-Urethral Resection of the Prostate	
<b>TZ:</b> Transition Zone	
<b>ULK1/2:</b> serine/threonine-protein kinase ULK1/2	
<b>uORF:</b> upstream Open Reading Frame	



---

<b>SUMMARY</b> .....	<b>37</b>
<b>INTRODUCTION</b> .....	<b>37</b>
<b>I CANCER</b> .....	<b>39</b>
<b>I.1 CANCER HALLMARKS AND TUMOR PROGRESSION</b> .....	<b>39</b>
<b>II PROSTATE CANCER</b> .....	<b>41</b>
<b>II.1 HUMAN AND MURINE PROSTATE PHYSIOLOGY</b> .....	<b>41</b>
<b>II.2 PROSTATE CANCER PROGRESSION MODEL</b> .....	<b>43</b>
<b>II.3 PROSTATE CANCER PATHOLOGY AND TREATMENT</b> .....	<b>44</b>
II.3.1 PROSTATE CANCER PATHOLOGY.....	44
II.3.2 PROSTATE CANCER TREATMENT.....	46
<b>III PI3K PATHWAY AND CANCER</b> .....	<b>46</b>
<b>III.1 PI3K PATHWAY</b> .....	<b>46</b>
III.1.1 STRUCTURAL AND BIOCHEMICAL CHARACTERISTICS OF CLASS I PI3K.....	46
III.1.2 SIGNALING DOWNSTREAM CLASS I PI3K.....	47
III.1.3 KEY MEDIATORS DOWNSTREAM PI3K.....	48
III.1.3.1 AKT.....	48
III.1.3.2 mTOR.....	49
III.1.3.3 PTEN.....	50
<b>III.2 PI3K PATHWAY DEREGLATION IN CANCER</b> .....	<b>51</b>
<b>III.3 GENETIC MODELS OF <i>PTEN</i> LOSS <i>IN VIVO</i></b> .....	<b>52</b>
III.3.1 GENETIC MODELS OF <i>PTEN</i> GERMLINE MUTATIONS.....	53
III.3.2 GENETIC MODELS OF PROSTATE-SPECIFIC <i>PTEN</i> DELETION.....	53
<b>IV METABOLIC DEREGLATION AND CANCER</b> .....	<b>55</b>
<b>IV.1 WARBURG EFFECT</b> .....	<b>55</b>
<b>IV.2 1C METABOLISM</b> .....	<b>56</b>
<b>IV.3 OTHER METABOLIC ALTERATIONS</b> .....	<b>56</b>
<b>V POLYAMINES</b> .....	<b>57</b>
<b>V.1 DEFINITION OF POLYAMINES</b> .....	<b>57</b>
<b>V.2 POLYAMINE FUNCTIONS</b> .....	<b>58</b>
V.2.1 REGULATION OF GENE EXPRESSION.....	58
V.2.2 CONTROL OF CELL PROLIFERATION.....	58

---

V.2.3	IMPLICATION IN CELLULAR STRESS .....	60
<b>V.3</b>	<b>POLYAMINE METABOLISM .....</b>	<b>60</b>
V.3.1	POLYAMINE SYNTHESIS .....	60
V.3.2	POLYAMINE CATABOLISM .....	61
V.3.3	POLYAMINE TRANSPORT .....	62
<b>V.4</b>	<b>RATE LIMITING ENZYMES OF THE PATHWAY .....</b>	<b>63</b>
V.4.1	ODC1 .....	63
V.4.2	AMD1 .....	64
V.4.2.1	AMD1 regulation .....	65
V.4.2.1.1	AMD1 processing .....	65
V.4.2.1.2	AMD1 transcription .....	65
V.4.2.1.3	AMD1 translation .....	65
V.4.2.1.4	AMD1 degradation .....	66
<b>V.5</b>	<b>POLYAMINES AND DISEASE .....</b>	<b>67</b>
V.5.1	POLYAMINES AND CANCER .....	68
<b>OBJECTIVES .....</b>		<b>72</b>
<b>MATERIALS AND METHODS .....</b>		<b>75</b>
<b>I IN VIVO AND EX VIVO ASSAYS .....</b>		<b>77</b>
<b>I.1</b>	<b>ANALYSIS OF TISSUE SAMPLES .....</b>	<b>77</b>
I.1.1	ANALYSIS OF MURINE SAMPLES .....	77
I.1.1.1	Genetically engineered mouse models (GEMM) .....	77
I.1.1.2	Xenograft models in nude mice .....	77
I.1.1.2.1	AMD1 OE <i>in vivo</i> .....	78
I.1.1.2.2	AMD1 Silencing <i>in vivo</i> .....	78
I.1.1.3	Preclinical trials .....	78
I.1.1.3.1	RAD001 treatment <i>in vivo</i> .....	78
I.1.1.3.2	SAM486A treatment <i>in vivo</i> .....	79
I.1.1.3.3	Methionine restriction <i>in vivo</i> .....	79
I.1.2	ANALYSIS OF HUMAN SPECIMENS .....	80
<b>I.2</b>	<b>METHODS .....</b>	<b>81</b>
I.2.1	GENOTYPING .....	81
I.2.1.1	Genomic DNA purification from mouse tail .....	81
I.2.1.2	Polymerase Chain Reaction (PCR) for genotyping .....	82
I.2.2	PATHOLOGICAL ANALYSIS OF PROSTATE TISSUES .....	83
I.2.2.1	Tissue processing, paraffin embedding and sectioning .....	83
I.2.2.2	Slide processing for immunohistochemistry .....	83
I.2.2.2.1	Haematoxylin and Eosin (H&E) staining .....	84
I.2.2.2.2	Ki67 and RpS6 <sup>S235-236</sup> staining .....	84
I.2.2.2.3	AMD1 staining and scoring .....	84
I.2.3	MOLECULAR ANALYSIS OF PROSTATE TISSUES .....	85

---

I.2.3.1	Gene expression analysis of murine prostate tissues .....	85
I.2.3.2	Protein expression analysis of murine prostate tissues .....	85
I.2.4	METABOLOMIC ANALYSIS OF MURINE PROSTATE TISSUES .....	85
I.2.4.1	Time of Flight-Mass Spectrometry (ToF-MS).....	85
I.2.4.2	Liquid Chromatography-Mass Spectrometry (LC/MS).....	86
I.2.4.3	Targeted metabolomics by UPLC-MS .....	86
I.2.4.4	Metabolic Flux Analysis (MFA) .....	86
<b>II IN VITRO ASSAYS .....</b>		<b>87</b>
<b>II.1 MATERIALS .....</b>		<b>87</b>
II.1.1	CELL LINES AND CULTURE CONDITIONS .....	87
II.1.2	DRUGS .....	88
<b>II.2 METHODS.....</b>		<b>89</b>
II.2.1	CLONING .....	89
II.2.2	VIRUS PRODUCTION AND TARGET CELL LINE INFECTION .....	91
II.2.2.1	Transient transfection in HEK293 cells.....	92
II.2.2.2	Lentivirus production and target cell-line infection .....	93
II.2.2.2.1	Second Generation Lentivirus production .....	93
II.2.2.2.2	Third Generation Lentivirus production.....	94
II.2.2.2.3	Constitutive Silencing of AMD1.....	96
II.2.2.2.4	Inducible AMD1silencing.....	96
II.2.2.3	Retrovirus production and target cell-line infection .....	96
II.2.3	CELLULAR ANALYSIS.....	98
II.2.3.1	Cell-growth analysis by crystal violet staining.....	98
II.2.3.2	Anchorage-independent growth (Soft agar) .....	98
II.2.3.3	Foci formation assay.....	98
II.2.3.4	DNA synthesis rate analysis by bromo deoxyurdine (BrdU) .....	99
II.2.3.4.1	BrdU Incorporation .....	99
II.2.3.4.2	BrdU exposure and detection by immunofluorescence (IF) .....	99
II.2.3.5	Cell cycle analysis .....	99
II.2.4	MOLECULAR ASSAYS .....	100
II.2.4.1	Gene expression analysis .....	100
II.2.4.1.1	RNA extraction and retrotranscription .....	100
II.2.4.1.2	Real time quantitative PCR (RT-Q-PCR).....	100
II.2.4.2	Protein expression analysis .....	101
II.2.4.2.1	Protein extraction.....	101
II.2.4.2.2	Western Blotting (WB) .....	102
II.2.4.2.3	Protein Immunoprecipitation (IP) Assay .....	102
II.2.4.2.4	AMD1 translation rate by <sup>35</sup> S-Met labelling .....	103
II.2.4.2.5	Polysome Profiling.....	103
II.2.4.2.5.1	Sample extraction .....	104
II.2.4.2.5.2	Sample processing.....	105
II.2.4.2.6	Phosphoproteomics .....	105
II.2.4.2.6.1	Sample Preparation.....	105

---

II.2.4.2.6.2	LC-MS/MS analysis.....	106
II.2.4.2.6.3	Data analysis .....	106
II.2.4.3	In-House targeted metabolomic approaches .....	107
II.2.4.3.1	One carbon Metabolism and Polyamine Pathway analysis by LC/MS <i>in vitro</i> .....	107
II.2.4.3.2	dcSAM and polyamine quantification <i>in vitro</i> .....	107
II.2.4.3.3	MFA <i>in vitro</i> .....	107
<b>III</b>	<b>STATISTICAL ANALYSIS.....</b>	<b>108</b>
	<b>RESULTS AND DISCUSSION .....</b>	<b>133</b>
<b>I</b>	<b>INTEGRATIVE METABOLIC STUDY TO UNCOVER METABOLIC ALTERATIONS UNDERLYING PROSTATE CANCER (PCA).....</b>	<b>111</b>
I.1.1	TOF-MS METABOLOMICS. ....	114
I.1.1.1	Tricarboxylic Acid Cycle (TCA) .....	115
I.1.1.2	Amino Sugar Synthesis Pathway.....	117
I.1.1.3	Branched Chain Amino Acid (BCAA) Metabolism .....	117
I.1.1.4	Serine, Glycine (Gly) and one-carbon (1C) Metabolism .....	117
I.1.2	LC/MS METABOLOMIC STUDY TO QUANTIFY METABOLIC ALTERATIONS IN PCA.....	121
I.1.2.1	LC/MS metabolomics in murine samples .....	121
I.1.2.1.1	Branched chain amino-acid metabolism .....	121
I.1.2.1.2	Urea cycle.....	121
I.1.2.1.3	Methionine cycle .....	121
I.1.2.1.4	Trans-sulphuration reactions.....	123
I.1.2.1.5	Polyamine synthesis and catabolism pathways.....	123
I.1.2.2	LC/MS metabolic study to validate GEMM findings in human prostate cancer specimens 124	
I.1.3	<i>IN VIVO</i> <sup>13</sup> C-LABELED METHIONINE MFA.....	127
I.1.3.1	Pilot experiment of <sup>13</sup> C <sub>5</sub> labeled metabolic flux analysis (MFA) to establish the experimental settings for <i>in vivo</i> analysis.....	127
I.1.3.2	<i>In vivo</i> <sup>13</sup> C-labeled methionine MFA demonstrates the increased flux of methionine towards polyamine metabolism in PCa .....	128
	<b>RESULTS AND DISCUSSION .....</b>	<b>133</b>
<b>II</b>	<b>ELUCIDATION OF THE MECHANISM OF ACTION UNDERLYING THE METABOLIC ALTERATIONS OBSERVED IN PCA .....</b>	<b>135</b>
<b>II.1</b>	<b>EVALUATION OF TRANSCRIPTIONAL CHANGES AS DRIVERS OF THE POLYAMINE METABOLIC SWITCH .....</b>	<b>135</b>
II.1.1	TRANSCRIPT ANALYSIS OF GENES WITHIN THE METHIONINE/POLYAMINE AND RELATED PATHWAYS ....	135
II.1.1.1	Gene expression of polyamine metabolism-related enzymes .....	135
II.1.1.2	Gene expression of enzymes implicated in polyamine catabolism.....	136
II.1.1.3	Gene expression of folate metabolism related enzymes .....	138



II.1.1.4	Gene expression of enzymes implicated in trans-sulphuration reactions .....	138
II.1.1.5	Gene expression of methionine metabolism related enzymes .....	138
II.1.2	EVALUATION OF GNMT AS A CANDIDATE GENE TO MEDIATE THE METABOLIC SWITCH .....	139
II.1.2.1	<i>In vivo</i> .....	139
II.1.2.1.1	<i>Gnmt</i> -loss as a single event. ....	140
II.1.2.1.2	Compound deletion of <i>Pten</i> and <i>Gnmt</i> .....	141
II.1.2.2	<i>In vitro</i> .....	143
II.1.2.2.1	GNMT over-expression to characterize its role in PCa.....	143
<b>II.2</b>	<b>EVALUATION OF POST-TRANSCRIPTIONAL CHANGES AS DRIVERS OF THE POLYAMINE METABOLIC SWITCH</b>	
	<b>146</b>	
II.2.1	ANALYSIS OF AMD1 PROTEIN LEVELS IN <i>PTEN</i> <sup>pc+/+</sup> VS. <i>PTEN</i> <sup>pc-/-</sup> MICE.....	146
II.2.2	REGULATION OF AMD1 DOWNSTREAM PTEN .....	147
II.2.3	DECONSTRUCTION OF PI3K CASCADE BY PHARMACOLOGICAL INHIBITION .....	148
II.2.4	PRECLINICAL TRIAL OF RAD001 TO VALIDATE MTORC1 REGULATION OF AMD1 IN VIVO .....	152
II.2.5	MOLECULAR MECHANISM OF REGULATION OF AMD1 DOWNSTREAM MTORC1 .....	153
II.2.5.1	Regulation through ODC1 upregulation and putrescine increase .....	154
II.2.5.2	Regulation through increased autophagy .....	156
II.2.5.3	Regulation through translation initiation control .....	157
II.2.5.4	Regulation of proAMD1 stability.....	158
II.2.5.5	mTORC1 regulation of AMD1 levels through direct phosphorylation .....	159
II.2.6	TARGETS DOWNSTREAM AMD1.....	161
	<b>RESULTS AND DISCUSSION.....</b>	<b>168</b>
	<b>III ANALYSIS OF THE THERAPEUTIC POTENTIAL OF TARGETING AMD1 AND</b>	
	<b>EVALUATION OF PROSPECTIVE THERAPIES.....</b>	<b>169</b>
<b>III.1</b>	<b>ANALYSIS OF THE THERAPEUTIC POTENTIAL OF TARGETING AMD1 .....</b>	<b>169</b>
III.1.1	GENETIC MODULATION OF AMD1 LEVELS <i>IN VITRO</i> .....	169
III.1.1.1	Ectopic expression of AMD1 by lentiviral transduction .....	169
III.1.1.2	AMD1 silencing by lentiviral transduction. ....	170
III.1.1.3	Pharmacological modulation of AMD1 levels <i>in vitro</i> .....	174
III.1.2	AMD1 MODULATION <i>IN VIVO</i> .....	175
III.1.2.1	AMD1 ectopic expression <i>in vivo</i> .....	175
III.1.2.2	AMD1 silencing <i>in vivo</i> .....	176
<b>III.2</b>	<b>EVALUATION OF POTENTIAL THERAPIES.....</b>	<b>178</b>
III.2.1	NUTRITIONAL MODULATION .....	178
III.2.2	SAM486A PRECLINICAL TRIAL .....	184
III.2.3	ANALYSIS OF AMD1 LEVELS IN A CLINICAL TRIAL OF RAD001 .....	188
	<b>GENERAL DISCUSSION.....</b>	<b>193</b>
	<b>I THE REVOLUTION OF OMICS: MILESTONES AND REMAINING CHALLENGES IN</b>	
	<b>CANCER RESEARCH.....</b>	<b>195</b>

OMICS DEVELOPMENT AND CANCER RESEARCH .....	195
CHALLENGES AND FUTURE PROSPECTS OF METABOLOMICS IN EUKARYOTES.....	196
<b>II THE INTERPLAY OF MTORC1 SIGNALING AND POLYAMINE METABOLISM IN CANCER AND BEYOND.....</b>	<b>198</b>
THE CROSSTALK BETWEEN SIGNALING AND METABOLISM IN CANCER .....	198
SIGNALING-METABOLISM CROSSTALK BEYOND CANCER .....	200
<b>III AMD1 AS A PREDICTIVE BIOMARKER AND TARGET IN PROSTATE CANCER.....</b>	<b>202</b>
<b>CONCLUSIONS.....</b>	<b>206</b>
<b>BIBLIOGRAPHY.....</b>	<b>210</b>

**INTRODUCTION**

Figure1.....	39
Representation of the multi-step tumor progression model.	
Figure2.....	40
Schematic representations showing the revisited hallmarks of cancer by Hanahan and Weinberg, 2011.	
Figure3.....	42
Anatomy and histology of male human and murine reproductive system.	
Figure4.....	43
Schematic showing the prostate cancer progression model.	
Figure5.....	45
Grading systems employed for histopathological evaluation of prostate cancer.	
Figure6.....	47
Schematic depicting domain structure of the catalytic and regulatory subunits of class I PI3Ks.	
Figure7.....	48
Signaling downstream class I PI3Ks.	
Figure8.....	50
mTOR forms two distinct complexes	
Figure9.....	54
Prostate-specific <i>Pten</i> knockout mouse model.	
Figure10.....	59
Role of polyamines in cell physiology	
Figure11.....	61
Methionine cycle and polyamine pathway connection.	
Figure12.....	62
Putative mechanism models for polyamine uptake, accumulation and sequestration into vesicles in mammalian cells.	
Figure13.....	64
Ornithine decarboxylase 1 (ODC1) and antizyme (AZ) regulation.	
Figure14.....	65
AMD1 processing mechanism.	
Figure15.....	66
Different levels of AMD1 regulation	

**MATERIALS AND METHODS**

FigureM1.....	78
Schematic showing the experimental design of the RAD001 preclinical trial.	
FigureM2.....	79
Schematic showing the experimental design of the SAM486A preclinical trial.	

FigureM3.....	79
Schematic showing the experimental design of the methionine restriction preclinical trial for four weeks.	
FigureM4.....	80
Schematic showing the experimental design of the methionine restriction preclinical trial for four months.	
FigureM5.....	82
PCR programs followed for mouse tail DNA amplification and genotyping.	
FigureM6.....	84
Schematic of immunohistochemistry procedures	
FigureM7.....	92
Schematic showing the experimental design followed for virus production.	
FigureM8.....	93
Representative image showing packaging system and lentivirus production in HEK293 cells.	
FigureM9.....	93
Informative image showing the fragmentation of the lentiviral genome into a second generation packaging system	
FigureM10.....	94
Informative image showing the fragmentation of the lentiviral genome into a third generation packaging system.	
FigureM11.....	95
Illustrative image explaining the third generation lentiviral production in HEK283 cells and posterior infection of target cells	
FigureM12.....	97
Informative image showing the fragmentation of the retroviral genome into the packaging system.	
FigureM13.....	97
Informative image showing different retroviral packaging methods.	
FigureM14.....	104
Schematic of the protocol followed to analyze AMD1 protein synthesis rate.	

## RESULTS AND DISCUSSION I

FigureR1.....	112
General experimental design of <i>in vivo</i> experiments.	
FigureR2.....	113
Experimental design of the integrative metabolomic study.	

FigureR3.....	116
ToF-MS study unraveled increasing number of metabolic alterations through PCa development.	
FigureR4.....	118
ToF-MS enrichment analysis uncovered alterations in amino sugar synthesis pathway, BCAA metabolism, TCA and Ser and Gly metabolism in PCa pathogenesis.	
FigureR5.....	120
The inclusion criteria established narrowed the number of consistently altered metabolites.	
FigureR6.....	122
LC/MS analysis confirmed the altered metabolic pathways detected by ToF-MS.	
FigureR7.....	123
Diagram summarizing the main metabolic alterations observed by LC/MS.	
FigureR8.....	125
LC/MS analysis of PCa patients' specimens compared to BPH samples confirmed the metabolic alterations observed in the PCa GEMM.	
FigureR9.....	126
Diagram summarizing the main metabolic alterations observed by LC/MS in PCa patients' specimens	
FigureR10.....	127
Experimental design of <i>in vivo</i> MFA pilot experiment.	
FigureR11.....	128
<i>In vivo</i> flux pilot experiment to set up optimal conditions.	
FigureR12.....	129
Experimental design of <i>in vivo</i> metabolic flux experiment.	
FigureR13.....	130
The <i>in vivo</i> metabolic flux experiment confirmed in a dynamic setting the increased flux towards polyamine synthesis pathway through SAM decarboxylation.	
FigureR14.....	130
The fractional labeling data from the <i>in vivo</i> MFA experiment reinforces the rewiring towards SAM decarboxylation and polyamine synthesis.	
FigureR15.....	131
Diagram summarizing the main metabolic alterations observed in the <i>in vivo</i> U- <sup>13</sup> C <sub>5</sub> -methionine MFA experiment by LC/MS.	
 <b>RESULTS AND DISCUSSION II</b>	
FigureR16.....	137
Transcript analysis of the expression levels of enzymes involved in 1C metabolism and polyamine synthesis pathways.	

FigureR17.....	140
Evaluation of <i>Gnmt</i> loss single event as a mediator in the metabolic switch	
FigureR18.....	142
Evaluation of compound deletion of <i>Pten</i> and <i>Gnmt</i> and its implication in the metabolic switch.	
FigureR19.....	143
GNMT overexpression reduces cell-growth in AR expressing prostate cancer cells.	
FigureR20.....	144
<i>GNMT</i> over-expression <i>in vitro</i> did not recapitulate the metabolic wiring observed in <i>Pten</i> <i>pc<sup>-/-</sup></i> mice.	
FigureR21.....	146
Amd1 protein, but not RNA, levels dramatically increase upon Pten loss <i>in vivo</i> .	
FigureR22.....	147
<i>PTEN</i> expression in Pten deficient cells decreases AMD1 protein levels.	
FigureR23.....	149
PI3K/mTOR pathway targeting.	
FigureR24.....	150
mTORC1 regulates AMD1 protein expression.	
FigureR25.....	151
mTORC1 regulates dcSAM production.	
FigureR26.....	152
mTORC1 downstream PI3K regulates AMD1 at protein levels.	
FigureR27.....	153
mTORC1 regulation of AMD1 is conserved <i>in vivo</i> .	
FigureR28.....	154
Hypothetical means of AMD1 regulation downstream mTORC1.	
FigureR29.....	155
mTORC1 regulation of AMD1 does not depend on ODC1 nor on putrescine levels.	
FigureR30.....	156
mTORC1 does not regulate AMD1 through autophagy induction.	
FigureR31.....	158
mTORC1 does not regulate initiation of AMD1 translation.	
FigureR32.....	159
mTORC1 regulates stability of proAMD1.	
FigureR33.....	160
proAMD1 phosphorylation in S298 residue is decreased upon mTORC1 inhibition.	
FigureR34.....	161
Phosphorylation of residue S298 in proAMD1 decreases its stability and processing.	

FigureR35.....	161
mTORC1 phosphorylates proAMD1 in residue S298 increasing its stability and allowing its processing.	
FigureR36.....	162
Proteomic study to elucidate the mechanistic program induced downstream AMD1.	
FigureR37.....	163
AMD1 inhibition and silencing induce a proteomic profile regulated by MYC, which shows similarity with profiles obtained upon mTORC1 inhibition.	
FigureR38.....	164
MYC levels correlate with AMD1 levels.	
FigureR39.....	165
AMD1 under the regulation of mTORC1 might induce a transcriptional program controlled by c-MYC.	
<b>RESULTS AND DISCUSSION III</b>	
FigureR40.....	170
Impact of AMD1 over-expression in PCa growth.	
FigureR41.....	171
Impact of constitutive AMD1 silencing in PCa growth in DU145 cells.	
Figure R42. ....	171
Impact of constitutive AMD1 silencing in PCa growth in PC3 cells.	
FigureR43.....	172
Impact of inducible AMD1 silencing in PCa growth.	
FigureR44.....	173
Rescue experiment to revert the phenotype upon inducible AMD1 silencing.	
FigureR45.....	174
Impact of pharmacological AMD1 inhibition with SAM486A in PCa growth.	
FigureR46.....	175
Impact of AMD1 over-expression in PCa oncogenicity <i>in vivo</i> .	
FigureR47.....	177
Impact of inducible AMD1 silencing in PCa oncogenicity <i>in vivo</i> .	
FigureR48.....	180
Impact of short-term methionine restriction in PCa metabolism <i>in vivo</i> .	
FigureR49.....	181
Impact of short-term methionine restriction in PCa metabolism <i>in vivo</i> .	
FigureR50.....	182
Impact of long-term methionine restriction in PCa metabolism <i>in vivo</i> .	
FigureR51.....	183
Impact of long-term methionine restriction in PCa metabolism <i>in vivo</i> .	

FigureR52.....	185
Impact of pharmacological AMD1 inhibition with SAM486A in PCa oncogenicity <i>in vivo</i> .	
FigureR53.....	186
Impact of pharmacological AMD1 inhibition with SAM486A in PCa metabolism.	
FigureR54.....	189
Impact of pharmacological mTORC1 inhibition with RAD001 on AMD1 levels in a clinical trial.	
FigureR55.....	190
Impact of pharmacological mTORC1 inhibition with RAD001 on AMD1 levels in a clinical trial.	

### GENERAL DISCUSSION

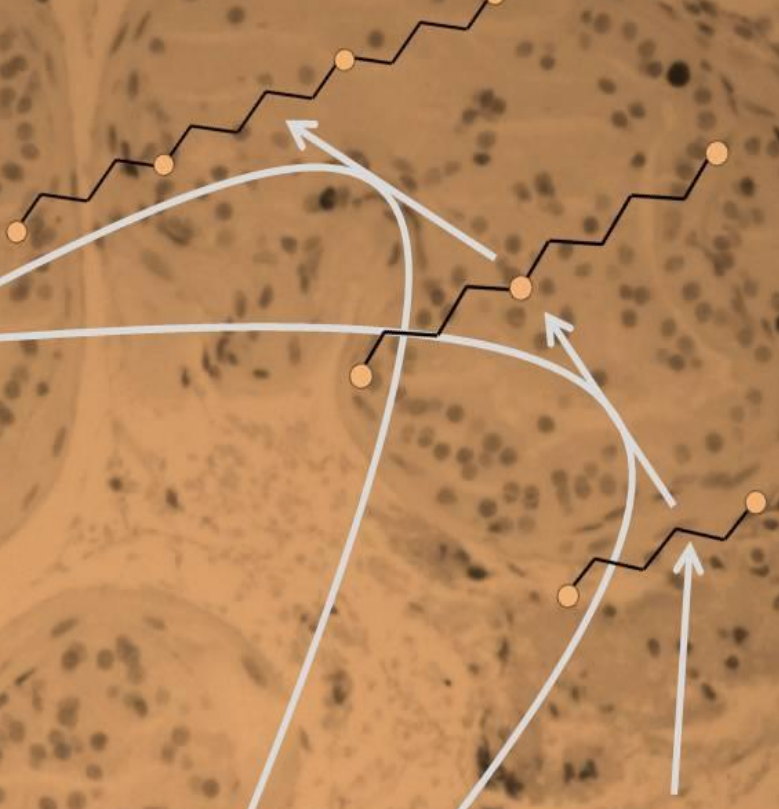
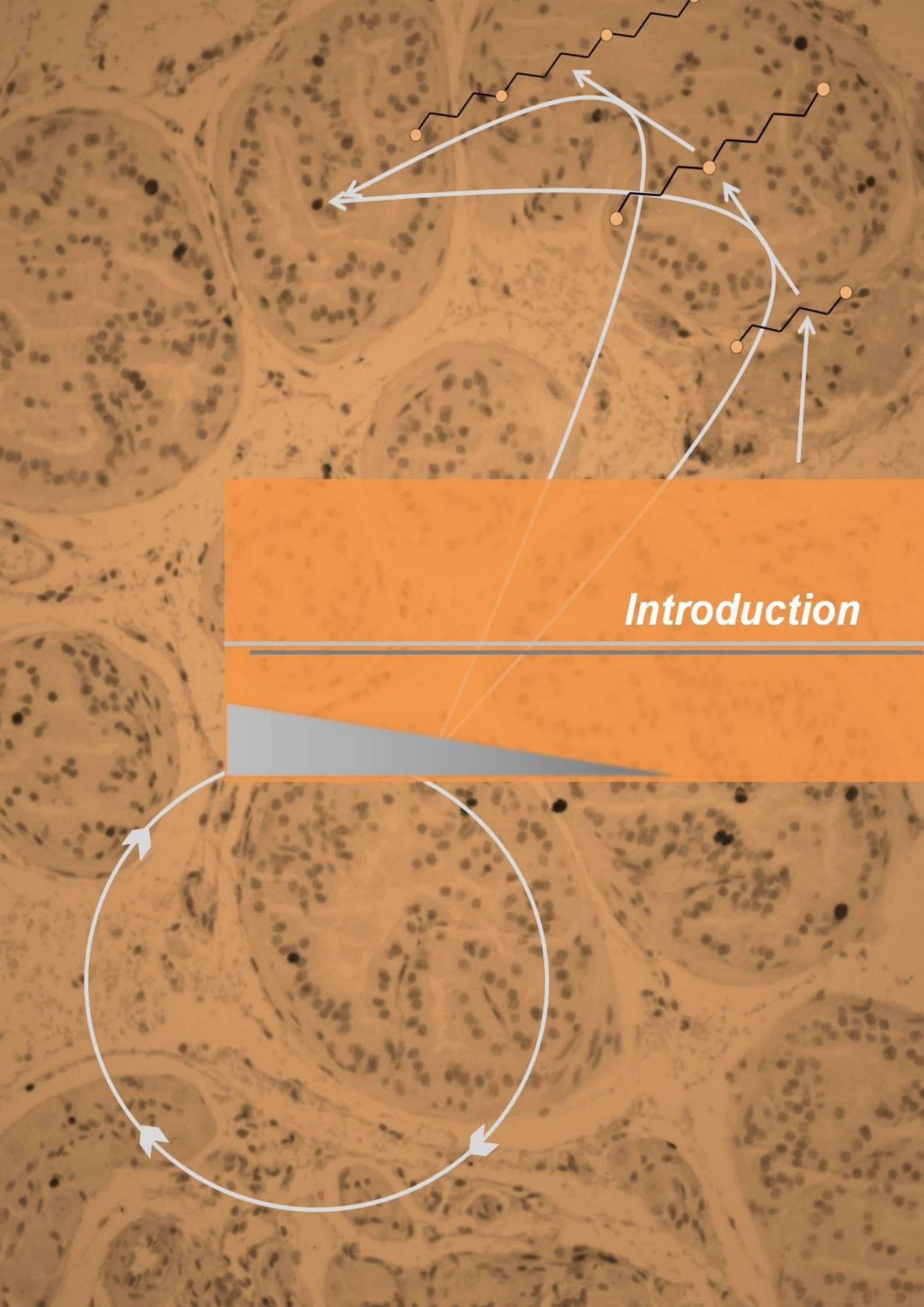
FigureD1.....	197
Schematic representation of polyamine pools according to the observed in Pten pc <sup>-/-</sup> mice and upon AMD1 inhibition with SAM486A.	
FigureD2.....	197
Schematic representation of the hypothesis postulating increased flux through polyamine pathway in prostate cancer.	
FigureD3.....	199
Scheme depicting the anabolic processes regulated downstream mTORC1, including AMD1 regulation and polyamine production.	
FigureD4.....	201
Interplay between PI3K-mTORC1 signaling and polyamine levels.	



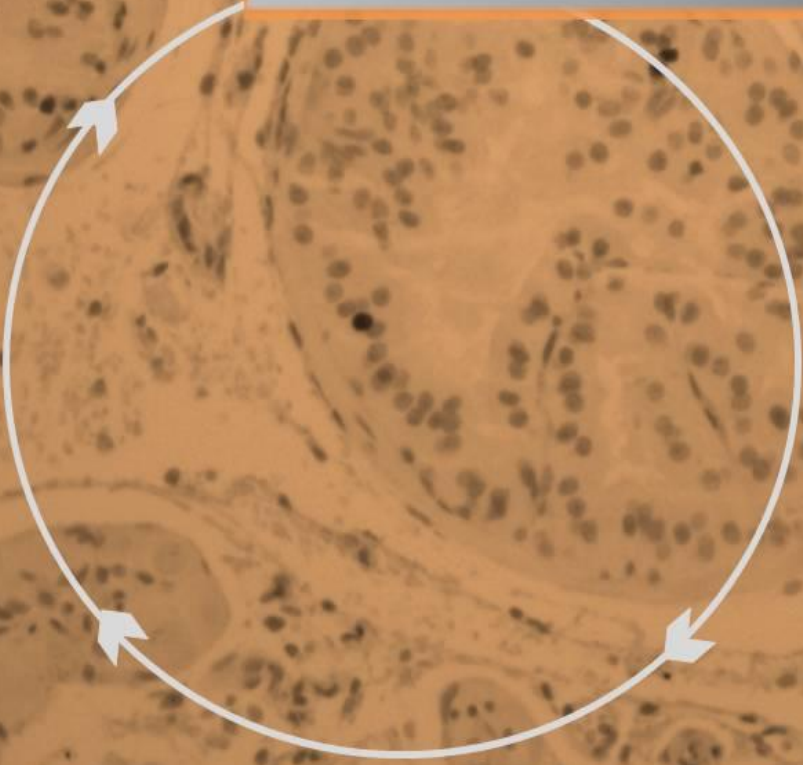
## SUMMARY

Activation of the PTEN-PI3K-mTORC1 pathway consolidates metabolic programs that sustain cell growth, proliferation and promote cancer initiation and progression. In this thesis work we describe a novel molecular mechanism by which mTORC1 regulates polyamine dynamics, a metabolic route that is essential for oncogenicity. Through the integrative metabolomics analysis of a mouse model and human biopsies of prostate cancer, we identified alterations in tumors impacting on the production of decarboxylated S-Adenosylmethionine (dcSAM) and polyamine synthesis. Mechanistically, we demonstrate that this metabolic rewiring stems from mTORC1-mediated post-transcriptional control of S-Adenosylmethionine decarboxylase 1 (AMD1). This novel molecular regulation was pharmacologically validated in samples from murine pre-clinical and human clinical trials with Everolimus. Importantly, we demonstrate that manipulation of AMD1 levels and activity dictates prostate cancer oncogenicity. The results in this thesis provide fundamental information about the complex regulatory landscape controlled by mTORC1 to integrate and translate growth signals into an oncogenic metabolic program.





***Introduction***

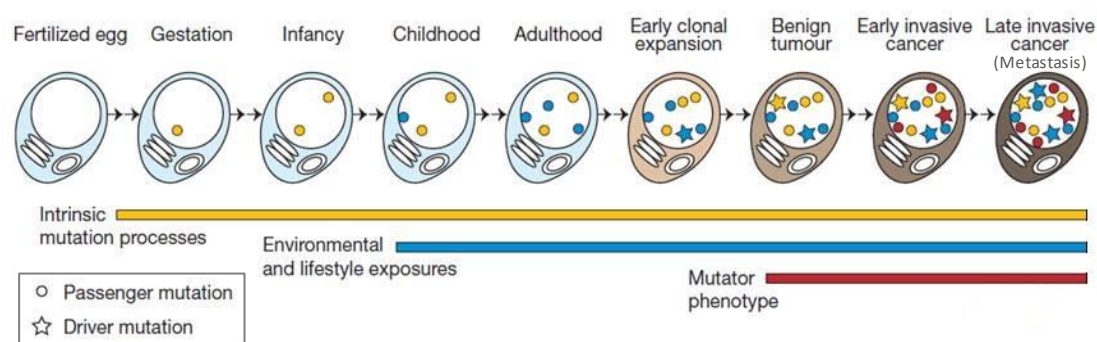




## I CANCER

Cancer refers to the uncontrolled proliferation of cells that leads to the formation of an abnormal cellular mass, denominated tumor. This term encompasses more than 100 different forms of the disease, as virtually every tissue can spawn one or more cancer types (Weinberg, 1996). Importantly, each of them requires unique diagnosis and treatment. Nevertheless, a common shared feature of tumors is the aberrant proliferation of malignant or transformed cells (Hanahan and Weinberg, 2000).

According to the World Health Organization (WHO, data collected by the International Agency for Research in Cancer (IARC) on the last Globocan 2012 report), cancer is one of the leading causes of morbidity and mortality worldwide. Indeed, more than 8 million people die from cancer every year, which covers 13% of all deaths worldwide. Of note, new cancer cases are estimated to increase in a 70% over the next two decades (<http://www.who.int/cancer/en/>). In Europe, 3.5 million new cases were estimated in 2012. The most common cancer types were breast (13.5%), colorectal (13%), prostate (12.1%) and lung (11.9%), representing 50.5% of the overall estimated burden of cancer in Europe in 2012 (Ferlay et al., 2013). All these key facts underscore the need and relevance for cancer research.



*Adapted from Stratton MR, Campbell PJ and Futreal PA, Nat Rev 2009*

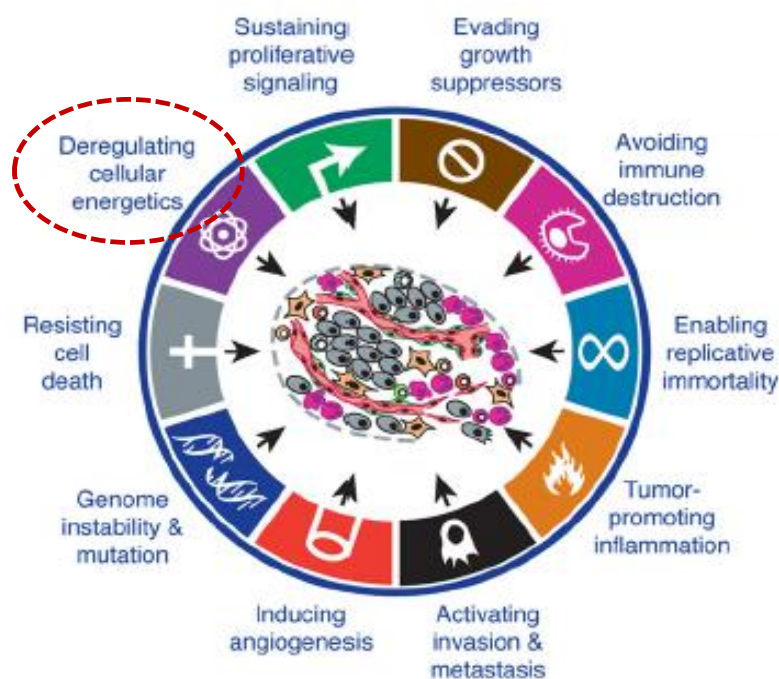
Figure I1. Representation of the multi-step tumor progression model.

### I.1 Cancer hallmarks and tumor progression

After decades of research, cancer is widely accepted as a primarily genetic disease (Vogelstein and Kinzler, 2004). Cancer development is a sequential, multistep and complex process of mutations that accumulate leading to transformation and clonal expansion of cells (3 to 7 mutagenic events are suggested to be required) (Vogelstein and Kinzler, 1993; Hahn and Weinberg, 2002). Multiple studies performing comparative analysis of genetic alterations in early versus late stage tumors support this notion (Yokota, 2000). Subsequent genetic and epigenetic alterations would convert normal cells into premalignant cells, premalignant cells into transformed cells and transformed cells into metastatic cells (**Fig. I1**). Thus, this progressive accumulation of

alterations would imply increasing malignancy and aggressiveness of the tumor (Nowell, 2002). The cumulative nature of this process and the monoclonal and polyclonal expansion of transformed cells, in turn supports the heterogeneity of primary and metastatic tumors (Yokota, 2000).

There are three type of genes whose alteration is considered relevant to tumorigenesis: oncogenes, tumor-suppressor genes and genomic stability genes. Both gain of function alterations of oncogenes and loss of function alterations of tumor-suppressor genes lead to uncontrolled proliferation of cells driving the neoplastic process. Alterations in the third group of genes lead to increased mutation rate, which can affect the function of oncogenes and tumor suppressors (Nowell, 2002; Vogelstein and Kinzler, 2004).



*Adapted from Hanahan D and Weinberg RA, Cell Rev 2011*

**Figure I2.** Schematic representations showing the revisited hallmarks of cancer by Hanahan and Weinberg, 2011.

In an effort to unify and identify common features of cancer cells, Hanahan and Weinberg proposed, more than a decade ago, six capabilities that a cell must acquire to engage malignant growth: i) self-sufficiency of growth signals, ii) insensitivity to growth-inhibitory signals, iii) evasion of apoptosis, iv) limitless replicative potential, v) sustained angiogenesis and vi) tissue invasion and metastasis (Hanahan and Weinberg, 2000). In order to acquire these capabilities, it was postulated that cells would need to acquire an enabling characteristic: genome instability (consequence of the malfunction of genomic integrity control mechanisms), hence increasing mutation rate (Nowell, 2002). With the intense research in the field during the following decade, increased knowledge regarding tumor initiation, progression and dissemination led to revisiting

these hallmarks. Together with the aforementioned genomic instability, the inflammatory state of premalignant and malignant cells arose as a second enabling characteristic. Indeed, cells of the immune system were suggested to act as promoters of tumor progression by producing growth, survival and angiogenic factors, extracellular matrix-modifying enzymes, epithelial-mesenchymal transition (EMT)-inducing signals and reactive oxygen species (ROS) in the tumor microenvironment (Hanahan and Weinberg, 2011). Importantly, two other capabilities of cancer cells were introduced in the list of cancer hallmarks due to their relevance in the development of the disease: avoiding immune destruction and reprogramming energy metabolism. Increasing evidence supports the notion that deregulation of metabolism is a direct response to growth factor signaling (Ward and Thompson, 2012) (**Fig. I2**).

## II PROSTATE CANCER

### II.1 Human and murine prostate physiology

The prostate is part of the male reproductive system, and is the largest accessory gland in the body (Bhavsar et al., 2014). The glandular tissue of the prostate secretes an alkaline fluid that helps maintain sperm motility. The smooth muscle of the prostate gland contracts during ejaculation to contribute to the expulsion of semen from the urethra (Scandalon VC and Sanders T, 2007). For further comprehension of this work we will describe in depth the anatomic and histological characteristics of human and murine prostate.

The human prostate gland is about 3 cm high by 4 cm wide by 2 cm deep, about the size of a walnut, and it is located just below the urinary bladder. It is conical in shape and surrounds the first 2,5 cm of the urethra as it emerges from the bladder (Scandalon VC and Sanders T, 2007) (**Fig. I3A-B**). The human prostate is a single organ that forms a pseudocapsule consisting of glandular and stromal elements (Bhavsar et al., 2014). In humans, this gland is organized in four zones following the branching pattern of the prostate ducts: the central (CZ), which surrounds the urethra; the transition zone (TZ), anterior to the urethra, the peripheral (PZ), posterior to the urethra and the fibromuscular stroma that separates the prostate from the rectum (Knoblauch and True, 2012) (**Fig. I3C**). The PZ is relatively accessible for transrectal biopsies to sample the prostate for prostatic adenocarcinoma. The PZ is the largest of the zones, encompassing approximately 70% of the glandular tissue, while the CZ and the PZ account for approximately 25% and 5% of the glandular tissue, respectively (Bhavsar et al., 2014).

The mouse prostate gland is divided into three distinct lobes: the dorsolateral lobe (DLP), which has butterfly shape and surrounds the urethra; the ventral (VP), leaf-shaped, gelatinous and located above the urethra and toward midline; and the anterior lobes (AP), located cranial to the other lobes and attached to the lesser curvature of the seminal vesicles (Knoblauch and True, 2012) (**Fig. I3D**). Histologically, each of the lobes is surrounded by a thin mesothelium-lined

delicate capsule. The glandular prostate is separated from the capsule by loose fibroadipose tissue containing major vessels, nerves, and ganglia. The individual mouse prostate lobes are composed of a series of branching ducts, which are formed by few layers of spindle cells and eosinophilic collagen (Shappell et al., 2004). The individual murine prostate lobes show distinctive histological features. The DLP is lined by cuboidal and columnar epithelium, with moderate infolding, granular cytoplasm with eosinophilic secretions and basally located uniform nuclei. The VP is mostly lined by cuboidal epithelium, with sparse infolding, abundant homogeneous pale secretions and small basally located nuclei. The AP lobes are lined by cuboidal to columnar epithelium with a papillary pattern, contain granular cytoplasm with homogeneous eosinophilic secretions and centrally located nuclei (Knoblauch and True, 2012).

Similarly, the human prostate ducts are constituted of cuboidal to columnar epithelium composed of a layer of basal cells and a luminal layer of differentiated secretory cells, with small subpopulations showing differentiated neuroendocrine (NE) phenotype, which represent less than 1% of prostate epithelial cells (Shappell et al., 2004; Knoblauch and True, 2012) (**Fig. I3E**).

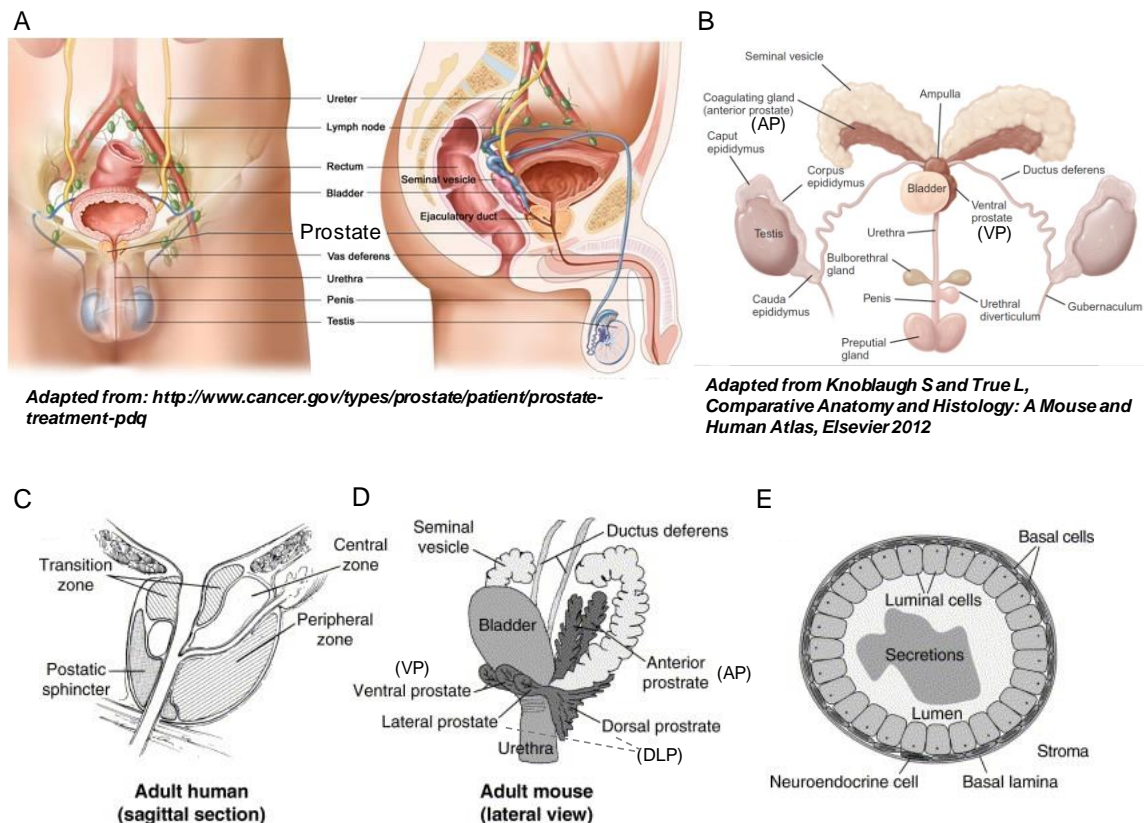


**Figure I3. Anatomy and histology of male human and murine reproductive system. A**, Picture of human anatomy showing the localization of the prostate gland. **B**, Picture of murine anatomy showing the different organs constituting the male reproductive system. **C-D**, Schematics of the anatomy of the different zones and lobes of human (**C**) and murine (**D**) prostates. **E**, Schematic depicting the different cellular types in a histological section of a human prostate duct.

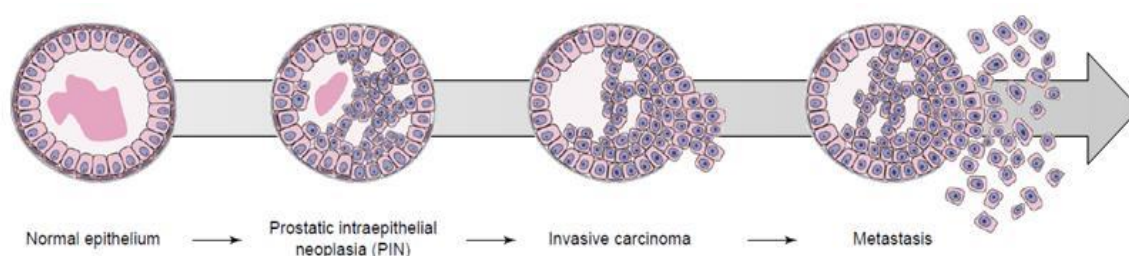


Importantly, the individual prostate zones or lobes have different embryologic origins and can be distinguished not only by the appearance and anatomic features, but by the biological functions and susceptibility to pathology (Bhavsar et al., 2014). Of note, although the mouse DLP has sometimes been assessed as the most homologous to the human PZ, the developing lobes are identifiable only in the embryo in humans. Thus there is no supporting evidence nor consensus agreement among pathologists for a direct correlation between the specific mouse prostate lobes and the human prostate zones (Shappell et al., 2004). Furthermore, overall, the mouse prostate has a modest stromal component compared to that of the human prostate (Knoblauch and True, 2012). Hence, there are fundamental anatomic differences between the human and murine prostates that should be considered when studying the neoplastic development of this organ.

## II.2 Prostate cancer progression model

In spite of the anatomic and histological differences between the human and murine prostate structures, prostate cancer progression occurs in a strikingly similar manner in mice and humans (Nardella et al., 2010a).

Prostate cancer starts from the accumulation of genetic alterations in the epithelium of the prostatic gland, which leads to prostatic intraepithelial neoplasia (PIN) and can progress to high-grade prostatic intraepithelial neoplasia (HGPIN). The progressive accumulation of further genetic insults leads to more aggressive and malignant lesions, which thereby disrupt the basement membrane and invade the surrounding stroma, leading to an invasive carcinoma (Nardella et al., 2010). This carcinoma can stay confined in the prostate or invade other organs, causing metastasis and ultimately resulting in lethality (Abate-Shen and Shen, 2002) (**Fig. I4**).



*Adapted from Abate-Shen C and Shen MM. Trends in Gen 2002*

**Figure I4.** Schematic showing the prostate cancer progression model.

PIN is characterized by cellular proliferating foci within preexisting ducts and acini with cytologic changes, such as nuclear and nucleolar enlargement. In this kind of premalignant neoplasia, inversion of the normal epithelial proliferation orientation occurs, cells proliferating from the basal cell compartment to the luminal space. PIN progresses into HGPIN, which is usually

multicentric and is commonly found in the PZ. Early stromal invasion, which is the earliest evidence of carcinoma, occurs at sites with basal cell disruption in ducts with HGPIN (Bostwick et al., 2004). Cancer cells require the acquisition of another capability in order to survive upon loss of contact with the basement membrane, evasion of *anoikis* signals. *Anoikis* is a programmed cell death induced upon cell detachment from extracellular matrix. Resistance to this type of cell death is of vital importance in cancer progression (Paoli et al., 2013). Prostate cancer invariably metastasizes to bone, although lung, liver and pleura are secondary metastasis sites (Bubendorf et al., 2000).

## **II.3 Prostate cancer pathology and treatment**

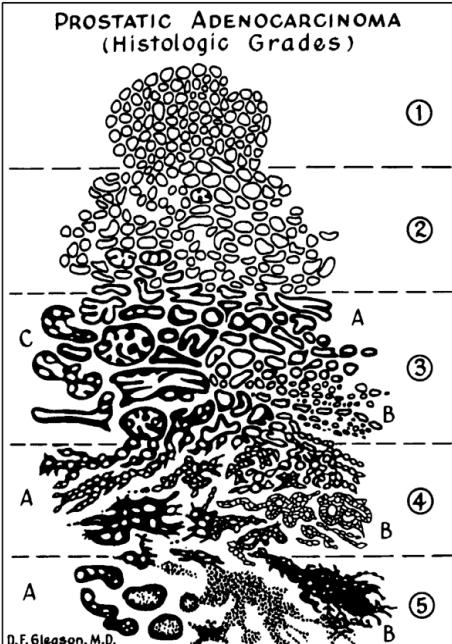
### **II.3.1 Prostate cancer pathology**

According to the last Globocan 2012 report of the IARC, 1.1 million men were diagnosed of prostate cancer in 2012 worldwide and the disease caused 307,000 deaths (<http://www.who.int/cancer/en/>). This cancer type is the second most frequent and the fifth cause of death from cancer in men worldwide. In Europe it represents the most frequent cancer type in men, with 417,000 new cases and 92,000 deaths in 2012 (Ferlay et al., 2013).

Age is the main risk factor for prostate cancer. Indeed, it is estimated that approximately 95% of men older than 70 present benign prostatic hyperplasia (BPH) (Valkenburg and Williams, 2011). In the same line, PIN and HGPIN incidence positively correlate with age. Indeed, PIN shows a frequency of 9% and 22% in men in their 20s and 30s respectively (Bostwick et al., 2004). However, the etiologic factors related to prostate cancer are various and encompass, apart from the age, familiar history, race, diet, lifestyle factors and hormonal influences (Isaacs et al., 2002).

BPH usually arises from the TZ. In contrast, PIN and HGPIN are rarely seen in this zone (Shappell et al., 2004) and commonly occur in the PZ. Indeed, the PZ harbors the majority of prostate carcinomas (70%) (Abate-Shen and Shen, 2002). Based on the zonal difference in the incidence of BPH and prostate carcinoma and the fact that stromal cell proliferation is a major feature of BPH, this benign lesion is not contemplated as the precursor of prostatic invasive carcinoma. Instead, PIN is considered the precursor lesion of this disease (Isaacs et al., 2002). BPH histological alterations are very common in the TZ and show increasing incidence with age. Actually, BPH lesions have been observed in 80-90% of radical prostatectomies (RP) performed, while only 20% of significant prostate cancers (PCas) have their origin in the TZ (Shappell et al., 2004).

Prostate cancer is suspected on the basis of digital rectal examination (DRE) and/or prostate-specific antigen (PSA) levels (<http://uroweb.org/individual-guidelines/oncology-guidelines/>). PSA is a kallikrein-related serine protease produced in normal prostatic tissue with the physiological role of liquefying seminal fluid. However, this peptidase is also produced in BPH and PCa and is thought to be released into the blood due to disruption of normal prostate architecture, especially in PCa where basal layer of cells is lost (Lilja et al., 2008). However, definitive diagnosis depends on histological verification of carcinoma in prostate biopsies obtained by trans-urethral resection of the prostate (TURP) or prostatectomy (<http://uroweb.org/individual-guidelines/oncology-guidelines/>). These biopsies are histopathologically evaluated and classified according to two different methods, the Gleason Score and the TNM (Tumor, Node, Metastasis) system (Shen and Abate-Shen, 2010). The Gleason Score classifies the tumors according to the differentiation level (from 1 to 5) of their most prevalent architecture and assigns a combined score, calculated from the sum of the two most common patterns (Mellinger et al., 1967; Humphrey, 2004) (**Fig. 15**). The TNM system encompasses evaluation of the primary tumor status, from prostate-confined to invasive (T1-4), absence or presence of lymph node involvement (N0 or 1) and absence or presence and degree of metastasis (M0-1a-c) (Ohori et al., 1994; Shen and Abate-Shen, 2010) (**Fig. 15**).

A	B																																																				
<p style="text-align: center;"><b>PROSTATIC ADENOCARCINOMA (Histologic Grades)</b></p>  <p style="text-align: right;">① ② ③ ④ ⑤</p> <p style="text-align: left;">A B A B</p> <p style="font-size: small;">D.F. Gleason, M.D.</p>	<table border="1" style="width: 100%; border-collapse: collapse;"> <thead> <tr> <th colspan="2" style="text-align: left; background-color: #f2f2f2;">T - Primary tumour</th> </tr> </thead> <tbody> <tr> <td style="width: 10%;">TX</td> <td>Primary tumour cannot be assessed</td> </tr> <tr> <td>T0</td> <td>No evidence of primary tumour</td> </tr> <tr> <td>T1</td> <td>Clinically inapparent tumour not palpable or visible by imaging</td> </tr> <tr> <td>  T1a</td> <td>Tumour incidental histological finding in 5% or less of tissue resected</td> </tr> <tr> <td>  T1b</td> <td>Tumour incidental histological finding in more than 5% of tissue resected</td> </tr> <tr> <td>  T1c</td> <td>Tumour identified by needle biopsy (e.g. because of elevated prostate-specific antigen (PSA) level)</td> </tr> <tr> <td>T2</td> <td>Tumour confined within the prostate<sup>1</sup></td> </tr> <tr> <td>  T2a</td> <td>Tumour involves one half of one lobe or less</td> </tr> <tr> <td>  T2b</td> <td>Tumour involves more than half of one lobe, but not both lobes</td> </tr> <tr> <td>  T2c</td> <td>Tumour involves both lobes</td> </tr> <tr> <td>T3</td> <td>Tumour extends through the prostatic capsule<sup>2</sup></td> </tr> <tr> <td>  T3a</td> <td>Extracapsular extension (unilateral or bilateral) including microscopic bladder neck involvement</td> </tr> <tr> <td>  T3b</td> <td>Tumour invades seminal vesicle(s)</td> </tr> <tr> <td>T4</td> <td>Tumour is fixed or invades adjacent structures other than seminal vesicles: external sphincter, rectum, levator muscles, and/or pelvic wall</td> </tr> <tr> <th colspan="2" style="text-align: left; background-color: #f2f2f2;">N - Regional lymph nodes<sup>3</sup></th> </tr> <tr> <td>NX</td> <td>Regional lymph nodes cannot be assessed</td> </tr> <tr> <td>N0</td> <td>No regional lymph node metastasis</td> </tr> <tr> <td>N1</td> <td>Regional lymph node metastasis<sup>4</sup></td> </tr> <tr> <th colspan="2" style="text-align: left; background-color: #f2f2f2;">M - Distant metastasis<sup>5</sup></th> </tr> <tr> <td>MX</td> <td>Distant metastasis cannot be assessed</td> </tr> <tr> <td>M0</td> <td>No distant metastasis</td> </tr> <tr> <td>M1</td> <td>Distant metastasis</td> </tr> <tr> <td>  M1a</td> <td>Non-regional lymph node(s)</td> </tr> <tr> <td>  M1b</td> <td>Bone(s)</td> </tr> <tr> <td>  M1c</td> <td>Other site(s)</td> </tr> </tbody> </table>	T - Primary tumour		TX	Primary tumour cannot be assessed	T0	No evidence of primary tumour	T1	Clinically inapparent tumour not palpable or visible by imaging	T1a	Tumour incidental histological finding in 5% or less of tissue resected	T1b	Tumour incidental histological finding in more than 5% of tissue resected	T1c	Tumour identified by needle biopsy (e.g. because of elevated prostate-specific antigen (PSA) level)	T2	Tumour confined within the prostate <sup>1</sup>	T2a	Tumour involves one half of one lobe or less	T2b	Tumour involves more than half of one lobe, but not both lobes	T2c	Tumour involves both lobes	T3	Tumour extends through the prostatic capsule <sup>2</sup>	T3a	Extracapsular extension (unilateral or bilateral) including microscopic bladder neck involvement	T3b	Tumour invades seminal vesicle(s)	T4	Tumour is fixed or invades adjacent structures other than seminal vesicles: external sphincter, rectum, levator muscles, and/or pelvic wall	N - Regional lymph nodes <sup>3</sup>		NX	Regional lymph nodes cannot be assessed	N0	No regional lymph node metastasis	N1	Regional lymph node metastasis <sup>4</sup>	M - Distant metastasis <sup>5</sup>		MX	Distant metastasis cannot be assessed	M0	No distant metastasis	M1	Distant metastasis	M1a	Non-regional lymph node(s)	M1b	Bone(s)	M1c	Other site(s)
T - Primary tumour																																																					
TX	Primary tumour cannot be assessed																																																				
T0	No evidence of primary tumour																																																				
T1	Clinically inapparent tumour not palpable or visible by imaging																																																				
T1a	Tumour incidental histological finding in 5% or less of tissue resected																																																				
T1b	Tumour incidental histological finding in more than 5% of tissue resected																																																				
T1c	Tumour identified by needle biopsy (e.g. because of elevated prostate-specific antigen (PSA) level)																																																				
T2	Tumour confined within the prostate <sup>1</sup>																																																				
T2a	Tumour involves one half of one lobe or less																																																				
T2b	Tumour involves more than half of one lobe, but not both lobes																																																				
T2c	Tumour involves both lobes																																																				
T3	Tumour extends through the prostatic capsule <sup>2</sup>																																																				
T3a	Extracapsular extension (unilateral or bilateral) including microscopic bladder neck involvement																																																				
T3b	Tumour invades seminal vesicle(s)																																																				
T4	Tumour is fixed or invades adjacent structures other than seminal vesicles: external sphincter, rectum, levator muscles, and/or pelvic wall																																																				
N - Regional lymph nodes <sup>3</sup>																																																					
NX	Regional lymph nodes cannot be assessed																																																				
N0	No regional lymph node metastasis																																																				
N1	Regional lymph node metastasis <sup>4</sup>																																																				
M - Distant metastasis <sup>5</sup>																																																					
MX	Distant metastasis cannot be assessed																																																				
M0	No distant metastasis																																																				
M1	Distant metastasis																																																				
M1a	Non-regional lymph node(s)																																																				
M1b	Bone(s)																																																				
M1c	Other site(s)																																																				

**Figure 15. Grading systems employed for histopathological evaluation of prostate cancer. A,** Schematic picture depicting the histological patterns for prostate cancer grading according to Gleason Score system. **B,** Table describing the extent of primary tumor (T), lymph node involvement (N) and presence/absence of metastasis according to TNM grading system.

### II.3.2 Prostate cancer treatment

Based on the DRE, PSA analysis and the histopathological evaluation of the biopsies, different therapeutic options are proposed to the patient following the *Guidelines on Prostate Cancer*, assessed by Urology Associations, and the treatment election is reached in agreement.

In general, the treatment options for prostate cancer comprise surgical excision of the prostate (RP), radiotherapy (irradiation through externalbeam therapy or implantation of radioactive “seeds” - brachytherapy), hormonal therapy (androgen deprivation therapy or chemical castration) and chemotherapy (docetaxel) (Shen and Abate-Shen, 2010).

In patients with low and intermediate risk PCa, RP or brachytherapy are normally the first-line therapy. Biochemical recurrence is considered when a gradual increase of PSA is observed after first line treatment. Then, chemical castration (androgen deprivation therapy) is suggested. In high risk PCa, RP or radiotherapy in combination with hormonal therapy is recommended. If the patient exhibits an increase of PSA or appearance of Fluorodeoxyglucose-PET (positron emission tomography) positive masses after androgen deprivation, alternative hormonal therapies or chemotherapy are recommended. Chemotherapy is usually the therapy of choice when cancer develops into metastasis. However, the therapeutic alternatives are subject to individual and personalized consideration. For those patients with low risk indolent prostate cancer, active surveillance is emerging as the main recommendation, with the aim of minimizing over-treatment and treatment-related side-effects (Wadman, 2015). According to this option, patients remain under close surveillance to decide on the therapeutic strategy if the cancer progresses (<http://uroweb.org/individual-guidelines/oncology-guidelines/>). Nevertheless, the lack of information on long-term outcome and biomarkers for eligibility criteria seeds uncertainty regarding this strategy (Chamie et al., 2015).

## III PI3K PATHWAY AND CANCER

### III.1 PI3K Pathway

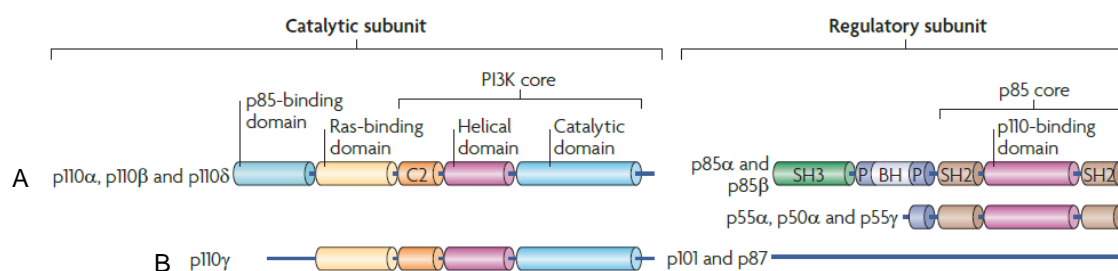
Phosphoinositide 3-kinases (PI3Ks) are a family of conserved lipid kinases that catalyze the phosphorylation of the 3'-hydroxyl group of phosphatidylinositol and phosphatidylinositides (Katso et al., 2001). This reaction unleashes an array of intracellular signaling pathways implicated in the control of cellular proliferation, growth, survival, motility and metabolism (Thorpe et al., 2015).

#### III.1.1 Structural and biochemical characteristics of class I PI3K

PI3Ks are classified into three classes (I-III) according to substrate specificity and structure. Little is known about the functional role of class II and III PI3Ks. In mammals, class I PI3Ks are divided into two subfamilies depending on the receptor they respond to. Class IA PI3Ks are activated by

growth factor receptor tyrosine kinases (RTKs), while class IB PI3Ks are activated by G-protein-coupled receptors (GPCRs). We will focus on class IA PI3Ks for in-depth description.

Class IA PI3Ks are heterodimers composed of two subunits, the catalytic subunit p110 and the regulatory subunit p85, which maintains p110 with low-activity in basal conditions and functions as an adaptor to couple it to activated protein tyrosine kinases (Hiles et al., 1992). There are three highly homologous catalytic subunit isoforms, p110 $\alpha$ , p110 $\beta$  and p110 $\delta$ , which associate with any of the five regulatory subunit isoforms: p85 $\alpha$ , p55 $\alpha$ , p50 $\alpha$ , p85 $\beta$  and p55 $\gamma$  (**Fig. 16**).

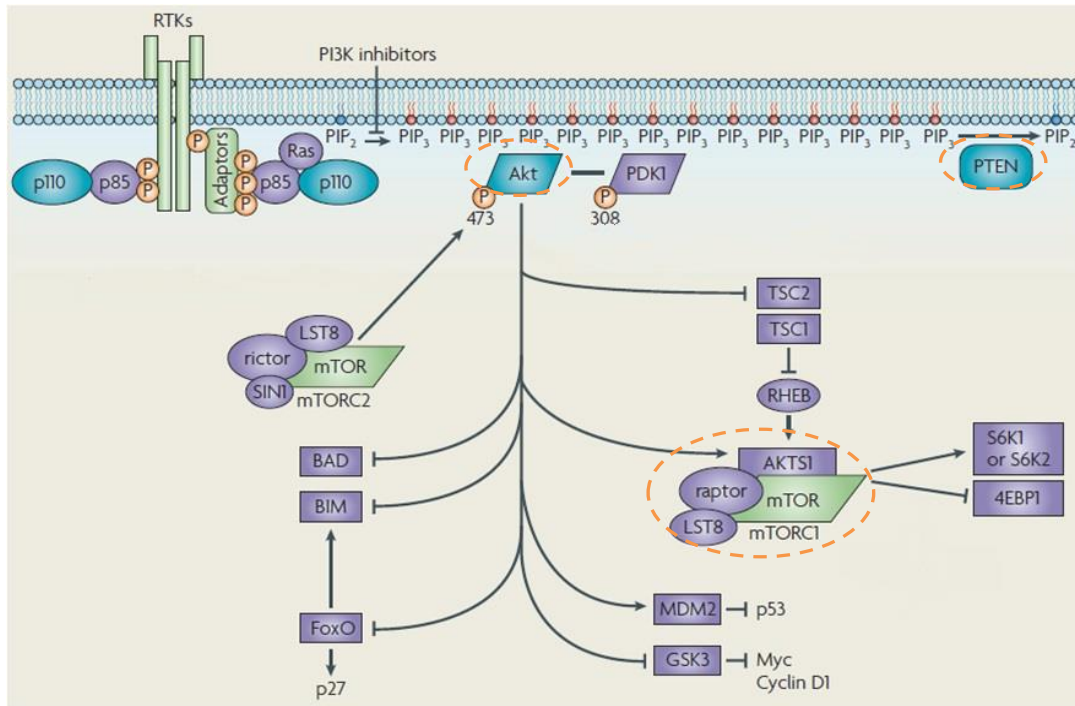


*Adapted from Vanhaesebroeck B, et al, Nat Rev Mol Cell Bio 2010*

**Figure 16.** Schematic depicting domain structure of the catalytic and regulatory subunits of class I PI3Ks.

### III.1.2 Signaling downstream class I PI3K

Growth factors signal through receptor tyrosine kinases, which recruit scaffold and signaling proteins (including PI3K) through autophosphorylation of their C-terminal tail. p85-p110 heterodimer interacts with phosphorylated tyrosines in RTKs, gets activated and converts plasma membrane lipid phosphatidylinositol-4,5-bisphosphate [PI(4,5)P<sub>2</sub>; PIP<sub>2</sub>] into phosphatidylinositol-3,4,5-trisphosphate [PI(3,4,5)P<sub>3</sub>; PIP<sub>3</sub>]. This lipid phosphorylation is the signal for proteins that contain pleckstrin-homology (PH) domains, to be recruited to the plasma membrane and bind to PIP<sub>3</sub> (Cantley, 2002). Examples of these proteins are serine-threonine kinase AKT (Protein kinase B, PKB) and phosphoinositide-dependent kinase 1 (PDK1). Once AKT is phosphorylated by PDK1 and mechanistic target of rapamycin (mTOR) complex 2 (mTORC2) and activated, it phosphorylates multiple downstream targets, including glycogen synthase kinase 3 (GSK3) and the forkhead box family of transcription factors (FOXOs). AKT also activates mTORC1 through phosphorylation of its upstream regulator proline-rich AKT substrate 40 kDa (PRAS40, activatory regulation) and tuberous sclerosis 2 protein (TSC2, inhibitory regulation) (Liu et al., 2009b). The control of the intensity and duration of this signaling pathway is controlled by three type of phosphatases. Src-homology 2 (SH2)-containing phosphatases (SHIP1 and SHIP2), inositol polyphosphate 4-phosphatase type II (INPP4B) and Phosphatase and tensin homolog (PTEN) dephosphorylate position 5, 4 or 3 of the inositol ring; respectively (**Fig. 17**).



Adapted from Engelman JA, *Nat Rev Cancer* 2009

**Figure 17. Signaling downstream class I PI3Ks.** Schematic representation of PI3K signaling cascade highlighting key downstream kinases and phosphatases.

### III.1.3 Key mediators downstream PI3K

We will focus in key effectors downstream PI3K for the correct understanding of this work.

#### III.1.3.1 AKT

AKT or PKB $\alpha$  was first discovered in the genome of the retrovirus AKT-8 in murine T-cell lymphoma (Alessi et al., 1996). There are three AKT isoforms (AKT1/PKB $\alpha$ , AKT2/PKB $\beta$  and AKT3/PKB $\gamma$ ), all belonging to the cAMP-dependent, cGMP-dependent and protein kinase C (AGC) kinase family (Lawlor and Alessi, 2001). The three distinct isoforms are ubiquitously expressed in all cell and tissue types, although AKT3 seems to have a more restricted expression pattern (Toker and Yoeli-Lerner, 2006).

Upon binding to PIP<sub>3</sub>, AKT gets phosphorylated and activated by PDK1 and mTORC2, in turn phosphorylating a variety of downstream targets to regulate many different cellular processes (Cantley, 2002) (**Fig. 17**). AKT is known to promote cell survival by inhibiting pro-apoptotic proteins, such as Bcl-2-associated death promoter protein (BAD) (Datta et al., 1997), or by inhibiting the transcription factors FOXO1/3/4 and tumor protein p53 (p53) (Tran et al., 2003). In the same line, an important role has been attributed to AKT in cell growth and proliferation (Manning and Cantley, 2007). AKT was reported to activate mTORC1 (through the inhibition of the negative regulator TSC2 (Inoki et al., 2002; Manning et al., 2002)), as well as to inhibit cyclin-dependent kinase inhibitors Cyclin-dependent kinase inhibitor p27 (p27<sup>Kip1</sup>) (Liang et al., 2002)

and Cyclin-dependent kinase inhibitor 1 (p21<sup>Cip1/WAF1cell</sup>) (Zhou et al., 2001), to promote cell growth and proliferation. Through the regulation of the aforementioned and other targets, AKT has been also implicated in the regulation of angiogenesis, cellular metabolism and cell migration and invasion (Manning and Cantley, 2007). Importantly, germline deletion of AKT1 or AKT3 have been reported to result in growth defects *in vivo* (Engelman et al., 2006).

### III.1.3.2 mTOR

mTOR was first discovered as the target complex of the immunosuppressant rapamycin, in complex with peptidyl-prolyl cis-trans isomerase FKBP12 (FKBP12), and it was therefore named rapamycin and FKBP12 target (RAFT) (Brown et al., 1994; Sabatini et al., 1994). This complex contains two components of 245KDa and 35KDa, which were designated RAFT1 and RAFT2 respectively. RAFT1 was found to show high homology with yeast proteins TOR1 and TOR2 and thereby it was considered the mammalian homolog of yeast TOR proteins (Sabatini et al., 1994).

mTOR is a serine/threonine protein kinase that belongs to the PI3K-related kinase (PIKK) family and forms two distinct complexes, mechanistic target of rapamycin complex 1 (mTORC1) and mTORC2 by interacting with some shared and other specific proteins (Abraham and Gibbons, 2007). The shared components of both complexes are the catalytic mTOR subunit, mammalian lethal withsec-13 protein 8 (mLST8), DEP domain containing mTOR-interacting protein (DEPTOR) and the Tti1/Tel2 complex. However, while mTORC1 specifically interacts with regulatory-associated protein of mammalian target of rapamycin (RAPTOR) and proline-rich Akt substrate40 KDa (PRAS40), mTORC2 is formed of rapamycin-insensitive companion of mTOR (RICTOR), mammalian stress-activated map kinase-interacting protein 1 (mSin1) and protein observed with rictor 1 and 2 (protor1/2) (Laplante and Sabatini, 2012) (**Fig. 18**).

This kinase shows a phylogenetically conserved amino acidic sequence that consists of: up to 20 HEAT motifs repeated in tandem, a FAT [FRAP (FKBP12–rapamycin-associated protein)-ATM (ataxiatangiectasi mutated)-TRRAP (transactivation/transformation-domain-associated protein) complex] domain and the catalytic kinase domain, which contains a FKBP12–rapamycin binding (FRB) domain, a LST8-binding element (LBE) and a FATC (C terminus of FRAP-ATM-TRRAP complex) domain (Bjornsti and Houghton, 2004; Saran et al., 2015).

Contrary to mTORC1, the knowledge regarding the function and signaling cascade of mTORC2 is scarce. While insensitive to nutrients, this mTOR complex responds to growth factors through PI3K (Laplante and Sabatini, 2012). mTORC2 regulates cellular processes such as growth, proliferation, survival, metabolism, apoptosis, ion transport and cytoskeletal rearrangements through the direct phosphorylation of several AGC kinase subfamily members, including AKT, serum- and glucocorticoid-induced protein kinase 1 (SGK1) and protein kinase C- $\alpha$  (PKC $\alpha$ ) (Saran et al., 2015). Although originally thought to be rapamycin insensitive, long term treatments have been shown to inhibit mTORC2 in a cell type-dependent fashion (Laplante and Sabatini, 2012).

The identification of rapamycin has allowed a deeper characterization of the functions and regulation of mTORC1 (Saran et al., 2015). mTORC1 is considered a master sensor of extracellular and intracellular nutrient and energy status, capable of translating multiple signals into the coordination and regulation of anabolic and catabolic processes to sustain cell growth (Dibble and Manning, 2013a). Through transcriptional, translational (Ma and Blenis, 2009) and post-translational mechanisms mediated by its downstream targets ribosomal protein S6 kinase (S6K) and eukaryotic translation initiation factor 4E-binding protein (4E-BP), mTORC1 stimulates the synthesis of macromolecules (lipids, proteins and nucleic acids), promotes the production of adenosine triphosphate (ATP), nicotinamide adenine dinucleotide phosphate (NADPH) and macromolecule precursors and inhibits degradative processes, such as lipolysis,  $\beta$ -oxidation and autophagy (Dibble and Cantley, 2015).

### III.1.3.3 PTEN

PTEN is a dual lipid and protein phosphatase and one of the phosphatases known to degrade

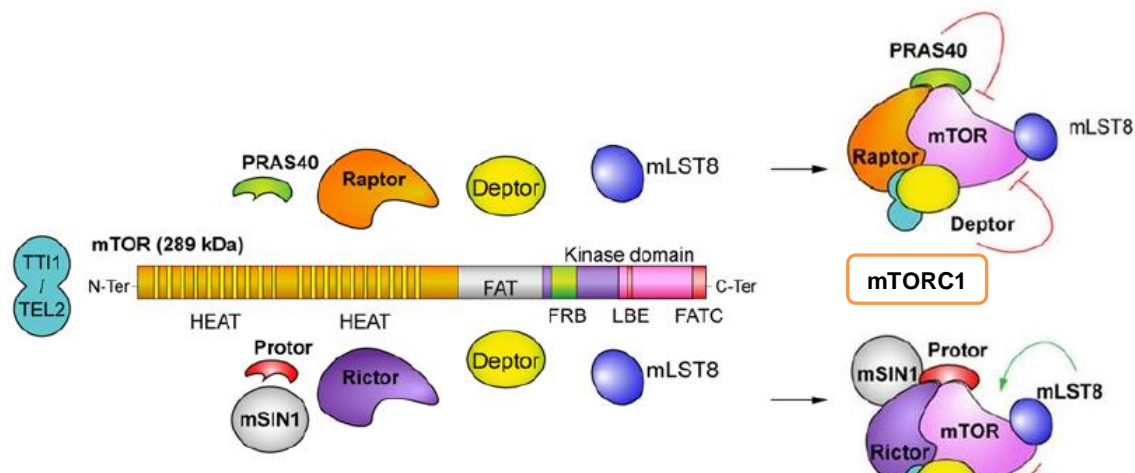


**Figure 18. mTOR forms two distinct complexes.** Schematic representation of mTOR structure and shared and specific components of each particular complex.

PIP<sub>3</sub> by dephosphorylating the phosphate group on position D3 of the inositol ring (Blanco-Aparicio et al., 2007) (**Fig. 17**). Due to its biochemical function, it plays a primordial role in the regulation of the PI3K-AKT-mTORC1 axis and it is involved in multiple cellular processes. Indeed, through many of the aforementioned mechanisms, PTEN activity has been related to cell metabolism, motility and polarity, self-renewal capacity, tumor microenvironment regulation and senescence (Song et al., 2012). Regarding this last mentioned function, *Pten* loss was reported to result in a distinct type of senescence, referred to as *Pten*-loss-induced cellular senescence (PICS) (Alimonti et al., 2010). Importantly, PTEN has been demonstrated to exert relevant phosphatase-independent functions in the nucleus (Serra H, 2015; Song et al., 2011a). PTEN has been also attributed PI3K-AKT-mTORC1 pathway independent roles. PTEN was shown to exert its tumor suppressive effect through c-jun N-terminal kinase (JNK) and IFN-induced double-stranded RNA-dependent protein kinase (PKR)-eukaryotic translation initiation factor 2 complex



(eIF2 $\alpha$ ) phosphorylation in an AKT-independent manner (Mounir et al., 2009; Vivanco et al., 2007).

### III.2 PI3K Pathway deregulation in cancer

Hyperactivation of the PI3K pathway is known to contribute to human cancer (Cantley, 2002). Human cancer genomic studies revealed that many components of the PI3K pathway are frequently affected by germline or somatic mutations in a wide variety of human tumors, underscoring the relevance of this signaling cascade in the disease (Liu et al., 2009b). Indeed, deregulation of this oncogenic cascade commonly occurs by activating mutations in growth factor receptors, the PIK3CA gene coding for the catalytic subunit p110 $\alpha$  or AKT, as well as loss of function of the tumor suppressor PTEN or TSC1/2 (Marone et al., 2008).

As aforementioned, activating alterations (mutations and amplification) in PI3K are frequent in multiple cancer types (Samuels et al., 2004). The oncogenic capacity of class I PI3K was first demonstrated in the late 1990s (Thorpe et al., 2015). However, the high incidence of mutations of this kinase in human cancers was discovered in 2004, when Samuels and colleagues found it to be altered in 32% of colorectal cancers, 27% of glioblastomas and 25% of gastric cancers, among others. Furthermore, these mutations were reported to arise late in tumorigenesis, suggesting a role in invasiveness (Samuels et al., 2004). Although missense mutations have been reported in all p110 $\alpha$  domains, mutations in each domain lead to different mechanisms of aberrantly activating the pathway. In turn, mutations in the helical domain prevent p110 $\alpha$  inhibition by p85 or facilitate its interaction with insulin receptor substrate 1 (IRS1), mutations in the kinase domain enhance the interaction with lipid membranes, and other mutations mimic conformational changes of active PI3K (Thorpe et al., 2015).

AKT is also amplified and mutated in cancer (Carracedo and Pandolfi, 2008). In fact, the activating mutation E17K in the PH domain of AKT makes it growth factor-independent, leading to its aberrant localization to the membrane and the stimulation of downstream signaling (Carpten et al., 2007). However, distinct AKT isoforms may show tumor-specific alterations. Indeed, while AKT1 amplification has mainly been detected in gastric cancer, somatic mutations on AKT1 have been described in breast, colorectal, ovarian, lung, and bladder cancers (Martini et al., 2014). In contrast, AKT2 amplification has been frequently detected in ovarian, breast, colorectal, and pancreatic tumors, while AKT3 appears amplified in breast and prostate cancers (Agarwal et al., 2013). Finally, the activating mutation E17K has been identified on AKT3 in melanoma (Davies et al., 2008).

Importantly, few cancer-related somatic mutations in *MTOR* have been functionally characterized, recently some mutations leading to mTOR hyperactivation and nutrient signaling

and resistance have been reported. In addition, hyperactivation of upstream kinases (PI3K, AKT) or growth factor receptors, as well as loss of upstream negative regulators (PTEN, TSC1/2) can lead to hyperactivation of mTOR (Dancey, 2010). Oncogenic PI3K-mTORC1 overactivation confers addiction to the pathway. Indeed, *PTEN* loss driven prostate cancer has been reverted by tissue-specific mTOR deletion in the mouse prostate (Guertin et al., 2009).

Nevertheless, the most common mechanism triggering hyperactivation of PI3K pathway is somatic loss of *PTEN* due to genetic or epigenetic alterations (Thorpe et al., 2015). In fact, when *PTEN* is deleted, mutated or otherwise inactivated, PI3K effectors, in particular AKT, are activated in the absence of any other stimulus (Cully et al., 2006). Sequencing of *PTEN* revealed that it is one of the most commonly mutated and deleted tumor suppressors among human cancers (Carracedo et al., 2011). In the same line, multiple tumors show alterations in its protein expression, in *PTEN* locus methylation or loss of heterozygosity (Marone et al., 2008). Genetic alterations in *PTEN* encompass from point mutations to large chromosomal deletions (Nardella et al., 2010a). These mutations are mostly missense and non-sense localized in exons 5,7 and 8, that encode the phosphatase domain (Marone et al., 2008). Of note, *PTEN* mutations can either affect both alleles (specially in endometrial cancer and glioblastoma) or only one allele, as observed in glioma, prostate, breast or lung, among others (Nardella et al., 2010a).

In prostate cancer, approximately 30% of patients with castration-resistant prostate cancer (CRPC) harbor mutations in *PIK3CA* (Sarker et al., 2009). However, the relevance of *PTEN* loss of function is better described. In fact, approximately 25% of prostate HG-PINs and 70% of prostate cancers at early stage show heterozygous alterations in *PTEN* (Yoshimoto et al., 2006). Of note, prostate tumors tend to select for *PTEN* heterozygous inactivation at presentation and loss the other allele later in the progression of the disease (Carracedo and Pandolfi, 2008).

### III.3 Genetic models of *Pten* loss *in vivo*

In line with its implication in a plethora of cellular processes, mutations in *PTEN* have been identified in multiple sporadic malignancies and in cancer-susceptibility syndromes (Nardella et al., 2010a). Germline mutations and deletions of *PTEN* are associated with the development of several autosomal dominant syndromes collectively named as PTEN hamartoma tumor syndromes (PHTS). PHTS include Cowden syndrome (CS), Bannayan-Riley-Ruvalcaba syndrome (BRRS), Lhermitte-Duclos disease (LDD), Proteus syndrome, and Proteus-like syndrome (Hollander et al., 2011). These patients suffer from hamartomas with cancer predisposition in different organs. Macrocephaly development has also been described in the first two syndromes (Nardella et al., 2010a). The relevance of the tumor-suppressor role of PTEN led to the development of multiple *Pten* knockout mouse models with the aim of studying the effects of its loss of function *in vivo*.

### III.3.1 Genetic models of *Pten* germline mutations

In the last decade of the twentieth century, mouse engineering experienced important advances, including the development of the *genetargeting* technology. Gene targeting brought the possibility of introducing specific mutations by homologous recombination into endogenous genes of embryonic stem (ES) cells, and transmitting these changes in the germline through mice breeding (Jonkers and Berns, 2002).

Homozygous *Pten* loss is lethal at day E7.5 post-fertilization, which highlights an essential role of *Pten* in embryonic development (Di Cristofano et al., 1998). In the same line, hypomorphic *Pten* mutants (*Pten<sup>hy/-</sup>*) showed a partial rescue of embryonic lethality, leading to some viable mice albeit at a lower frequency than expected according to Mendelian ratios (Trotman et al., 2003). *Pten* heterozygosity (*Pten<sup>+/-</sup>*) was reported to cause dysplastic and hyperplastic alterations in prostate, skin and colon resembling CS, BRRS and LDD features. Furthermore, spontaneous development of tumors of various histological origins was described in *Pten<sup>+/-</sup>* mice (Di Cristofano et al., 1998). Importantly, *Pten* hypomorphic mice showed increased aggressiveness, with massive prostatic hyperplasia and invasive PCa (Trotman et al., 2003). In conclusion, these “hypomorphic *Pten* allelic series” revealed that subtle variations in *Pten* expression levels result in dose-dependent pathological alterations (Nardella et al., 2010a).

### III.3.2 Genetic models of prostate-specific *Pten* deletion

Germline knockouts have been widely employed for the study of gene function *in vivo*. Although these conventional knockouts are useful to ascertain gene function during development, they exhibit intrinsic limitations to model postnatal pathologies, mostly due to their whole body range of action (Wu et al., 2001). To circumvent the consequence of losing *Pten* in all cells of the body, and to study the impact of *Pten* loss in a given tissue, conditional tissue-specific *Pten* knockout mouse models were employed (Jonkers and Berns, 2002). Conditional gene knockout techniques, such as the Cre-loxP recombination system, bypass some of the limitations of conventional gene-targeting. This technique combines the use of the bacteriophage P1 site-specific DNA recombinase (Cre) and the creation of conditional target alleles in mice expressing Cre under the control of cell type-specific or inducible promoters (Wu et al., 2001). Cre excises DNA sequences located between two unidirectional loxP recognition sequences (“flox”), leaving one loxP site on the linear DNA.

To achieve specific deletion of *Pten* in the prostate, *Pten*<sup>loxP/loxP</sup> mice were crossed with *Probasin-Cre* (*PB-Cre*) transgenic mice. In *PB-Cre* transgenic mice *Cre* recombinase is expressed specifically in the prostate epithelium post-puberty due to its regulation by the rat *Probasin* (*PB*) gene promoter, which is an androgen responsive promoter (Nardella et al., 2010a). Two distinct versions of the *PB* promoter have been utilized to perform these crosses, *PB-Cre* and *PB-Cre4*, where in *PB-Cre4* mice *Cre* expression is driven by a composite promoter, *ARR<sub>2</sub>PB*, which is a more potent derivative of the original rat *PB*. Indeed, *Cre* expression under *ARR<sub>2</sub>PB* promoter led to widespread *Pten* deletion in the prostate epithelium, prostate enlargement and more aggressive invasive PCa with multifocal origin compared to original *PB* promoter driven phenotype (Trotman et al., 2003). We will focus on *PB-Cre4* mice phenotype for further considerations regarding prostate-specific deletion driven models, which is the model that was employed in this thesis work. Homozygous prostate-specific *Pten* deletion leads to HG-PIN development at 9 weeks of age. Moreover, after bypassing *Pten* loss induced senescence at 11 weeks of age, these HG-PIN lesions further progress into full penetrance invasive PCa by 6 months. Although disease aggressiveness increased with time, these mice did not show metastatic lesions (Chen et al., 2005) (**Fig. I9**).

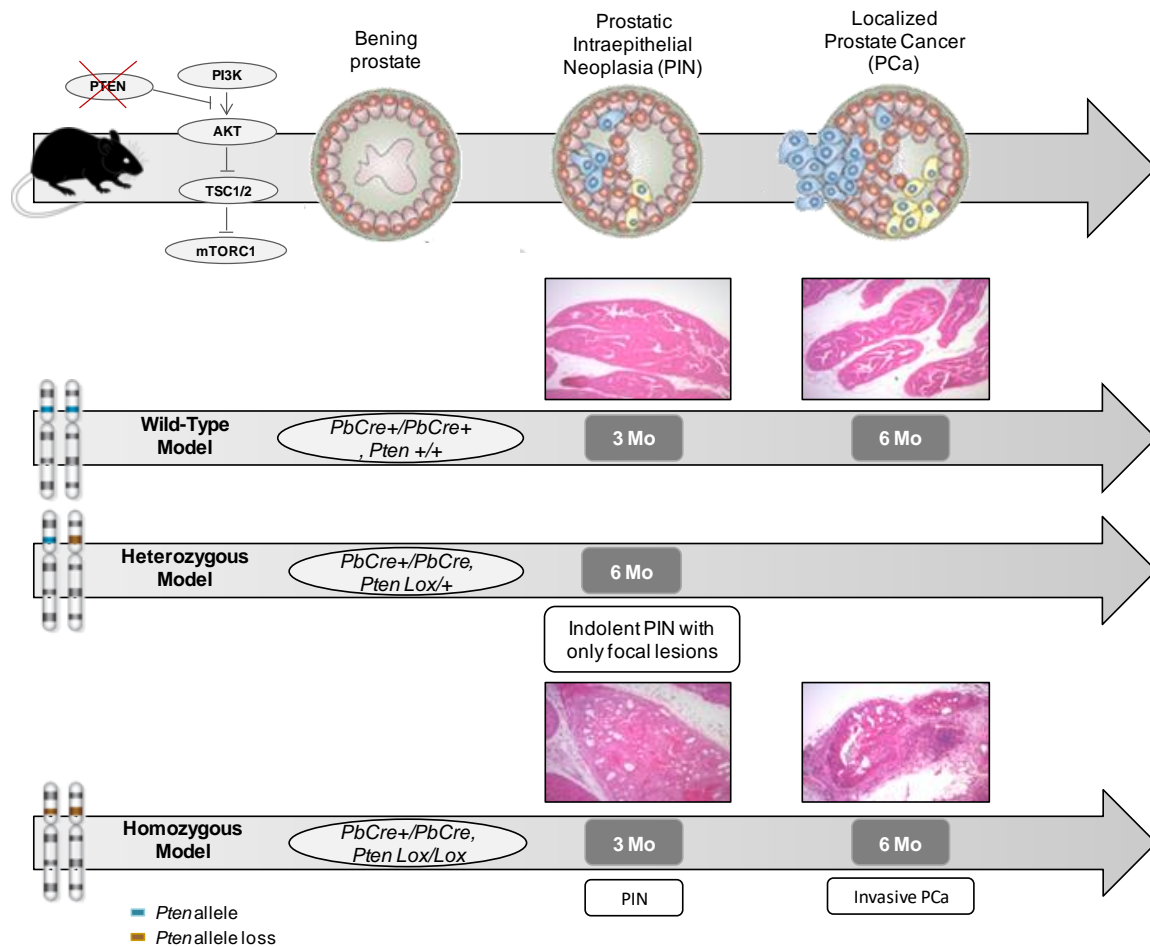


**Figure I9. Prostate-specific *Pten* knockout mouse model.** Representation of the genotype (wild-type, heterozygous or homozygous)-phenotype (PIN or PCa) correlation at early (3Mo) and late (6 Mo) stages of the disease.

## IV METABOLIC DEREGULATION AND CANCER

### IV.1 Warburg effect

The first evidence reporting the deregulation of metabolism in cancer were provided by Otto Warburg in the early 1920s (Warburg et al., 1927). This German physiologist observed that tumor cells consumed more glucose than normal tissues, which suggested a relevant differential characteristic of normal *versus* cancerous cells (Warburg, 1956a). However, this data was left aside for many years in cancer research until the beginning of twenty first century, when reports claiming the importance of alterations in metabolic enzymes in cancer pathogenesis started to arise (Possemato et al., 2011; Reitman et al., 2011). Increasing evidence claim that oncogenic alterations in metabolic enzymes can directly trigger the deregulation of cancer cell metabolism (Ward and Thompson, 2012), but it is widely accepted that metabolism in cancer is regulated at large by signaling alterations. The consolidation of this field has led to the consideration of the deregulation of metabolism in cancer as a hallmark of the disease (Hanahan and Weinberg, 2011).

Normal cells uptake glucose, they convert it into pyruvate and incorporate it in the Tricarboxylic Acid Cycle (TCA) to obtain 36 molecules of ATP from a single molecule of glucose through oxidative phosphorylation. However, tumoral cells or cells with high proliferation rates uptake higher amounts of glucose and convert it into lactate even in the presence of oxygen, yielding 4 ATP in a process defined as aerobic glycolysis or “Warburg effect” (Vander Heiden et al., 2009). Recently, more information about how the Warburg effect can be energetically sustained has been provided. Lactate production from glucose in cancer cells occurs 10-100 times faster than complete glucose oxidation through oxidative phosphorylation in the mitochondria (Shestov et al., 2014). Hence, this inherent difference in kinetics would explain the choice for anaerobic glycolysis of cancer cells (Liberti and Locasale, 2016). It is worth noting that cells with a higher metabolic rate would also exhibit a selective advantage under limited nutrient and energy availability conditions (such as the tumor microenvironment) and conditions of high rapid ATP demand (Epstein et al., 2014).

Aerobic glycolysis has also been proposed as an adaptation to use glucose for the production of anabolic intermediates and NADPH (Vander Heiden et al., 2009). In fact, glycolytic intermediates in cancer cells are diverted into branching pathways, such as, pentose phosphate pathway (PPP), hexosamine biosynthesis pathway or *de novo* serine synthesis (50% of glucose) and one carbon (1C) metabolism, in order to obtain biosynthetic precursors (Pavlova and Thompson, 2016).

## IV.2 1C metabolism

1C metabolism accepts inputs, such as glucose or amino acids and processes them to produce outputs for anabolic processes. Thus, this pathway is considered a nutrient status integrator (Locasale, 2013). 1C metabolism encompasses folate and methionine (Met) cycle. This cyclic metabolic network is fueled by a carbon unit from serine (Ser) conversion to glycine (Gly) and subsequent glycine cleavage, which then is transferred through biochemical reactions to other metabolic pathways. Folate is reduced by a number of enzymes, leading to the production of methyl-tetrahydrofolate (m-THF), which couples folate cycle to Met cycle, and further tetrahydrofolate (THF) generation (Amelio et al., 2014). Importantly, virtually all biomolecules require substrates from 1C metabolism for their synthesis. 1C metabolism is also connected to trans-sulphuration pathway through an intermediate of Met cycle, homocysteine, and is implicated in the maintenance of cellular Redox balance, through the NADPH/NADP ratio balance and glutathione production, and in the methylation capacity of the cell, through the regulation of S-adenosylmethionine (SAM) levels (Locasale, 2013).

Ser, one of the fuels of this pathway, can be synthesized *de novo*, from a glycolysis intermediate, 3-phosphoglycerate (3PG) (Locasale, 2013). Importantly, this pathway has been shown to correlate with tumorigenesis (Snell, 1984). Indeed, Ser and not Gly, was demonstrated to selectively support 1C metabolism and proliferation of cancer cells (Labuschagne et al., 2014). Likewise, glycine metabolism, glycine decarboxylase (GLDC) and the glycine-cleavage system have also been implicated in cell transformation and tumorigenesis (Zhang et al., 2012; Wang et al., 2009).

## IV.3 Other metabolic alterations

Recent advances in cancer research have proven that deregulation of metabolism in cancer extends beyond the previously thought unique objective of adapting to the enhanced anabolic processes required for proliferation (Ward and Thompson, 2012). Cancer cells exhibit increased uptake of other growth-supporting substrates, like glutamine, which was observed more than 50 years ago (Eagle, 1955). The transcription factor myc proto-oncogene protein (c-MYC) (often amplified in tumors) induces glutamine utilization (Wang et al., 2011), providing nitrogen for purine and pyrimidine synthesis, non-essential amino acids and polyamines (Pavlova and Thompson, 2016), as well as carbons for anaplerosis (a process through which the activity of the tricarboxylic acid cycle is sustained by providing additional alpha ketoglutarate).

Some cancer cells also exhibit opportunistic modes of nutrient acquisition (Pavlova and Thompson, 2016). In fact, mutant RAS-transformed cells recover free amino acids from extracellular proteins, through internalization by macropinocytosis and lysosomal degradation (Commisso et al., 2013). Remarkably, this mode of amino acid uptake is inhibited by mTORC1 (Palm et al., 2015). In the same line, mutant GTPase KRas (KRAS)-expressing cells are more prone to elicit entosis, the engulfment and digestion of entire living cells, as a means of amino acid

recovery (Krajcovic et al., 2013). Furthermore, upon inhibition of stearyl-CoA desaturase (SCD)1 in hypoxic conditions, these cells are able to scavenge serum fatty acids (Kamphorst et al., 2013).

Metabolic reprogramming of cancer cells leads to the production of metabolites such as acetyl-CoA, that are substrate for histone acetyl transferases, resulting in increased acetylation of growth-related genes and subsequent increased growth (Cai et al., 2011). Thus, the metabolic reprogramming in cancer allows the direct transmission of growth signals to metabolic enzymes (Pavlova and Thompson, 2016).

## V POLYAMINES

Polyamine metabolism is a physiologically relevant pathway that has been extensively related to proliferation. Owing to their multiple roles in essential cellular processes, their concentrations are strictly controlled at several levels, by regulation of the enzymes implicated in their synthesis and catabolism. This fact underscores the importance of fine-tuning the availability of polyamines. The deregulation of these enzymes has been therefore implicated in multiple diseases, and especially in cancer pathogenesis.

### V.1 Definition of polyamines

Polyamines are ubiquitous essential small polycationic molecules derived from amino acids. Since Antonie Van Leewenheuk identified some crystals in seminal fluid corresponding to spermine (Spm) in 1678, more polyamines have been described, such as putrescine (Put) (in the late 1800s), spermidine (Spd) (at the beginning of twentieth century), cadaverine (Cad) and 1,3-diaminopropane (1,3-DAP). The first three are the most common ones, especially in mammals. Polyamines contain two amino groups in the case of primary diamines (Put, 1,4-diaminobutane; and Cad, 1,5-diaminopentane), while three and four amino groups are present in the structure of Spd (N-(3-aminopropyl)butane-1,4-diamine) and Spm (N,N'-bis(3-aminopropyl)butane-1,4-diamine), respectively. Polyamine content varies among species. For instance, intracellular content of Spd (1-3 mM) is higher than Put content (0.1-0.2 mM) in most bacteria, whereas in *Escherichia coli* Put is the predominant polyamine (10-30 mM) (Shah and Swiatlo, 2008). In the same line, Cad is mainly present in bacteria and plants, with a reduced abundance in the remaining species (Kusano et al., 2008).

These positively charged aliphatic hydrocarbon molecules are relevant for the maintenance of essential cellular processes. Indeed, due to their overall positive charge at physiological pH, they are known to bind macromolecules with acidic nature, such as nucleic acids, proteins and phospholipids (Pegg, 2009a) and cause effects on gene expression, cell proliferation and cellular stress (Miller-Fleming et al., 2015). Owing to their high interactive capacity, the free polyamine concentration is markedly lower than total polyamine content, which

also explains the fact that slight alterations in polyamine levels may have critical consequences on cell function (Pegg, 2009a).

## V.2 Polyamine functions

### V.2.1 Regulation of gene expression

Polyamines are able to affect gene expression by different means (**Fig. I10**). These molecules are considered condensation agents that remodel chromatin structure by creating electrostatic bonds between desoxyribonucleic acid (DNA) and phosphate charges that stabilize the nucleic acid. In the same line, natural and synthetic polyamines precipitate DNA, depending on their concentration (Childs et al., 2003). Polyamines regulate the transcription rate of several genes, the oncogenic transcription factor c-MYC among them (Kumar et al., 2009). Interestingly, amplification of N-myc proto-oncogene protein (N-MYC), another transcription factor from the same family, has been reported to induce overexpression of ornithine decarboxylase 1 (ODC1), one of the rate-limiting enzymes of the polyamine synthesis pathway, in neuroblastoma (Hogarty et al., 2008). This fact emphasizes the presence of feedback loops in polyamine related regulation.

To try to understand the physiological role of polyamines, their distribution among acidic molecules in cells has been determined. Importantly, most polyamines form a ribonucleic acid (RNA)-bound complex, as assessed in bovine lymphocytes and rat liver, what suggests that these polycations could alter the structure of RNA (Igarashi and Kashiwagi, 2010) and regulate protein translation. Indeed, polyamines can induce the translation of a group of genes, named the "Polyamine modulon", both in prokaryotes (Yoshida et al., 2004) and eukaryotes (Nishimura et al., 2009a). Interestingly, polyamines regulate translation initiation and elongation (Yoshida et al., 2002) as well as the phosphorylation of factors involved in translation (Landau et al., 2010).

### V.2.2 Control of cell proliferation

Polyamines have been widely related to proliferation and growth (**Fig. I10**). Apparently, this regulation occurs through different mechanisms in prokaryotes and eukaryotes. In prokaryotes, as aforementioned, translation of growth-related transcription factors is induced in response to polyamines, according to the metabolic conditions. However, polyamines show a putative role in cell cycle progression in eukaryotes (Oredsson, 2003), although the exact mechanism underlying this activity remains to be elucidated (Miller-Fleming et al., 2015).



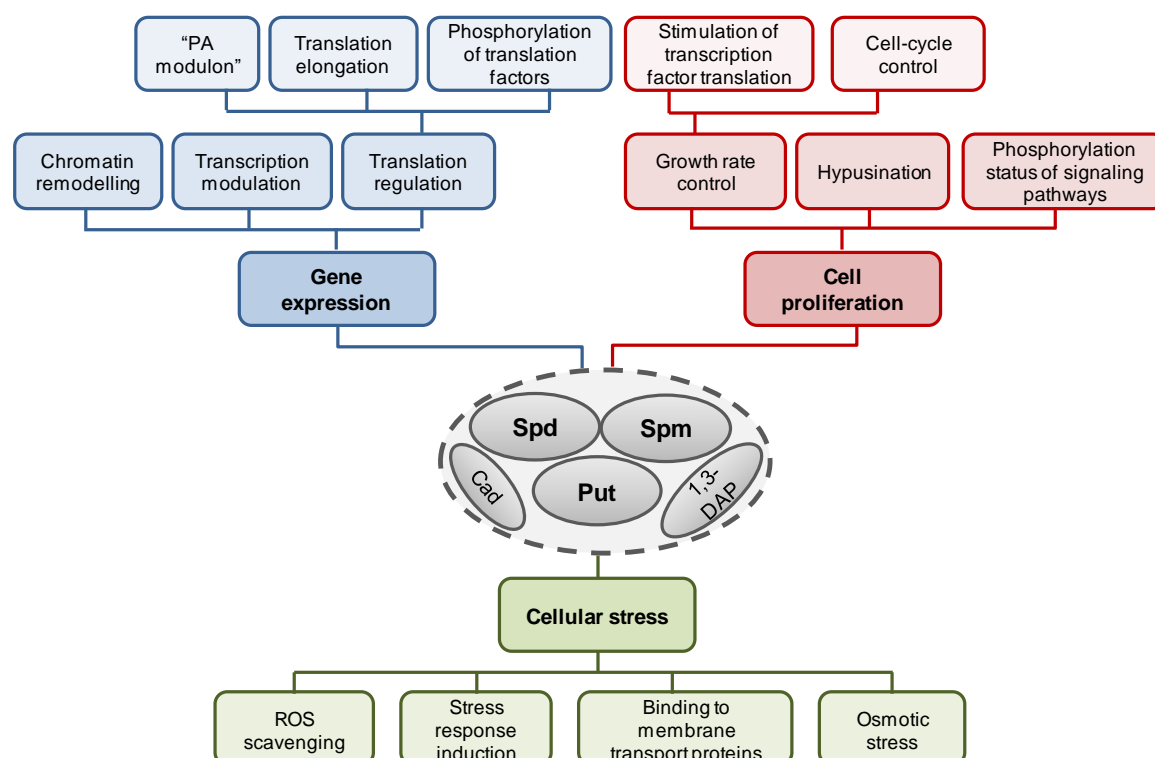


**Figure 110. Role of polyamines in cell physiology.** Schematic representation of the main cellular processes and specific functions in which polyamines are involved at physiological level.

Another proliferation-related function of polyamines, especially of Spd, is to serve as substrate for the unique post-translational modification of eukaryotic translation initiation factor 5A (eIF5A), hypusination (Cooper et al., 1982). This exclusive modification is based on the formation of hypusine, a basic amino acid, by adding the 4-aminobutyl moiety of Spd to Lys50 in eIF5A (Park et al., 2009). The hypusination process consists of two enzymatic steps, deoxyhypusine intermediate formation by deoxyhypusine synthase (DHS), which transfers the 4-aminobutyl moiety from Spd to Lys50; and hydroxylation of deoxyhypusine by deoxyhypusine hydroxylase (DOHH) to form active eIF5A (Park et al., 2009). These two enzymes responsible for hypusination and eIF5A are highly conserved from archaea to eukaryotes, which suggests a vital role of this translation initiation factor in cell viability. Indeed, deletion of both eIF5A homologues in yeast (Hyp2 and Anb2) is lethal (Schnier et al., 1991), as well as eIF5A homozygous deletion in mice (Nishimura et al., 2012). Although eIF5A was initially described as a translation initiation factor, it was later demonstrated that it does not play an essential role in initiation, but binds to translating ribosomes and elongation factors, in an hypusine-dependent manner (Zanelli et al., 2006).

Finally, polyamines have been reported to affect signaling pathways by modulating phosphorylation of key regulatory proteins, such as kinases (AKT, GSK-3 $\beta$ , cyclin-dependent kinase 4, CDK-4), transcription factors (p53), E3 ubiquitin-protein ligases (murine double minute 2, Mdm2) and signaling receptors (EGFR), among others (Pegg, 2009a).

### V.2.3 Implication in cellular stress

Polyamines have been associated to the protection of cells against multiple types of cellular stresses, such as ROS, changes in pH, osmotic pressure and temperature (Miller-Fleming et al., 2015) (**Fig. I10**).

Due to their polycationic nature, polyamines can function as ROS scavengers, by binding to alkyl, hydroxyl and peroxy radicals and superoxide to protect DNA from oxidative stress (Fujisawa and Kadoma, 2005; Ha et al., 1998). Another reported function of polyamines is the induction of the defense mechanisms against stress. Evidence supporting this fact have been provided in *E. coli*, where Put and Spd upregulate the transcription of the stress-related transcription factors OxyR, SoxRS and RpoS (Tkachenko and Nesterova, 2003); in yeast, where overexpression of the polyamine exporter Tpo1 sensitizes cells to H<sub>2</sub>O<sub>2</sub> (Krüger et al., 2013); and plants, where polyamines protect *Arabidopsis* from heat stress (Sagor et al., 2012). Polyamines also have the capacity to bind to proteins. This ability allows them, for instance, to bind to porins (membrane proteins that form channels) and inhibit them to prevent acidic and osmotic stress (Iyer and Delcour, 1997). In response to osmotic stress, polyamines can further act as “osmolytes”, accumulating for protection (Groppa and Benavides, 2007) or being excreted to balance charge alterations (Schiller et al., 2000).

We will focus on naturally occurring polyamines in mammals to delve into their synthesis, catabolism and transport. These processes are very tightly controlled through the specialized and unconventional means of regulation of the enzymes in polyamine metabolism.

## V.3 Polyamine metabolism

### V.3.1 Polyamine synthesis

Polyamines are synthesized from two proteinogenic amino acids, the essential amino acid methionine (Met, M) and the non-essential amino acid arginine (Arg, R). Arg is converted into ornithine, a non-proteinogenic amino acid that is the real substrate for the synthesis of the first polyamine synthesized in the pathway, Put (Lee and MacLean, 2011). There are two rate-limiting and equally relevant enzymes implicated in the synthesis of polyamines, ODC1 and S-adenosylmethionine decarboxylase (AMD1) (Pegg, 2009a) (**Fig. I11**). Both branches of the pathway start with a decarboxylation reaction. Ornithine is decarboxylated by ODC1 to form Put (Nowotarski et al., 2013). The other branch of the pathway is fueled with methionine, which is converted into SAM, the substrate that is then decarboxylated by AMD1 to form decarboxylated S-adenosylmethionine (dcSAM) (Miller-Fleming et al., 2015). This metabolite is the aminopropyl donor for the synthesis of the other two polyamines present in mammals, Spd and Spm (Pegg, 2013).

The aminopropyl group is transferred to Put and Spd in consecutive reactions catalyzed by two aminopropyltransferases, spermidine synthase (SpdS) and spermine synthase (SpmS), respectively (Rhee et al., 2007) (**Fig. I11**).

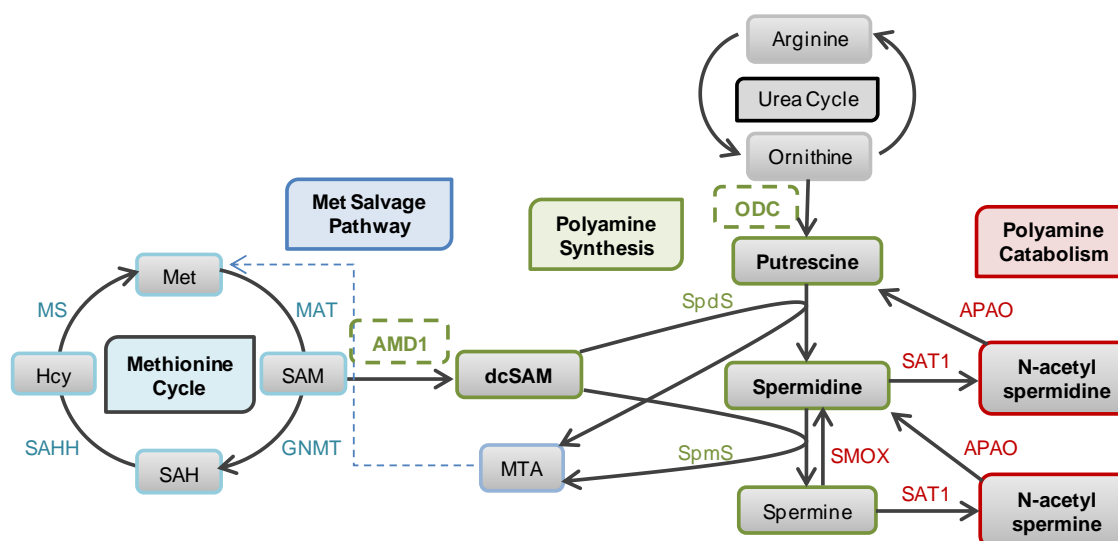


**Figure I11. Methionine cycle and polyamine pathway connection.** Schematic representation of the metabolic reactions of methionine cycle and polyamine synthesis and catabolism pathways.

### V.3.2 Polyamine catabolism

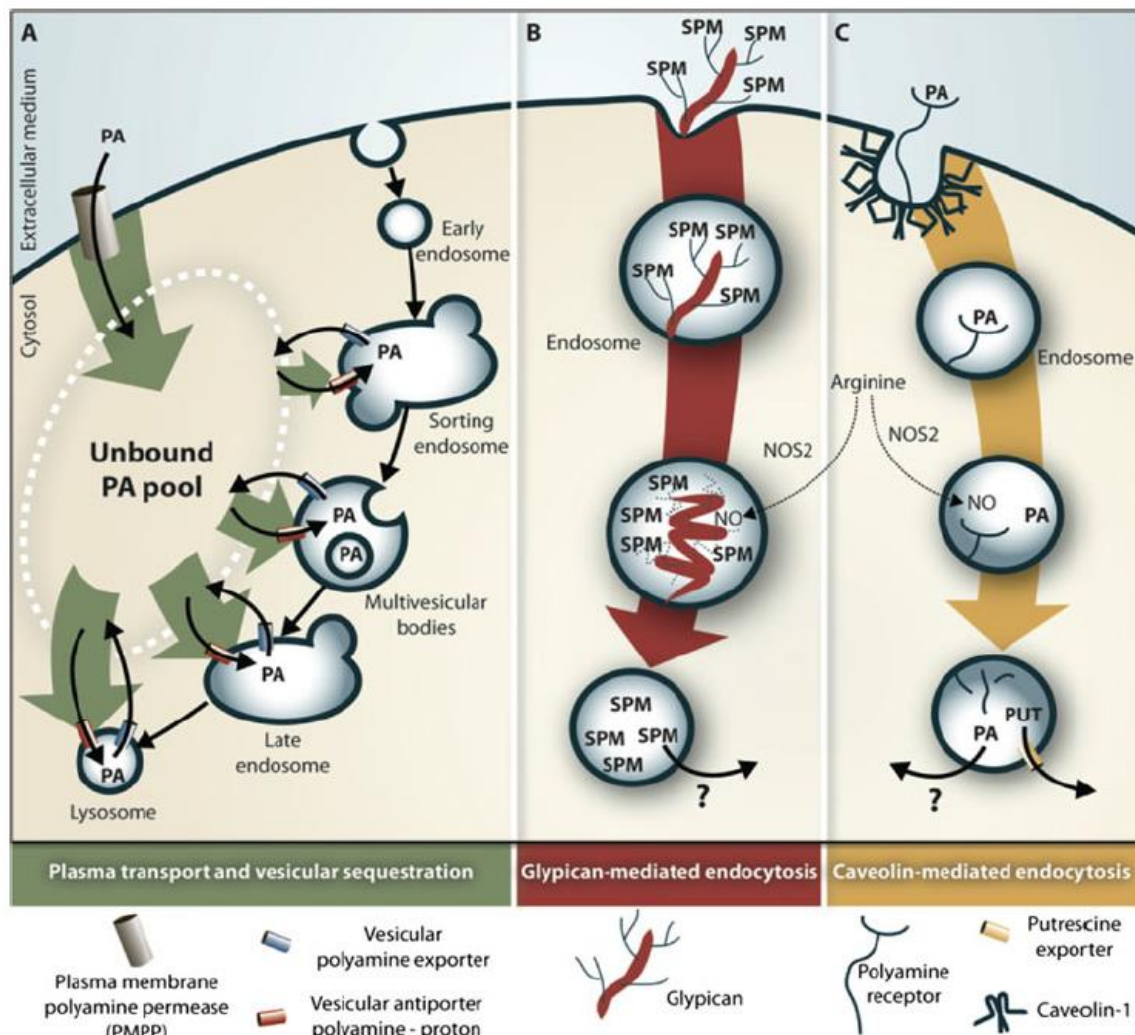
Polyamine concentration is not only regulated through their synthesis, but also through tightly regulated catabolic reactions. Polyamine catabolism consists of two main reactions, acetylation and oxidation (**Fig. I11**).

Acetylation of Spd and Spm, is catalyzed by Spermidine/spermine N<sub>1</sub>-acetyltransferase (SSAT). This inducible enzyme transfers the acetyl group from acetyl-coenzyme A to the N<sub>1</sub> position of either Spd or Spm (Casero and Marton, 2007), forming N<sub>1</sub>-acetylspermidine or N<sub>1</sub>-acetylspermine. Acetylation of polyamines reduces their positive charge, which decreases their ability to bind to macromolecules and makes them prone to be excreted (Pegg, 2013). Alternatively, they become substrates for acetylpolyamine oxidase (APAO). Oxidases can be classified according to the cofactor they require, flavin adenine dinucleotide (FAD) or copper (Cu<sup>2+</sup>). On the one hand, FAD-dependent oxidases include: APAO, which efficiently acts on N<sub>1</sub>-acetylspermine and N<sub>1</sub>-acetylspermidine and converts them into Spd and Put, respectively; and spermine oxidase (SMO), which shows a very high selectivity for spermine. These two enzymes generate reactive aldehydes and H<sub>2</sub>O<sub>2</sub> thereby causing oxidative stress (Pegg, 2009a). On the other hand, there are Cu<sup>2+</sup>-containing oxidases, including: diamine oxidase, which degrades putrescine into Δ<sup>1</sup>-pyrroline, ammonia and H<sub>2</sub>O<sub>2</sub>; and serum amine oxidase, which transforms Spd and Spm to produce amino aldehydes, ammonia and H<sub>2</sub>O<sub>2</sub>. Importantly, oxidation products of

serum polyamine oxidase or SMO can undergo spontaneous  $\beta$  elimination producing acrolein, a metabolite that shows very high toxicity (Pegg, 2013) (**Fig. I11**).

### V.3.3 Polyamine transport

Polyamine transport may play an important role in the regulation of total polyamine pools through their uptake (Casero and Marton, 2007) and excretion (Pegg, 2009a). Despite their central function, polyamine-specific transport systems in mammals are not very well understood yet, although several mechanisms implying endocytosis have been suggested (Miller-Fleming et al., 2015) (**Fig. I12**).



Adapted from Poulin R, Casero RA and Soulet D, *Amino Acids* 2012

**Figure I12. Putative mechanism models for polyamine uptake, accumulation and sequestration into vesicles in mammalian cells.** **A**, Model adapted from (Soulet et al.2004) illustrating a two-step mechanism. **B**, Model adapted from (Belting et al.2003) proposing Spm internalization bound to glycosaminoglycans and released from glypican-1 via NO-mediated oxidation. **C**, Model based on (Uemura et al.2010) suggesting a caveolin-1-dependent internalization bound to a potential polyamine receptor. NO, nitric oxide; NOS2, nitric oxide synthase-2; PA, polyamines; PUT, putrescine; SPM, spermine.

Soulet *et al.* proposed a mechanism by which polyamines may be transported into the cell through an unknown transporter powered by membrane potential (model 1). Immediately after internalization, polyamines would accumulate into polyamine-sequestering vesicles (PSVs) through V-ATPase activity-bearing transporters (Soulet et al., 2004). Other models claim the implication of glycosaminoglycans (model 2) (Belting et al., 2003) or caveolin-1 (model 3) (Uemura et al., 2010) in the internalization process of polyamines. Model 2 only provides an explanation for spermine transport and both model 2 and 3 do not solve the steps of polyamine release from vesicles (Poulin et al., 2011). In the last years, a number of membrane proteins from solute carrier (SLC) and ATP-binding cassette (ABC) protein superfamilies have been suggested as putative polyamine transporters, such as SLC22A1 and SLC22A2, SLC3A2, SLC12A8A, SLC22A16 and MDR1 (from ABC superfamily) (Abdulhussein and Wallace, 2013).

## V.4 Rate Limiting enzymes of the pathway

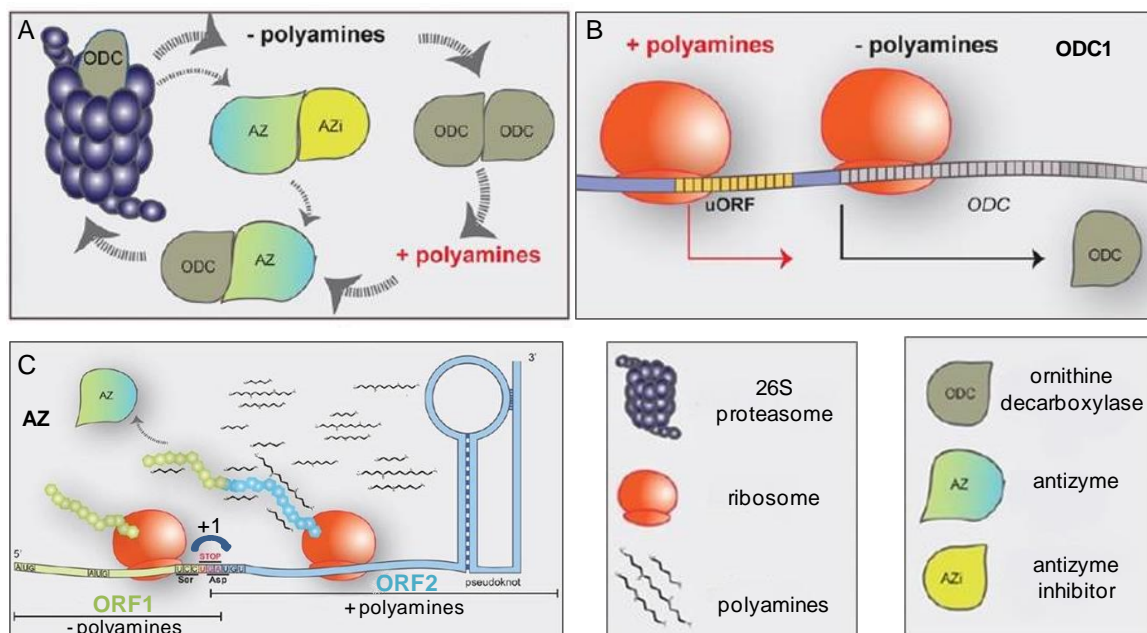
The polyamine pathway is tightly regulated by two rate-limiting enzymes implicated in the synthesis of these molecules. On the one hand, synthesis of the first polyamine in the synthetic pathway from decarboxylation of the amino acid ornithine is catalyzed by ODC1. On the other hand, the pathway relies on another important checkpoint control at the production of the other main substrate required for polyamine synthesis, dcSAM. This reaction is driven by AMD1, which decarboxylates SAM to produce dcSAM.

### V.4.1 ODC1

ODC1 is the first rate-limiting enzyme in the synthesis of polyamines. This enzyme requires pyridoxal phosphate (PLP) as a cofactor (Pegg, 2009a). An active ODC1 homodimer is the responsible for the synthesis of the diamine Put by decarboxylating ornithine (Pegg, 2006). The expression of ODC1 is tightly regulated at multiple levels, from transcription to degradation (Shantz and Pegg, 1999) (**Fig. I13**). This enzyme is of key importance for life, as demonstrated by *Odc1* deletion *in vivo*, which results in early lethality at E3.5 days post-fertilization (Pendeville et al., 2001).

At transcriptional level, ODC1 expression responds to multiple stimuli, such as growth factors, hormones and tumor promoter signals. At the translational level, ODC1 messenger RNA (mRNA) contains both elements that reduce translation efficiency (a 5' untranslated region (UTR)

with a strong secondary structure, a small upstream open reading frame, uORF, and a GC-rich sequence) (Shantz and Pegg, 1999) and elements that enhance translation (internal ribosome entry sites, IRES) (Pyronnet et al., 2000). However, the most unusual and complex regulatory step of ODC1 is its degradation. ODC1 shows a half-life of 10-30 minutes, which suggests a very tight regulation of protein stability. This decarboxylase is degraded through the proteasome, although this process is independent of ubiquitination. Instead, ODC1 depends on antizyme (AZ) binding, which has high affinity for ODC1 monomers, for recognition by the proteasome and degradation (Coffino, 2001). AZ is encoded by two adjacent ORFs and its synthesis is regulated by a +1 frameshift event that happens in high polyamine concentration conditions (Hayashi and Murakami, 1995; Nilsson et al., 1997). Importantly, AZ is also regulated by an antizyme inhibitor (AZi), which is highly homologous to ODC1 but lacks catalytic activity (Fujita et al., 1982). AZ has higher affinity for AZi than ODC1, thus allowing ODC1 dimerization and activation upon AZi expression.



Adapted from Miller-Fleming J, et al, *J Mol Biol* 2015

**Figure I13. Ornithine decarboxylase 1 (ODC1) and antizyme (AZ) regulation.** **A**, Schematic picture describing ODC1 and AZ regulation by polyamine levels. **B**, Schematic picture showing the mechanism of regulation of ODC1. **C**, Schematic picture showing the mechanism of regulation of AZ.

#### V.4.2 AMD1

AMD1 is the second rate limiting enzyme in polyamine synthesis pathway and the responsible for dcSAM production. To ensure that AMD1 does not deplete the pool of SAM, which is essential to maintain the methylation capacity of the cell (Locasale, 2013), this enzyme is expressed at very low levels. dcSAM is an essential substrate for polyamine synthesis, because it donates the aminopropyl group for Spd and Spm synthesis. In turn, AMD1 levels are very strictly regulated at

multiple levels, such as transcription, translation, processing and degradation. Put positively regulates AMD1 levels, whereas Spd and Spm negatively regulate the enzyme (Pegg, 2009b). The vital relevance of AMD1 is further supported by the fact that homozygous deletion of AMD1 is lethal between E3.5 and E6.5 days post-fertilization (Nishimura et al., 2002).

### V.4.2.1 AMD1 regulation

#### V.4.2.1.1 AMD1 processing

This decarboxylase has a pyruvoyl prosthetic group covalently bound. AMD1 is synthesized as an inactive proenzyme (proAMD1) of 38 KDa, which requires to undergo an autocatalytic serinolysis between glutamic acid 67 and Ser68 (Stanley et al., 1989) to generate the two different subunits (a and b) that will in turn dimerize and form the active heterotetramer (Pegg et al., 1998) (**Fig. I14**). This process is activated by Put in mammals (Stanley and Pegg, 1991).

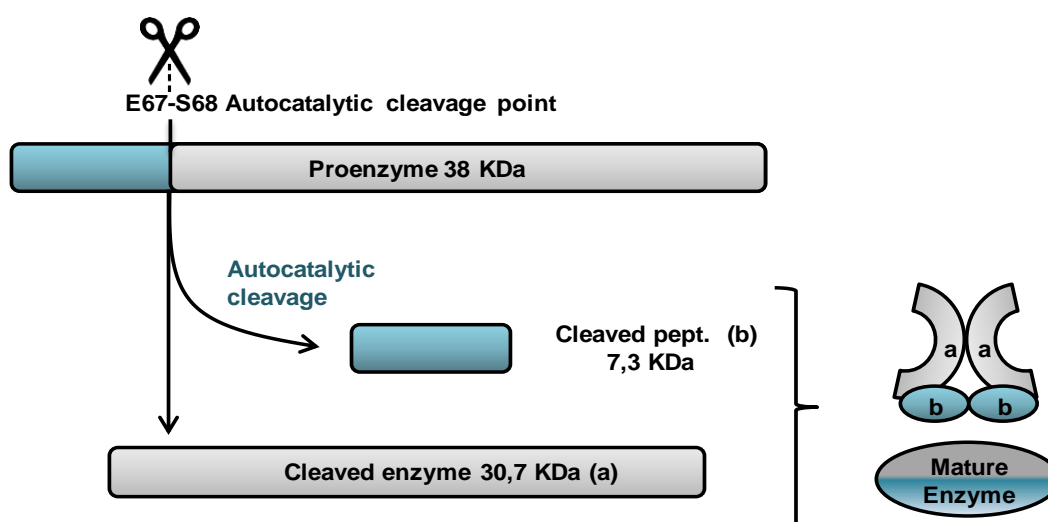


**Figure I14. AMD1 processing mechanism.** Schematic representation of the autocatalytic serinolysis process that the inactive proenzyme form of AMD1 suffers in order to produce the subunits “a” and “b” that will in turn dimerize giving the active mature enzyme.

#### V.4.2.1.2 AMD1 transcription

Regulation of AMD1 transcription has not been clarified yet. There is some evidence suggesting that AMD1 mRNA levels are upregulated in response to growth factors and Spd depletion. Indeed, human AMD1 promoter has been reported to contain a spd-responsive element (or polyamine-responsive element, PRE), although the experimental evidence are inconclusive (Pegg et al., 1998) (**Fig. I15**).

#### V.4.2.1.3 AMD1 translation

AMD1 translation is regulated by uORFs. AMD1 mRNA contains a small ORF 14 nucleotides downstream the 5' CAP that encodes for the hexapeptide MAGDIS (Hill and Morris, 1992).

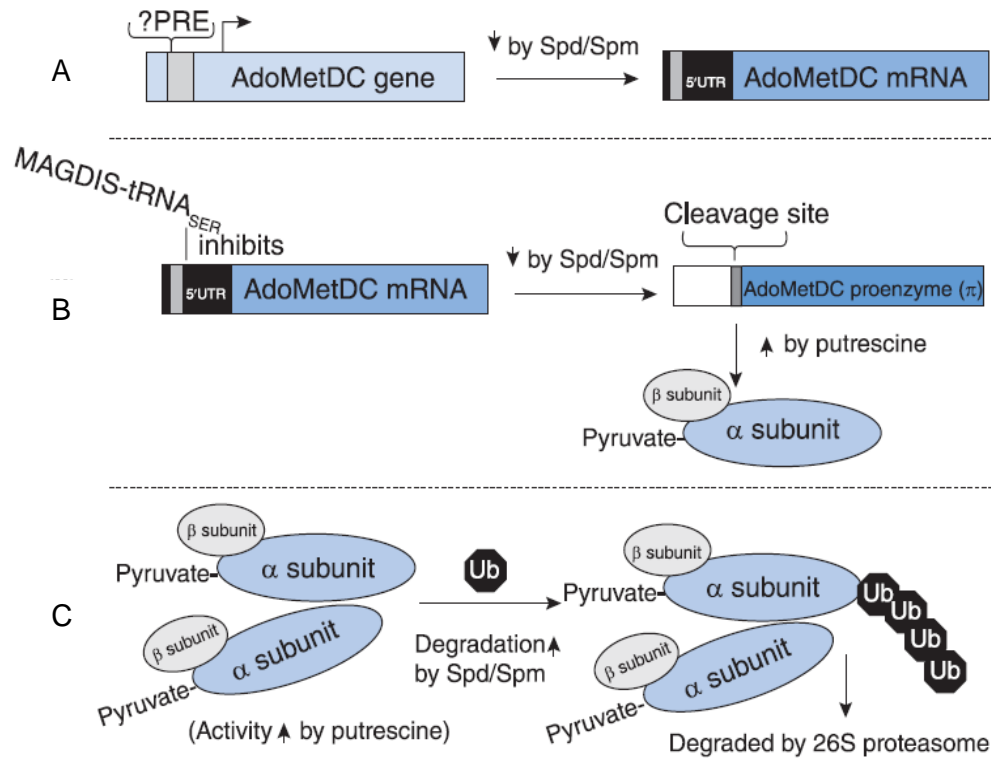


**Figure I15. Different levels of AMD1 regulation.** A-C, Mechanism of regulation of AMD1 transcription (A), translation (B) and degradation (C).

During translation of this peptide, when ribosomes reach the translation of last Ser (S) ribosomal stalling occurs, blocking the entrance of the ribosome to the AMD1 start codon. Spd and Spm stabilize the complex formed by the peptidyl-tRNA associated to the ribosome, inhibiting translation of AMD1 (Law et al., 2001; Raney et al., 2002) (**Fig. I15**).

#### V.4.2.1.4 AMD1 degradation

AMD1 in its proenzyme form shows a very short half-life (less than 1 h), and in some species the turnover takes less than five minutes. Importantly, the turnover is accelerated when Spd and Spm concentrations are high and no further polyamine synthesis is required (Miller-Fleming et al., 2015). AMD1 degradation occurs through polyubiquitination via the 26S proteasome (Yerlikaya and Stanley, 2004). In the reaction chain that takes place to produce dcSAM, the last step consists on protonation of C $\alpha$  of the product for the correct release of dcSAM and regeneration of the pyruvate. However, under some circumstances, C $\alpha$  of the prosthetic group is protonated leading to the formation of alanine instead of pyruvate and to the release of an aldehyde group. This substrate-mediated transamination process irreversibly inactivates AMD1 (Pegg, 2009b).



Furthermore, this transformation has been suggested to cause conformational changes in the enzyme that would make it more accessible to ubiquitination and prone to proteasome-dependent degradation (Yerlikaya and Stanley, 2004) (**Fig. I15**).

## V.5 Polyamines and disease

As a consequence of their multiple and varied physiological roles, polyamines have been implicated in a considerable number of pathologies. Nevertheless, there is only one inherited human disease directly associated to a genetic alteration in polyamine synthesis pathway, the Snyder-Robinson syndrome (SRS). This syndrome is caused by a splice mutation in *SpmS* gene located in chromosome X and characteristic features of this disorder encompass mental retardation, osteoporosis, facial asymmetry, hypotonia and movement disorders (Lauren Cason et al., 2003). There is also evidence reporting duplication of *Ssat1* gene (encoding for SSAT1) as the responsible for keratosis follicularis spinulosa decalvans (KFSD), although further patient studies are required to conclude a direct relationship (Pegg, 2009a).

Ageing has been shown to negatively correlate with polyamine levels. In line with this fact, some age-related neurodegenerative diseases, such as Parkinson's disease (PD) or Alzheimer's disease (AD) show increased polyamine levels, suggesting a deranged polyamine pathway. However, these observations in PD and AD were reported to be polyamine and cell-type specific and no causative demonstration has been achieved yet (Miller-Fleming et al., 2015; Minois et al., 2011). At molecular level, polyamines have been shown to promote  $\alpha$ -synuclein (Antony et al., 2003; Krasnoslobodtsev et al., 2012) and  $\beta$ -amyloid (Luo et al., 2013) aggregation in PD and AD, respectively. These results were not unexpected, based on the interaction capacity of polyamines, and thus, *in vivo* experiments showing the extent and relevance of the effect of polyamines on the formation of these aggregates are warranted (Minois et al., 2011). In the same line, while some polyamines, such as Spm, have been related to ischemic neuronal injury in stroke (Duan et al., 2011), others, as Put, have been shown neuroprotective effects against epilepsy (Bell et al., 2011). Polyamines are also associated with inflammatory responses, leading to an overall increase in inflammatory conditions, such as pancreatitis (Minois et al., 2011) and the capacity to recruit macrophages. Whether polyamines play a pro- or anti-inflammatory role still remains elusive (Puntambekar et al., 2011). In the same line, polyamines ameliorate parasitic infection-related symptoms, probably by improving the adaptive immune response and leading to a beneficial outcome of the disease (Nishimura et al., 2009b).

Of note, byproducts of polyamine metabolism have been involved in multiple diseases. The potential toxic role of acrolein was already suggested a century ago. Ever since, this aldehyde has been associated with neurological damage due to stroke or dementia, neurological disease and renal failure (Minois et al., 2011).

### V.5.1 Polyamines and cancer

Polyamines have been widely associated to active proliferation and cancer (Gerner and Meyskens, 2004a; Soda, 2011). The association of polyamines with this disease was first reported by Russell and Snyder in 1968, who demonstrated a dramatic increase of ODC1 in STAT-I sarcoma (Russell and Snyder, 1968). Thenceforth, higher polyamine concentration upon neoplastic transformation has been reported in a variety of cancer types, such as colorectal, breast or prostate cancer (Kingsnorth et al., 1984; Cañizares et al., 1999; Schipper et al., 2000).

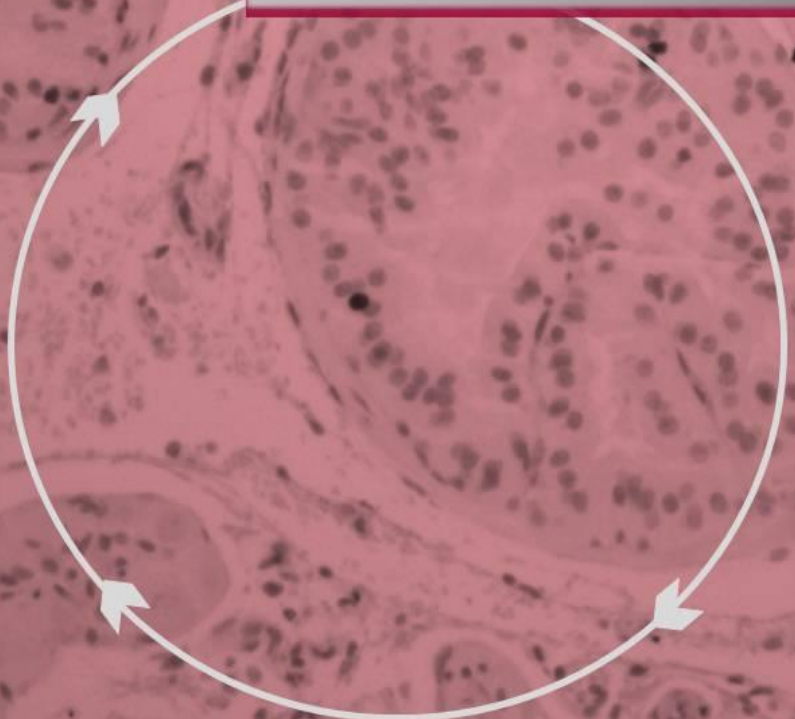
Expression and activity of polyamine biosynthetic and catabolic enzymes have been related to cancer status (Soda, 2011). In this sense, upregulation of ODC1 in the intestinal mucosa of familial adenomatous polyposis (FAP) patients is the best described example. In this inheritable form of colon cancer, the tumor suppressor adenomatous polyposis coli (APC) appears mutated or lost, which upregulates the expression of *MYC* oncogene, leading to aberrant growth and cancer (Gerner and Meyskens, 2004a). ODC1 is a direct transcriptional target of *MYC* (Bello-Fernandez et al., 1993; Peña et al., 1993), and its expression has been correlated with colon cancer risk. Moreover, a single-nucleotide polymorphism (SNP) (G315A) in intron 1 of *ODC1*, which lies between two consensus *MYC* binding sites (E boxes), was reported to affect *ODC1* transcription, due to the selective binding of the transcriptional repressor and *MYC* antagonist MAD1. Based on this molecular mechanism, it was found that individuals homozygous for this allele showed a reduction in colon polyp development and cancer risk. Of note, aspirin use was observed to further decrease colon cancer risk in an allele-independent manner, through the activation of SSAT (Martínez et al., 2003). *In vivo*, ODC1 overexpression alone was not sufficient to induce tumorigenesis (Alhonen et al., 1995; Smith et al., 1998), whereas targeted ODC1 expression to the skin, under the control of K6 keratin promoter, caused increased susceptibility to skin tumor development upon different carcinogen induction (Chen et al., 2000; O'Brien et al., 1997). Of note, the development of skin tumors is polyamine-dependent, as it is reduced upon ODC1 inhibition with difluoromethylornithine (DFMO) (Smith et al., 1998), targeted AZ overexpression in the skin (Feith et al., 2001) or *ODC1* heterozygosity (Guo et al., 2005). Likewise, ODC1 has also been related to other oncogenes. This enzyme is necessary to induce active H-Ras GTPase-driven oncogenic transformation *in vitro* (Shantz and Pegg, 1998) and to cooperate with H-Ras in the promotion of epidermal tumors *in vivo* (Smith et al., 1998).

Catabolic enzymes such as SSAT1 or SMO have also been related to the disease. These enzymes are also under the regulation of mutant *KRAS*. *KRAS* inactivates peroxisome proliferator-activated receptor gamma (PPAR $\gamma$ ), which in turn fails to bind the PPAR response element (PPRE) in *SSAT1* promoter (Gerner and Meyskens, 2004a). Nonetheless, studies using transgenic SSAT1 overexpression exhibit conflicting results. Overexpression of *Ssat1* in the skin (K6/SSAT) (Coleman et al., 2002) or whole *Ssat1* overexpression in combination with *Apc*<sup>Min/+</sup> mutation (which develop colon cancer) (Tucker et al., 2005) showed increased incidence of skin and intestinal tumors, respectively. Conversely, transgenic expression of *Sat1* (Pietilä et al., 2001) in the transgenic adenocarcinoma of the mouse prostate (TRAMP) model (which

develops prostate cancer) (Kee et al., 2004) led to significant reduction in tumor incidence. However, germline *Ssat1* overexpression is known to cause multiple pleiotropic phenotypes that difficult drawing carcinogenesis-related conclusions. Furthermore, contrary to the targeted K6/SSAT mice, the SSAT1 transgenic expression in TRAMP mice led to a profound depletion of polyamines, through the inhibition of a compensatory increase of polyamine synthesis that would support tumor growth (Casero and Pegg, 2009).

SMO has recently been linked to carcinogenesis. Increased expression of this polyamine catabolic enzyme has been observed in inflammatory-associated cancers. Specifically, infectious agents such as enterotoxigenic *Bacteroides fragilis* (ETBF) and *Helicobacter pylori* induce an inflammatory state that increases colorectal cancer risk (bowel disease and colitis) and colon cancer (Ulger Toprak et al., 2006), and gastric cancer (Chaturvedi et al., 2011), respectively. In both cases the bacterial infection was demonstrated to increase SMO expression, resulting in DNA damage and apoptosis (Xu et al., 2004). This data was validated with the inhibitor of SMO MDL72527 and SMO knockdown. In this line, SMO expression was reported to be increased as an early event in PCa development, although further studies are warranted in order to assess the role of SMO-induced ROS in prostate carcinogenesis (Goodwin et al., 2008).







Despite decades of investigation on prostate cancer (PCa), it remains the fifth cause of death among men worldwide. This fact underscores the necessity to develop more selective and efficient therapies that would ensure disease eradication. Deregulation of energetic metabolism has recently been postulated as one of the hallmarks of cancer (Hanahan and Weinberg, 2011). This thesis work stems from the interest in deciphering the metabolic cues implicated in PCa initiation and progression, and is based in the following hypothesis: ***Oncogenic events trigger the deregulation of metabolism in prostate cancer, thus revealing potential therapeutic strategies.***

We based our work on the premise that there is strong conservation in the metabolic signals that regulate murine and human PCa pathogenesis. Therefore, we propose to perform a discovery study based on integrative metabolomics, starting from a conditional tissue specific *Pten* knockout mouse model of PCa (Chen et al., 2005; Nardella et al., 2010b). We integrated, validated and deconstructed this data using PCa patient specimens and PCa cell lines.

In order to test this hypothesis, we establish the following specific aims:

➤ **Aim1: To identify metabolic alterations underlying prostate cancer pathogenesis**

To characterize metabolic alterations at the core of PCa, we undertook an integrative metabolomics approach. Recent innovation in metabolomics instrumentation and development of bioinformatic tools (Patti et al., 2012) offers the opportunity to select the most suitable metabolomics approach:

- 1.1 Time-of-flight Mass Spectrometry (ToF-MS) to establish the panoramic semiquantitative view of prostate cancer metabolism.
- 1.2 Liquid Chromatography-Mass Spectrometry (LC/MS) to focus on most altered and relevant pathways and analyze them quantitatively.
- 1.3 Metabolic Flux Analysis (MFA) to validate the data in a dynamic setting, which accurately represents metabolic nature.

➤ **Aim2: To elucidate the molecular mechanism underlying the metabolic regulation observed in PCa**

PTEN is a tumor suppressor that regulates the oncogenic PI3K pathway, which has been reported to be altered in a large fraction of human cancers (Carracedo and Pandolfi, 2008; Engelman et al., 2006). Importantly, alterations in *Pten* have been observed in up to seventy percent of prostate cancers (Song et al., 2012). Hence, our mouse model, driven by the loss of *Pten*, will allow us to study the interconnection between the metabolic alterations observed and the hyper-activation of this oncogenic cascade. To ascertain the molecular mechanism triggering the metabolic alterations we will rely on two main strategies:

- 2.1 Evaluation of transcriptional changes as drivers of the polyamine metabolic switch.
- 2.2 Evaluation of post-transcriptional changes as drivers of the polyamine metabolic switch.

➤ **Aim3: To ascertain the therapeutic potential of targeting the altered metabolic pathway and evaluation of prospective therapies**

Based on the need of new selective and efficient therapies that would drive us towards precision medicine, we will approach this aim in two ways:

- 3.1 Genetic and pharmacological modulation of potential targets *in vitro* and *in vivo* to test their therapeutic potential.
- 3.2 Evaluation of *in vivo* therapeutic strategies based on the target with highest potential.



The background of the slide is a microscopic image of biological tissue, possibly showing cross-sections of cells or fibers. Overlaid on this are several diagrams: a jagged black line with purple dots at its peaks, several white arrows pointing in various directions, and a circular diagram at the bottom left with three white arrows forming a clockwise loop. A dark purple rectangular box is positioned in the lower-middle section, containing the text 'Materials and Methods'.

***Materials and Methods***



## I IN VIVO AND EX VIVO ASSAYS

### I.1 Analysis of tissue samples

#### I.1.1 Analysis of murine samples

All mouse experiments were carried out following the ethical guidelines established by the Biosafety and Animal Welfare Committee at CIC bioGUNE. The procedures employed were carried out following the recommendations from AAALAC. Mice were housed under controlled environmental conditions, such as time controlled lighting on standard 12:12 light:dark cycles, controlled temperature at  $22 \pm 2^\circ\text{C}$  and 30-50% relative humidity. Mice were fed regular Chow diet *ad libitum*, unless otherwise specified based on experimental designs. Mice were fasted for 6h prior to tissue harvest (9 am-3 pm) in order to prevent metabolic alterations due to immediate food intake. At experimental end-point, all mice were sacrificed by  $\text{CO}_2$  inhalation followed by cervical dislocation.

##### I.1.1.1 Genetically engineered mouse models (GEMM)

In this thesis work we have studied three genetic alterations in mice: Cre recombinase-dependent *Pten* conditional deletion (Chen et al., 2005), whole body *Gnmt* mutation (Luka et al., 2006) and Cre recombinase expression under the control of androgen-dependent *ARR2B Probasin* promoter (*Pb-Cre4*). The *Pb-Cre4* transgene allowed us to delete *Pten* in the prostate epithelium at puberty. The conditional tissue specific *Pten* knockout (C57BL6/129sv;*Pb-Cre4*; *Pten*<sup>lox/lox</sup>) model was kindly provided by Dr. Pandolfi (Chen et al., 2005). The whole body *Gnmt* knockout (C57BL6) was kindly provided by Dr. Martinez-Chantar (Luka et al., 2006). We generated a mouse line which we named PGN by breeding *Pten* prostate-specific knockout mice (*Pb-Cre4Pten*<sup>lox/lox</sup>) and *Gnmt* knockout mice. We intercrossed these two lines for at least three generations to obtain a founder colony with mixed homogeneous background. Probasin Cre was always retained in male mice, since in females *Pb-Cre4* expression in utero can lead to recombination in embryos during pregnancy. Prostate *Pten*-deleted male mice were termed *Pten*<sup>pc+/-</sup> (heterozygous) or *Pten*<sup>pc-/-</sup> (homozygous knockout). We generated a mouse colony of *Pten*<sup>pc-/-</sup> for metabolomic characterization and preclinical studies. *Gnmt*<sup>-/-</sup> and wildtype counterparts were generated to evaluate the relevance of this gene in prostate cancer (PCa) pathogenesis and metabolism. For the PGN line, *Pten*<sup>pc+/-</sup> *Gnmt*<sup>+/+</sup> and *Pten*<sup>pc+/-</sup> *Gnmt*<sup>-/-</sup> mice were generated for pathological and metabolomics studies. The time of analysis was based on the experimental design, and it is indicated in the results section.

##### I.1.1.2 Xenograft models in nude mice

DU145 cells in suspension were injected subcutaneously into immunocompromised 8-10-week-old male nude mice (Harlan). Measurement of tumor size was performed every two-three days

and tumor volume was estimated using the following formula: **volume = length x width<sup>2</sup> x 0.526**. Final tumor weight was measured upon tissue harvest at the experimental end point.

### I.1.1.2.1 AMD1 OE in vivo

DU145 cells transduced with either empty vector (Mock) or AMD1 expressing construct (DU145<sup>MYC-AMD1-HA WT</sup>) ( $4 \times 10^6$  cells per condition) in PBS (supplemented with  $5 \mu\text{M}$  glucose) suspension were mixed at 1:1 ratio with Matrigel (Corning Cat# 354230) in a final volume of  $100 \mu\text{L}$  and injected subcutaneously in two flanks per mouse (6 mice,  $n=12$  per condition).

### I.1.1.2.2 AMD1 Silencing in vivo

A suspension of DU145 cells (in PBS supplemented with  $5 \mu\text{M}$  glucose) transduced with a lentiviral inducible vector (TET-pLKO; Addgene Plasmid #21915) containing shRNA for AMD1 (SIGMATRCN0000078462) ( $7,5 \times 10^6$  cells per condition) was mixed at 2:1 ratio with Matrigel (Corning Cat# 354230) in a final volume of  $150 \mu\text{L}$  and injected subcutaneously in two flanks per mouse. Injected nude mice were fed regular Chow diet until tumors reached an average volume of  $150 \text{mm}^3$ . Then mice (according to cage distribution) were fed doxycycline-containing diet (specifications are reflected in the datasheet in Anex) to induce AMD1 silencing or were maintained in chow food as control (7 mice,  $n=14$  per condition).

### I.1.1.3 Preclinical trials

#### I.1.1.3.1 RAD001 treatment *in vivo*

The RAD001 preclinical trial was performed following the experimental design in **Fig. M1**. Two month-old *Pten<sup>pc/-</sup>* mice were administered either vehicle (polyethylene glycol, PEG) or RAD001 (10mg/Kg) six days a week during four weeks by oral gavage. At the experimental end-point, mice were euthanized as specified in I.1.1. and tissues of experimental interest were harvested.

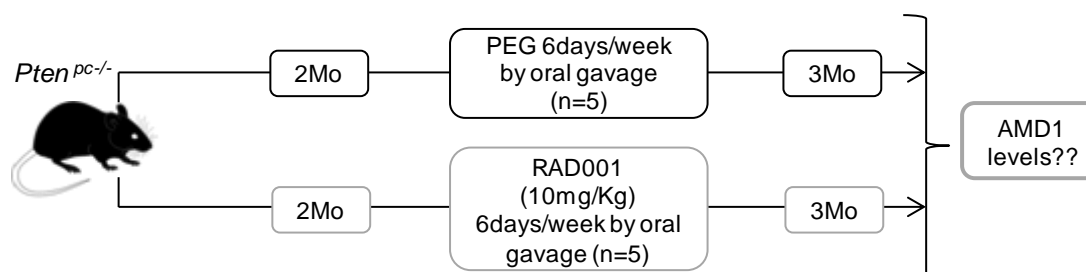


Figure M1. Schematic showing the experimental design of the RAD001 preclinical trial.

### I.1.1.3.2 SAM486A treatment *in vivo*

The SAM486A preclinical trial was performed following the experimental design in **Fig. M2**. Two month-old *Pten<sup>pc/-</sup>* mice were administered either vehicle (0,9% NaCl) or SAM486A (2mg/Kg or 5mg/Kg) five days a week during four weeks by intraperitoneal injection. At the experimental end-point, mice were sacrificed as specified in I.1.1. and tissues of experimental interest were harvested.

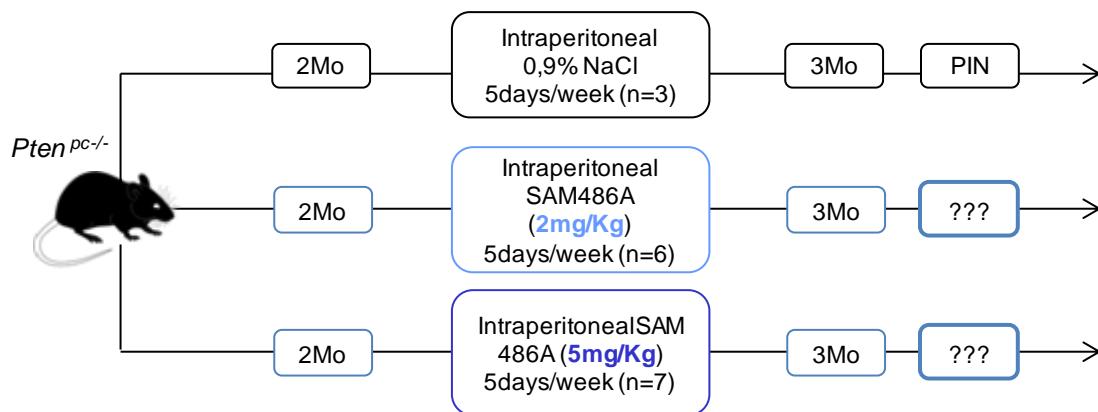


Figure M2. Schematic showing the experimental design of the SAM486A preclinical trial.

### I.1.1.3.3 Methionine restriction *in vivo*

Methionine restriction preclinical trials were performed following the experimental design detailed in **Fig. M3** and **Fig. M4** for one month- and four month-long experiments, respectively. Mice were weighed weekly to control diet safety. See Annex for diet specifications. At the experimental end-point, mice were sacrificed as specified in I.1.1. and tissues of experimental interest were harvested.

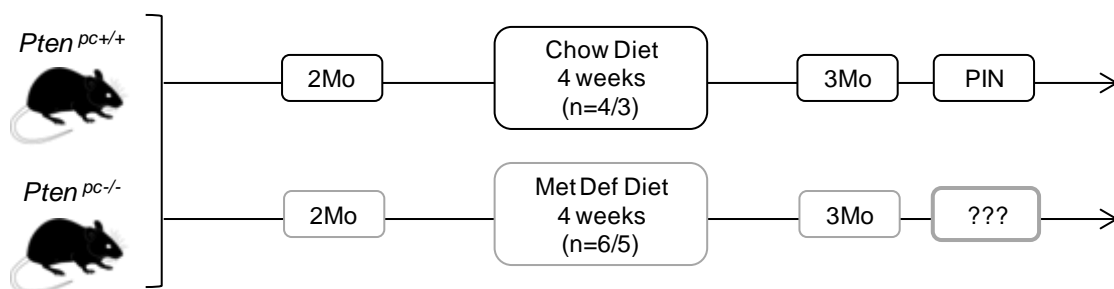


Figure M3. Schematic showing the experimental design of the methionine restriction preclinical trial for four weeks.

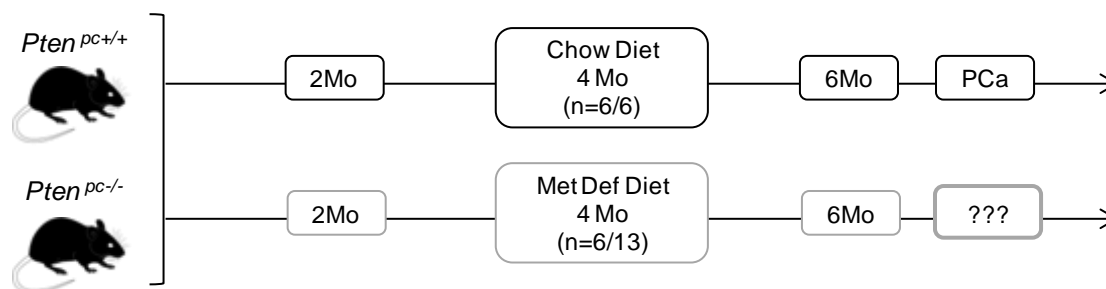


Figure M4. Schematic showing the experimental design of the methionine restriction preclinical trial for four months.

### I.1.2 Analysis of human specimens

All prostate specimens were obtained upon informed consent and with evaluation and approval from the corresponding ethics committee (CEIC code OHEUN11-12 and OHEUN14-14). Sample and pathological information from PCa and benign prostatic hyperplasia (BPH) patients used for LC/MS was obtained from the Basque biobank for research (BIOEF), and is specified in **Table M1**. The clinical-pathological information about the biopsies from the clinical trial with Everolimus is described in **Table M2**.

**Table M1:** Detailed data of patient specimens from The Bioef Foundation biobank, describing sample type, specific characteristics of the sample and aggressiveness parameters of prostate cancer samples (Gleason Score and TNM Classification)

Patient	Sample type	Characteristics	Gleason	TNM
Patient 1	BPH	Hiperplasia. Squamousmetaplasia foci		
Patient 2	BPH	Glandular hiperplasia mixed with estroma		
Patient 3	BPH	Glandular hiperplasia		
Patient 4	BPH	Glandular hiperplasia		
Patient 5	BPH	60% glandular, 40% estromal hiperplasia		
Patient 6	BPH	40% glandular, 60% estromal hiperplasia		
Patient 7	PCa	Prostate adenocarcinoma	7	T2
Patient 8	PCa	Prostate adenocarcinoma with mucinous component	7	T1c
Patient 9	PCa	Prostate adenocarcinoma	7	T2a
Patient 10	PCa	Prostate adenocarcinoma	6	T1c
Patient 11	PCa	Prostate adenocarcinoma	7	T2c
Patient 12	PCa	Prostate adenocarcinoma	6	T2b

**Table M2:** Detailed data of patient biopsies from the clinical trial with Everolimus.

Patient	Biopsies		Primary Tumor	Localization	Dose (mg)	Administration	Response
	Day	Localization					
P1	Pre-tr.	liver Mx	colon	liver Mx	20	weekly	PD
	On-tr.	liver Mx					
P2	Pre-tr.	breast	breast	liver M	5	daily	PD
	On-tr.	liver Mx					
P3	Pre-tr.	breast	breast	skin	5	daily	PD
	On-tr.	breast					
P4	Pre-tr.	breast	breast	skin	20	weekly	PD
	On-tr.	breast					
P5	Pre-tr.	liver Mx	colon	liver Mx	50	weekly	PD
	On-tr.	liver Mx					
P6	Pre-tr.	liver Mx	pancreas	liver Mx	50	weekly	PD
	On-tr.	liver Mx					
P7	Pre-tr.	breast	breast	skin	50	weekly	PD
	On-tr.	breast					
P8	Pre-tr.	melanoma axila	melanoma	axilar lymph node	10	daily	PD
	On-tr.	melanoma axila					
P9	Pre-tr.	liver Mx	liver Mx	liver Mx	5	daily	SD
	On-tr.	liver Mx					
P10	Pre-tr.	breast	breast	skin	50	weekly	PD
	On-tr.	breast					
P11	Pre-tr.	breast	breast	skin	5	daily	PD
	On-tr.	breast					
P12	Pre-tr.	liver Mx	liver Mx	liver Mx	10	daily	PD
	On-tr.	liver Mx					
P13	Pre-tr.	maxilar	H&N	maxillar	10	daily	NA
	On-tr.	maxilar					
P14	Pre-tr.	breast	breast	skin	20	weekly	NA
	On-tr.	breast					

## I.2 Methods

### I.2.1 Genotyping

Breeding and tag and tailing was carried out by animal house personnel. Genotyping was performed by technicians in the Carracedo lab, Sonia Fernández and Pilar Sanchez-Mosquera (CIC bioGUNE).

#### I.2.1.1 Genomic DNA purification from mouse tail

Mouse tail samples (0,2-1cm) were lysed in 195uL of lysis buffer [100mM NaCl, 50mM Tris-HCl (pH 8.0), 25mM EDTA, 0.5% SDS or 100mM NaCl, 50mM Tris-HCl (pH 8.0), 5mM EDTA, 1% SDS] with 5uL of Proteinase K (stock 10mg/ml; *Fluka*) for 3-6h at 55°C.

Once soft tissue was solubilized, 200µl of phenol/chloroform/isoamyl (25:24:1) were added to separate DNA (in upper aqueous phase) from denaturalized proteins (in interphase) and RNA and lipids (in lower organic phase) by mixing well by inversion and centrifugation for 15 min at 14,000rpm at room temperature. DNA containing aqueous phase was transferred to new tubes and washed/precipitated by adding 15uL sodium acetate (3M) and 400uL of 100% ethanol and

incubated at -20°C overnight to enhance precipitation. Samples were centrifuged 10min at 14000rpm at 4°C and supernatant was discarded to dry DNA pellets. Dry pellets were resuspended in 50-100uL H<sub>2</sub>O (up to 500uL for tail fragments of 1cm).

### I.2.1.2 Polymerase Chain Reaction (PCR) for genotyping

For genotyping, extracted mouse tail DNAs (1µL) were subjected to Polymerase Chain Reactions (PCR), optimized with specific primers (specified in Table M3) and PCR programs (See Fig. M5) for each gene of interest. All PCR assays were performed with DNA Polymerase Mix *AccuStart™II PCR SuperMix (Quanta Biosciences)*.

**Table M3:** Specific primer sequences used for genotyping mouse colonies.

Gene	Forward 5'-3'	Reverse 5'-3'	Band size
<i>Pten</i>	TGTTTTGACCAATTAAGTAGGCTGTG	AAAAGTCCCCTGCTGATGATTTGT	<i>Pten</i> <sup>pc+</sup> : 350bp <i>Pten</i> <sup>pc lox</sup> : 480bp
<i>Cre</i>	GGTGCAAGTTGAATAACCGGA	CGGTATTGAACTCCAGCGC	850bp
<i>Gnmt</i> <sup>+</sup>	GTACCGCAGAGTACAAGGCG	CAATCGCAGGAGGAACAGCGC	330bp
<i>Gnmt</i> <sup>-</sup>	CAATCGCAGGAGGAACAGCGC	CTGAATGAACTGCAGGACGAG	1151bp

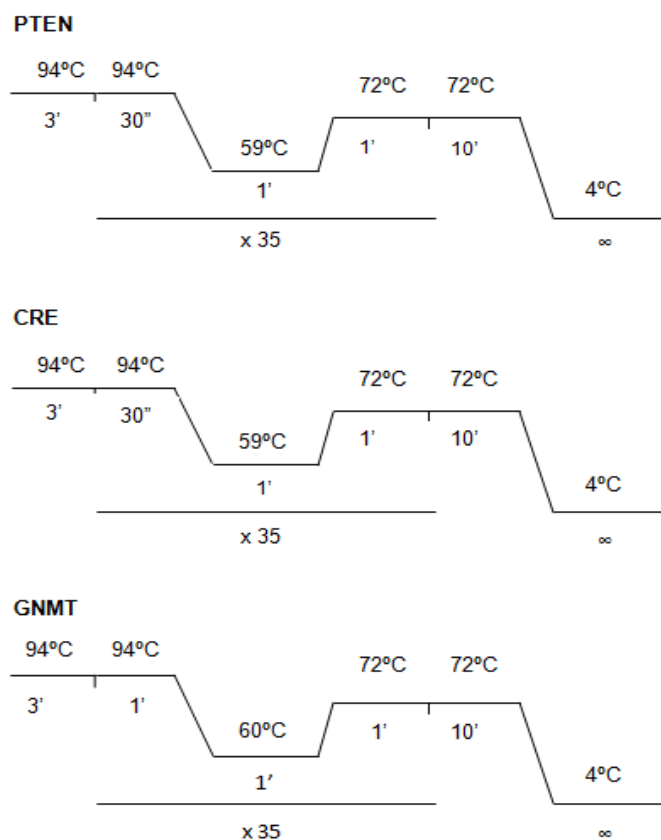


**Figure M5.** PCR programs followed for mouse tail DNA amplification and genotyping.



## I.2.2 Pathological analysis of prostate tissues

At the experimental end-point of all *in vivo* genetic mouse model experiments, one of each prostate lobes (AP, DLP and VP) was fixed in 10% neutral buffered formalin and stored at 4°C for 24 hours to allow tissue fixation for pathological analysis. All the tissue processing and staining steps were performed by Sonia Fernández (CIC bioGUNE).

### I.2.2.1 Tissue processing, paraffin embedding and sectioning

After 24 hour fixation tissues were dehydrated and infiltrated with paraffin following the steps in **Table M4**. Infiltrated tissues were then embedded in paraffin blocks.

**Table M4:** Steps followed to process mice tissues.

Tray	Time	Reagent	Fuction
T1	10 min	50% alcohol	Dehydration
T2	1 h 30 min	70% alcohol	Dehydration
T3	1 h 30 min	80% alcohol	Dehydration
T4	1 h 30 min	96% alcohol	Dehydration
T5	1 h 30 min	100% alcohol	Dehydration
T6	1 h 30 min	100% alcohol	Dehydration
T7	1 h 30 min	100% alcohol	Dehydration
T8	45min	Citrosol or Xylene substitute	Rinse, replace the alcohol with citrosol
T9	2h	Paraffin	Replace the citrosol with paraffin
T10	2h	Paraffin	Replace the citrosol with paraffin

Ice-cold paraffin blocks were sectioned to obtain 3  $\mu$ m sections, which were then adhered to slides for tissue staining and analysis.

### I.2.2.2 Slide processing for immunohistochemistry

Tissue slides were de-paraffined and hydrated, following steps in **Table M5**, to allow immunohistochemical analysis.

**Table M5:** Steps followed to process tissue slides for immuhistochemistry.

Time	Repeats	Reagent	Fuction
10-15 min	Twice	Citrosol or Xylene substitute	Hydration
3 min	Twice	100% alcohol	Hydration
3 min	Twice	95% alcohol	Hydration
3 min	Twice	dH <sub>2</sub> O	Hydration

After the desired staining in each case, slides were dehydrated with 95% and 100% alcohol and cleared in xylene for final coverslip mounting with DPX.

### I.2.2.2.1 Haematoxylin and Eosin (H&E) staining

Slides were incubated in haematoxylin for 5 min and rinsed in water for 1 min. After haematoxylin staining, they were incubated in acid alcohol (70% alcohol, 3% HCl) for 2 seconds for controlled leaching of non-specific background coloration and rinsed again in water (1 min). Finally, slides were incubated in eosin for 2 min and mounted.

### I.2.2.2.2 Ki67 and RpS6<sup>S235-236</sup> staining

Antigen retrieval was performed with citrate buffer (pH 6) in steamer (30 min). H<sub>2</sub>O<sub>2</sub> was used to block the endogenous peroxidase, followed by blocking with goat serum and primary antibody [Ki67, Thermo MA5-14520 (1:100); RpS6<sup>S235-236</sup>, CST #4858 (1:500)] incubation overnight at 4 °C. Goat anti-rabbit IgG antibody [Vector Laboratories, Cat# BA-1000 (1:1000)] was incubated at room temperature for 30 min. IHC detection was performed with the VECTASTAIN Elite ABC Kit (Cat# PK-6100) from Vector Laboratories and developed with DAB. A schematic of the procedure is shown in **Fig. M6**.

### I.2.2.2.3 AMD1 staining and scoring

Immunohistochemical analysis of AMD1 [Proteintech, 11052-1-AP (1:100)] was performed using DAKO EnVision™ Flex High pH (Tris/EDTA pH 9) (DAKO) (Technical details are shown in **Fig. M6**) The scoring system was based on the quantification of the percentage of cells negative (0), low (1+), medium (2+) or high (3+) immunoreactivity. Subsequently, h-score was calculated as follows:  $H = [\text{percentage of cells } 1+] + [2 \times (\text{percentage of cells } 2+)] + [3 \times (\text{percentage of cells } 3+)]$ .

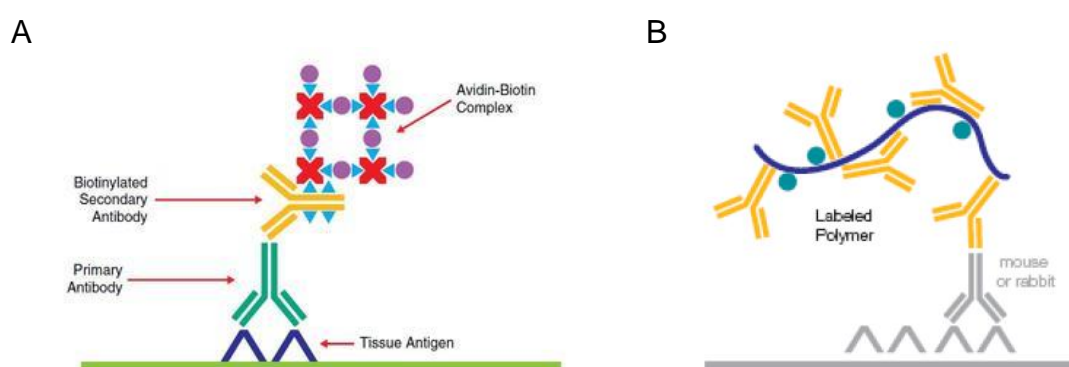


**Figure M6. Schematic of immunohistochemistry procedures. A, Avidin/Biotin Complex (ABC) method. B, DAKO EnVision Flex method.**

### **I.2.3 Molecular analysis of prostate tissues**

At the experimental end-point of all the *in vivo* experiments, one of the prostate lobes (AP, DLP and VP) was snap frozen in liquid nitrogen immediately after extraction for molecular or metabolomic analysis.

For molecular analysis, prostate tissues were homogenized with Precellys technology in the presence of ceramic beads, using two cycles of 30 seconds at 5000rpm.

#### **I.2.3.1 Gene expression analysis of murine prostate tissues**

For RNA extraction from prostatic tissue, samples were incubated overnight in the presence of RNAlater ICE® (Thermo) at -20°C. Prostate tissues were homogenized in the presence of TRIzol® reagent (Thermo) and RNA extraction was performed by TRIzol method and subsequent Macherey Nagel RNA extraction kit (Ref# 740955.250) (Ugalde-Olano et al., 2015). Retrotranscription and gene expression analysis by Real Time-Quantitative-Polymerase Chain Reaction (RT-QPCR) were then performed as explained in II.2.4.1.1. and II.2.4.1.2.

#### **I.2.3.2 Protein expression analysis of murine prostate tissues**

For protein extraction from prostatic tissue, the homogenization was performed in the presence of 400µL of RIPA lysis buffer containing 2mM phosphatase inhibitors (sodium fluoride, sodium orthovanadate and β-glycerophosphate) and two tablets of protease inhibitor cocktail (Roche). Protein extraction and western blotting were then performed as explained in II.2.4.2.1. and II.2.4.2.2.

### **I.2.4 Metabolomic analysis of murine prostate tissues**

Prostate tissues for metabolomic analysis were directly shipped frozen in dry ice for metabolite extraction by Agios Pharmaceuticals.

#### **I.2.4.1 Time of Flight-Mass Spectrometry (ToF-MS)**

Following normalization to cell number or tissue weight, metabolites were extracted with cold 80/20 (v/v) methanol/water. Samples were then dried and stored at -80°C until MS analysis. High-throughput Time-Of-Flight analysis was conducted using flow injection analysis as previously described (Fuhrer et al., 2011.). In short, samples were re-suspended and injected on an Agilent 1100 coupled with an Agilent 6520 QToF mass spectrometer with an electrospray ionization source. Mobile phase consisted of 60/40 methanol/water with 0.1% formic acid and was used to deliver 2µL of each sample to the MS, flowing at 150µL/min. Data was collected in positive mode with 4 GHz HiRes resolving power with internal lock masses. Data processing was conducted with Matlab R2010b.

#### **I.2.4.2 Liquid Chromatography-Mass Spectrometry (LC/MS)**

Quantitative liquid chromatography/mass spectrometry (LCMS) was conducted as previously described (Jha et al., 2015). A Thermo Accela 1250 pump delivered a gradient of 0.025% heptafluorobutyric acid, 0.1% formic acid in water and acetonitrile at 400 $\mu$ L/min. Stationary phase was an Atlantis T3, 3 $\mu$ m, 2.1x150mm column. A QExactive Mass Spectrometer was used at 70,000 resolving power to acquire data in full-scan mode. Data analysis was conducted in MAVEN (Melamud et al., 2010) and Spotfire.

#### **I.2.4.3 Targeted metabolomics by UPLC-MS**

Levels of dcSAM in cell cultures and tissues were analyzed by ultra-high performance liquid-chromatography coupled to mass spectrometry (UPLC-MS). Briefly, extraction and homogenization was done in methanol/acetic acid (80/20 %v/v) Speed-vacuum-dried metabolites were solubilized in 100  $\mu$ L of a mixture of water/acetonitrile (40/60 %v/v) and injected onto the UPLC/MS system (Acquity and SYNAPT G2, Waters, Manchester). The extracted ion traces were obtained for dcSAM (RT = 3.0',  $m/z$  355.16) and putrescine (RT = 2.67',  $m/z$  89.1079). Corrected signals were normalized to relative cell number.

#### **I.2.4.4 Metabolic Flux Analysis (MFA)**

U-<sup>13</sup>C<sub>5</sub>-L-methionine was purchased from Cambridge Isotope laboratories and administered intravenously (by tail vein injection, performed by Dr. Beraza). A pilot experiment was performed to establish final concentrations and time-points. For the pilot experiment, final concentrations of 100mg/Kg or 400mg/Kg for 3, 6, 10 and 24 hour pulses were tested. From the pilot experiment, 100mg/Kg dose and two time-points (1hour to detect methionine cycle related metabolites; 10hours to detect polyamine pathway related metabolites) were set. After 1hour and 10 hour pulses with U-<sup>13</sup>C<sub>5</sub>-L-methionine mice were sacrificed as specified in I.1.1. and tissues of experimental interest were harvested.

## II IN VITRO ASSAYS

### II.1 Materials

#### II.1.1 Cell lines and culture conditions

Human prostate carcinoma cell lines (PC3, LNCaP, DU145) were purchased from Leibniz-Institut DSMZ (Deutsche Sammlung von Mikroorganismen und Zellkulturen GmbH), who provided authentication certificate, or American Type Culture Collection (ATCC) in the case of RWPE1, PWR1E and 22RV1 cell-lines. Virus packaging cell lines 293FT and Phoenix Ampho and C4.2 were generously provided by the laboratory of Dr. Rosa Barrio and Pier Paolo Pandolfi, respectively. PC3, DU145, Phoenix Ampho and 293FT cell lines were cultured in Dulbecco's Modified Eagle Medium (DMEM; *Gibco Cat# 41966-029*), while LNCaP, C4.2 and 22RV1 were cultured in RPMI 1640 Medium (*Gibco Cat# 61870-010*; with GlutaMAX supplement). Both culture medias were complemented with 10% inactivated Fetal Bovine Serum (FBS) (*Gibco*), from same lot and previously analyzed to ensure experimental reproducibility, and 1% Penicillin/Streptomycin (*Gibco*) (complete media). RWPE1 and PWR1E benign prostate primary cell lines were cultured in Keratinocyte-Serum Free Medium (K-SFM; *Gibco Cat# 17005-034*), supplemented with human recombinant Epidermal Growth Factor 1-53 (EGF 1-53) and Bovine Pituitary Extract (BPE). See **Table M6** for cell line specifications.

**Table M6:** Detailed list of the characteristics of the different PCa cell-lines employed in the work.

Cell-line	Cell type	Morphology	Derivation	<i>Pten</i> status	Cultur media
<b>RWPE1</b> CRL-11609™	Prostate epithelial	Epithelial	From the peripheral zone of a histologically normal adult human prostate transfected with HPV-18	Positive	K-SFM
<b>PWR1E</b> CRL-11611™	Prostate epithelial	Epithelial	From a normal prostate with mild hyperplasia, immortalized with Ad12-SV40	Positive	K-SFM
<b>PC3</b> (ACC 465)	Prostate adenocarcinoma	Epithelial-like	Bone marrow metastasis of grade IV prostate cancer after androgen suppression therapy	Negative	DMEM
<b>DU145</b> (ACC 261)	Prostate carcinoma	Epithelial-like	From metastatic central nervous system lesion	Positive	DMEM
<b>LNCaP</b> (ACC 256)	Prostate carcinoma	Fibroblastoid	From supraclavicular lymph node metastasis	Negative	RPMI
<b>C4-2</b>	Prostate carcinoma	Fibroblastoid	LNCaP derived androgen-resistant	Negative	RPMI
<b>22RV1</b> CRL-2505™	Prostate carcinoma	Epithelial	From CWR22 xenograft propagation after castration-induced regression and relapse	Positive	RPMI
<b>HEK293FT</b>	Human Embryonic Kidney Cells	Fibroblastoid	From human primary embryonal kidney transformed by adenovirus type 5	Negative	DMEM
<b>HEK293 Ampho</b>	Human Embryonic Kidney Cells	Fibroblastoid	From human primary embryonal kidney transformed by adenovirus type 5	Negative	DMEM

All cell lines were grown at 37°C in a humidified atmosphere of 5% CO<sub>2</sub>. Cells were regularly cultured in 100mm dishes and split every 2-3 days, maintaining them below 80-90% density, up to 30 passages maximum. To split the cells they were incubated in a trypsin-EDTA solution (*Gibco*) at 0.05% for 3-5 minutes at 37°C and resuspended in fresh complete media. All cell-lines were periodically analyzed by PCR for mycoplasma presence and replaced or treated in case of positive result. For cell counting, after trypsinization, cells were diluted 1:2 in Trypan Blue Dye (*Amresco*) and 10µL were loaded in a Neubauer chamber to count viable cells by optical microscopy (*Olympus CKX31*). The Trypan Blue dye allows to determine cell viability based in the fact that damaged or dead cells show disrupted plasma membrane and allow the internalization of the dye staining their cytoplasm in blue, while alive cells remain non-stained. In general experiments were performed with technical duplicates or triplicates and a minimum of three biological replicates (n=3 minimum).

**Table M7:** Approximate cell-number seeded according to each experimental technique.

Assay	Cellular density per well				Plate type	
	PC3	LNCaP	DU145	22RV1		
Protein/RNA extraction	100000	300000	120000		6-well plate	
Growth Curves	5000	30000	7500		12-well plate	
Soft Agar	2500	5000	3000		6-well plate	
Foci Formation			500			
Cell-Cycle		250000			6-well plate	
BrDU Incorporation		40000			12-well plate	
Metabolo mics	GNTM OE	350000	1000000	425000	2000000	100mm
	AMD1 acute Silencing	100000- 110000		120000- 200000		6-well plate
	AMD1 Inducible Silencing			50000- 100000		6-well plate
	AMD1 OE			200000		6-well plate

## II.1.2 Drugs

Information regarding the different inhibitors and drugs used for this thesis work are depicted in **Table M8**.

**Table M8:** Commercial information and experimental specifications for the different drugs used throughout the thesis work.

Drug	Supplier	Dose	Function
<b>Rapamycin</b>	LC Laboratories (Cat.# R-5000)	20nM	Specific mTOR inhibitor
<b>RAD001 (Everolimus)</b>	Provided by Dr. Alimonti and Dr. Serra	10mg/Kg	Rapamycin derivative, mTOR inhibitor
<b>Torin-1</b>	Tocris Bioscience (Cat.#4247)	125-250nM	Potent and selective ATP-competitive mTORC1 and mTORC2 inhibitor
<b>MK2206</b>	Shellectchem (Cat.# S1078)	500nM	Highly selective allosteric pan-AKT inhibitor
<b>SAM486A</b>	Novartis	0.5-1µM	Competitive AMD1 inhibitor
<b>Cicloheximide</b>	Sigma	5µg/mL	Protein synthesis inhibitor in eukaryotes
<b>MG132</b>	Provided by Dr. Rodriguez	5µM	Potent, membrane-permeable proteasome inhibitor

## II.2 Methods

### II.2.1 Cloning

Different cloning strategies were followed to obtain the lentiviral and retroviral vectors required for GNMT overexpression, PTEN (Wild-Type, WT; and C124S) re-expression, and AMD1 overexpression and silencing. The different strategies are briefly detailed below (See **Table M9** for primer specifications):

#### **HA-GNMT-TRIPZ:**

PCEP4-GNMT vector was amplified using high-fidelity PCR with the primers specified in **Table M9** (GNMT01 and GNMT02) to generate a HA-GNMT cassette containing the restriction sites for AgeI-MluI. GNMT01 and GNMT02 provide Kozak, ATG, and stop sequences. The resulting amplicon was subcloned with TOPO Cloning technology. Then, TOPO was digested with AgeI-MluI and the GNMT bearing fragment was introduced in an inducible TRIPZ vector.

#### **TRIPZ-YFP-PTEN (WT and C124S, catalytic-dead mutant):**

TRIPZ-FF3shRNA was digested with AgeI-MluI, which releases the tRFP, shRNA mir, and barcode from the plasmid backbone. Vector was gel-purified. Using PTEN expression clones (WT or C124S; from Dr. Pandolfi's lab), a YFP-GSG-PTEN cassette was created by overlap-extension PCR using high-fidelity PCR (KAPA Biosystems). Outer primers PTEN03 and PTEN02 provide Kozak, ATG, and stop sequences. Inner bridging primers (PTEN04 and PTEN05) join the YFP and PTEN portions with a flexible Gly-Ser linker. The final resulting amplicon (~1.9kb) was cleaned up, digested with AgeI-MluI, gel-purified and cloned into TRIPZ-FF3shRNA AgeI-MluI. Colonies were screened by restriction digest and positives confirmed by Sanger sequencing.

#### **sh3 AMD1 pLKO Tet ON:**

Lentiviral inducible pLKO Tet ON vector was opened using AgeI-EcoRI (Fermentas/Takara-Clontech). Specific shRNA sequences for AMD1 were obtained from SIGMA (MISSION® shRNA) (see **Table M9**). Complementary primers were designed, in which an EcoRI site was added in the 5' end, coinciding with complementary AgeI site in the template sequence. For the annealing, 11.25 µL of each primer were added to a 25 µL reaction with 2.5 µL 10X annealing buffer (100mM NaCl, 50 mM HEPES, pH=7.4). The reaction was added to a preheated thermoblock (95°C), allowed to incubate for 5 min, and then the thermoblock was switched off, allowing slow cooling to room temperature. 2.5 µL of annealed oligos were ligated to 4 µL of linearized vector, in a reaction of 10 µL, with 2 µL of 5x Invitrogen ligase buffer and 1.5 µL of NBE ligase (Invitrogen). After 1hr of incubation at room temperature (RT), ligation was transformed into competent XL-10 Gold E. coli and selected on Amp plates. Positive colonies were confirmed by restriction digest and Sanger sequencing.

**Table M9:** Information about the specific primers utilized for the different cloning approaches.

Number	Name	Purpose	Sequence
GNMT01	AgeI-HA-GNMT F	To produce a PCR product with AgeI restriction site in 5' end	ACCGGTGCCACCatggcttatccttacgacg tgctgactacgccATGGTGGACAGCGT GTACCGGACCCGC
GNMT02	HA-GNMT-MluI R	To produce a PCR product with AgeI restriction site	ACGCGTTCAGTCTGTCTCTTGAG CACGTGGATG
PTEN02	MluI.PTEN.rev	2-step PCR cloning of PTEN WT and mutants with YFP tag; for cloning as AgeI-MluI into TRIPZ	gatatcaccggtTCAGACTTTTGTAAATTT GTGTATGCTGATC
PTEN03	AgeI.KozGFP.f or	2-step PCR cloning of PTEN WT and mutants with YFP tag; for cloning as AgeI-MluI into TRIPZ	agatcaccggtgccaccATGGTGAGCAAG GGCGAGGAGC
PTEN04	GFP.GSG.PTEN.for	2-step PCR cloning of PTEN WT and mutants with YFP tag; for cloning as AgeI-MluI into TRIPZ	GGCATGGACGAGCTGTACAAGggca gcggtATGACAGCCATCATCAAAGAG
PTEN05	GFP.GSG.PTEN.rev	2-step PCR cloning of PTEN WT and mutants with YFP tag; for cloning as AgeI-MluI into TRIPZ	CTCTTTGATGATGGCTGTCATaccgct gccCTTGACAGCTCGTCCATGCC
sh3AMD T01	sh3 AMD top	To introduce the shRNA in the pLKO Tet ON vector	CCGGGTCTCCAAGAGACGTTTCAT TCTCGAGAATGAAACGTCTCTTGGGA GACTTTTTG
sh3AMD B01	sh3 AMD bottom	To introduce the shRNA in the pLKO Tet ON vector	AATTCAAAAAGTCTCCAAGAGACGT TTCATTCTCGAGAATGAAACGTCTC TTGGAGACCCGG
AC.AMD 01	HABMSXNC.for	Linker for LNCX; HIII-Age1-Bgl2-Mlu1-Sal1-Xho1-Not1-Cla1	AGCTTACCGGTAGATCTACGCGTG TCGACCTCGAGGCGGCCGCAT
AC.AMD 02	HABMSXNC.rev	Linker for LNCX; HIII-Age1-Bgl2-Mlu1-Sal1-Xho1-Not1-Cla1	CGATGCGGCCGCTCGAGGTCGA CACGCGTAGATCTACCGGTA
AC.AMD 07	BamHI.NheI.MYC.AMD1.for	to amplify AMD1/mutants with a N-terminal MYC tag	GATCGGATCCGCTAGCGCCACCAT GGAGCAGAAGCTGATCTCCGAGGA GGACCTGGGCTCCATGGAAGCTGC ACATTTTTTCGAA
AC.AMD 10	BamHI.Sall.HA. rev	to amplify AMD1/mutants with C-terminal HA	GATCGGATCCGATCGTCTGACTCAA GCGTAATCTGGAACATCGTATGGG TA
3336	AMD1.S298A.qc. for	to mutate S298 in AMD1	aaatgtcgcacagtgtgctGCCccccagaag attgaaggtttaagc
3337	AMD1.S298A.qc. rev	to mutate S298 in AMD1	gcttaaaccttcaatcttctggggGGCagc aagcactgtgcgacattt
3338	AMD1.S298D.qc. for	to mutate S298 in AMD1	aaatgtcgcacagtgtgctGACccccagaaga ttgaaggtttaagc
3339	AMD1.S298D.qc. rev	to mutate S298 in AMD1	gcttaaaccttcaatcttctggggGTCagcaagc actgtgcgacattt

### LNCX-neo (HCX):

Retroviral expression vector LNCX-neo was opened using HindIII-ClaI (Fermentas/Thermo). A multiple cloning site was created by inserting a double-stranded synthetic oligo pair into the HindIII-ClaI site, to create LNCX-neo (HCX). For the annealing, 5µl of each oligo (100 µM stock) (Metabion) were added to a 50µl reaction, including 200 mM NaCl, 10 mM Tris-HCl pH 7.9, 20mM MgCl<sub>2</sub> (2X NEB Buffer 3). The reaction was added to a preheated thermoblock (95 °C), allowed to



incubate for 5 min, and then the thermoblock was switched off, allowing slow cooling to room temperature. Finally, ~100 ng of linearized vector was ligated to 1 µl of annealed oligos, in a reaction of 10 µl, with 2 µl of 5x T4 DNA ligase buffer and 1 µl of T4 DNA ligase (Invitrogen). After 1h of incubation at RT, ligation was transformed into competent XL-10 Gold E. coli and selected on Amp plates. Positive colonies were screened by PCR, confirmed by restriction digest and Sanger sequencing.

#### **LNCX-MYC-AMD1(WT)-HA:**

A retroviral expression construct for N-terminal MYC- and C-terminal HA-tagged AMD1 was created. Primer AC.AMD07 and AC.AMD08 were used to amplify the AMD1 ORF using high-fidelity PCR (KAPA Biosystems). The resulting amplicon (~1kb) was digested with BamH1-Sal1, and cloned into LNCX-neo (HCX) Bgl2-Sal1.

#### **LNCX-MYC-AMD1(S298A)-HA (phospho-dead mutant):**

These mutants were created by 2-step overlap extension PCR. Briefly, oligos AC.AMD07 and mutagenic oligos 3337 (or 3339) were used to create a 5' amplicon, while mutagenic oligos 3336 (or 3338) and AC.AMD10 were used to create a 3' amplicon, using AMD1(WT) ORF as a template. Amplicons were gel-purified, mixed, elongated using 10 cycles of melting/annealing/extension, without amplification. Outer primers AC.AMD07 and AC.AMD10 were added and PCR with amplification was carried out for 25 cycles. The resulting composite amplicons were cleaned up, digested with BamH1-Sal1, gel-purified, and then cloned into LNCX-neo (HCX) Bgl2-Sal1. Colonies were screened by restriction digest and positives confirmed by Sanger sequencing.

## **II.2.2 Virus production and target cell line infection**

Virus production was performed by employing a packaging cell line and the target cell line in which the transgene was aimed to be introduced.

The general protocol was similar for both lentivirus and retrovirus production (**Fig. M7**):

- **Day1:**
  - Morning: Packaging cells were seeded at high density ( $4 \times 10^6$  cells/100mm plate)
  - Afternoon: Packaging cells were transfected
  
- **Day2:** Packaging cells' media was changed to fresh culture-media and target cell line was seeded.
  
- **Day3:** Target cells were first infected with virus containing supernatant (SN) from packaging cells and fresh media was added to these cells for further virus production

- **Day4:** Second infection of target cells was performed with virus containing SN and packaging cells were discarded.

For infection, SN from packaging cells was filtered with 0.45µm filters and 4mL of fresh media were added to a total of 13mL. Protamine sulfate (Stock 8mg/ml) was added to the mixture (1:1000 dilution) to increase infection efficiency.

- ◆ **Day5:** Target cells were submitted to selection with the corresponding antibiotic each

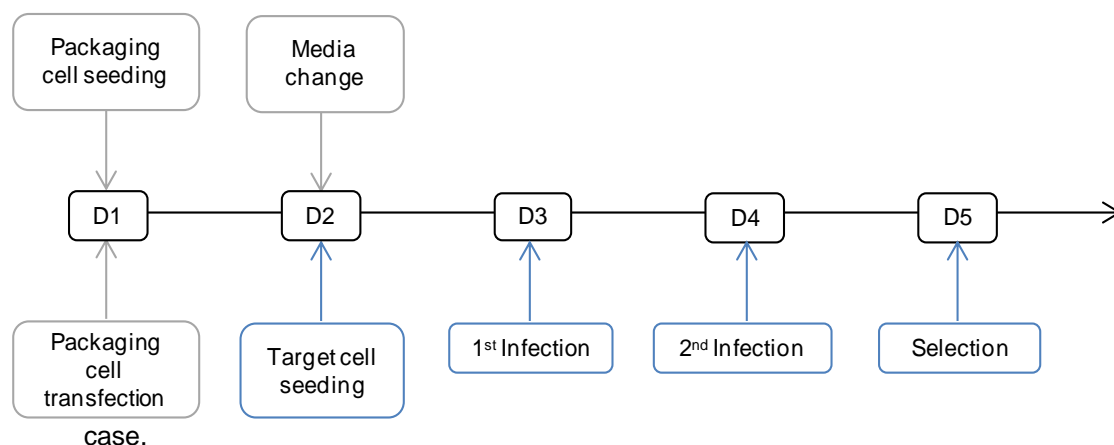


Figure M7. Schematic showing the experimental design followed for virus production.

### II.2.2.1 Transient transfection in HEK293 cells

Virus production was performed by transient transfection of Human Embryonic Kidney 293 cells (HEK293). In transient transfection, the exogenous DNA is not inserted into the genome, and hence, it is diluted in subsequent cellular divisions.

Cells were transfected with packaging vectors and the vector of interest (transfer vector), by calcium phosphate method, to produce viral particles. DNA was first diluted in milliQ-water and then CaCl<sub>2</sub> was added to a final concentration of 125 mM. This DNA solution was then mixed with same volume of a 2x HEPES-Buffered Solution (HBS) [50mM HEPES, 280mM NaCl, 10mM KCl, 1.5mM Na<sub>2</sub>HPO<sub>4</sub> · 2H<sub>2</sub>O, 12mM dextrose, pH=7.05] in the presence of oxygen to facilitate the formation of calcium phosphate crystals. These crystals form pores in the cytoplasmic membrane allowing exogenous DNA entrance.

4x10<sup>6</sup> HEK293 cells were seeded for each transfection and culture media was changed to fresh media 16h post-transfection to induce viral particle production. Then, the viral particles produced were used to infect target cell lines for genetic modification.

## II.2.2.2 Lentivirus production and target cell-line infection

Lentivirus production was performed in HEK293FT cells transfected with packaging vectors and the vector carrying the transgene (**Fig M8**). We used lentiviral infection to over-express GNMT and to silence AMD1 in PCa cell lines. Depending on the back-bone vector containing our gene or shRNA of interest, second generation or third generation packaging vectors were employed.

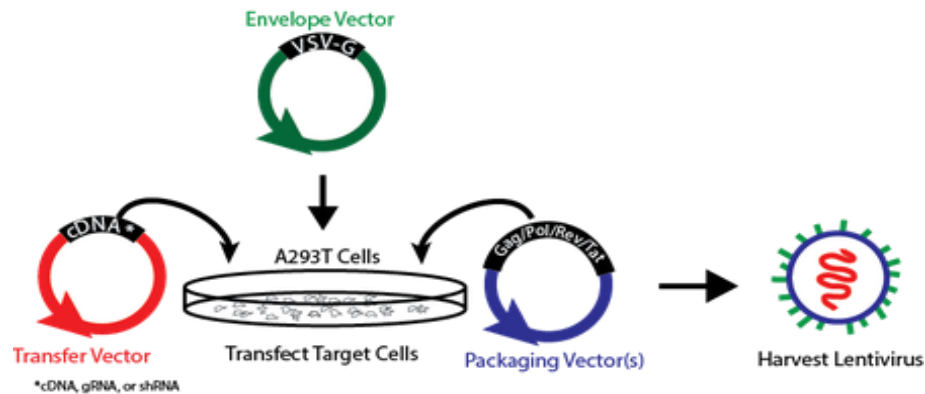


Figure M8. Representative image showing packaging system and lentivirus production in HEK293 cells.

### II.2.2.2.1 Second Generation Lentivirus production

GNMT and PTEN (WT and C124S mutant) were introduced in a doxycycline inducible TRIPZ vector. TRIPZ vectors are not compatible with third generation packaging systems. Thus, a second generation strategy was followed to produce the virus. Second generation lentiviral vectors consist of three plasmids normally: the transfer vector, containing all the *cis*-acting sequences required and the transgene to be delivered, and two packaging vectors psPAX2 and pVSV-G, which provide the *trans*-acting factors (**Fig. M9**). The separation of *cis*-acting and *trans*-acting sequences reduces the probability of recombination producing replication-competent viral particles. In this particular case, due to the TRIPZ backbone of the GNMT and PTEN bearing vector, as aforementioned, a pTAT vector was needed to help in transcription (See **Table M10**).

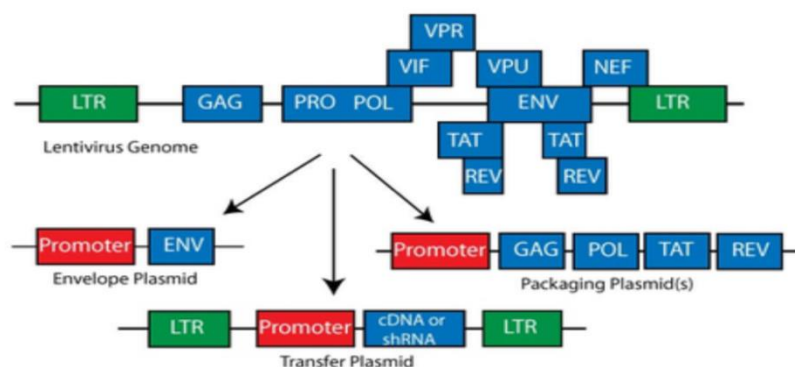


Figure M9. Informative image showing the fragmentation of the lentiviral genome into a second generation packaging system.

Second generation lentivirus production was performed following standard protocol mentioned in II.2.1. Target cell-lines (PC3, DU145, LNCaP and 22RV1) were submitted to puromycin (2ug/mL) selection for 48-72h.

**Table M10:** Information regarding the specific vectors employed for second generation lentivirus production.

Vector Name	Role	Encoding sequences	Function	Origin	Amount transfected
<b>psPAX2</b>	Packaging vector	Gag-Pol	integrase, reverse transcriptase, and structural proteins	Dr. James D. Sutherland	1.66µg
		RRE	Rev-responsive element		
		Rev	Enhancer of unspliced viral genomic RNA nuclear export		
<b>pVSV-G</b>	Packaging vector	VSV-G	Envelope protein	Dr. James D. Sutherland	1.66µg
<b>pTAT</b>	Helper vector	TAT	Enhances transcription efficiency	Dr. James D. Sutherland	1.66µg
<b>HA-GNMT-TRIPZ</b>	Transfer vector	<i>GNMT</i>	Gene to over-express	Dr. James D. Sutherland	5µg
<b>TRIPZ-YFP-PTEN-WT</b>	Transfer vector	<i>PTEN-WT</i>	Gene to over-express	Dr. James D. Sutherland	5µg
<b>TRIPZ-YFP-PTEN-C124S</b>	Transfer vector	<i>PTEN-C124S</i>	Mutant to over-express	Dr. James D. Sutherland	5µg

### II.2.2.2.2 Third Generation Lentivirus production

Third generation virus (**Fig. M10**) were generated for constitutive and inducible silencing of AMD1 in DU145 and PC3 cells. A set of five short-hairpin RNA (shRNA) sequences against AMD1 in a pLKO backbone were purchased from SIGMA (MISSION® shRNA Bacterial Glycerol Stock).

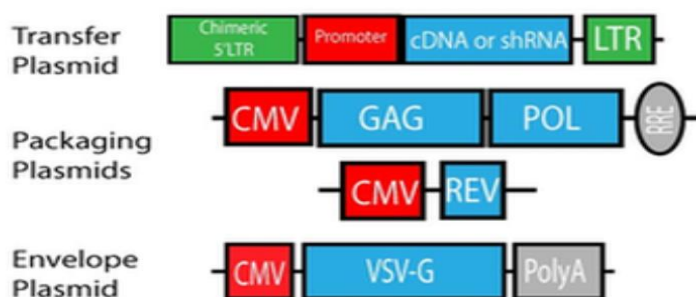
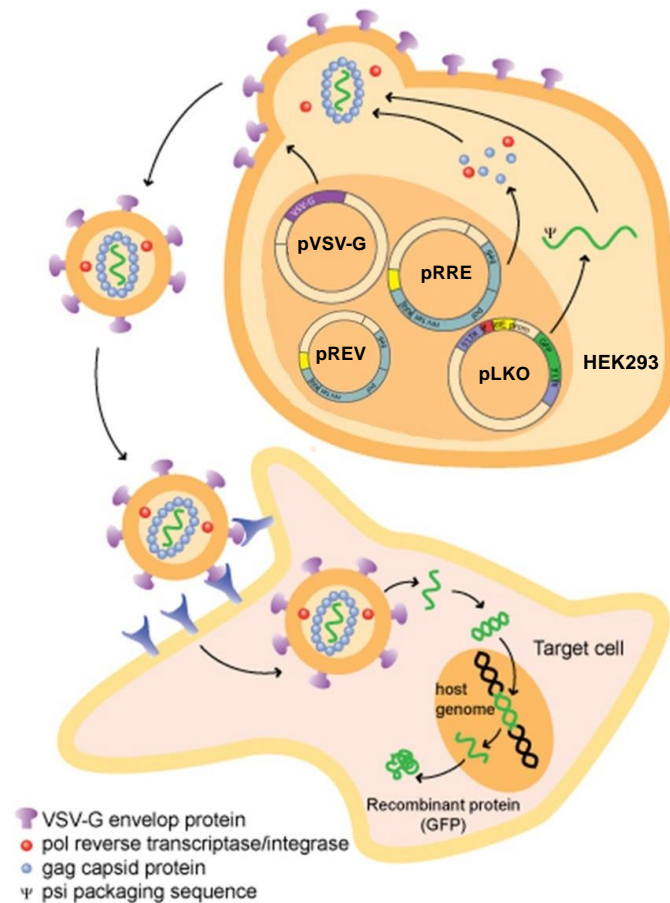


**Figure M10.** Informative image showing the fragmentation of the lentiviral genome into a third generation packaging system.

The set of shRNAs was validated and two efficient shRNAs were selected for further experiments. One of those two selected sequences was then cloned into a doxycycline inducible pLKO backbone in collaboration with Dr. Sutherland. pLKO vectors are compatible with third generation lentivirus production. Third generation lentivirus require three packaging vectors (pRRE, pREV, pVSV-G; which decreases recombination probability and makes them more secure to handle than second generation ones) and transfer vector (See **Figure M10,11** and **Table M11**).



Adapted from <http://www.invivogen.com/review-lentiviral-vectors>

**Figure M11.** Illustrative image explaining the third generation lentiviral production in HEK293 cells and posterior infection of target cells.

**Table M11:** Information regarding the specific vectors employed for third generation lentivirus production

Vector Name	Role	Encoding sequences	Function/Sequence	Origin	Amount
<b>pRRE</b>	Packaging vector	Gag-Pol	Integrase, reverse transcriptase, and structural proteins	Dr. James D. Sutherland	1.66µg
		RRE	Rev-responsive element		
<b>pREV</b>	Packaging vector	Rev	Enhancer of unspliced viral genomic RNA nuclear export	Dr. James D. Sutherland	1.66µg
<b>pVSV-G</b>	Packaging vector	VSV-G	Envelope protein	Dr. James D. Sutherland	1.66µg
<b>sh3 AMD1-pLKO</b>	Transfer vector	shRNA against AMD1	CCGGGTCTCCAAGAGACGT TTCATTCTCGAGAATGAAAC GTCTCTTGGAGACTTTTTG	SIGMA TRCN0000078 462	5µg
<b>sh4 AMD1-pLKO</b>	Transfer vector	shRNA against AMD1	CCGGCCCATTAAAGTAGTGT TCTATACTCGAGTATAGAAC ACTACTTAATGGGTTTTTG	SIGMA TRCN0000078 458	5µg
<b>sh3 AMD1 pLKO TeT ON</b>	Transfer vector	shRNA against AMD1	CCGGGTCTCCAAGAGACGT TTCATTCTCGAGAATGAAAC GTCTCTTGGAGACTTTTTG	Dr. James D. Sutherland	5µg

### II.2.2.2.3 Constitutive Silencing of AMD1

First attempts to silence AMD1 were performed with SN infection as explained in II.2.1.2. However, due to the high silencing efficiency and the aggressive phenotype (high percentage of dead) observed upon AMD1 silencing, freshly infected cells were required per experiment, because stable growth of AMD1 silenced cells was not viable.

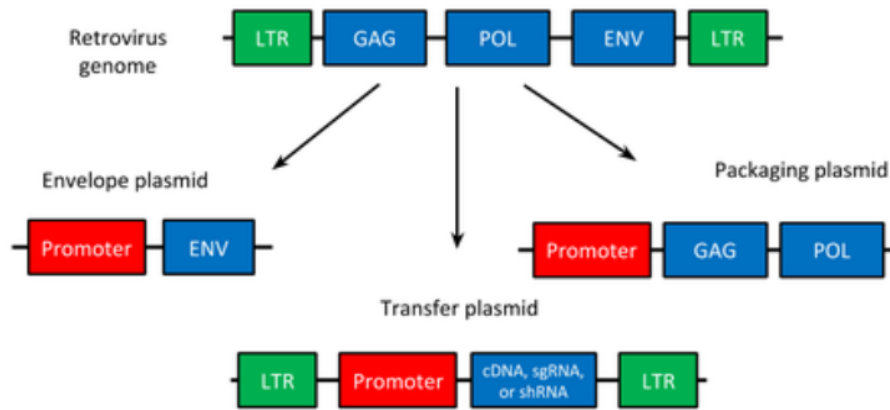
To optimize the timing per infection, virus was submitted to concentration procedures. Concentrated virus aliquots were generated following the time-schedule mentioned in Fig. M7. until day 3, in which the SN was collected, filtered and fresh media was added to HEK293FT cells. 3 volumes of clarified supernatant were combined with 1 volume of Lenti-X Concentrator and, after gently mixing it by inversion, it was incubated at 4°C until next day SN collection. On day 4, same procedure was repeated and SN was incubated at 4°C for 1-3 hours. SN from both days were mixed and centrifuged at 1500G for 45 minutes at 4°C. After centrifugation, SN was discarded and the pellet was resuspended in 400µl of PBS and aliquoted in 20uL aliquots, based on previous experience. Once the virus was concentrated, target cells were seeded on day 1 in the morning, infected with an aliquot in the afternoon, infected for the second time on day 2 and submitted to puromycin (2ug/mL) selection on day 3 for three days. In this ways infection protocol was shortened from 5 days to 3 days.

### II.2.2.2.4 Inducible AMD1silencing

Inducible silencing of AMD1 was performed by SN infection with a third generation system following the timing aforementioned in II.2.1. Target cells were submitted to selection pressure with puromycin (2ug/mL). Packaging and transfer vector information is mentioned in II.2.1.2.2. (See **Table M10**).

### II.2.2.3 Retrovirus production and target cell-line infection

Retrovirus production was performed transfecting HEK293 Ampho cells. These cells derive from HEK 293 cells, but were generated to stably express the viral *gag-pol* and *env* genes (**Fig. M12**), allowing rapid production of high-titer replication-incompetent amphotropic retrovirus. Thus, for retrovirus generation these packaging cells were transfected with the transfer vector only (**Fig. M13, right**), following the time-line specified in II.2.1. Target DU145 cells were submitted to G418 (Geneticin) selection (starting from 200ug/mL and scaling the dose to 1mg/mL to reach total selection) during 3-4 weeks, because puromycin was used to maintain stable expression of the viral genes in HEK293 Ampho cell generation. Retrovirus mediated transduction was performed to over-express wild-type and phospho-mutant (S298A) AMD1 in DU145 cells (**Table M12**).

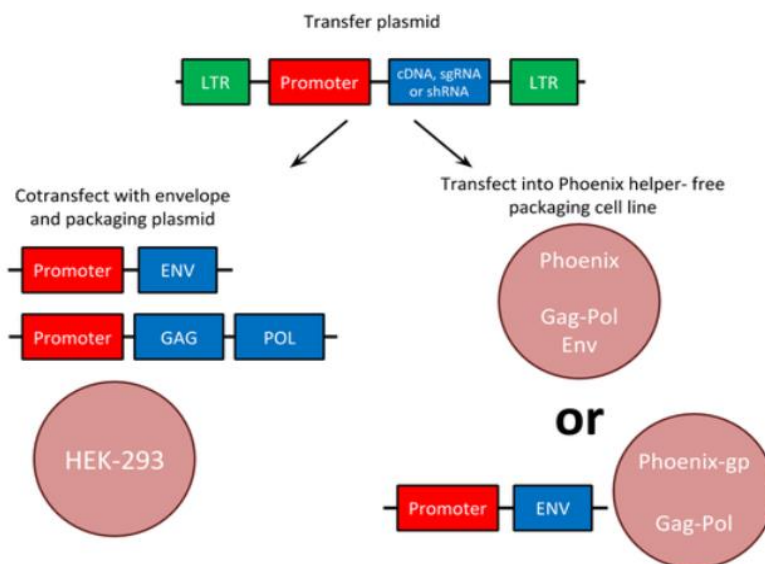


Adapted from <https://www.addgene.org/viral-vectors/retrovirus/retro-guide/>

Figure M12. Informative image showing the fragmentation of the retroviral genome into the packaging system.

Table M12: Information regarding the specific vectors employed for retrovirus production.

Vector Name	Role	Encoding sequences	Function	Origin	Amount transfected
LNCX Neo (HCX) HABMSXNC linker	Transfer vector	Empty vector	Control cells	Dr. James D. Sutherland	5µg
LNCX-MYC-AMD1-HA	Transfer vector	AMD1-WT	Gene to over-express	Dr. James D. Sutherland	5µg
LNCX-MYC-AMD1 <sup>S298A</sup> -HA	Transfer vector	AMD1-S298A	Mutant to over-express	Dr. James D. Sutherland	5µg



Adapted from <https://www.addgene.org/viral-vectors/retrovirus/retro-guide/>

Figure M13. Informative image showing different retroviral packaging methods.

## **II.2.3 Cellular analysis**

### **II.2.3.1 Cell-growth analysis by crystal violet staining**

Cells were seeded in 12 well-plates (5000-8000 cells/well) for days 0, 2, 4 and 6 or 0, 1, 2 and 3 (depending on the experiment). Each plate was washed with 10% PBS, fixed with 10% formalin and stored at 4°C for further processing of all plates at the same time. Once fixed (> 15 minutes with formalin), cells were stained with crystal violet (0,1% crystal violet, 20%) for 40 minutes. After washing (4xdH<sub>2</sub>O) and air drying the plates, precipitates were dissolved with 10% acetic acid for 30 minutes and absorbance was measured in 96well-plates by spectrophotometer at 595nm.

### **II.2.3.2 Anchorage-independent growth (Soft agar)**

Anchorage independent growth is considered an aggressiveness parameter, utilized to characterize cellular phenotypes in vitro. For cell plating in anchorage independent conditions, 6 well-plates were previously coated with a lower layer of 0,6% agar (SeaKem LE agarose, Lonza)/medium mixture (3mL/well) and stored at 4°C for at least 30 minutes to let the agar solidify. Previous to the upper layer seeding, cells (3000-5000 cells/well) were suspended in a 0.3% low melting agar/medium mixture and 1,5mL/well were plated. Low melting agar allows to maintain the agar/cell mixture liquified at lower temperature, to avoid harming cells. Plates were stored at 4°C (around 20 mins) to allow the solidification of upper layer and then incubated at 37°C in a humidified atmosphere of 5% CO<sub>2</sub> for 3-4 weeks, until colony detection.

### **II.2.3.3 Foci formation assay**

Foci formation assay measures the clonogenic capacity of transformed cells (Alvarez et al., 2014), by means of number of foci formed at very low seeding cellular density. To perform these experiments, 500 cells/well were seeded in 6well/plates in adherence and incubated at 37°C in a humidified atmosphere of 5% CO<sub>2</sub> for 10 days. Plates were then fixed with 10% formalin solution at 4°C for at least 15 minutes, washed with PBS and stained with crystal violet (0.1% crystal violet, 20% methanol) for 40 minutes. After washing (4 x dH<sub>2</sub>O) and air drying, plates were scanned to obtain digitalized images for foci counting. After scanning the plates, crystal violet precipitates were dissolved in 10% acetic acid for 30 minutes and absorbance was measured in 96 well-plates by spectrophotometer at 595 nm, for cell number quantification.



### II.2.3.4 DNA synthesis rate analysis by bromo deoxyuridine (BrdU)

One of the most commonly used techniques to analyze cell proliferation is the incorporation of the thymidine pyrimidine analogue BrdU (5-bromodeoxyuridine) into newly replicated DNA, based on the direct correlation between DNA replication and cell division.

#### II.2.3.4.1 BrdU Incorporation

This analogue when added in culture media gets incorporated into DNA, during DNA replication process (Darzynkiewicz and Juan, 2001). Since monoclonal antibodies were developed to target incorporated BrdU into DNA (Gratzner, 1982), BrdU has been extensively used to estimate cell proliferation by immunofluorescence. In this thesis work BrdU was used in asynchronous cultures. Cells were seeded onto coverslips and once adhered BrdU was added to culture media to a final concentration of 0,2µg/mL and incubated for 3-4h at 37°C. After incubation cells were washed with PBS and fixed with 4% paraformaldehyde (PFA) solution in PBS for 15 minutes. Cells were washed twice to eliminate remaining PFA and coverslips were stored in PBS at 4°C until processing.

#### II.2.3.4.2 BrdU exposure and detection by immunofluorescence (IF)

BrdU needs to be exposed to detect it with monoclonal antibodies. To this end, coverslips were incubated with HCl 2N for 5 minutes and quickly washed twice with PBS to further neutralize the acid with Borax (Sodium tetraborate 0.1M, pH8.5) for two minutes. Cells were permeabilized with Triton X100 0.1% for 5 minutes and 10% goat serum was employed as blocking reagent for 30 minutes at RT. Primary antibody against BrdU (BD Pharmingen™, Cat# 555627) was incubated at 1:100 dilution overnight at 4°C. The next day, secondary anti-mouse antibody (labelled with Alexa Fluor® 594 dye) was incubated at 1:1000 dilution in 10% goat serum for 1h in the dark. Finally, cells were stained with DAPI (1:1000 dilution in PBS) for nuclear staining and coverslips were mounted onto slides with home-made Mowiol. The slides were stored at 4°C in the dark until analysis with the upright fluorescent microscope Axio Imager D1 (Carl Zeiss).

### II.2.3.5 Cell cycle analysis

Propidium Iodide (PI) is an intercalating fluorescent agent extensively used for cell cycle analysis (Krishan, 1975). Harvested cells were suspended in 1mL of PBS and fixed drop by drop with 2.5 mL of absolute ethanol (70% final ethanol concentration). Samples were incubated overnight at -20°C for fixation. Next, cells were centrifuged and suspended in 200-500µL of PI staining solution [RNase 25ug/ml (stock 1mg/ml), Triton X-100 0,05%, PI: 1 µg/ml (stock 1mg/ml)]. Samples were incubated for 20-40 minutes at 37°C and analyzed by flowcytometry.

## II.2.4 Molecular Assays

Cells were seeded for a final density of around 70-80% in 6 well plates. Plates were washed with PBS and processed or snap-frozen in liquid-nitrogen for later protein or RNA extraction, unless otherwise specified.

### II.2.4.1 Gene expression analysis

#### II.2.4.1.1 RNA extraction and retrotranscription

RNA was extracted using NucleoSpin® RNA isolation kit from Macherey-Nagel (ref: 740955.240C) according to manufacturer's protocol and concentration was determined by Nanodrop ND-1000 Spectrophotometer.

1µg of the obtained RNA was used for complementary DNA (cDNA) synthesis using qScript cDNA Supermix from Quanta (ref. 95048). Resulting cDNA was diluted 1/6-1/30 in fresh mQ water (depending on the expression levels of each gene) and 1µL was used for RT-QPCR reaction.

#### II.2.4.1.2 Real time quantitative PCR (RT-Q-PCR)

RT-QPCR was performed using Viiia7 system from Life Technologies'. The RT-QPCRs were performed according to the following program: 2min at 50°C and 10min at 95°C (Hold Stage) followed by 40 cycles of 15sec at 95°C (denaturalization) and 1min for 60°C (annealing and elongation). Polyamine pathway related enzyme gene expression was analyzed with primers and probes from Universal Probe Library from Roche. The Universal Probe Library Assay Design Center is available on-line in: <http://lifescience.roche.com/shop/en/mx/overviews/brand/universal-probe-library>. This tool allows the design of primers and assigns the respective probe needed for each reaction in order to build a TaqMan assay. Methionine cycle-related enzyme gene expression was analyzed by SYBRGreen Technology and primers were kindly provided by Dr. Woodhoo (CIC bioGUNE). For the analysis of reference house-keeping genes (*Gapdh*, *GAPDH* and  $\beta$ -*ACTIN*) Taqman Probes were used. Two different master mixes were used to catalyze the reaction: FastStart Universal Probe Master (Roche ref. 04914058001) and TaqMan® Universal Master Mix II (Life Technologies ref. 4440046). For quantification of changes in gene expression, Comparative Ct method was selected. See **Table M13** for specific primer sequences and references.

**Table M13:** Table detailing the specific primer sequences and probe numbers from Universal Probe Library from Roche, specific primers for SYBR technology and references of Taqman technology probes used for RT-QPCRs.

Gene	Species	Technology	Forward 5'-3'	Reverse 5'-3'	Probe
<i>SpmS</i>	Mouse	UPL Roche	CAGCAGCTCGACTTCAA	CCAGGTGTGCACTGACTCTG	#68
<i>SpdS</i>	Mouse	UPL Roche	TCCAGTGCGAGATTGATGAG	CCCACGTGGAGAGTCAGC	#78
<i>Amd1</i>	Mouse	UPL Roche Taqman	GACGCATGAATTCTGACTGC Mm04207265	TGGGTCAAGCTCACTCATCA	#47
<i>Odc1</i>	Mouse	UPL Roche	GCTAAGTCGACCTTGAGGA	AGCTGCTCATGGTTCTCGAT	#80
<i>Sat1</i>	Mouse	UPL Roche	TCTTGAAGACTTCTTCGTGATGAG	CATACTGCTGCAGCGACACT	#110
<i>Paox</i>	Mouse	UPL Roche	ACCGTTCGGGGAGTATACAGT	TCGGTAAGTCCTTGGTAGCC	#26
<i>Slc3a2</i>	Mouse	UPL Roche	CAAAGTGCCAAAGAAAAGAGC	CTGAGCAGGGAGGAACCCAC	#81
<i>Cbs</i>	Mouse	SYBR	CTTCAGGGACATCCCAGTGT	AGCTGCCAGGTACATCTGCT	
<i>Cth</i>	Mouse	SYBR	TGTTAAGGCCTTCCTCAAAA	GTCCTTCTCAGGCACAGAGG	
<i>Mthfr</i>	Mouse	SYBR	CAGGTCATCCTCGAAGCTCT	AGACCTGGTGAAGCACATCC	
<i>Ms</i>	Mouse	SYBR	CATCCAAGAGTGTGGTGGTG	ATAAACGTGGGCTTCACTGG	
<i>Sahh</i>	Mouse	SYBR	CCTGGCATCTCATTCTCAGC	CGCCAGCATGTCTGATAAAC	
<i>Bhmt</i>	Mouse	SYBR	GAACTCCCGATGAAGCTGAC	CTTTGCACTGGAAAAGAGGG	
<i>Pemt</i>	Mouse	SYBR	AGTTCTCTGCTCCCATCTCG	AGTTCTCTGCTCCCATCTCG	
<i>Mat2a</i>	Mouse	SYBR	CTTCCTTCAGAGAGCAGTGCTTT	CTTACGCCATACCCAGAATACA	
<i>Mat2b</i>	Mouse	SYBR	CCAGTGGCACCAGTAATGAG	AGCTCTCCATCCACTTCGTC	
<i>Gnmt</i>	Mouse	SYBR Taqman	AAGCCCTCTCCACCAGC Mm 4689 m1	AGTACAAGGCGTGGTTGCTT	
<i>Gnmt 338</i>	Mouse	SYBR	AAAGGATGGCTCTTTCTCC	GTGCTGACGTAGCCTGTG	
<i>Sardh</i>	Mouse	SYBR Taqman	GACAAAGGACAGCCTGATGG M 4657 m	GCAGGATGTGCTTGATGCT	
<i>Gapdh</i>	Mouse	Taqman	Mm99999915_g1		
<i>AMD1</i>	Human	UPL Roche Taqman	CAGACCTCCTATGATGACCTGA Hs00750876s1	TCAGGTCACGAATCCACTCT	#72
<i>ODC1</i>	Human	UPL Roche	AAAACATGGGCGCTTACACT	TGGAATTGCTGCATGAGTTG	#3
<i>GAPDH</i>	Human	Taqman	Hs02758991_g1		
<i>β-ACTIN</i>	Human	Taqman	Hs99999903_m1		

## II.2.4.2 Protein expression analysis

### II.2.4.2.1 Protein extraction

Cells were lysed with radioimmunoprecipitation assay (RIPA) buffer (See **Table M14** for recipe) for protein extraction, based on predicted protein molecular weights smaller than 200kDa. Lysates were rocked at 4°C for 20 minutes, centrifuged at 13500 rpm for 10 minutes and the supernatant was recovered. Protein concentration was quantified with Pierce™ BCA Protein Assay Kit (Thermo Fisher Scientific Cat# 23225), and lowest protein concentration in the sample set was used as reference for normalization. Samples were prepared in Laemmli sample buffer.

**Table M14:** Reagent concentrations used to prepare RIPA buffer for protein extraction

RIPA Buffer	Stock concentration	Final concentration
TrisHCl (pH 7.5)	2 M	50 mM
NaCl	5 M	150 mM
EDTA	0.5 M	1 mM
SDS	10 %	0.10 %
Sodium Deoxycholate	10 %	1 %
NP-40	10 %	1 %
Complete Protease inhibitors		1 pill/50mL
NaF, NaOv, $\beta$ -GP	100 mM	1 mM

#### II.2.4.2.2 Western Blotting (WB)

Protein lysates were boiled at 95°C for 5 minutes for denaturalization, resolved in NuPAGE® Novex® 4-12% Bis-Tris Midi Protein gels (ref: WG1403BOX) at 180V for 1h 20mins in MES Buffer 1X or MOPS Buffer 1X and transferred to nitrocellulose membranes at 100V for 1h 45mins.

The membranes were blocked with 5% non-fat milk prepared in Tris-buffered saline solution containing 0,01% Tween-20 (TBS-T) and primary antibodies were incubated at 4°C over-night (o/n). See **table M15** for references of antibodies used for Western Blotting.

**Table M15:** References and conditions of primary and secondary antibodies employed for western blotting and immunoprecipitation.

Antibody (Clone)	Reference	Species	Dilution
AMD1	Proteintech 11052-1-AP	Rabbit	1:1000
AKT <sup>S473</sup> (D9E)	Cell Signaling Technology #4060	Rabbit	1:1000
AKT	Cell Signaling Technology #9272	Rabbit	1:1000
RpS6 <sup>S240/244</sup>	Cell Signaling Technology #2215	Rabbit	1:1000
RpS6(54D2)	Cell Signaling Technology #2317	Mouse	1:1000
PTEN(6H2.1)	CASCADEABM-2052	Mouse	1:1000
c-MYC (D3N8F)	Cell Signaling Technology #13987	Rabbit	1:1000
HA-tag (16B12)	COVANCE	Mouse	1:1000
$\beta$ -ACTIN	SIGMA A5316	Mouse	1:1000
HSP90	Cell Signaling Technology #4874	Rabbit	1:1000
$\alpha$ -TUBULIN	?	-	1:1000
Secondary Rabbit ab	Jackson ImmunoResearch	Rabbit	1:4000
Secondary Mouse ab	Jackson ImmunoResearch	Mouse	1:4000

#### II.2.4.2.3 Protein Immunoprecipitation (IP) Assay

Protein immunoprecipitation was performed to analyze AMD1 synthesis rate and for the phosphoproteomics study of AMD1 phosphorylation sites. Cell plates were washed with ice cold PBS (3 ml/p60; 5mL/p100; 10mL/p150) directly after removing medium and placed on a bed of ice. Cells were scrapped with RIPA lysis buffer and protein extraction and quantification was

performed as explained in II.2.3.2.1. 1mg of protein incubated diluted in a total volume of 800 $\mu$ L using pre-cold IP buffer (See **table M16** for recipe) for immunoprecipitation with the primary antibody. For endogenous AMD1 precipitation, anti-AMD1 antibody (11052-1-AP, Proteintech) and Protein A/G agarose beads (Pierce™ Thermo, Cat# 20421) were utilized, while exogenous AMD1 was immunoprecipitated with agarose HA-beads (A2095 SIGMA). Beads were centrifuged (30 seconds at 10000rpm at 4°C) and washed with IP buffer (800 $\mu$ L) five times. After last washing step beads were dried with capillary tips and suspended in 2x Laemmli sample buffer for elution by boiling them at 95°C for 5 minutes. Bead supernatants were loaded in a bis-acrylamide gel for migration.

**Table M16:** Reagent concentrations used to prepare immunoprecipitation buffer.

	Stock [ ]	For 50 mL	Final [ ]
<b>Tris pH 7,6</b>	2 M	1 mL	40 mM
<b>EDTA pH 8</b>	0.5 M	0.1 mL	1 mM
<b>MgCl<sub>2</sub></b>	1 M	50 $\mu$ L	1 mM
<b>NaCl</b>	5 M	1.5 mL	150 mM
<b>Triton-100</b>	10 %	500 $\mu$ L	0.1 %
<b>NaF, Na Orthovanadate, <math>\beta</math>-GP</b>	100 mM	500 $\mu$ L/each	1 mM
<b>Protease Inhibitor Cocktail</b>		1 pill	

#### II.2.4.2.4 AMD1 translation rate by <sup>35</sup>S-Met labelling

For AMD1 synthesis with radio-labelling assay, PC3 and DU145 cells were treated with either vehicle (dimethylsulfoxide (DMSO)) or Rapamycin (20 nM) for 20h in 60mm (PC3) and 100 mm (DU145) dishes. To assess AMD1 synthesis, cells were starved for 40 min from methionine and cystine and radio-labelled for 30 min with a <sup>35</sup>S-Met/Cys mix (Cat# NEG772002MC EasyTag™ EXPRESS<sup>35</sup>S Protein Labeling Mix, [<sup>35</sup>S]-, 2 mCi (74 MBq), Stabilized Aqueous Solution) before lysis. Protein lysates were incubated with protein A/G agarose beads (30  $\mu$ L) for 1h to pre-clear non-specific binding to the beads. Precleared lysates were then incubated with anti-AMD1 polyclonal antibody (11052-1-AP, Proteintech) overnight at 4°C in 400  $\mu$ L of RIPA buffer. Next, samples were incubated with protein A/G agarose beads for 1h and following immunoprecipitation bead washing steps were performed as explained in II.2.3.2.3. Lysate migration was performed in a NuPAGE™ (Novex™ 4-12% Bis-Tris Protein Gels, 1.0 mm, 12-well, Life Technologies) precast gel, in parallel with Input samples as a control of total AMD1 levels and rapamycin effect. After migration, the gel was submitted to fixation in a trichloroacetic acid (TCA) solution [10 % TCA, 10 % acetic acid, and 30 % ethanol] for 30 minutes and to signal amplification in sodium salicylate (1 M) for 1h. The gel was then dried (Model 583 gel dryer, BIORAD) and exposed to a film at -80°C for at least 96h (**Fig. M12**).

#### II.2.4.2.5 Polysome Profiling

Distribution of mRNAs across sucrose gradients was performed as described earlier (Fumagalli et al., 2012), except for minor modifications.

### II.2.4.2.5.1 Sample extraction

Briefly,  $3,5 \times 10^6$  DU145 cells were plated in 150mm plates to ensure a final density no higher than 50-60%. After 24h, cells were treated with either vehicle (DMSO) or rapamycin (20 nM) for 8 hours. After treatment, cycloheximide (CHX) was added to the medium at 37°C for 5 min at a concentration of 100 µg/mL. Cells were washed twice with cold PBS supplemented with CHX (100 µg/mL), scraped on ice and pelleted by centrifugation at 3000 rpm for 3'. Cell pellets were suspended in 250 µl of fresh hypotonic lysis buffer [1.5 mM KCl, 2.5 mM MgCl<sub>2</sub>, 5mM Tris HCl pH7.4, 1 mM dithiothreitol (DTT), 1% sodium deoxycholate, 1 % Triton X-100, 100 µg/ml CHX] supplemented with protease inhibitors Cocktail (Roche) and RNase inhibitor (New England Biolabs) at a concentration of 100 U/ml and left on ice for 5 minutes. Cell lysates were cleared of debris and nuclei by centrifugation for 5 minutes at 13000 rpm and 4°C, and the polysomal lysate in supernatant was transferred to new tubes. Protein concentrations were determined by BCA assay and aliquots of 900 µg-1,5 mg protein in 200 µL (same protein amount and volume among conditions per experiment) were prepared. Aliquots were snap frozen in liquid nitrogen, stored at -80°C and shipped to Dr. Thomas laboratory in IDIBELL for polysome profiling by Dr. Antonio Gentilella.

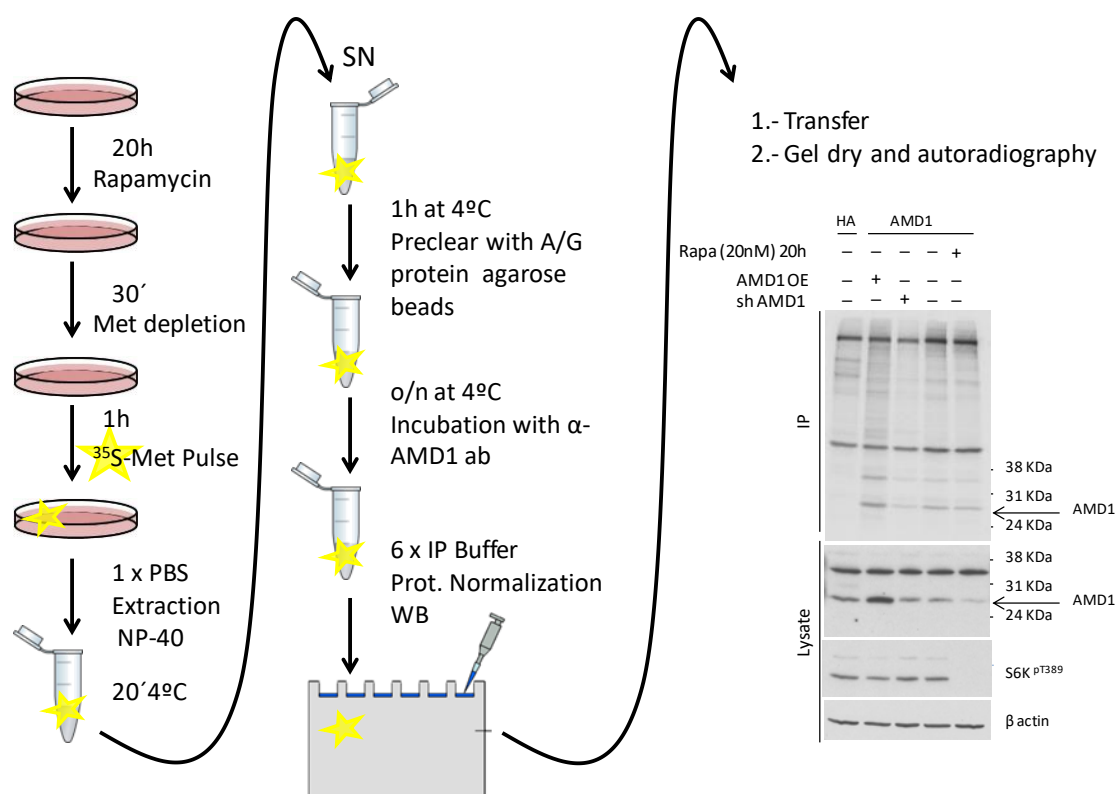


Figure M12. Schematic of the protocol followed to analyze AMD1 protein synthesis rate.

#### II.2.4.2.5.2 Sample processing

500 µg of lysate were loaded on 10-50% sucrose linear gradients containing 80 mM NaCl, 5 mM MgCl<sub>2</sub>, 20 mM Tris HCl pH7.4, 1 mM DTT, 10 U/ml RNase inhibitor with a BIOCAMP gradient master. Gradients were centrifuged on a SW40 rotor for 3 hours at 35000 rpm. Gradients were analyzed on a BIOCAMP gradient station and collected in 12 fractions ranging from light to heavy sucrose. Fractions were supplemented with SDS at a final concentration of 1% and placed for 10 min at 65°C. To each fraction was added 1ng of firefly luciferase mRNA, followed by phenol-chloroform extraction and precipitation with isopropanol. Purified RNAs from each fraction were reverse-transcribed and subjected to RT-QPCR. mRNA quantification was normalized to firefly mRNA.

#### II.2.4.2.6 Phosphoproteomics

DU145 cells stably expressing Myc-AMD1-HA were plated in 2-3 150mm plates per condition to ensure a final density no higher than 50-60% and sufficient protein amount to immunoprecipitate ectopic AMD1 and detect the corresponding band by Sypro-Ruby (Invitrogen, S12000) gel staining. Cells were treated for 8 hours with rapamycin (20nM) and Torin-1 (250nM) prior to immunoprecipitation,

##### II.2.4.2.6.1 Sample Preparation

Cells were washed with PBS on a bed of ice and lysed in 300µL RIPA lysis buffer per plate. Plates were scrapped and protein extraction was performed as explained in II.2.3.2.1. Ectopic AMD1 was immunoprecipitated as detailed in II.2.3.2.3. Specifically, the IP was performed in a total volume of 1mL with 40µL of HA-beads (A2095 SIGMA) for 1hour rolling at 4°C. Beads were washed 5 times with IP Buffer and immunoprecipitate was prepared in 80 µL 2xLaemmli by boiling the samples at 95°C for 5 min. After migrating samples in a 10% Sodium Dodecyl Sulfate Polyacrylamide MiniGel, the gel was fixed in fixing solution [10% acetic acid and 30% ethanol, fresh prepared] for 30 min and stained overnight with Sypro-Ruby (Invitrogen, S12000) under agitation in the dark. Next, the gel was rinsed in unstaining solution and water several times prior to image acquisition in theTyphoon Trio scanner (Variable Mode imager) (GE Healthcare life sciences).

The bands were unstained with several washes of 40% acetonitrile (ACN) in 50 mM ammonium bicarbonate. Then the proteins were reduced with 15 mM tris(2-carboxyethyl)phosphine (TCEP) in 50 mM ammonium bicarbonate for 30 min at room temperature and alkylated with 55mM for 30 min in the dark. Proteins were digested overnight at 37°C with trypsin. The resulting peptides were desalted and concentrated using homemade reversed phase micro-columns filled with Poros Oligo R3 beads (Life Technologies). The samples were dried using the Speed-Vac and dissolved in 22 µL of loading buffer (0.1% formic acid).

#### II.2.4.2.6.2 LC-MS/MS analysis

LC-MS/MS was performed by Pilar Ximenez and Javier Muñoz at CNIO. Peptides were separated by reversed-phase chromatography using a nanoLC Ultra system (Eksigent), directly coupled with a LTQ-Orbitrap Velos instrument (Thermo Fisher Scientific) via nanoelectrospray source (ProxeonBiosystem). Peptides were loaded onto the column (Dr. Maisch, ReproSil-Pur C18-AQ GmbH 2.4  $\mu\text{m}$ , 500x0.075 mm), with a previous trapping column step (NS-MP-10 BioSphere C18 5  $\mu\text{m}$  120  $\text{\AA}$  360/100  $\mu\text{m}$ , L=20 mm, Nanoseparations), during 10 min with a flow rate of 2.5  $\mu\text{l}/\text{min}$  of loading buffer (0.1% formaldehyde, FA). Elution from the column was made with a 60 min linear gradient (buffer A: 4 % ACN, 0.1 % FA; buffer B: 100 % ACN, 0.1 % FA) at 250 nL/min. The peptides were directly electrosprayed into the mass spectrometer using a PicoTip emitter (360/20 OD/ID  $\mu\text{m}$  tip ID 10  $\mu\text{m}$ , New Objective), a 1.4 kV spray voltage with a heated capillary temperature of 325°C and S-Lens of 60 %. Mass spectra were acquired in a data-dependent manner, with an automatic switch between MS and MS/MS scans using a top 5 method with a threshold signal of 800 counts. MS spectra were acquired with a resolution of 60000 (FWHM) at 400 m/z in the Orbitrap, scanning a mass range between 350 and 1500 m/z. Peptide fragmentation was performed using collision induced dissociation (CID/CAD) and fragment ions were detected in the linear ion trap. The normalized collision energy was set to 35%, the Q value to 0.25 and the activation time to 10 ms. The maximum ion injection times for the survey scan and the MS/MS scans were 500 ms and 100 ms respectively and the ion target values were set to 1E6 and 5000, respectively for each scan mode.

#### II.2.4.2.6.3 Data analysis

Data analysis was performed by Pilar Ximenez and Javier Muñoz at CNIO. Raw files were analyzed either by Proteome Discoverer (version 1.4.1.2) or by MaxQuant (Cox and Mann, 2008) (version 1.5.3.30) against a forward-reverse concatenated human database (UniProtKB/Swiss-Prot 20,187 sequences), including common contaminants. Carbamidomethylation of cysteines was considered as fixed modification whereas oxidation of methionines and phosphorylation on serine, threonine and tyrosine residues were set as variable modifications in both Sequest HT and Andromeda search engine (v2.2). Sequest HT, in conjunction with Percolator provided the list of proteins for Proteome Discoverer. Minimal peptide length was set to 6 amino acids and a maximum of two missed-cleavages were allowed. Peptides were filtered at 1% FDR (False Discovery Rate). For protein assessment in MaxQuant, at least one peptide provided by Andromeda search engine (Cox et al., 2011) with a FDR = 1% was required. Other parameters were set as default. Results at peptide label were exported to excel for further analysis. Extracted ion Chromatograms (XIC) of the identified phosphopeptides were manually obtained from Xcalibur (version 2.2). In order to normalize the XICs to the total protein amount, absolute intensities from MaxQuant were considered.



### II.2.4.3 In-House targeted metabolomic approaches

All samples were seeded in 6-well plates, unless otherwise specified, to a final density of no more than 80% of confluence, adjusting seeding cell numbers per condition to reach similar final density. At the experimental end-point, cells were washed three times with ammonium carbonate pH=7.4 (adjusted with acetic acid and sodium hydroxide), prepared in High-Performance Liquid Chromatography (HPLC) water, snap frozen in liquid nitrogen and stored at -80°C until processing.

#### II.2.4.3.1 One carbon Metabolism and Polyamine Pathway analysis by LC/MS *in vitro*

Cell samples were shipped in frozen plates to Agios Pharmaceuticals, where metabolites were extracted and processed by LC/MS as specified in I.2.5.2.

#### II.2.4.3.2 dcSAM and polyamine quantification *in vitro*

Frozen plates were processed by the metabolomics platform in CIC bioGUNE to extract the metabolites and analyze them by UPLC-MS as specified in I.2.5.3.

#### II.2.4.3.3 MFA *in vitro*

Seeded cells were treated with either vehicle (DMSO) or rapamycin (20nM) in fresh medium for 30 hours. After the treatment, cells were washed with methionine free (Gibco, Cat. # 21013-024) medium (with dialyzed FBS or no serum) and incubated with U-<sup>13</sup>C<sub>5</sub>-L-methionine (30 µg/mL) resuspended in same methionine-free medium (with dialyzed FBS or no serum) for 15 min to detect metabolites related to methionine cycle and 2 hours to detect metabolites related to polyamine synthesis pathway.

### III STATISTICAL ANALYSIS

All experiments were performed a minimum of three times (biological replicates), except for the exploratory experiments, such as metabolomics by ToF-MS, LC/MS, UPLC-MS or preclinical trials with mice, that were done once, but with independent biological replicates ( $n \geq 3$ ).

Values in histograms represent average value, while values in plot graphs show individual values, with a line representing the mean in parametric analyses or the median in non-parametric analyses. The error bars represent the standard error (Std Er) in the parametric analyses, while they depict the interquartile range in non-parametric analyses. The confidence interval (CI) established for the statistical analysis was 95% ( $\alpha=0.05$ ).

When comparing datasets from cell culture origin, a normal distribution was assumed and the statistic used for the analysis was paired or unpaired Student T-test, depending on the existence of dependency among samples. However, when analyzing differences among datasets from murine or human origin, a Gaussian distribution could not be assumed and thus, non-parametric Mann Whitney U-test was chosen for the analysis. Two-tailed analysis were the choice for experiments with non-predicted result, while one-tailed analysis was performed for hypothesis driven validations.

The background of the slide is a microscopic image of biological tissue, possibly showing cross-sections of cells or fibers. Overlaid on this are several diagrams: a jagged black line with blue dots at its peaks, several yellow arrows pointing in various directions, and a circular diagram at the bottom left with three yellow arrows forming a clockwise loop. A dark blue rectangular box is positioned in the lower-middle section of the slide, containing the text 'Results & Discussion I'.

## *Results & Discussion I*



## I Integrative metabolic study to uncover metabolic alterations underlying prostate cancer (PCa)

The first aim of this thesis work was to uncover the metabolic alterations underlying the pathogenesis of PCa in order to understand the metabolic requirements of cancer cells.

### HYPOTHESIS

Prostate cancer harbors metabolic alterations relevant to the pathogenesis of the disease

In the last fifteen years, multiple studies have attempted to tackle this question by developing and applying metabolomics technologies to cancer models. These efforts have allowed to establish that the metabolome (the compendium of low-molecular weight intermediates produced by cellular biochemical reactions) (Oliver et al., 1998) is intrinsically different in normal and cancer cells, as well as among different cancer types (Liesenfeld et al., 2013). After the genomic and proteomic eras, metabolomics is considered the closest approach to understand cellular phenotypes (Liesenfeld et al., 2013).

Several metabolomics studies have been performed on cancer patient specimens, to elucidate key molecular alterations underlying tumorigenesis that would in turn help to find early diagnostic biomarkers (Ren et al., 2015). However, there is intrinsic noise in these analyses, coming from the complexity of human samples and inter-individual variability. This highlights the challenge of defining consistent and relevant altered pathways. In turn, metabolic studies identifying novel metabolic biomarkers remain controversial, such as sarcosine for prostate cancer diagnosis (Sreekumar et al., 2009). To avoid such heterogeneity, in this project we decided to take advantage of our *Pten* prostate-specific knockout genetic engineered mouse model (GEMM) (*Pten*<sup>pc-/-</sup>), that faithfully recapitulates the pathogenesis of the human disease, for a profound metabolic study. In order to better understand the development of the disease, we analyzed tissue from three different prostate lobes (the ventral, VP; the anterior, AP, and the dorsolateral, DLP) and two different ages, three and six month-old mice, as representative of early (prostate intraepithelial neoplasia - PIN - lesions) and late (prostate invasive carcinoma - PCa) disease, respectively (**Fig. R1**).

With these representative samples we performed an integrative metabolomics study by combining the power of untargeted metabolomics, the resolution of targeted metabolomics and the dynamism of isotope-labeled metabolite tracing.

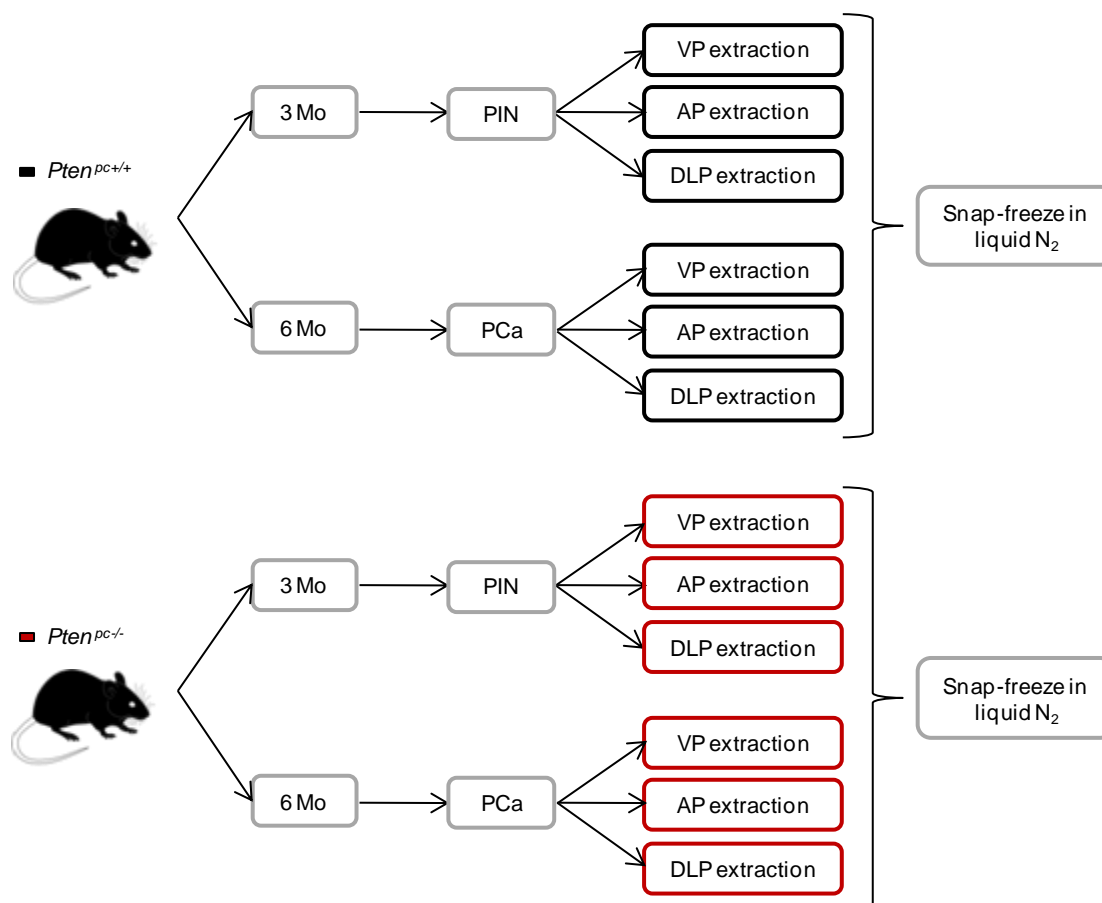


**Figure R1. General experimental design of *in vivo* experiments.** *Pten<sup>pc-/-</sup>* mice were compared to *Pten<sup>pc+/+</sup>* mice at three (when mice develop PIN lesions) and six (when mice develop PCa) months of age. The three different lobes (VP, AP and DLP) of mouse prostate were extracted and snap-frozen in liquid N<sub>2</sub> for metabolomics analysis.

### A. High-throughput Flow Injection-Time-of-Flight Mass Spectrometry (FI-ToF-MS)

We first decided to perform an untargeted metabolic study by Time-of-Flight Mass Spectrometry (ToF-MS) to have an overall idea of the metabolic alterations that the loss of *Pten* could trigger during prostate tumorigenesis. We therefore measured hundreds of ionized peptides in an unbiased way (Hypothesis-generating approach) (**Fig. R2A**).

In this technique, the flow injection, omitting the usual chromatography, allows to analyze more than 1400 samples a day, making possible the analysis of all the samples of the study in a day to avoid the variability derived from measurements performed in different days. Furthermore, ToF-MS enables the detection and identification of metabolites, based on their mass to charge ratio ( $m/z$ ). However, this technique only provides a semi-quantitative measurement of the altered metabolites (Fuhrer et al., 2011).

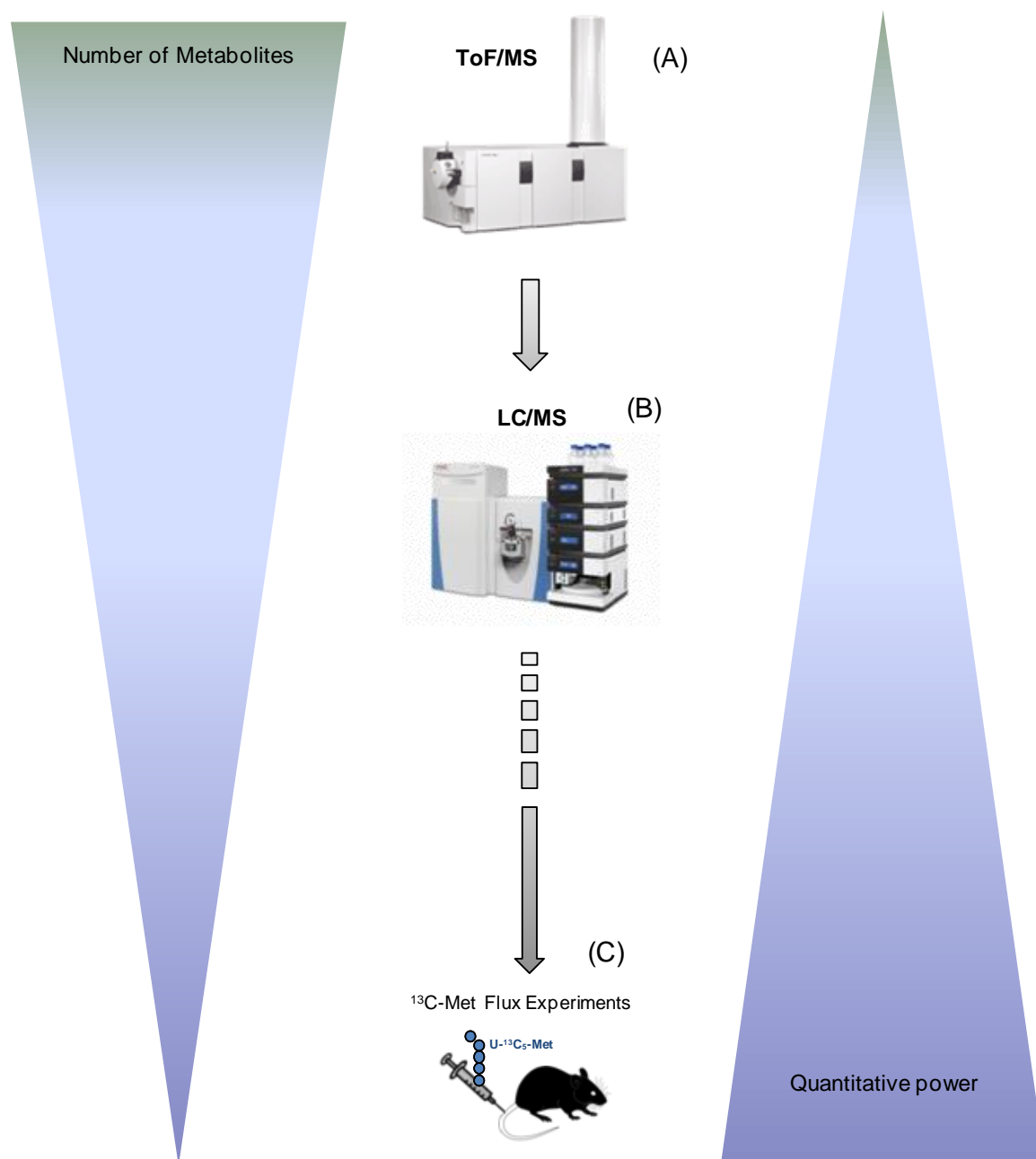


**Figure R2. Experimental design of the integrative metabolomic study.** The first study was approached by untargeted ToF-MS analysis (A). The second study was performed by targeted quantitative LC/MS analysis (B). Finally, results were corroborated by a dynamic U-<sup>13</sup>C<sub>5</sub>-labeled methionine tracing experiment.

## B. Liquid Chromatography / Mass Spectrometry (LC/MS)

Based on the data obtained by FI-ToF-MS, we then decided to perform a hypothesis driven targeted metabolic experiment by LC/MS (**Fig. R2B**). With this strategy, we aimed at confirming the previous observations and obtaining a more accurate quantification. Thus, in this approach we only included the altered pathways and related routes detected by ToF-MS, hence decreasing the number of metabolites analyzed, and in accordance with the separation limit of the

chromatography (Fuhrer et al., 2011). Nevertheless, LC/MS shows very high specificity and quantitative reproducibility (Patti et al., 2012), what has promoted its use as a main option of choice for numerous metabolic studies (Liesenfeld et al., 2013). This second approach provided us with important accurate information and quantification of altered metabolites in PCa. However, these data were limited by its static nature. Due to the dynamic nature of metabolism, we perceived that these results were insufficient to understand the biochemical cues that drive those alterations (Zamboni et al., 2015). In order to overcome this limitation, we sought to apply metabolite tracing (**Fig. R2C**), a technique that allows the interpretation of dynamic metabolic data (Feng et al., 2012).

### C. *In vivo* $^{13}\text{C}$ labeling Metabolic Flux Analysis (MFA) by LC/MS

The purpose of labeling a metabolite of interest with  $^{13}\text{C}$  is to trace the fate of carbons derived from that metabolite in the metabolic pathway of choice. In this work we designed an *in vivo* non-stationary MFA experiment, which focuses on the kinetics of the labeled isotope propagation before reaching isotopic equilibrium (Zamboni et al., 2015) (**Fig. R2C**). In this way, we have not only the measurement of the concentration of each metabolite by LC/MS, but also information about the flux from a particular metabolite into the related pathways. The fluxes provide directionality to the metabolic analysis, and the combination of  $^{13}\text{C}$  vs.  $^{12}\text{C}$  abundance for a carbon in a metabolite, informs about the reaction that originates the molecule. This knowledge is crucial in order to understand the mechanisms for metabolic regulation and in disease vs. healthy settings provides very valuable information in order to ascertain potential therapeutic targets (Zamboni et al., 2015).

#### I.1.1 ToF-MS metabolomics.

As mentioned in the description of the general experimental design followed for the integrative metabolomics study (**Fig. R2**), the first analysis was performed using FI-ToF-MS. In this first untargeted metabolomics experiment we analyzed prostate tissues from VP, AP and DLP lobes of *Pten*<sup>pc+/+</sup> and *Pten*<sup>pc-/-</sup> mice at the age of three and six months in order to have representative time points of early (PIN) and advanced (PCa) disease.

At first glance, data represented in volcano plots showed multiple increased (Fold Change (FC)>1.5; p-value<0.05) and decreased (FC<1.5; p-value<0.05) ions, corresponding to altered metabolites (**Fig. R3A**). Furthermore, the number of altered metabolites increased as the disease progressed. However, that increase was variable among the prostate lobes: VP showed a 13.1% (61 significantly altered ions/3Mo; 69 significantly altered ions/6Mo) increase in altered metabolites in the *Pten*<sup>pc-/-</sup> mice compared to *Pten*<sup>pc+/+</sup> (**Table S1**), while we could observe a 25% (80 significantly altered ions /3Mo; 100 significantly altered ions/6Mo) (**Fig. R3B**) increase in the DLP and a further increase of a 110% (60 significantly altered ions/3Mo; 126 significantly altered



ions/6Mo) (**Fig. R3C**) in the AP. These results suggest different metabolic impact of *Pten* deletion and prostate tumorigenesis in the different lobes.

We identified 156 total metabolites (**Fig. R3**), based on their mass-to-charge ratio. From those, 130 were significantly altered in *Pten*<sup>pc-/-</sup> mice compared to *Pten*<sup>pc+/+</sup>, in at least one of the lobes and time points. Such a numerous amount of alterations made it complicated to identify at a glance the metabolic pathways relevant to the disease. Thus, to further understand the implication of the deregulated metabolites observed, we analyzed the data by an enrichment analysis. This computational method identified several altered metabolic pathways in the different lobes of *Pten*<sup>pc-/-</sup> mice. Thus, data was represented as percentage of altered metabolites (**Fig. R4**).

In coherence with our previous observations, VP seemed to follow different disease evolution compared to AP and DLP, by means of altered pathway number. Indeed, no significant hits arose at three months of age in this lobe and only three metabolic pathways stood out as significantly altered at six months (**Fig. R4A**). These results could be explained by the different histological features of the three mouse prostate lobes and the higher similarity between DLP and AP. VP is composed of a flat monolayer of luminal cells, DLP shows a slightly stratified simple epithelium and AP is the lobe with the most marked papillary structure (Shappell et al., 2004). Based on the previous observations and the differential histological structure, we decided to focus in AP and DLP lobes for consistency for further analysis. Among the top hits, we observed consistent alterations in pathways related to amino acids (aa) (threonine, Thr/T; cysteine, Cys/C; glutamate, Glu/E; glutamine, Gln/Q; branched chain aa and Urea cycle), sugar (amino sugars) and mitochondrial metabolism (TCA, electron transport chain, ETC; oxidative phosphorylation, OXPHOS; and reactive oxygen species, ROS) (**Fig. R3A,B**). We then decided to consider pathways robustly altered in at least three of the four experimental settings:

#### 1.1.1.1 Tricarboxylic Acid Cycle (TCA)

The Warburg effect establishes that cancer cells exhibit a preference for glycolysis as source of energy and metabolic intermediates, alternatively to the TCA, even in the presence of oxygen (Vander Heiden et al., 2009; Warburg, 1956b). In this respect, despite the fact that mutations in TCA enzymes have been associated to tumorigenesis, it has been found that these metabolic alterations stem primarily from the deregulation of oncogenes or tumor suppressors (Desideri et al., 2015). The enrichment analysis of the ToF-MS data (**Fig. R4, in orange**) revealed alterations in TCA related metabolites, such as a decrease in succinyl-CoA levels, which correlated with a less oxidative phenotype (Cardaci et al., 2012; Torrano et al., 2016). However, many other alterations were related to less TCA-specific metabolites, such as nicotinamide adenine dinucleotide (NAD) or quinone.

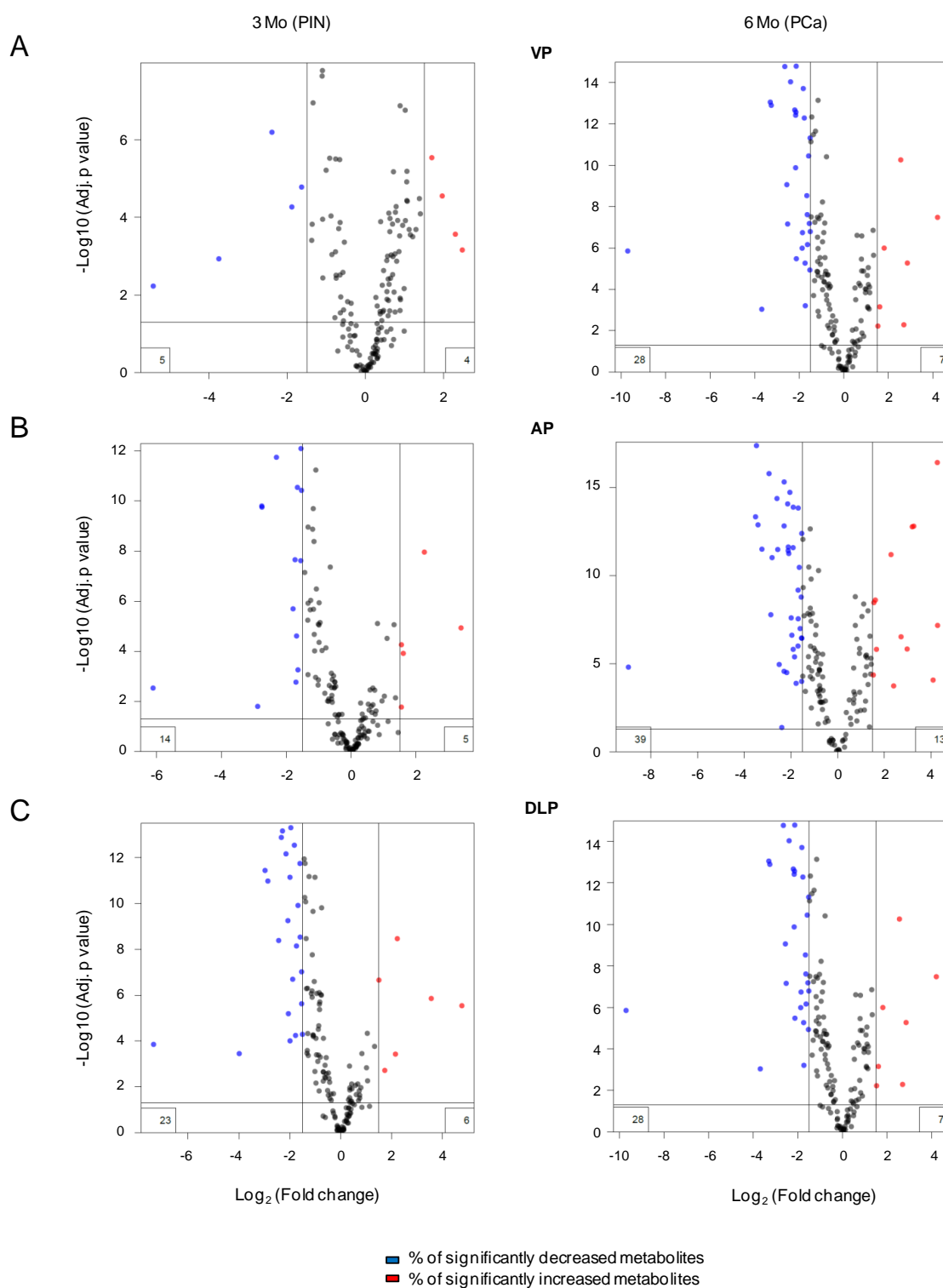


**Figure R3. ToF-MS study unraveled increasing number of metabolic alterations through PCa development.** Volcano plots representing each decreased (blue dots) or increased (red dots) ion detected by ToF-MS ( $\text{FC} > 1.5$  and  $\text{FC} < 1.5$ ;  $p\text{-value} < 0.05$ ) in VP (A), AP (B) and DLP (C) lobes at three months of age (left column) and six months of age (right column). Y axis represents negative  $\text{Log}_{10}$  of the adjusted p-values. X axis represents  $\text{Log}_2 Pten^{pc/-}$  to  $Pten^{pc+/+}$  fold change percentage of altered metabolites.

The Warburg effect was originally attributed to mitochondrial dysfunction and ROS production, although a causal effect remains unclear (Senyilmaz and Teleman, 2015). Other lines of research in the lab are focused in the regulation of this metabolic pathway (Torrano et al., 2016).

#### I.1.1.2 Amino Sugar Synthesis Pathway

Another top hit of the ToF-MS enrichment analysis was the amino sugar synthesis pathway or hexosamine biosynthetic pathway (HBP) (**Fig. R4, in purple**). N-acetylglucosamine (GlcNAc) was among the top altered metabolites in this group. GlcNAc is covalently bound to the hydroxyl group of serine (Ser, S) or Thr residues in proteins by the O-GlcNAc transferase (OGT), a post-translational modification process called O-Glc-N-acylation. Cancer cells have higher glucose uptake (Vander Heiden et al., 2009; DeBerardinis et al., 2008; Warburg, 1956b) which favors the synthesis of GlcNAc and consequent O-Glc-N-acylation. Indeed, the latter has been suggested as a nutrient sensor and metabolic regulator (Hanover et al., 2010; Józwiak et al., 2014). Hyper-O-Glc-N-acylation and/or increased OGT expression have been related to different cancer type pathogenesis in multiple publications in the last five years (Ma and Vosseller, 2013), which is in line with our data. This pathway was first reported to increase breast cancer aggressiveness (Gu et al., 2010), but was later demonstrated to participate in various other cancer types, including PCa (Lynch et al., 2012) and pancreatic cancer (Guillaumond et al., 2013).

#### I.1.1.3 Branched Chain Amino Acid (BCAA) Metabolism

BCAA (**Fig. R4, in light grey**) are leucine (Leu, L), isoleucine (Ile, I) and valine (Val, V), and they compose around the 35% of essential amino acids in muscle proteins (O'Connell, 2013). BCAAs are first transaminated by the enzyme branched chain aminotransferase to produce branched chain ketoacids (BCKA) (O'Connell, 2013). This first reaction requires  $\alpha$ -KG for the transamination, producing Glu in the reaction, which links BCAA metabolism to the previously mentioned TCA, also altered in our data.

mTORC1, a master nutrient sensor, depends on amino acid signals to become fully active (Bar-Peled and Sabatini, 2014). Furthermore, it has been reported that Sestrin-2, a protein that interacts with GATOR-2 complex to inhibit mTORC1, is a Leu sensor, what makes this amino acid (one of the three BCAAs) necessary for mTORC1 activation (Wolfson et al., 2015). These data reveal a close relationship between BCAAs and mTORC1 signaling pathway, which confers coherence to our data. However, Val was the only altered specific signal among BCAA in the ToF-MS data and the changes were very mild and inconsistent to make any conclusion.

#### I.1.1.4 Serine, Glycine (Gly) and one-carbon (1C) Metabolism

Ser and Gly (G) metabolism was the most altered pathway in our analysis (**Fig. R4, in wine-red**). Importantly, it remained altered in both lobes and the alteration was conserved along the two stages of the disease.

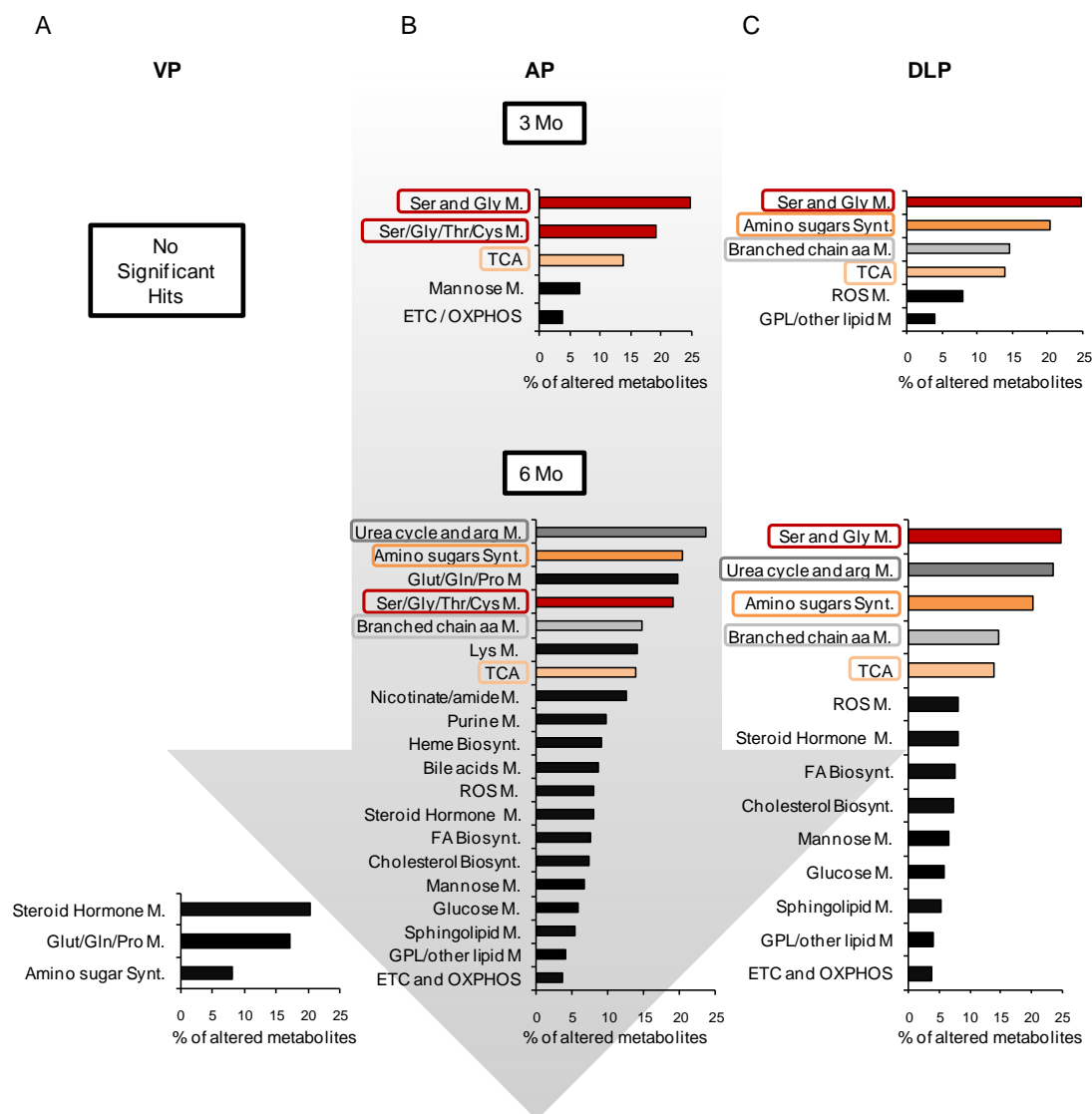


**Figure R4. ToF-MS enrichment analysis uncovered alterations in amino sugar synthesis pathway, BCAA metabolism, TCA and Ser and Gly metabolism in PCa pathogenesis.** Enrichment analysis of the ToF-MS data at three and six months of age in VP (A), AP (B) and DLP (C). The data is represented as percentage of altered metabolites.

Ser and Gly fuel 1C metabolism, composed of two cyclic pathways, namely folate and Met cycle. The two routes are coupled through the production of methyl-tetrahydrofolate (m-THF), which donates one carbon to homocysteine (HCys) to generate methionine (Met, M). The name of this pathway refers to the fact that these two cycles are fueled with a carbon residue from Ser and Gly that afterwards can be followed from one metabolite to another, reaction by reaction. Those carbon donors can be incorporated from the extracellular environment, can be synthesized *de novo* (from glucose) in the case of Ser or from other metabolites in the case of Gly (such as choline, betaine, dimethylglycine and sarcosine). The metabolic pathways involving Ser, Gly and 1C metabolism have been related to tumorigenesis in multiple studies (Locasale, 2013). However,

carbons incorporated into 1C metabolism can be further followed through many other related pathways as the trans-sulphuration pathway, which is linked to Met cycle through HCys; or the synthesis of polyamines through the decarboxylation of S-adenosylmethionine (SAM). For polyamine synthesis, another carbon source coming from the urea cycle is needed, ornithine (Pegg, 2009a).

From the 130 differentially altered metabolites upon *Pten* loss, 107 appeared to be significantly increased or decreased in two of the experimental settings, meaning that were altered in AP and DLP at three or six months of age, or were altered at both stages of the disease in AP or DLP. From those 107 metabolites, 80 showed alterations in three of the four experimental settings, meaning that were altered in both lobes, but either AP or DLP did not show the alteration at one of the timepoints. Finally, 49 of the significantly altered metabolites showed consistent changes in location (both prostate lobes) and time points of the disease, as shown by the Venn diagram in **Fig. R5A**.

In order to identify a pathway of relevance through the pathogenesis of the disease, we decided to focus on those consistently altered 49 metabolites for further analysis (**highlighted in Fig. R5B Waterfall**). Among those 49 metabolites, the highest decrease was observed in 3-Hexenedioic acid. This metabolite is an unsaturated dicarboxylic acid inversely correlated with fatty acid oxidation (FAO) (Jin and Tserng, 1989), which is coherent with the relevance of FAO in various cancerous settings (Wu et al., 2014; Carracedo et al., 2013; Liu, 2006).

On the other hand, three metabolites related to polyamine synthesis pathway were the top increased metabolites: decarboxylated SAM (dcSAM), N1-Acetylspermine and N1-Acetylspermidine. dcSAM comes from decarboxylation of SAM, the master methyl donor in the cell belonging to Met cycle. dcSAM provides carbons for polyamine synthesis (Locasale, 2013). N1-Acetylspermine and N1-Acetylspermidine are acetylated forms of polyamines, a product of their catabolism by the enzyme spermidine/spermine N1-acetyltransferase 1 (SSAT1), a key regulator of polyamine levels (Pegg, 2008).

In conclusion, these data suggest an increase in polyamine-related metabolites, from one of the essential substrates for their synthesis (dcSAM) to their catabolized form, the acetylated-polyamines. Polyamines have been widely associated to proliferation, although the mechanism underlying their role in cancer remains to be elucidated (Gerner and Meyskens, 2004b). Thus, with this data, we focused our efforts on studying alterations in 1C-metabolism and polyamine pathway in prostate cancer pathogenesis. To further confirm these data with a more accurate quantification of these metabolites we addressed in a second step of our integrative metabolic design by LC/MS, as explained in **Fig. R2**.

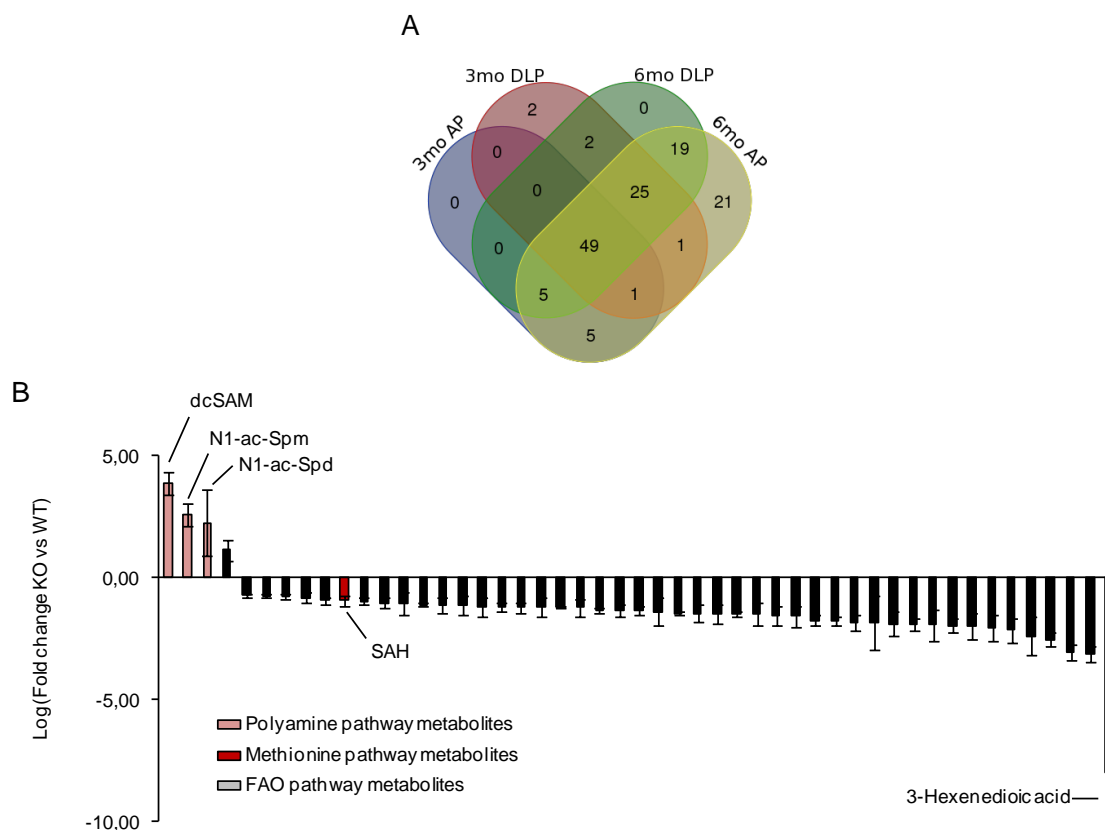


**Figure R5. The inclusion criteria established narrowed the number of consistently altered metabolites. A-B, VENN diagram (anterior prostate (AP) and dorsolateral prostate (DLP), A) and Waterfall pathway enrichment (AP and DLP, B) from the analysis of altered metabolites in TOF-MS metabolomic analysis carried out in *Pten<sup>pc-/-</sup>* vs. *Pten<sup>pc+/+</sup>* mouse prostate samples at the indicated age (n=4-5). Values in (B) represent the average of the Log (Fold change) of the two lobes and two time points (3 and 6 months of age) per metabolite.**

### SECTION SUMMARY

- The untargeted metabolomic study by FI-ToF-MS revealed alterations in TCA, amino sugar synthesis pathway, BCAA metabolism and Ser, Gly and 1C Metabolism in *Pten<sup>pc-/-</sup>* mice compared to *Pten<sup>pc+/+</sup>* at both stages of the disease.
- From the integration of alterations in both AP and DLP prostate lobes and time-points we could identify 49 consistently altered metabolites, among which polyamine pathway related metabolites were predominantly increased.

## I.1.2 LC/MS metabolomic study to quantify metabolic alterations in PCa

### I.1.2.1 LC/MS metabolomics in murine samples

For the LC/MS study, we included polyamines and related pathways in the set of analysis. As previously mentioned, we analyzed AP and DLP tissues of *Pten*<sup>pc+/+</sup> and *Pten*<sup>pc-/-</sup> mice at three and six months of age.

#### I.1.2.1.1 Branched chain amino-acid metabolism

The ToF-MS analysis showed an enrichment in BCAA metabolism in three of the four conditions (six months AP, three months DLP and six months DLP) of the experimental design (**Fig. R4B,C**). Interestingly, valine (BCAA) levels measured by LC/MS were slightly but significantly decreased, while leucine and isoleucine (also BCAAs) showed the same trend although without reaching statistical significance, in *Pten*<sup>pc-/-</sup> mice AP at three months of age. No significant alteration was observed in the rest of conditions (**Fig. R6A,B**). There are different potential explanations for this lack of coherence. Firstly, some of the metabolites that arose in the BCAA enrichment could have been misidentified. Secondly, other metabolites implicated in BCAA metabolism could be the responsible of the enrichment rather than the three BCAA themselves. Lastly, although the altered metabolites in *Pten*<sup>pc-/-</sup> mice seemed to be enriched in BCAA metabolism, those alterations could be quantitatively not significant and relevant enough to appear in the LC/MS analysis.

#### I.1.2.1.2 Urea cycle

Although excluded for consideration in our ToF-MS analysis, Urea cycle and arginine (Arg, R) metabolism showed significant alterations by LC/MS. Ornithine levels were consistently increased, whereas Arg levels were significantly decreased at three months of age in both lobes and showed the same tendency at six months of age (**Fig. R6A, B**). These data suggest a decrease in Arg in favor of ornithine production, the substrate for ornithine decarboxylase 1 (ODC1), to further produce the polyamine putrescine (Put).

#### I.1.2.1.3 Methionine cycle

Met cycle metabolites also showed clear alterations in the LC/MS analysis, confirming the data obtained by ToF-MS. Met levels were only slightly decreased in *Pten*<sup>pc-/-</sup> mice AP at three months of age (**Fig. R6A**), while they remained unaltered in the rest of conditions. Notwithstanding, SAM levels were consistently increased in both lobes and time-points, whereas we could observe a less consistent (due to variability among samples) but clear decrease of SAH levels (**Fig. R6A, B**). SAH levels did not correlate with the increased sarcosine levels. However, this increase could be explained by the increase in Gly, one of the substrates of the reaction, catalyzed by GNMT, to produce sarcosine. The increase in Gly, together with the increase in betaine observed in *Pten*<sup>pc-/-</sup> mice prostates at six months of age compared to *Pten*<sup>pc+/+</sup>, could also be the reflect of higher

metabolites in mice treated with either dose of SAM486A compared to vehicle-treated mice (**Fig. R53**). Put levels were dramatically increased in both treatment regimens. The increase in Put correlated with the alterations observed in ornithine and Arg, both metabolites of the urea cycle implicated in the synthesis of Put. These results indicate that SAM486A induces a robust increase in putrescine synthesis, presumably acting on ODC1 activity. The fact that the changes in Put occur in the absence of a consistent reduction in dcSAM strongly suggests that this event is not due to the intricate compensatory mechanisms of polyamine synthesis, but rather to some direct effect of the compound on Put synthesis. Our data was in line with previous *in vitro* studies (Regenass et al., 1994; Svensson et al., 1997), preclinical trials (Dorhout et al., 1995a, 1995b) and with some of the mentioned phase I and phase II clinical trials (Millward et al., 2005; Siu et al., 2002), in which SAM486A treatment caused an increase in Put. The authors in these studies argued that the increase in putrescine was due to a compensatory mechanism rising from the decrease in dcSAM. However, although SAM486A treatment was able to decrease Spd and Spm levels in the *in vitro* studies and in the preclinical leukemia trials, none of them had any data about dcSAM levels. According to the clinical trials, PA levels showed in most cases very high inter-patient variability and inconsistency. It should be noted that the analysis of PA pools in those cases was done in peripheral blood leucocytes, and not in the target tissue (Eskens et al., 2000). Only in one phase I trial were able to confirm a decrease from pre-treatment to post-treatment analysis of dcSAM levels in a biopsy of a melanoma patient with apparently very high initial levels of dcSAM (Siu et al., 2002). In that particular patient, they were also able to detect decreased Put/Spd ratio and a reduction in Spm levels. Interestingly in the phase II melanoma trial reductions in Spd levels were also achieved (Millward et al., 2005), suggesting tumor type-specific efficacy of the treatment.

In our preclinical trial, SAM486A 2mg/Kg dose was not able to alter the levels of PA pools or dcSAM (**Fig. R53 left**). However, the higher dose caused an increase in the putrescine/Spd ratio and a mild but significant decrease in Spm levels. In the same line, dcSAM levels showed a tendency to decrease (**Fig. R53 right**).

Polyamine synthesis is tightly regulated through multiple feedback mechanisms. We speculate that SAM486A might retain structural similarities with SAM and dcSAM to interfere with ODC1 regulation, leading to an activation of putrescine synthesis. Our results suggest that local dose reached in the tumor tissue is sufficient to activate ODC1, but it does not inhibit AMD1 efficiently, as shown in the metabolomics analysis. Further research is needed in order to define whether such an off-target effect could hamper the therapeutic efficacy of SAM486A and explain the poor therapeutic efficacy observed in the preclinical and clinical trials with the compound.



## SECTION SUMMARY

- Methionine deficient diet resulted insufficient to revert the metabolic alterations observed in *Pten<sup>pc-/-</sup>* mice and did not show therapeutic advantage, compared to regular Chow diet fed mice.
- Pharmacological AMD1 inhibition with SAM486A *in vivo* showed no efficacy in decreasing dcSAM levels, and lacked therapeutic potential.

### III.2.3 Analysis of AMD1 levels in a clinical trial of RAD001

Our data demonstrated that regulation of AMD1 by mTORC1 is preserved *in vivo* in mice and that AMD1 levels can be modulated upon mTORC1 inhibition with Everolimus (RAD001). To further study the extent of our findings, we sought to validate our data in human specimens from a clinical trial with RAD001. Thanks to the collaboration with Dr. Baselga and Dr. Taberero's laboratory at Vall D'Hebron Hospital, we had access to pre- and post-treatment biopsy samples from cancer patients with advanced solid tumors treated with either daily (5 or 10 mg) or weekly (20 or 50 mg) administration (**Fig. R54A**) of RAD001 (Taberero et al., 2008).

Paired pre- and post-treatment biopsies were processed by IHC to assess AMD1 immunoreactivity and analyze changes upon RAD001 treatment. To quantify AMD1 protein expression, an H-Scoring was performed. Strikingly, 62% of the patient biopsies analyzed exhibited a decrease in AMD1 levels upon RAD001 treatment in the tumor (**Fig. R54B**), as appreciable in the decreased immunoreactivity of AMD1 in the post-treatment staining of biopsies (**Fig. R54C, lower panels**) compared to pre-treatment samples (**Fig. R54C, upper panels**).

To further analyze whether AMD1 levels were differently altered in the RAD001 treatment regimens, we evaluated differential AMD1 immunoreactivity for each regime. Interestingly, AMD1 levels were significantly decreased only in patients treated with low doses of Everolimus (a maximum cumulative dose of 35mg/week; 5mg/day or 20mg/week), but not in response to high dose regimens (a minimum cumulative dose of 50mg/week; 10mg/day or 50mg/week) (**Fig. R55A**). Strikingly, the Everolimus regime resulting in AMD1 reduction was the only capable of impacting tumor cell proliferation, assessed by Ki67 staining (**Fig. R55B**).

Analysis of the phosphorylation level of molecular markers of mTOR pathway showed that phosphorylation of all markers downstream mTOR (S6<sup>S235/236</sup>, S6<sup>S240/244</sup>, 4EBP<sup>T70</sup> and eukaryotic initiation factor 4G, eIF4G<sup>S1106</sup>) was significantly inhibited at the time-points analyzed irrespective of the Everolimus regime (**Fig. R55C**). This data suggests that AMD1 is a more sensitive biomarker of therapeutic efficacy for mTORC1 than other targets evaluated. AKT

phosphorylation, which stands upstream mTOR, showed trend to upregulation upon high dose administration (Tabernero et al., 2008). This upregulation is caused by a negative feedback loop inducing upstream insulin-like growth factor 1 receptor (IGF-1R) signaling, which in term would result in AKT activation (O'Reilly et al., 2006; Tabernero et al., 2008). This feedback loop would also explain higher polyamine content upon re-phosphorylation of AKT (Rajeeve et al., 2013) and the rationale for the attenuation of the clinical activity of this agent .

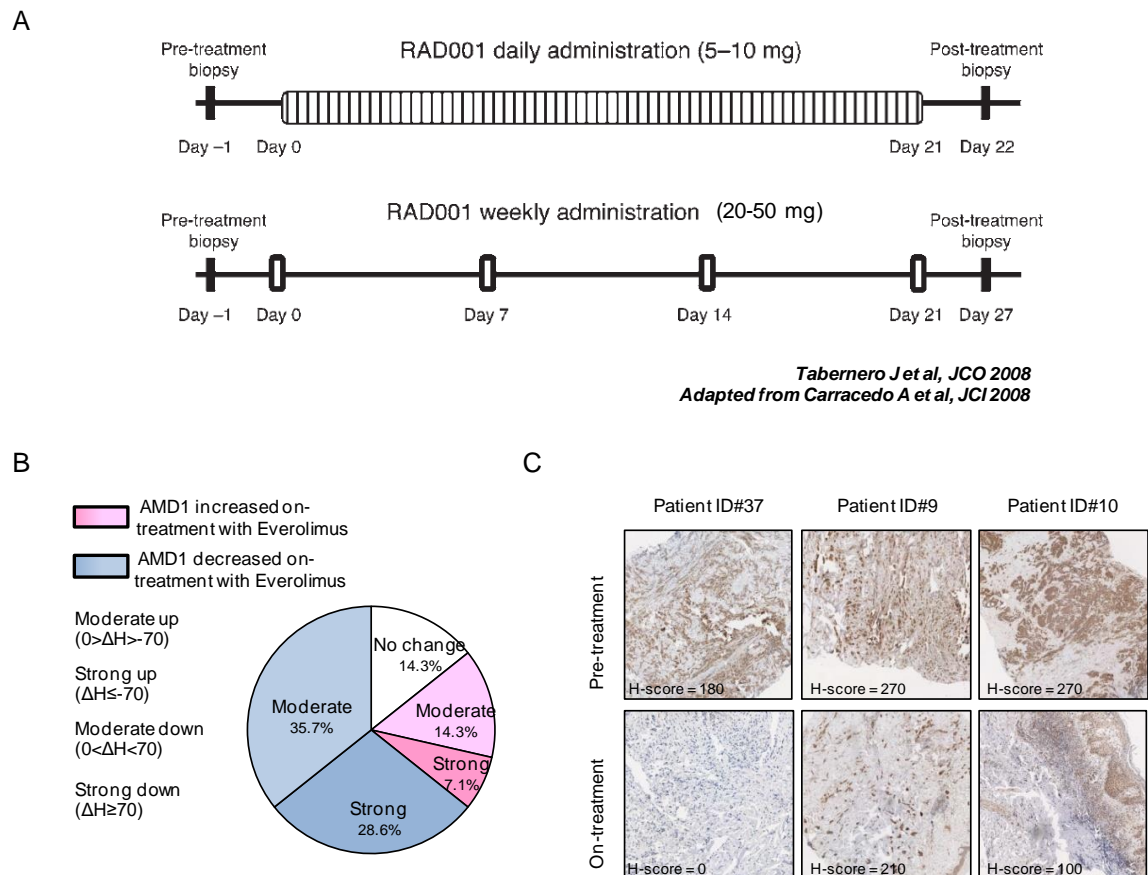


**Figure R54. Impact of pharmacological mTORC1 inhibition with RAD001 on AMD1 levels in a clinical trial.** **A**, Schematic of the different dose regimens administered in the clinical trial (5-10 mg/day or 20-50 mg/week) **B**, Quantification of AMD1 immunoreactivity difference (H-score change) between pre- and post-treatment biopsies. **C**, Representative images of AMD1 staining by IHQ in pre- and post-treatment biopsies and H-score quantification of each case.  $\Delta H$ : H-score difference.

In conclusion, our data led us to hypothesize that the effect on AMD1 upon mTORC1 inhibition is responsible of the reduced cancer cell proliferation and thus, unveil AMD1 as an important marker to monitor in mTOR-targeting therapies.

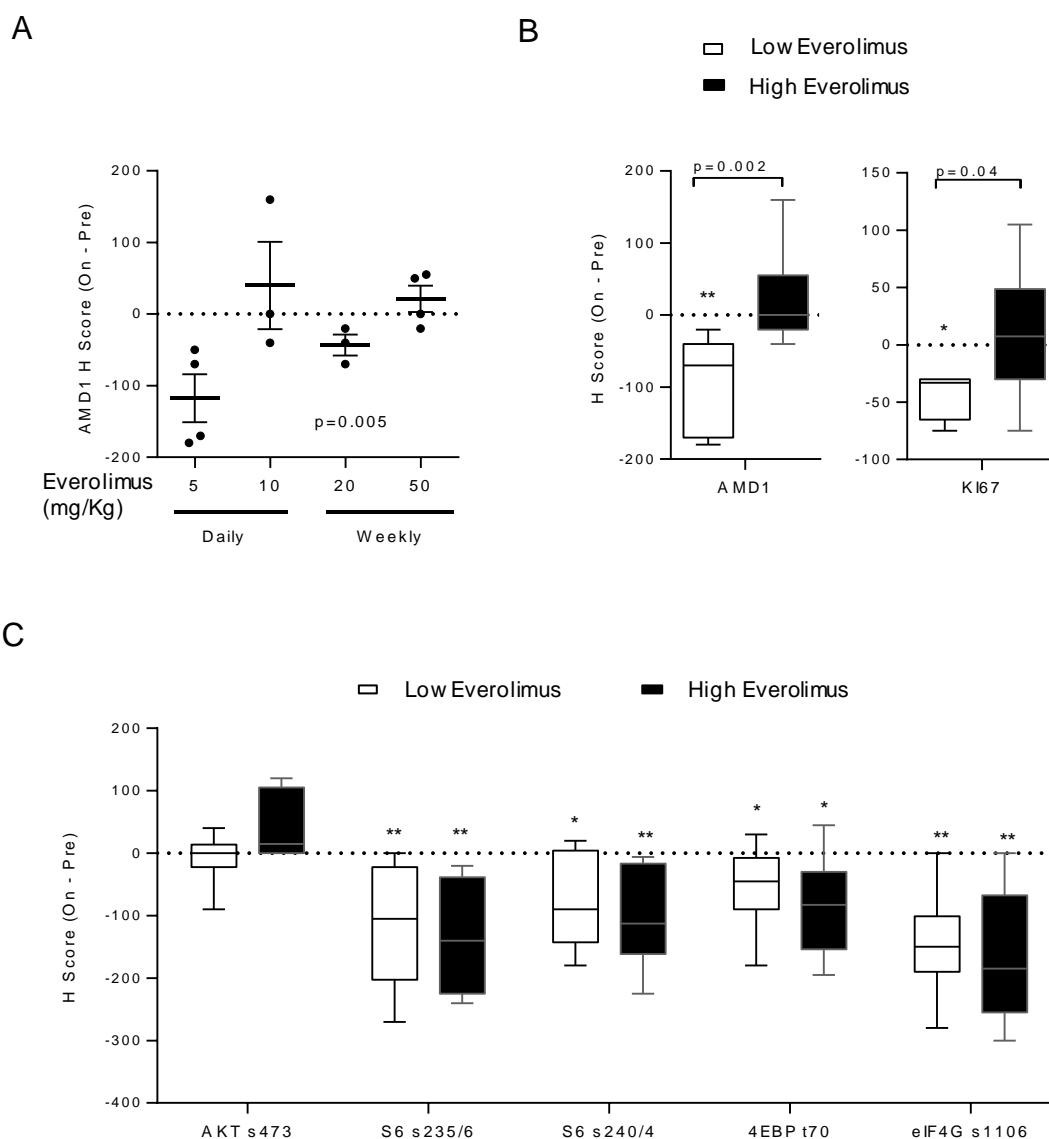


**Figure R55. Impact of pharmacological mTORC1 inhibition with RAD001 on AMD1 levels in a clinical trial.** **A**, Differential AMD1 immunoreactivity (quantified as H-score post-treatment – H-score pre-treatment) in each dose regime (5-10 mg/day or 20-50 mg/week). **B**, Differential AMD1 (**left panel**) or Ki67 (**right panel**) immunoreactivity (quantified as differential H-score) according to combined low dose regimens (5 mg/day or 20 mg/week) or combined high dose regimens (10 mg/day or 50 mg/week). **C**, Differential H-scores of molecular biomarkers (phospho-AKT, phospho-RpS6, phospho-4EBP1 and phospho-eIF4G) for mTOR pathway inhibition according to combined dose regimens mentioned in **B**.

### SECTION SUMMARY

- Regulation of AMD1 levels upon mTORC1 inhibition (Rapamycin, RAD001 or Everolimus *in vivo*) is preserved in human specimens and associated to its anti-proliferative activity, enforcing the relevance of this enzyme for therapeutic purposes.

### CONCLUSION III

- Genetic and pharmacological modulation of AMD1 underscored the therapeutic potential of targeting this enzyme
- Methionine restriction alone and pharmacological AMD1 inhibition with SAM486A *in vivo* did not show any therapeutic benefit against PCa development, arguably due to reduced pathway inhibitory effects
- AMD1 downstream mTORC1 might be a critical component of the cytostatic effect of mTORC1 inhibitors

### EXPERIMENTAL IMPROVEMENTS AND FUTURE PERSPECTIVES

- The polyamine rescue experiment could be validated by overexpressing AMD1 ectopically and then performing AMD1 silencing with an shRNA that targets endogenous, but not exogenous AMD1, mimicking in that way endogenous polyamine depletion and further polyamine addition.
- Methionine restriction beyond 0.15% would be more appropriate to evaluate the impact of nutritional manipulation in PCa
- Combination of SAM486A treatment with DFMO (ODC1 inhibitor) could prevent the increase of putrescine and increase the therapeutic benefit in pre-clinical trials



The background of the slide is a microscopic image of biological tissue, showing several large, roughly circular structures with internal granular details. Overlaid on this are several diagrams: a jagged black line with blue dots at its peaks, several curved white arrows pointing in various directions, and a circular white arrow at the bottom left. A dark teal horizontal bar is positioned in the middle of the slide, containing the text 'General Discussion'.

***General Discussion***



## I THE REVOLUTION OF OMICS: MILESTONES AND REMAINING CHALLENGES IN CANCER RESEARCH

### Omics development and cancer research

Large-scale profiling methods have been innovatively employed to elucidate metabolic pathways implicated in tumor initiation, progression and metastasis (Benjamin et al., 2012). The last of the “*omics*”, metabolomics, has transformed cancer research (Klupczyńska et al., 2015). Previously developed “*omics*”, such as genomics, transcriptomics or proteomics, offered valuable information about the expression levels of oncogenes or tumor-suppressors, which led to the discovery of altered signaling pathways that play relevant roles in cancer pathogenesis (Stratton et al., 2009; Hanash and Taguchi, 2010). However, the information provided by these large-scale profiling methods was limited to the quantification of gene alterations and transcript or protein levels, which do not necessarily correlate with the enzymatic activities, reaction rates and, in general, metabolic dynamics (Holmes et al., 2008). Metabolomics conferred the capacity of measuring metabolite pools, which provide faithful information about substrate, intermediate and product amounts of the biochemical reactions that sustain cellular metabolism (Patti et al., 2012). Furthermore, this data can provide a speculative idea of the regulation status of involved metabolic enzymes. Consequently, metabolomics is considered the OMIC that most closely relates to the phenotype (Klupczyńska et al., 2015).

The technological blooming of instrumentation offered a broad variety of metabolomic techniques, from untargeted screenings to targeted MFA. Steady-state metabolomics provide valuable information regarding deregulated metabolic pathways. However, this type of metabolomics offers a static view, a snapshot of the metabolome, providing cues about the altered biochemical reactions in a particular moment (Zhao and Yang, 2015). The challenge of capturing the dynamic essence of metabolism was achieved by the development of metabolic flux techniques (Zamboni et al., 2015). Non-stationary metabolic flux analysis provides reaction rate information and directionality based on the  $^{13}\text{C}/^{12}\text{C}$  labeling ratio, and recapitulates more closely the dynamism of metabolism (Wiechert and Nöh, 2013).

In this work we combined untargeted (ToF/MS), targeted (LC-MS) and MFA metabolomics in an integrative metabolomics study to faithfully uncover, narrow down and validate the most relevant metabolic alterations underlying PCa pathogenesis in murine and human specimens. This approach allowed us to characterize a metabolic wiring showing increased flux from methionine cycle towards polyamine metabolic pathway in PCa. Importantly, the metabolic routes identified by ToF/MS in the murine prostates, were then validated by LC/MS and MFA employing murine, human and cell line samples to elucidate the extent and relevance of this metabolic switch in PCa.



## Challenges and future prospects of metabolomics in eukaryotes

Despite the informative potential of metabolomics and the valuable information obtained by this approach, the technology exhibits limitations and faces challenges in the analysis of samples of eukaryotic origin. Contrary to prokaryotic cells, eukaryotic cells are compartmentalized into specialized organelles, with compartment-specific and shared metabolic activities (Wahrheit et al., 2011). Furthermore, cells have achieved sophisticated mechanisms to separate zones inside each compartment, as liquid-liquid phase separation, leading to membraneless compartmentalization (Aguzzi and Altmeyer, 2016). Compartmented subcellular structure results in numerous cellular metabolic microenvironments (Wahrheit et al., 2011), which allow the isolation and regulation of the numerous reactions that take place within a cell. However, compartmentalization has a price: the development of communication mechanisms to transmit signals and exchange material among the different organelles (Prinz, 2014). In turn, subcellular compartmentalization remarkably complicates the interpretation of metabolic networks from whole cell lysates (Niklas et al., 2010). Most current techniques obviate this variable and measure average labeling and metabolite levels of all mixed compartments in a cell (Buescher et al., 2015).

These facts are in support of our results. Indeed, although increased entrance (dcSAM) and exit (ac-polyamines) metabolites were detected, polyamine pools did not show consistent alterations, but rather remained fairly constant throughout the different experimental approaches addressed. In a metaphoric comparison, we could imagine polyamine reservoir as a water tank with continuous enter/exit flux, where an increased influx will be immediately compensated with a proportional efflux. In a biological context where the influx is increased (in our case *Pten* loss), the metabolomics data would reveal as increased influx and efflux metabolites, without major changes in the total pool of the central metabolites. Our hypothesis was reinforced by the metabolic flux experiments. The dynamic essence of this technique provided us the opportunity to demonstrate the increased production of dcSAM with carbons being incorporated into polyamines and subsequently into their acetylated derivatives (**Fig. D2**). Thus, our results highlight the relevance changes in polyamine influx and efflux, rather than total polyamine pools. Compartmentalization is particularly relevant when studying polyamine dynamics. Polyamines have been suggested to exhibit vesicle sequestration upon cell internalization through yet undefined mechanisms (Poulin et al., 2011). Importantly, quick polyamine import/export capacity from these putative vesicles could explain the rapid regulation of polyamine levels in response to exogenous alterations. Moreover, most polyamines are found in RNA-bound complexes (Igarashi and Kashiwagi, 2010). These two factors combined imply that the free polyamine pool is minor relative to total polyamine amounts. In turn, changes in free polyamines that are negligible when measuring total polyamine pool size, could exert profound effects in cell biology.

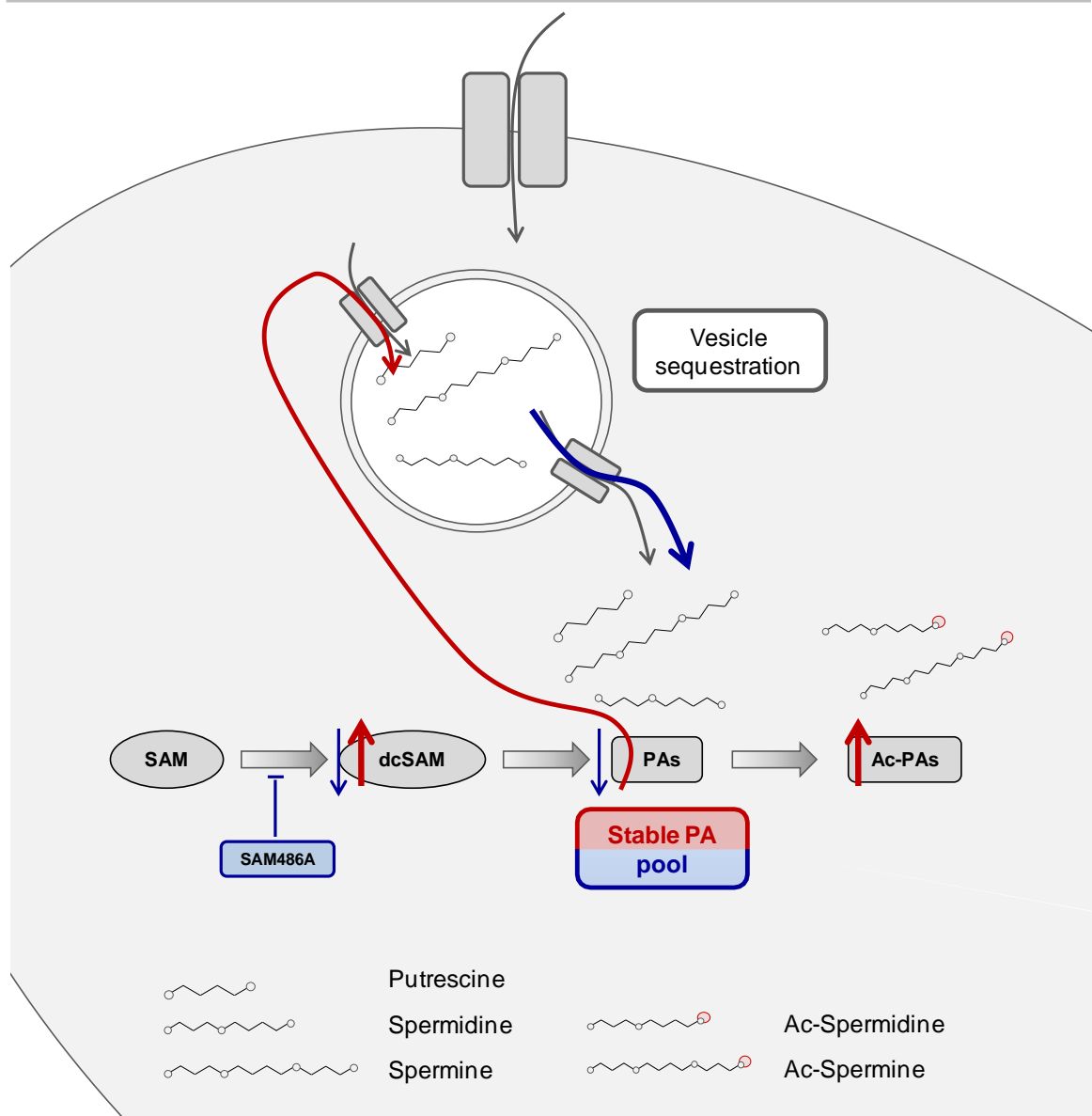


Figure D1. Schematic representation of polyamine pools according to the observed in *Pten* *pc*<sup>-/-</sup> mice and upon AMD1 inhibition with SAM486A.

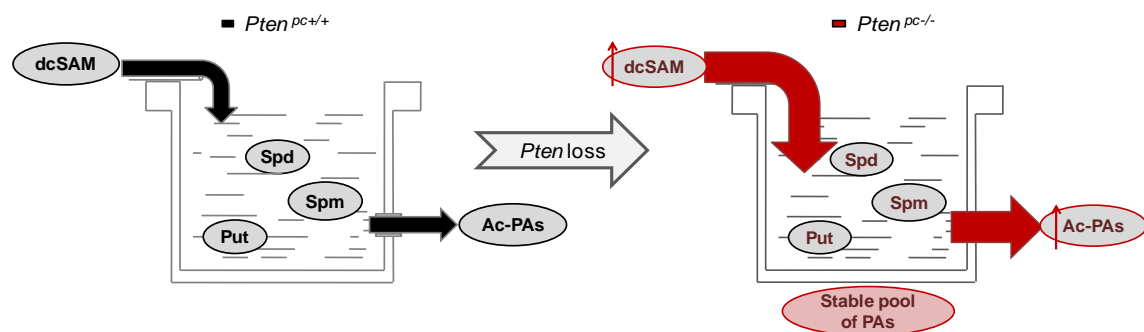


Figure D2. Schematic representation of the hypothesis postulating increased flux through polyamine pathway in prostate cancer. The representation reflects the importance of altered enter and exit fluxes despite unaltered total polyamine pools.

The considerations postulated herein might be of vital importance for therapies targeting polyamine metabolism. Indeed, despite the promising results *in vitro* and in *in vivo* models, drugs targeting polyamine synthesis enzymes, such as DFMO (ODC1) or SAM486A (AMD1) failed to show clear antitumoral benefit in clinical trials (Millward et al., 2005; Vlastos et al., 2005; Pless et al., 2004; Siu et al., 2002; Paridaens et al., 2000; Eskens et al., 2000; Loprinzi and Messing, 1992; Horn et al., 1987). The lack of therapeutic efficacy of these and other polyamine pathway modulators could be explained in part by the aforementioned data. By targeting *de novo* polyamine synthesis, these drugs should alter free polyamine levels. However, it is plausible that these pools are rapidly equilibrated by polyamine export from sequestering vesicles. Following this rationale, polyamine pathway-targeting therapies might need to be rethought. Probably, specific therapies targeting polyamine vesicle sequestration upon internalization would show higher benefit.

The possibility of measuring metabolites in a compartment-dependent manner could profoundly change our understanding of polyamine pathway regulation. In this work we have demonstrated that AMD1 is regulated by mTORC1. This serine-threonine kinase complex is reported to localize to the lysosome (Sancak et al., 2010). Based on these data, it is tempting to speculate that AMD1 could temporarily localize to the lysosome to be subject to mTORC1-dependent regulation.

## II THE INTERPLAY OF mTORC1 SIGNALING AND POLYAMINE METABOLISM IN CANCER AND BEYOND

### The crosstalk between signaling and metabolism in cancer

Most oncogenes and tumor suppressor genes discovered during the genomics era encode proteins implicated in signal transduction (Ward and Thompson, 2012). In the last decade of the twentieth century, cancer research focused on characterizing the oncogenic or tumor suppressive nature of genes based on gain or loss of function analysis with genetic tools. Traditionally, these genes have been attributed the capacity to support the acquisition of cancer hallmarks (Hanahan and Weinberg, 2000). However, increasing evidence reveal an alternative scenario, where oncogenes and tumor suppressors are essential mediators of the metabolic reprogramming, leading to the possibility of metabolic regulation as the ancient function of many of these genes (Ward and Thompson, 2012). In the same line, downstream aberrantly activated oncogenic signals, cell metabolism is reprogrammed to comply with anabolic needs. Nevertheless, metabolism also remodels the signaling network through the control of the epigenetic landscape (Pavlova and Thompson, 2016). This renewed understanding of cancer hallmarks implies an exquisite crosstalk between signaling and metabolism. In this sense, we provide a direct link between one of the master sensors that integrates and interprets growth signals, mTORC1, and a

metabolic route essential for cell proliferation and survival, the polyamine pathway. In support of our data, other metabolic enzymes related to polyamine synthesis and catabolism have previously been reported to be under the regulation of oncogenes and tumor suppressor genes. Indeed, the other rate limiting enzyme in polyamine synthesis, ODC1, is an established direct target of the oncogene *c-MYC* (Bello-Fernandez et al., 1993; Peña et al., 1993). Moreover, this decarboxylase cooperates with the oncogene H-RAS in fibroblast transformation *in vitro* (Shantz and Pegg, 1998) and in skin carcinogenesis *in vivo* (Smith et al., 1998). Likewise, the catabolic enzyme SSAT1 has been shown to lie under the control of the oncogene K-RAS (Ignatenko et al., 2004).

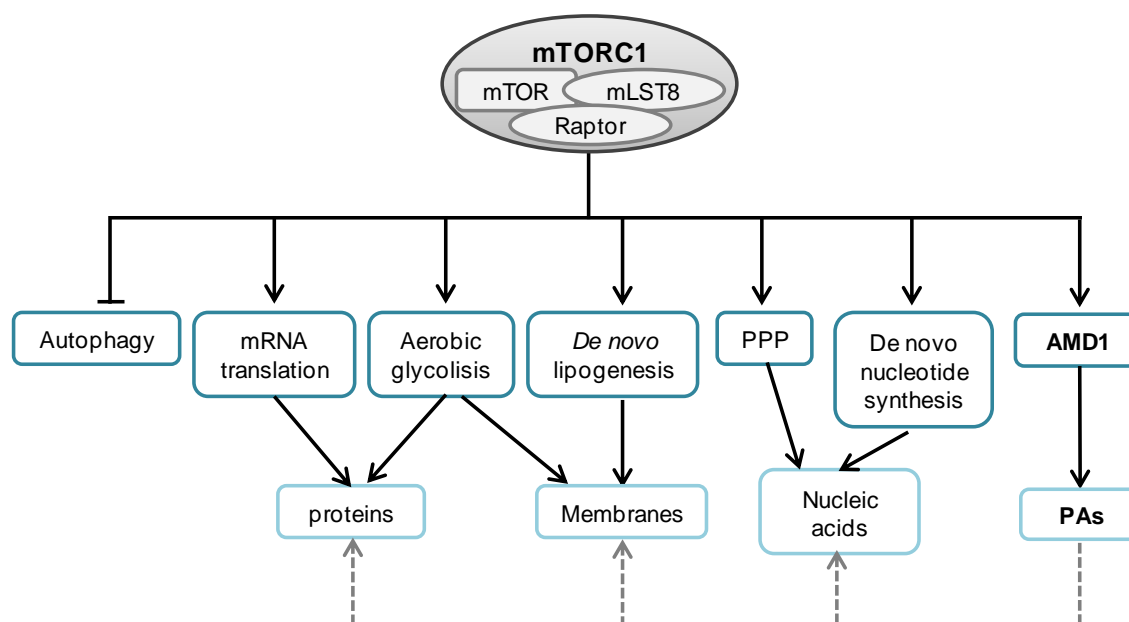


**Figure D3.** Scheme depicting the anabolic processes regulated downstream mTORC1, including AMD1 regulation and polyamine production.

mTORC1 promotes growth and proliferation depending on the nutrient and energy status of the cell (Howell and Manning, 2011). This complex induces anabolic metabolism by orchestrating several biosynthetic pathways. Under energy and nutrient-availability conditions, mTORC1 blocks autophagy by inhibiting a protein complex containing the kinases ULK1/2, which is essential for the autophagic process (Yecies and Manning, 2011; Neufeld, 2010). However, mTORC1 is also capable of directly regulating the synthesis of macromolecules, such as proteins, lipids and nucleic acids (Dibble and Manning, 2013a). The implication of mTORC1 in protein synthesis regulation is the best characterized of its functions. Indeed, this master regulator controls not only cap-dependent translation through phosphorylation of its targets 4EBP1 and S6K, but also protein degradation to ensure protein homeostasis (Zhang et al., 2014; Ma and Blenis, 2009). mTORC1 is also implicated in the regulation of lipid homeostasis. In fact, this protein complex induces lipid synthesis and storage, while inhibiting processes that imply lipid consumption (Ricoult and Manning, 2013). In the same line, mTORC1 induces purine synthesis, through the regulation of folate cycle (Ben-Sahra et al., 2016), as well as, *de novo* pyrimidine production by direct phosphorylation of carbamoyl-phosphate synthetase 2 (CAD) by its

downstream target S6K (Ben-Sahra et al., 2013). In this work we have described a previously unidentified branch under the control of mTORC1 (**Fig. D3**). Based on our preliminary data, this regulatory pathway would stem from direct phosphorylation of AMD1, although ongoing validation experiments are warranted to validate this assumption. If our hypothesis is confirmed, AMD1 would be a direct target immediately downstream mTORC1, together with 4EBP1 and S6K. The regulation of AMD1 by mTORC1 is of vital importance since connects a signaling cascade and a metabolic pathway, both relevantly implicated in such an essential cellular process as proliferation (Dibble and Cantley, 2015; Miller-Fleming et al., 2015). Importantly, this connection also integrates polyamines and the synthesis of macromolecules. Polyamines induce adipogenesis (Hyvönen et al., 2013; Ishii et al., 2011) and bind to DNA and RNA affecting their structure and stability (Iacomino et al., 2012; Igarashi and Kashiwagi, 2010). Furthermore, Spd is essential for eIF5A hypusination, a post-translational modification required for its activation and subsequent correct mRNA translation elongation (Park et al., 2009; Cooper et al., 1982). In conclusion, we have identified a mTORC1-AMD1-PAs axis, which enriches the metabolic landscape downstream mTORC1.

## Signaling-metabolism crosstalk beyond cancer

The fact that polyamine pathway enzymes are so tightly regulated under the control of oncogenes and tumor suppressors underscores the relevance of these molecules in cancer and, potentially, in physiology. We show that mTORC1 regulates polyamine synthesis to support proliferation. Indeed, both mTORC1 signaling and polyamines are involved in relevant processes throughout our lifespan. This perspective well correlates with new perspectives on aging, which define this vital process as "*any change in an organism over time*", thus aging being synonymous of change rate (Bowen and Atwood, 2004). In view of this, the developmental processes occurring in mammals sequentially through lifespan could reasonably be separated into a "positive phase", from conception to adulthood; followed by a "negative phase", senescence, from adulthood to death (Scalabrino and Ferioli, 1984).

Embryonic development and tissue growth are processes that imply high proliferation and change rates ("positive phase"). In this context, mTORC1 is of vital importance. In fact, germline deletion of mTOR components showed that both mTORC1 and mTORC2 are essential during embryogenesis, although mTORC1 is primordial at early stages of the development, whereas mTORC2 plays its decisive role at midgestation (Guertin et al., 2009). In fact, mTOR is critical for gastrulation and tissue growth during organogenesis (Land et al., 2014). Interestingly, polyamines are essential during embryonic development. Knockout of both polyamine biosynthetic enzymes (AMD1 and ODC1) lead to embryonic lethality at early stages of development (Nishimura et al., 2002; Pendeville et al., 2001). In the same line, polyamines play a relevant role during pregnancy, especially during first half of development (Sooranna et al., 1998). These data support a role for mTORC1-AMD1-PAs in early life stages.

The connection of this axis might result less certain in later stages of life, when proliferation requirements are reduced. Experimental evidence suggest that mTOR controls aging through the regulation of several downstream processes (Blagosklonny and Hall, 2009). Researchers in the gerontology field support the notion of non-programmed aging, which hypothesizes that aging is the consequence of the incorrect inactivation of the growth program (Blagosklonny, 2013). Aging impacts on the entire organism, through the accumulation of damage in molecules, cells and tissues over time. Tissue dysfunction in aging has been correlated with a switch in cellular status, from reversible G0 quiescence to irreversible G0 senescence, a proliferation block driven by mTOR (Demidenko and Blagosklonny, 2008) and named "geroconversion". This process leads to hypertrophic cells, due to active mTOR signaling despite cell-cycle inhibition (Blagosklonny, 2014). Importantly, both mTORC1 specific and dual mTORC1 and mTORC2 inhibitors have been demonstrated to efficiently prevent geroconversion, preserving proliferative potential (Leontieva et al., 2015; Sousa-Victor et al., 2015; Demidenko et al., 2009). However, polyamine levels show a sustained inverse correlation with ageing, although there is certain tissue specificity. (Nishimura et al., 2006; Scalabrino and Ferioli, 1984). For instance, spermidine and spermine levels decrease with age in mice (Nishimura et al., 2006) and humans (Pucciarelli et al., 2012). Strikingly, in this study nona/centenarian people showed an enrichment in Spd and Spm concentrations relative to total polyamines, suggesting that maintaining these polyamines in aging contribute to longevity (Pucciarelli et al., 2012). This evidence supports the notion that polyamines are required for the extension of lifespan.

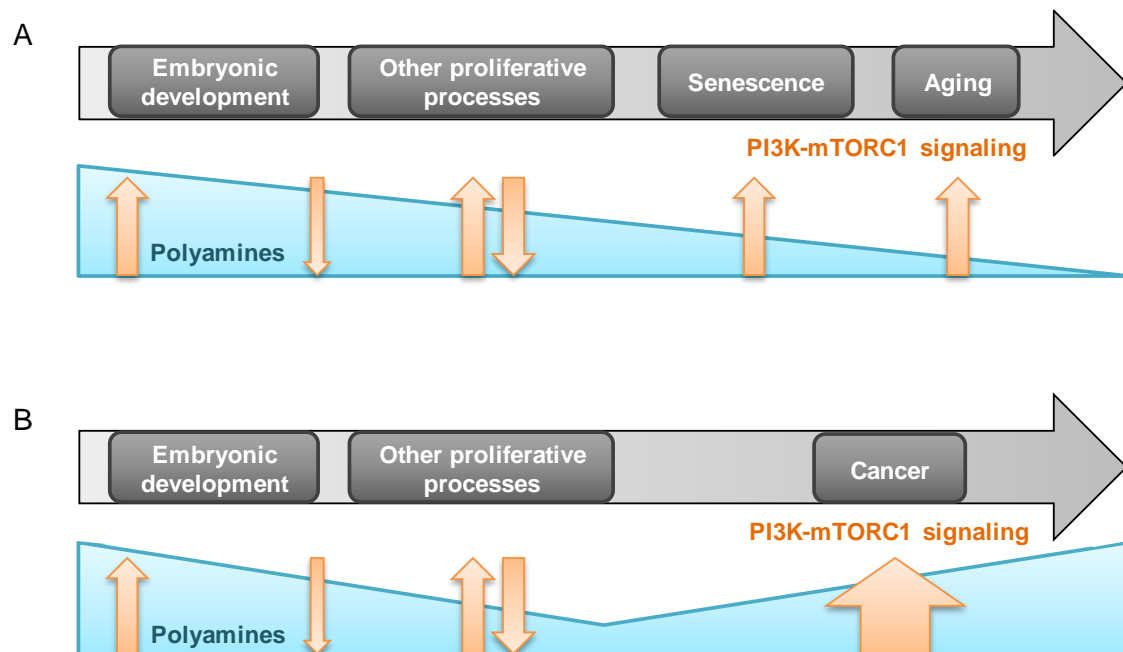


**Figure D4.** Interplay between PI3K-mTORC1 signaling and polyamine levels. A-B, Crosstalk throughout proliferation-related processes in lifespan (A) and cancer (B).

In the search for anti-aging strategies, genetic or pharmacological inhibition of mTOR was found to extend lifespan in yeast, nematodes, flies and mice (Harrison et al., 2009; Powers et al., 2006; Kaeberlein et al., 2005; Kapahi et al., 2004; Jia et al., 2004; Vellai et al., 2003). In turn, rapamycin and its derivatives (Rapalogs) have become the best-supported candidates as anti-aging therapeutics. Likewise, exogenous Spd supplementation was demonstrated to increase the lifespan of yeast, flies, worms, human immune cells and to decrease oxidative stress in aging mice. In this study Eisenberg and coworkers showed that Spd addition caused general hypoacetylation of histone H3 and induced autophagy by promoting acetylation of autophagy-related autophagy related 7 (*ATG7*) gene promoter (Eisenberg et al., 2009). Thus, polyamines, and especially Spd, have aroused as anti-aging molecules, which can be supplemented in food or water to increase their levels in the organism (Minois, 2014). Rapamycin also shares with Spd multiple potential mechanisms by which it exerts its anti-aging effect, such as regulation of cell growth, autophagy induction and anti-inflammatory mechanisms. Nonetheless, despite its encouraging effects rapamycin, it seems unlikely that this drug will be approved for preventive use, due to its side effects (Lamming et al., 2013).

Our data demonstrate a direct regulation of AMD1 downstream mTORC1, which led us to speculate that this axis also operates throughout development and aging. This might be true until the axis is disconnected from proliferation. Nevertheless, in conditions where proliferation is sustained, such as cancer, the axis might be preserved, as we observed in PCa. In conclusion, the analogous activities of PI3K signaling and polyamines, are observed in several facets of life. Elucidating this complex relationship would help us better understand physiological processes at the cellular and systemic level, and could reveal novel therapeutic avenues for pathological alterations related to cell growth and senescence.

### III AMD1 AS A PREDICTIVE BIOMARKER AND TARGET IN PROSTATE CANCER

The combination of established clinical-pathological acquaintance with state-of-the-art molecular profiling to achieve diagnostic, prognostic and therapeutic strategies is termed precision medicine (Mirnezami et al., 2012). In this regard, genomic technologies have inspired this stratification approach, whereas other high throughput technologies that provide better information about the phenotype of the tumor remain underdeveloped in this area of research (Friedman et al., 2015). In the particular case of PCa, precision medicine is yet far from becoming a reality. Indeed, stratification of PCa patients depends on very general parameters, such as PSA, Gleason Score and TNM classification, and targeted therapy is limited to the inhibition of androgen signaling. Therefore, novel stratification markers and targeted therapies are needed to treat the disease once first line therapy (surgery or radiotherapy) fails. This fact underscores the need for reliable and reproducible prognostic biomarkers to discriminate patients that would benefit from early adjuvant treatment from those requiring more aggressive therapy (Sedelaar and Schalken, 2015). Patient derived tumor xenograft (PDX) models, which maintain the molecular, genetic and

histological heterogeneity of the tumor of origin, might represent excellent platforms to predict clinical efficacy based on potential biomarkers (Cho et al., 2016; Tentler et al., 2012).

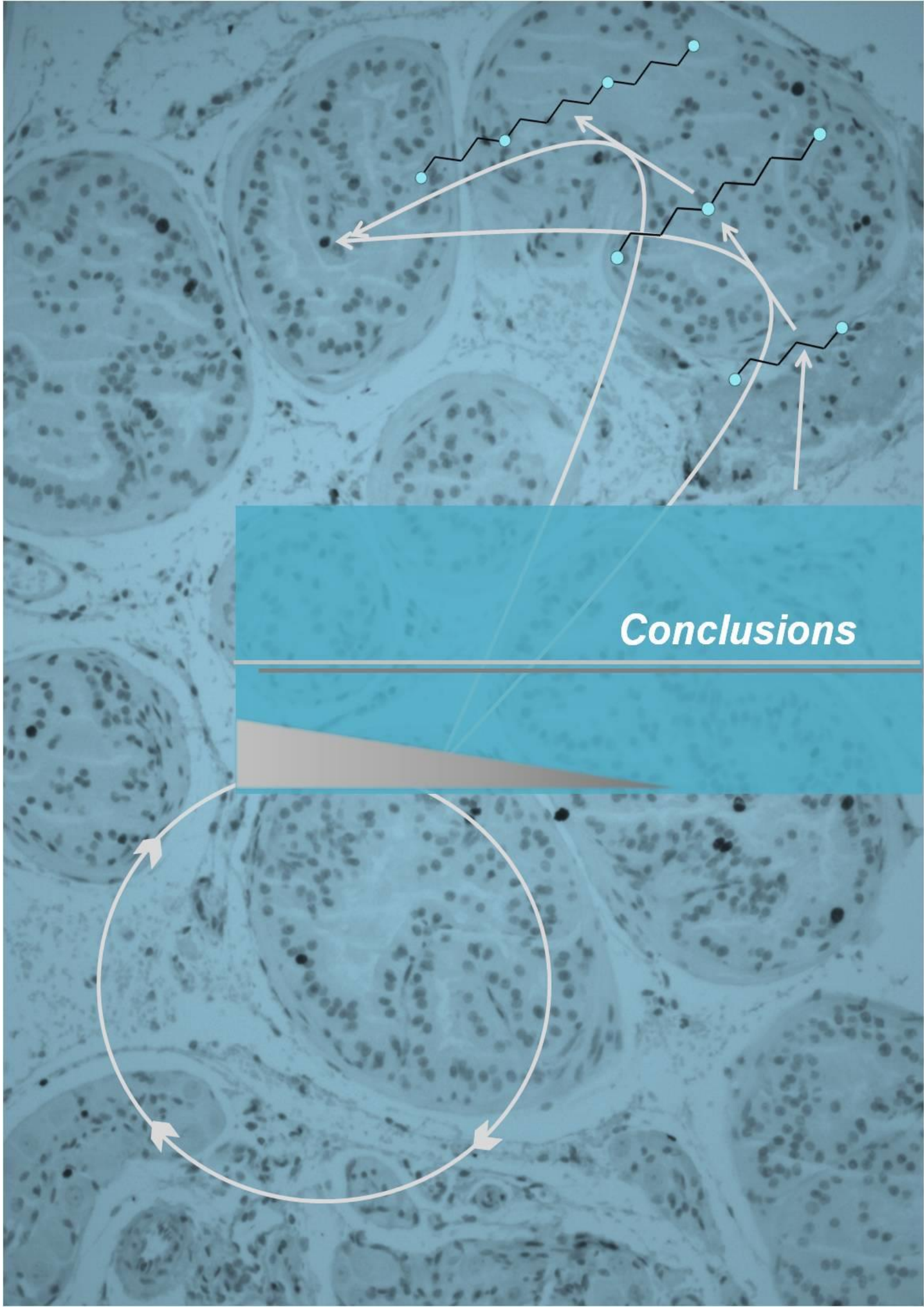
In this project we have shown that the rapamycin-derivative Everolimus is capable of decreasing AMD1 levels *in vivo*. Interestingly, a decrease in AMD1 immunoreactivity exhibits better association to a decrease in tumor cell proliferation than the rest of mTORC1 activity readout proteins (Tabernero et al., 2008), that remained inhibited regardless of Everolimus regime and therapeutic effects. Thus, we hypothesize that AMD1 might be a key contributing factor to the cytostatic effect triggered by Everolimus. This fact would be of relevance to predict therapeutic efficacy, and underscore the relevance of AMD1 as a potential predictive biomarker for response to mTORC1 inhibition-based therapies.

Genetic and pharmacological inhibition of AMD1 *in vitro* and in xenograft models demonstrated the therapeutic potential of targeting this metabolic enzyme for PCa treatment. However, in contrast to previous studies showing an antitumoral effect of SAM486A in xenograft models (Dorhout et al., 1995a, 1995b), pharmacological inhibition of AMD1 *in vivo* failed to support an antitumoral effect in our PCa model. This drug reached the prostate, but was unable to efficiently decrease neither dcSAM, nor polyamine levels. For yet unclear reasons, SAM486A led to a dramatic induction of putrescine levels (**Fig. R53**). One plausible explanation for this effect is that SAM486A would not reach prostate cancer cells at sufficient concentration to exert its pharmacological activity. In this regard, the emerging field of drug nanoencapsulation might provide advantageous alternatives. Nanoparticles (NP) possess unique properties, such as nanoscopic size, large surface-to-volume ratio, the capacity to encapsulate large payloads and a modifiable external surface. These characteristics provide them with advantages over bulk drugs: the possibility of adding targeting-ligands on their surface, efficient navigation through the often hostile microenvironments in the body, the capability of co-transporting multiple drugs, controlled release of the drug and increased cellular uptake (Davis et al., 2008). Furthermore, NPs offer the possibility of targeting them to specific organelles to achieve maximal therapeutic benefit, with minimal side-effects (Biswas and Torchilin, 2014). Thus, encapsulation of SAM486A into nanoparticles would allow directly targeting the drug to the prostate and would facilitate its incorporation, thereby enhancing the probabilities of achieving an effective therapeutic concentration. This approach could potentiate the efficacy of this drug.

Our data reflects another alternative for targeting AMD1, mTORC1 inhibition. We have shown that mTORC1 inhibition with rapamycin and Torin-1 effectively decreases AMD1 protein levels and dcSAM production *in vitro* and *in vivo*. We propose that Everolimus could show therapeutic benefit in patients with high AMD1 levels. Importantly, Everolimus-based combinatorial therapy might increase treatment efficacy, decrease the emergence of resistance and avoid therapy-induced metastasis (Nastiuk and Krolewski, 2016). Despite the discouraging results in the latest attempts to test rapamycin for combination therapies in prostate cancer clinical trials (Vaishampayan et al., 2015; Nakabayashi et al., 2012), the elucidation of AMD1 as



the plausible downstream effector of mTORC1 raises the alternative of combining Everolimus with another polyamine pathway inhibitor, such as the ODC1 inhibitor, difluoromethylornithine (DFMO). Previous studies in which DFMO in combination with SAM486A showed beneficial effect against leukemic xenografts support this hypothesis. In summary, we believe AMD1 shows predictive capacity for mTORC1 inhibition-based therapies and represents a potential target for combination therapies in PCa.



*Conclusions*



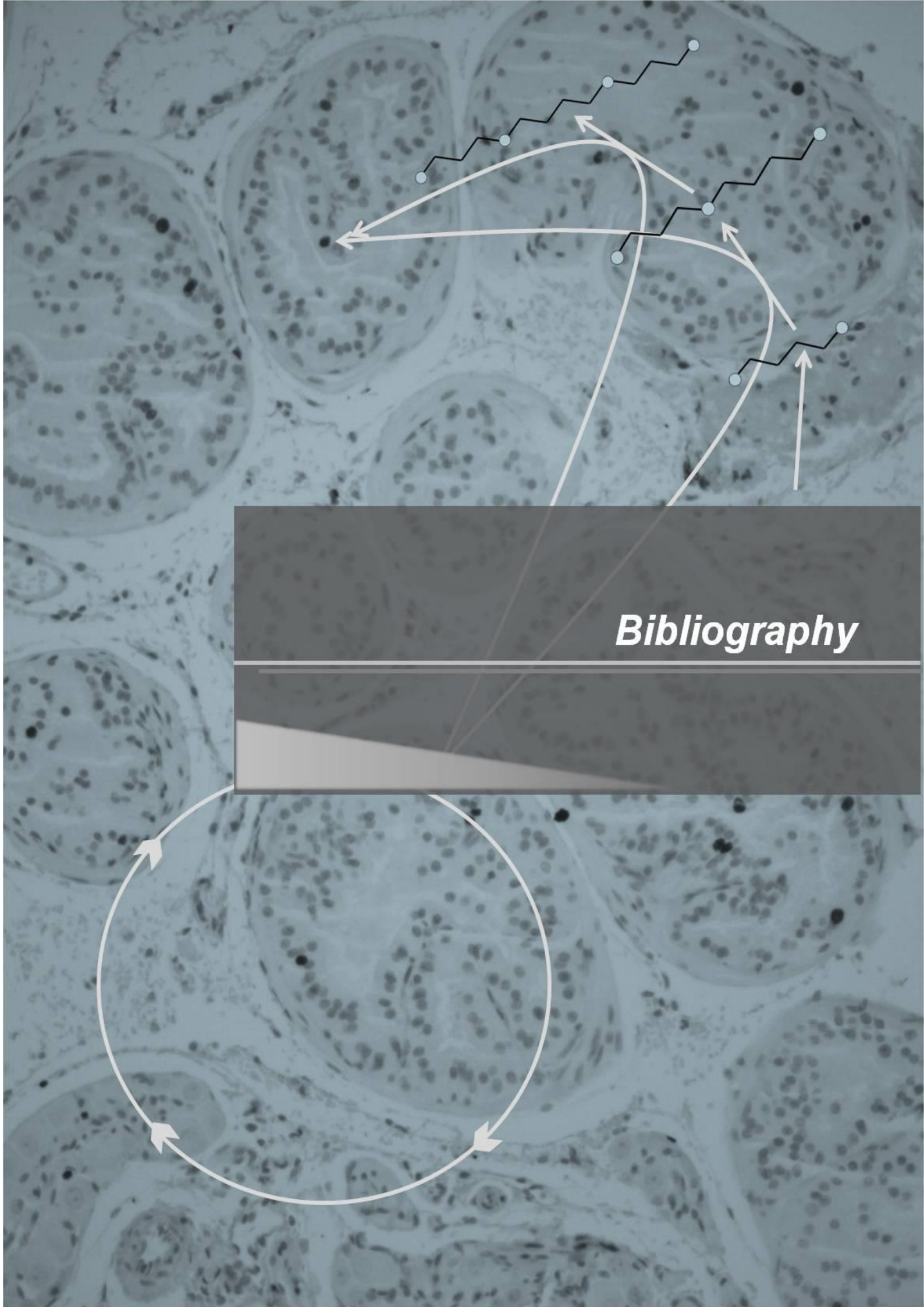
The results obtained throughout this thesis work confirm our initial hypothesis and demonstrate that oncogenic events trigger the deregulation of metabolism in prostate cancer. The results are summarized as follows:

- ◆ *Pten* loss induces a metabolic switch from methionine cycle towards polyamine synthesis pathway in murine and human prostate cancer.
- ◆ *Gnmt* loss as a single or compound genetic event is not relevant for disease initiation.
- ◆ AMD1 increase upon *Pten* loss induces the metabolic switch observed in prostate cancer.
- ◆ AMD1 is under the control of mTORC1.
- ◆ We propose the direct phosphorylation of proAMD1 by mTORC1 as the mechanism of regulation, leading to stabilization of the proenzyme and subsequent processing.
- ◆ Genetic and pharmacological inhibition of AMD1 exhibits therapeutic potential.

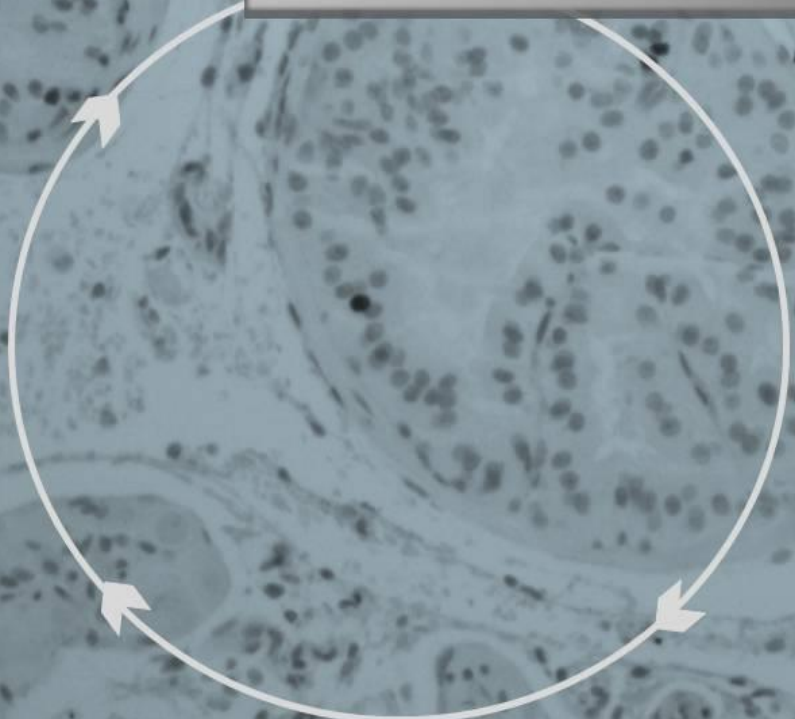
### GENERAL CONCLUSION

The results obtained in this thesis work demonstrate that the oncogenic loss of *Pten* induces the metabolic deregulation in prostate cancer, through the increase of AMD1. Furthermore, we propose a mechanism of AMD1 regulation downstream mTORC1, which opens new alternatives to target this enzyme.





***Bibliography***





- Abate-Shen, C., and Shen, M.M. (2002). Mouse models of prostate carcinogenesis. *Trends Genet.* *18*, S1–S5.
- Abdulhussein, A.A., and Wallace, H.M. (2013). Polyamines and membrane transporters. *Amino Acids* *46*, 655–660.
- Abraham, R.T., and Gibbons, J.J. (2007). The Mammalian Target of Rapamycin Signaling Pathway: Twists and Turns in the Road to Cancer Therapy. *Clin. Cancer Res.* *13*, 3109–3114.
- Agarwal, E., Brattain, M.G., and Chowdhury, S. (2013). Cell survival and metastasis regulation by Akt signaling in colorectal cancer. *Cell. Signal.* *25*, 1711–1719.
- Aguzzi, A., and Altmeyer, M. (2016). Phase Separation: Linking Cellular Compartmentalization to Disease. *Trends Cell Biol.*
- Alessi, D.R., Andjelkovic, M., Caudwell, B., Cron, P., Morrice, N., Cohen, P., and Hemmings, B.A. (1996). Mechanism of activation of protein kinase B by insulin and IGF-1. *EMBO J.* *15*, 6541–6551.
- Alhonen, L., Halmekytö, M., Kosma, V.M., Wahlfors, J., Kauppinen, R., and Jänne, J. (1995). Life-long over-expression of ornithine decarboxylase (ODC) gene in transgenic mice does not lead to generally enhanced tumorigenesis or neuronal degeneration. *Int. J. Cancer* *63*, 402–404.
- Alimonti, A., Nardella, C., Chen, Z., Clohessy, J.G., Carracedo, A., Trotman, L.C., Cheng, K., Varmeh, S., Kozma, S.C., Thomas, G., et al. (2010). A novel type of cellular senescence that can be enhanced in mouse models and human tumor xenografts to suppress prostate tumorigenesis. *J. Clin. Invest.* *120*, 681–693.
- Alvarez, A., Barisone, G.A., and Diaz, E. (2014). Focus formation: a cell-based assay to determine the oncogenic potential of a gene. *J. Vis. Exp. JoVE.*
- Amelio, I., Cutruzzolá, F., Antonov, A., Agostini, M., and Melino, G. (2014). Serine and glycine metabolism in cancer. *Trends Biochem. Sci.* *39*, 191–198.
- Antony, T., Hoyer, W., Cherny, D., Heim, G., Jovin, T.M., and Subramaniam, V. (2003). Cellular Polyamines Promote the Aggregation of  $\alpha$ -Synuclein. *J. Biol. Chem.* *278*, 3235–3240.
- Bar-Peled, L., and Sabatini, D.M. (2014). Regulation of mTORC1 by amino acids. *Trends Cell Biol.* *24*, 400–406.
- Bell, M.R., Belarde, J.A., Johnson, H.F., and Aizenman, C.D. (2011). A neuroprotective role for polyamines in a *Xenopus* tadpole model of epilepsy. *Nat. Neurosci.* *14*, 505–512.
- Bello-Fernandez, C., Packham, G., and Cleveland, J.L. (1993). The ornithine decarboxylase gene is a transcriptional target of c-Myc. *Proc. Natl. Acad. Sci. U. S. A.* *90*, 7804–7808.
- Belting, M., Mani, K., Jönsson, M., Cheng, F., Sandgren, S., Jonsson, S., Ding, K., Delcros, J.-G., and Fransson, L.-A. (2003). Glypican-1 is a vehicle for polyamine uptake in mammalian cells: a pivotal role for nitrosothiol-derived nitric oxide. *J. Biol. Chem.* *278*, 47181–47189.
- Benjamin, D.I., Cravatt, B.F., and Nomura, D.K. (2012). Global Profiling Strategies for Mapping Dysregulated Metabolic Pathways in Cancer. *Cell Metab.* *16*, 565–577.
- Ben-Sahra, I., Howell, J.J., Asara, J.M., and Manning, B.D. (2013). Stimulation of de Novo Pyrimidine Synthesis by Growth Signaling Through mTOR and S6K1. *Science* *339*, 1323–1328.
- Ben-Sahra, I., Hoxhaj, G., Ricoult, S.J.H., Asara, J.M., and Manning, B.D. (2016). mTORC1 induces purine synthesis through control of the mitochondrial tetrahydrofolate cycle. *Science* *351*, 728–733.



Bhavsar, A., Verma, S., Bhavsar, A., and Verma, S. (2014). Anatomic Imaging of the Prostate, Anatomic Imaging of the Prostate. *BioMed Res. Int.* *2014*, *2014*, e728539.

Biswas, S., and Torchilin, V.P. (2014). Nanopreparations for organelle-specific delivery in cancer. *Adv. Drug Deliv. Rev.* *66*, 26–41.

Bjornsti, M.-A., and Houghton, P.J. (2004). The TOR pathway: a target for cancer therapy. *Nat. Rev. Cancer* *4*, 335–348.

Blagosklonny, M.V. (2013). Aging is not programmed. *Cell Cycle* *12*, 3736–3742.

Blagosklonny, M.V. (2014). Geroconversion: irreversible step to cellular senescence. *Cell Cycle* *13*, 3628–3635.

Blagosklonny, M.V., and Hall, M.N. (2009). Growth and aging: a common molecular mechanism. *Aging* *1*, 357–362.

Blanco-Aparicio, C., Renner, O., Leal, J.F.M., and Carnero, A. (2007). PTEN, more than the AKT pathway. *Carcinogenesis* *28*, 1379–1386.

Bostwick, D.G., Liu, L., Brawer, M.K., and Qian, J. (2004). High-Grade Prostatic Intraepithelial Neoplasia. *Rev. Urol.* *6*, 171–179.

Bowen, R.L., and Atwood, C.S. (2004). Living and dying for sex. *Gerontology* *50*, 265–290.

Brana, I., Berger, R., Golan, T., Haluska, P., Edenfield, J., Fiorica, J., Stephenson, J., Martin, L.P., Westin, S., Hanjani, P., et al. (2014). A parallel-arm phase I trial of the humanised anti-IGF-1R antibody dalotuzumab in combination with the AKT inhibitor MK-2206, the mTOR inhibitor ridaforolimus, or the NOTCH inhibitor MK-0752, in patients with advanced solid tumours. *Br. J. Cancer* *111*, 1932–1944.

Breillout, F., Hadida, F., Echinard-Garin, P., Lascaux, V., and Poupon, M.F. (1987). Decreased rat rhabdomyosarcoma pulmonary metastases in response to a low methionine diet. *Anticancer Res.* *7*, 861–867.

Brown, E.J., Albers, M.W., Bum Shin, T., Ichikawa, K., Keith, C.T., Lane, W.S., and Schreiber, S.L. (1994). A mammalian protein targeted by G1-arresting rapamycin–receptor complex. *Nature* *369*, 756–758.

Bubendorf, L., Schöpfer, A., Wagner, U., Sauter, G., Moch, H., Willi, N., Gasser, T.C., and Mihatsch, M.J. (2000). Metastatic patterns of prostate cancer: an autopsy study of 1,589 patients. *Hum. Pathol.* *31*, 578–583.

Buescher, J.M., Antoniewicz, M.R., Boros, L.G., Burgess, S.C., Brunengraber, H., Clish, C.B., DeBerardinis, R.J., Feron, O., Frezza, C., Ghesquiere, B., et al. (2015). A roadmap for interpreting 13C metabolite labeling patterns from cells. *Curr. Opin. Biotechnol.* *34*, 189–201.

Cai, L., Sutter, B.M., Li, B., and Tu, B.P. (2011). Acetyl-CoA Induces Cell Growth and Proliferation by Promoting the Acetylation of Histones at Growth Genes. *Mol. Cell* *42*, 426–437.

Cañizares, F., Salinas, J., Heras, M. de las, Diaz, J., Tovar, I., Martinez, P., and Peñafiel, R. (1999). Prognostic Value of Ornithine Decarboxylase and Polyamines in Human Breast Cancer: Correlation with Clinicopathologic Parameters. *Clin. Cancer Res.* *5*, 2035–2041.

Cantley, L.C. (2002). The Phosphoinositide 3-Kinase Pathway. *Science* *296*, 1655–1657.

Cardaci, S., Ciriolo, M.R., Cardaci, S., and Ciriolo, M.R. (2012). TCA Cycle Defects and Cancer: When Metabolism Tunes Redox State, TCA Cycle Defects and Cancer: When Metabolism Tunes Redox State. *Int. J. Cell Biol.* *2012*, *2012*, e161837.

- Carpten, J.D., Faber, A.L., Horn, C., Donoho, G.P., Briggs, S.L., Robbins, C.M., Hostetter, G., Boguslawski, S., Moses, T.Y., Savage, S., et al. (2007). A transforming mutation in the pleckstrin homology domain of AKT1 in cancer. *Nature* *448*, 439–444.
- Carracedo, A., and Pandolfi, P.P. (2008). The PTEN–PI3K pathway: of feedbacks and cross-talks. *Oncogene* *27*, 5527–5541.
- Carracedo, A., Ma, L., Teruya-Feldstein, J., Rojo, F., Salmena, L., Alimonti, A., Egia, A., Sasaki, A.T., Thomas, G., Kozma, S.C., et al. (2008). Inhibition of mTORC1 leads to MAPK pathway activation through a PI3K-dependent feedback loop in human cancer. *J. Clin. Invest.* *118*, 3065–3074.
- Carracedo, A., Alimonti, A., and Pandolfi, P.P. (2011). PTEN Level in Tumor Suppression: How Much Is Too Little? *Cancer Res.* *71*, 629–633.
- Carracedo, A., Cantley, L.C., and Pandolfi, P.P. (2013). Cancer metabolism: fatty acid oxidation in the limelight. *Nat. Rev. Cancer* *13*, 227–232.
- Casero, R.A., and Marton, L.J. (2007). Targeting polyamine metabolism and function in cancer and other hyperproliferative diseases. *Nat. Rev. Drug Discov.* *6*, 373–390.
- Casero, R.A., and Pegg, A.E. (2009). Polyamine catabolism and disease. *Biochem. J.* *421*, 323–338.
- Casero, R.A., Wang, Y., Stewart, T.M., Devereux, W., Hacker, A., Wang, Y., Smith, R., and Woster, P.M. (2003). The role of polyamine catabolism in anti-tumour drug response. *Biochem. Soc. Trans.* *31*, 361–365.
- Cavuto, P., and Fenech, M.F. (2012). A review of methionine dependency and the role of methionine restriction in cancer growth control and life-span extension. *Cancer Treat. Rev.* *38*, 726–736.
- Chamie, K., Williams, S.B., Hershman, D.L., Wright, J.D., Nguyen, P.L., and Hu, J.C. (2015). Population-based assessment of determining predictors for quality of prostate cancer surveillance. *Cancer* *121*, 4150–4157.
- Chaturvedi, R., Asim, M., Romero-Gallo, J., Barry, D.P., Hoge, S., de Sablet, T., Delgado, A.G., Wroblewski, L.E., Piazuelo, M.B., Yan, F., et al. (2011). Spermine oxidase mediates the gastric cancer risk associated with *Helicobacter pylori* CagA. *Gastroenterology* *141*, 1696–1708-2.
- Chen, Y., Megosh, L.C., Gilmour, S.K., Sawicki, J.A., and O'Brien, T.G. (2000). K6/ODC transgenic mice as a sensitive model for carcinogen identification. *Toxicol. Lett.* *116*, 27–35.
- Chen, Z., Trotman, L.C., Shaffer, D., Lin, H.-K., Dotan, Z.A., Niki, M., Koutcher, J.A., Scher, H.I., Ludwig, T., Gerald, W., et al. (2005). Crucial role of p53-dependent cellular senescence in suppression of Pten-deficient tumorigenesis. *Nature* *436*, 725–730.
- Childs, A.C., Mehta, D.J., and Gerner, E.W. (2003). Polyamine-dependent gene expression. *Cell. Mol. Life Sci. CMLS* *60*, 1394–1406.
- Cho, S.-Y., Kang, W., Han, J.Y., Min, S., Kang, J., Lee, A., Kwon, J.Y., Lee, C., and Park, H. (2016). An Integrative Approach to Precision Cancer Medicine Using Patient-Derived Xenografts. *Molecules Cells* *39*, 77–86.
- Coffino, P. (2001). Regulation of cellular polyamines by antizyme. *Nat. Rev. Mol. Cell Biol.* *2*, 188–194.

Coleman, C.S., Pegg, A.E., Megosh, L.C., Guo, Y., Sawicki, J.A., and O'Brien, T.G. (2002). Targeted expression of spermidine/spermine N1-acetyltransferase increases susceptibility to chemically induced skin carcinogenesis. *Carcinogenesis* 23, 359–364.

Commisso, C., Davidson, S.M., Soydaner-Azeloglu, R.G., Parker, S.J., Kamphorst, J.J., Hackett, S., Grabocka, E., Nofal, M., Drebin, J.A., Thompson, C.B., et al. (2013). Macropinocytosis of protein is an amino acid supply route in Ras-transformed cells. *Nature* 497, 633–637.

Cooper, H.L., Park, M.H., and Folk, J.E. (1982). Posttranslational formation of hypusine in a single major protein occurs generally in growing cells and is associated with activation of lymphocyte growth. *Cell* 29, 791–797.

Cox, J., and Mann, M. (2008). MaxQuant enables high peptide identification rates, individualized p.p.b.-range mass accuracies and proteome-wide protein quantification. *Nat. Biotechnol.* 26, 1367–1372.

Cox, J., Neuhauser, N., Michalski, A., Scheltema, R.A., Olsen, J.V., and Mann, M. (2011). Andromeda: A Peptide Search Engine Integrated into the MaxQuant Environment. *J. Proteome Res.* 10, 1794–1805.

Cully, M., You, H., Levine, A.J., and Mak, T.W. (2006). Beyond PTEN mutations: the PI3K pathway as an integrator of multiple inputs during tumorigenesis. *Nat. Rev. Cancer* 6, 184–192.

Dancey, J. (2010). mTOR signaling and drug development in cancer. *Nat. Rev. Clin. Oncol.* 7, 209–219.

Dang, C.V. (2012). MYC on the Path to Cancer. *Cell* 149, 22–35.

Darzynkiewicz, Z., and Juan, G. (2001). Analysis of DNA Content and BrdU Incorporation. In *Current Protocols in Cytometry*, (John Wiley & Sons, Inc.), p. 7.7.1-7.7.9.

Datta, S.R., Dudek, H., Tao, X., Masters, S., Fu, H., Gotoh, Y., and Greenberg, M.E. (1997). Akt Phosphorylation of BAD Couples Survival Signals to the Cell-Intrinsic Death Machinery. *Cell* 91, 231–241.

Davies, M.A., Stemke-Hale, K., Tellez, C., Calderone, T.L., Deng, W., Prieto, V.G., Lazar, A.J.F., Gershenwald, J.E., and Mills, G.B. (2008). A novel AKT3 mutation in melanoma tumours and cell lines. *Br. J. Cancer* 99, 1265–1268.

Davis, M.E., Chen, Z. (Georgia), and Shin, D.M. (2008). Nanoparticle therapeutics: an emerging treatment modality for cancer. *Nat. Rev. Drug Discov.* 7, 771–782.

DeBerardinis, R.J., Lum, J.J., Hatzivassiliou, G., and Thompson, C.B. (2008). The Biology of Cancer: Metabolic Reprogramming Fuels Cell Growth and Proliferation. *Cell Metab.* 7, 11–20.

DebRoy, S., Kramarenko, I.I., Ghose, S., Oleinik, N.V., Krupenko, S.A., and Krupenko, N.I. (2013). A Novel Tumor Suppressor Function of Glycine N-Methyltransferase Is Independent of Its Catalytic Activity but Requires Nuclear Localization. *PLoS ONE* 8, e70062.

Demidenko, Z.N., and Blagosklonny, M.V. (2008). Growth stimulation leads to cellular senescence when the cell cycle is blocked. *Cell Cycle* 7, 3355–3361.

Demidenko, Z.N., Zubova, S.G., Bukreeva, E.I., Pospelov, V.A., Pospelova, T.V., and Blagosklonny, M.V. (2009). Rapamycin decelerates cellular senescence. *Cell Cycle* 8, 1888–1895.

Desideri, E., Vegliante, R., and Ciriolo, M.R. (2015). Mitochondrial dysfunctions in cancer: Genetic defects and oncogenic signaling impinging on TCA cycle activity. *Cancer Lett.* 356, 217–223.

- Di Cristofano, A.D., Pesce, B., Cordon-Cardo, C., and Pandolfi, P.P. (1998). Pten is essential for embryonic development and tumour suppression. *Nat. Genet.* 19, 348–355.
- Dibble, C.C., and Cantley, L.C. (2015). Regulation of mTORC1 by PI3K signaling. *Trends Cell Biol.* 25, 545–555.
- Dibble, C.C., and Manning, B.D. (2013a). Signal integration by mTORC1 coordinates nutrient input with biosynthetic output. *Nat. Cell Biol.* 15, 555–564.
- Dibble, C.C., and Manning, B.D. (2013b). Signal integration by mTORC1 coordinates nutrient input with biosynthetic output. *Nat. Cell Biol.* 15, 555–564.
- Dorhout, B., Te Velde, R.J., Ferwerda, H., Kingma, A.W., de Hoog, E., and Muskiet, F.A.J. (1995a). *in vivo* effects of 4-amidinoindan-1-one 2'-amidinohydrazone (CGP 48664A) and  $\alpha$ -difluoromethylornithine (DFMO) on L1210 growth, cell-cycle phase distribution and polyamine contents. *Int. J. Cancer* 62, 738–742.
- Dorhout, B., Velde, R.J.T., Kingma, H.F.W., De Hoog, E., and Muskiet, F.A.J. (1995b). *In vivo* growth inhibition of leukemia by 4-amidinoindan-1-one 2'-amidinohydrazone (CGP 48664a), a new inhibitor of S-adenosylmethionine decarboxylase. *Int. J. Cancer* 61, 214–217.
- Dorhout, B., Poortenga, P.J., Kingma, A.W., de Hoog, E., and Muskiet, F.A.J. (1998). *In vitro* manipulation of L1210 cell cycle kinetics with 4-amidinoindan-1-one 2'-amidinohydrazone,  $\alpha$ -difluoromethylornithine and N1-acetylspermine. *Biochim. Biophys. Acta BBA - Gen. Subj.* 1381, 95–103.
- Douros, J., and Suffness, M. (1981). New antitumor substances of natural origin. *Cancer Treat. Rev.* 8, 63–87.
- Duan, B., Wang, Y.-Z., Yang, T., Chu, X.-P., Yu, Y., Huang, Y., Cao, H., Hansen, J., Simon, R.P., Zhu, M.X., et al. (2011). Extracellular Spermine Exacerbates Ischemic Neuronal Injury through Sensitization of ASIC1a Channels to Extracellular Acidosis. *J. Neurosci.* 31, 2101–2112.
- Eagle, H. (1955). The Minimum Vitamin Requirements of the L and Hela Cells in Tissue Culture, the Production of Specific Vitamin Deficiencies, and Their Cure. *J. Exp. Med.* 102, 595–600.
- Eisenberg, T., Knauer, H., Schauer, A., Büttner, S., Ruckenstuhl, C., Carmona-Gutierrez, D., Ring, J., Schroeder, S., Magnes, C., Antonacci, L., et al. (2009). Induction of autophagy by spermidine promotes longevity. *Nat. Cell Biol.* 11, 1305–1314.
- Engelman, J.A., Luo, J., and Cantley, L.C. (2006). The evolution of phosphatidylinositol 3-kinases as regulators of growth and metabolism. *Nat. Rev. Genet.* 7, 606–619.
- Epner, D.E., Morrow, S., Wilcox, M., and Houghton, J.L. (2002). Nutrient Intake and Nutritional Indexes in Adults With Metastatic Cancer on a Phase I Clinical Trial of Dietary Methionine Restriction. *Nutr. Cancer* 42, 158–166.
- Epstein, T., Xu, L., Gillies, R.J., and Gatenby, R.A. (2014). Separation of metabolic supply and demand: aerobic glycolysis as a normal physiological response to fluctuating energetic demands in the membrane. *Cancer Metab.* 2, 1.
- Eskens, F.A.L.M., Greim, G.A., Zuylen, C. van, Wolff, I., Denis, L.J., Planting, A.S.T., Muskiet, F.A., Wanders, J., Barbet, N.C., Choi, L., et al. (2000). Phase I and Pharmacological Study of Weekly Administration of the Polyamine Synthesis Inhibitor SAM 486A (CGP 48 664) in Patients with Solid Tumors. *Clin. Cancer Res.* 6, 1736–1743.
- Fasolo, A., and Sessa, C. (2008). mTOR inhibitors in the treatment of cancer. *Expert Opin. Investig. Drugs* 17, 1717–1734.

Feith, D.J., Shantz, L.M., and Pegg, A.E. (2001). Targeted antizyme expression in the skin of transgenic mice reduces tumor promoter induction of ornithine decarboxylase and decreases sensitivity to chemical carcinogenesis. *Cancer Res.* *61*, 6073–6081.

Feng, X., Zhuang, W.-Q., Colletti, P., and Tang, Y.J. (2012). Metabolic pathway determination and flux analysis in nonmodel microorganisms through <sup>13</sup>C-isotope labeling. *Methods Mol. Biol. Clifton NJ* *881*, 309–330.

Ferlay, J., Steliarova-Foucher, E., Lortet-Tieulent, J., Rosso, S., Coebergh, J.W.W., Comber, H., Forman, D., and Bray, F. (2013). Cancer incidence and mortality patterns in Europe: Estimates for 40 countries in 2012. *Eur. J. Cancer* *49*, 1374–1403.

Friedman, A.A., Letai, A., Fisher, D.E., and Flaherty, K.T. (2015). Precision medicine for cancer with next-generation functional diagnostics. *Nat. Rev. Cancer* *15*, 747–756.

Fuhrer, T., Heer, D., Begemann, B., and Zamboni, N. (2011). High-throughput, accurate mass metabolome profiling of cellular extracts by flow injection-time-of-flight mass spectrometry. *Anal. Chem.* *83*, 7074–7080.

Fujimura, K., Wright, T., Strnadell, J., Kaushal, S., Metildi, C., Lowy, A.M., Bouvet, M., Kelber, J.A., and Klemke, R.L. (2014). A Hypusine-eIF5A-PEAK1 Switch Regulates the Pathogenesis of Pancreatic Cancer. *Cancer Res.* *74*, 6671–6681.

Fujisawa, S., and Kadoma, Y. (2005). Kinetic Evaluation of Polyamines as Radical Scavengers. *Anticancer Res.* *25*, 965–969.

Fujita, K., Murakami, Y., and Hayashi, S. (1982). A macromolecular inhibitor of the antizyme to ornithine decarboxylase. *Biochem. J.* *204*, 647–652.

Fumagalli, S., Ivanenkov, V.V., Teng, T., and Thomas, G. (2012). Suprainduction of p53 by disruption of 40S and 60S ribosome biogenesis leads to the activation of a novel G2/M checkpoint. *Genes Dev.* *26*, 1028–1040.

Gerner, E.W., and Meyskens, F.L. (2004a). Polyamines and cancer: old molecules, new understanding. *Nat. Rev. Cancer* *4*, 781–792.

Gerner, E.W., and Meyskens, F.L. (2004b). Polyamines and cancer: old molecules, new understanding. *Nat. Rev. Cancer* *4*, 781–792.

Gonzalez-Angulo, A.M., Krop, I., Akcakanat, A., Chen, H., Liu, S., Li, Y., Culotta, K.S., Tarco, E., Piha-Paul, S., Moulder-Thompson, S., et al. (2015). SU2C Phase Ib Study of Paclitaxel and MK-2206 in Advanced Solid Tumors and Metastatic Breast Cancer. *J. Natl. Cancer Inst.* *107*, dju493.

Goodwin, A.C., Jadallah, S., Toubaji, A., Lecksell, K., Hicks, J.L., Kowalski, J., Bova, G.S., De Marzo, A.M., Netto, G.J., and Casero, R.A. (2008). Increased spermine oxidase expression in human prostate cancer and prostatic intraepithelial neoplasia tissues. *The Prostate* *68*, 766–772.

Gratzner, H.G. (1982). Monoclonal antibody to 5-bromo- and 5-iododeoxyuridine: A new reagent for detection of DNA replication. *Science* *218*, 474–475.

Groppa, M.D., and Benavides, M.P. (2007). Polyamines and abiotic stress: recent advances. *Amino Acids* *34*, 35–45.

Gu, Y., Mi, W., Ge, Y., Liu, H., Fan, Q., Han, C., Yang, J., Han, F., Lu, X., and Yu, W. (2010). GlcNAcylation Plays an Essential Role in Breast Cancer Metastasis. *Cancer Res.* *70*, 6344–6351.

Guertin, D.A., Stevens, D.M., Saitoh, M., Kinkel, S., Crosby, K., Sheen, J.-H., Mullholland, D.J., Magnuson, M.A., Wu, H., and Sabatini, D.M. (2009). mTOR Complex 2 Is Required for the Development of Prostate Cancer Induced by Pten Loss in Mice. *Cancer Cell* *15*, 148–159.

- Guillaumond, F., Leca, J., Olivares, O., Lavaut, M.-N., Vidal, N., Berthezène, P., Dusetti, N.J., Loncle, C., Calvo, E., Turrini, O., et al. (2013). Strengthened glycolysis under hypoxia supports tumor symbiosis and hexosamine biosynthesis in pancreatic adenocarcinoma. *Proc. Natl. Acad. Sci.* *110*, 3919–3924.
- Guo, H., Lishko, V.K., Herrera, H., Groce, A., Kubota, T., and Hoffman, R.M. (1993). Therapeutic Tumor-specific Cell Cycle Block Induced by Methionine Starvation in Vivo. *Cancer Res.* *53*, 5676–5679.
- Guo, Y., Cleveland, J.L., and O'Brien, T.G. (2005). Haploinsufficiency for *Odc* Modifies Mouse Skin Tumor Susceptibility. *Cancer Res.* *65*, 1146–1149.
- Gupta, E.D., Pachauri, M., Ghosh, P.C., and Rajam, M.V. (2015). Targeting polyamine biosynthetic pathway through RNAi causes the abrogation of MCF 7 breast cancer cell line. *Tumor Biol.* 1–13.
- Ha, H.C., Sirisoma, N.S., Kuppusamy, P., Zweier, J.L., Woster, P.M., and Casero, R.A. (1998). The natural polyamine spermine functions directly as a free radical scavenger. *Proc. Natl. Acad. Sci.* *95*, 11140–11145.
- Hahn, W.C., and Weinberg, R.A. (2002). Rules for Making Human Tumor Cells. *N. Engl. J. Med.* *347*, 1593–1603.
- Halim, A.-B., LeGros, L., Geller, A., and Kotb, M. (1999). Expression and Functional Interaction of the Catalytic and Regulatory Subunits of Human Methionine Adenosyltransferase in Mammalian Cells. *J. Biol. Chem.* *274*, 29720–29725.
- Hanahan, D., and Weinberg, R.A. (2000). The Hallmarks of Cancer. *Cell* *100*, 57–70.
- Hanahan, D., and Weinberg, R.A. (2011). Hallmarks of Cancer: The Next Generation. *Cell* *144*, 646–674.
- Hanash, S., and Taguchi, A. (2010). The grand challenge to decipher the cancer proteome. *Nat. Rev. Cancer* *10*, 652–660.
- Hanover, J.A., Krause, M.W., and Love, D.C. (2010). The hexosamine signaling pathway: O-GlcNAc cycling in feast or famine. *Biochim. Biophys. Acta BBA - Gen. Subj.* *1800*, 80–95.
- Harrison, D.E., Strong, R., Sharp, Z.D., Nelson, J.F., Astle, C.M., Flurkey, K., Nadon, N.L., Wilkinson, J.E., Frenkel, K., Carter, C.S., et al. (2009). Rapamycin fed late in life extends lifespan in genetically heterogeneous mice. *Nature* *460*, 392–395.
- Hayashi, S., and Murakami, Y. (1995). Rapid and regulated degradation of ornithine decarboxylase. *Biochem. J.* *306*, 1–10.
- Hellmich, M.R., Coletta, C., Chao, C., and Szabo, C. (2014). The Therapeutic Potential of Cystathionine  $\beta$ -Synthetase/Hydrogen Sulfide Inhibition in Cancer. *Antioxid. Redox Signal.* *22*, 424–448.
- Hiles, I.D., Otsu, M., Volinia, S., Fry, M.J., Gout, I., Dhand, R., Panayotou, G., Ruiz-Larrea, F., Thompson, A., Totty, N.F., et al. (1992). Phosphatidylinositol 3-kinase: Structure and expression of the 110 kd catalytic subunit. *Cell* *70*, 419–429.
- Hill, J.R., and Morris, D.R. (1992). Cell-specific translation of S-adenosylmethionine decarboxylase mRNA. Regulation by the 5' transcript leader. *J. Biol. Chem.* *267*, 21886–21893.
- Hirai, H., Sootome, H., Nakatsuru, Y., Miyama, K., Taguchi, S., Tsujioka, K., Ueno, Y., Hatch, H., Majumder, P.K., Pan, B.-S., et al. (2010). MK-2206, an Allosteric Akt Inhibitor, Enhances

Antitumor Efficacy by Standard Chemotherapeutic Agents or Molecular Targeted Drugs In vitro and In vivo. *Mol. Cancer Ther.* 9, 1956–1967.

Hogarty, M.D., Norris, M.D., Davis, K., Liu, X., Evageliou, N.F., Hayes, C.S., Pawel, B., Guo, R., Zhao, H., Sekyere, E., et al. (2008). ODC1 Is a Critical Determinant of MYCN Oncogenesis and a Therapeutic Target in Neuroblastoma. *Cancer Res.* 68, 9735–9745.

Hollander, M.C., Blumenthal, G.M., and Dennis, P.A. (2011). PTEN loss in the continuum of common cancers, rare syndromes and mouse models. *Nat. Rev. Cancer* 11, 289–301.

Holmes, E., Wilson, I.D., and Nicholson, J.K. (2008). Metabolic Phenotyping in Health and Disease. *Cell* 134, 714–717.

Horn, Y., Schechter, P.J., and Marton, L.J. (1987). Phase I-II clinical trial with alpha-difluoromethylornithine--an inhibitor of polyamine biosynthesis. *Eur. J. Cancer Clin. Oncol.* 23, 1103–1107.

Howell, J.J., and Manning, B.D. (2011). mTOR couples cellular nutrient sensing to organismal metabolic homeostasis. *Trends Endocrinol. Metab.* 22, 94–102.

Hsieh, A.L., Walton, Z.E., Altman, B.J., Stine, Z.E., and Dang, C.V. (2015). MYC and metabolism on the path to cancer. *Semin. Cell Dev. Biol.* 43, 11–21.

Hsu, P.P., Kang, S.A., Rameseder, J., Zhang, Y., Ottina, K.A., Lim, D., Peterson, T.R., Choi, Y., Gray, N.S., Yaffe, M.B., et al. (2011). The mTOR-Regulated Phosphoproteome Reveals a Mechanism of mTORC1-Mediated Inhibition of Growth Factor Signaling. *Science* 332, 1317–1322.

<http://uroweb.org/individual-guidelines/oncology-guidelines/> Oncology Guidelines.

<http://www.who.int/cancer/en/> WHO | Cancer.

Hu, X., Washington, S., Verderame, M.F., Demers, L.M., Mauger, D., and Manni, A. (2004). Biological activity of the S-adenosylmethionine decarboxylase inhibitor SAM486A in human breast cancer cells in vitro and in vivo. *Int. J. Oncol.* 25, 1831–1838.

Huang, Y.-C., Lee, C.-M., Chen, M., Chung, M.-Y., Chang, Y.-H., Huang, W.J.-S., Ho, D.M.-T., Pan, C.-C., Wu, T.T., Yang, S., et al. (2007). Haplotypes, Loss of Heterozygosity, and Expression Levels of Glycine N-Methyltransferase in Prostate Cancer. *Clin. Cancer Res.* 13, 1412–1420.

Hubbard, G.K., Mutton, L.N., Khalili, M., McMullin, R.P., Hicks, J.L., Bianchi-Frias, D., Horn, L.A., Kulac, I., Moubarek, M.S., Nelson, P.S., et al. (2015). Combined MYC Activation and Pten Loss Are Sufficient to Create Genomic Instability and Lethal Metastatic Prostate Cancer. *Cancer Res.*

Hudis, C., Swanton, C., Janjigian, Y.Y., Lee, R., Sutherland, S., Lehman, R., Chandarlapaty, S., Hamilton, N., Gajria, D., Knowles, J., et al. (2013). A phase 1 study evaluating the combination of an allosteric AKT inhibitor (MK-2206) and trastuzumab in patients with HER2-positive solid tumors. *Breast Cancer Res.* 15, R110.

Humphrey, P.A. (2004). Gleason grading and prognostic factors in carcinoma of the prostate. *Mod. Pathol.* 17, 292–306.

Hyvönen, M.T., Koponen, T., Weisell, J., Pietilä, M., Khomutov, A.R., Vepsäläinen, J., Alhonen, L., and Keinänen, T.A. (2013). Spermidine promotes adipogenesis of 3T3-L1 cells by preventing interaction of ANP32 with HuR and PP2A. *Biochem. J.* 453, 467–474.

Iacomino, G., Picariello, G., and D'Agostino, L. (2012). DNA and nuclear aggregates of polyamines. *Biochim. Biophys. Acta* 1823, 1745–1755.

- Igarashi, K., and Kashiwagi, K. (2010). Modulation of cellular function by polyamines. *Int. J. Biochem. Cell Biol.* *42*, 39–51.
- Ignatenko, N.A., Babbar, N., Mehta, D., Casero, R.A., and Gerner, E.W. (2004). Suppression of polyamine catabolism by activated Ki-ras in human colon cancer cells. *Mol. Carcinog.* *39*, 91–102.
- Inoki, K., Li, Y., Zhu, T., Wu, J., and Guan, K.-L. (2002). TSC2 is phosphorylated and inhibited by Akt and suppresses mTOR signalling. *Nat. Cell Biol.* *4*, 648–657.
- Isaacs, W., De Marzo, A., and Nelson, W.G. (2002). Focus on prostate cancer. *Cancer Cell* *2*, 113–116.
- Ishii, I., Ikeguchi, Y., Mano, H., Wada, M., Pegg, A.E., and Shirahata, A. (2011). Polyamine metabolism is involved in adipogenesis of 3T3-L1 cells. *Amino Acids* *42*, 619–626.
- Iyer, R., and Delcour, A.H. (1997). Complex Inhibition of OmpF and OmpC Bacterial Porins by Polyamines. *J. Biol. Chem.* *272*, 18595–18601.
- Jasiulionis, M.G., Luchessi, A.D., Moreira, A.G., Souza, P.P.C., Suenaga, A.P.M., Correa, M., Costa, C.A.S., Curi, R., and Costa-Neto, C.M. (2007). Inhibition of eukaryotic translation initiation factor 5A (eIF5A) hypusination impairs melanoma growth. *Cell Biochem. Funct.* *25*, 109–114.
- Jhee, K.-H., and Kruger, W.D. (2005). The Role of Cystathionine  $\beta$ -Synthase in Homocysteine Metabolism. *Antioxid. Redox Signal.* *7*, 813–822.
- Jia, K., Chen, D., and Riddle, D.L. (2004). The TOR pathway interacts with the insulin signaling pathway to regulate *C. elegans* larval development, metabolism and life span. *Dev. Camb. Engl.* *131*, 3897–3906.
- Jin, S.J., and Tserng, K.Y. (1989). Identification of isomeric unsaturated medium-chain dicarboxylic acids in human urine. *J. Lipid Res.* *30*, 1611–1619.
- Jonkers, J., and Berns, A. (2002). Conditional mouse models of sporadic cancer. *Nat. Rev. Cancer* *2*, 251–265.
- Jóźwiak, P., Forma, E., Bryś, M., and Krześlak, A. (2014). O-GlcNAcylation and Metabolic Reprograming in Cancer. *Front. Endocrinol.* *5*.
- Jung, C.H., Ro, S.-H., Cao, J., Otto, N.M., and Kim, D.-H. (2010). mTOR regulation of autophagy. *FEBS Lett.* *584*, 1287–1295.
- Kaeberlein, M., Powers, R.W., Steffen, K.K., Westman, E.A., Hu, D., Dang, N., Kerr, E.O., Kirkland, K.T., Fields, S., and Kennedy, B.K. (2005). Regulation of yeast replicative life span by TOR and Sch9 in response to nutrients. *Science* *310*, 1193–1196.
- Kaiser, A. (2011). Translational control of eIF5A in various diseases. *Amino Acids* *42*, 679–684.
- Kameji, T., and Pegg, A.E. (1987). Effect of putrescine on the synthesis of S-adenosylmethionine decarboxylase. *Biochem. J.* *243*, 285–288.
- Kamphorst, J.J., Cross, J.R., Fan, J., Stanchina, E. de, Mathew, R., White, E.P., Thompson, C.B., and Rabinowitz, J.D. (2013). Hypoxic and Ras-transformed cells support growth by scavenging unsaturated fatty acids from lysophospholipids. *Proc. Natl. Acad. Sci.* *110*, 8882–8887.
- Kapahi, P., Zid, B.M., Harper, T., Koslover, D., Sapin, V., and Benzer, S. (2004). Regulation of lifespan in *Drosophila* by modulation of genes in the TOR signaling pathway. *Curr. Biol. CB* *14*, 885–890.



Katso, R., Okkenhaug, K., Ahmadi, K., White, S., Timms, J., and Waterfield, M.D. (2001). Cellular Function of Phosphoinositide 3-Kinases: Implications for Development, Immunity, Homeostasis, and Cancer. *Annu. Rev. Cell Dev. Biol.* 17, 615–675.

Kee, K., Foster, B.A., Merali, S., Kramer, D.L., Hensen, M.L., Diegelman, P., Kisiel, N., Vujcic, S., Mazurchuk, R.V., and Porter, C.W. (2004). Activated Polyamine Catabolism Depletes Acetyl-CoA Pools and Suppresses Prostate Tumor Growth in TRAMP Mice. *J. Biol. Chem.* 279, 40076–40083.

Khan, A.P., Rajendiran, T.M., Ateeq, B., Asangani, I.A., Athanikar, J.N., Yocum, A.K., Mehra, R., Siddiqui, J., Palapattu, G., Wei, J.T., et al. (2013). The Role of Sarcosine Metabolism in Prostate Cancer Progression. *Neoplasia N. Y. N* 15, 491–501.

Kingsnorth, A.N., Lumsden, A.B., and Wallace, H.M. (1984). Polyamines in colorectal cancer. *Br. J. Surg.* 71, 791–794.

Klupczyńska, A., Dereziński, P., and Kokot, Z.J. (2015). METABOLOMICS IN MEDICAL SCIENCES--TRENDS, CHALLENGES AND PERSPECTIVES. *Acta Pol. Pharm.* 72, 629–641.

Knoblauch, S., and True, L. (2012). 18 - Male Reproductive System A2 - Treuting, Piper M. In *Comparative Anatomy and Histology*, S.M. Dintzis, ed. (San Diego: Academic Press), pp. 285–308.

Komninou, D., Leutzinger, Y., Reddy, B.S., and Jr, J.P.R. (2006). Methionine Restriction Inhibits Colon Carcinogenesis. *Nutr. Cancer* 54, 202–208.

Krajcovic, M., Krishna, S., Akkari, L., Joyce, J.A., and Overholtzer, M. (2013). mTOR regulates phagosome and entotic vacuole fission. *Mol. Biol. Cell* 24, 3736–3745.

Krasnoslobodtsev, A.V., Peng, J., Asiago, J.M., Hindupur, J., Rochet, J.-C., and Lyubchenko, Y.L. (2012). Effect of Spermidine on Misfolding and Interactions of Alpha-Synuclein. *PLOS ONE* 7, e38099.

Krishan, A. (1975). Rapid flow cytofluorometric analysis of mammalian cell cycle by propidium iodide staining. *J. Cell Biol.* 66, 188–193.

Krüger, A., Vowinckel, J., Mülleder, M., Grote, P., Capuano, F., Bluemlein, K., and Ralser, M. (2013). Tpo1-mediated spermine and spermidine export controls cell cycle delay and times antioxidant protein expression during the oxidative stress response. *EMBO Rep.* 14, 1113–1119.

Kumar, N., Basundra, R., and Maiti, S. (2009). Elevated polyamines induce c-MYC overexpression by perturbing quadruplex–WC duplex equilibrium. *Nucleic Acids Res.* 37, 3321–3331.

Kusano, T., Berberich, T., Tateda, C., and Takahashi, Y. (2008). Polyamines: essential factors for growth and survival. *Planta* 228, 367–381.

Labuschagne, C.F., van den Broek, N.J.F., Mackay, G.M., Vousden, K.H., and Maddocks, O.D.K. (2014). Serine, but Not Glycine, Supports One-Carbon Metabolism and Proliferation of Cancer Cells. *Cell Rep.* 7, 1248–1258.

Lamming, D.W., Ye, L., Sabatini, D.M., and Baur, J.A. (2013). Rapalogs and mTOR inhibitors as anti-aging therapeutics. *J. Clin. Invest.* 123, 980–989.

Land, S.C., Scott, C.L., and Walker, D. (2014). mTOR signalling, embryogenesis and the control of lung development. *Semin. Cell Dev. Biol.* 36, 68–78.

- Landau, G., Bercovich, Z., Park, M.H., and Kahana, C. (2010). The Role of Polyamines in Supporting Growth of Mammalian Cells Is Mediated through Their Requirement for Translation Initiation and Elongation. *J. Biol. Chem.* 285, 12474–12481.
- Laplante, M., and Sabatini, D.M. (2012). mTOR Signaling in Growth Control and Disease. *Cell* 149, 274–293.
- Lauren Cason, A., Ikeguchi, Y., Skinner, C., Wood, T.C., Holden, K.R., Lubs, H.A., Martinez, F., Simensen, R.J., Stevenson, R.E., Pegg, A.E., et al. (2003). X-linked spermine synthase gene (SMS) defect: the first polyamine deficiency syndrome. *Eur. J. Hum. Genet.* 11, 937–944.
- Law, G.L., Raney, A., Heusner, C., and Morris, D.R. (2001). Polyamine regulation of ribosome pausing at the upstream open reading frame of S-adenosylmethionine decarboxylase. *J. Biol. Chem.*
- Lawlor, M.A., and Alessi, D.R. (2001). PKB/Akt. *J. Cell Sci.* 114, 2903–2910.
- Lee, N.K.L., and MacLean, H.E. (2011). Polyamines, androgens, and skeletal muscle hypertrophy. *J. Cell. Physiol.* 226, 1453–1460.
- Lee, S.B., Park, J.H., Folk, J.E., Deck, J.A., Pegg, A.E., Sokabe, M., Fraser, C.S., and Park, M.H. (2011). Inactivation of eukaryotic initiation factor 5A (eIF5A) by specific acetylation of its hypusine residue by spermidine/spermine acetyltransferase 1 (SSAT1). *Biochem. J.* 433, 205–213.
- Leontieva, O.V., Demidenko, Z.N., Blagosklonny, M.V., Leontieva, O.V., Demidenko, Z.N., and Blagosklonny, M.V. (2015). Dual mTORC1/C2 inhibitors suppress cellular geroconversion (a senescence program). *Oncotarget* 6, 23238–23248.
- Li, W., Liu, X., Wang, W., Sun, H., Hu, Y., Lei, H., Liu, G., and Gao, Y. (2008). Effects of antisense RNA targeting of ODC and AdoMetDC on the synthesis of polyamine synthesis and cell growth in prostate cancer cells using a prostatic androgen-dependent promoter in adenovirus. *The Prostate* 68, 1354–1361.
- Liang, J., Zubovitz, J., Petrocelli, T., Kotchetkov, R., Connor, M.K., Han, K., Lee, J.-H., Ciarallo, S., Catzavelos, C., Beniston, R., et al. (2002). PKB/Akt phosphorylates p27, impairs nuclear import of p27 and opposes p27-mediated G1 arrest. *Nat. Med.* 8, 1153–1160.
- Liberti, M.V., and Locasale, J.W. (2016). The Warburg Effect: How Does it Benefit Cancer Cells? *Trends Biochem. Sci.*
- Liesenfeld, D.B., Habermann, N., Owen, R.W., Scalbert, A., and Ulrich, C.M. (2013). Review of Mass Spectrometry–Based Metabolomics in Cancer Research. *Cancer Epidemiol. Biomarkers Prev.* 22, 2182–2201.
- Lilja, H., Ulmert, D., and Vickers, A.J. (2008). Prostate-specific antigen and prostate cancer: prediction, detection and monitoring. *Nat. Rev. Cancer* 8, 268–278.
- Liu, Y. (2006). Fatty acid oxidation is a dominant bioenergetic pathway in prostate cancer. *Prostate Cancer Prostatic Dis.* 9, 230–234.
- Liu, L., Rao, J.N., Zou, T., Xiao, L., Wang, P.-Y., Turner, D.J., Gorospe, M., and Wang, J.-Y. (2009a). Polyamines Regulate c-Myc Translation through Chk2-dependent HuR Phosphorylation. *Mol. Biol. Cell* 20, 4885–4898.
- Liu, P., Cheng, H., Roberts, T.M., and Zhao, J.J. (2009b). Targeting the phosphoinositide 3-kinase pathway in cancer. *Nat. Rev. Drug Discov.* 8, 627–644.
- Locasale, J.W. (2013). Serine, glycine and one-carbon units: cancer metabolism in full circle. *Nat. Rev. Cancer* 13, 572–583.

Loenen, W. a. M. (2006). S-Adenosylmethionine: jack of all trades and master of everything? *Biochem. Soc. Trans.* *34*, 330–333.

López-Lázaro, M. (2015). Selective amino acid restriction therapy (SAART): a non-pharmacological strategy against all types of cancer cells. *Oncoscience* *2*, 857–866.

Loprinzi, C.L., and Messing, E.M. (1992). A prospective clinical trial of difluoromethylornithine (DFMO) in patients with resected superficial bladder cancer. *J. Cell. Biochem. Suppl.* *161*, 153–155.

Luka, Z., Capdevila, A., Mato, J.M., and Wagner, C. (2006). A Glycine N-methyltransferase Knockout Mouse Model for Humans with Deficiency of this Enzyme. *Transgenic Res.* *15*, 393–397.

Luo, J., Yu, C.-H., Yu, H., Borstnar, R., Kamerlin, S.C.L., Gräslund, A., Abrahams, J.P., and Wärmländer, S.K.T.S. (2013). Cellular Polyamines Promote Amyloid-Beta (A $\beta$ ) Peptide Fibrillation and Modulate the Aggregation Pathways. *ACS Chem. Neurosci.* *4*, 454–462.

Lynch, T.P., Ferrer, C.M., Jackson, S.R., Shahriari, K.S., Vosseller, K., and Reginato, M.J. (2012). Critical Role of O-Linked  $\beta$ -N-Acetylglucosamine Transferase in Prostate Cancer Invasion, Angiogenesis, and Metastasis. *J. Biol. Chem.* *287*, 11070–11081.

Ma, X.M., and Blenis, J. (2009). Molecular mechanisms of mTOR-mediated translational control. *Nat. Rev. Mol. Cell Biol.* *10*, 307–318.

Ma, Z., and Vosseller, K. (2013). O-GlcNAc in cancer biology. *Amino Acids* *45*, 719–733.

Mailloux, R.J., McBride, S.L., and Harper, M.-E. (2013). Unearthing the secrets of mitochondrial ROS and glutathione in bioenergetics. *Trends Biochem. Sci.* *38*, 592–602.

Mamane, Y., Petroulakis, E., LeBacquer, O., and Sonenberg, N. (2006). mTOR, translation initiation and cancer. *Oncogene* *25*, 6416–6422.

Manni, A., Fischer, S., Franks, M., Washington, S., De Arment, R., Griffith, J., Demers, L., Verderame, M., Leiby, B., and Mauger, D. (2001). S-adenosylmethionine decarboxylase overexpression reduces invasiveness and tumorigenicity in nude mice of MCF-7 breast cancer cells. *Int. J. Oncol.* *19*, 317–323.

Manning, B.D., and Cantley, L.C. (2007). AKT/PKB Signaling: Navigating Downstream. *Cell* *129*, 1261–1274.

Manning, B.D., Tee, A.R., Logsdon, M.N., Blenis, J., and Cantley, L.C. (2002). Identification of the Tuberous Sclerosis Complex-2 Tumor Suppressor Gene Product Tuberin as a Target of the Phosphoinositide 3-Kinase/Akt Pathway. *Mol. Cell* *10*, 151–162.

Marone, R., Cmiljanovic, V., Giese, B., and Wymann, M.P. (2008). Targeting phosphoinositide 3-kinase—Moving towards therapy. *Biochim. Biophys. Acta BBA - Proteins Proteomics* *1784*, 159–185.

Martínez, M.E., O'Brien, T.G., Fultz, K.E., Babbar, N., Yerushalmi, H., Qu, N., Guo, Y., Boorman, D., Einspahr, J., Alberts, D.S., et al. (2003). Pronounced reduction in adenoma recurrence associated with aspirin use and a polymorphism in the ornithine decarboxylase gene. *Proc. Natl. Acad. Sci.* *100*, 7859–7864.

Martínez-Chantar, M.L., García-Trevijano, E.R., Latasa, M.U., Martín-Duce, A., Fortes, P., Caballería, J., Avila, M.A., and Mato, J.M. (2003a). Methionine adenosyltransferase II  $\beta$  subunit gene expression provides a proliferative advantage in human hepatoma. *Gastroenterology* *124*, 940–948.

Martínez-Chantar, M.L., Latasa, M.U., Varela-Rey, M., Lu, S.C., García-Trevijano, E.R., Mato, J.M., and Avila, M.A. (2003b). L-Methionine Availability Regulates Expression of the Methionine Adenosyltransferase 2A Gene in Human Hepatocarcinoma Cells ROLE OF S-ADENOSYLMETHIONINE. *J. Biol. Chem.* 278, 19885–19890.

Martínez-Chantar, M.L., Vázquez-Chantada, M., Ariz, U., Martínez, N., Varela, M., Luka, Z., Capdevila, A., Rodríguez, J., Aransay, A.M., Matthiesen, R., et al. (2008). Loss of the glycine N-methyltransferase gene leads to steatosis and hepatocellular carcinoma in mice. *Hepatology* 47, 1191–1199.

Martínez-Uña, M., Varela-Rey, M., Cano, A., Fernández-Ares, L., Beraza, N., Aurrekoetxea, I., Martínez-Arranz, I., García-Rodríguez, J.L., Buqué, X., Mestre, D., et al. (2013). Excess S-adenosylmethionine reroutes phosphatidylethanolamine towards phosphatidylcholine and triglyceride synthesis. *Hepatology* 58, 1296–1305.

Martini, M., Santis, M.C.D., Braccini, L., Gulluni, F., and Hirsch, E. (2014). PI3K/AKT signaling pathway and cancer: an updated review. *Ann. Med.* 46, 372–383.

Mato, J.M., and Lu, S.C. (2011). The Hepatocarcinogenic Effect of Methionine and Choline Deficient Diets: An Adaptation to the Warburg Effect? *Alcohol. Clin. Exp. Res.* 35, 811–814.

Mato, J.M., Corrales, F.J., Lu, S.C., and Avila, M.A. (2002). S-Adenosylmethionine: a control switch that regulates liver function. *FASEB J.* 16, 15–26.

Mellinger, G.T., Gleason, D., and Bailar, J. (1967). The histology and prognosis of prostatic cancer. *J. Urol.* 97, 331–337.

Miller-Fleming, L., Olin-Sandoval, V., Campbell, K., and Ralser, M. (2015). Remaining Mysteries of Molecular Biology: The Role of Polyamines in the Cell. *J. Mol. Biol.* 427, 3389–3406.

Millward, M.J., Joshua, A., Kefford, R., Aamdal, S., Thomson, D., Hersey, P., Toner, G., and Lynch, K. (2005). Multi-centre Phase II trial of the polyamine synthesis inhibitor SAM486A (CGP48664) in patients with metastatic melanoma. *Invest. New Drugs* 23, 253–256.

Minois, N. (2014). Molecular Basis of the “Anti-Aging” Effect of Spermidine and Other Natural Polyamines - A Mini-Review. *Gerontology* 60, 319–326.

Minois, N., Carmona-Gutierrez, D., and Madeo, F. (2011). Polyamines in aging and disease. *Aging* 3, 716–732.

Mirnezami, R., Nicholson, J., and Darzi, A. (2012). Preparing for Precision Medicine. *N. Engl. J. Med.* 366, 489–491.

Mounir, Z., Krishnamoorthy, J.L., Robertson, G.P., Scheuner, D., Kaufman, R.J., Georgescu, M.-M., and Koromilas, A.E. (2009). Tumor Suppression by PTEN Requires the Activation of the PKR-eIF2 $\alpha$  Phosphorylation Pathway. *Sci. Signal.* 2, ra85-ra85.

Nagy, B., Szendroi, A., and Romics, I. (2008). Overexpression of CD24, c-myc and Phospholipase 2A in Prostate Cancer Tissue Samples Obtained by Needle Biopsy. *Pathol. Oncol. Res.* 15, 279–283.

Nakabayashi, M., Werner, L., Courtney, K.D., Buckle, G., Oh, W.K., Bublely, G.J., Hayes, J.H., Weckstein, D., Elfiky, A., Sims, D.M., et al. (2012). Phase II trial of RAD001 and bicalutamide for castration-resistant prostate cancer. *BJU Int.* 110, 1729–1735.

Nardella, C., Carracedo, A., Salmena, L., and Pandolfi, P.P. (2010a). Faithfull Modeling of PTEN Loss Driven Diseases in the Mouse (Springer Berlin Heidelberg).

Nardella, C., Carracedo, A., Salmena, L., and Pandolfi, P.P. (2010b). Faithful Modeling of PTEN Loss Driven Diseases in the Mouse. In *Phosphoinositide 3-Kinase in Health and Disease*, C. Rommel, B. Vanhaesebroeck, and P.K. Vogt, eds. (Springer Berlin Heidelberg), pp. 135–168.

Nastiuk, K.L., and Krolewski, J.J. (2016). Opportunities and challenges in combination gene cancer therapy. *Adv. Drug Deliv. Rev.* **98**, 35–40.

Neufeld, T.P. (2010). TOR-dependent control of autophagy: biting the hand that feeds. *Curr. Opin. Cell Biol.* **22**, 157–168.

Niklas, J., Schneider, K., and Heinzle, E. (2010). Metabolic flux analysis in eukaryotes. *Curr. Opin. Biotechnol.* **21**, 63–69.

Nilsson, J., Koskiniemi, S., Persson, K., Grahn, B., and Holm, I. (1997). Polyamines Regulate Both Transcription and Translation of the Gene Encoding Ornithine Decarboxylase Antizyme in Mouse. *Eur. J. Biochem.* **250**, 223–231.

Nishimura, K., Nakatsu, F., Kashiwagi, K., Ohno, H., Saito, T., and Igarashi, K. (2002). Essential role of S-adenosylmethionine decarboxylase in mouse embryonic development. *Genes Cells* **7**, 41–47.

Nishimura, K., Shiina, R., Kashiwagi, K., and Igarashi, K. (2006). Decrease in Polyamines with Aging and Their Ingestion from Food and Drink. *J. Biochem. (Tokyo)* **139**, 81–90.

Nishimura, K., Okudaira, H., Ochiai, E., Higashi, K., Kaneko, M., Ishii, I., Nishimura, T., Dohmae, N., Kashiwagi, K., and Igarashi, K. (2009a). Identification of proteins whose synthesis is preferentially enhanced by polyamines at the level of translation in mammalian cells. *Int. J. Biochem. Cell Biol.* **41**, 2251–2261.

Nishimura, K., Yanase, T., Nakagawa, H., Matsuo, S., Ohnishi, Y., and Yamasaki, S. (2009b). Effect of Polyamine-deficient Chow on *Trypanosoma brucei brucei* Infection in Rats. *J. Parasitol.* **95**, 781–786.

Nishimura, K., Lee, S.B., Park, J.H., and Park, M.H. (2012). Essential role of eIF5A-1 and deoxyhypusine synthase in mouse embryonic development. *Amino Acids* **42**, 703–710.

Nowell, P.C. (2002). Tumor progression: a brief historical perspective. *Semin. Cancer Biol.* **12**, 261–266.

Nowotarski, S.L., Woster, P.M., and Casero, R.A. (2013). Polyamines and cancer: Implications for chemoprevention and chemotherapy. *Expert Rev. Mol. Med.* **15**, e3.

O'Brien, T.G., Megosh, L.C., Gilliard, G., and Soler, A.P. (1997). Ornithine Decarboxylase Overexpression Is a Sufficient Condition for Tumor Promotion in Mouse Skin. *Cancer Res.* **57**, 2630–2637.

O'Connell, T.M. (2013). The Complex Role of Branched Chain Amino Acids in Diabetes and Cancer. *Metabolites* **3**, 931–945.

Ohori, M., Wheeler, T.M., and Scardino, P.T. (1994). The new american joint committee on cancer and international union against cancer tm classification of prostate cancer. *Cancer* **74**, 104–114.

Oredsson, S.M. (2003). Polyamine dependence of normal cell-cycle progression. *Biochem. Soc. Trans.* **31**, 366–370.

O'Reilly, K.E., Rojo, F., She, Q.-B., Solit, D., Mills, G.B., Smith, D., Lane, H., Hofmann, F., Hicklin, D.J., Ludwig, D.L., et al. (2006). mTOR Inhibition Induces Upstream Receptor Tyrosine Kinase Signaling and Activates Akt. *Cancer Res.* **66**, 1500–1508.

- Origanti, S., Nowotarski, S.L., Carr, T.D., Sass-Kuhn, S., Xiao, L., Wang, J.-Y., and Shantz, L.M. (2012). Ornithine decarboxylase mRNA is stabilized in an mTORC1-dependent manner in Ras-transformed cells. *Biochem. J.* **442**, 199–207.
- Ouyang, D.-Y., Xu, L.-H., He, X.-H., Zhang, Y.-T., Zeng, L.-H., Cai, J.-Y., and Ren, S. (2013). Autophagy is differentially induced in prostate cancer LNCaP, DU145 and PC-3 cells via distinct splicing profiles of ATG5. *Autophagy* **9**, 20–32.
- Paasinen-Sohns, A., Kielosto, M., Kääriäinen, E., Eloranta, T., Laine, A., Jänne, O.A., Birrer, M.J., and Hölttä, E. (2000). C-Jun Activation-Dependent Tumorigenic Transformation Induced Paradoxically by Overexpression or Block of S-Adenosylmethionine Decarboxylase. *J. Cell Biol.* **151**, 801–810.
- Paasinen-Sohns, A., Kääriäinen, E., Yin, M., Järvinen, K., Nummela, P., and Hölttä, E. (2011). Chaotic neovascularization induced by aggressive fibrosarcoma cells overexpressing S-adenosylmethionine decarboxylase. *Int. J. Biochem. Cell Biol.* **43**, 441–454.
- Palm, W., Park, Y., Wright, K., Pavlova, N.N., Tuveson, D.A., and Thompson, C.B. (2015). The Utilization of Extracellular Proteins as Nutrients Is Suppressed by mTORC1. *Cell* **162**, 259–270.
- Paoli, P., Giannoni, E., and Chiarugi, P. (2013). Anoikis molecular pathways and its role in cancer progression. *Biochim. Biophys. Acta BBA - Mol. Cell Res.* **1833**, 3481–3498.
- Paridaens, R., Uges, D.R.A., Barbet, N., Choi, L., Seeghers, M., Graaf, W.T.A. van der, Groen, H.J.M., Dumez, H., Buuren, I.V., Muskiet, F., et al. (2000). A phase I study of a new polyamine biosynthesis inhibitor, SAM486A, in cancer patients with solid tumours. *Br. J. Cancer* **83**, 594–601.
- Park, M.H., Wolff, E.C., Lee, Y.B., and Folk, J.E. (1994). Antiproliferative effects of inhibitors of deoxyhypusine synthase. Inhibition of growth of Chinese hamster ovary cells by guanidyl diamines. *J. Biol. Chem.* **269**, 27827–27832.
- Park, M.H., Nishimura, K., Zanelli, C.F., and Valentini, S.R. (2009). Functional significance of eIF5A and its hypusine modification in eukaryotes. *Amino Acids* **38**, 491–500.
- Park, S., Pak, J., Jang, I., and Cho, J. (2014). Inhibition of mTOR affects protein stability of OGT. *Biochem. Biophys. Res. Commun.* **453**, 208–212.
- Parreiras-e-Silva, L.T., Luchessi, A.D., Reis, R.I., Oliver, C., Jamur, M.C., Ramos, R.G.P., Oliveira, E.B., Curi, R., and Costa-Neto, C.M. (2010). Evidences of a role for eukaryotic translation initiation factor 5A (eIF5A) in mouse embryogenesis and cell differentiation. *J. Cell. Physiol.* **225**, 500–505.
- Patel, A.R., and Wang, J.Y. (1997). Polyamines modulate transcription but not posttranscription of c-myc and c-jun in IEC-6 cells. *Am. J. Physiol.* **273**, C1020-1029.
- Patti, G.J., Yanes, O., and Siuzdak, G. (2012). Innovation: Metabolomics: the apogee of the omics trilogy. *Nat. Rev. Mol. Cell Biol.* **13**, 263–269.
- Pavlova, N.N., and Thompson, C.B. (2016). The Emerging Hallmarks of Cancer Metabolism. *Cell Metab.* **23**, 27–47.
- Pegg, A.E. (2006). Regulation of Ornithine Decarboxylase. *J. Biol. Chem.* **281**, 14529–14532.
- Pegg, A.E. (2008). Spermidine/spermine-N1-acetyltransferase: a key metabolic regulator. *Am. J. Physiol. - Endocrinol. Metab.* **294**, E995–E1010.
- Pegg, A.E. (2009a). Mammalian Polyamine Metabolism and Function. *IUBMB Life* **61**, 880–894.

- Pegg, A.E. (2009b). S-Adenosylmethionine decarboxylase. *Essays Biochem.* 46, 25–46.
- Pegg, A.E. (2013). Toxicity of Polyamines and Their Metabolic Products. *Chem. Res. Toxicol.* 26, 1782–1800.
- Pegg, A.E., and Feith, D.J. (2007). Polyamines and neoplastic growth. *Biochem. Soc. Trans.* 35, 295–299.
- Pegg, A.E., Wechter, R.S., Clark, R.S., Wiest, L., and Erwin, B.G. (1986). Acetylation of decarboxylated S-adenosylmethionine by mammalian cells. *Biochemistry (Mosc.)* 25, 379–384.
- Pegg, A.E., Xiong, H., Feith, D.J., and Shantz, L.M. (1998). S-Adenosylmethionine decarboxylase: structure, function and regulation by polyamines. *Biochem. Soc. Trans.* 26, 580–586.
- Peña, A., Reddy, C.D., Wu, S., Hickok, N.J., Reddy, E.P., Yumet, G., Soprano, D.R., and Soprano, K.J. (1993). Regulation of human ornithine decarboxylase expression by the c-Myc.Max protein complex. *J. Biol. Chem.* 268, 27277–27285.
- Pendeville, H., Carpino, N., Marine, J.-C., Takahashi, Y., Muller, M., Martial, J.A., and Cleveland, J.L. (2001). The Ornithine Decarboxylase Gene Is Essential for Cell Survival during Early Murine Development. *Mol. Cell. Biol.* 21, 6549–6558.
- Peng, T., Golub, T.R., and Sabatini, D.M. (2002). The Immunosuppressant Rapamycin Mimics a Starvation-Like Signal Distinct from Amino Acid and Glucose Deprivation. *Mol. Cell. Biol.* 22, 5575–5584.
- Pietilä, M., Parkkinen, J.J., Alhonen, L., and Jänne, J. (2001). Relation of skin polyamines to the hairless phenotype in transgenic mice overexpressing spermidine/spermine N-acetyltransferase. *J. Invest. Dermatol.* 116, 801–805.
- Pless, M., Belhadj, K., Menssen, H.D., Kern, W., Coiffier, B., Wolf, J., Herrmann, R., Thiel, E., Bootle, D., Sklenar, I., et al. (2004). Clinical Efficacy, Tolerability, and Safety of SAM486A, a Novel Polyamine Biosynthesis Inhibitor, in Patients with Relapsed or Refractory Non-Hodgkin's Lymphoma Results from a Phase II Multicenter Study. *Clin. Cancer Res.* 10, 1299–1305.
- Pogribny, I.P., James, S.J., and Beland, F.A. (2012). Molecular alterations in hepatocarcinogenesis induced by dietary methyl deficiency. *Mol. Nutr. Food Res.* 56, 116–125.
- Poirson-Bichat, F., Gonfalone, G., Bras-Gonçalves, R.A., Dutrillaux, B., and Poupon, M.F. (1997). Growth of methionine-dependent human prostate cancer (PC-3) is inhibited by ethionine combined with methionine starvation. *Br. J. Cancer* 75, 1605–1612.
- Possemato, R., Marks, K.M., Shaul, Y.D., Pacold, M.E., Kim, D., Birsoy, K., Sethumadhavan, S., Woo, H.-K., Jang, H.G., Jha, A.K., et al. (2011). Functional genomics reveal that the serine synthesis pathway is essential in breast cancer. *Nature* 476, 346–350.
- Poulin, R., Casero, R.A., and Soulet, D. (2011). Recent advances in the molecular biology of metazoan polyamine transport. *Amino Acids* 42, 711–723.
- Powers, R.W., Kaeberlein, M., Caldwell, S.D., Kennedy, B.K., and Fields, S. (2006). Extension of chronological life span in yeast by decreased TOR pathway signaling. *Genes Dev.* 20, 174–184.
- Prinz, W.A. (2014). Bridging the gap: Membrane contact sites in signaling, metabolism, and organelle dynamics. *J. Cell Biol.* 205, 759–769.
- Pucciarelli, S., Moreschini, B., Micozzi, D., De Fronzo, G.S., Carpi, F.M., Polzonetti, V., Vincenzetti, S., Mignini, F., and Napolioni, V. (2012). Spermidine and Spermine Are Enriched in Whole Blood of Nona/Centenarians. *Rejuvenation Res.* 15, 590–595.

- Puntambekar, S.S., Davis, D.S., Hawel III, L., Crane, J., Byus, C.V., and Carson, M.J. (2011). LPS-induced CCL2 expression and macrophage influx into the murine central nervous system is polyamine-dependent. *Brain. Behav. Immun.* 25, 629–639.
- Pyronnet, S., Pradayrol, L., and Sonenberg, N. (2000). A Cell Cycle-Dependent Internal Ribosome Entry Site. *Mol. Cell* 5, 607–616.
- Rajeeve, V., Pearce, W., Cascante, M., Vanhaesebroeck, B., and Cutillas, P.R. (2013). Polyamine production is downstream and upstream of oncogenic PI3K signalling and contributes to tumour cell growth. *Biochem. J.* 450, 619–628.
- Raney, A., Law, G.L., Mize, G.J., and Morris, D.R. (2002). Regulated Translation Termination at the Upstream Open Reading Frame in S-Adenosylmethionine Decarboxylase mRNA. *J. Biol. Chem.* 277, 5988–5994.
- Regenass, U., Mett, H., Stanek, J., Mueller, M., Kramer, D., and Porter, C.W. (1994). CGP 48664, a New S-Adenosylmethionine Decarboxylase Inhibitor with Broad Spectrum Antiproliferative and Antitumor Activity. *Cancer Res.* 54, 3210–3217.
- Reitman, Z.J., Jin, G., Karoly, E.D., Spasojevic, I., Yang, J., Kinzler, K.W., He, Y., Bigner, D.D., Vogelstein, B., and Yan, H. (2011). Profiling the effects of isocitrate dehydrogenase 1 and 2 mutations on the cellular metabolome. *Proc. Natl. Acad. Sci.* 108, 3270–3275.
- Ren, S., Shao, Y., Zhao, X., Hong, C.S., Wang, F., Lu, X., Li, J., Ye, G., Zhuang, Z., Xu, C., et al. (2015). Integration of metabolomics and transcriptomics reveals major metabolic pathways and potential biomarker involved in prostate cancer. *Mol. Cell. Proteomics* mcp.M115.052381.
- Rhee, H.J., Kim, E.-J., and Lee, J.K. (2007). Physiological polyamines: simple primordial stress molecules. *J. Cell. Mol. Med.* 11, 685–703.
- Ricoult, S.J.H., and Manning, B.D. (2013). The multifaceted role of mTORC1 in the control of lipid metabolism. *EMBO Rep.* 14, 242–251.
- Russell, D., and Snyder, S.H. (1968). Amine synthesis in rapidly growing tissues: ornithine decarboxylase activity in regenerating rat liver, chick embryo, and various tumors. *Proc. Natl. Acad. Sci. U. S. A.* 60, 1420–1427.
- Sabatini, D.M., Erdjument-Bromage, H., Lui, M., Tempst, P., and Snyder, S.H. (1994). RAFT1: A mammalian protein that binds to FKBP12 in a rapamycin-dependent fashion and is homologous to yeast TORs. *Cell* 78, 35–43.
- Sabò, A., and Amati, B. (2014). Genome Recognition by MYC. *Cold Spring Harb. Perspect. Med.* 4, a014191.
- Sagor, G.H.M., Berberich, T., Takahashi, Y., Niitsu, M., and Kusano, T. (2012). The polyamine spermine protects Arabidopsis from heat stress-induced damage by increasing expression of heat shock-related genes. *Transgenic Res.* 22, 595–605.
- Salmena, L., Carracedo, A., and Pandolfi, P.P. (2008). Tenets of PTEN Tumor Suppression. *Cell* 133, 403–414.
- Samuels, Y., Wang, Z., Bardelli, A., Silliman, N., Ptak, J., Szabo, S., Yan, H., Gazdar, A., Powell, S.M., Riggins, G.J., et al. (2004). High Frequency of Mutations of the PIK3CA Gene in Human Cancers. *Science* 304, 554–554.
- Sancak, Y., Bar-Peled, L., Zoncu, R., Markhard, A.L., Nada, S., and Sabatini, D.M. (2010). Ragulator-Rag Complex Targets mTORC1 to the Lysosomal Surface and Is Necessary for Its Activation by Amino Acids. *Cell* 141, 290–303.



Saran, U., Foti, M., and Dufour, J.-F. (2015). Cellular and molecular effects of the mTOR inhibitor everolimus. *Clin. Sci.* 129, 895–914.

Sarker, D., Reid, A.H.M., Yap, T.A., and de Bono, J.S. (2009). Targeting the PI3K/AKT pathway for the treatment of prostate cancer. *Clin. Cancer Res. Off. J. Am. Assoc. Cancer Res.* 15, 4799–4805.

Scalabrino, G., and Ferioli, M.E. (1984). Polyamines in mammalian ageing: an oncological problem, too? A review. *Mech. Ageing Dev.* 26, 149–164.

Scandalon VC, and Sanders T (2007). *Essentials of Anatomy and Physiology*, 7 edition - PDF Download.

Schiller, D., Kruse, D., Kneifel, H., Krämer, R., and Burkovski, A. (2000). Polyamine Transport and Role of potE in Response to Osmotic Stress in *Escherichia coli*. *J. Bacteriol.* 182, 6247–6249.

Schipper, R.G., Penning, L.C., and Verhofstad, A.A. (2000). Involvement of polyamines in apoptosis. Facts and controversies: effectors or protectors? *Semin. Cancer Biol.* 10, 55–68.

Schipper, R.G., Romijn, J.C., Cuijpers, V.M.J.I., and Verhofstad, A. a. J. (2003). Polyamines and prostatic cancer. *Biochem. Soc. Trans.* 31, 375–380.

Schnier, J., Schwelberger, H.G., Smit-McBride, Z., Kang, H.A., and Hershey, J.W. (1991). Translation initiation factor 5A and its hypusine modification are essential for cell viability in the yeast *Saccharomyces cerevisiae*. *Mol. Cell. Biol.* 11, 3105–3114.

Scuoppo, C., Miething, C., Lindqvist, L., Reyes, J., Ruse, C., Appelmann, I., Yoon, S., Krasnitz, A., Teruya-Feldstein, J., Pappin, D., et al. (2012). A tumour suppressor network relying on the polyamine-hypusine axis. *Nature* 487, 244–248.

Sedelaar, J.M., and Schalken, J.A. (2015). The need for a personalized approach for prostate cancer management. *BMC Med.* 13, 1.

Seiler, N., and Raul, F. (2005). Polyamines and apoptosis. *J. Cell. Mol. Med.* 9, 623–642.

Senyilmaz, D., and Teleman, A.A. (2015). Chicken or the egg: Warburg effect and mitochondrial dysfunction. *F1000Prime Rep.* 7.

Serra H (2015). PTEN mediates Notch-dependent stalk cell arrest in angiogenesis: *Nature Communications*: Nature Publishing Group.

Shah, P., and Swiatlo, E. (2008). A multifaceted role for polyamines in bacterial pathogens. *Mol. Microbiol.* 68, 4–16.

Shantz, L.M., and Pegg, A.E. (1998). Ornithine Decarboxylase Induction in Transformation by H-Ras and RhoA. *Cancer Res.* 58, 2748–2753.

Shantz, L.M., and Pegg, A.E. (1999). Translational regulation of ornithine decarboxylase and other enzymes of the polyamine pathway. *Int. J. Biochem. Cell Biol.* 31, 107–122.

Shappell, S.B., Thomas, G.V., Roberts, R.L., Herbert, R., Ittmann, M.M., Rubin, M.A., Humphrey, P.A., Sundberg, J.P., Rozengurt, N., Barrios, R., et al. (2004). Prostate Pathology of Genetically Engineered Mice: Definitions and Classification. The Consensus Report from the Bar Harbor Meeting of the Mouse Models of Human Cancer Consortium Prostate Pathology Committee. *Cancer Res.* 64, 2270–2305.

Sharmin, S., Sakata, K., Kashiwagi, K., Ueda, S., Iwasaki, S., Shirahata, A., and Igarashi, K. (2001). Polyamine Cytotoxicity in the Presence of Bovine Serum Amine Oxidase. *Biochem. Biophys. Res. Commun.* 282, 228–235.

- Shen, M.M., and Abate-Shen, C. (2010). Molecular genetics of prostate cancer: new prospects for old challenges. *Genes Dev.* 24, 1967–2000.
- Shestov, A.A., Liu, X., Ser, Z., Cluntun, A.A., Hung, Y.P., Huang, L., Kim, D., Le, A., Yellen, G., Albeck, J.G., et al. (2014). Quantitative determinants of aerobic glycolysis identify flux through the enzyme GAPDH as a limiting step. *eLife* 3, e03342.
- Shi, C., Cooper, T.K., McCloskey, D.E., Glick, A.B., Shantz, L.M., and Feith, D.J. (2012). S-adenosylmethionine decarboxylase overexpression inhibits mouse skin tumor promotion. *Carcinogenesis* 33, 1310–1318.
- Shor, B., Gibbons, J.J., Abraham, R.T., and Yu, K. (2009). Targeting mTOR globally in cancer: Thinking beyond rapamycin. *Cell Cycle* 8, 3831–3837.
- Sievert, H., Pällmann, N., Miller, K.K., Hermans-Borgmeyer, I., Venz, S., Sandoel, A., Preukschas, M., Schweizer, M., Boettcher, S., Janiesch, P.C., et al. (2014). A novel mouse model for inhibition of DOHH-mediated hypusine modification reveals a crucial function in embryonic development, proliferation and oncogenic transformation. *Dis. Model. Mech.* 7, 963–976.
- Singh, R., and Cuervo, A.M. (2011). Autophagy in the Cellular Energetic Balance. *Cell Metab.* 13, 495–504.
- Siu, L.L., Rowinsky, E.K., Hammond, L.A., Weiss, G.R., Hidalgo, M., Clark, G.M., Moczygemba, J., Choi, L., Linnartz, R., Barbet, N.C., et al. (2002). A Phase I and Pharmacokinetic Study of SAM486A, a Novel Polyamine Biosynthesis Inhibitor, Administered on a Daily-times-five every-three-week Schedule in Patients with Advanced Solid Malignancies. *Clin. Cancer Res.* 8, 2157–2166.
- Smith, M.K., Trempus, C.S., and Gilmour, S.K. (1998). Co-operation between follicular ornithine decarboxylase and v-Ha-ras induces spontaneous papillomas and malignant conversion in transgenic skin. *Carcinogenesis* 19, 1409–1415.
- Snell, K. (1984). Enzymes of serine metabolism in normal, developing and neoplastic rat tissues. *Adv. Enzyme Regul.* 22, 325–400.
- Soda, K. (2011). The mechanisms by which polyamines accelerate tumor spread. *J. Exp. Clin. Cancer Res. CR* 30, 95.
- Song, M.S., Carracedo, A., Salmena, L., Song, S.J., Egia, A., Malumbres, M., and Pandolfi, P.P. (2011a). Nuclear PTEN Regulates the APC-CDH1 Tumor-Suppressive Complex in a Phosphatase-Independent Manner. *Cell* 144, 187–199.
- Song, M.S., Salmena, L., and Pandolfi, P.P. (2012). The functions and regulation of the PTEN tumour suppressor. *Nat. Rev. Mol. Cell Biol.* 13, 283–296.
- Song, Y.H., Shiota, M., Kuroiwa, K., Naito, S., and Oda, Y. (2011b). The important role of glycine N-methyltransferase in the carcinogenesis and progression of prostate cancer. *Mod. Pathol.* 24, 1272–1280.
- Sooranna, S.R., Hirani, J., and Das, I. (1998). The role of polyamines in pregnancy. *Biochem. Soc. Trans.* 26, S101–S101.
- Soulet, D., Gagnon, B., Rivest, S., Audette, M., and Poulin, R. (2004). A Fluorescent Probe of Polyamine Transport Accumulates into Intracellular Acidic Vesicles via a Two-step Mechanism. *J. Biol. Chem.* 279, 49355–49366.
- Sousa-Victor, P., García-Prat, L., Muñoz-Cánoves, P., Sousa-Victor, P., García-Prat, L., and Muñoz-Cánoves, P. (2015). Dual mTORC1/C2 inhibitors: gerosuppressors with potential anti-aging effect. *Oncotarget* 6, 23052–23054.

Sreekumar, A., Poisson, L.M., Rajendiran, T.M., Khan, A.P., Cao, Q., Yu, J., Laxman, B., Mehra, R., Lonigro, R.J., Li, Y., et al. (2009). Metabolomic profiles delineate potential role for sarcosine in prostate cancer progression. *Nature* 457, 910–914.

Stambolic, V., Suzuki, A., de la Pompa, J.L., Brothers, G.M., Mirtsos, C., Sasaki, T., Ruland, J., Penninger, J.M., Siderovski, D.P., and Mak, T.W. (1998). Negative Regulation of PKB/Akt-Dependent Cell Survival by the Tumor Suppressor PTEN. *Cell* 95, 29–39.

Stanley, B.A., and Pegg, A.E. (1991). Amino acid residues necessary for putrescine stimulation of human S-adenosylmethionine decarboxylase proenzyme processing and catalytic activity. *J. Biol. Chem.* 266, 18502–18506.

Stanley, B.A., Pegg, A.E., and Holm, I. (1989). Site of pyruvate formation and processing of mammalian S-adenosylmethionine decarboxylase proenzyme. *J. Biol. Chem.* 264, 21073–21079.

Steiner, M.S., Anthony, C.T., Lu, Y., and Holt, J.T. (1998). Antisense c-myc Retroviral Vector Suppresses Established Human Prostate Cancer. *Hum. Gene Ther.* 9, 747–755.

Stine, Z.E., Walton, Z.E., Altman, B.J., Hsieh, A.L., and Dang, C.V. (2015). MYC, Metabolism, and Cancer. *Cancer Discov.* 5, 1024–1039.

Stolzing, A., and Grune, T. (2004). Neuronal apoptotic bodies: phagocytosis and degradation by primary microglial cells. *FASEB J.*

Stratton, M.R., Campbell, P.J., and Futreal, P.A. (2009). The cancer genome. *Nature* 458, 719–724.

Sugimura, T., Birnbaum, S.M., Winitz, M., and Greenstein, J.P. (1959). Quantitative nutritional studies with water-soluble, chemically defined diets. VIII. The forced feeding of diets each lacking in one essential amino acid. *Arch. Biochem. Biophys.* 81, 448–455.

Sun, H., Lesche, R., Li, D.-M., Liliental, J., Zhang, H., Gao, J., Gavriloza, N., Mueller, B., Liu, X., and Wu, H. (1999). PTEN modulates cell cycle progression and cell survival by regulating phosphatidylinositol 3,4,5,-trisphosphate and Akt/protein kinase B signaling pathway. *Proc. Natl. Acad. Sci.* 96, 6199–6204.

Svensson, F., Mett, H., and Persson, L. (1997). CGP 48664, a potent and specific S-adenosylmethionine decarboxylase inhibitor: effects on regulation and stability of the enzyme. *Biochem. J.* 322, 297–302.

Taberner, J., Rojo, F., Calvo, E., Burris, H., Judson, I., Hazell, K., Martinelli, E., Cajal, S.R. y, Jones, S., Vidal, L., et al. (2008). Dose- and Schedule-Dependent Inhibition of the Mammalian Target of Rapamycin Pathway With Everolimus: A Phase I Tumor Pharmacodynamic Study in Patients With Advanced Solid Tumors. *J. Clin. Oncol.* 26, 1603–1610.

Tabib, A., and Bachrach, U. (1994). Activation of the Proto-oncogene c-myc and c-fos by c-ras: Involvement of Polyamines. *Biochem. Biophys. Res. Commun.* 202, 720–727.

Tan, C.Y., and Hagen, T. (2013). mTORC1 Dependent Regulation of REDD1 Protein Stability. *PLoS ONE* 8, e63970.

Tentler, J.J., Tan, A.C., Weekes, C.D., Jimeno, A., Leong, S., Pitts, T.M., Arcaroli, J.J., Messersmith, W.A., and Eckhardt, S.G. (2012). Patient-derived tumour xenografts as models for oncology drug development. *Nat. Rev. Clin. Oncol.* 9, 338–350.

Thoreen, C.C., Kang, S.A., Chang, J.W., Liu, Q., Zhang, J., Gao, Y., Reichling, L.J., Sim, T., Sabatini, D.M., and Gray, N.S. (2009). An ATP-competitive Mammalian Target of Rapamycin Inhibitor Reveals Rapamycin-resistant Functions of mTORC1. *J. Biol. Chem.* 284, 8023–8032.

- Thoreen, C.C., Chantranupong, L., Keys, H.R., Wang, T., Gray, N.S., and Sabatini, D.M. (2012). A unifying model for mTORC1-mediated regulation of mRNA translation. *Nature* 485, 109–113.
- Thorpe, L.M., Yuzugullu, H., and Zhao, J.J. (2015). PI3K in cancer: divergent roles of isoforms, modes of activation and therapeutic targeting. *Nat. Rev. Cancer* 15, 7–24.
- Tkachenko, A.G., and Nesterova, L.Y. (2003). Polyamines as Modulators of Gene Expression under Oxidative Stress in *Escherichia coli*. *Biochem. Mosc.* 68, 850–856.
- Toker, A., and Yoeli-Lerner, M. (2006). Akt Signaling and Cancer: Surviving but not Moving On. *Cancer Res.* 66, 3963–3966.
- Torrano, V., Valcarcel-Jimenez, L., Cortazar, A.R., Liu, X., Urosevic, J., Castillo-Martin, M., Fernández-Ruiz, S., Morciano, G., Caro-Maldonado, A., Guiu, M., et al. (2016). The metabolic co-regulator PGC1 $\alpha$  suppresses prostate cancer metastasis. *Nat. Cell Biol.* 18, 645–656.
- Tran, H., Brunet, A., Griffith, E.C., and Greenberg, M.E. (2003). The Many Forks in FOXO's Road. *Sci STKE* 2003, re5-re5.
- Trotman, L.C., Niki, M., Dotan, Z.A., Koutcher, J.A., Cristofano, A.D., Xiao, A., Khoo, A.S., Roy-Burman, P., Greenberg, N.M., Dyke, T.V., et al. (2003). Pten Dose Dictates Cancer Progression in the Prostate. *PLOS Biol* 1, e59.
- Tucker, J.M., Murphy, J.T., Kisiel, N., Diegelman, P., Barbour, K.W., Davis, C., Medda, M., Alhonen, L., Jänne, J., Kramer, D.L., et al. (2005). Potent Modulation of Intestinal Tumorigenesis in *Apcmin/+* Mice by the Polyamine Catabolic Enzyme Spermidine/Spermine N1-acetyltransferase. *Cancer Res.* 65, 5390–5398.
- Uemura, T., Stringer, D.E., Blohm-Mangone, K.A., and Gerner, E.W. (2010). Polyamine transport is mediated by both endocytic and solute carrier transport mechanisms in the gastrointestinal tract. *Am. J. Physiol. - Gastrointest. Liver Physiol.* 299, G517–G522.
- Ugalde-Olano, A., Egia, A., Fernández-Ruiz, S., Loizaga-Iriarte, A., Zuñiga-García, P., Garcia, S., Royo, F., Lacasa-Viscasillas, I., Castro, E., Cortazar, A.R., et al. (2015). Methodological aspects of the molecular and histological study of prostate cancer: Focus on PTEN. *Methods* 77–78, 25–30.
- Ulger Toprak, N., Yagci, A., Gulluoglu, B.M., Akin, M.L., Demirkalem, P., Celenk, T., and Soyletir, G. (2006). A possible role of *Bacteroides fragilis* enterotoxin in the aetiology of colorectal cancer. *Clin. Microbiol. Infect.* 12, 782–786.
- Vaishampayan, U., Shevrin, D., Stein, M., Heilbrun, L., Land, S., Stark, K., Li, J., Dickow, B., Heath, E., Smith, D., et al. (2015). Phase II Trial of Carboplatin, Everolimus, and Prednisone in Metastatic Castration-resistant Prostate Cancer Pretreated With Docetaxel Chemotherapy: A Prostate Cancer Clinical Trial Consortium Study. *Urology* 86, 1206–1211.
- Valkenburg, K.C., and Williams, B.O. (2011). Mouse Models of Prostate Cancer. *Prostate Cancer* 2011.
- Vander Heiden, M.G., Cantley, L.C., and Thompson, C.B. (2009). Understanding the Warburg effect: the metabolic requirements of cell proliferation. *Science* 324, 1029–1033.
- Vellai, T., Takacs-Vellai, K., Zhang, Y., Kovacs, A.L., Orosz, L., and Müller, F. (2003). Genetics: influence of TOR kinase on lifespan in *C. elegans*. *Nature* 426, 620.
- Vézina C et al. (2006). RAPAMYCIN (AY-22, 989), A NEW ANTIFUNGAL ANTIBIOTIC I. TAXONOMY OF THE PRODUCING STREPTOMYCETE AND ISOLATION OF THE ACTIVE PRINCIPLE. *J. Antibiot. (Tokyo)* 721.

Vita, M., and Henriksson, M. (2006). The Myc oncoprotein as a therapeutic target for human cancer. *Semin. Cancer Biol.* 16, 318–330.

Vivanco, I., Palaskas, N., Tran, C., Finn, S.P., Getz, G., Kennedy, N.J., Jiao, J., Rose, J., Xie, W., Loda, M., et al. (2007). Identification of the JNK Signaling Pathway as a Functional Target of the Tumor Suppressor PTEN. *Cancer Cell* 11, 555–569.

Vlastos, A.-T., West, L.A., Atkinson, E.N., Boiko, I., Malpica, A., Hong, W.K., and Follen, M. (2005). Results of a phase II double-blinded randomized clinical trial of difluoromethylornithine for cervical intraepithelial neoplasia grades 2 to 3. *Clin. Cancer Res. Off. J. Am. Assoc. Cancer Res.* 11, 390–396.

Vogelstein, B., and Kinzler, K.W. (1993). The multistep nature of cancer. *Trends Genet.* 9, 138–141.

Vogelstein, B., and Kinzler, K.W. (2004). Cancer genes and the pathways they control. *Nat. Med.* 10, 789–799.

Wadman, M. (2015). Treatment: When less is more. *Nature* 528, S126–S127.

Wahrheit, J., Nicolae, A., and Heinzle, E. (2011). Eukaryotic metabolism: Measuring compartment fluxes. *Biotechnol. J.* 6, 1071–1085.

Wallace, H.M., Fraser, A.V., and Hughes, A. (2003). A perspective of polyamine metabolism. *Biochem. J.* 376, 1–14.

Wang, J., Alexander, P., Wu, L., Hammer, R., Cleaver, O., and McKnight, S.L. (2009). Dependence of Mouse Embryonic Stem Cells on Threonine Catabolism. *Science* 325, 435–439.

Wang, R., Dillon, C.P., Shi, L.Z., Milasta, S., Carter, R., Finkelstein, D., McCormick, L.L., Fitzgerald, P., Chi, H., Munger, J., et al. (2011). The Transcription Factor Myc Controls Metabolic Reprogramming upon T Lymphocyte Activation. *Immunity* 35, 871–882.

Warburg, O. (1956a). On the Origin of Cancer Cells. *Science* 123, 309–314.

Warburg, O. (1956b). On the origin of cancer cells. *Science* 123, 309–314.

Warburg, O., Wind, F., and Negelein, E. (1927). The Metabolism of Tumors in the Body. *J. Gen. Physiol.* 8, 519–530.

Ward, P.S., and Thompson, C.B. (2012). Metabolic Reprogramming: A Cancer Hallmark Even Warburg Did Not Anticipate. *Cancer Cell* 21, 297–308.

Weinberg, R.A. (1996). How cancer arises. *Sci. Am.* 275, 62–70.

Wiechert, W., and Nöh, K. (2013). Isotopically non-stationary metabolic flux analysis: complex yet highly informative. *Curr. Opin. Biotechnol.* 24, 979–986.

Wolfson, R.L., Chantranupong, L., Saxton, R.A., Shen, K., Scaria, S.M., Cantor, J.R., and Sabatini, D.M. (2015). Sestrin2 is a leucine sensor for the mTORC1 pathway. *Science* aab2674.

Wu, X., Wu, J., Huang, J., Powell, W.C., Zhang, J., Matusik, R.J., Sangiorgi, F.O., Maxson, R.E., Sucov, H.M., and Roy-Burman, P. (2001). Generation of a prostate epithelial cell-specific Cre transgenic mouse model for tissue-specific gene ablation. *Mech. Dev.* 101, 61–69.

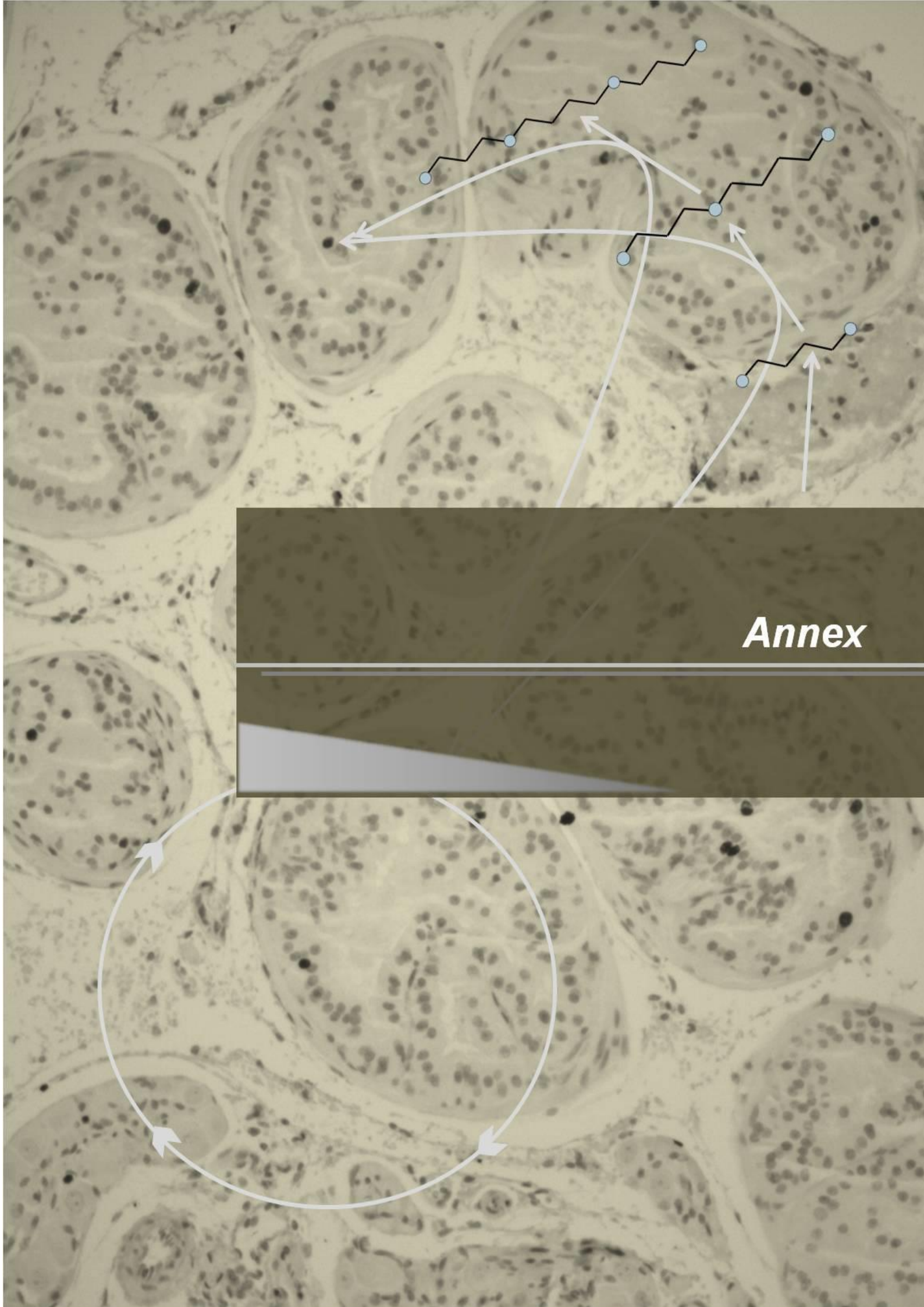
Wu, X., Daniels, G., Lee, P., and Monaco, M.E. (2014). Lipid metabolism in prostate cancer. *Am. J. Clin. Exp. Urol.* 2, 111–120.

- Xu, H., Chaturvedi, R., Cheng, Y., Bussiere, F.I., Asim, M., Yao, M.D., Potosky, D., Meltzer, S.J., Rhee, J.G., Kim, S.S., et al. (2004). Spermine oxidation induced by *Helicobacter pylori* results in apoptosis and DNA damage: implications for gastric carcinogenesis. *Cancer Res.* *64*, 8521–8525.
- Yang, Z.J., Chee, C.E., Huang, S., and Sinicrope, F.A. (2011). The Role of Autophagy in Cancer: Therapeutic Implications. *Mol. Cancer Ther.* *10*, 1533–1541.
- Yap, T.A., Yan, L., Patnaik, A., Fearen, I., Olmos, D., Papadopoulos, K., Baird, R.D., Delgado, L., Taylor, A., Lupinacci, L., et al. (2011). First-in-Man Clinical Trial of the Oral Pan-AKT Inhibitor MK-2206 in Patients With Advanced Solid Tumors. *J. Clin. Oncol.* *29*, 4688–4695.
- Yecies, J.L., and Manning, B.D. (2011). mTOR links oncogenic signaling to tumor cell metabolism. *J. Mol. Med.* *89*, 221–228.
- Yen, C.-H., Lu, Y.-C., Li, C.-H., Lee, C.-M., Chen, C.-Y., Cheng, M.-Y., Huang, S.-F., Chen, K.-F., Cheng, A.-L., Liao, L.-Y., et al. (2011). Functional Characterization of Glycine N-Methyltransferase and Its Interactive Protein DEPDC6/DEPTOR in Hepatocellular Carcinoma. *Mol. Med.* *18*, 286–296.
- Yerlikaya, A., and Stanley, B.A. (2004). S-Adenosylmethionine Decarboxylase Degradation by the 26 S Proteasome Is Accelerated by Substrate-mediated Transamination. *J. Biol. Chem.* *279*, 12469–12478.
- Yokota, J. (2000). Tumor progression and metastasis. *Carcinogenesis* *21*, 497–503.
- Yoshida, M., Kashiwagi, K., Kawai, G., Ishihama, A., and Igarashi, K. (2002). Polyamines Enhance Synthesis of the RNA Polymerase  $\zeta$ 38 Subunit by Suppression of an Amber Termination Codon in the Open Reading Frame. *J. Biol. Chem.* *277*, 37139–37146.
- Yoshida, M., Kashiwagi, K., Shigemasa, A., Taniguchi, S., Yamamoto, K., Makinoshima, H., Ishihama, A., and Igarashi, K. (2004). A Unifying Model for the Role of Polyamines in Bacterial Cell Growth, the Polyamine Modulon. *J. Biol. Chem.* *279*, 46008–46013.
- Yoshimoto, M., Cutz, J.-C., Nuin, P.A.S., Joshua, A.M., Bayani, J., Evans, A.J., Zielenska, M., and Squire, J.A. (2006). Interphase FISH analysis of PTEN in histologic sections shows genomic deletions in 68% of primary prostate cancer and 23% of high-grade prostatic intra-epithelial neoplasias. *Cancer Genet. Cytogenet.* *169*, 128–137.
- Zamboni, N., Saghatelian, A., and Patti, G.J. (2015). Defining the Metabolome: Size, Flux, and Regulation. *Mol. Cell* *58*, 699–706.
- Zanelli, C.F., and Valentini, S.R. (2007). Is there a role for eIF5A in translation? *Amino Acids* *33*, 351–358.
- Zanelli, C.F., Maragno, A.L.C., Gregio, A.P.B., Komili, S., Pandolfi, J.R., Mestriner, C.A., Lustri, W.R., and Valentini, S.R. (2006). eIF5A binds to translational machinery components and affects translation in yeast. *Biochem. Biophys. Res. Commun.* *348*, 1358–1366.
- Zhang, Y., and Manning, B.D. (2015). mTORC1 signaling activates NRF1 to increase cellular proteasome levels. *Cell Cycle* *14*, 2011–2017.
- Zhang, W.C., Shyh-Chang, N., Yang, H., Rai, A., Umashankar, S., Ma, S., Soh, B.S., Sun, L.L., Tai, B.C., Nga, M.E., et al. (2012). Glycine Decarboxylase Activity Drives Non-Small Cell Lung Cancer Tumor-Initiating Cells and Tumorigenesis. *Cell* *148*, 259–272.
- Zhang, Y., Nicholatos, J., Dreier, J.R., Ricoult, S.J.H., Widenmaier, S.B., Hotamisligil, G.S., Kwiatkowski, D.J., and Manning, B.D. (2014). Coordinated regulation of protein synthesis and degradation by mTORC1. *Nature* *513*, 440–443.

Zhao, Y., and Yang, Y. (2015). Profiling metabolic states with genetically encoded fluorescent biosensors for NADH. *Curr. Opin. Biotechnol.* 31, 86–92.

Zhou, B.P., Liao, Y., Xia, W., Spohn, B., Lee, M.-H., and Hung, M.-C. (2001). Cytoplasmic localization of p21Cip1/WAF1 by Akt-induced phosphorylation in HER-2/neu-overexpressing cells. *Nat. Cell Biol.* 3, 245–252.

Zingg, D., Debbache, J., Schaefer, S.M., Tuncer, E., Frommel, S.C., Cheng, P., Arenas-Ramirez, N., Haeusel, J., Zhang, Y., Bonalli, M., et al. (2015). The epigenetic modifier EZH2 controls melanoma growth and metastasis through silencing of distinct tumour suppressors. *Nat. Commun.* 6, 6051.



*Annex*



Supplementary table. Time of Flight analysis of murine prostate tissue from Pten wt or prostate deficient mice at 3 months (X3M) or 6 months (X6M) in AP and DLP lobes.

ion	mz	assignedMetabolite	Sum of signif	Ave Signal ALL	SD signal ALL	X3m_KO_DLP_VS_X3m_wt_DLP.signifClass	X3m_KO_DLP_VS_X3m_wt_DLP.logFC	X3m_KO_DLP_VS_X3m_wt_DLP.adj.P.Val	X3m_KO_AP_VS_X3m_wt_AP.signifClass	X3m_KO_AP_VS_X3m_wt_AP.logFC	X3m_KO_AP_VS_X3m_wt_AP.adj.P.Val	X6m_KO_DLP_VS_X6m_wt_DLP.signifClass	X6m_KO_DLP_VS_X6m_wt_DLP.logFC	X6m_KO_DLP_VS_X6m_wt_DLP.adj.P.Val	X6m_KO_AP_VS_X6m_wt_AP.signifClass	X6m_KO_AP_VS_X6m_wt_AP.logFC	X6m_KO_AP_VS_X6m_wt_AP.adj.P.Val
m3121	355.1572	S-Adenosylmethionine // HMDB00988:H(+) // 355.1572 // 40	4.0000	3.8596	0.4530	1.0000	3.5599	0.0000	1.0000	3.3865	0.0000	1.0000	4.2056	0.0000	1.0000	4.2866	0.0000
m1902	245.2357	N1-Acetylspermine // HMDB01186:H(+) // 245.2357 // 49	4.0000	2.5583	0.4530	1.0000	2.2243	0.0000	1.0000	2.2557	0.0000	1.0000	2.5526	0.0000	1.0000	3.2005	0.0000
m1253	188.1765	N1-Acetylspermidine // HMDB01276:H(+) // 188.1765 // 100 // N8-Acetylspermidine // HMDB02189:H(+) // 188.1765 // 100	4.0000	2.2403	1.3709	1.0000	1.3295	0.0002	1.0000	1.5478	0.0001	1.0000	1.8083	0.0000	1.0000	4.2756	0.0000
m574	135.0410	(S)-Ureidoglycolic acid // HMDB01005:H(+) // 135.0410 // 100 // trans-1,2-Dihydrobenzene-1,2-diol // HMDB01164:Na(+) // 135.0410 // 30 // trans-1,2-Dihydrobenzene-1,2-diol // HMDB01164:H/Na.H(+) // 135.0410 // 30	4.0000	1.1221	0.4189	1.0000	0.8319	0.0004	1.0000	0.7250	0.0036	1.0000	1.3103	0.0000	1.0000	1.6211	0.0000
m85	85.0641	Methyl propenyl ketone // HMDB01184:H(+) // 85.0641 // 100 // 3-Methyl-2-butenal // HMDB12157:H(+) // 85.0641 // 100	4.0000	-0.7481	0.0722	1.0000	-0.7522	0.0000	1.0000	-0.6463	0.0000	1.0000	-0.7813	0.0000	1.0000	-0.8125	0.0000
m4116	459.2372	3-Sulfodeoxycholic acid // HMDB02504:H(+) // 459.2372 // 100 // MG(P-18:0e(0:0:0)) // HMDB11153:(NaCl)2.H(+) // 459.2372 // 43 // Retinoyl b-glucuronide // HMDB03141:H2O.H(+) // 459.2372 // 13 // DHAP(18:0) // HMDB11133:H/Na.H(+) // 459.2372 // 10	4.0000	-0.7579	0.0941	1.0000	-0.8818	0.0000	1.0000	-0.6769	0.0023	1.0000	-0.7798	0.0002	1.0000	-0.6933	0.0015
m3014	345.0746	Thiamine monophosphate // HMDB02666:H(+) // 345.0746 // 100 // L-isoleucyl-L-proline // HMDB11174:(NaCl)2.H(+) // 345.0746 // 12 // L-leucyl-L-proline // HMDB11175:(NaCl)2.H(+) // 345.0746 // 12 // Salicin // HMDB03546:NaCl.H(+) // 345.0746 // 12	4.0000	-0.7836	0.1381	1.0000	-0.5996	0.0041	1.0000	-0.8991	0.0001	1.0000	-0.8798	0.0000	1.0000	-0.7557	0.0007
m3054	349.1120	Riboflavin reduced // HMDB01557:H(+) // 349.1120 // 98 // 6,7-Dimethyl-8-(1-D-ribityl)lumazine // HMDB03826:H/Na.H(+) // 349.1120 // 44 // 2-O-a-L-Fucopyranosyl-galactose // HMDB06590:H/Na.H(+) // 349.1120 // 29 // 3-O-a-L-Fucopyranosyl-D-glucose // HMDB06701:H/Na.H(+) // 349.1120 // 29	4.0000	-0.8354	0.2292	1.0000	-1.1297	0.0000	1.0000	-0.6061	0.0081	1.0000	-0.8932	0.0000	1.0000	-0.7127	0.0016
m3411	384.1205	Succinyladenosine // HMDB00912:H(+) // 384.1205 // 59 // Dityrosine // HMDB06045:[+1].Na(+) // 384.1205 // 9	4.0000	-0.9400	0.1410	1.0000	-1.1190	0.0000	1.0000	-0.7793	0.0001	1.0000	-0.9593	0.0000	1.0000	-0.9026	0.0000
m3421	385.1211	S-Adenosylhomocysteine // HMDB00939:H(+) // 385.1211 // 53 // Succinyladenosine // HMDB00912:[+1].H(+) // 385.1211 // 33	4.0000	-0.9441	0.2320	1.0000	-1.0422	0.0000	1.0000	-0.6040	0.0028	1.0000	-1.1239	0.0000	1.0000	-1.0062	0.0000
m1131	177.0405	Ascorbic acid // HMDB00044:H(+) // 177.0405 // 88 // D-Glucurono-6,3-lactone // HMDB06355:H(+) // 177.0405 // 88 // 2,4-Diaminobutyric acid // HMDB02362:NaCl.H(+) // 177.0405 // 10 // L-2,4-diaminobutyric acid // HMDB06284:NaCl.H(+) // 177.0405 // 10	4.0000	-0.9702	0.1324	1.0000	-0.9446	0.0000	1.0000	-0.9898	0.0000	1.0000	-0.8127	0.0000	1.0000	-1.1336	0.0000
m2958	339.0723	AICAR // HMDB01517:H(+) // 339.0723 // 100 // L-Aspartyl-L-phenylalanine // HMDB00706:NaCl.H(+) // 339.0723 // 23 // L-beta-aspartyl-L-phenylalanine // HMDB11167:NaCl.H(+) // 339.0723 // 23	4.0000	-1.0534	0.2248	1.0000	-1.0784	0.0001	1.0000	-0.7296	0.0097	1.0000	-1.1763	0.0000	1.0000	-1.2294	0.0000
m759	147.1139	L-Lysine // HMDB00182:H(+) // 147.1139 // 94 // D-Lysine // HMDB03405:H(+) // 147.1139 // 94 // (3S,5S)-3,5-Diaminohexanoate // HMDB12115:H(+) // 147.1139 // 94 // (3S)-3,6-Diaminohexanoate // HMDB12114:H(+) // 147.1139 // 94 // Pipecolic acid // HMDB00070:NH4(+) // 147.1139 // 10 // L-Pipecolic acid // HMDB00716:NH4(+) // 147.1139 // 10 // N4-Acetylamino butanal // HMDB04226:NH4(+) // 147.1139 // 10 // D-Pipecolic acid // HMDB05960:NH4(+) // 147.1139 // 10	4.0000	-1.0879	0.4549	1.0000	-0.8222	0.0000	1.0000	-1.1900	0.0000	1.0000	-0.6566	0.0001	1.0000	-1.6827	0.0000
m1617	219.1481	5-Methoxydimethyltryptamine // HMDB02004:H(+) // 219.1481 // 100 // Gamma-glutamyl-L-putrescine // HMDB12230:[+1].H(+) // 219.1481 // 5	4.0000	-1.1083	0.0721	1.0000	-1.0134	0.0000	1.0000	-1.0916	0.0000	1.0000	-1.1595	0.0000	1.0000	-1.1689	0.0000
m144	98.9860	Phosphoric acid // HMDB02142:H(+) // 98.9860 // 73 // Acetic acid // HMDB00042:H/K.H(+) // 98.9860 // 8 // Glycolaldehyde // HMDB03344:H/K.H(+) // 98.9860 // 8	4.0000	-1.1257	0.3138	1.0000	-0.9543	0.0004	1.0000	-0.8140	0.0047	1.0000	-1.2055	0.0000	1.0000	-1.5289	0.0000

m510	130.0872	Pipecolic acid // HMDB00070: H(+) // 130.0872 // 100 // L-Pipecolic acid // HMDB00716: H(+) // 130.0872 // 100 // N4-Acetylaminobutanol // HMDB04226: H(+) // 130.0872 // 100 // D-Pipecolic acid // HMDB05960: H(+) // 130.0872 // 100 // trans-1,2-Dihydrobenzene-1,2-diol // HMDB01164: NH4(+) // 130.0872 // 10	4.0000	-1.1554	0.3959	1.0000	-1.0800	0.0001	1.0000	-1.1290	0.0001	1.0000	-0.7275	0.0056	1.0000	-1.6853	0.0000
m4407	491.1316	L-2-Amino adipate adenylate // HMDB06941: H(+) // 491.1316 // 100 // 11beta,20-Dihydroxy-3-oxopregn-4-en-21-oi-c acid // HMDB11651: (NaCl)2.H(+) // 491.1316 // 13	4.0000	-1.1949	0.4107	1.0000	-1.3480	0.0000	1.0000	-0.6970	0.0099	1.0000	-1.6632	0.0000	1.0000	-1.0714	0.0001
m965	162.0772	Amino adipic acid // HMDB00510: H(+) // 162.0772 // 87 // 3-Hexenedioic acid // HMDB00393: NH4(+) // 162.0772 // 10 // 3-Methylglutaconic acid // HMDB00522: NH4(+) // 162.0772 // 10 // (E)-2-Methylglutaconic acid // HMDB02266: NH4(+) // 162.0772 // 10 // 7-Aminomethyl-7-carbaguanine // HMDB11690: H2O.H(+) // 162.0772 // 10 // Glucosamine // HMDB01514: H2O.H(+) // 162.0772 // 9 // Fructosamine // HMDB02030: H2O.H(+) // 162.0772 // 9	4.0000	-1.2200	0.1892	1.0000	-1.1564	0.0000	1.0000	-0.9914	0.0000	1.0000	-1.3016	0.0000	1.0000	-1.4307	0.0000
m1566	214.9955	2-Oxo-3-hydroxy-4-phosphobutanoic acid // HMDB06801: H(+) // 214.9955 // 100 // Ascorbic acid // HMDB00044: H.K.H(+) // 214.9955 // 16 // D-Glucurono-6,3-lactone // HMDB06355: H.K.H(+) // 214.9955 // 16 // Ascorbic acid // HMDB00044: K(+) // 214.9955 // 8 // D-Glucurono-6,3-lactone // HMDB06355: K(+) // 214.9955 // 8 // Cyclohexanone // HMDB03315: (NaCl)2.H(+) // 214.9955 // 6	4.0000	-1.2285	0.2206	1.0000	-1.1241	0.0000	1.0000	-1.1637	0.0000	1.0000	-1.0715	0.0000	1.0000	-1.5546	0.0000
m663	142.0268	O-Phosphoethanolamine // HMDB00224: H(+) // 142.0268 // 100 // Dimethylglycine // HMDB00092: H.K.H(+) // 142.0268 // 10 // Gamma-Aminobutyric acid // HMDB00112: H.K.H(+) // 142.0268 // 10 // L-Alpha-aminobutyric acid // HMDB00452: H.K.H(+) // 142.0268 // 10 // D-Alpha-aminobutyric acid // HMDB00650: H.K.H(+) // 142.0268 // 10 // 2-Aminoisobutyric acid // HMDB01906: H.K.H(+) // 142.0268 // 10 // (S)-b-aminoisobutyric acid // HMDB02166: H.K.H(+) // 142.0268 // 10 // (R)-b-aminoisobutyric acid // HMDB02299: H.K.H(+) // 142.0268 // 10 // 3-Aminoisobutanoic acid // HMDB03911: H.K.H(+) // 142.0268 // 10 // Dimethylglycine // HMDB00092: K(+) // 142.0268 // 5 // Gamma-Aminobutyric acid // HMDB00112: K(+) // 142.0268 // 5 // L-Alpha-aminobutyric acid // HMDB00452: K(+) // 142.0268 // 5 // D-Alpha-aminobutyric acid // HMDB00650: K(+) // 142.0268 // 5 // 2-Aminoisobutyric acid // HMDB01906: K(+) // 142.0268 // 5 // (S)-b-aminoisobutyric acid // HMDB02166: K(+) // 142.0268 // 5 // (R)-b-aminoisobutyric acid // HMDB02299: K(+) // 142.0268 // 5 // 3-Aminoisobutanoic acid // HMDB03911: K(+) // 142.0268 // 5	4.0000	-1.2293	0.4047	1.0000	-0.8021	0.0005	1.0000	-1.4331	0.0000	1.0000	-0.9928	0.0000	1.0000	-1.6891	0.0000
m982	163.0750	Safrole // HMDB02333: H(+) // 163.0750 // 100	4.0000	-1.2307	0.0436	1.0000	-1.2461	0.0000	1.0000	-1.1713	0.0000	1.0000	-1.2748	0.0000	1.0000	-1.2304	0.0000
m3458	389.2524	5,6-Dihydroxyprostaglandin F1a // HMDB12109: H(+) // 389.2524 // 100	4.0000	-1.2369	0.3401	1.0000	-1.6806	0.0000	1.0000	-1.2490	0.0000	1.0000	-1.1608	0.0000	1.0000	-0.8571	0.0004
m264	109.0287	Quinone // HMDB03364: H(+) // 109.0287 // 100 // 1,2-Benzoquinone // HMDB12133: H(+) // 109.0287 // 100 // Gamma-Butyrolactone // HMDB00549: H/Na.H(+) // 109.0287 // 8 // Oxolan-3-one // HMDB02523: H/Na.H(+) // 109.0287 // 8 // Diacetyl // HMDB03407: H/Na.H(+) // 109.0287 // 8 // But-2-enoic acid // HMDB10720: H/Na.H(+) // 109.0287 // 8	4.0000	-1.3449	0.1220	1.0000	-1.3798	0.0000	1.0000	-1.3312	0.0000	1.0000	-1.4810	0.0000	1.0000	-1.1875	0.0000
m1276	189.1612	N6,N6,N6-Trimethyl-L-lysine // HMDB01325: H(+) // 189.1612 // 69 // Gabapentin // HMDB05015: NH4(+) // 189.1612 // 10	4.0000	-1.3504	0.2480	1.0000	-1.2960	0.0000	1.0000	-1.0984	0.0011	1.0000	-1.3151	0.0000	1.0000	-1.6922	0.0000
m2	55.0189	2-Propyn-1-al // HMDB06803: H(+) // 55.0189 // 96 // Pyruvaldehyde // HMDB01167: H2O.H(+) // 55.0189 // 10 // Malondialdehyde // HMDB06112: H2O.H(+) // 55.0189 // 10	4.0000	-1.3712	0.1631	1.0000	-1.4370	0.0000	1.0000	-1.1481	0.0000	1.0000	-1.3684	0.0000	1.0000	-1.5314	0.0000
m5505	608.0843	Uridine diphosphate-N-acetylglucosamine // HMDB00290: H(+) // 608.0843 // 98 // Uridine diphosphate-N-acetylglactosamine // HMDB00304: H(+) // 608.0843 // 98	4.0000	-1.3955	0.5839	1.0000	-1.3068	0.0000	1.0000	-0.6927	0.0080	1.0000	-1.4690	0.0000	1.0000	-2.1137	0.0000

m1641	221.1175	N-Acetyl-D-glucosaminylamine // HMDB01104:.H(+)// 221.1175 // 63	4.0000	-1.4692	0.0633	1.0000	-1.4014	0.0000	1.0000	-1.5496	0.0000	1.0000	-1.4417	0.0000	1.0000	-1.4838	0.0000
m1874	243.0247	Inositol cyclic phosphate // HMDB01125:.H(+)// 243.0247 // 100	4.0000	-1.4757	0.3377	1.0000	-1.4158	0.0000	1.0000	-1.0751	0.0000	1.0000	-1.5160	0.0000	1.0000	-1.8958	0.0000
m2402	290.0858	N-Succinyl-2-amino-6-ketopimelate // HMDB12266:.H(+)// 290.0858 // 100 // Adenosine // HMDB00050:.H/Na.H(+)// 290.0858 // 38 // Deoxyguanosine // HMDB00085:.H/Na.H(+)// 290.0858 // 38 // Neuraminic acid // HMDB00830:.H/Na.H(+)// 290.0858 // 33 // Adenosine // HMDB00050:.Na(+)// 290.0858 // 14 // Deoxyguanosine // HMDB00085:.Na(+)// 290.0858 // 14 // Neuraminic acid // HMDB00830:.Na(+)// 290.0858 // 12	4.0000	-1.4777	0.3933	1.0000	-0.9745	0.0068	1.0000	-1.6864	0.0000	1.0000	-1.8739	0.0000	1.0000	-1.3760	0.0004
m5570	615.1504	Cytidine monophosphate N-acetylneuraminic acid // HMDB01176:.H(+)// 615.1504 // 75	4.0000	-1.5080	0.1152	1.0000	-1.5394	0.0000	1.0000	-1.3397	0.0000	1.0000	-1.5527	0.0000	1.0000	-1.6003	0.0000
m4421	492.9931	2-Deoxyinosine triphosphate // HMDB03537:.H(+)// 492.9931 // 100	4.0000	-1.5238	0.4706	1.0000	-1.3615	0.0000	1.0000	-1.0142	0.0000	1.0000	-1.5834	0.0000	1.0000	-2.1360	0.0000
m2504	298.0977	5-Methylthioadenosine // HMDB01173:.H(+)// 298.0977 // 100	4.0000	-1.5445	0.3976	1.0000	-1.5381	0.0000	1.0000	-1.0222	0.0022	1.0000	-1.6333	0.0000	1.0000	-1.9844	0.0000
m2313	282.0985	4-Hydroxyphenylacetylglutamine // HMDB06061:.H(+)// 282.0985 // 100	4.0000	-1.5930	0.4208	1.0000	-1.9625	0.0000	1.0000	-0.9941	0.0000	1.0000	-1.7774	0.0000	1.0000	-1.6380	0.0000
m38	73.0288	Pyruvaldehyde // HMDB01167:.H(+)// 73.0288 // 100 // Malondialdehyde // HMDB06112:.H(+)// 73.0288 // 100	4.0000	-1.7501	0.2295	1.0000	-1.6041	0.0000	1.0000	-1.5329	0.0000	1.0000	-1.8233	0.0000	1.0000	-2.0402	0.0000
m1003	165.0765	L-Fucose // HMDB00174:.H(+)// 165.0765 // 100 // Rhamnose // HMDB00849:.H(+)// 165.0765 // 100 // 1,5-Anhydrosorbitol // HMDB02712:.H(+)// 165.0765 // 100 // Beta-D-Fucose // HMDB03081:.H(+)// 165.0765 // 100 // L-Rhamnulose // HMDB10207:.H(+)// 165.0765 // 100 // 2-Deoxygalactopyranose // HMDB12327:.H(+)// 165.0765 // 100 // 5-(2-carboxypropyl)-Cysteamine // HMDB02169:[+1].H(+)// 165.0765 // 12 // Galactitol // HMDB00107:-H2O.H(+)// 165.0765 // 7 // Sorbitol // HMDB00247:-H2O.H(+)// 165.0765 // 7 // Mannitol // HMDB00765:-H2O.H(+)// 165.0765 // 7 // L-Iditol // HMDB11632:-H2O.H(+)// 165.0765 // 7	4.0000	-1.7919	0.1879	1.0000	-1.8893	0.0000	1.0000	-1.7940	0.0000	1.0000	-1.5283	0.0000	1.0000	-1.9560	0.0000
m1185	183.0504	3-Methyluric acid // HMDB01970:.H(+)// 183.0504 // 100 // 9-Methyluric acid // HMDB01973:.H(+)// 183.0504 // 100 // 1-Methyluric acid // HMDB03099:.H(+)// 183.0504 // 100 // 7-Methyluric acid // HMDB11107:.H(+)// 183.0504 // 100	4.0000	-1.8532	0.3210	1.0000	-1.5959	0.0000	1.0000	-1.5560	0.0000	1.0000	-2.1519	0.0000	1.0000	-2.1090	0.0000
m7245	876.2956	Lacto-N-fucopentaose III // HMDB06576:.H/Na.H(+)// 876.2956 // 63 // Lacto-N-fucopentaose-2 // HMDB06577:.H/Na.H(+)// 876.2956 // 63 // Lex-lactose // HMDB06696:.H/Na.H(+)// 876.2956 // 63 // Lacto-n-fucopentaose I // HMDB06705:.H/Na.H(+)// 876.2956 // 63 // Lacto-N-fucopentaose V // HMDB06706:.H/Na.H(+)// 876.2956 // 63	4.0000	-1.8635	1.1104	1.0000	-1.0908	0.0001	1.0000	-1.7322	0.0000	1.0000	-1.1589	0.0000	1.0000	-3.4723	0.0000
m17	62.0606	Ethanolamine // HMDB00149:.H(+)// 62.0606 // 100 // L-Serine // HMDB00187:-CO2.H(+)// 62.0606 // 10 // D-Serine // HMDB03406:-CO2.H(+)// 62.0606 // 10 // O-Phosphoethanolamine // HMDB00224:-HPO3.H(+)// 62.0606 // 8	4.0000	-1.8965	0.5065	1.0000	-2.1527	0.0000	1.0000	-1.1403	0.0000	1.0000	-2.2060	0.0000	1.0000	-2.0872	0.0000
m7199	868.1383	Succinyl-CoA // HMDB01022:.H(+)// 868.1383 // 100 // Methylmalonyl-CoA // HMDB01269:.H(+)// 868.1383 // 100 // R-Methylmalonyl-CoA // HMDB02255:.H(+)// 868.1383 // 100 // 5-Methylmalonyl-CoA // HMDB02310:.H(+)// 868.1383 // 100	4.0000	-1.9301	0.2726	1.0000	-1.9944	0.0001	1.0000	-1.7047	0.0017	1.0000	-1.7323	0.0006	1.0000	-2.2890	0.0000
m4582	511.1162	3-Methyl-1-hydroxybutyl-ThPP // HMDB06865:.H(+)// 511.1162 // 100 // 2-Methyl-1-hydroxybutyl-ThPP // HMDB12310:.H(+)// 511.1162 // 100 // 8-iso-PGA1 // HMDB02236:.(NaCl)3.H(+)// 511.1162 // 8 // Prostaglandin A1 // HMDB02656:.(NaCl)3.H(+)// 511.1162 // 8 // Prostaglandin B1 // HMDB02982:.(NaCl)3.H(+)// 511.1162 // 8	4.0000	-1.9542	0.6627	1.0000	-2.0776	0.0000	1.0000	-1.0114	0.0014	1.0000	-2.1673	0.0000	1.0000	-2.5606	0.0000

m717	145.0499	3-Hexenedioic acid // HMDB00393:.H(+) // 145.0499 // 100 // 3-Methylglutaconic acid // HMDB00522:.H(+) // 145.0499 // 100 // (E)-2-Methylglutaconic acid // HMDB02266:.H(+) // 145.0499 // 100 // 2-Hydroxyadipic acid // HMDB00321:-H2O.H(+) // 145.0499 // 10 // 3-Hydroxyadipic acid // HMDB00345:-H2O.H(+) // 145.0499 // 10 // 3-Hydroxymethylglutaric acid // HMDB00355:-H2O.H(+) // 145.0499 // 10 // 2(R)-Hydroxyadipic acid // HMDB00368:-H2O.H(+) // 145.0499 // 10 // Glucosan // HMDB00640:-H2O.H(+) // 145.0499 // 10 // Inositol cyclic phosphate // HMDB01125:-H3PO4.H(+) // 145.0499 // 8 // Erythritol // HMDB02994:.H/Na.H(+) // 145.0499 // 7 // D-Threitol // HMDB04136:.H/Na.H(+) // 145.0499 // 7	4.0000	-1.9775	0.2866	1.0000	-1.8237	0.0000	1.0000	-1.6594	0.0000	1.0000	-2.1413	0.0000	1.0000	-2.2855	0.0000
m2968	340.1038	6-Hydroxy-5-methoxyindole glucuronide // HMDB10362:.H(+) // 340.1038 // 92 // 5-Hydroxy-6-methoxyindole glucuronide // HMDB10363:.H(+) // 340.1038 // 92 // Topiramate // HMDB05034:.H(+) // 340.1038 // 44	4.0000	-2.0220	0.5242	1.0000	-1.9965	0.0000	1.0000	-1.3318	0.0000	1.0000	-2.1662	0.0000	1.0000	-2.5935	0.0000
m1584	216.0641	Glycerylphosphorylethanolamine // HMDB00114:.H(+) // 216.0641 // 100 // Phenylacetylglycine // HMDB00821:.Na(+) // 216.0641 // 20 // Methylhippuric acid // HMDB00859:.Na(+) // 216.0641 // 20 // 2-Methylhippuric acid // HMDB11723:.Na(+) // 216.0641 // 20 // Phenylacetylglycine // HMDB00821:.H/Na.H(+) // 216.0641 // 20 // Methylhippuric acid // HMDB00859:.H/Na.H(+) // 216.0641 // 20 // 2-Methylhippuric acid // HMDB11723:.H/Na.H(+) // 216.0641 // 20 // Glucosamine-1P // HMDB01109:-CO2.H(+) // 216.0641 // 6 // Glucosamine 6-phosphate // HMDB01254:-CO2.H(+) // 216.0641 // 6	4.0000	-2.0593	0.5319	1.0000	-2.2906	0.0000	1.0000	-1.2649	0.0000	1.0000	-2.3939	0.0000	1.0000	-2.2876	0.0000
m2129	265.1125	Thiamine // HMDB00235:.H(+) // 265.1125 // 100	4.0000	-2.1733	0.5043	1.0000	-2.0592	0.0000	1.0000	-1.6429	0.0006	1.0000	-2.1345	0.0000	1.0000	-2.8567	0.0000
m4337	483.0610	Gestrinone // HMDB02720:.NaCl3.H(+) // 483.0610 // 59	4.0000	-2.3934	0.7886	1.0000	-2.4408	0.0000	1.0000	-1.3339	0.0009	1.0000	-2.5615	0.0000	1.0000	-3.2375	0.0000
m1640	221.0784	L-beta-aspartyl-L-serine // HMDB11168:.H(+) // 221.0784 // 100 // Guaifenesin // HMDB04998:.H/Na.H(+) // 221.0784 // 60 // Guaifenesin // HMDB04998:.Na(+) // 221.0784 // 13 // (-)-Nicotine pestanali // HMDB01934:.NaCl.H(+) // 221.0784 // 10 // Anabasine // HMDB04350:.NaCl.H(+) // 221.0784 // 10 // 3,4,5-Trimethoxycinnamic acid // HMDB02511:-H2O.H(+) // 221.0784 // 5 // Trans-2, 3, 4-Trimethoxycinnamate // HMDB11721:-H2O.H(+) // 221.0784 // 5	4.0000	-2.5567	0.2958	1.0000	-2.3355	0.0000	1.0000	-2.3063	0.0000	1.0000	-2.6518	0.0000	1.0000	-2.9333	0.0000
m981	163.0612	2-Hydroxyadipic acid // HMDB00321:.H(+) // 163.0612 // 94 // 3-Hydroxyadipic acid // HMDB00345:.H(+) // 163.0612 // 94 // 3-Hydroxymethylglutaric acid // HMDB00355:.H(+) // 163.0612 // 94 // 2(R)-Hydroxyadipic acid // HMDB00368:.H(+) // 163.0612 // 94 // Glucosan // HMDB00640:.H(+) // 163.0612 // 94 // Fructose 6-phosphate // HMDB00124:-H3PO4.H(+) // 163.0612 // 7 // Myo-inositol 1-phosphate // HMDB00213:-H3PO4.H(+) // 163.0612 // 7 // Galactose 1-phosphate // HMDB00645:-H3PO4.H(+) // 163.0612 // 7 // Dolichyl phosphate D-mannose // HMDB00994:-H3PO4.H(+) // 163.0612 // 7 // Fructose 1-phosphate // HMDB01076:-H3PO4.H(+) // 163.0612 // 7 // Mannose 6-phosphate // HMDB01078:-H3PO4.H(+) // 163.0612 // 7 // Myo-inositol 4-phosphate // HMDB01313:-H3PO4.H(+) // 163.0612 // 7 // Glucose 6-phosphate // HMDB01401:-H3PO4.H(+) // 163.0612 // 7 // Glucose 1-phosphate // HMDB01586:-H3PO4.H(+) // 163.0612 // 7 // Inositol phosphate // HMDB02985:-H3PO4.H(+) // 163.0612 // 7 // Beta-D-Glucose 6-phosphate // HMDB03498:-H3PO4.H(+) // 163.0612 // 7 // Beta-D-Fructose 6-phosphate // HMDB03971:-H3PO4.H(+) // 163.0612 // 7 // D-Tagatose 1-phosphate // HMDB06328:-H3PO4.H(+) // 163.0612 // 7 // D-Mannose 1-	4.0000	-3.0721	0.3097	1.0000	-2.8657	0.0000	1.0000	-2.7577	0.0000	1.0000	-3.2591	0.0000	1.0000	-3.4057	0.0000

m1155	180.0879	7-Aminomethyl-7-carbaguanine // HMDB11690:.H(+)// 180.0879 // 100 /// Glucosamine // HMDB01514:.H(+)// 180.0879 // 79 /// Fructosamine // HMDB02030:.H(+)// 180.0879 // 79 /// 2-Hydroxyadipic acid // HMDB00321:.NH4(+)// 180.0879 // 10 // 3-Hydroxyadipic acid // HMDB00345:.NH4(+)// 180.0879 // 10 // 3-Hydroxymethylglutaric acid // HMDB00355:.NH4(+)// 180.0879 // 10 // 2(R)-Hydroxyadipic acid // HMDB00368:.NH4(+)// 180.0879 // 10 // Glucosan // HMDB00640:.NH4(+)// 180.0879 // 10	4.0000	-3.1365	0.3375	1.0000	-2.9768	0.0000	1.0000	-2.7526	0.0000	1.0000	-3.3053	0.0000	1.0000	-3.5112	0.0000
m727	146.0534	3-Hexenedioic acid // HMDB00393:[+1].H(+)// 146.0534 // 60 // 3-Methylglutaconic acid // HMDB00522:[+1].H(+)// 146.0534 // 60 // (E)-2-Methylglutaconic acid // HMDB02266:[+1].H(+)// 146.0534 // 60	4.0000	-8.0329	1.6120	1.0000	-7.3597	0.0001	1.0000	-6.1108	0.0029	1.0000	-9.7047	0.0000	1.0000	-8.9564	0.0000
m3132	356.1582	5-Adenosylmethioninamine // HMDB00988:[+1].H(+)// 356.1582 // 28	3.0000	2.2382	0.5438	1.0000	2.1516	0.0004	0.0000	1.5467	0.0169	1.0000	2.8496	0.0000	1.0000	2.4047	0.0002
m6109	682.3244	(3a,5b)-24-oxo-24-[(2-sulfoethyl)amino]cholan-3-yl-b-D-Glucopyranosiduronic acid // HMDB02429:.H/Na.H(+)// 682.3244 // 100	3.0000	1.8443	0.7981	1.0000	1.7312	0.0019	0.0000	1.1363	0.0631	1.0000	1.5269	0.0060	1.0000	2.9828	0.0000
m639	140.0691	Trigonelline // HMDB00875:.H(+)// 140.0691 // 66 // 3,4-Dihydroxybenzylamine // HMDB12153:.H(+)// 140.0691 // 66 // Betaine // HMDB00043:.Na(+)// 140.0691 // 20 // L-Valine // HMDB00883:.Na(+)// 140.0691 // 20 // Vaporole // HMDB01382:.Na(+)// 140.0691 // 20 // N-Methyl-a-aminoisobutyric acid // HMDB02141:.Na(+)// 140.0691 // 20 // 5-Aminopentanoic acid // HMDB03355:.Na(+)// 140.0691 // 20 // Betaine // HMDB00043:.H/Na.H(+)// 140.0691 // 20 // L-Valine // HMDB00883:.H/Na.H(+)// 140.0691 // 20 // Vaporole // HMDB01382:.H/Na.H(+)// 140.0691 // 20 // N-Methyl-a-aminoisobutyric acid // HMDB02141:.H/Na.H(+)// 140.0691 // 20 // 5-Aminopentanoic acid // HMDB03355:.H/Na.H(+)// 140.0691 // 20	3.0000	1.6322	0.7956	0.0000	0.8322	0.0779	1.0000	1.3658	0.0072	1.0000	1.6087	0.0007	1.0000	2.7220	0.0000
m1277	189.1799	N1-Acetylspermidine // HMDB01276:[+1].H(+)// 189.1799 // 60 // N8-Acetylspermidine // HMDB02189:[+1].H(+)// 189.1799 // 60	3.0000	1.5120	1.1827	0.0000	0.6981	0.0398	1.0000	0.9494	0.0096	1.0000	1.1350	0.0009	1.0000	3.2657	0.0000
m3289	372.3133	Tetradecanoylcarnitine // HMDB05066:.H(+)// 372.3133 // 65	3.0000	1.3306	0.7064	0.0000	0.6101	0.0218	1.0000	1.3211	0.0000	1.0000	1.0992	0.0001	1.0000	2.2920	0.0000
m1766	232.1551	Isobutyryl-L-carnitine // HMDB00736:.H(+)// 232.1551 // 100 // Butyrylcarnitine // HMDB02013:.H(+)// 232.1551 // 100	3.0000	1.1760	0.3065	1.0000	1.0555	0.0055	1.0000	1.6064	0.0001	0.0000	0.8906	0.0186	1.0000	1.1516	0.0043
m5934	660.8692	Myo-inositol hexakisphosphate // HMDB03502:.H(+)// 660.8692 // 100	3.0000	1.1639	0.3730	1.0000	1.5010	0.0000	0.0000	0.6398	0.0278	1.0000	1.3334	0.0000	1.0000	1.1816	0.0000
m2336	284.1279	N-Phenylacetylphenylalanine // HMDB02372:.H(+)// 284.1279 // 100 // Morphine // HMDB03563:.H(+)// 284.1279 // 100 // 2-Methylbutyrylcarnitine // HMDB00378:.H/K.H(+)// 284.1279 // 8 // Isovalerylcarnitine // HMDB00688:.H/K.H(+)// 284.1279 // 8	3.0000	1.0616	0.2792	1.0000	1.0132	0.0015	0.0000	0.7391	0.0327	1.0000	1.0758	0.0008	1.0000	1.4184	0.0000
m3546	398.3281	trans-Hexadec-2-enoyl carnitine // HMDB06317:.H(+)// 398.3281 // 100	3.0000	1.0032	0.3887	0.0000	0.4641	0.0530	1.0000	1.1047	0.0000	1.0000	1.0539	0.0000	1.0000	1.3901	0.0000
m6244	701.2895	Pentacarboxyl porphyrinogen III // HMDB01957:.H(+)// 701.2895 // 66	3.0000	0.8541	0.4913	1.0000	1.0451	0.0000	0.0000	0.1413	0.6398	1.0000	0.9679	0.0001	1.0000	1.2622	0.0000
m1024	167.0322	Phthalic acid // HMDB02107:.H(+)// 167.0322 // 59 // Benzoquinoneacetic acid // HMDB02334:.H(+)// 167.0322 // 59 // Terephthalic acid // HMDB02428:.H(+)// 167.0322 // 59 // 3-Hexenedioic acid // HMDB00393:.Na(+)// 167.0322 // 20 // 3-Methylglutaconic acid // HMDB00522:.Na(+)// 167.0322 // 20 // (E)-2-Methylglutaconic acid // HMDB02266:.Na(+)// 167.0322 // 20 // 3-Hexenedioic acid // HMDB00393:.H/Na.H(+)// 167.0322 // 20 // 3-Methylglutaconic acid // HMDB00522:.H/Na.H(+)// 167.0322 // 20 // (E)-2-Methylglutaconic acid // HMDB02266:.H/Na.H(+)// 167.0322 // 20	3.0000	0.8229	0.1766	1.0000	0.6706	0.0075	0.0000	0.6714	0.0136	1.0000	1.0002	0.0001	1.0000	0.9492	0.0004
m3009	344.2812	Dodecanoylcarnitine // HMDB02250:.H(+)// 344.2812 // 94	3.0000	0.7399	0.3188	0.0000	0.3525	0.0298	1.0000	0.8102	0.0000	1.0000	0.6754	0.0001	1.0000	1.1217	0.0000
m3837	429.0170	IDP // HMDB03335:.H(+)// 429.0170 // 69 // 1-Phosphatidyl-D-myo-inositol // HMDB06953:.H/K.H(+)// 429.0170 // 10 // Homoanserine // HMDB05767:.[NaCl]3.H(+)// 429.0170 // 5	3.0000	-0.5269	0.6281	1.0000	-0.6840	0.0022	0.0000	0.3839	0.1182	1.0000	-1.0542	0.0000	1.0000	-0.7534	0.0015

m2422	292.0444	Parathion // HMDB01355: H(+) // 292.0444 // 72 // L-Threonineopterin // HMDB00727: H/K.H(+) // 292.0444 // 29 // Neopterin // HMDB00845: H/K.H(+) // 292.0444 // 29 // Umanopterin // HMDB00877: H/K.H(+) // 292.0444 // 29 // Hydroxysepiapterin // HMDB02109: H/K.H(+) // 292.0444 // 29	3.0000	-0.6161	0.2475	1.0000	-0.6167	0.0011	0.0000	-0.2706	0.1972	1.0000	-0.8384	0.0000	1.0000	-0.7385	0.0003
m719	145.1052	Proline betaine // HMDB04827: [1+].H(+) // 145.1052 // 60	3.0000	-0.6973	0.0857	1.0000	-0.6808	0.0001	0.0000	-0.5846	0.0013	1.0000	-0.7433	0.0000	1.0000	-0.7807	0.0000
m5119	565.0325	3-carboxy-1-hydroxypropylthiamine diphosphate // HMDB06744: H/K.H(+) // 565.0325 // 77	3.0000	-0.7523	0.4224	1.0000	-0.8329	0.0000	0.0000	-0.1619	0.4140	1.0000	-0.8484	0.0000	1.0000	-1.1659	0.0000
m2822	326.0468	Uridine 5'-monophosphate // HMDB00288: [1+].H(+) // 326.0468 // 61 // Pseudouridine 5'-phosphate // HMDB01271: [1+].H(+) // 326.0468 // 61 // Uridine 2'-phosphate // HMDB11641: [1+].H(+) // 326.0468 // 61	3.0000	-0.7582	0.2700	1.0000	-0.8387	0.0000	0.0000	-0.3879	0.0345	1.0000	-1.0320	0.0000	1.0000	-0.7742	0.0000
m6801	791.5228	Solaneyl-PP // HMDB02367: H(+) // 791.5228 // 82	3.0000	-0.7654	0.4952	1.0000	-0.9746	0.0001	0.0000	-0.0291	0.9261	1.0000	-0.9552	0.0001	1.0000	-1.1026	0.0000
m3412	384.1488	N-Acetyllactosamine // HMDB01542: H(+) // 384.1488 // 100 // Beta-1,4-mannose-N-acetylglucosamine // HMDB06535: H(+) // 384.1488 // 100 // Lacto-N-biose I // HMDB06575: H(+) // 384.1488 // 100 // Poly-N-acetyllactosamine // HMDB06583: H(+) // 384.1488 // 100	3.0000	-0.8025	0.1917	1.0000	-0.8474	0.0000	0.0000	-0.5206	0.0027	1.0000	-0.9028	0.0000	1.0000	-0.9394	0.0000
m3679	413.0477	dADP // HMDB01508: [1+].H(+) // 413.0477 // 94 // 1-Phosphatidyl-D-myo-inositol // HMDB06953: H/Na.H(+) // 413.0477 // 37	3.0000	-0.8057	0.6067	1.0000	-0.8729	0.0004	0.0000	0.0714	0.8166	1.0000	-1.1758	0.0000	1.0000	-1.2456	0.0000
m245	106.0497	L-Serine // HMDB00187: H(+) // 106.0497 // 100 // D-Serine // HMDB03406: H(+) // 106.0497 // 100	3.0000	-0.8063	0.2701	1.0000	-0.7598	0.0000	0.0000	-0.4763	0.0025	1.0000	-0.8584	0.0000	1.0000	-1.1305	0.0000
m1652	222.0962	N-Acetylgalactosamine // HMDB00212: H(+) // 222.0962 // 100 // N-Acetyl-D-glucosamine // HMDB00215: H(+) // 222.0962 // 100 // Beta-N-Acetylglucosamine // HMDB00803: H(+) // 222.0962 // 100 // N-Acetyl-b-D-galactosamine // HMDB00853: H(+) // 222.0962 // 100 // N-Acetylmannosamine // HMDB01129: H(+) // 222.0962 // 100 // N-Acetyl-D-mannosamine // HMDB11744: H(+) // 222.0962 // 100 // 2-Deoxysepiapterin // HMDB00389: H(+) // 222.0962 // 43	3.0000	-0.8491	0.7314	1.0000	-0.9022	0.0008	0.0000	0.1824	0.5677	1.0000	-1.5104	0.0000	1.0000	-1.1663	0.0001
m2239	276.1574	Epsilon-(gamma-Glutamyl)-lysine // HMDB03869: H(+) // 276.1574 // 75 // L-alpha-glutamyl-L-lysine // HMDB04207: H(+) // 276.1574 // 75	3.0000	-0.8687	0.2529	1.0000	-1.0913	0.0000	0.0000	-0.5061	0.0017	1.0000	-0.9614	0.0000	1.0000	-0.9162	0.0000
m4388	489.1123	Citicoline // HMDB01413: H(+) // 489.1123 // 100	3.0000	-0.9818	0.4606	1.0000	-0.8649	0.0000	0.0000	-0.3992	0.0647	1.0000	-1.1921	0.0000	1.0000	-1.4710	0.0000
m2314	282.1202	1-Methyladenosine // HMDB03331: H(+) // 282.1202 // 100 // N6-Methyladenosine // HMDB04044: H(+) // 282.1202 // 100 // 2-O-Methyladenosine // HMDB04326: H(+) // 282.1202 // 100 // 3-O-Methyladenosine // HMDB06023: H(+) // 282.1202 // 100	3.0000	-1.0661	0.3876	1.0000	-1.2781	0.0004	0.0000	-0.5039	0.2065	1.0000	-1.3605	0.0002	1.0000	-1.1217	0.0033
m7048	838.0606	Diadenosine tetraphosphate // HMDB01211: [1+].H(+) // 838.0606 // 60	3.0000	-1.2019	0.6040	1.0000	-1.3157	0.0003	0.0000	-0.4314	0.2786	1.0000	-1.1610	0.0011	1.0000	-1.8993	0.0000
m6788	789.0787	Diguanosine triphosphate // HMDB01379: H(+) // 789.0787 // 100 // Diguanosine tetraphosphate // HMDB01340: HPO3.H(+) // 789.0787 // 24	3.0000	-1.2433	0.5731	1.0000	-1.5053	0.0001	0.0000	-0.5055	0.2085	1.0000	-1.1213	0.0020	1.0000	-1.8412	0.0000
m6397	725.0656	Molybdopterin-AMP // HMDB12262: H(+) // 725.0656 // 61	3.0000	-1.3239	0.6416	1.0000	-1.7413	0.0000	0.0000	-0.3695	0.2149	1.0000	-1.6446	0.0000	1.0000	-1.5401	0.0000
m7043	837.0612	Diadenosine tetraphosphate // HMDB01211: H(+) // 837.0612 // 100	3.0000	-1.3286	0.4464	1.0000	-1.3268	0.0003	0.0000	-0.7095	0.0786	1.0000	-1.7431	0.0000	1.0000	-1.5349	0.0001
m1193	184.0748	Phosphorylcholine // HMDB01565: H(+) // 184.0748 // 67 // Tryptophanol // HMDB03447: H/Na.H(+) // 184.0748 // 13 // 3-Dehydroxycarnitine // HMDB06831: H/K.H(+) // 184.0748 // 7 // Acetylcholine // HMDB00895: H/K.H(+) // 184.0748 // 7	3.0000	-1.3954	1.3083	1.0000	-1.7767	0.0001	0.0000	0.4940	0.3082	1.0000	-2.5256	0.0000	1.0000	-1.7733	0.0001
m5960	664.1161	NAD // HMDB00902: H(+) // 664.1161 // 100	3.0000	-1.4594	1.1332	1.0000	-1.0161	0.0021	0.0000	-0.1594	0.6934	1.0000	-1.8585	0.0000	1.0000	-2.8035	0.0000
m3563	400.3444	L-Palmitoylcarnitine // HMDB00222: H(+) // 400.3444 // 100	2.0000	1.0739	0.4195	0.0000	0.7930	0.0108	0.0000	0.7656	0.0240	1.0000	1.0680	0.0007	1.0000	1.6688	0.0000
m2210	273.1097	5C-aglycone // HMDB04810: H(+) // 273.1097 // 99 // Ubiquinone // HMDB02012: H/Na.H(+) // 273.1097 // 48 // N-Succinyl-L-2,6-diaminopimelate // HMDB12267: H2O.H(+) // 273.1097 // 7	2.0000	0.9872	0.3964	0.0000	0.7471	0.0306	1.0000	1.0222	0.0062	0.0000	0.6474	0.0609	1.0000	1.5322	0.0000

m5354	591.2973	Dimethylprotoporphyrin IX dimethyl ester // HMDB00810:.H(+) // 591.2973 // 100 /// Protoporphyrinogen IX // HMDB01097:.H/Na.H(+) // 591.2973 // 54 /// Protoporphyrinogen IX // HMDB01097:.Na(+) // 591.2973 // 54 /// D-Urobilinogen // HMDB04158:.H(+) // 591.2973 // 41 /// Urobilin // HMDB04160:.H(+) // 591.2973 // 41 /// Lithocholate 3-O-glucuronide // HMDB02513:.H/K.H(+) // 591.2973 // 20 /// (3a,5b,7a)-23-Carboxy-7-hydroxy-24-norcholan-3-yl-b-D-Glucopyranosiduronic acid // HMDB02430:.Na(+) // 591.2973 // 10 /// Deoxycholic acid 3-glucuronide // HMDB02596:.Na(+) // 591.2973 // 10 /// (3a,5b,7a)-23-Carboxy-7-hydroxy-24-norcholan-3-yl-b-D-Glucopyranosiduronic acid // HMDB02430:.H/Na.H(+) // 591.2973 // 10 /// Deoxycholic acid 3-glucuronide // HMDB02596:.H/Na.H(+) // 591.2973 // 10 /// Stigmastanol // HMDB00494:(NaCl)3.H(+) // 591.2973 // 5	2.0000	0.8909	0.5290	0.0000	0.7271	0.0149	0.0000	0.2319	0.5094	1.0000	1.1604	0.0001	1.0000	1.4440	0.0000
m1831	239.0912	3,4,5-Trimethoxycinnamic acid // HMDB02511:.H(+) // 239.0912 // 100 /// Trans-2,3,4-Trimethoxycinnamate // HMDB11721:.H(+) // 239.0912 // 100	2.0000	0.8765	0.4974	0.0000	0.5354	0.0604	0.0000	0.3860	0.2224	1.0000	1.1522	0.0001	1.0000	1.4325	0.0000
m4123	460.1959	5-Methyltetrahydrofolic acid // HMDB01396:.H(+) // 460.1959 // 100 /// Dodecanoylcarnitine // HMDB02250:(NaCl)2.H(+) // 460.1959 // 18	2.0000	0.8071	0.4191	0.0000	0.3091	0.1976	0.0000	0.6175	0.0157	1.0000	1.0944	0.0000	1.0000	1.2076	0.0000
m773	148.0382	Indole-5,6-quinone // HMDB06779:.H(+) // 148.0382 // 87	2.0000	0.7777	0.4078	0.0000	0.3952	0.0433	0.0000	0.5259	0.0129	1.0000	0.8852	0.0000	1.0000	1.3046	0.0000
m1843	240.0945	3,4,5-Trimethoxycinnamic acid // HMDB02511:[+].H(+) // 240.0945 // 60 /// Trans-2,3,4-Trimethoxycinnamate // HMDB11721:[+].H(+) // 240.0945 // 60 /// N-a-Acetylcitrulline // HMDB00856:.Na(+) // 240.0945 // 20 /// N-a-Acetylcitrulline // HMDB00856:.H/Na.H(+) // 240.0945 // 20	2.0000	0.7325	0.4390	0.0000	0.4047	0.0937	0.0000	0.3278	0.2197	1.0000	0.9594	0.0001	1.0000	1.2380	0.0000
m3809	426.3551	Elaidic carnitine // HMDB06464:.H(+) // 426.3551 // 100	2.0000	0.6550	0.4549	0.0000	0.3901	0.1411	0.0000	0.2162	0.4788	1.0000	0.7714	0.0033	1.0000	1.2421	0.0000
m798	150.0274	2-Oxo-4-methylthiobutanoic acid // HMDB01553:[+].H(+) // 150.0274 // 46	2.0000	0.6517	0.3267	0.0000	0.4310	0.0075	0.0000	0.3408	0.0541	1.0000	0.7880	0.0000	1.0000	1.0470	0.0000
m1097	174.0888	2-Oxoarginine // HMDB04225:.H(+) // 174.0888 // 69 /// N-Methylphenylethanolamine // HMDB01387:.Na(+) // 174.0888 // 20 /// Phenylpropanolamine // HMDB01942:.Na(+) // 174.0888 // 20 /// N-Methyltyramine // HMDB03633:.Na(+) // 174.0888 // 20 /// N-Methylphenylethanolamine // HMDB01387:.H/Na.H(+) // 174.0888 // 20 /// Phenylpropanolamine // HMDB01942:.H/Na.H(+) // 174.0888 // 20 /// N-Methyltyramine // HMDB03633:.H/Na.H(+) // 174.0888 // 20	2.0000	0.6421	0.2748	0.0000	0.4407	0.0121	0.0000	0.3811	0.0479	1.0000	0.7991	0.0000	1.0000	0.9475	0.0000
m1844	240.1199	Propionylcarnitine // HMDB00824:.H/Na.H(+) // 240.1199 // 45 /// Propionylcarnitine // HMDB00824:.Na(+) // 240.1199 // 26 /// Bupropion // HMDB01510:.H(+) // 240.1199 // 11	2.0000	0.5778	0.3087	0.0000	0.3111	0.0845	0.0000	0.3289	0.0972	1.0000	0.7353	0.0001	1.0000	0.9357	0.0000
m1119	176.0677	Guanidinosuccinic acid // HMDB03157:.H(+) // 176.0677 // 94 /// Indoleacetic acid // HMDB00197:.H(+) // 176.0677 // 34 /// 5-Hydroxyindoleacetaldehyde // HMDB04073:.H(+) // 176.0677 // 34 /// Dopamine // HMDB00073:.H/Na.H(+) // 176.0677 // 20 /// p-Octopamine // HMDB04825:.H/Na.H(+) // 176.0677 // 20 /// Vanillylamine // HMDB12309:.H/Na.H(+) // 176.0677 // 20 /// Dopamine // HMDB00073:.Na(+) // 176.0677 // 20 /// p-Octopamine // HMDB04825:.Na(+) // 176.0677 // 20 /// Vanillylamine // HMDB12309:.Na(+) // 176.0677 // 20	2.0000	0.5539	0.3066	0.0000	0.3565	0.0137	0.0000	0.2282	0.1551	1.0000	0.8037	0.0000	1.0000	0.8271	0.0000
m2714	316.2498	Decanoylcarnitine // HMDB00651:.H(+) // 316.2498 // 86	2.0000	0.5290	0.2199	0.0000	0.2131	0.3166	1.0000	0.6676	0.0029	0.0000	0.5457	0.0083	1.0000	0.6897	0.0018
m1508	209.0803	4-Hydroxybenzyl alcohol // HMDB11724:.H(+) // 209.0803 // 100 /// (R)-2-Benzylsuccinate // HMDB12127:.H(+) // 209.0803 // 100	2.0000	0.4966	0.2195	0.0000	0.3447	0.0012	0.0000	0.2900	0.0117	1.0000	0.5907	0.0000	1.0000	0.7611	0.0000
m395	123.0558	Niacinamide // HMDB01406:.H(+) // 123.0558 // 100	2.0000	0.1739	0.5493	0.0000	0.2399	0.2390	1.0000	-0.5963	0.0058	0.0000	0.3535	0.0775	1.0000	0.6986	0.0011

m3159	359.1101	Pantetheine 4 -phosphate // HMD801416:.H(+) // 359.1101 // 59 /// N1-(5-Phospho-a-D- ribosyl)-5,6-dimethylbenzimidazole // HMD803882:.H(+) // 359.1101 // 39 /// Valproic acid glucuronide // HMD800901:.H/K.H(+) // 359.1101 // 38 /// Octanoylglucuronide // HMD810347:.H/K.H(+) // 359.1101 // 38 /// 3- Oxotetradecanoic acid // HMD810730:.NaCl.H(+) // 359.1101 // 12	2.0000	-0.3685	0.4129	1.0000	-0.6870	0.0056	0.0000	0.1998	0.4906	1.0000	-0.6606	0.0076	0.0000	-0.3261	0.2310
m3216	365.0447	Xanthylic acid // HMD801554:.H(+) // 365.0447 // 100 /// 6-Hydroxymelatonin // HMD804081:.NaCl.H(+) // 365.0447 // 9 /// Histidylproline diketopiperazine // HMD802053:.NaCl.H(+) // 365.0447 // 5	2.0000	-0.4705	0.4109	0.0000	-0.4361	0.0063	0.0000	0.0936	0.6281	1.0000	-0.7069	0.0000	1.0000	-0.8327	0.0000
m1703	227.0531	Chorismate // HMD812199:.H(+) // 227.0531 // 100 /// Prephenate // HMD812283:.H(+) // 227.0531 // 100 /// Pyridoxamine // HMD801431:.NaCl.H(+) // 227.0531 // 7	2.0000	-0.5085	0.2040	0.0000	-0.5655	0.0027	0.0000	-0.2061	0.3332	1.0000	-0.6286	0.0009	1.0000	-0.6337	0.0016
m3398	383.1527	Loratadine // HMD805000:.H(+) // 383.1527 // 92	2.0000	-0.5227	0.2443	1.0000	-0.7799	0.0000	0.0000	-0.5067	0.0017	1.0000	-0.6064	0.0001	0.0000	-0.1977	0.2265
m3236	367.0660	Phosphoribosyl formamidocarboxamide // HMD801439:.H(+) // 367.0660 // 100 /// 7- Hydroxy-6-methyl-8-ribityl lumazine // HMD804256:.H/K.H(+) // 367.0660 // 55 /// Thiamine monophosphate // HMD802666:.H/Na.H(+) // 367.0660 // 18 /// Malvidin // HMD803201:.H(+) // 367.0660 // 17 /// Warfarin // HMD801935:.NaCl.H(+) // 367.0660 // 12 /// Bisdemethoxycurcumin // HMD802114:.NaCl.H(+) // 367.0660 // 12	2.0000	-0.5452	0.2243	0.0000	-0.5165	0.0144	0.0000	-0.2469	0.3004	1.0000	-0.7709	0.0003	1.0000	-0.6466	0.0040
m46	75.0448	Propionic acid // HMD800237:.H(+) // 75.0448 // 100 /// Lactaldehyde // HMD803052:.H(+) // 75.0448 // 100 /// 3-Hydroxypropanal // HMD803453:.H(+) // 75.0448 // 100 /// D- Lactaldehyde // HMD806458:.H(+) // 75.0448 // 100 /// Hydroxyacetone // HMD806961:.H(+) // 75.0448 // 100	2.0000	-0.5488	0.1776	0.0000	-0.3859	0.0205	1.0000	-0.6118	0.0008	0.0000	-0.4268	0.0102	1.0000	-0.7708	0.0000
m1112	175.1203	L-Arginine // HMD800517:.H(+) // 175.1203 // 74 /// D-Arginine // HMD803416:.H(+) // 175.1203 // 74 /// N-Methyltryptamine // HMD804370:.H(+) // 175.1203 // 37	2.0000	-0.5522	0.4749	0.0000	-0.3062	0.1121	1.0000	-0.9608	0.0000	0.0000	-0.0040	0.9849	1.0000	-0.9377	0.0000
m1663	223.0760	Flavone // HMD803075:.H(+) // 223.0760 // 100 /// L-Cystathionine // HMD800099:.H(+) // 223.0760 // 76 /// Allocystathionine // HMD800455:.H(+) // 223.0760 // 76	2.0000	-0.5767	0.3265	0.0000	-0.3722	0.0386	0.0000	-0.2444	0.2215	1.0000	-0.7368	0.0001	1.0000	-0.9534	0.0000
m2537	300.0977	8-Hydroxyguanosine // HMD802044:.H(+) // 300.0977 // 70 /// Gamma glutamyl ornithine // HMD802248:.H/K.H(+) // 300.0977 // 13 /// Aspartylsine // HMD804985:.H/K.H(+) // 300.0977 // 13 /// Alpha-Aspartyl-lysine // HMD804987:.H/K.H(+) // 300.0977 // 13	2.0000	-0.6109	0.1387	1.0000	-0.6262	0.0037	0.0000	-0.4976	0.0342	0.0000	-0.5188	0.0158	1.0000	-0.8010	0.0005
m3606	405.0116	Uridine 5 -diphosphate // HMD800295:.H(+) // 405.0116 // 100	2.0000	-0.6647	0.4331	0.0000	-0.2869	0.1403	0.0000	-0.4293	0.0409	1.0000	-0.6740	0.0005	1.0000	-1.2685	0.0000
m3672	412.0435	dADP // HMD801508:.H(+) // 412.0435 // 100	2.0000	-0.6745	0.2940	0.0000	-0.5700	0.0005	0.0000	-0.3777	0.0334	1.0000	-0.6756	0.0001	1.0000	-1.0749	0.0000
m3828	428.0385	Adenosine 3, 5 -diphosphate // HMD800061:.H(+) // 428.0385 // 100 /// dGDP // HMD800960:.H(+) // 428.0385 // 100 /// ADP // HMD801341:.H(+) // 428.0385 // 100 /// Acetyl adenylate // HMD806880:.H/K.H(+) // 428.0385 // 15 /// N-Acetylneuraminic acid 9- phosphate // HMD804381:.H/K.H(+) // 428.0385 // 8 /// N-Acetylneuraminic acid 9- phosphate // HMD806268:.H/K.H(+) // 428.0385 // 8	2.0000	-0.8815	0.8469	0.0000	-0.4874	0.0231	0.0000	0.0474	0.8640	1.0000	-1.1835	0.0000	1.0000	-1.9026	0.0000
m7051	838.2349	3 -Sialyl-3-fucosyllactose // HMD806606:.NaCl.H(+) // 838.2349 // 72	1.0000	3.2499	1.4786	0.0000	4.7631	0.0000	0.0000	1.4486	0.1753	0.0000	2.6929	0.0052	1.0000	4.0950	0.0001
m966	162.1136	4-Trimethylammoniobutanoic acid // HMD801161:.H(+) // 162.1136 // 92 /// L- Carnitine // HMD800062:.H(+) // 162.1136 // 92	1.0000	0.6324	0.2945	0.0000	0.2981	0.3793	0.0000	0.5187	0.1531	0.0000	0.7236	0.0269	1.0000	0.9890	0.0045
m347	118.0869	Betaine // HMD800043:.H(+) // 118.0869 // 100 /// L-Valine // HMD800883:.H(+) // 118.0869 // 100 /// Vaporole // HMD801382:.H(+) // 118.0869 // 100 /// N-Methyl-a-aminoisobutyric acid // HMD802141:.H(+) // 118.0869 // 100 /// 5-Aminopentanoic acid // HMD803355:.H(+) // 118.0869 // 100 /// Seneciolic acid // HMD800509:.NH4(+) // 118.0869 // 10 // Tiglic acid // HMD801470:.NH4(+) // 118.0869 // 10 /// 2-Ethylacrylic acid // HMD801862:.NH4(+) // 118.0869 // 10 /// 3-Methylbutyrolactone // HMD802167:.NH4(+) // 118.0869 // 10 /// Aminoadipic acid // HMD800510:.CO2.H(+) // 118.0869 // 10 /// Glycerylphosphorylethanolamine // HMD800114:.H3PO4.H(+) // 118.0869 // 5	1.0000	0.5917	0.4486	0.0000	0.1205	0.7554	0.0000	0.5510	0.1564	0.0000	0.4948	0.1651	1.0000	1.2004	0.0013



m983	163.1167	4-Trimethylammonibutanoic acid // HMDB01161:[+1].H(+)// 163.1167 // 60 /// L-Carnitine // HMDB00062:[+1].H(+)// 163.1167 // 60 /// 4-Hydroxycyclohexylcarboxylic acid // HMDB01988:[+1].NH4(+)// 163.1167 // 6	1.0000	0.5344	0.2489	0.0000	0.2610	0.3734	0.0000	0.4262	0.1753	0.0000	0.6101	0.0310	1.0000	0.8405	0.0053
m2194	271.1394	2-(3-Carboxy-3-(methylammonio)propyl)-L-histidine // HMDB11654:.H(+)// 271.1394 // 100	1.0000	0.5287	0.5895	0.0000	-0.1193	0.7340	0.0000	0.4100	0.2531	0.0000	0.5155	0.1096	1.0000	1.3087	0.0002
m1966	252.1045	Muramic acid // HMDB03254:.H(+)// 252.1045 // 100 /// Deoxyadenosine // HMDB00101:.H(+)// 252.1045 // 95 /// 5-Deoxyadenosine // HMDB01983:.H(+)// 252.1045 // 95 /// Prollyhydroxyproline // HMDB06695:[+1].Na(+)// 252.1045 // 53 /// Deoxyadenosine monophosphate // HMDB00905:-HPO3.H(+)// 252.1045 // 5	1.0000	0.5094	0.1593	0.0000	0.3641	0.0483	0.0000	0.5818	0.0035	0.0000	0.3924	0.0325	1.0000	0.6994	0.0004
m340	117.1033	5-Aminopentanamide // HMDB12176:.H(+)// 117.1033 // 91 /// 2-Piperidinone // HMDB11749:.NH4(+)// 117.1033 // 10	1.0000	0.4978	0.7146	0.0000	-0.0002	0.9994	0.0000	0.1812	0.4887	0.0000	0.2524	0.2728	1.0000	1.5578	0.0000
m1148	179.1051	5-Phenylvaleric acid // HMDB02043:.H(+)// 179.1051 // 63 /// 4-Hydroxynonenal // HMDB04362:.H/Na.H(+)// 179.1051 // 20 /// Monoisobutyl phthalic acid // HMDB02056:-CO2.H(+)// 179.1051 // 6 /// Amino adipic acid // HMDB00510:.NH4(+)// 179.1051 // 5	1.0000	0.4017	0.2877	0.0000	0.2162	0.0816	0.0000	0.1299	0.3554	0.0000	0.4974	0.0001	1.0000	0.7635	0.0000
m2275	279.2305	Alpha-Linolenic acid // HMDB01388:.H(+)// 279.2305 // 100 /// Gamma-Linolenic acid // HMDB03073:.H(+)// 279.2305 // 100 /// Palmitic acid // HMDB00220:.H/Na.H(+)// 279.2305 // 27 /// Trimethyltridecanoic acid // HMDB02396:.H/Na.H(+)// 279.2305 // 27	1.0000	0.3686	0.2359	0.0000	0.1503	0.3213	0.0000	0.2494	0.1263	0.0000	0.3825	0.0093	1.0000	0.6924	0.0000
m288	112.0522	Cytosine // HMDB00630:.H(+)// 112.0522 // 61	1.0000	0.3477	0.3367	0.0000	0.2787	0.1714	0.0000	0.4386	0.0458	0.0000	-0.0675	0.7592	1.0000	0.7411	0.0006
m2946	338.0519	Famotidine // HMDB01919:.H(+)// 338.0519 // 100 /// Dihydrozeatin // HMDB12215:.(NaCl)2.H(+)// 338.0519 // 8	1.0000	-0.1275	0.4154	1.0000	-0.6856	0.0023	0.0000	-0.0430	0.8812	0.0000	-0.0992	0.6840	0.0000	0.3177	0.1944
m3599	404.0202	CDP // HMDB01546:.H(+)// 404.0202 // 76 /// Molybdopterin precursor Z // HMDB11683:.NaCl.H(+)// 404.0202 // 6 /// Cyclic GMP // HMDB01314:.NaCl.H(+)// 404.0202 // 6 /// Guanosine 2,3-cyclic phosphate // HMDB11629:.NaCl.H(+)// 404.0202 // 6	1.0000	-0.2193	0.4499	0.0000	0.0577	0.7833	0.0000	0.2277	0.2857	0.0000	-0.3957	0.0365	1.0000	-0.7667	0.0002
m6727	777.9710	Phosphoribosyl-ATP // HMDB03665:.NaCl.H(+)// 777.9710 // 98	1.0000	-0.2217	0.3005	0.0000	-0.0556	0.7277	0.0000	0.0435	0.8135	0.0000	-0.2372	0.1055	1.0000	-0.6373	0.0001
m2641	309.0955	Glutathione // HMDB00125:[+1].H(+)// 309.0955 // 86 /// Salicin // HMDB03546:.H/Na.H(+)// 309.0955 // 30 /// Salicin // HMDB03546:.Na(+)// 309.0955 // 30 /// 2-(3-Carboxy-3-(methylammonio)propyl)-L-histidine // HMDB11654:.H/K.H(+)// 309.0955 // 16 /// 2-(3-Carboxy-3-(methylammonio)propyl)-L-histidine // HMDB11654:.K(+)// 309.0955 // 8	1.0000	-0.2512	0.3532	0.0000	0.0554	0.7333	0.0000	-0.0155	0.9366	0.0000	-0.3255	0.0279	1.0000	-0.7193	0.0000
m1146	179.0489	Cysteinylglycine // HMDB00078:.H(+)// 179.0489 // 100	1.0000	-0.3310	0.3865	0.0000	-0.1361	0.4911	0.0000	0.0512	0.8315	0.0000	-0.3989	0.0337	1.0000	-0.8403	0.0000
m2629	308.0926	Glutathione // HMDB00125:.H(+)// 308.0926 // 65	1.0000	-0.3717	0.5962	0.0000	0.1154	0.6118	0.0000	0.0661	0.8046	0.0000	-0.5103	0.0158	1.0000	-1.1579	0.0000
m338	117.0536	Alpha-ketoisovaleric acid // HMDB00019:.H(+)// 117.0536 // 100 /// Methylacetoacetic acid // HMDB00310:.H(+)// 117.0536 // 100 /// Levulinic acid // HMDB00720:.H(+)// 117.0536 // 100 /// 2-Oxovaleric acid // HMDB01865:.H(+)// 117.0536 // 100 /// 2-Methylacetoacetic acid // HMDB03771:.H(+)// 117.0536 // 100 /// Glutarate semialdehyde // HMDB12233:.H(+)// 117.0536 // 100	1.0000	-0.3911	0.1665	0.0000	-0.2850	0.0199	0.0000	-0.2850	0.0329	0.0000	-0.3594	0.0034	1.0000	-0.6353	0.0000
m7631	971.9021	Dolichol-14 // HMDB05181:.H(+)// 971.9021 // 100	1.0000	-0.4851	0.7255	0.0000	-0.0553	0.8836	0.0000	0.1351	0.7501	0.0000	-0.5315	0.1194	1.0000	-1.4889	0.0001
m48	76.0399	Glycine // HMDB00123:.H(+)// 76.0399 // 100	1.0000	-0.5103	0.2109	0.0000	-0.4254	0.0320	0.0000	-0.2738	0.2145	0.0000	-0.5747	0.0038	1.0000	-0.7674	0.0003
m990	164.0683	4-(3-Pyridyl)-3-butenic acid // HMDB01424:.H(+)// 164.0683 // 84 /// 3-Methylthioxindole // HMDB04186:.H(+)// 164.0683 // 84 /// S-(2-carboxypropyl)-Cysteamine // HMDB02169:.H(+)// 164.0683 // 34 /// 2-Hydroxyadipic acid // HMDB00321:[+1].H(+)// 164.0683 // 6 /// 3-Hydroxyadipic acid // HMDB00345:[+1].H(+)// 164.0683 // 6 /// 3-Hydroxymethylglutaric acid // HMDB00355:[+1].H(+)// 164.0683 // 6 /// 2[R]-Hydroxyadipic acid // HMDB00368:[+1].H(+)// 164.0683 // 6 /// Glucosan // HMDB00640:[+1].H(+)// 164.0683 // 6	1.0000	-0.5262	0.0680	0.0000	-0.4609	0.0043	0.0000	-0.5200	0.0029	0.0000	-0.5026	0.0019	1.0000	-0.6212	0.0003
m1441	204.2270	Spermine // HMDB01256:[+1].H(+)// 204.2270 // 60	1.0000	-1.0216	0.7944	0.0000	-0.6055	0.2158	0.0000	-0.4102	0.4639	0.0000	-0.8957	0.0625	1.0000	-2.1750	0.0000

m1413	203.2242	Spermine // HMDB01256:.H(+) // 203.2242 // 85	1.0000	-1.1929	0.8880	0.0000	-0.6931	0.1882	0.0000	-0.5782	0.3239	0.0000	-1.0027	0.0527	1.0000	-2.4974	0.0000
m4772	530.2008	O-6-deoxy-a-L-galactopyranosyl-(1->2)-O-b-D-galactopyranosyl-(1->3)-2-(acetylamino)-2-deoxy-D-Galactose // HMDB02060:.H(+) // 530.2008 // 63 // Lewis X trisaccharide // HMDB06568:.H(+) // 530.2008 // 63 // Lewis a trisaccharide // HMDB06582:.H(+) // 530.2008 // 63	1.0000	-3.2375	0.7342	1.0000	-3.9912	0.0004	0.0000	-2.8848	0.0159	0.0000	-3.6867	0.0009	0.0000	-2.3872	0.0424
m105	89.1076	Putrescine // HMDB01414:.H(+) // 89.1076 // 100	0.0000	0.9402	0.4181	0.0000	1.1322	0.0703	0.0000	0.8636	0.2127	0.0000	0.3952	0.5532	0.0000	1.3699	0.0392
m651	140.9953	Acetylphosphate // HMDB01494:.H(+) // 140.9953 // 100 // Phosphonoacetate // HMDB04110:.H(+) // 140.9953 // 100 // 2-Ketobutyric acid // HMDB00005:.H/K.H(+) // 140.9953 // 10 // 10 // Acetoacetic acid // HMDB00060:.H/K.H(+) // 140.9953 // 10 // 2-Methyl-3-oxopropanoic acid // HMDB01172:.H/K.H(+) // 140.9953 // 10 // Succinic acid semialdehyde // HMDB01259:.H/K.H(+) // 140.9953 // 10 // (S)-Methylmalonic acid semialdehyde // HMDB02217:.H/K.H(+) // 140.9953 // 10 // 4-Hydroxycrotonic acid // HMDB03381:.H/K.H(+) // 140.9953 // 10 // 2-Ketobutyric acid // HMDB00005:.K(+) // 140.9953 // 5 // Acetoacetic acid // HMDB00060:.K(+) // 140.9953 // 5 // 2-Methyl-3-oxopropanoic acid // HMDB01172:.K(+) // 140.9953 // 5 // Succinic acid semialdehyde // HMDB01259:.K(+) // 140.9953 // 5 // (S)-Methylmalonic acid semialdehyde // HMDB02217:.K(+) // 140.9953 // 5 // 4-Hydroxycrotonic acid // HMDB03381:.K(+) // 140.9953 // 5	0.0000	0.7655	0.0719	0.0000	0.7468	0.0231	0.0000	0.6719	0.0634	0.0000	0.8146	0.0130	0.0000	0.8286	0.0178
m4911	543.4860	7,7,8,8,11,11,12,12 -Hexahydro-γ,γ-Carotene // HMDB02272:.H(+) // 543.4860 // 100 // Phytofluene // HMDB02871:.H(+) // 543.4860 // 100 // cis-7,7,8,8,11,12-Hexahydro-Carotene // HMDB02936:.H(+) // 543.4860 // 100	0.0000	0.4255	0.1331	0.0000	0.3364	0.1804	0.0000	0.2938	0.2902	0.0000	0.4943	0.0451	0.0000	0.5775	0.0279
m473	127.0243	Taurine // HMDB00251:[+1].H(+) // 127.0243 // 59	0.0000	0.4195	0.1145	0.0000	0.3039	0.0366	0.0000	0.3392	0.0322	0.0000	0.5310	0.0003	0.0000	0.5037	0.0012
m3550	399.1471	S-Adenosylmethionine // HMDB01185:.H(+) // 399.1471 // 39	0.0000	0.3893	0.2899	0.0000	0.5820	0.0087	0.0000	0.5520	0.0222	0.0000	0.4621	0.0367	0.0000	-0.0388	0.8892
m4567	509.3381	Reduced Vitamin K (phylloquinone) // HMDB04198:.H/K.H(+) // 509.3381 // 71	0.0000	0.2803	0.2954	0.0000	0.4231	0.0419	0.0000	-0.1292	0.6054	0.0000	0.2759	0.1921	0.0000	0.5516	0.0124
m5550	613.1583	Oxidized glutathione // HMDB03337:.H(+) // 613.1583 // 100	0.0000	0.2746	0.4037	0.0000	-0.1440	0.7639	0.0000	0.8146	0.0899	0.0000	0.1279	0.7884	0.0000	0.3000	0.5534
m758	147.0765	L-Glutamine // HMDB00641:.H(+) // 147.0765 // 100 // Ureidoisobutyric acid // HMDB02031:.H(+) // 147.0765 // 100 // D-Glutamine // HMDB03423:.H(+) // 147.0765 // 100 // Alanylglycine // HMDB06899:.H(+) // 147.0765 // 100 // Pyroglutamic acid // HMDB00267:.NH4(+) // 147.0765 // 5 // Pyrrolidonecarboxylic acid // HMDB00805:.NH4(+) // 147.0765 // 5 // Pyrroline hydroxycarboxylic acid // HMDB01369:.NH4(+) // 147.0765 // 5 // N-Acryloylglycine // HMDB01843:.NH4(+) // 147.0765 // 5 // 1-Pyrroline-4-hydroxy-2-carboxylate // HMDB02234:.NH4(+) // 147.0765 // 5	0.0000	0.1792	0.2155	0.0000	0.3585	0.0110	0.0000	0.2934	0.0583	0.0000	0.1924	0.1804	0.0000	-0.1274	0.4267
m2741	318.2966	Phytosphingosine // HMDB04610:.H(+) // 318.2966 // 100	0.0000	0.1701	0.1084	0.0000	0.3143	0.0835	0.0000	0.1258	0.5599	0.0000	0.1813	0.3331	0.0000	0.0590	0.7913
m2752	319.2575	Allopregnanolone // HMDB01449:.H(+) // 319.2575 // 60 // Alloepipregnanolone // HMDB01455:.H(+) // 319.2575 // 60 // Epipregnanolone // HMDB01471:.H(+) // 319.2575 // 60 // Epimetendiol // HMDB06012:.H(+) // 319.2575 // 60 // 3a-Hydroxy-5b-pregnane-20-one // HMDB06759:.H(+) // 319.2575 // 60 // 2,6-dimethylheptanoyl carnitine // HMDB06320:.NH4(+) // 319.2575 // 16	0.0000	0.1639	0.1541	0.0000	0.2466	0.1552	0.0000	-0.0670	0.7553	0.0000	0.2456	0.1572	0.0000	0.2303	0.2202

m3799	425.2859	1b-Hydroxycholeic acid // HMD800307:.H(+) // 425.2859 // 94 // 3b,4b,7a,12a-Tetrahydroxy-5b-cholanoic acid // HMD800311:.H(+) // 425.2859 // 94 // 2b,3a,7a,12a-Tetrahydroxy-5b-cholanoic acid // HMD800316:.H(+) // 425.2859 // 94 // 3a,7a,12a,19-Tetrahydroxy-5b-cholanoic acid // HMD800340:.H(+) // 425.2859 // 94 // 3a,6b,7b,12a-Tetrahydroxy-5b-cholanoic acid // HMD800367:.H(+) // 425.2859 // 94 // 3a,6b,7b,12b-Tetrahydroxy-5b-cholanoic acid // HMD800377:.H(+) // 425.2859 // 94 // 3a,6b,7a,12a-Tetrahydroxy-5b-cholanoic acid // HMD800399:.H(+) // 425.2859 // 94 // 1,3,7,12-Tetrahydroxycholanoic acid // HMD800433:.H(+) // 425.2859 // 94 // 3a,4b,7a,12a-Tetrahydroxy-5b-cholanoic acid // HMD800437:.H(+) // 425.2859 // 94	0.0000	0.1523	0.2659	0.0000	0.2161	0.3004	0.0000	0.2749	0.2253	0.0000	-0.2373	0.2555	0.0000	0.3555	0.1050
m3559	400.1495	S-Adenosylmethionine // HMD801185:[+1].H(+) // 400.1495 // 37	0.0000	0.1274	0.2576	0.0000	0.3584	0.1368	0.0000	0.1476	0.6071	0.0000	0.2404	0.3298	0.0000	-0.2368	0.3771
m1329	195.0091	p-Cresol sulfate // HMD811635:.H/Na.H(+) // 195.0091 // 66 // p-Cresol sulfate // HMD811635:.Na(+) // 195.0091 // 19 // Glycerol 3-phosphate // HMD800126:.H/Na.H(+) // 195.0091 // 11 // Beta-Glycerophosphoric acid // HMD802520:.H/Na.H(+) // 195.0091 // 11 // Hypoxanthine // HMD800157:.NaCl.H(+) // 195.0091 // 7 // Erythronic acid // HMD800613:.NaCl.H(+) // 195.0091 // 5 // Threonic acid // HMD800943:.NaCl.H(+) // 195.0091 // 5	0.0000	0.1093	0.1457	0.0000	-0.0981	0.5921	0.0000	0.2056	0.2861	0.0000	0.1138	0.5346	0.0000	0.2160	0.2530
m3057	349.2395	3b,15b,17a-Trihydroxy-pregnenone // HMD800353:.H(+) // 349.2395 // 100 // 3b,17a,21-Trihydroxypregnenone // HMD800382:.H(+) // 349.2395 // 100 // 3a,21-Dihydroxy-5b-pregnane-11,20-dione // HMD806755:.H(+) // 349.2395 // 100 // 11b,21-Dihydroxy-5b-pregnane-3,20-dione // HMD806757:.H(+) // 349.2395 // 100 // 17a,21-Dihydroxypreg-nenolone // HMD806762:.H(+) // 349.2395 // 100	0.0000	0.1087	0.2307	0.0000	-0.0469	0.7410	0.0000	-0.1166	0.4355	0.0000	0.2211	0.0876	0.0000	0.3771	0.0059
m524	131.1183	N-Acetylputrescine // HMD802064:.H(+) // 131.1183 // 100	0.0000	0.0205	0.0459	0.0000	0.0599	0.5508	0.0000	-0.0458	0.6942	0.0000	0.0324	0.7558	0.0000	0.0356	0.7597
m329	116.0708	L-Proline // HMD800162:.H(+) // 116.0708 // 100 // D-Proline // HMD803411:.H(+) // 116.0708 // 100	0.0000	-0.0494	0.1101	0.0000	-0.0141	0.9333	0.0000	-0.0508	0.7857	0.0000	0.0650	0.6862	0.0000	-0.1978	0.2225
m760	147.1694	Spermidine // HMD801257:[+1].H(+) // 147.1694 // 60	0.0000	-0.0666	0.2396	0.0000	0.1153	0.6977	0.0000	0.1492	0.6548	0.0000	-0.1835	0.5304	0.0000	-0.3476	0.2483
m731	146.1660	Spermidine // HMD801257:.H(+) // 146.1660 // 100	0.0000	-0.0679	0.2470	0.0000	0.1106	0.7334	0.0000	0.1702	0.6358	0.0000	-0.2134	0.4988	0.0000	-0.3387	0.3029
m109	90.1106	Putrescine // HMD801414:[+1].H(+) // 90.1106 // 60	0.0000	-0.1182	0.1365	0.0000	-0.1343	0.8058	0.0000	-0.1640	0.7932	0.0000	-0.2480	0.6447	0.0000	0.0733	0.9070
m4640	517.3012	Taurocholic acid // HMD800036:[+1].H(+) // 517.3012 // 100 // Tauroursocholic acid // HMD800889:[+1].H(+) // 517.3012 // 100 // Taurallocholic acid // HMD800922:[+1].H(+) // 517.3012 // 100 // Tauro-b-muricholic acid // HMD800932:[+1].H(+) // 517.3012 // 100 // Taurohydrocholate // HMD811637:[+1].H(+) // 517.3012 // 100 // Campesterol // HMD802869:(NaCl)2.H(+) // 517.3012 // 8 // 4-alpha-Methyl-5-alpha-cholest-7-en-3-beta-ol // HMD811605:(NaCl)2.H(+) // 517.3012 // 8 // (5Alpha)-campestan-3-one // HMD812116:(NaCl)2.H(+) // 517.3012 // 8	0.0000	-0.1690	0.2887	0.0000	-0.1336	0.5510	0.0000	-0.5839	0.0108	0.0000	0.0690	0.7665	0.0000	-0.0273	0.9189
m868	156.0762	L-Histidine // HMD800177:.H(+) // 156.0762 // 100	0.0000	-0.1915	0.2785	0.0000	0.0283	0.9073	0.0000	-0.3185	0.1817	0.0000	0.0483	0.8369	0.0000	-0.5243	0.0217
m123	94.9982	Dimethylsulfide // HMD805879:.H(+) // 94.9982 // 100	0.0000	-0.2167	0.0451	0.0000	-0.2246	0.2218	0.0000	-0.1547	0.4619	0.0000	-0.2244	0.2239	0.0000	-0.2631	0.1813
m1568	215.0535	Quinic acid // HMD803072:.H/Na.H(+) // 215.0535 // 63 // Canavanine // HMD802706:.H/K.H(+) // 215.0535 // 31 // Serotonin // HMD800259:.H/K.H(+) // 215.0535 // 7 // Cotinine // HMD801046:.H/K.H(+) // 215.0535 // 7 // Phosphoguanidinooacetate // HMD803705:.NH4(+) // 215.0535 // 6	0.0000	-0.2375	0.1567	0.0000	-0.2287	0.1955	0.0000	-0.1453	0.4725	0.0000	-0.1148	0.5361	0.0000	-0.4611	0.0125
m799	150.0581	L-Methionine // HMD800696:.H(+) // 150.0581 // 100	0.0000	-0.3051	0.2633	0.0000	-0.0742	0.6504	0.0000	-0.5454	0.0010	0.0000	-0.0803	0.6255	0.0000	-0.5204	0.0013
m2237	276.0848	N-Acetylvallalanine // HMD811716:.H/Na.H(+) // 276.0848 // 77	0.0000	-0.3694	0.1454	0.0000	-0.4848	0.0025	0.0000	-0.1576	0.3890	0.0000	-0.4345	0.0064	0.0000	-0.4006	0.0183
m4162	464.0653	Chondroitin sulfate // HMD800580:.H(+) // 464.0653 // 65	0.0000	-0.6532	0.2521	0.0000	-0.8510	0.0151	0.0000	-0.3061	0.4526	0.0000	-0.6282	0.0738	0.0000	-0.8275	0.0265

## Teklad Global 14% Protein Rodent Maintenance Diet

**Product Description-** 2014 is a fixed formula, non-autoclavable diet manufactured with high quality ingredients and designed to promote longevity and normal body weight in rodents. 2014 does not contain alfalfa or soybean meal, thus minimizing the occurrence of natural phytoestrogens. Typical isoflavone concentrations (daidzein + genistein aglycone equivalents) range from non-detectable to 20 mg/kg. Exclusion of alfalfa reduces chlorophyll, improving optical imaging clarity. Absence of animal protein and fish meal minimizes the presence of nitrosamines.

**Also available certified (2014C) and irradiated (2914). For autoclavable diet, refer to 2014S (Sterilizable).**

### Macronutrients

Crude Protein	%	14.3
Fat (ether extract) <sup>a</sup>	%	4.0
Carbohydrate (available) <sup>b</sup>	%	48.0
Crude Fiber	%	4.1
Neutral Detergent Fiber <sup>c</sup>	%	18.0
Ash	%	4.7
Energy Density <sup>d</sup>	kcal/g (kJ/g)	2.9 (12.1)
Calories from Protein	%	20
Calories from Fat	%	13
Calories from Carbohydrate	%	67

### Minerals

Calcium	%	0.7
Phosphorus	%	0.6
Non-Phytate Phosphorus	%	0.3
Sodium	%	0.1
Potassium	%	0.6
Chloride	%	0.3
Magnesium	%	0.2
Zinc	mg/kg	70
Manganese	mg/kg	100
Copper	mg/kg	15
Iodine	mg/kg	6
Iron	mg/kg	175
Selenium	mg/kg	0.23

### Amino Acids

Aspartic Acid	%	0.9
Glutamic Acid	%	2.9
Alanine	%	0.9
Glycine	%	0.7
Threonine	%	0.5
Proline	%	1.2
Serine	%	0.7
Leucine	%	1.4
Isoleucine	%	0.6
Valine	%	0.7
Phenylalanine	%	0.7
Tyrosine	%	0.4
Methionine	%	0.3
Cystine	%	0.3
Lysine	%	0.7
Histidine	%	0.4
Arginine	%	0.8
Tryptophan	%	0.2

Teklad Diets are designed and manufactured for research purposes only.



**Ingredients** (in descending order of inclusion)- Wheat middlings, ground wheat, ground corn, corn gluten meal, calcium carbonate, soybean oil, dicalcium phosphate, iodized salt, L-lysine, vitamin E acetate, DL-methionine, magnesium oxide, choline chloride, manganous oxide, ferrous sulfate, menadione sodium bisulfite complex (source of vitamin K activity), zinc oxide, copper sulfate, niacin, calcium pantothenate, calcium iodate, pyridoxine hydrochloride, riboflavin, thiamin mononitrate, vitamin A acetate, vitamin B<sub>12</sub> supplement, folic acid, cobalt carbonate, biotin, vitamin D<sub>3</sub> supplement.

Standard Product Form: **Pellet**

### Vitamins

Vitamin A <sup>e, f</sup>	IU/g	6.0
Vitamin D <sub>3</sub> <sup>e, g</sup>	IU/g	0.6
Vitamin E	IU/kg	120
Vitamin K <sub>3</sub> (menadione)	mg/kg	20
Vitamin B <sub>1</sub> (thiamin)	mg/kg	12
Vitamin B <sub>2</sub> (riboflavin)	mg/kg	6
Niacin (nicotinic acid)	mg/kg	54
Vitamin B <sub>6</sub> (pyridoxine)	mg/kg	10
Pantothenic Acid	mg/kg	17
Vitamin B <sub>12</sub> (cyanocobalamin)	mg/kg	0.03
Biotin	mg/kg	0.26
Folate	mg/kg	2
Choline	mg/kg	1030

### Fatty Acids

C16:0 Palmitic	%	0.5
C18:0 Stearic	%	0.1
C18:1ω9 Oleic	%	0.7
C18:2ω6 Linoleic	%	2.0
C18:3ω3 Linolenic	%	0.1
Total Saturated	%	0.6
Total Monounsaturated	%	0.7
Total Polyunsaturated	%	2.1

### Other

Cholesterol	mg/kg	--
-------------	-------	----

<sup>a</sup> Ether extract is used to measure fat in pelleted diets, while an acid hydrolysis method is required to recover fat in extruded diets. Compared to ether extract, the fat value for acid hydrolysis will be approximately 1% point higher.

<sup>b</sup> Carbohydrate (available) is calculated by subtracting neutral detergent fiber from total carbohydrates.

<sup>c</sup> Neutral detergent fiber is an estimate of insoluble fiber, including cellulose, hemicellulose, and lignin. Crude fiber methodology underestimates total fiber.

<sup>d</sup> Energy density is a calculated estimate of *metabolizable energy* based on the Atwater factors assigning 4 kcal/g to protein, 9 kcal/g to fat, and 4 kcal/g to available carbohydrate.

<sup>e</sup> Indicates added amount but does not account for contribution from other ingredients.

<sup>f</sup> 1 IU vitamin A = 0.3 µg retinol

<sup>g</sup> 1 IU vitamin D = 25 ng cholecalciferol

For nutrients not listed, insufficient data is available to quantify.

Nutrient data represent the best information available, calculated from published values and direct analytical testing of raw materials and finished product. Nutrient values may vary due to the natural variations in the ingredients, analysis, and effects of processing.



## ***Contributed publications***

---

---



## Methodological aspects of the molecular and histological study of prostate cancer: Focus on PTEN



Aitziber Ugalde-Olano <sup>a,1</sup>, Ainara Egia <sup>b,1</sup>, Sonia Fernández-Ruiz <sup>c,1</sup>, Ana Loizaga-Iriarte <sup>d,1</sup>, Patricia Zuñiga-García <sup>c,1</sup>, Stephane Garcia <sup>e</sup>, Félix Royo <sup>c,f</sup>, Isabel Lacasa-Viscasillas <sup>d</sup>, Erika Castro <sup>b</sup>, Ana R. Cortazar <sup>c</sup>, Amaia Zabala-Letona <sup>c</sup>, Natalia Martín-Martín <sup>c</sup>, Amaia Arruabarrena-Aristorena <sup>c</sup>, Verónica Torrano-Moya <sup>c</sup>, Lorea Valcárcel-Jiménez <sup>c</sup>, Pilar Sánchez-Mosquera <sup>c</sup>, Alfredo Caro-Maldonado <sup>c</sup>, Jorge González-Tampan <sup>d</sup>, Guido Cachi-Fuentes <sup>d</sup>, Elena Bilbao <sup>d</sup>, Rocío Montero <sup>d</sup>, Sara Fernández <sup>a,b</sup>, Edurne Arrieta <sup>b</sup>, Kerman Zorroza <sup>b</sup>, Mireia Castillo-Martín <sup>g</sup>, Violeta Serra <sup>h,i</sup>, Eider Salazar <sup>b</sup>, Nuria Macías-Cámara <sup>c</sup>, Jose Tabernero <sup>h,i</sup>, Jose Baselga <sup>h,i,j</sup>, Carlos Cordon-Cardo <sup>g</sup>, Ana M. Aransay <sup>c,f</sup>, Amaia Del Villar <sup>b</sup>, Juan L. Iovanna <sup>e</sup>, Juan M. Falcón-Pérez <sup>c,f,k</sup>, Miguel Unda <sup>d,2</sup>, Roberto Bilbao <sup>b,2</sup>, Arkaitz Carracedo <sup>c,k,l,\*</sup>

<sup>a</sup> Department of Pathology, Basurto University Hospital, 48013 Bilbao, Spain

<sup>b</sup> Basque Biobank, Basque Foundation for Health Innovation and Research-BIOEF, Barakaldo, Spain

<sup>c</sup> CIC bioGUNE, Bizkaia Technology Park, 801 Building, 48160 Derio, Spain

<sup>d</sup> Department of Urology, Basurto University Hospital, 48013 Bilbao, Spain

<sup>e</sup> Centre de Recherche en Cancérologie de Marseille (CRCM), INSERM UMR 1068, CNRS UMR 7258, Aix-Marseille University and Institut Paoli-Calmettes, Parc Scientifique et Technologique de Luminy, Marseille, France

<sup>f</sup> Centro de Investigación Biomédica en Red de Enfermedades Hepáticas y Digestivas (Ciberehd), Spain

<sup>g</sup> Department of Pathology, Icahn School of Medicine at Mount Sinai, New York, NY, USA

<sup>h</sup> Molecular Therapeutics Research Unit, Medical Oncology Department, Vall d'Hebron University Hospital, Barcelona, Spain

<sup>i</sup> Experimental Therapeutics Group, Vall d'Hebron University Hospital, Barcelona, Spain

<sup>j</sup> Human Oncology & Pathogenesis Program, Memorial Sloan-Kettering Cancer Center, New York, NY, USA

<sup>k</sup> Ikerbasque, Basque Foundation for Science, Bilbao, Spain

<sup>l</sup> Biochemistry and Molecular Biology Department, University of the Basque Country (UPV/EHU), Bilbao, Spain

### ARTICLE INFO

#### Article history:

Received 3 October 2014

Received in revised form 9 February 2015

Accepted 10 February 2015

Available online 16 February 2015

#### Keywords:

PTEN

Prostate cancer

Fresh tissue

Molecular biology

### ABSTRACT

Prostate cancer is among the most frequent cancers in men, and despite its high rate of cure, the high number of cases results in an elevated mortality worldwide. Importantly, prostate cancer incidence is dramatically increasing in western societies in the past decades, suggesting that this type of tumor is exquisitely sensitive to lifestyle changes. Prostate cancer frequently exhibits alterations in the *PTEN* gene (inactivating mutations or gene deletions) or at the protein level (reduced protein expression or altered sub-cellular compartmentalization). The relevance of *PTEN* in this type of cancer is further supported by the fact that the sole deletion of *PTEN* in the murine prostate epithelium recapitulates many of the features of the human disease. In order to study the molecular alterations in prostate cancer, we need to overcome the methodological challenges that this tissue imposes. In this review we present protocols and methods, using *PTEN* as proof of concept, to study different molecular characteristics of prostate cancer.

© 2015 Published by Elsevier Inc.

### 1. Introduction

Prostate cancer (PCa) is among the deadliest forms of cancer (WHO), and represents the third cause of death by cancer in men ([www.globocan.iarc.fr](http://www.globocan.iarc.fr)). The tumor suppressor *PTEN* is among the most mutated and lost tumor suppressors in PCa [1]. Up to 70% of PCa harbor loss of *PTEN* at presentation. This

\* Corresponding author. CIC bioGUNE, Bizkaia Technology Park, 801 Building, 48160 Derio, Spain.

E-mail address: [acarracedo@cicbiogune.es](mailto:acarracedo@cicbiogune.es) (A. Carracedo).

<sup>1</sup> Equal contribution.

<sup>2</sup> Equal contribution.

tumor suppressor is located at the top of a highly oncogenic signaling pathway, the PI-3 Kinase (PI-3K) cascade, which contains many other oncogenes and tumor suppressors [2]. In addition, regulatory feedback loops stem from the PTEN/PI-3K pathway to ensure cell homeostasis, which decrease the efficacy of single agent therapies [2,3].

PTEN down-regulation is not restricted to genetic events, and regulation of its transcription, translation and stability can play an important role. PTEN is frequently lost in heterozygosity, whereas mostly advanced cancers exhibit complete loss of the tumor suppressor. Interestingly, the prostate epithelium is exquisitely sensitive to the reduction in PTEN levels. This concept has been formally proven in mice through the use of genetic interference, which allows a partial reduction of the expression of the interfered allele [4,5]. While PTEN heterozygous mice present PIN lesions in the prostate with long latency [6], PTEN hypomorphic mice show progression of the prostate lesions to invasive cancer at higher penetrance [5]. Importantly, while a gradual decrease of PTEN promotes prostate cancer progression, acute and complete PTEN-loss elicits the activation of a fail-safe senescence response, which is driven by the up-regulation of the tumor suppressor p53 [7]. This novel type of senescence is genuinely distinct from the classic oncogene-induced senescence [8]. Importantly, genetic or environmental events regulating this process may be key players in the progression of prostate cancer and therefore attractive targets for anti-cancer therapy [9,10].

All these evidence point to the need of studying PTEN-dependent pathways in prostate cancer. However, the technical challenges related to the study of this type of tumor require special attention, and hence, in this review we aim at describing a series of methodologies to study prostate cancer biology, with a reference to the pathway aforementioned.

## 2. Methods and results

### 2.1. Preparation of well-diagnosed prostate cancer specimens for molecular studies

Cancerous lesions in the prostate, unlike in other tissues, are difficult to identify macroscopically. This poses a challenge when the aim is to obtain well-diagnosed frozen tissue. To overcome this limitation, we have set up together with the Basque Biobank and Basurto University Hospital (OSI-Basurto, Bilbao, Spain), in

collaboration with the Dept. of Pathology at Mount Sinai, a procedure to obtain this type of specimen.

### 2.2. Key materials

- A biopsy punch (Miltex Ref. 33–34).

Due to the characteristics of prostate cancer, we established a procedure by which fresh tissue obtained from radical prostatectomy is sliced into left and right lobe (after delimiting the margins of the surgical piece with ink and fixing the ink with acetic acid). All prostate specimens were obtained upon informed consent and with evaluation and approval from the corresponding ethics committee (CEIC code OHEUN11–12 and OHEUN14–14). From each lobe, the dermatologic punch is employed to harvest 8 tissue cylinders of 4 mm diameter. The site of the punches is selected blindly due to the lack of macroscopic alterations associated to cancerous lesions. However, we did notice that the expertise of the pathologist does influence the rate of success in harvesting cylinders with cancer. Of note, this approach prevents from damaging the capsule and a drop of eosin on the site of tissue harvest can help monitoring the histological alterations surrounding the area for diagnostic purposes. Tissue cylinders are then divided longitudinally with a scalpel and dedicated to snap-freeze (in liquid nitrogen or isopentane at  $-80^{\circ}\text{C}$ ) and to paraffin embedding for diagnostic purposes (procedure in Fig. 1A–D). Due to the width of the cylinder (4 mm diameter), the diagnosed tissue fraction will closely represent the histological properties of the frozen adjacent tissue. In Fig. 1E, hematoxylin/eosin staining of whole tissue sections from cylinders with different tumor abundance are shown, together with a zoom that shows the correct preservation of the histological properties of the sections. Importantly, this protocol allows us to closely estimate the tumor abundance that we have in the frozen tissue piece, hence solving an otherwise challenge in the acquisition of frozen material. The material obtained from this approach is sufficient to carry out different molecular biology studies, including RNA preparation (described below), protein extraction and metabolite profiling (data not shown).

### 2.3. Molecular biology analysis from frozen tissue: tips for good quality RNA preparation

Preparation of RNA of high quality from prostate cancer specimens remains a challenge, primarily due to the abundance of RNAses and proteases in the prostate and prostatic fluid. A variety

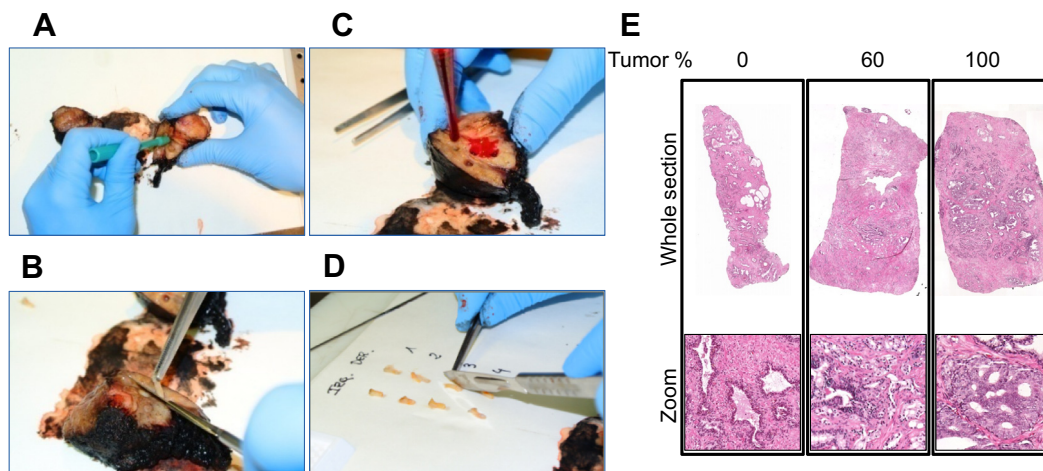


**Fig. 1.** Preparation of well-diagnosed fresh frozen biopsies. (A–D) Preparation of the punch biopsy (A) and excision with scalpel (B), identification of the harvest point in surgical piece with eosin (C) and longitudinal separation of the punch with scalpel (D). (E) Histological features of punch biopsies with different abundance of tumoral tissue, whole section hematoxylin/eosin staining is shown together with a zoom to show the histological features of the piece.



of protocols have been proposed to maximize the quality and yield from biopsies of different origin [11–14] (see also protocols from Prostate Cancer Biorepository Network; SOP N:006 <http://www.prostatebiorepository.org>). While real time PCR is a low-demanding approach in terms of RNA integrity, the latest OMIC technologies, including RNA sequencing, require material in optimal conditions.

To define the technical needs of an appropriate RNA extraction strategy, we have tested one main technical implementation (the use of phenolic extraction agents) and one variable (the presence of ink and acetic acid in the preparation).

#### 2.4. Key materials

- Trizol (Life Technologies/Invitrogen Ref. 15596-018).
- Total RNA extraction kit (NucleoSpin® miRNA Ref. 740971.10/50/250).

The protocol is the following, where the alternative procedure with and without Trizol is underlined (the Trizol-based implementation is described in the user manual of the NucleoSpin® miRNA kit):

1. RNase inhibition and tissue thawing (a minimal amount of tissue of 10 mg is sufficient for the procedure). RNA later ICE (Life Technologies Ref. AM7030) is used to ensure the maximal inhibition of RNases and the optimization of tissue homogenization afterwards. The protocol is based on transferring frozen tissue (stored dry at  $-80^{\circ}\text{C}$ ) to RNA later ICE (also at  $-80^{\circ}\text{C}$ ) and thawing the tissue at  $-20^{\circ}\text{C}$  overnight.
2. Regular lysis buffer. Tissue is transferred to the recommended volume of NucleoSpin® miRNA lysis buffer.

Trizol-based lysis. Tissue is transferred to 400  $\mu\text{L}$  volume of Trizol. Additional 400  $\mu\text{L}$  are added after homogenization.

3. Homogenization. 5–6 beads/tube (Ceramic Bead Tubes 2.8 mm, Cat.: 13114-50; MO BIO Laboratories). Homogenization is carried out in *Precellys* in two cycles of 6000 rpm and 30 s.
4. RNA extraction. Following the manufacturer's instructions.

RNA extraction. Following homogenization, we add 160  $\mu\text{L}$  of Chloroform, mix by vortex, incubate 3 min and centrifuge 15 min at 12,000g in tabletop centrifuge. The supernatant (350–400  $\mu\text{L}$ ) is transferred to a new tube and mixed with 1 mL of MX buffer. After vortex, the product is loaded in the column and the same process indicated in point 4 is followed.

The results obtained from frozen tissues with a stabilizing agent (RNA later ICE), a total RNA extraction kit, and with or without Trizol implementation are shown in Fig. 2. RNA stabilizing agents and the standard non-phenol based lysis buffer is not sufficient to prevent the RNA from degrading (Fig. 2A), while Trizol implementation results in total RNA of optimal quality for transcriptomic studies (Fig. 2B, RNA Integrity Number – RIN – values in Fig. 2C). Of note, although small RNAs have not been monitored in this procedure, the kit presented herein would allow for their isolation.

On the other hand, we have evaluated with an independent phenol-based RNA extraction kit (Absolutely RNA miRNA KIT. Cat. 400814, Agilent) whether the presence of ink and acetic acid from the margins of the non-tumoral prostate tissue could influence RNA quality. To this end, we selected biopsies containing increasing amounts of these contaminants (Fig. 2D). The presence of these agents did not impact the quality of RNA, as quantified by Agilent Bioanalyzer (Fig. 2E). We further studied if despite yielding good quality RNA, ink and acetic acid could interfere with

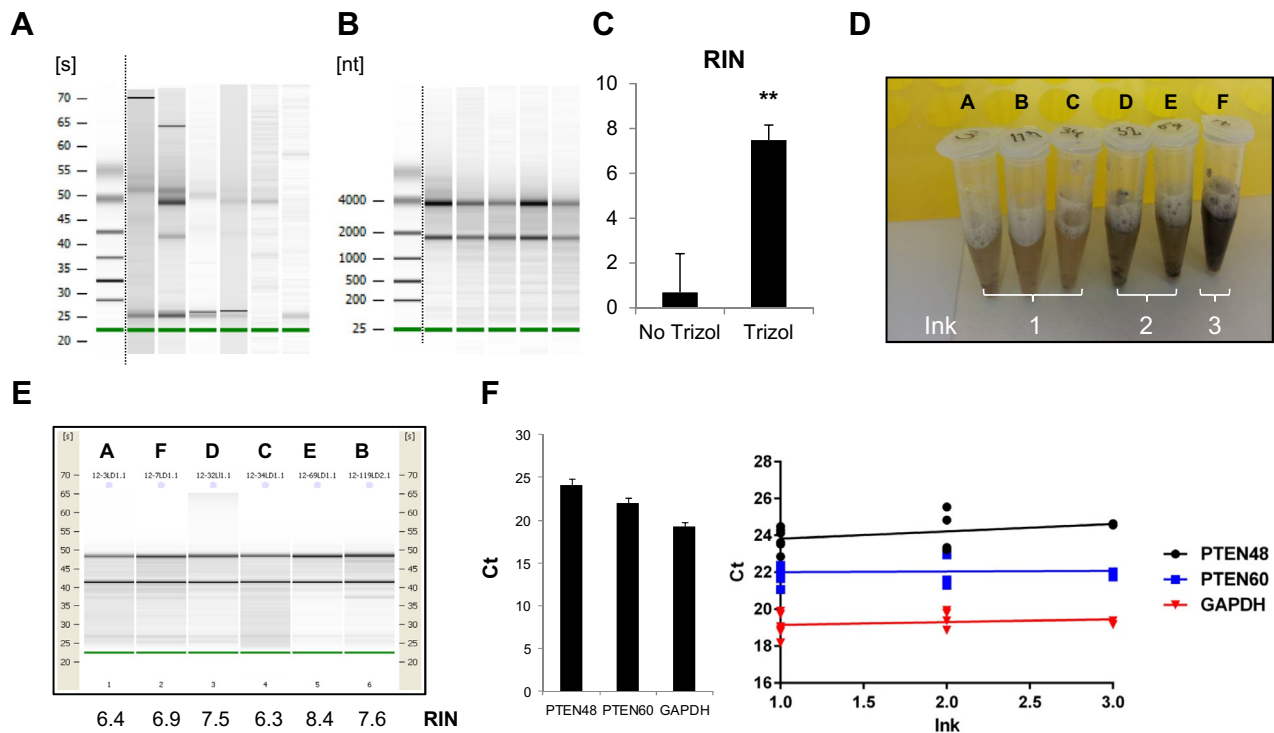


**Fig. 2.** Evaluation of the impact on phenol-based lysis and ink/acetic acid contaminants in RNA quality. (A–C) Bioanalyzer analysis of RNA preparations performed in the absence (A) or presence (B) of Trizol lysis (average RIN values for the samples analyzed are presented in C; \*\*, significance  $p < 0.01$ ). (D and E) Representative images of the lysis of samples with increasing amount of ink (the intensity of the dark color reflects the increasing concentration of ink in the sample of origin, which has been separated in three groups as indicated) (D), and RIN values obtained from the RNA preparation (E). (F) Real time quantitative PCR of PTEN (two Taqman probes) and GAPDH shows average Ct amplification values in all samples (left panel) and the lack of correlation between Ct values and the increase in ink (right panel).

the retrotranscription and real time quantitative PCR process. We predicted that if the ink/acetic acid interferes with the retrotranscription or real time PCR, we would observe an increase in the Ct values of the genes studied in the high ink conditions. However, evaluation of *PTEN* expression with two independent Taqman probes (*PTEN* 48: Universal Probe library [Roche] #48; primer F: ggggaagtaaggaccagagac Primer R: tccagatgattcttaacaggtagc; *PTEN* 60: Universal Probe library [Roche] #60; primer F: gcacaagaggccc-tagatttc Primer R: cgcctctgactgggaatagt) and *GAPDH* (REF. Life Technologies Hs02758991\_g1) as housekeeping gene clearly showed a lack of correlation between the amount of ink and any alteration in gene expression (Fig. 2F). In summary, phenol-based RNA extraction coupled to column-based purification significantly improves RNA quality and the presence of ink/acetic acid in the tissue sample does not influence RNA preparation, retrotranscription, or real time PCR amplification.

### 2.5. Monitoring *PTEN* expression in prostate cancer: an immunohistochemical (IHC) procedure

Immunodetection of *PTEN* could become critical in the coming years to stratify patients and define the best therapeutic strategies [15,16]. Therefore, good standardized IHC procedures need to be established. Lotan et al. recently established an immunohistochemical protocol for *PTEN* [17]. We have employed a different clone from Cell Signaling Technology *PTEN* (138G6) and we have established a sensitive and specific IHC protocol for research purposes.

### 2.6. Key material

- Rabbit monoclonal *PTEN* antibody, clone 138G6 (Cell Signaling Technology, Ref. 9559).

Antigen retrieval was performed with Tris–EDTA (pH 9) in microwave (4 min).  $H_2O_2$  was used to block the endogenous peroxidase, followed by blocking with goat serum and primary antibody (1:100) incubation overnight at 4 °C. Goat anti-rabbit IgG antibody (1:1000) was incubated at room temperature for 30 min. IHC detection was performed with the ABC Kit from Vector

Laboratories. This protocol with DAB-based development results in specific detection of *PTEN*, which was setup in DU145 (*PTEN* positive) and PC3 (*PTEN* negative) xenograft-derived formalin fixed, paraffin embedded (FFPE) slides. Sections were counterstained with hematoxylin.

With this protocol, tumors with known *PTEN* status (described above) were correctly identified (Fig. 3A and B). We also stained human biopsies consisting of benign hyperplasias and prostate cancer. We could identify *PTEN* positive epithelia in the hyperplasia cases as well as prostate cancer biopsies with and without detectable *PTEN* immunoreactivity (Fig. 3C). Of note, we observed that often the stromal component exhibited greater *PTEN* expression than the adjacent epithelial tissue (see asterisks in Fig. 3). In summary, we present here a protocol that is valuable for the detection of *PTEN* in human specimens for research purposes.

### 2.7. Extracellular vesicle isolation from urine samples of prostate cancer patients

Due to the close proximity of the prostate to the urinary track, urine-mediated diagnosis of prostate cancer has remained an attractive concept. Extracellular vesicles (EVs) have been described to contain mRNA, protein and metabolites that could be selectively loaded [18]. Importantly, EVs have been identified in urine and cancerous alterations in the bladder have been shown to impact on their composition, suggesting that they could serve as a source for non-invasive biomarker identification. Since current non-invasive prostate cancer biomarkers have been proven to have limitations [19–21], urine EVs might provide a future source of novel biomarkers. Here, we describe the current protocol for urine EV isolation we are employing (a setup carried out by the group of Dr. Falcón-Pérez).

### 2.8. Key material

- Ultracentrifuge.

Urine EVs can be isolated through this methodology starting from 50 mL of urine. Urine is centrifuged in a tabletop centrifuge

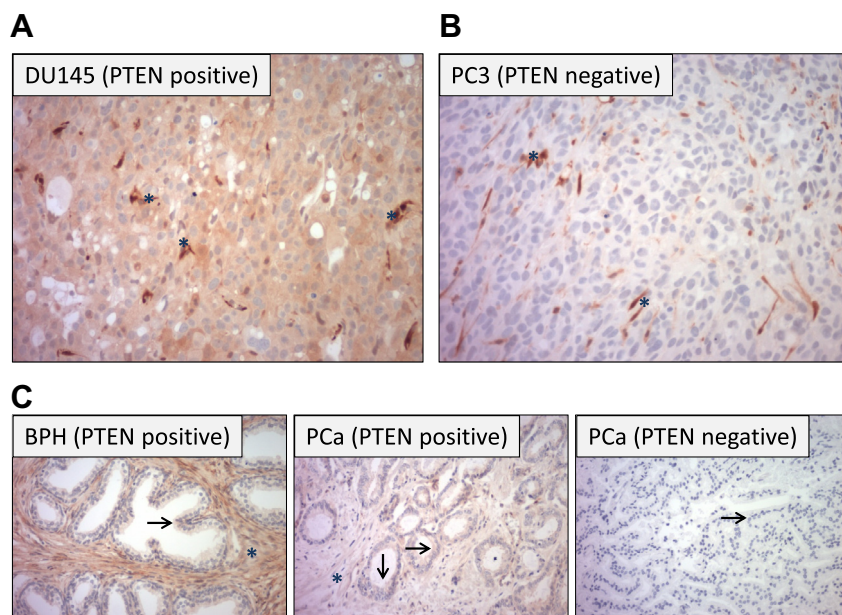


**Fig. 3.** An immunostaining protocol for *PTEN* in human prostate cancer specimens. (A and B) Representative immunohistochemical images (200×) of *PTEN* expressing (DU145) and *PTEN* deficient (PC3) human tumor xenografts. Asterisks indicate stromal cells. (C) Representative micrographs (200×) of *PTEN* staining in benign hyperplasia tissue (BPH) and prostate cancer (PCa) biopsies with *PTEN* high and low immunoreactivity, arrows indicate epithelial cells and asterisk depict stromal area.

at 3000 rpm for 5 min and the supernatant is filtered (0.22 micra) at the moment of collection, and then frozen at  $-80^{\circ}\text{C}$ . At the time of processing, urine is subjected to a first centrifugation of 11,500g for 30 min, and the supernatant is subjected to a second centrifugation of 118,000g for 90 min. The pellet (containing EVs) is then collected, resuspended in 150  $\mu\text{L}$  of cold PBS and frozen for later processing. The EV pellet is subjected to RNA extraction, for which purpose we employ the miRCURY RNA isolation kit (EXIQON, following manufacturer's instructions, DNase I – Qiagen – digestion) and we carried out the retrotranscription with SuperScript III (Invitrogen). 35  $\mu\text{L}$  of total RNA is isolated, and despite the low yield of RNA in the preparation (in the range of nanograms), 60–80  $\mu\text{L}$  of cDNA can be prepared for qPCR analysis (Fig. 4A and B). As proof of concept of the validity of this method, we have carried out qPCR analysis in 10 benign hyperplasias and 13 prostate cancers (paired samples to the biopsies presented in the histochemical analysis). We have used as positive control a gene known to be present in EVs, *GAPDH* [22] (Fig. 4C).

PTEN has been recently reported to be secreted [23,24], and PTEN protein abundance in blood exosomes has been suggested to reflect status of the tumor suppressor in the prostate tumor [25]. Hence we sought to ascertain to which extent the transcript abundance of PTEN would be altered in urine EVs from prostate cancer patients. The results revealed that both *PTEN* and *GAPDH* were present in all EV preparations analyzed at a similar abundance regardless of the benign of the tumoral status. This result was in discordance with PTEN protein expression, since the urine samples analyzed include cases that we identified as negative for PTEN immunoreactivity (displayed in Fig. 3). This lack of differences could be due to two main factors: first, the content of EVs in urine might be strongly influenced by bladder cells, perhaps more than by prostate cells. Second, PTEN is down-regulated at multiple levels, through mutations, deletions, but also through post-transcriptional regulation, which would not necessarily impact on the transcript levels.

### 3. Discussion

In this methods manuscript, we present approaches that allow us to study the biology of prostate cancer. While much work

remains to be carried out in order to understand the molecular changes in this disease, we believe that the technological improvements that we present herein could serve as the basis to ensure the acquisition of (i) fresh and well diagnosed prostate cancer tissue, (ii) RNA of high quality for OMIC studies, (iii) immunostaining methodology to ascertain the expression of PTEN in human tissues and (iv) isolation of urine EVs for molecular studies.

The interaction between pathologists, uro-oncologists and basic scientists is fundamental in order to reach clinically relevant conclusions in prostate cancer research. The fresh tissue preparation procedure that we present has proven to be sustainable in a hospital with biobanking support and, importantly, to preserve the integrity of the surgical material for diagnostic purposes. Unpublished evidence also suggest that the area/volume ratio of the biopsy is directly proportional to the quality of the RNA obtained, and it is therefore plausible that the dimensions of these punch biopsies will allow molecular studies of the highest quality requirements. It is worth noting that the surgical material in our studies was obtained from robotic surgeries, where the warm ischemia period (the time the surgical piece stays excised and inside the patient) is of 60–80 min, while the cold ischemia (the time elapsed from the extraction of the piece to the snap-freeze of the punch biopsy) is at least of 30 min. These ischemic periods do not alter the RNA quality of the biopsy (which we consider a good readout of tissue integrity) and can be achieved in any urology and pathology service.

Importantly, the molecular studies described herein can greatly benefit from the analysis of public databases. In the recent years, bioinformatic platforms have been developed in order to aid in the analysis of publicly available genomic, epigenomic, transcriptomic and proteomic studies. These platforms now allow quickly browsing through tens of studies (which imply thousands of samples) looking at a gene or pathway of interest. Two outstanding examples of this effort are Oncomine ([www.oncomine.org](http://www.oncomine.org)) [26] and cbiportal ([www.cbiportal.org](http://www.cbiportal.org)) [27,28]. These sites allow the researcher to get information about the status of a gene or genes of interest in a given cancer, the mutational landscape throughout different cancers, the epigenetic modifications regulating its expression and the clinical variables associated with its expression. Therefore, these platforms can serve both as a

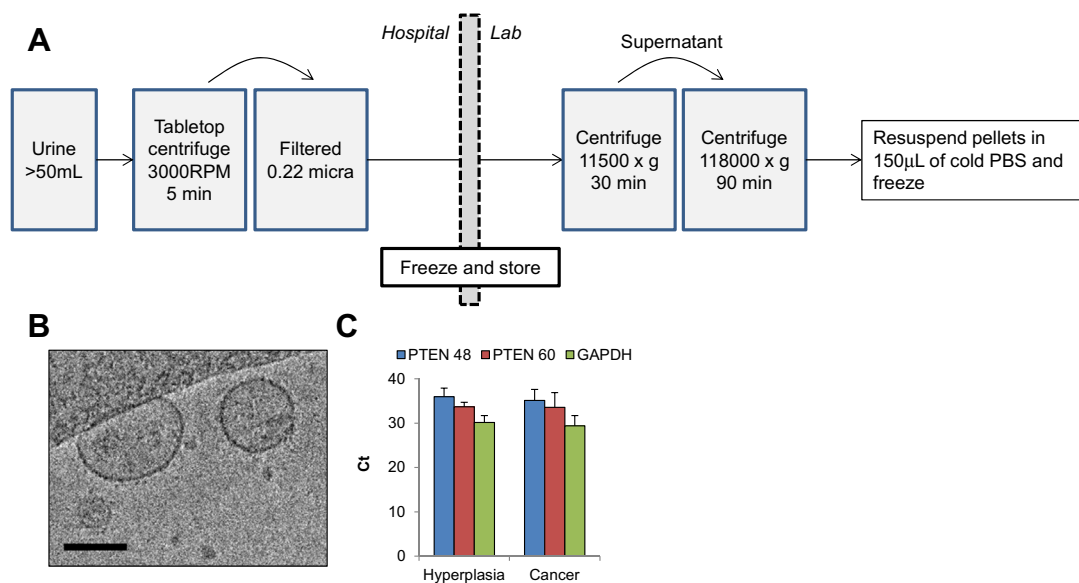


**Fig. 4.** A method to harvest RNA from urine EVs. (A) Experimental procedure of the EV isolation from urine samples. (B) Representative image by cryo-Transmission Electron Microscopy (TEM) of the isolated EVs with this approach (scale represents 100 nm). (C) Abundance of *PTEN* (with two probes) and *GAPDH* transcript in urine EVs by real time quantitative PCR.

discovery starting point or a clinical validation end point. In summary, a good balance between experimental approaches with human cancer specimens and data mining studies can maximize the relevance of the conclusions met by the researcher.

### Acknowledgments

Apologies to those whose related publications were not cited due to space limitations. We thank Paolo Nuciforo, Maurizio Scaltriti and Pau Castell for technical advice. David Gil and Sandra Delgado from electron microscopy CIC bioGUNE platform for their technical assistance in the cryo-TEM analysis of EVs. The work of AC is supported by the Ramón y Cajal award, the Basque Department of Industry, Tourism and Trade (Etortek), Health (2012111086) and Education (PI2012-03), Marie Curie (277043), Movember Foundation (GAP1), ISCIII (PI10/01484, PI13/00031) and ERC (336343). N.M.-M. is supported by the Spanish Association Against Cancer (AECC). A.A.-A and L.V.-J are supported by the Basque Government of education. RB is supported by ISCIII (PT13/0010/0052) and A.E. is supported by MICINN (PTA2011-5805-1).

### References

- [1] L. Salmena, A. Carracedo, P.P. Pandolfi, *Cell* 133 (2008) 403–414.
- [2] A. Carracedo, P.P. Pandolfi, *Oncogene* 27 (2008) 5527–5541.
- [3] A. Carracedo, L. Ma, J. Teruya-Feldstein, F. Rojo, L. Salmena, A. Alimonti, A. Egia, A.T. Sasaki, G. Thomas, S.C. Kozma, A. Papa, C. Nardella, L.C. Cantley, J. Baselga, P.P. Pandolfi, *J. Clin. Invest.* 118 (2008) 3065–3074.
- [4] A. Alimonti, A. Carracedo, J.G. Clohessy, L.C. Trotman, C. Nardella, A. Egia, L. Salmena, K. Sampieri, W.J. Haveman, E. Brogi, A.L. Richardson, J. Zhang, P.P. Pandolfi, *Nat. Genet.* 42 (2010) 454–458.
- [5] L.C. Trotman, M. Niki, Z.A. Dotan, J.A. Koutcher, A. Di Cristofano, A. Xiao, A.S. Khoo, P. Roy-Burman, N.M. Greenberg, T. Van Dyke, C. Cordon-Cardo, P.P. Pandolfi, *PLoS Biol.* 1 (2003) E59.
- [6] A. Di Cristofano, B. Pesce, C. Cordon-Cardo, P.P. Pandolfi, *Nat. Genet.* 19 (1998) 348–355.
- [7] Z. Chen, L.C. Trotman, D. Shaffer, H.K. Lin, Z.A. Dotan, M. Niki, J.A. Koutcher, H.I. Scher, T. Ludwig, W. Gerald, C. Cordon-Cardo, P.P. Pandolfi, *Nature* 436 (2005) 725–730.
- [8] A. Alimonti, C. Nardella, Z. Chen, J.G. Clohessy, A. Carracedo, L.C. Trotman, K. Cheng, S. Varmeh, S.C. Kozma, G. Thomas, E. Rosivatz, R. Woscholski, F. Cognetti, H.I. Scher, P.P. Pandolfi, *J. Clin. Invest.* 120 (2010) 681–693.
- [9] D. DiMitri, A. Toso, J.J. Chen, M. Sarti, S. Pinton, T.R. Jost, R. D'Antuono, E. Montani, R. Garcia-Escudero, I. Guccini, S. Da Silva-Alvarez, M. Collado, M. Eisenberger, Z. Zheng, C. Catapano, F. Grassi, A. Alimonti, *Nature* (2014).
- [10] A. Toso, A. Revandkar, D. Di Mitri, I. Guccini, M. Proietti, M. Sarti, S. Pinton, J. Zhang, M. Kalathur, G. Civenni, D. Jarrossay, E. Montani, C. Marini, R. Garcia-Escudero, E. Scanziani, F. Grassi, P.P. Pandolfi, C.V. Catapano, A. Alimonti, *Cell Rep.* (2014).
- [11] H. Bertilsson, A. Angelsen, T. Viset, E. Anderssen, J. Halgunset, *Scand. J. Clin. Lab. Invest.* 70 (2010) 45–53.
- [12] Y. Fukabori, K. Yoshida, K. Nakano, Y. Shibata, H. Yamanaka, T. Oyama, *J. Urol.* 176 (2006) 1204–1207.
- [13] S.H. Margan, D.J. Handelsman, S. Mann, P. Russell, J. Rogers, M.H. Khadra, Q. Dong, *J. Urol.* 163 (2000) 613–615.
- [14] K.M. Scott, P. Fanta, R. Calaluze, B. Dalkin, R.S. Weinstein, R.B. Nagle, *Prostate* 44 (2000) 296–302.
- [15] P.J. Eichhorn, M. Gili, M. Scaltriti, V. Serra, M. Guzman, W. Nijkamp, R.L. Beijersbergen, V. Valero, J. Seoane, R. Bernards, J. Baselga, *Cancer Res.* 68 (2008) 9221–9230.
- [16] E. Gonzalez-Billalabeitia, N. Seitzer, S.J. Song, M.S. Song, A. Patnaik, X.S. Liu, M.T. Epping, A. Papa, R.M. Hobbs, M. Chen, A. Lunardi, C. Ng, K.A. Webster, S. Signoretti, M. Loda, J.M. Asara, C. Nardella, J.G. Clohessy, L.C. Cantley, P.P. Pandolfi, *Cancer Discov.* 4 (2014) 896–904.
- [17] T.L. Lotan, B. Gurel, S. Sutcliffe, D. Esopi, W. Liu, J. Xu, J.L. Hicks, B.H. Park, E. Humphreys, A.W. Partin, M. Han, G.J. Netto, W.B. Isaacs, A.M. De Marzo, *Clin. Cancer Res.* 17 (2011) 6563–6573.
- [18] S. Mathivanan, C.J. Fahner, G.E. Reid, R.J. Simpson, *Nucleic Acids Res.* 40 (2012) D1241–D1244.
- [19] F.H. Schroder, J. Hugosson, M.J. Roobol, T.L. Tammela, S. Ciatto, V. Nelen, M. Kwiatkowski, M. Lujan, H. Lilja, M. Zappa, L.J. Denis, F. Recker, A. Paez, L. Maattanen, C.H. Bangma, G. Aus, S. Carlsson, A. Villers, X. Rebillard, T. van der Kwast, P.M. Kujala, B.G. Blijenberg, U.H. Stenman, A. Huber, K. Taari, M. Hakama, S.M. Moss, H.J. de Koning, A. Auvinen, *N. Engl. J. Med.* 366 (2012) 981–990.
- [20] H.C. Sox, *N. Engl. J. Med.* 367 (2012) 669–671.
- [21] E.M. Wever, J. Hugosson, E.A. Heijnsdijk, C.H. Bangma, G. Draisma, H.J. de Koning, *Br. J. Cancer* 107 (2012) 778–784.
- [22] E. Zeringer, M. Li, T. Barta, J. Schageman, K.W. Pedersen, A. Neurauter, S. Magdaleno, R. Setterquist, A.V. Vlassov, *World J. Methodol.* 3 (2013) 11–18.
- [23] B.D. Hopkins, B. Fine, N. Steinbach, M. Dendy, Z. Rapp, J. Shaw, K. Pappas, J.S. Yu, C. Hodakoski, S. Mense, J. Klein, S. Pegno, M.L. Sulis, H. Goldstein, B. Amendolara, L. Lei, M. Maurer, J. Bruce, P. Canoll, H. Hibshoosh, R. Parsons, *Science* 341 (2013) 399–402.
- [24] U. Putz, J. Howitt, A. Doan, C.P. Goh, L.H. Low, J. Silke, S.S. Tan, *Sci Signal* 5 (2012) ra70.
- [25] K. Gabriel, A. Ingram, R. Austin, A. Kapoor, D. Tang, F. Majeed, T. Qureshi, K. Al-Nedawi, *PLoS ONE* 8 (2013) e70047.
- [26] D.R. Rhodes, J. Yu, K. Shanker, N. Deshpande, R. Varambally, D. Ghosh, T. Barrette, A. Pandey, A.M. Chinnaiyan, *Neoplasia* 6 (2004) 1–6.
- [27] E. Cerami, J. Gao, U. Dogrusoz, B.E. Gross, S.O. Sumer, B.A. Aksoy, A. Jacobsen, C.J. Byrne, M.L. Heuer, E. Larsson, Y. Antipin, B. Reva, A.P. Goldberg, C. Sander, N. Schultz, *Cancer Discov.* 2 (2012) 401–404.
- [28] J. Gao, B.A. Aksoy, U. Dogrusoz, G. Dresdner, B. Gross, S.O. Sumer, Y. Sun, A. Jacobsen, R. Sinha, E. Larsson, E. Cerami, C. Sander, N. Schultz, *Sci. Signal.* 6 (2013) p11.

## ORIGINAL ARTICLE

## Pharmacological inhibition of fatty-acid oxidation synergistically enhances the effect of L-asparaginase in childhood ALL cells

I Hermanova<sup>1</sup>, A Arruabarrena-Aristorena<sup>2</sup>, K Valis<sup>3,4</sup>, H Nuskova<sup>5</sup>, M Alberich-Jorda<sup>6</sup>, K Fiser<sup>1</sup>, S Fernandez-Ruiz<sup>2</sup>, D Kavan<sup>3,4</sup>, A Pecinova<sup>5</sup>, M Niso-Santano<sup>7,8</sup>, M Zaliova<sup>1</sup>, P Novak<sup>3,4</sup>, J Houstek<sup>5</sup>, T Mracek<sup>5</sup>, G Kroemer<sup>7,8,9,10</sup>, A Carracedo<sup>2,11,12</sup>, J Trka<sup>1,13</sup> and J Starkova<sup>1</sup>

L-asparaginase (ASNase), a key component in the treatment of childhood acute lymphoblastic leukemia (ALL), hydrolyzes plasma asparagine and glutamine and thereby disturbs metabolic homeostasis of leukemic cells. The efficacy of such therapeutic strategy will depend on the capacity of cancer cells to adapt to the metabolic challenge, which could relate to the activation of compensatory metabolic routes. Therefore, we studied the impact of ASNase on the main metabolic pathways in leukemic cells. Treating leukemic cells with ASNase increased fatty-acid oxidation (FAO) and cell respiration and inhibited glycolysis. FAO, together with the decrease in protein translation and pyrimidine synthesis, was positively regulated through inhibition of the RagB-mTORC1 pathway, whereas the effect on glycolysis was RagB-mTORC1 independent. As FAO has been suggested to have a pro-survival function in leukemic cells, we tested its contribution to cell survival following ASNase treatment. Pharmacological inhibition of FAO significantly increased the sensitivity of ALL cells to ASNase. Moreover, constitutive activation of the mammalian target of rapamycin pathway increased apoptosis in leukemic cells treated with ASNase, but did not increase FAO. Our study uncovers a novel therapeutic option based on the combination of ASNase and FAO inhibitors.

*Leukemia* (2016) 30, 209–218; doi:10.1038/leu.2015.213

## INTRODUCTION

L-asparaginase (ASNase) is an essential component in the treatment of childhood acute lymphoblastic leukemia (ALL).<sup>1</sup> Intensified use of ASNase increases event-free survival in children with ALL by 10–15%.<sup>2,3</sup> ASNase has the potential to be used in other types of cancers besides childhood ALL – at present, it is already used in the treatment protocol of adult T-ALL and lymphomas.<sup>4,5</sup> There are also ongoing *in vitro* studies on its use in solid tumors (brain, prostate and ovarian cancers).<sup>6–10</sup> Although ASNase has been in clinical use for the treatment of childhood ALL for several decades, our knowledge of mechanisms behind its therapeutic effect is still incomplete. ASNase catalyzes deamination of asparagine (Asn) and glutamine (Gln).<sup>11,12</sup> Intracellular Asn is typically produced by Asn synthetase (ASNS). The cytotoxic effect of ASNase on leukemic cells was traditionally explained by the lower activity of ASNS in leukemic cells compared with healthy cells.<sup>13,14</sup> However, recent studies reported that basal ASNS expression does not predict resistance to ASNase among ALL patients<sup>15–18</sup> and has no biological or clinical consequences in ALL patients.<sup>19</sup> These findings indicate that the mechanism of action of ASNase is more complex and cannot be explained by the expression of a single gene.

Proliferating cancer cells are characterized by considerably different metabolic requirements compared with normal differentiated cells.<sup>20,21</sup> Cancer cell metabolism is therefore studied with a focus on potential therapeutic targets. As metabolic modulators are widely used for pathologies beyond cancer, drug repurposing has become a very appealing concept in the field, as exemplified by metformin, an antidiabetic that has been newly investigated for its inhibitory effect on cancer progression.<sup>22–24</sup> By deaminating Asn and Gln, ASNase obviously also perturbs metabolism, but these metabolic consequences have not yet been described. The main sensor of amino-acid deprivation is mammalian target of rapamycin (mTOR), which has been associated with the activity of ASNase.<sup>25</sup> Moreover, it has been shown that Gln depletion can efficiently inhibit downstream mTOR signaling in acute myeloid leukemia and ovarian cancer cells.<sup>26,27</sup> Under nutrient-rich conditions, mTORC1 promotes cell growth by stimulating biosynthetic pathways. Meanwhile, cellular catabolism, such as autophagy, is inhibited. Signaling via mTOR also influences a wide range of metabolic mechanisms<sup>28–31</sup> and the impact of ASNase on the downstream mTOR targets that are involved in metabolic processes has not yet been studied thoroughly. This study for the first time describes the profound effect of ASNase on the

<sup>1</sup>CLIP-Childhood Leukaemia Investigation Prague, Department of Pediatric Hematology/Oncology, Charles University Prague, Prague, Czech Republic; <sup>2</sup>CIC bioGUNE Technology Park of Bizkaia, Derio, Spain; <sup>3</sup>Laboratory of Structural Biology and Cell Signaling, Institute of Microbiology, Academy of Sciences of the Czech Republic, Prague, Czech Republic; <sup>4</sup>Department of Biochemistry, Charles University, Prague, Czech Republic; <sup>5</sup>Department of Bioenergetics, Institute of Physiology of the Czech Academy of Sciences, Prague, Czech Republic; <sup>6</sup>Laboratory of Molecular Immunology, Institute of Molecular Genetics of the Czech Academy of Sciences, Prague, Czech Republic; <sup>7</sup>Equipe 11 labellisée par la Ligue Nationale Contre le Cancer; INSERM U1138; Centre de Recherche des Cordeliers, Paris, France; <sup>8</sup>Metabolomics and Molecular Cell Biology Platforms; Gustave Roussy, Villejuif, France; <sup>9</sup>Pôle de Biologie; Hôpital Européen Georges Pompidou; AP-HP, Paris, France; <sup>10</sup>Université Paris Descartes; Sorbonne Paris Cité, Paris, France; <sup>11</sup>Ikerbasque, Basque Foundation for Science, Bilbao, Spain; <sup>12</sup>Department of Biochemistry and Molecular biology, University of the Basque Country, Leioa, Spain and <sup>13</sup>University Hospital Motol, Prague, Czech Republic. Correspondence: Professor J Trka, CLIP-Childhood Leukaemia Investigation Prague, Department of Pediatric Hematology/Oncology, Charles University and University Hospital Motol, V Úvalu 84, Prague 15006, Czech Republic. E-mail: jan.trka@lfmotol.cuni.cz

Received 24 February 2015; revised 3 July 2015; accepted 10 July 2015; accepted article preview online 4 August 2015; advance online publication, 28 August 2015

metabolism of lymphoid leukemic cells that is driven by mTOR. The characterization of these cellular processes reveals novel potential targets for the treatment of ALL to enhance the effects of chemotherapy and improve clinical outcome in patients.

## MATERIALS AND METHODS

### Cell culture

REH (human B-cell precursor leukemia, ets variant 6/runt-related transcription factor 1 (ETV6/RUNX1, TEL/AML1) - positive); NALM-6 (human B-cell precursor leukemia, TEL/platelet derived growth factor receptor beta 1 (PDGFRB1); (TEL/PDGFRB1) - positive) and RS4;11 (human B-cell precursor leukemia, mixed-lineage leukemia/AF4/FMR2 family, member 1 (AF4); MLL/AF4-positive) cell lines were purchased from German Collection of Microorganisms and Cell Cultures (DSMZ-Deutsche Sammlung von Mikroorganismen und Zellkulturen GmbH, Braunschweig, Germany) and cultivated according to the producer's instructions. Cell lines were negative for mycoplasma contamination.

### Patient samples

Bone marrow samples from untreated children initially diagnosed with B-cell precursor ALL were collected from the Czech Pediatric Hematology Centers. Within 24 h after aspiration, mononuclear cells were isolated by density gradient centrifugation using Ficoll-Paque PLUS (GE Healthcare, Chalfont St Giles, UK). Ethical committee approved the study no. NT12429. All samples were obtained with the informed consent of the children's parents or guardians. Isolated blasts were maintained in Roswell Park Memorial Institute media with 10% fetal bovine serum (Life Technologies, Carlsbad, CA, USA) and insulin-transferrin-sodium selenite supplement (Sigma-Aldrich, St Louis, MO, USA).<sup>32</sup> The characteristics of the patients whose samples were used for western blot analysis (1–3), Annexin V/4',6-diamidino-2-phenylindole (Annexin V/DAPI) staining (4–8) and measurement of respiration (9–11) are listed in Supplementary Table 1.

### Isolation of B lymphocytes

Human B-Cell Enrichment Cocktail (Stemcell Technologies, Vancouver, BC, Canada) was used according to the manufacturer's instructions to isolate B cells from the buffy coat of healthy donors. B cells were incubated in Roswell Park Memorial Institute media supplemented with 10% fetal bovine serum, interleukin-21 (50 ng/ml) and interleukin-2 (50 ng/ml) (Sigma-Aldrich). B cells were isolated from three healthy donors.

### Electrophoresis and western blotting

Protein lysates were prepared as previously described.<sup>19</sup> Proteins (10–40 µg per well) were resolved by NuPAGE Novex 4–12% Bis-Tris Gels (Life Technologies) and transferred to a nitrocellulose membrane (Bio-Rad, Hercules, CA, USA). The membrane was probed overnight with primary antibodies listed in Supplementary Table 2. The bound antibodies were detected with the appropriate secondary antibodies (Bio-Rad) conjugated with horseradish peroxidase and visualized using enhanced chemiluminescence reagent followed by exposure to X-ray film (Kodak, Rochester, NY, USA). Rapamycin (Sigma-Aldrich) served as a positive control of mTORC1 inhibition. Densitometry was performed using Image J software. The densitometry value was normalized against the value for β-actin.

### RNA extraction, complementary DNA synthesis and quantitative real-time PCR

Total cellular RNA was extracted using the RNeasy mini-kit (Qiagen GmbH, Hilden, Germany) according to the manufacturer's instructions and converted to complementary DNA using an iScript complementary DNA synthesis kit (Bio-Rad). The c-Myc transcript was detected using the Power SYBR Green PCR Master Mix (Life Technologies). The primer sequences of c-Myc are listed in Supplementary Table 3. β2 microglobulin served as a house-keeping gene. PCR reactions were performed in a LightCycler 480 real-time PCR machine (Roche Diagnostics GmbH, Mannheim, Germany).

### Assessment of cell death

Cells were treated with ASNase (Medac GmbH, Hamburg, Germany), etomoxir (Sigma-Aldrich) or both and apoptosis was quantified by Annexin V-FITC (Exbio Praha, a.s., Czech Republic) and DAPI (Life Technologies) or

propidium iodide (PI) (Miltenyi Biotec, Bergisch Gladbach, Germany) staining using flow cytometer. Measurements were performed in triplicate.

### Combination index (CI) calculation

CI values were calculated using CompuSyn software (www.combosyn.com). The calculation of dose-effect relationship for each drug we used was done via serial dilution. CI was calculated from serial dilution of ASNase and each dose of etomoxir. CI was used to express synergism (CI < 1), additive effect (CI = 1) or antagonism (CI > 1).<sup>33</sup>

### Assessment of autophagic flux

Cells were treated with ASNase and bafilomycin (Sigma-Aldrich) for 6, 12 and 24 h. Autophagic flux was quantified by western blotting.

### Detection of *de novo* intermediates of pyrimidine synthesis by UPLC-ToF-MS

The cells were seeded to fresh media and incubated overnight. Next we treated the cells with ASNase (4 IU/ml) for 24 h. Five million of cells were harvest for each condition and washed in phosphate-buffered saline. Dried cell pellets were resuspended in 500 µl of a methanol/water (50/50; v/v%) mixture containing 10 mM acetic acid. After precipitation of the protein content, the supernatant was evaporated. The dried pellets were resuspended in 150 µl of water/acetonitrile/formic acid (39.9/60/0.1v/v/v%) and centrifuged. The resulting extracts were injected into the LC-MS system using ACQUITY UPLC with Acquity UPLC amide column 1.7 µm (2.1 × 100 mm) and ToF MS, SYNAPT G2 (Waters Corporation, Milford, MA, USA). Retention time for uridine monophosphate and uridine was 2.95 and 1.68 min, respectively. The limit of detection of those compounds: uridine monophosphate 0.5 µM, uridine 0.05 µM. The measurement was performed in three independent experiments.

### High performance liquid chromatography analysis

High performance liquid chromatography analysis of amino acids was performed using Waters AccQ-Tag Chemistry Package (WAT052875) on two pump Beckman Coulter Gold chromatograph with Merck-Hitachi F-1080 fluorescence detector (ex.250 nm, em. 395 nm). Data were collected and evaluated with DataApex CSW32 chromatography software.

### Glucose-uptake measurement

Cells were washed twice with Krebs-Ringer-4-(2-hydroxyethyl)-1-piperazineethanesulfonic acid buffer (20 mM 4-(2-hydroxyethyl)-1-piperazineethanesulfonic acid, pH 7.4, 136 mM NaCl, 4.7 mM KCl, 1.25 mM MgSO<sub>4</sub>, 1.25 mM CaCl<sub>2</sub>), resuspended in 900 µl of Krebs-Ringer-4-(2-hydroxyethyl)-1-piperazineethanesulfonic acid buffer and incubated for 15 min at 37 °C. Next, we added 100 µl of 10 × START solution (1 mM 2-deoxyglucose, 5 µCi/ml [<sup>3</sup>H]-2-deoxyglucose, PerkinElmer Life Sciences, Waltham, MA, USA) and incubated the cells for 10 min at 37 °C. Cells were washed with phosphate-buffered saline, collected by centrifugation, and the cell pellet was solubilized in 1 ml of 0.03% sodium dodecyl sulphate for 10 min at 37 °C. Radioactivity was measured using a 1900TR liquid scintillation analyzer (Packard). The measurement was performed in four independent experiments.

### Extracellular lactate

Extracellular lactate was measured using the Lactate Kit (Trinity Biotech, Bray, Ireland) according to the manufacturer's directions. Changes in lactate production were normalized to the protein content. The measurement was performed in five independent experiments.

### FAO measurement

Cells were incubated for 4 h in culture medium containing 100 µM palmitic acid, 1 mM carnitine and 1.7 µCi [9,10(n)-<sup>3</sup>H]palmitic acid (GE Healthcare) in the presence or absence of etomoxir (100 µM, Sigma-Aldrich), and the medium was collected to analyze the amount of released <sup>3</sup>H<sub>2</sub>O that was formed during the cellular oxidation of [<sup>3</sup>H]-palmitate.<sup>34–36</sup> Medium was precipitated with 10% TCA, and supernatants were neutralized with 6 M NaOH and loaded onto ion exchange columns packed with DOWEX 1 × 2-400 resin (Sigma-Aldrich). <sup>3</sup>H<sub>2</sub>O was eluted with water and quantitated by liquid scintillation counting. The oxidation of [<sup>3</sup>H]-palmitate

was normalized to the protein content, as determined using a DC Protein Assay (Bio-Rad). Non-mitochondrial FAO and background signal (FAO measured in samples after incubation with etomoxir) was extracted, and mitochondrial FAO (etomoxir counts extracted from total counts) was presented in nCi/mg protein/h. The measurement was performed in four independent experiments.

### Respiration

The endogenous respiration of intact cells was measured in the culture medium at 37 °C using Oxygraph-2k-respirometer (OROBOROS Instruments Corporation, Innsbruck, Austria). Respiratory rates were determined in both coupled and uncoupled states, the latter after titration of the uncoupler carbonyl cyanide-4-(trifluoromethoxy)phenylhydrazone (Sigma-Aldrich). Inhibition by ATP synthase inhibitor oligomycin (Sigma-Aldrich) was used to verify dependence of coupled respiration on mitochondrial  $F_0F_1$ -ATP synthase. The following concentrations of cells and respiratory inhibitors were applied: 0.4 mg/ml cells, 1  $\mu$ M oligomycin, 200–300 nM carbonyl cyanide-4-(trifluoromethoxy)phenylhydrazone and 0.5  $\mu$ M antimycin A (respiratory chain inhibitor; Sigma-Aldrich). The measurement was performed in four (REH, NALM-6) and three (healthy B lymphocytes, BCP-ALL) independent experiments.

### NAD<sup>+</sup>/NADH ratio

The ratio of oxidized and reduced form of nicotinamide adenine dinucleotide (NAD<sup>+</sup>/NADH) was measured using the NAD<sup>+</sup>/NADH Glo assay (Promega, Madison, WI, USA) according to the manufacturer's protocol. The ratio was measured in three independent experiments.

### Lentiviral RagB cell models

We have used Flag pLJM1 RagB wild-type (RagB wt; Addgene plasmid 19313) and Flag pLJM1 RagB 99L (Addgene plasmid 19315) lentiviral constructs (Addgene, Cambridge, MA, USA).<sup>37</sup> Lentiviral particles were produced as previously described<sup>38</sup> and used for the transduction of NALM-6 cells. Positive clones were selected by puromycin resistance and further used for experiments.

### Statistical analysis

Student's *t*-tests were performed in GraphPad Prism software (GraphPad Software, Inc., San Diego, CA, USA) for statistical analyses.

## RESULTS

### ASNase treatment extensively alters cellular metabolism

As ASNase disrupts nutrient homeostasis, we studied its effect on key metabolic pathways in leukemic cells. Effect of applied ASNase dosage (RS4;11: 0.5 IU/ml; REH, NALM-6: 4 IU/ml) chosen according to the pharmacokinetics of ASNase<sup>39</sup> was confirmed as a change in extracellular amino-acid levels by high-performance liquid chromatography (Supplementary Figure S1). First, we focused on the impact of ASNase on FAO. We incubated REH, NALM-6 and RS4;11 B-precursor leukemic cells with ASNase for 18 h and measured the activity of FAO. ASNase treatment significantly increased FAO in these cell lines (Figure 1a). The effect of etomoxir on FAO in ALL cells is shown in Supplementary Figure S2. Next, we determined the effect of ASNase on glucose metabolism in REH and NALM-6 cells and observed that ASNase treatment significantly reduced glucose uptake in both cell lines (Figure 1b). This was accompanied by decreased lactate production in NALM-6 cells (Supplementary Figure S3). Lactate production in RS4;11 was also significantly reduced after ASNase treatment. There were no observable changes in REH cells; however, the basal lactate level was substantially lower in REH cells compared with NALM-6 (data not shown). Furthermore, we determined the levels of the glycolysis regulator *c*-Myc and glucose transporter type 1 (GLUT1). As shown in Supplementary Figure S4, ASNase significantly decreased *c*-Myc messenger RNA expression in ALL cell lines with a concomitant decrease in the protein levels of *c*-Myc and GLUT1. Consistent with these results observed in ALL cell lines, we detected decreased

*c*-Myc protein levels also in some primary ALL cells following ASNase treatment (Supplementary Figure S4).

Both FAO and glucose oxidation yield NADH, which is then oxidized by mitochondrial respiratory chain. In the subsequent experiment we therefore investigated the impact of ASNase on the mitochondrial respiration in ALL cells. ASNase significantly increased basal oxygen consumption (routine respiration) of REH cells ( $P=0.0276$ ) (Figure 1c and Supplementary Figure S5). In the uncoupled state, which serves as a measure of the maximum capacity of the respiratory chain, we observed a significant increase in oxygen consumption in ALL cell lines (Figure 1c and Supplementary Figure S5). More interestingly, we observed significant increase of the spare respiratory capacity (uncoupled/coupled respiration) in REH and NALM-6 cell lines treated with ASNase (Figure 1d). The increase of spare respiratory capacity was borderline significant ( $P=0.062$ ) in RS4;11 cell line. We found a similar increase in the spare respiratory capacity also in the primary ALL cells on ASNase treatment (Figure 1d). In contrast, this was not the case for the control B lymphocytes isolated from peripheral blood of healthy subjects (Figure 1d), indicating that the effect of ASNase is specific to leukemic cells. The increase in the respiratory capacity was not accompanied by a change in the content of oxidative phosphorylation proteins (Supplementary Figure S6), meaning that it likely represents a shift in the balance of available substrates. Indeed, we detected a significant increase in the NAD<sup>+</sup>/NADH ratio in ALL cell lines following ASNase treatment (Supplementary Figure S7).

### ASNase modulates pyrimidine synthesis and autophagy via mTORC1 inhibition

Our previous experiments have shown that ASNase treatment affects key metabolic pathways in ALL cells. Based on the sensitivity of mTORC1 to amino-acid levels and the evidence that ASNase treatment inhibits mTORC1 signaling,<sup>25</sup> we hypothesized that the effect of ASNase on metabolism is driven through mTORC1. First, we confirmed the effect of ASNase on main mTORC1 targets. We detected dephosphorylated p-P70S6K and p-S6 in ALL cell lines and some primary ALL samples treated with ASNase (Figure 2a and Supplementary Figure S8). Furthermore, we detected dephosphorylated carbamoyl phosphate synthase II (p-CAD), suggesting a decrease in the *de novo* synthesis of pyrimidines (Figure 2a).<sup>40</sup> Similar effect on p-CAD status was also observed using specific mTOR inhibitor rapamycin (Figure 2a). We also measured the intermediates of *de novo* pyrimidine synthesis using UPLC-ToF-MS in REH and NALM-6 cells treated with ASNase. In concordance with the dephosphorylation of p-CAD, we observed significantly decreased synthesis of uridine monophosphate and uridine in REH and NALM-6 cells treated with ASNase (Figure 2b). Another mechanism that may be activated on mTORC1 inhibition is autophagy. To investigate whether ASNase treatment augments autophagic flux, we detected the conversion of the marker of autophagosome, microtubule-associated protein light chain 3 (LC3), LC3-I to LC3-II, by western blot. Treatment with ASNase induced a time-dependent increase in the expression of LC3-II in the NALM-6 cell line (Figure 2c), indicating that ASNase activates autophagy. Consistent with increased autophagic flux following treatment with ASNase, there was a time-dependent decrease in the level of p62 (selective substrate of autophagy). LC3-II accumulation following ASNase treatment was intensified in the NALM-6 cell line after treatment with bafilomycin A1 (Figure 2c). Bafilomycin A1 is an inhibitor of the vacuolar ATPase, which blocks the fusion of autophagosomes with lysosomes, leading to an accumulation of autophagosomes.<sup>41</sup> This result confirms that the observed increase in LC3-II after ASNase treatment was due to increased autophagic flux and not because of decreased degradation of lipidated LC3.

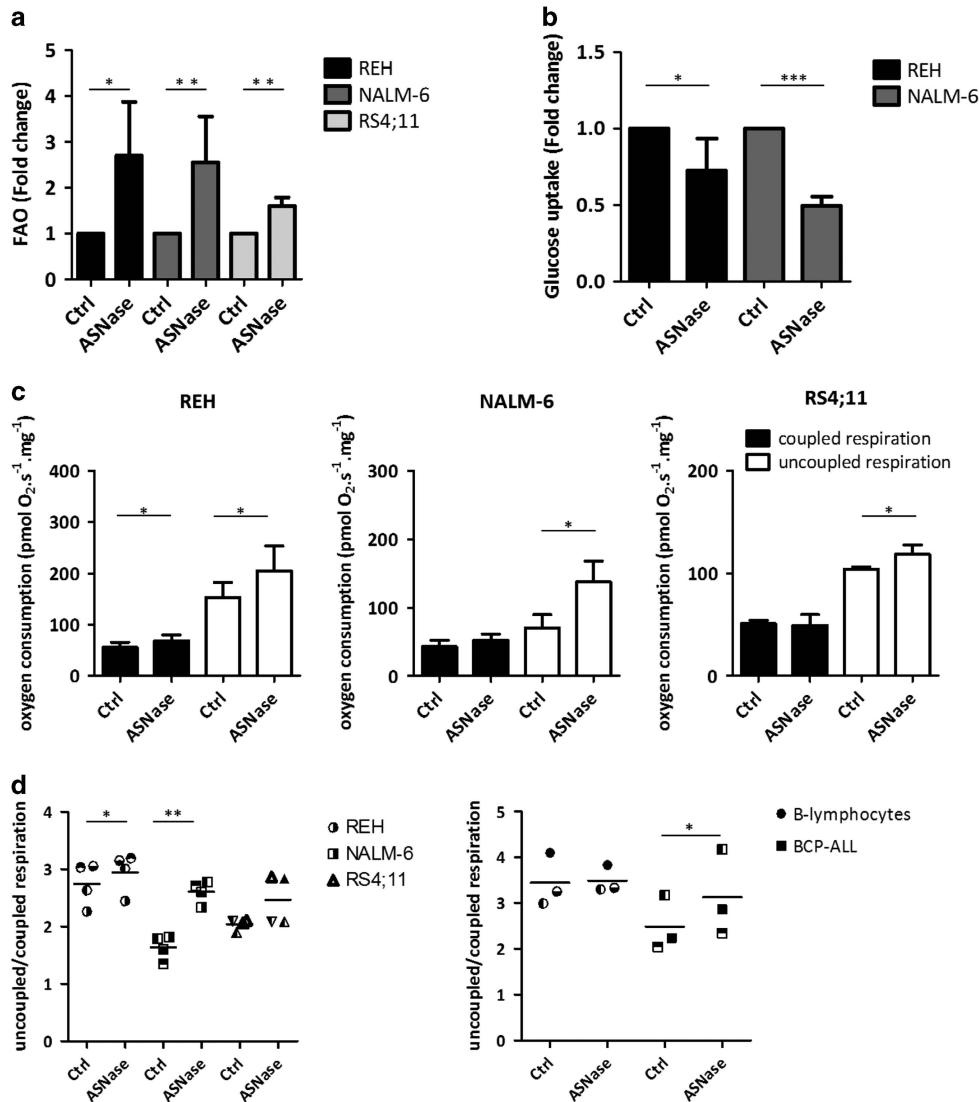


**Figure 1.** Effect of ASNase on the metabolism of leukemic cells. **(a)** ALL cell lines were cultured for 18 h with or without ASNase and the rate of fatty-acid oxidation was assessed. The concentration of ASNase was 4 IU/ml (REH, NALM-6) and 0.5 IU/ml (RS4;11). The experiment was performed in quadruplicate. **(b)** ALL cell lines were cultured overnight with or without ASNase (4 IU/ml). Changes in glucose uptake were measured by the accumulation of [<sup>3</sup>H]-2-deoxyglucose in cells. **(c)** ALL cell lines **(d)** healthy B lymphocytes and BCP-ALL patient samples were cultured with or without ASNase for 24 h. The dose of ASNase was 4 IU/ml for all samples except of RS4;11 (0.5 IU/ml). The endogenous respiratory rates were determined in both coupled and uncoupled states (the latter after titration of the uncoupler FCCP) and also after the addition of oligomycin. The spare respiratory capacity was calculated. The following concentrations of cells and respiratory inhibitors were applied: 0.4 mg/ml cells, 1  $\mu$ M oligomycin, 200–300 nM FCCP. Asterisks represent significant changes. \*\*\* $P < 0.001$ ; \*\* $P < 0.01$ ; \* $P < 0.05$ .

ASNase acts through the RagB-mTORC1 pathway

Next, we investigated the mechanism whereby ASNase inhibits the mTORC1 pathway. The activation of mTORC1 in the presence of amino acids is mediated by the Rag GTPases (guanosine-5'-triphosphatases) A, B, C and D. A key event in the amino-acid-dependent activation of mTORC1 is the conversion of RagA or RagB from a guanosine-5'-diphosphate (GDP) to guanosine-5'-triphosphate (GTP)-bound state.<sup>31,37,42</sup> To determine whether ASNase inhibits mTORC1 by the same mechanism as general amino-acid deprivation, we established RagB wt and RagB mutant (RagB 99L) cells (Figure 3). The mutation of RagB causes constitutive activation of mTORC1 by permanent conversion to GTP and localization of mTOR in the vesicle compartments regardless of amino-acid deprivation.<sup>37</sup> We used a lentiviral system to achieve permanent expression of RagB in the NALM-6 cell line. The resistance of the mTOR pathway inhibition to

amino-acid deprivation by ASNase treatment was confirmed in RagB 99L. There was no change in p-S6 level in the RagB 99L cells, whereas ASNase treatment inhibited p-S6 protein in RagB wt cells. Concordantly, p-CAD protein was inhibited more extensively in RagB wt cells than in RagB 99L cells (Figure 3a). Importantly, the ability to enhance FAO was impaired in RagB 99L cells exposed to ASNase (Figure 3b). These results suggest that the effect of ASNase on protein translation, *de novo* pyrimidine synthesis and FAO is mediated through the RagB-mTORC1 pathway. By contrast, c-Myc expression was decreased in both RagB wt and RagB 99L cells (Figure 3a). Consistent with this result, there was a significant decrease in the level of extracellular lactate in RagB 99L cells (Supplementary Figure S9), indicating that ASNase inhibits glycolysis in a RagB-mTORC1-independent manner. To test whether c-Myc inhibition following ASNase treatment is mTORC1 independent, we detected the c-Myc protein level in REH and NALM-6 cells treated with the mTORC1 inhibitor rapamycin.



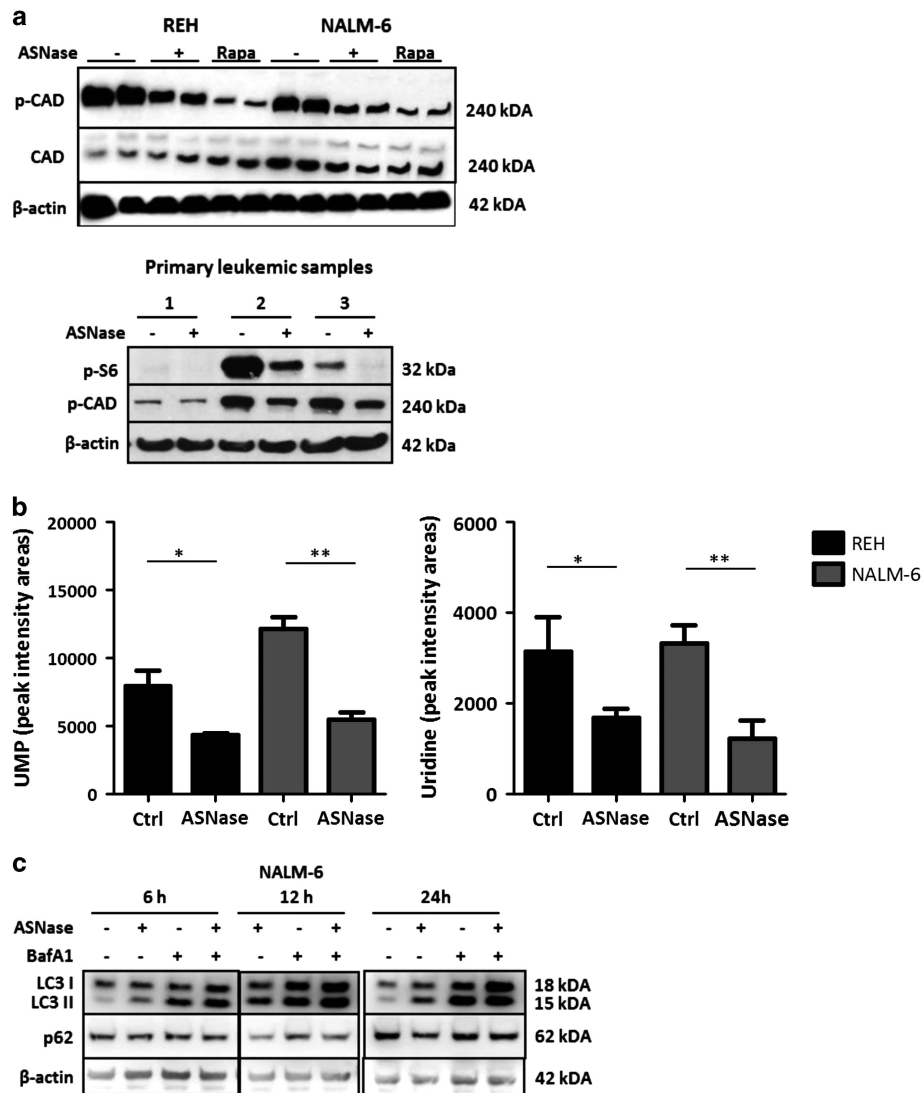


**Figure 2.** Effect of ASNase on mTORC1 targets. (a) ALL cell lines were cultured for 24 h with or without ASNase (4 IU/ml). Levels of phospho-CAD and CAD proteins were measured by immunoblotting, with  $\beta$ -actin used as a loading control. Rapamycin (Rapa; 10 nM) served as a positive control of mTORC1 inhibition. Phospho-S6 and phospho-CAD proteins were measured in ASNase-treated cells (4 IU/ml; 24 h) from three different patients by immunoblotting, using  $\beta$ -actin as a loading control. (b) ALL cell lines were cultured for 24 h with or without ASNase (4 IU/ml). Uridine monophosphate (UMP) and uridine levels were measured using UPLC-ToF-MS. (c) NALM-6 cells were cultured with or without ASNase (4 IU/ml) in the presence or absence of bafilomycin A1 (BafA1, 100 nM) for 6, 12 and 24 h to analyze autophagic flux. LC3 I/II and p62 protein levels were measured by immunoblotting, with  $\beta$ -actin used as a loading control. Asterisks represent significant changes.  $**P < 0.01$ ;  $*P < 0.05$ .

Contrary to the effects of ASNase, inhibition of mTORC1 by rapamycin did not cause a substantial decrease in c-Myc (Supplementary Figure S10).

These results suggest that ASNase inhibits protein translation and DNA synthesis directly through RagB-mTORC1, and inhibition of the mTORC1 pathway also causes enhancement of FAO. However, glycolysis seems to be regulated through a different mechanism.

Inhibition of FAO increases the cytotoxic effect of ASNase in ALL cells

The activation of FAO has been suggested to exert a pro-survival function in leukemic cells under nutrient stress conditions. We tested whether the increase of FAO upon ASNase treatment allows leukemic cells to cope with metabolic stress. We treated REH and NALM-6 cells with the FAO inhibitor etomoxir, ASNase, or both drugs, and measured its effect on the viability of the cells. The concentrations of etomoxir were 25, 50, 100, 200 and 400  $\mu$ M.

The range of etomoxir was chosen according to previous publications.<sup>43,44</sup> Pharmacological inhibition of FAO in combination with ASNase increased apoptosis in REH and NALM-6 cells. As shown in Figure 4a, CI for etomoxir with ASNase were  $< 1$ , indicating synergistic mode of action in both cell lines.<sup>33</sup> Complete data on the effect of both drugs are shown in Supplementary Figure S11. The most effective concentrations of etomoxir in the combination with ASNase were 100 and 200  $\mu$ M. Importantly, similar results were obtained in primary diagnostic ALL patient samples co-treated with ASNase and etomoxir. Etomoxir increased the cytotoxic effect of ASNase in *ex vivo* conditions in four out of five diagnostic BCP-ALL patient samples (Figure 4b). These results reveal that increased FAO is crucial for the survival of ALL cells treated with ASNase. Moreover, cells with the inability to induce FAO (RagB 99L) were significantly more sensitive to ASNase compared with RagB wt cells, shown by the cleavage of PARP (Figure 3a) and the assessment of apoptosis by Annexin V/DAPI staining (Figure 4c).

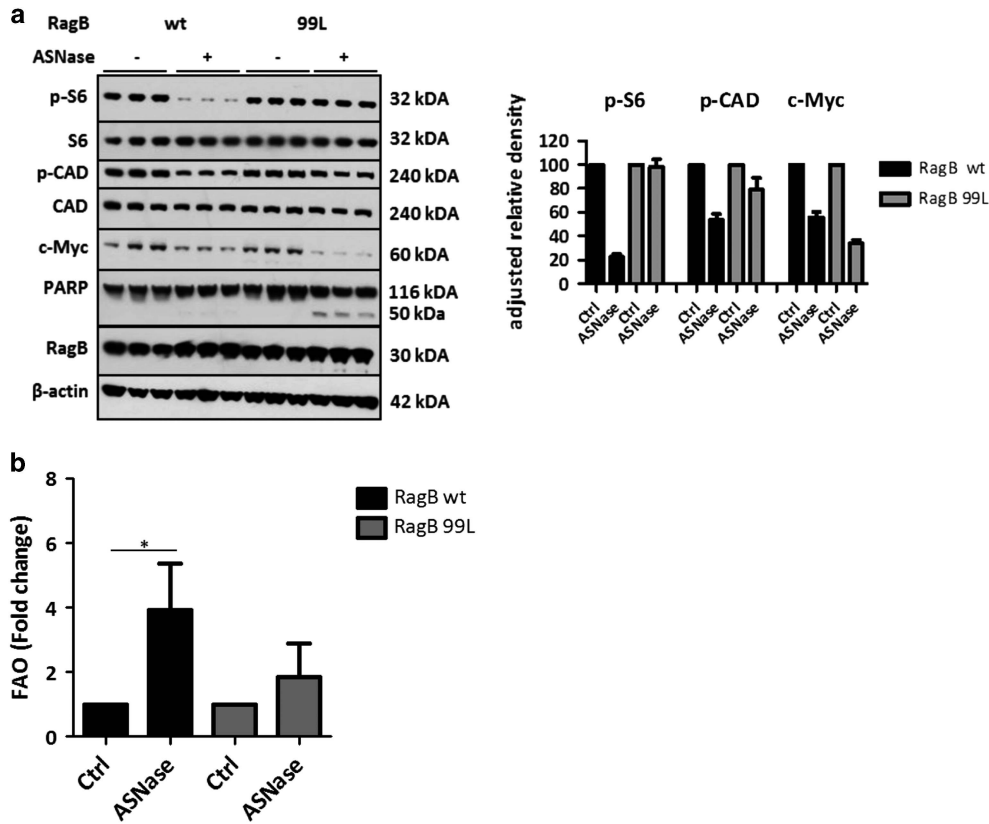


**Figure 3.** Effect of ASNase on RagB wild-type and RagB mutant cells. (a) RagB wild-type (RagB wt) and mutant (RagB 99L) NALM-6 cells were cultured with or without ASNase (4 IU/ml) for 24 h. Expression levels of phospho-S6, S6, phospho-CAD, CAD, c-Myc, cleaved PARP and RagB proteins were measured by immunoblotting, with  $\beta$ -actin used as a loading control and quantified by densitometry (lower graph). The measurement was performed in three independent experiments. (b) RagB wt and RagB 99L cells were cultured overnight with or without ASNase (4 IU/ml) and the rate of fatty-acid oxidation was measured. The experiment was performed in quadruplicate. Asterisks represent significant changes. \* $P < 0.05$ .

Altogether, our results revealed enhanced cytotoxic effect of ASNase owing to FAO inhibition.

#### Distinct effect of Asn and Gln on mTOR downstream targets and FAO activity

At last, we examined the individual roles of Gln and Asn on cellular processes. We cultured ALL cell lines under four different conditions: complete media, media without Asn, media without Gln and complete media treated with ASNase. In REH and NALM-6, p-S6 and c-Myc protein levels were decreased after cultivation in media without Asn or Gln but the effect of Gln depletion was more pronounced in NALM-6 cells. On the other hand, in RS4;11 we detected a substantial reduction of p-S6 and c-Myc in the cells cultured in media without Asn. Apoptosis detected by cleaved PARP was not increased by depletion of any amino acid in NALM-6, whereas in REH and RS4;11 apoptosis was triggered by Asn depletion. Depletion of either Asn or Gln had similar impact on p-CAD levels in all studied cell lines (Figure 5a). RS4;11 cells are dependent on Asn presence as also documented by a significant increase of FAO in this cell line after cultivation in media without Asn. FAO was significantly increased after cultivation in Gln-depleted media in NALM-6 cells (Figure 5b). Cell respiration did not follow the FAO activation upon individual amino-acid depletion (Supplementary Figure S12). In general, Gln depletion causes suppression of NADH production which, in our experiments, was reflected as the inhibition of maximum capacity of cell respiration. Moreover, we studied the rescue effect of Asn and Gln after ASNase treatment. We pre-treated NALM-6 and REH

cell line with ASNase for 8 h and then changed the media to complete media, media without Asn or without Gln, respectively. Media without Asn represent addition of Gln and vice versa, media without Gln represent addition of Asn. After overnight cultivation we detected mTOR targets (p-S6, S6) and PARP cleavage. Rescue effect of Asn after ASNase treatment is more evident in REH cells. There is an increase in p-S6 as well as a decrease of cleaved PARP compared with addition of Gln in the media. In the NALM-6 cell line though, p-S6 was increased by addition of either Asn or Gln after ASNase treatment. Apoptosis was decreased after addition of both amino acids (Supplementary Figure S13).

#### DISCUSSION

ASNase was incorporated into the treatment protocol for childhood ALL in 1970. Despite the successful use of this drug for decades, the mechanism underlying its cytotoxic effect remains surprisingly obscure. ASNase depletes two extracellular amino acids, Asn and Gln. The depletion of amino acids changes nutrient availability and consequently influences metabolic signaling. Metabolic pathways in malignant cells can be rewired depending on the cellular availability of the nutrients<sup>45</sup> and thus participate in the mechanisms of drug resistance. This study, for the first time, presents evidence that ASNase triggers extensive metabolic reprogramming in leukemic cells and reveals the adaptive activation of pro-survival metabolic pathways following ASNase treatment. Our data show increased levels of FAO, inhibition of glycolysis and elevated respiratory activities after ASNase treatment. FAO serves as a source of NADH, FADH<sub>2</sub> and acetyl-CoA

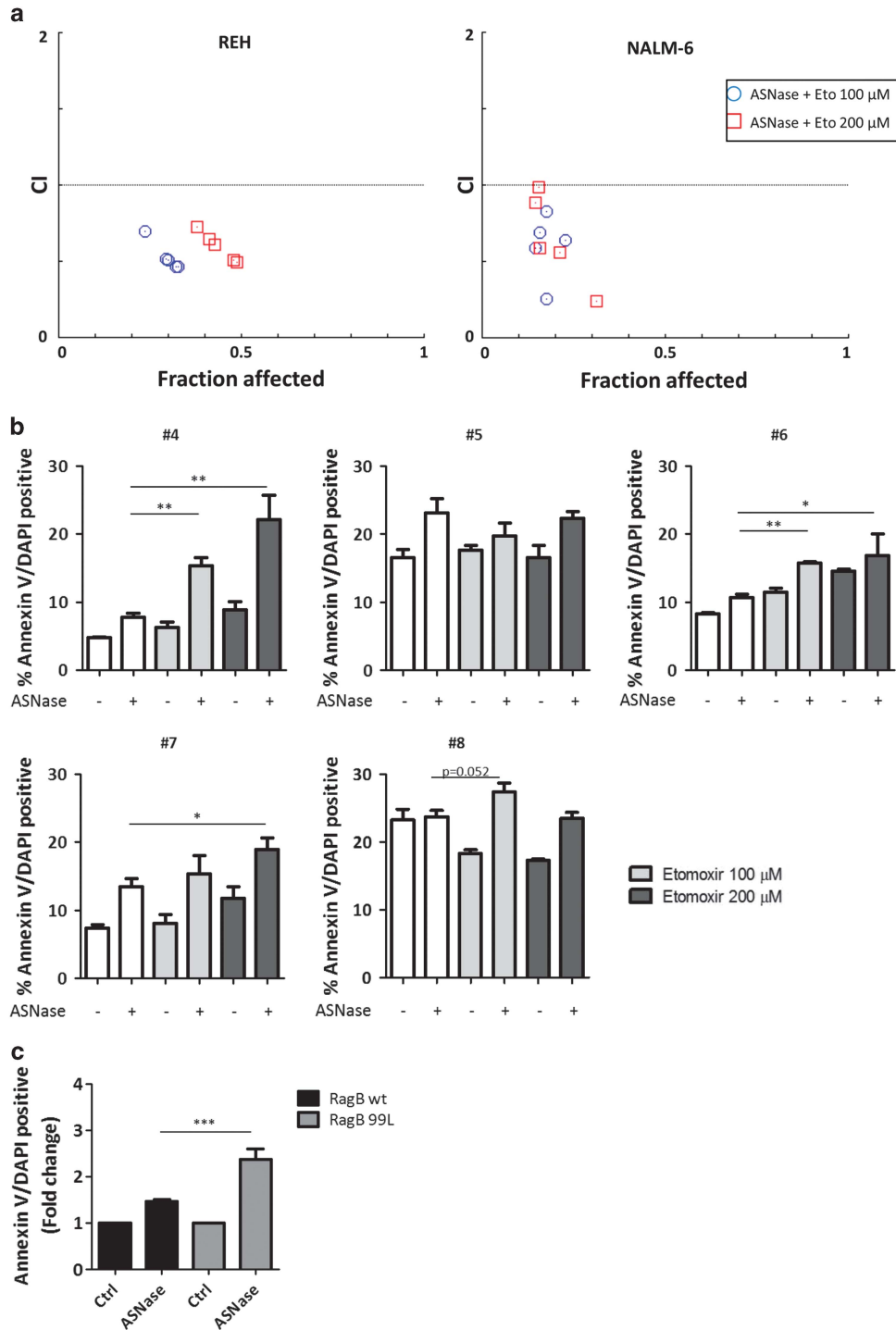


**Figure 4.** Effect of FAO inhibition on ASNase-mediated cytotoxicity. **(a)** REH and NALM-6 cells were treated with ASNase (1, 2, 4, 8 and 16 IU/ml) in combination with etomoxir (Eto1, 100  $\mu$ M; Eto2, 200  $\mu$ M) for 24 h. The percentage of cell death was determined by Annexin V/PI staining followed by FACS analysis. Combination indexes (CI) were obtained by entering the resulting specific death values into the CompuSyn program. Fraction affected (FA; Percentage of Annexin V/PI positive cells)-CI plots indicate that the combinations of ASNase with etomoxir are synergistic (CI < 1). **(b)** Leukemic blasts isolated from the bone marrow of patients with ALL were cultivated with or without ASNase (4 IU/ml) in the presence or absence of the FAO inhibitor etomoxir (Eto1, 100  $\mu$ M; Eto2, 200  $\mu$ M) for 24 h. **(c)** RagB wt and RagB 99L NALM-6 cells were cultivated with or without ASNase (4 IU/ml) for 24 h. The percentage of cell death was determined by Annexin V/DAPI staining followed by FACS analysis. Values represent the mean of triplicate measurements. Asterisks represent significant changes. \*\*\* $P$  < 0.001; \*\* $P$  < 0.01; \* $P$  < 0.05.

feeding the Krebs cycle and mitochondrial oxidative phosphorylation. Utilization of FAO for energy provision is thus important for the growth and survival of cancer cells under both normal and metabolic stress conditions.<sup>36,46–50</sup> The metabolic rescue role of FAO has been described in different tumors such

as diffuse large B-cell lymphoma, multiple myeloma and glioblastoma.<sup>50–52</sup> Moreover, FAO can contribute to chemoresistance.<sup>51,52</sup> Pharmacological inhibition of FAO showed a therapeutic benefit in combination with chemotherapy in mouse models of human myeloid leukemia, suggesting that the shift

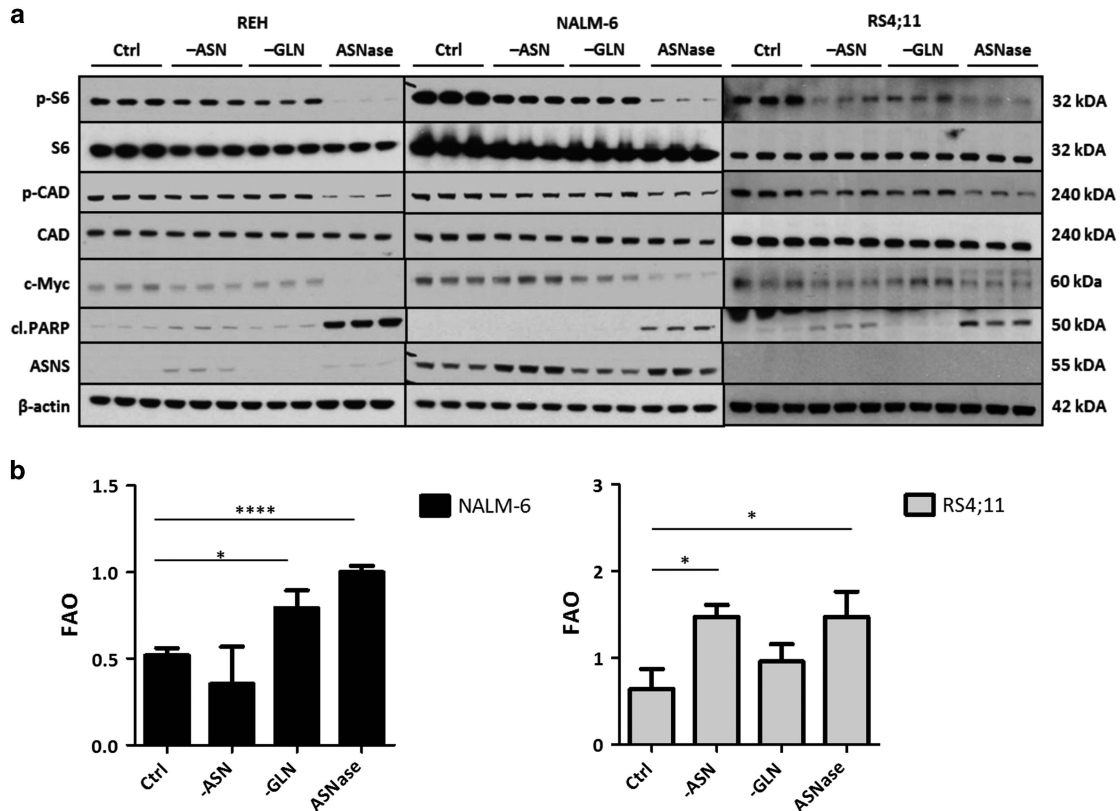


**Figure 5.** Effect of Asn and Gln depletion on ALL cells. **(a)** ALL cell lines were incubated in complete RPMI media (Ctrl), RPMI media without Asn (-ASN), RPMI media without Gln (-GLN) or complete RPMI media with ASNase for 24 h. The concentration of ASNase was 4 IU/ml (REH, NALM-6) and 0.5 IU/ml (RS4;11). Levels of phospho-S6, S6, phospho-CAD, CAD, c-Myc, cleaved PARP (cl.PARP), ASNS proteins were measured by immunoblotting, with  $\beta$ -actin used as a loading control. **(b)** ALL cell lines were incubated in complete RPMI media (Ctrl), RPMI media without Asn (-ASN), RPMI media without Gln (-GLN) or complete RPMI media with ASNase for 18 h and the rate of fatty-acid oxidation was assessed. Asterisks represent significant changes. \*\*\*\* $P < 0.0001$ ; \* $P < 0.05$ .

toward FAO could be a target for the treatment of hematological malignancies.<sup>43,53</sup> In this study, we combined ASNase and the FAO inhibitor etomoxir in the treatment of childhood ALL samples for the first time. Our experiments showed an increase in FAO after ASNase treatment, providing a rationale for the combination treatment. Etomoxir-sensitized leukemic cells to ASNase in two leukemic cell lines *in vitro* as well as under *ex vivo* conditions when treating BCP-ALL patient samples. These data support the pro-survival effect of FAO in the treatment of ALL cells with ASNase and demonstrate the potential of this combination treatment. Previous studies have described a negative association between mTOR and FAO and a positive relation of mTOR upregulation with fatty-acid synthesis.<sup>54–56</sup> Our results show that ASNase inhibited mTORC1 through RagB (Ras-related GTPase), which is a mediator of amino-acid signaling.<sup>37</sup> Importantly, in the presence of ASNase, RagB mutant cells with the constitutively activated mTOR pathway exhibited a reduction of FAO compared with the significant FAO elevation observed in RagB wt cells. Accordingly, RagB mutant cells were significantly more sensitive to ASNase than RagB wt cells. These results demonstrate that RagB-mTOR inhibition senses metabolic stress, which induces FAO. We hypothesize that the limited elevation of FAO after ASNase treatment in RagB mutant cells was not sufficient to protect these cells from amino-acid deprivation.

As ASNase treatment inhibited mTORC1, we focused on the downstream targets of mTORC1 that are involved in cellular metabolism. ASNase treatment inhibited protein translation and pyrimidine synthesis in ALL cells as part of the apoptotic process. Concurrently, leukemic cells treated with ASNase increased autophagy as has been already shown in other cancer type.<sup>10,26</sup>

Autophagy may serve to maintain intracellular metabolic homeostasis through the degradation of unfolded or aggregated proteins and organelles.<sup>57</sup> Thus, autophagy may serve as another rescue mechanism by producing amino acids or even fatty acids<sup>58</sup> that restore the nutrient balance disrupted by ASNase. Glycolysis was yet another metabolic pathway affected by ASNase. ASNase inhibited c-Myc, but it is not clear if this was a direct effect or a feedback loop resulting from the inhibition of glycolysis. Of particular note is our finding that treatment with ASNase increases spare respiration exclusively in leukemic cells. Increase in respiration may reflect increased flux of nutrients that can be oxidized by mitochondria. Although this could be both FAO-dependent and FAO-independent, the observed increase in FAO (involving the whole pathway from uptake of palmitate from culture media to its final oxidation to water) argues that at least substantial part of these fatty acids originated from extracellular environment and was oxidized by mitochondria. The increased ratio of  $NAD^+$ / $NADH$  measured after ASNase treatment further supports the increased mitochondrial oxidation of reducing equivalents.

The role of individual amino acids in these cellular processes is cell line specific. The tested leukemic cell lines differ in their sensitivity to ASNase and also in ASNS protein level. RS4;11 cells are the most sensitive with undetectable ASNS protein, REH cells are intermediate sensitive and have higher ASNS protein levels, and NALM-6 cells are the most resistant of the studied cell lines with higher ASNS protein level.<sup>19,59</sup> Most importantly, we did not see any differences in the effect of ASNase in ALL cell lines on mTOR targets and metabolic processes. Next, we propose that the higher the sensitivity, the deeper the cells' dependence on Asn.

In other words, the cells' dependence on Asn is inversely proportional to the ASNS protein expression. Accordingly, the rescue effect of Asn was pronounced in sensitive cells (REH) after ASNase treatment, whereas in NALM-6 cells both amino acids displayed rescue properties. Our data support previous finding presenting that glutaminase activity of ASNase is not essential in anticancer effect of ASNS-negative cancer cells.<sup>59</sup>

In conclusion, our results demonstrate that ASNase has a strong effect on the bioenergetics and biosynthesis in leukemic cells. Our data further show that increased FAO has a pro-survival effect on leukemic cells. Moreover, our results also suggest that pharmacological blocking of FAO sensitizes leukemic cells to ASNase treatment. Metabolic changes similar to those described here in acute leukemia cells are rather frequent among other cancer subtypes; therefore, using ASNase in combination with etomoxir may represent a treatment option not only for ALL but also for other types of cancers.

### CONFLICT OF INTEREST

The authors declare no conflict of interest.

### ACKNOWLEDGEMENTS

This work was supported by the Grant Agency of the Ministry of Health of the Czech Republic (NT12429) (IH, JS, JT), (NT12370-5) (TM); The Charles University Grant Agency (632513) (IH, JS, JT), (14-21095P) (KV); UNCE 204025/2012 (KV, PN); Ministry of Health, Czech Republic, (00064203 University Hospital Motol, Prague, Czech Republic) (IH, JS, JT, KF); Czech Science Foundation (P302/12/G01) (MZ); 15-28848A (JS, JT); MSMT Navrat grant LK21307 (MAJ); the Grant Agency of the Czech Republic (14-36804G) (TM); the Ramón y Cajal award, the Basque Department of Industry, Tourism and Trade (Etorrek), health (2012111086) and education (PI2012-03), Marie Curie (277043), Movember, ISCIII (PI10/01484, PI13/00031) and ERC (336343) (AC); The Basque Government of education (AAA).

### REFERENCES

- Pui CH, Evans WE. Treatment of acute lymphoblastic leukemia. *N Engl J Med* 2006; **354**: 166–178.
- Amylon MD, Shuster J, Pullen J, Berard C, Link MP, Wharam M *et al*. Intensive high-dose asparaginase consolidation improves survival for pediatric patients with T cell acute lymphoblastic leukemia and advanced stage lymphoblastic lymphoma: a Pediatric Oncology Group study. *Leukemia* 1999; **13**: 335–342.
- Moghribi A, Levy DE, Asselin B, Barr R, Clavell L, Hurwitz C *et al*. Results of the Dana-Farber Cancer Institute ALL Consortium Protocol 95-01 for children with acute lymphoblastic leukemia. *Blood* 2007; **109**: 896–904.
- Jaccard A, Gachard N, Marin B, Rogez S, Audrain M, Suarez F *et al*. Efficacy of L-asparaginase with methotrexate and dexamethasone (AspaMetDex regimen) in patients with refractory or relapsing extranodal NK/T-cell lymphoma, a phase 2 study. *Blood* 2011; **117**: 1834–1839.
- Douer D, Yampolsky H, Cohen LJ, Watkins K, Levine AM, Periclou AP *et al*. Pharmacodynamics and safety of intravenous pegaspargase during remission induction in adults aged 55 years or younger with newly diagnosed acute lymphoblastic leukemia. *Blood* 2007; **109**: 2744–2750.
- Lorenzi PL, Llamas J, Gonsior M, Ozbun L, Reinhold WC, Varma S *et al*. Asparagine synthetase is a predictive biomarker of L-asparaginase activity in ovarian cancer cell lines. *Mol Cancer Ther* 2008; **7**: 3123–3128.
- Panosyan EH, Wang Y, Xia P, Lee WN, Pak Y, Laks DR *et al*. Asparagine depletion potentiates the cytotoxic effect of chemotherapy against brain tumors. *Mol Cancer Res* 2014; **12**: 694–702.
- Purwaha P, Lorenzi PL, Silva LP, Hawke DH, Weinstein JN. Targeted metabolomic analysis of amino acid response to L-asparaginase in adherent cells. *Metabolomics* 2014; **10**: 909–919.
- Sircar K, Huang H, Hu L, Cogdell D, Dhillion J, Tzelepi V *et al*. Integrative molecular profiling reveals asparagine synthetase is a target in castration-resistant prostate cancer. *Am J Pathol* 2012; **180**: 895–903.
- Yu M, Henning R, Walker A, Kim G, Perroy A, Alessandro R *et al*. L-asparaginase inhibits invasive and angiogenic activity and induces autophagy in ovarian cancer. *J Cell Mol Med* 2012; **16**: 2369–2378.
- Capizzi RL, Bertino JR, Skeel RT, Creasey WA, Zanes R, Olayon C *et al*. L-asparaginase: clinical, biochemical, pharmacological, and immunological studies. *Ann Intern Med* 1971; **74**: 893–901.
- Cooney DA, Capizzi RL, Handschumacher RE. Evaluation of L-asparagine metabolism in animals and man. *Cancer Res* 1970; **30**: 929–935.
- Miller HK, Salsler JS, Balis ME. Amino acid levels following L-asparagine amidohydrolase (EC.3.5.1.1) therapy. *Cancer Res* 1969; **29**: 183–187.
- Ohnuma T, Holland JF, Freeman A, Sinks LF. Biochemical and pharmacological studies with asparaginase in man. *Cancer Res* 1970; **30**: 2297–2305.
- Fine BM, Kaspers GJ, Ho M, Loonen AH, Boxer LM. A genome-wide view of the in vitro response to L-asparaginase in acute lymphoblastic leukemia. *Cancer Res* 2005; **65**: 291–299.
- Holleman A, Cheok MH, den Boer ML, Yang W, Veerman AJ, Kazemier KM *et al*. Gene-expression patterns in drug-resistant acute lymphoblastic leukemia cells and response to treatment. *N Engl J Med* 2004; **351**: 533–542.
- Kaspers GJ, Veerman AJ, Pieters R, Van Zantwijk CH, Smets LA, Van Wering ER *et al*. In vitro cellular drug resistance and prognosis in newly diagnosed childhood acute lymphoblastic leukemia. *Blood* 1997; **90**: 2723–2729.
- Krejci O, Starkova J, Otova B, Madzo J, Kalinova M, Hrusak O *et al*. Upregulation of asparagine synthetase fails to avert cell cycle arrest induced by L-asparaginase in TEL/AML1-positive leukaemic cells. *Leukemia* 2004; **18**: 434–441.
- Hermanova I, Zaliova M, Trka J, Starkova J. Low expression of asparagine synthetase in lymphoid blasts precludes its role in sensitivity to L-asparaginase. *Exp Hematol* 2012; **40**: 657–665.
- Vander Heiden MG, Cantley LC, Thompson CB. Understanding the Warburg effect: the metabolic requirements of cell proliferation. *Science* 2009; **324**: 1029–1033.
- Boag JM, Beesley AH, Firth MJ, Freitas JR, Ford J, Hoffmann K *et al*. Altered glucose metabolism in childhood pre-B acute lymphoblastic leukaemia. *Leukemia* 2006; **20**: 1731–1737.
- Scotland S, Saland E, Skuli N, de Toni F, Boutzen H, Micklow E *et al*. Mitochondrial energetic and AKT status mediate metabolic effects and apoptosis of metformin in human leukemic cells. *Leukemia* 2013; **27**: 2129–2138.
- Buzzai M, Jones RG, Amaravadi RK, Lum JJ, DeBerardinis RJ, Zhao F *et al*. Systemic treatment with the antidiabetic drug metformin selectively impairs p53-deficient tumor cell growth. *Cancer Res* 2007; **67**: 6745–6752.
- Hirsch HA, Iliopoulos D, Tschlis PN, Struhl K. Metformin selectively targets cancer stem cells, and acts together with chemotherapy to block tumor growth and prolong remission. *Cancer Res* 2009; **69**: 7507–7511.
- liboshi Y, Papst PJ, Hunger SP, Terada N. L-Asparaginase inhibits the rapamycin-targeted signaling pathway. *Biochem Biophys Res Commun* 1999; **260**: 534–539.
- Willems L, Jacque N, Jacquelin A, Neveux N, Maciel TT, Lambert M *et al*. Inhibiting glutamine uptake represents an attractive new strategy for treating acute myeloid leukemia. *Blood* 2013; **122**: 3521–3532.
- Yang L, Moss T, Mangala LS, Marini J, Zhao H, Wahlig S *et al*. Metabolic shifts toward glutamine regulate tumor growth, invasion and bioenergetics in ovarian cancer. *Mol Syst Biol* 2014; **10**: 728.
- Behrends C, Sowa ME, Gygi SP, Harper JW. Network organization of the human autophagy system. *Nature* 2010; **466**: 68–76.
- Hay N, Sonenberg N. Upstream and downstream of mTOR. *Genes Dev* 2004; **18**: 1926–1945.
- Holz MK, Ballif BA, Gygi SP, Blenis J. mTOR and S6K1 mediate assembly of the translation preinitiation complex through dynamic protein interchange and ordered phosphorylation events. *Cell* 2005; **123**: 569–580.
- Kim E, Goraksha-Hicks P, Li L, Neufeld TP, Guan KL. Regulation of TORC1 by Rag GTPases in nutrient response. *Nat Cell Biol* 2008; **10**: 935–945.
- Pieters R, Loonen AH, Huismans DR, Broekema GJ, Dirven MW, Heyenbroek MW *et al*. In vitro drug sensitivity of cells from children with leukemia using the MTT assay with improved culture conditions. *Blood* 1990; **76**: 2327–2336.
- Chou TC. Theoretical basis, experimental design, and computerized simulation of synergism and antagonism in drug combination studies. *Pharmacol Rev* 2006; **58**: 621–681.
- Deberardinis RJ, Lum JJ, Thompson CB. Phosphatidylinositol 3-kinase-dependent modulation of carnitine palmitoyltransferase 1A expression regulates lipid metabolism during hematopoietic cell growth. *J Biol Chem* 2006; **281**: 37372–37380.
- Gerhart-Hines Z, Rodgers JT, Bare O, Lerin C, Kim SH, Mostoslavsky R *et al*. Metabolic control of muscle mitochondrial function and fatty acid oxidation through SIRT1/PGC-1alpha. *EMBO J* 2007; **26**: 1913–1923.
- Ito K, Carracedo A, Weiss D, Arai F, Ala U, Avigan DE *et al*. A PML-PPAR-delta pathway for fatty acid oxidation regulates hematopoietic stem cell maintenance. *Nat Med* 2012; **18**: 1350–1358.
- Sancak Y, Peterson TR, Shaul YD, Lindquist RA, Thoreen CC, Bar-Peled L *et al*. The Rag GTPases bind raptor and mediate amino acid signaling to mTORC1. *Science* 2008; **320**: 1496–1501.
- Alberich-Jorda M, Wouters B, Balastik M, Shapiro-Koss C, Zhang H, Di Ruscio A *et al*. C/EBPgamma deregulation results in differentiation arrest in acute myeloid leukemia. *J Clin Invest* 2012; **122**: 4490–4504.

- 39 Muller HJ, Beier R, Loning L, Blutters-Sawatzki R, Dorffel W, Maass E *et al*. Pharmacokinetics of native *Escherichia coli* asparaginase (Asparaginase medac) and hypersensitivity reactions in ALL-BFM 95 reinduction treatment. *Br J Haematol* 2001; **114**: 794–799.
- 40 Robitaille AM, Christen S, Shimobayashi M, Cornu M, Fava LL, Moes S *et al*. Quantitative phosphoproteomics reveal mTORC1 activates *de novo* pyrimidine synthesis. *Science* 2013; **339**: 1320–1323.
- 41 Yamamoto A, Tagawa Y, Yoshimori T, Moriyama Y, Masaki R, Tashiro Y. Bafilomycin A1 prevents maturation of autophagic vacuoles by inhibiting fusion between autophagosomes and lysosomes in rat hepatoma cell line, H-4-II-E cells. *Cell Struct Funct* 1998; **23**: 33–42.
- 42 Duran RV, Oppliger W, Robitaille AM, Heiserich L, Skendaj R, Gottlieb E *et al*. Glutaminolysis activates Rag-mTORC1 signaling. *Mol Cell* 2012; **47**: 349–358.
- 43 Samudio I, Harmancey R, Fiegl M, Kantarjian H, Konopleva M, Korchin B *et al*. Pharmacologic inhibition of fatty acid oxidation sensitizes human leukemia cells to apoptosis induction. *J Clin Invest* 2010; **120**: 142–156.
- 44 Estan MC, Calvino E, Calvo S, Guillen-Guio B, Boyano-Adanez Mdel C, de Blas E *et al*. Apoptotic efficacy of etomoxir in human acute myeloid leukemia cells. Cooperation with arsenic trioxide and glycolytic inhibitors, and regulation by oxidative stress and protein kinase activities. *PLoS One* 2014; **9**: e115250.
- 45 Vander Heiden MG. Targeting cancer metabolism: a therapeutic window opens. *Nat Rev Drug Discov* 2011; **10**: 671–684.
- 46 Lumeng L, Bremer J, Davis EJ. Suppression of the mitochondrial oxidation of (-)-palmitoylcarnitine by the malate-aspartate and alpha-glycerophosphate shuttles. *J Biol Chem* 1976; **251**: 277–284.
- 47 Schafer ZT, Grassian AR, Song L, Jiang Z, Gerhart-Hines Z, Irie HY *et al*. Antioxidant and oncogene rescue of metabolic defects caused by loss of matrix attachment. *Nature* 2009; **461**: 109–113.
- 48 Carracedo A, Cantley LC, Pandolfi PP. Cancer metabolism: fatty acid oxidation in the limelight. *Nat Rev Cancer* 2013; **13**: 227–232.
- 49 Carracedo A, Weiss D, Leljaert AK, Bhasin M, de Boer VC, Laurent G *et al*. A metabolic prosurvival role for PML in breast cancer. *J Clin Invest* 2012; **122**: 3088–3100.
- 50 Jeon SM, Chandel NS, Hay N. AMPK regulates NADPH homeostasis to promote tumour cell survival during energy stress. *Nature* 2012; **485**: 661–665.
- 51 Li J, Zhao S, Zhou X, Zhang T, Zhao L, Miao P *et al*. Inhibition of lipolysis by mercaptoacetate and etomoxir specifically sensitize drug-resistant lung adenocarcinoma cell to paclitaxel. *PLoS One* 2013; **8**: e74623.
- 52 Tung S, Shi Y, Wong K, Zhu F, Gorczyński R, Laister RC *et al*. PPARalpha and fatty acid oxidation mediate glucocorticoid resistance in chronic lymphocytic leukemia. *Blood* 2013; **122**: 969–980.
- 53 Barger JF, Gallo CA, Tandon P, Liu H, Sullivan A, Grimes HL *et al*. S6K1 determines the metabolic requirements for BCR-ABL survival. *Oncogene* 2013; **32**: 453–461.
- 54 Sengupta S, Peterson TR, Laplante M, Oh S, Sabatini DM. mTORC1 controls fasting-induced ketogenesis and its modulation by ageing. *Nature* 2010; **468**: 1100–1104.
- 55 Um SH, Frigerio F, Watanabe M, Picard F, Joaquin M, Sticker M *et al*. Absence of S6K1 protects against age- and diet-induced obesity while enhancing insulin sensitivity. *Nature* 2004; **431**: 200–205.
- 56 Laplante M, Sabatini DM. An emerging role of mTOR in lipid biosynthesis. *Curr Biol* 2009; **19**: R1046–R1052.
- 57 Degenhardt K, Mathew R, Beaudoin B, Bray K, Anderson D, Chen G *et al*. Autophagy promotes tumor cell survival and restricts necrosis, inflammation, and tumorigenesis. *Cancer Cell* 2006; **10**: 51–64.
- 58 Galluzzi L, Pietrocola F, Levine B, Kroemer G. Metabolic control of autophagy. *Cell* 2014; **159**: 1263–1276.
- 59 Chan WK, Lorenzi PL, Anishkin A, Purwaha P, Rogers DM, Sukharev S *et al*. The glutaminase activity of L-asparaginase is not required for anticancer activity against ASNS-negative cells. *Blood* 2014; **123**: 3596–3606.

Supplementary Information accompanies this paper on the Leukemia website (<http://www.nature.com/leu>)

ARTICLE

Received 7 Dec 2014 | Accepted 26 Jun 2015 | Published 31 Jul 2015

DOI: 10.1038/ncomms8935

OPEN

# PTEN mediates Notch-dependent stalk cell arrest in angiogenesis

Helena Serra<sup>1,\*</sup>, Iñigo Chivite<sup>1,\*</sup>, Ana Angulo-Urarte<sup>1</sup>, Adriana Soler<sup>1</sup>, James D. Sutherland<sup>2</sup>, Amaia Arruabarrena-Aristorena<sup>2</sup>, Anan Ragab<sup>3</sup>, Radiance Lim<sup>4</sup>, Marcos Malumbres<sup>5</sup>, Marcus Fruttiger<sup>6</sup>, Michael Potente<sup>4</sup>, Manuel Serrano<sup>5</sup>, Àngels Fabra<sup>7</sup>, Francesc Viñals<sup>8,9</sup>, Oriol Casanovas<sup>8</sup>, Pier Paolo Pandolfi<sup>10</sup>, Anna Bigas<sup>11</sup>, Arkaitz Carracedo<sup>2,12,13</sup>, Holger Gerhardt<sup>3,14</sup> & Mariona Graupera<sup>1</sup>

Coordinated activity of VEGF and Notch signals guides the endothelial cell (EC) specification into tip and stalk cells during angiogenesis. Notch activation in stalk cells leads to proliferation arrest via an unknown mechanism. By using gain- and loss-of-function gene-targeting approaches, here we show that PTEN is crucial for blocking stalk cell proliferation downstream of Notch, and this is critical for mouse vessel development. Endothelial deletion of PTEN results in vascular hyperplasia due to a failure to mediate Notch-induced proliferation arrest. Conversely, overexpression of PTEN reduces vascular density and abrogates the increase in EC proliferation induced by Notch blockade. PTEN is a lipid/protein phosphatase that also has nuclear phosphatase-independent functions. We show that both the catalytic and non-catalytic APC/C-Fzr1/Cdh1-mediated activities of PTEN are required for stalk cells' proliferative arrest. These findings define a Notch-PTEN signalling axis as an orchestrator of vessel density and implicate the PTEN-APC/C-Fzr1/Cdh1 hub in angiogenesis.

<sup>1</sup> Vascular Signalling Laboratory, Institut d'Investigació Biomèdica de Bellvitge (IDIBELL), Gran Via de l'Hospitalet 199-203, 08908 L'Hospitalet de Llobregat, Barcelona, Spain. <sup>2</sup> CIC-bioGUNE, Technology Park of Bizkaia, 48160 Derio, Bizkaia, Spain. <sup>3</sup> Vascular Biology Laboratory, London Research Institute-Cancer Research UK, London WC2A 3LY, UK. <sup>4</sup> Max Planck Institute for Heart and Lung Research, D61231 Bad Nauheim, Germany. <sup>5</sup> Spanish National Cancer Research Center (CNIO), Madrid 28029, Spain. <sup>6</sup> UCL Institute of Ophthalmology, University College of London, London EC1V9EL, UK. <sup>7</sup> Centre d'Oncologia Molecular, IDIBELL, Universitat de Barcelona, 08907 L'Hospitalet de Llobregat, Barcelona, Spain. <sup>8</sup> Translation Research Laboratory, Catalan Institute of Oncology, IDIBELL, Universitat de Barcelona, 08907 L'Hospitalet de Llobregat, Barcelona, Spain. <sup>9</sup> Departament de Ciències Fisiològiques II, Universitat de Barcelona, 08907 L'Hospitalet de Llobregat, Spain. <sup>10</sup> Cancer Research Institute, Beth Israel Deaconess Cancer Center, Department of Medicine and Pathology, Harvard Medical School, Boston, Massachusetts 02115, USA. <sup>11</sup> Program in Cancer Research, Hospital del Mar Medical Research Institute (IMIM), Barcelona Biomedical Research Park, 08003 Barcelona, Spain. <sup>12</sup> IKERBASQUE, Basque Foundation of Science, 48011 Bilbao, Bizkaia, Spain. <sup>13</sup> Department of Biochemistry and Molecular Biology, University of the Basque Country (UPV/EHU), Bilbao 48940, Spain. <sup>14</sup> Max-Delbrueck Center for Molecular Medicine (MDC), Robert-Rössle-Strasse 10, Berlin 13125, Germany. \* These authors contributed equally to this work. Correspondence and requests for materials should be addressed to M.G. (email: mgraupera@idibell.cat).

Vessel sprouting is a central mechanism of blood vessel growth<sup>1,2</sup> and it relies on the induction of specialized endothelial cell (EC) populations, each accounting for distinct functions. At the very front of the sprouts, tip cells provide guidance and migrate towards gradients of vascular endothelial growth factor (VEGF)-A, but rarely proliferate<sup>2–4</sup>. Instead, trailing stalk cells located at the base of the sprout proliferate, establish adherent and tight junctions and form the vascular lumen<sup>1,2,5</sup>.

The tip cell phenotype is usually associated with high levels of Delta-like 4 (Dll4), which activate Notch in neighbouring stalk cells, preventing them from becoming a new tip cell. Notch signalling is initiated by receptor–ligand recognition between adjacent cells. This interaction results in two sequential proteolytic events that release the Notch intracellular domain (NICD). Subsequently, NICD translocates to the nucleus, where it forms a complex with the transcriptional factor Rbpj/Cbf1 and the Mastermind-like proteins to drive target gene expression<sup>6,7</sup>. Activation of Notch in ECs leads to cell cycle arrest both *in vitro*<sup>8</sup> and *in vivo*<sup>9–11</sup>. However, it is still unclear how Notch exerts its negative effects on EC proliferation, and the transcriptional programme that triggers stalk cell function is not understood<sup>2,5,12</sup>. Furthermore, it is not clear how stalk cells are ultimately released from this arrest to provide sufficient cell numbers for the sprout to elongate and stabilize.

PTEN (phosphate and tensin homologue deleted on chromosome TEN) is a dual lipid/protein phosphatase, which is often underexpressed in cancer<sup>13–15</sup>. The main activity of PTEN is to dephosphorylate the lipid phosphatidylinositol 3,4,5-trisphosphate (PtdIns(3,4,5)P<sub>3</sub>) at the 3-position, thereby counterbalancing class I phosphoinositide 3-kinase (PI3K) signalling that mediates growth, cell division, survival, migration and metabolism<sup>13,16–18</sup>. Genetic studies in mouse and zebrafish point to a restrictive role of PTEN in angiogenesis. Mice lacking PTEN specifically in ECs exhibit cardiac failure and severe haemorrhages due to defects of the myocardial wall and impaired mural cell coverage of blood vessels<sup>19</sup>. Mutant zebrafish embryos lacking functional PTEN show enhanced angiogenesis<sup>20</sup>; whether this is due to a cell-autonomous effect of PTEN in ECs or is simply a consequence of increased VEGF levels is unclear. Importantly, the specific functions of PTEN in endothelial behaviour and vascular patterning remain unknown.

In most cells and tissues, PTEN localizes to the cytoplasm and the nucleus<sup>13,15</sup>. There is evidence to suggest that PTEN has nuclear, non-lipid phosphatase-dependent functions<sup>21,22</sup>. Interestingly, PTEN localization is cell cycle-dependent, with higher levels of nuclear PTEN during the G<sub>0</sub>–G<sub>1</sub> phase than during the S phase<sup>23,24</sup>. This is in line with the observation that nuclear PTEN negatively regulates cell cycle progression<sup>13,22</sup>. Indeed, in late mitosis and G<sub>1</sub>, nuclear PTEN enhances the E3 ligase activity of APC/C by facilitating the association of APC/C with its activator Fzr1/Cdh1 (encoded by the *Fzr1* gene), with no requirement of its phosphatase activity<sup>22</sup>. The APC/C–Fzr1/Cdh1 complex controls G<sub>1</sub> progression by targeting several proteins for degradation, including mitotic cyclins (Cyclin-A), mitotic kinases (Aurora Kinase A (Aurora A) and Polo-like kinase 1 (Plk1)), proteins involved in chromosome segregation and DNA replication (Geminin; ref. 25). Despite the large body of molecular evidence, the role and relevance of nuclear PTEN in physiology is poorly understood.

Here we report that endothelial PTEN regulates stalk cell proliferation during vessel development. Our data further identify PTEN as a key mediator of the antiproliferative responses of Notch. We show that Dll4/Notch signalling arrests stalk cell proliferation by inducing expression of PTEN to balance stalk cell numbers and coordinate patterning. On PTEN deletion, Notch

signalling fails to arrest early stalk cells and result in defective sprout length and patterning. Our results strongly indicate that both catalytic and non-catalytic activities of PTEN contribute to this function, providing evidence for an important *in vivo* physiological function for the PTEN-APC/C–Fzr1/Cdh1/axis.

## Results

### PTEN negatively regulates vascular density in angiogenesis.

To study the EC-autonomous role of PTEN in sprouting angiogenesis, we crossed *Pten*<sup>flox/flox</sup> mice with *PdgfrbCreER*<sup>T2</sup> transgenic mice that express a tamoxifen-activatable Cre recombinase in ECs<sup>26</sup> (further referred to as PTEN<sup>iΔEC/iΔEC</sup>) and assessed postnatal retinal angiogenesis. 4-hydroxytamoxifen (4-OHT) was administered *in vivo* at postnatal day 1 (P1) and P2, followed by analysis of the retinal vasculature at different time points. Comparing whole-mount-stained retinas of control (*Pten*<sup>flox/flox</sup>) to PTEN<sup>iΔEC/iΔEC</sup> mice at P5 revealed a mild increase in vessel width (Supplementary Fig. 1a–g). By P7, loss of PTEN resulted in excessive branching and substantially increased vessel width (Fig. 1a–d), a phenotype that was further exacerbated at P10 (Fig. 1h,i). PTEN<sup>iΔEC/iΔEC</sup> P7 retinas showed efficient recombination of the Cre-reporter R26-R and depletion of PTEN in the retinal endothelium (Supplementary Fig. 1h,i), with an increase in staining for phosphoS6 (pS6), a marker of PI3K pathway activation (Supplementary Fig. 1j). Isolated mouse lung ECs (mECs) from PTEN<sup>iΔEC/iΔEC</sup> mice confirmed that effective depletion of PTEN protein in mECs was achieved 96 h following 4-OHT administration (Supplementary Fig. 1k,l). To further characterize the cell-autonomous role of PTEN in ECs, we therefore focused on the P7 time point. No differences in radial expansion (Fig. 1e) and in the number of sprouts per 100 μm of leading endothelial membrane were found in PTEN<sup>iΔEC/iΔEC</sup> when compared with control retinas (Fig. 1f). Instead, the length of the sprouts was significantly reduced in the PTEN<sup>iΔEC/iΔEC</sup> retinal vasculature compared with controls (Fig. 1g). The hyperplastic phenotype observed on PTEN loss was validated in an independent cellular system based on embryoid body (EB) formation, in which clusters of embryonic stem cells respond to VEGF by forming vascular tubes<sup>27</sup>. Compared with wild type (WT), PTEN null EBs showed increased sprout width and length (Supplementary Fig. 2a–d), with no differences in the number of sprouts (Supplementary Fig. 2e).

Next, we sought to address whether regulated elevation in PTEN expression *in vivo* would oppose the phenotype induced by loss of PTEN. To this end, we used super-PTEN transgenic mice (PTEN<sup>TG</sup>)<sup>28</sup>, a mouse model that allows moderate organismal elevation of PTEN levels (two-fold over WT littermates), including in the vasculature (Supplementary Fig. 1m). PTEN<sup>TG</sup> retinas exhibited decreased vessel width and increased sprout length (Fig. 1j,k,m,p), with no changes in the number of branches (Fig. 1l) and sprouts (Fig. 1o). A slight reduction in radial expansion was also observed on moderate PTEN overexpression (Fig. 1n), similar to retinas from mice that are heterozygous for a kinase-dead p110α PI3K allele<sup>29</sup>. Neither loss nor gain of PTEN function resulted in changes in Dll4 or Notch target genes (Supplementary Fig. 3a–c), further supporting that PTEN is not required for tip/stalk selection. Analysis of *EphB4*, *EphrinB2* and *Nr2f2* gene expression, key genes involved in arteriovenous differentiation, did also not reveal any obvious difference between control and loss and gain of PTEN function in ECs, suggesting that PTEN signalling does not play a predominant role in this process (Supplementary Fig. 3d,e).

Taken together, these data uncover a selective role for PTEN in angiogenesis, regulating vascular density and consequently vessel growth *in vivo*.



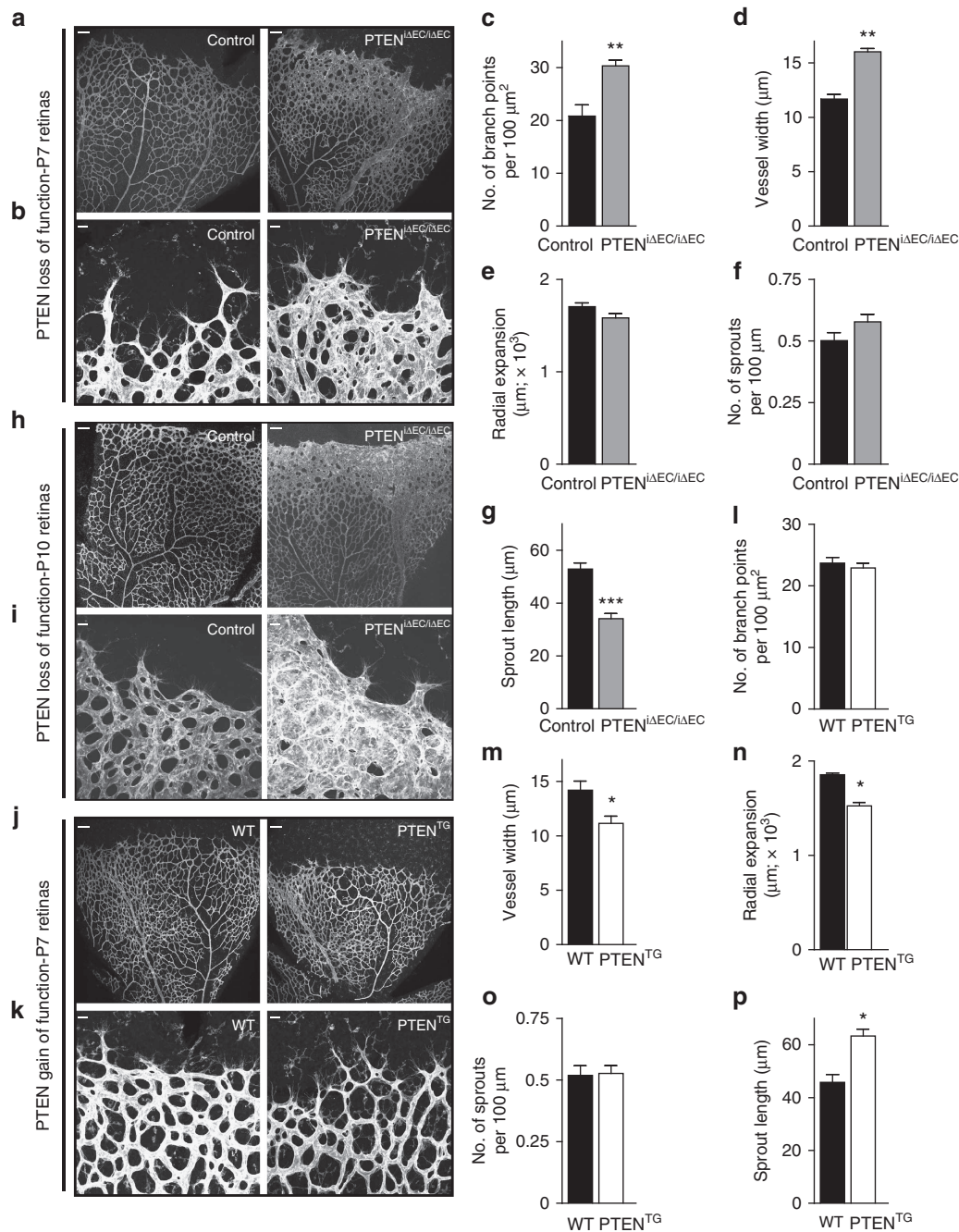


**Figure 1 | PTEN regulates vascular density.** (a,b) Whole-mount visualization of blood vessels by isolectin B4 (IB4) staining of control and PTEN<sup>iAEC/iAEC</sup> littermates at P7. (c–g) Quantitative analysis of the retinas shown in a,b. (c) Vascular branch points per unit area ( $n \geq 6$ ). (d) Vessel width ( $n \geq 4$ ). (e) Radial expansion of blood vessels ( $n \geq 7$ ). (f) Number of sprouts per vascular front length ( $n \geq 7$ ). (g) Sprout length from the tip to the base of the sprout ( $n \geq 7$ ). (h,i) Whole-mount visualization of blood vessels by IB4 staining of control and PTEN<sup>iAEC/iAEC</sup> littermates at P10. (j,k) Whole-mount visualization of blood vessels by IB4 staining of WT and PTEN<sup>TG</sup> littermates at P7. (l–p) Quantitative analysis of the retinas shown in j,k. (l) Vascular branch points per unit area ( $n = 8$ ). (m) Vessel width ( $n = 12$ ). (n) Radial expansion of blood vessels ( $n = 4$ ). (o) Number of sprouts per vascular front length ( $n = 6$ ). (p) Sprout length from the tip to the base of the sprout ( $n = 6$ ). Scale bars, 100 μm (a,h,i) and 20 μm (b,i,k). Error bars are s.e.m. \* $P < 0.05$ , \*\* $P < 0.01$  and \*\*\* $P < 0.001$  were considered statistically significant. Statistical analysis was performed by nonparametric Mann–Whitney test.

**PTEN regulates endothelial stalk cell number.** Previous data have shown that constitutive targeting of PTEN in ECs results in altered mural cell coverage<sup>19</sup>. Instead, immunostaining with desmin, a retinal pericyte marker<sup>30</sup>, did not reveal any obvious defect in mural cell coverage in PTEN<sup>iAEC/iAEC</sup> retinas compared with control, consistent with the lack of sprouting defects on PTEN loss (Supplementary Fig. 3f).

Analysis of PTEN<sup>iAEC/iAEC</sup> retinas stained with a nuclear endothelial marker (Erg) revealed increased EC numbers in the angiogenic vasculature (Fig. 2a,b). Conversely, elevated PTEN expression resulted in reduced EC numbers at the sprouting front (Fig. 2c,d). We sought to validate whether these differences relate to changes in EC proliferation. Surprisingly, no difference in the number of proliferative ECs located in the subfront retinal area,

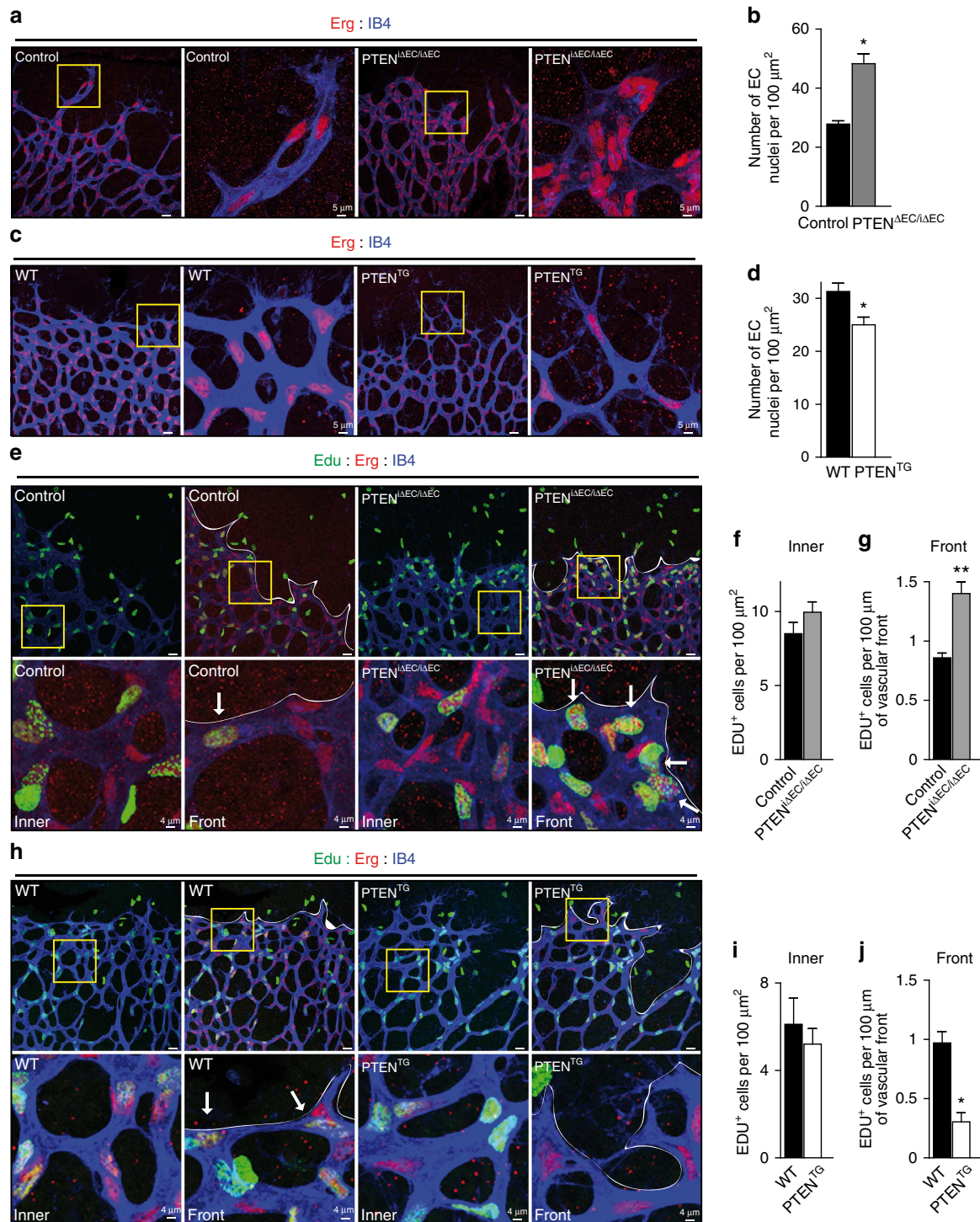


**Figure 2 | PTEN negatively regulates stalk cell proliferation.** (a) IB4 (blue) and Erg (red) staining of control and PTEN<sup>ΔEC/ΔEC</sup> littermate retinas at P7. Islets show higher magnification of selected regions shown to the right. (b) Quantification of EC nuclei per unit area assessed by Erg positivity in control and PTEN<sup>ΔEC/ΔEC</sup> P7 retinas ( $n \geq 4$ ). (c) IB4 (blue) and Erg (red) staining of WT and PTEN<sup>TG</sup> littermate retinas at P7. Islets show higher magnification of selected regions shown to the right. (d) Quantification of EC nuclei per unit area assessed by Erg positivity in WT and PTEN<sup>TG</sup> P7 retinas ( $n = 8$ ). (e) IB4 (blue), Erg (red) and Edu (green) staining of control and PTEN<sup>ΔEC/ΔEC</sup> P7 retinas. Islets show higher magnification of selected regions shown below. Arrows indicate Edu-positive ECs in the sprouting front. (f) Quantification of Edu-positive cells per unit area assessed in control and PTEN<sup>ΔEC/ΔEC</sup> P7 retinas ( $n \geq 7$ ). (g) Quantification of number of Edu-positive cells located at the sprouting front expressed per vascular front length in control and PTEN<sup>ΔEC/ΔEC</sup> P7 retinas ( $n = 7$ ). (h) IB4 (blue), Erg (red) and Edu (green) staining of WT and PTEN<sup>TG</sup> littermate retinas at P7. Islets show higher magnification of selected regions shown below. Arrows indicate Edu-positive ECs in the sprouting front. (i) Quantification of Edu-positive cells per unit area assessed in WT and PTEN<sup>TG</sup> P7 retinas ( $n = 4$ ). (j) Quantification of number of Edu-positive cells located at the sprouting front expressed per vascular front length in WT and PTEN<sup>TG</sup> retinas ( $n = 4$ ). Scale bars, 20 μm (a,c,e,h). Error bars are s.e.m. \* $P < 0.05$  and \*\* $P < 0.01$  were considered statistically significant. Statistical analysis was performed by nonparametric Mann-Whitney test.

behind the sprouting front, was found on either loss (Fig. 2e,f) or gain of PTEN function (Fig. 2h,i). This is unexpected, given that in the growing vasculature ECs with high turnover are located in this subfront area (Supplementary Fig. 4a,b). To test whether PTEN regulated proliferation of ECs in other retinal locations, we focused on the first line of cells located at the sprouting front where proliferating cells are rarely observed (Supplementary Fig. 4a,b). Interestingly, a 40% increase in proliferation in PTEN<sup>iΔEC/iΔEC</sup> retinas (Fig. 2g) or 60% reduction in PTEN<sup>TG</sup> retinas (Fig. 2j) compared with control retinas was observed in ECs at the front. These data point towards a selective role of PTEN in restricting EC proliferation in cells located at the sprouting front.

**PTEN executes Notch-dependent cell cycle arrest.** Given that the impact of PTEN loss or overexpression *in vivo* on proliferation are restricted to the sprouting front that is highly Notch-dependent<sup>9</sup>, we hypothesized that a functional connection exists between these two signalling pathways. Activation of Notch in mECs, both *in vivo* and *in vitro*, resulted in cell cycle arrest, shown by reduced 5-bromo-2'-deoxyuridine (BrdU) incorporation (Supplementary Fig. 4c,d and Fig. 3a) and downregulation of cell cycle regulators including Cyclin D and A, Plk1, Aurora A and Geminin (Fig. 3b). Interestingly, genetic manipulation of PTEN levels in ECs altered the antiproliferative response to Notch activation (Fig. 3c,e). PTEN<sup>iΔEC/iΔEC</sup> mECs failed to stop proliferation on Notch activation (Fig. 3c,d), whereas PTEN<sup>TG</sup> mECs showed a 50% increase in the cell cycle arrest response (Fig. 3e,f). Consistent with a role of PTEN in regulating the cell cycle arrest, higher PTEN levels in ECs *in vivo* corresponded to nonproliferative cells (Supplementary Fig. 4e,f). Our results suggest that PTEN is necessary for the growth-suppressive activity of Notch signalling in ECs and imply that the PTEN loss-of-function phenotype is the result of an impaired response to Dll4 stimulation.

Because PTEN is required for the Notch-dependent regulation of endothelial proliferation, we tested whether PTEN expression is regulated by Notch. Bioinformatic analysis of the *PTEN* locus identified the presence of three Rbpj motifs that are conserved in both the human and mouse *PTEN* gene (Fig. 3g). We used chromatin immunoprecipitation (ChIP) analysis on human ECs to determine the recruitment of NICD protein to the *PTEN* promoter after 2 h of incubation with Dll4. PTEN promoter occupancy was determined using real-time quantitative PCR (qPCR) probes that amplify seven regions spanning from -2,380 to -590 relative to the transcription initiation site. Our analysis revealed NICD occupancy in the -1,492 region, which contains one of the three predicted Rbpj-binding sites (Fig. 3g). We next validated the functional significance of Rbpj binding to the promoter in luciferase reporter assays. Indeed, analysis of PTEN promoter activity showed activation in response to Dll4 (Fig. 3h) and on overexpression of the intracellular domain of the Notch receptor (NICD; Fig. 3i). Importantly, enhanced PTEN promoter responsiveness to Dll4 was abrogated by the  $\gamma$ -secretase inhibitor dibenzazepine (DBZ; Fig. 3i). Western blot experiments confirmed that Dll4 stimulation results in elevated protein levels of PTEN in human ECs and mECs (Fig. 3j,k). Using lungs as highly vascularized tissue, we validated that overactivation of Notch signalling by inhibiting the Notch ligand, Jagged 1 (Jag1)<sup>11</sup>, resulted in higher PTEN expression levels (Fig. 3l). Taken together, these results demonstrate that PTEN is a target gene of Notch signalling in ECs, which becomes induced by Dll4 stimulation.

**PTEN is required for Notch function *in vivo*.** We sought to confirm the Notch/PTEN functional interaction *in vivo*. We took

advantage of endothelial Jag1 inactivation, which results in reduced EC proliferation and decreased vascular branching due to overactivation of Notch signalling<sup>11</sup>. We hypothesized that, if the regulation of the angiogenic process by Notch requires the increase in PTEN function, loss of PTEN would prevent the phenotype of Jag1 deletion. We tested this hypothesis in inducible endothelial-cell-specific PTEN<sup>iΔEC/iΔEC</sup>;Jag1<sup>iΔEC/iΔEC</sup> double mutants. The vasculature of Jag1<sup>iΔEC/iΔEC</sup> retinas showed reduced endothelial proliferation and reduced vessel width, confirming previous reports (Fig. 4a–g and Supplementary Fig. 5a)<sup>11</sup>. However, concomitant PTEN deletion abrogated the phenotype observed in Jag1<sup>iΔEC/iΔEC</sup> retinas (Fig. 4a–g), while the phenotype of PTEN loss remained unaffected by Jag1 deletion (the increase in endothelial proliferation at the sprouting front). Next, we validated our hypothesis in the PTEN<sup>TG</sup> mice by blocking Notch activation with the  $\gamma$ -secretase inhibitor DAPT (N-[N-(3,5-difluorophenacetyl)-L-alanyl]-S-phenylglycine t-butyl ester) that strongly enhances angiogenesis partially due to increased EC proliferation<sup>9</sup>. Remarkably, DAPT-induced increase in vascular density at the angiogenic front was abolished by increased levels of PTEN (Fig. 4h,j,m,n and Supplementary Fig. 5b). However, elevated levels of PTEN did not prevent the enhanced sprouting caused by DAPT (Fig. 4i,k,l), further indicating that PTEN is not required for Notch-dependent tip/stalk selection.

**Dual function of PTEN in angiogenesis.** To gain insight into the biological mechanism underlying the role of PTEN in sprouting angiogenesis, we investigated the contribution of phosphatase-dependent and -independent activities of PTEN at the organismal and cellular levels. We observed a compartmentalization of PTEN in the nucleus and cytoplasm in cultured control cells (Fig. 5a), whereas PTEN<sup>iΔEC/iΔEC</sup> mECs showed no nuclear staining with some residual positivity in the cytoplasm. PTEN depletion in mECs resulted in increased Akt phosphorylation and in accumulation of the E3 ubiquitin ligase APC/C-Fzr1/Cdh1 complex substrates Aurora A, Plk1 and Geminin (Fig. 5b). Control mECs treated with 4-OHT did not show any of the aforementioned changes (Fig. 5c). In contrast, mECs isolated from PTEN<sup>TG</sup> lungs showed reduced Akt phosphorylation and reduced accumulation of E3 ubiquitin ligase APC/C-Fzr1/Cdh1 complex substrates compared with WT cells (Fig. 5d).

To investigate whether increased levels of the APC/C-Fzr1/Cdh1 targets were only a consequence of increased PI3K activity, we tested the impact of GDC-0941 (a pan-class I PI3K inhibitor that blocks p110 $\alpha$ , p110 $\beta$ , p110 $\delta$  and p110 $\gamma$ ; ref. 31). While pretreatment with GDC-0941 abrogated Akt activation in PTEN<sup>iΔEC/iΔEC</sup> mECs (Fig. 5e), it did not modify the levels of Aurora A and Geminin (Fig. 5e), further corroborating that the function of PTEN promoting the APC/C-Fzr1/Cdh1 activity is independent of its ability to inhibit PI3K signalling through its lipid phosphatase activity<sup>22</sup>.

As our data indicate that the principal function of PTEN in sprouting angiogenesis is to regulate EC proliferation, we tested to what extent phosphatase-dependent and -independent activities of PTEN participate in this regulation. *In vitro* isolated PTEN<sup>iΔEC/iΔEC</sup> and PTEN<sup>TG</sup> mECs showed increased and decreased BrdU incorporation, respectively (Fig. 5f and Supplementary Fig. 6a,b). Inhibition of PI3K activity and Aurora kinase, one of the main targets of APC/C-Fzr1/Cdh1 (ref. 22), partially rescued normal proliferation rate in PTEN<sup>iΔEC/iΔEC</sup> mECs (Fig. 5f and Supplementary Fig. 6a). A synergistic effect was observed on pretreatment with both GDC-0941 and VX680, further implying a dual function of PTEN in this process. Next, we complemented PTEN-depleted ECs with either WT

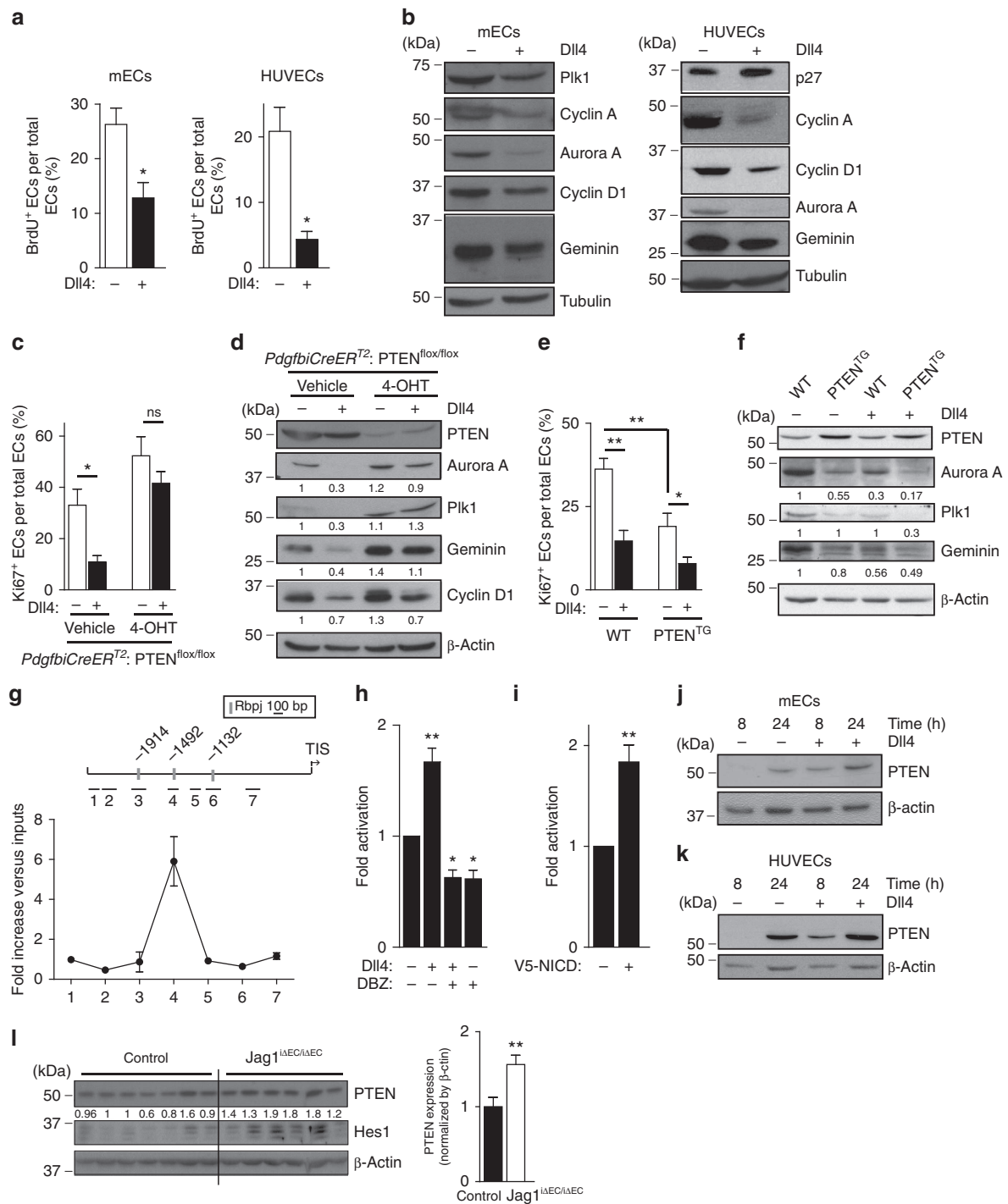


**Figure 3 | Notch limits EC proliferation by upregulating PTEN levels.** (a) Quantification of *in vitro* proliferation of mECs and HUVECs plated for 24 h in vehicle or DII4-coated dishes, pulsed with BrdU for 2 h and subjected to immunostaining analysis. At least 100 cells per condition were counted ( $n = 4$ ). (b) Immunoblot analysis of mECs and HUVECs plated for 24 h in vehicle or DII4-coated plates using the indicated antibodies ( $n = 3$ ). Molecular weight marker (kDa) is indicated. (c,e) Quantification of *in vitro* proliferation by Ki67 immunofluorescence of control and PTEN<sup>ΔEC/ΔEC</sup> mEC (c) and WT and PTEN<sup>TG</sup> mEC (e) plated for 24 h in vehicle or DII4-coated plates. Overall 100 cells per condition were counted ( $n = 4$ ). (d) Control and PTEN<sup>ΔEC/ΔEC</sup> or (f) WT and PTEN<sup>TG</sup> mEC were plated for 24 h in vehicle or DII4-coated dishes, followed by immunoblot analysis using the indicated antibodies. The quantification of the relative immunoreactivity of each protein normalized to β-actin is represented as the mean of four different experiments in d,f. Molecular weight marker (kDa) is indicated. (g) ChIP with the anti-NICD antibody from HUVECs and the analysis of the PTEN locus by qPCR. A pool of two independent experiments is shown. (h,i) PTEN-luciferase reporter assays were performed in HUVECs with a 2,666-bp PTEN promoter construct (pGL3 PTEN *Hind III-NotI*). (h) Cells were plated for 6 h in vehicle or DII4-coated dishes and (i) HUVECs were transfected with V5-NICD ( $n = 3$ ). (j,k) Immunoblot analysis of PTEN in lung mECs (j) and in HUVECs (k) plated for 8 or 24 h in vehicle or DII4-coated plates ( $n = 4$ ). Molecular weight marker (kDa) is indicated. (l) Immunoblot analysis of PTEN and Hes1 in lung lysates from control ( $n = 7$ ) and Jag1<sup>ΔEC/ΔEC</sup> ( $n = 6$ ) pups. Molecular weight marker (kDa) is indicated. Error bars are s.e.m. \* $P < 0.05$  and \*\* $P < 0.01$  were considered statistically significant. ns, not statistically significant. Statistical analysis was performed by nonparametric Mann-Whitney test.

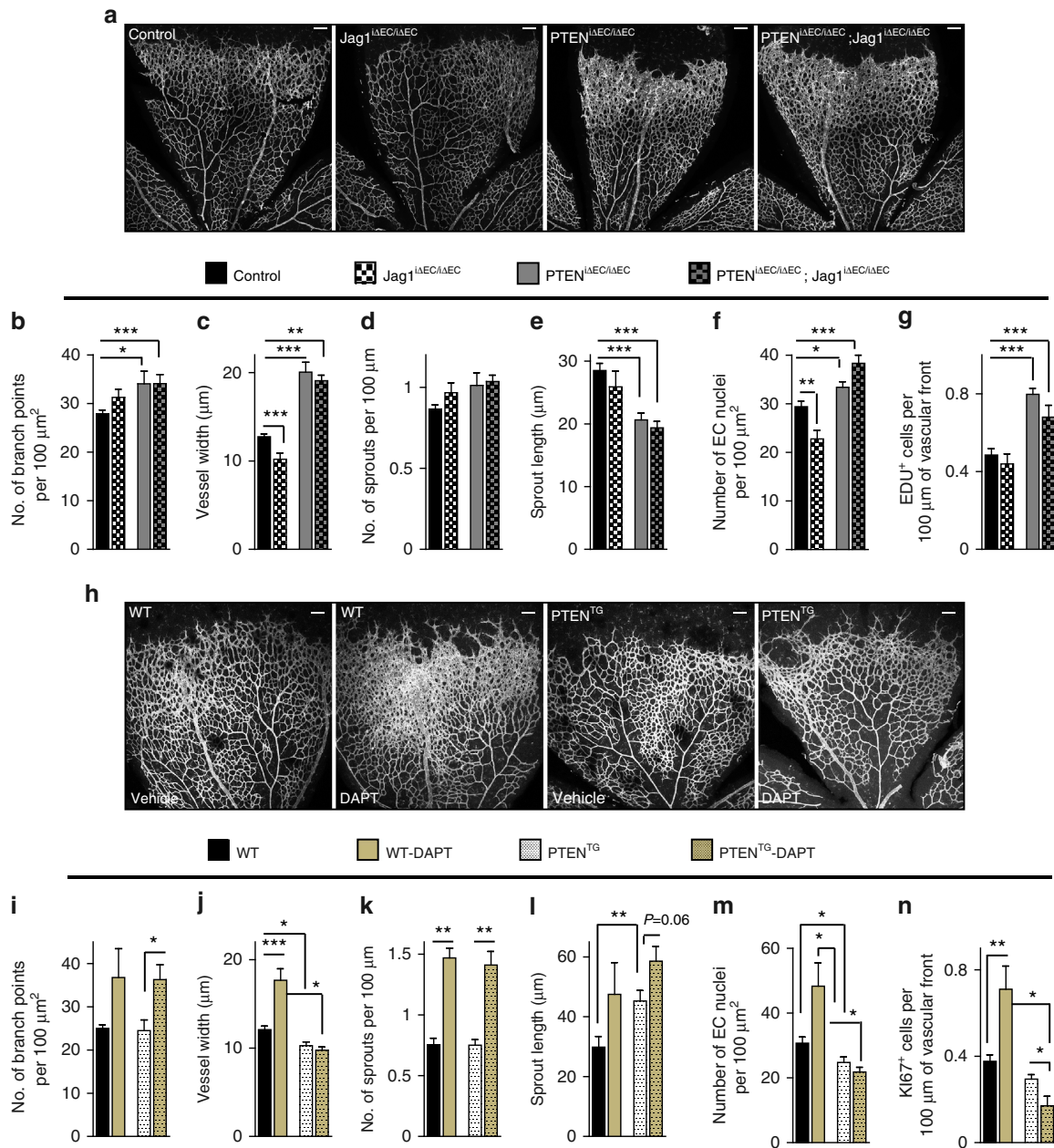


**Figure 4 | PTEN interacts with Notch *in vivo* to negatively control stalk cell proliferation.** (a) Whole-mount visualization of blood vessels by IB4 staining of control, Jag1<sup>ΔEC/ΔEC</sup>, PTEN<sup>ΔEC/ΔEC</sup> and PTEN<sup>ΔEC/ΔEC</sup>; Jag1<sup>ΔEC/ΔEC</sup> littermates at P7. (b–g) Quantitative analysis of the retinas shown in a. Retinas from five independent litters were pooled for quantification. (b) Vascular branch points (n ≥ 4). (c) Vessel width (n ≥ 4). (d) Number of sprouts per vascular front length (n ≥ 4). (e) Sprout length from the tip to the base of the sprout (n ≥ 4). (f) Quantification of EC nuclei per unit area assessed by Erg positivity (n ≥ 4). (g) Quantification of number of Edu-positive cells located at the vascular front expressed per sprouting front length (n ≥ 3). (h) Whole-mount visualization of blood vessels by IB4 staining of WT and PTEN<sup>TG</sup> P7 retinas treated with vehicle or DAPT (100 mg kg<sup>-1</sup>). (i–n) Quantitative analysis of the retinas shown in h. Retinas from three independent litters were pooled for quantification. (i) Vascular branch points per unit area (n ≥ 4). (j) Vessel width (n ≥ 4). (k) Number of sprouts per vascular front length (n ≥ 4). (l) Sprout length from the tip to the base of the sprout (n ≥ 4). (m) Quantification of endothelial nuclei per unit area assessed by Erg positivity (n ≥ 4). (n) Quantification of number of Ki67-positive cells located at the vascular front expressed per sprouting front length (n = 6). Scale bars, 100 μm (a,h). Error bars are s.e.m. \*P < 0.05, \*\*P < 0.01 and \*\*\*P < 0.001 were considered statistically significant. Statistical analysis was performed by nonparametric Mann-Whitney test.

(PTEN<sup>WT</sup>), phosphatase-inactive (C124S; PTEN<sup>C124S</sup>; refs 32,33) or nuclear-excluded (K13,289E; PTEN<sup>K13,289E</sup>) PTEN (ref. 22). Expression of PTEN<sup>WT</sup>, PTEN<sup>C124S</sup> and PTEN<sup>K13,289E</sup> abrogated the increase in EC proliferation (Fig. 5g and Supplementary Fig. 6c) of PTEN null ECs, albeit most prominently seen with PTEN<sup>WT</sup>. All together, these data indicate that phosphatase-dependent and -independent activities of PTEN are important to regulate EC proliferation.

Next, we tested the differential contribution of each of these functions *in vivo*, by first analysing the retinas of PTEN<sup>ΔEC/ΔEC</sup> on inhibition of class I PI3K activity with GDC-0941. The hyperplasia induced by PTEN loss was rescued by inhibiting PtdIns(3,4,5)P<sub>3</sub> production (Fig. 6a–d and Supplementary Fig. 7a), indicating, as expected, an important role of PTEN lipid phosphatase activity in vascular growth. Next, we assessed the contribution of phosphatase-independent activity of PTEN to

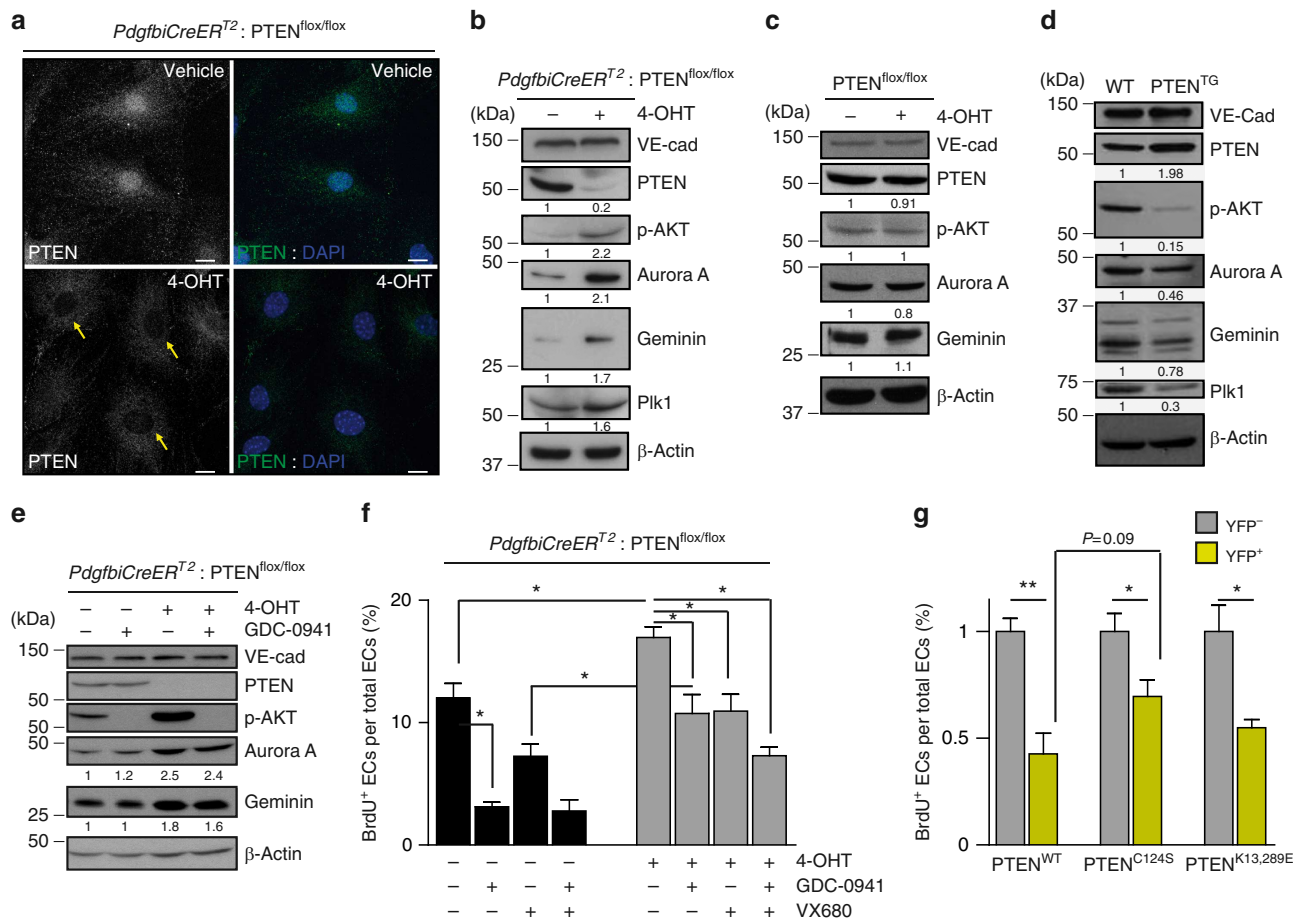


**Figure 5 | Catalytic and non-catalytic roles of PTEN regulate EC proliferation.** (a) Confocal images of PTEN (green) and DAPI immunofluorescence in *PdgfbiCreERT<sup>2</sup>; PTEN<sup>flox/flox</sup>* mECs treated with vehicle or with 4-OHT for 96 h. Yellow arrows indicate the lack of PTEN staining in the nucleus of PTEN null cells. Scale bars, 10  $\mu$ m ( $n = 3$ ). (b–d) Exponentially growing mECs were lysated, followed by immunoblotting using the indicated antibodies. *PdgfbiCreERT<sup>2</sup>; PTEN<sup>flox/flox</sup>* (b) and *PTEN<sup>flox/flox</sup>* (c) mECs were treated for 96 h with vehicle or 4-OHT. (d) WT and *PTEN<sup>TG</sup>* mECs were cultured for 48 h before cell lysis and immunoblotting. (e) *PdgfbiCreERT<sup>2</sup>; PTEN<sup>flox/flox</sup>* mECs were treated for 96 h with vehicle or 4-OHT. Before cell lysis, cells were pretreated for 2 h with GDC-0941 (1  $\mu$ M). The quantification of the relative immunoreactivity of each protein normalized to  $\beta$ -actin is represented as the mean from at least three different experiments in b–e. Molecular weight marker (kDa) is indicated. (f) Exponentially growing control and *PTEN<sup>iΔEC/iΔEC</sup>* mECs were treated for 48 h with test compounds or vehicle, and then were pulsed with BrdU for 2 h and subjected to immunostaining analysis. Inhibitors and doses used were as follows: GDC-0941 (pan-class I PI3K inhibitor; 1  $\mu$ M) and VX680 (Aurora Kinase inhibitor; 0.5  $\mu$ M). Data shown are means of four independent experiments. (g) *PdgfbiCreERT<sup>2</sup>; PTEN<sup>flox/flox</sup>* mECs were infected with *PTEN<sup>WT</sup>*, *PTEN<sup>C124S</sup>* or *PTEN<sup>K13,289E</sup>*, treated with 4-OHT for 72 h, plated for 48 h in the presence of doxycycline, pulsed with BrdU for 2 h and subjected to immunostaining analysis. Data shown are the means of six independent experiments. Error bars are s.e.m. \* $P < 0.05$  and \*\* $P < 0.01$  were considered statistically significant. Statistical analysis was performed by nonparametric Mann–Whitney test.

sprouting angiogenesis by inhibiting Aurora kinase. Strikingly, the phenotype of *PTEN<sup>iΔEC/iΔEC</sup>* was abrogated by Aurora kinase inhibition (Fig. 6e–h), which is consistent with the contribution of the phosphatase-independent activity of PTEN to sprouting angiogenesis *in vivo*. This was further corroborated by genetic conditional and inducible deletion of *Fzr1* in ECs. Complete depletion of *Fzr1/Cdh1* protein was achieved 48 h post incubation with 4-OHT (Supplementary Fig. 7b,c). Therefore, pups were treated with 4-OHT at P5 and P6, followed by analysis of the retinal vasculature at P7. The retinas of *Fzr1<sup>iΔEC/iΔEC</sup>* showed increased vascular density and reduced length of sprouts (Fig. 6i–n) comparable to *PTEN<sup>iΔEC/iΔEC</sup>*. All together, these data suggest that, in ECs, there is a dual contribution of PTEN, counterbalancing the PI3K signalling pathway through its lipid phosphatase activity and facilitating the APC/C-*Fzr1/Cdh1* complex activity, which has been reported to be independent of its catalytic function<sup>22</sup>.

## Discussion

Here we report that PTEN in ECs is required in a cell-autonomous and dose-dependent manner for the control of vascular density and vessel growth, but is dispensable for the regulation of the sprouting activity of tip cells. We show that endothelial PTEN restricts vascular growth by limiting stalk cell proliferation during sprouting angiogenesis. An important conclusion from this study is that PTEN is not required in all ECs to regulate proliferation *in vivo*, as shown in cultured ECs (our data and ref. 19). Instead, our results indicate that the consequence of PTEN loss or overexpression *in vivo* is restricted specifically to the zone of the vasculature that is highly Notch-dependent.

Constitutive targeting of PTEN in ECs leads to embryonic lethality due to aberrant angiogenesis<sup>19</sup>. Although these studies have established that PTEN regulates EC proliferation, the analysis of vasculature in *Tie2Cre-PTEN<sup>flox/flox</sup>* embryos did

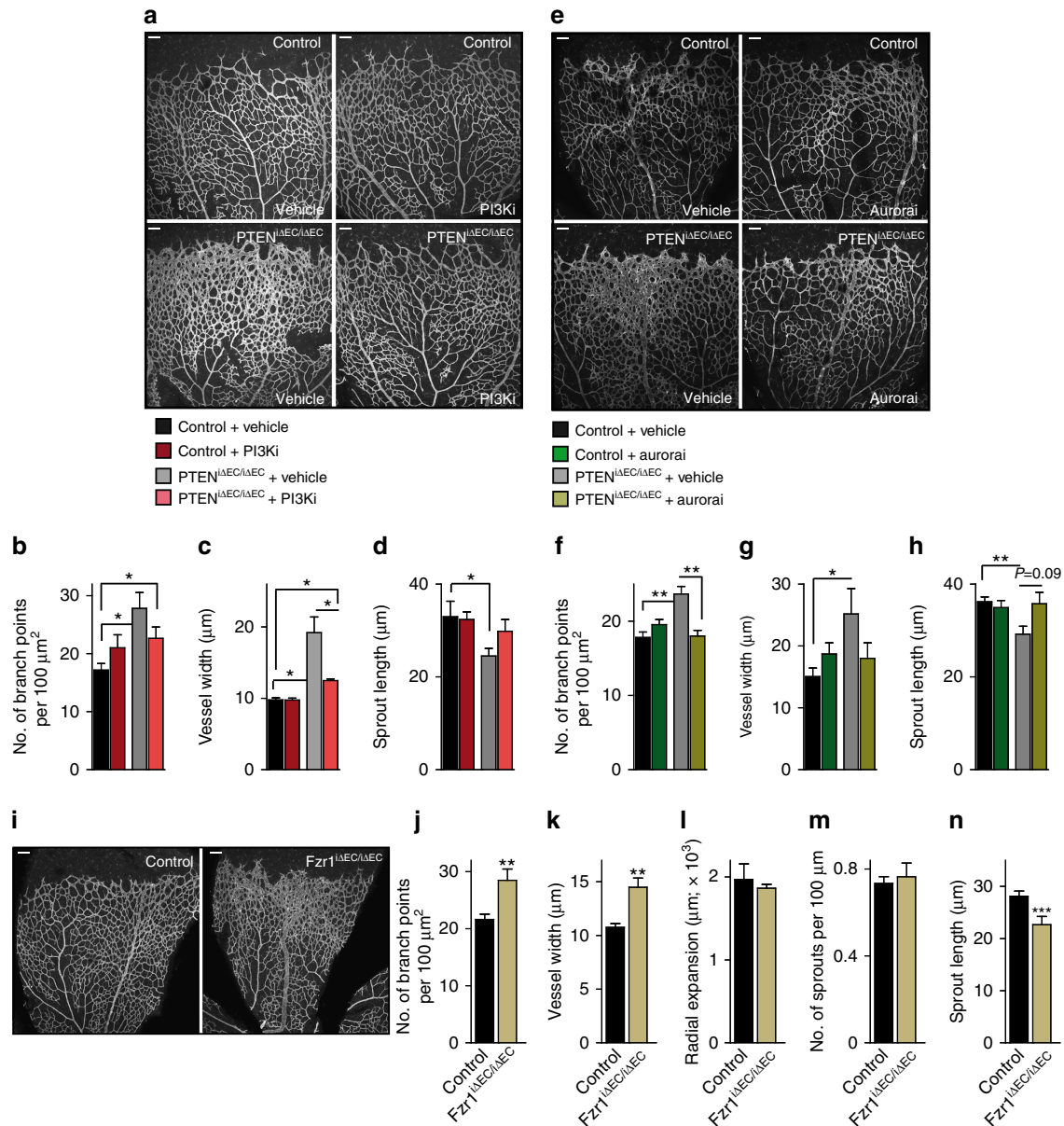


**Figure 6 | Dual function of PTEN in sprouting angiogenesis.** (a) IB4-stained control and PTEN<sup>ΔEC/ΔEC</sup> P7 retinas (4-OHT administration from P1 to P2) treated with vehicle or GDC-0941 at P6 and P7. (b–d) Quantitative analysis of the retinas shown in a. (b) Vascular branch points per unit area ( $n \geq 4$ ). (c) Vessel width ( $n \geq 4$ ). (d) Sprout length from the tip to the base of the sprout ( $n \geq 4$ ). (e) IB4-stained control and PTEN<sup>ΔEC/ΔEC</sup> P7 retinas (4-OHT administration from P1 to P2) treated with vehicle or VX680 at P6 and P7. (f–h) Quantitative analysis of the retinas shown in e. (f) Vascular branch points per unit area ( $n \geq 6$ ). (g) Vessel width ( $n \geq 6$ ). (h) Sprout length from the tip to the base of the sprout ( $n \geq 6$ ). (i) Overview of P7 control and Fzr1<sup>ΔEC/ΔEC</sup> iB4-stained. (j–n) Quantitative analysis of the retinas shown in i. (j) Vascular branch points per unit area ( $n = 11$ ). (k) Vessel width ( $n = 11$ ). (l) Radial expansion of blood vessels ( $n \geq 5$ ). (m) Number of sprouts per 100 μm vessel front length ( $n = 11$ ). (n) Sprout length from the tip to the base of the sprout ( $n = 6$ ). Scale bars, 100 μm (a,e,i). Error bars are s.e.m. \* $P < 0.05$ , \*\* $P < 0.01$  and \*\*\* $P < 0.001$  were considered statistically significant. Statistical analysis was performed by nonparametric Mann–Whitney test.

not allow unravelling precisely how PTEN regulates sprouting angiogenesis. Furthermore, Hamada *et al.* were unclear of whether the aberrant vasculature, which results on PTEN loss, was a consequence of aberrant PTEN signalling in ECs or simply a consequence of an altered pro-angiogenic cytokine profile<sup>19</sup>. Similarly, zebrafish studies have shown that loss of PTEN leads to increased VEGF levels and in turn vessel hyperplasia, highlighting indeed that PTEN also regulates angiogenesis in a paracrine manner<sup>20</sup>. Another difference between Hamada *et al.* and our study is that constitutive loss of PTEN in ECs also results in altered mural cell coverage, while induced loss of postnatal

endothelial PTEN does not. These discrepancies suggest that PTEN may differently regulate angiogenesis in different vascular beds.

Activation of Notch leads to cell cycle arrest<sup>8–11,34</sup>. In this study, we identify PTEN as a critical mediator of Notch antiproliferative response in stalk cells. If PTEN is not expressed in ECs, stalk cells become insensitive to the antiproliferative signals of Notch and exhibit unrestricted expansion, hence perturbing sprout length and pattern and eventually resulting in profound hyperplasia. Interestingly, our results also reveal that stalk cells located further away from the

front are insensitive to changes in PTEN expression. Given that these stalk cells at the subfront area are highly proliferative, our data support the existence of two biological states for stalk cells. A first state in which stalk cells must remain arrested to ensure the correct patterning of the sprout, and a second state in which cells enter the cell cycle to expand the plexus. These two states are likely the consequence of dynamic changes in Notch signalling, with high Notch activity in early nonproliferative stalk cells and low Notch activity in the late proliferative stalk cells. Our data predict a rise and fall in PTEN levels that will accompany the early quiescent and late proliferative phases, respectively. This is supported by the observation that, in WT cultured ECs, higher PTEN levels are seen 8 h post stimulation with Dll4 compared with 24 h post stimulation. Furthermore, co-staining of PTEN and 5-ethynyl-2'-deoxyuridine (Edu) in the growing vasculature showed that Edu-negative cells express higher levels of PTEN than Edu-positive cells, supporting the notion that PTEN protein levels rise to guarantee cell cycle arrest. Whether high PTEN cells correspond to high Notch signalling still needs to be determined. Moya *et al.* speculated that early and late stalk cell behaviours might be orchestrated by oscillation in Notch activity. The authors proposed that Id proteins, members of HLH proteins, govern these two states by releasing the negative autoregulatory loop of Hes1 (ref. 35). While our results are consistent with the idea of two states, they identify PTEN as the key mediator of early stalk cell function in response to Notch.

Why and how Notch exerts a unique negative regulation in the endothelium while driving proliferation in virtually every other cell type and in cancer has been a mystery<sup>5,36</sup>. Our data show that PTEN negatively regulates cell cycle progression in ECs through conserved pathways. Critically, what our results illustrate is a novel interaction between Notch and PTEN in ECs. We find that Notch stimulates PTEN transcription in the endothelium, an effect that is required for Notch-mediated cell cycle arrest. Interestingly, in cell types where Notch stimulates cell cycle progression, PTEN is transcriptionally repressed by Notch/Hes<sup>36–38</sup>. The PTEN gene locus contains both Rbpj- and Hes-binding sites, suggesting that binding to one or another is what determines the final biological output.

In line with the observation that PTEN restricts stalk cell proliferation, endothelial gain and loss of PTEN proliferation

phenotypes are reminiscent of gain and loss of Notch function in stalk cells<sup>9–11</sup>. However, in response to Notch signalling PTEN appears to only regulate EC proliferation while it is not required for tip and stalk specification. This is shown by the observation that Notch mutants not only show aberrant proliferation phenotypes in the nascent plexus but also sprouting defects<sup>9,11</sup>, while PTEN mutants only show vascular density defects. In the same line, increased levels of PTEN protect angiogenic ECs treated with DAPT from uncontrolled proliferation but fail to prevent excessive tip cell numbers. Conversely, a recent study has shown that inhibitors of the VEGFR3 kinase activity rescue the hypersprouting phenotype of Notch loss-of-function mutants, without reducing EC proliferation<sup>39</sup>. Taken together, these data suggest that Notch regulates tip cell numbers and stalk cell proliferation independently through VEGFR3 and PTEN pathways, respectively.

The predominant activity of PTEN is the dephosphorylation of PtdIns(3,4,5)P<sub>3</sub> and thus the counteraction of class I PI3K-mediated functions<sup>13,15</sup>. However, PTEN also exhibits PtdIns(3,4,5)P<sub>3</sub>-independent functions, including protein phosphatase<sup>14</sup> and non-catalytic activities<sup>13,15</sup>. In this context, PTEN can be found in the nucleus where it regulates DNA stability and cell cycle progression<sup>22,40</sup>. Several reports have highlighted the relevance of nuclear PTEN in disease<sup>22,41–43</sup>. To date, the physiological relevance of nuclear PTEN *in vivo* remains elusive. Our results reveal that both lipid phosphatase-dependent and non-catalytic activities of PTEN regulate stalk cell proliferation during sprouting angiogenesis. Inhibition of class I PI3K activity with GDC-0941 or Aurora kinase with VX680 significantly abrogates the phenotype observed on PTEN loss. However, the observation that pretreatment with either GDC-0941 or VX680 is not able to completely rescue the hyperplasia phenotype of PTEN<sup>iAEC/iAEC</sup> retinas and cultured ECs indicates that both types of activities of PTEN are required to drive the PTEN response in angiogenesis. Furthermore, genetic deletion of *Fzr1* in ECs recapitulates the phenotype observed on endothelial loss of PTEN, reinforcing the relevance of nuclear PTEN facilitating the APC/C-Fzr1/Cdh1 function. Taken together, our study provides *in vivo* evidence that nuclear PTEN is not only involved in disease such as cancer or cerebral ischaemia<sup>22,41–43</sup> but is also critical to regulate a fundamental physiological process such as angiogenesis.

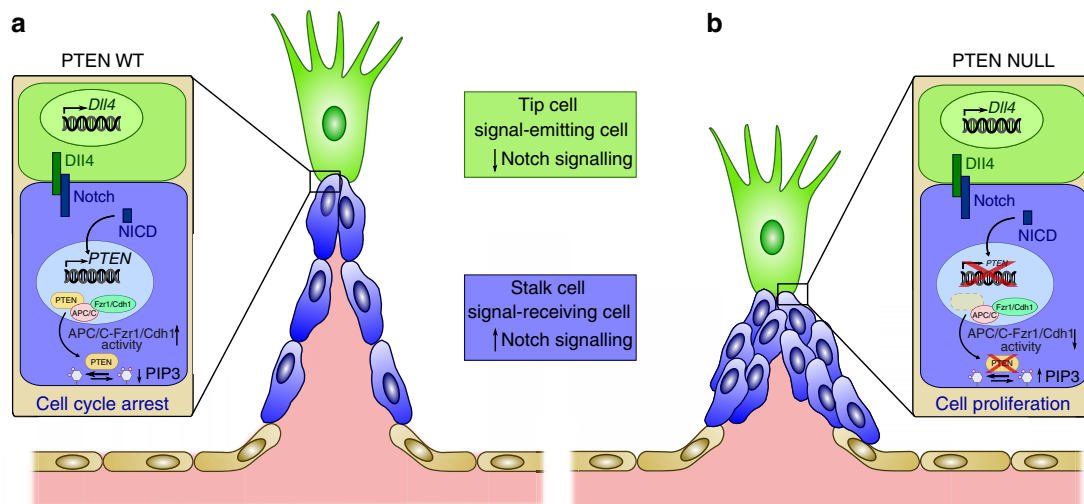


**Figure 7 | Schematic model of the role of PTEN in Dll4/Notch-mediated stalk cell cycle arrest.** (a) Activation of Notch by Dll4 induces expression of PTEN, which through its lipid phosphates activity and its nuclear function as a scaffold of the APC/C-Fzr1/Cdh1 blocks stalk cell proliferation. (b) On PTEN loss, Notch signalling fails to arrest stalk cells and result in defective sprout length and patterning.



We and others have previously shown that inhibition of class I PI3K isoform *in vivo* does not lead to blockade of EC proliferation<sup>29,44–46</sup>. Although contradictory, these observations may reflect that PTEN principally regulates EC proliferation independently of its lipid phosphatase activity<sup>22</sup>. In line with this, our data also reveal that the regulation of APC/C-Fzr1/Cdh1 by PTEN seems to play a major role in response to Notch signalling in angiogenesis. This is shown by the altered APC/C-Fzr1/Cdh1 target expression under conditions of PTEN loss and Notch activation. This observation, together with the fact that Notch stimulation in ECs results in phosphorylation of Akt<sup>47,48</sup>, suggest that Notch stimulates PTEN nuclear translocation. These findings would be in agreement with the notion that higher nuclear PTEN levels are found during G0–G1 phase than during the S phase<sup>23,24</sup>. Further experiments are needed to elucidate how PTEN accumulates in the nucleus on Notch activation.

The unique direction of the coupling of Notch and PTEN in the endothelium (Fig. 7), and the highly selective effects on the active vascular front raise the prospect that targeting this interaction and stimulation of PTEN signalling may be used therapeutically to render EC quiescence in aberrant tumour angiogenesis and in turn promote a normalization effect. Clinically, our results imply that stimulating both arms of PTEN function in ECs could render a more quiescence phenotype of highly proliferative tumour ECs<sup>2,49</sup>. However, inhibition of PI3K in the tumour stroma not only results in reduced EC proliferation but also in reduced vascular function<sup>47</sup>. It is thus tempting to speculate that promoting nuclear PTEN may offer more selectivity towards a tight control of EC proliferation.

## Methods

**Reagents.** Sources and catalogue numbers of antibodies were as follows: Cell Signaling Technology: PTEN (#9559), pS473-Akt (#4060) and pSer240/244-S6 (#2215); BD Pharmingen: p27 (#610242), cyclin-D1 (#556470), BrdU (#347580) and Aurora A Kinase (#610939); NeoMarkers: Ki67 (#RM-9106-S); Abcam: NICD (#ab27526), desmin (ab15200) and PTEN (ab32199); Santa Cruz Biotechnology: VE-cadherin (sc-6458), Geminin (sc-13015), cyclin-A (#sc-53230), Hes1 (#sc-25392) and Erg (sc-353); Millipore: Plk1 (#06-813) and Fzr1/Cdh1 (#CC43); Sigma-Aldrich:  $\beta$ -actin (A5441) and  $\alpha$ -tubulin (T6074). Isolectin GS-IB<sub>4</sub> and secondary antibodies conjugated to Alexa 488, Alexa 568 and Alexa 633, and Click-iT Edu Alexa 488 and 647 Imaging Kit were from Molecular Probes. Human (#1506-D4) and mouse Dll4 (#1389-D4) were from R&D Systems. The GDC-0941 compound was from Chem Express Haoyuan (China). The VX680 (MK-0457) compound was from Selleckchem (USA). All chemicals, unless otherwise stated, were from Sigma-Aldrich.

**Inducible genetic protocols and pharmacological inhibition in mice.** Mice were kept in individually ventilated cages and cared for according to the guidelines and legislation of the UK Home Office and Catalan Departament d'Agricultura, Ramaderia i Pesca, with procedures accepted by the Ethics Committees of CRUK-London Research Institute and IDIBELL-CEEA.

To delete PTEN in postnatal vessels, we crossed the PTEN<sup>fllox</sup> mice<sup>50</sup> into the transgenic mice expressing the tamoxifen-inducible recombinase CreER<sup>T2</sup> under the control of the endothelial *Pdgfb* promoter<sup>26</sup>. To generate *Pdgfb*CreER<sup>T2</sup>, PTEN<sup>fllox/fllox</sup> and PTEN<sup>fllox/fllox</sup> littermates, *Pdgfb*CreER<sup>T2</sup>; PTEN<sup>fllox/fllox</sup> were interbred with PTEN<sup>fllox/fllox</sup>. Cre activity and gene deletion were induced by intraperitoneal injection of 25  $\mu$ g 4-OHT (Sigma, H7904 10 mg ml<sup>-1</sup>) in all pups of the litter at P1 and P2, and retinas were collected at different time points (P5, P7 and P10). Class I PI3K signalling or Aurora kinase was inhibited in half of the pups by subcutaneous injection at 18:00 pm of P6 and 10:00 am of P7 with 37.5  $\mu$ g g<sup>-1</sup> GDC-0941 (ref. 31) or with 50  $\mu$ g g<sup>-1</sup> VX680, respectively, dissolved in dimethylsulphoxide (DMSO). Retinas were harvested at 18:00 pm of P7. Control mice were injected with DMSO only.

PTEN<sup>TG</sup> (ref. 28) was maintained in C57/BL6 background and were fed with a 19% protein-extruded rodent diet (Harlan, 2019) in a 1:1 proportion with normal diet. Notch signalling was inhibited in half of the pups by subcutaneous injection at P5 and P6, with 100 mg kg<sup>-1</sup> DAPT (Calbiochem, #565770) and retinas being harvested at P7.

*Pdgfb*CreER<sup>T2</sup>; Fzr1<sup>fllox/fllox</sup> were interbred with Fzr1<sup>fllox/fllox</sup> (ref. 51) to generate *Pdgfb*CreER<sup>T2</sup>; Fzr1<sup>fllox/fllox</sup> and Fzr1<sup>fllox/fllox</sup> littermates. Pups were injected with 25  $\mu$ g 4-OHT (10 mg ml<sup>-1</sup>) at P5 and P6 and dissected at P7.

For combined endothelial-cell-specific loss-of-function of PTEN and Jag1, we crossed PTEN<sup>fllox/fllox</sup> (ref. 50) with Jagged1<sup>fllox/fllox</sup> (ref. 52) and *Pdgfb*CreER<sup>T2</sup>

(ref. 26). To generate *Pdgfb*CreER<sup>T2</sup>; PTEN<sup>fllox/fllox</sup>; Jag1<sup>fllox/fllox</sup> (PTEN<sup>iAEC/iAEC</sup>; Jag1<sup>iAEC/iAEC</sup>), *Pdgfb*CreER<sup>T2</sup>; PTEN<sup>fllox/fllox</sup> (PTEN<sup>iAEC/iAEC</sup>) and *Pdgfb*CreER<sup>T2</sup>; Jag1<sup>fllox/fllox</sup> (Jag1<sup>iAEC/iAEC</sup>) littermates, two different types of breeding were set up; *Pdgfb*CreER<sup>T2</sup>; PTEN<sup>fllox/fllox</sup>; Jag1<sup>fllox/fllox</sup> were interbred with PTEN<sup>fllox/fllox</sup>; Jag1<sup>fllox/WT</sup> or with PTEN<sup>fllox/WT</sup>; Jag1<sup>fllox/fllox</sup>. Cre activity and gene deletion were induced by intraperitoneal injection of 25  $\mu$ g 4-OHT (10 mg ml<sup>-1</sup>) in all pups of the litter, at P1 and P3 and retinas were collected at P7. To assess proliferating ECs, the pups were injected intraperitoneally with 60  $\mu$ l of Edu (0.5  $\mu$ g<sup>-1</sup>  $\mu$ l<sup>-1</sup>) 2 h before being killed. Edu was dissolved in a 1:1 ratio DMSO:PBS.

**Immunofluorescence.** Eyes were fixed in 4% paraformaldehyde (PFA) for 2 h at 4 °C. For PTEN staining, mice were exsanguinated by transcardiac perfusion of PBS, followed by perfusion with 4% PFA before dissecting and continuing fixing the retinas with methanol at -20 °C. Samples were rehydrated for 30 min at room temperature (RT). After washing twice in PBS, retinas were permeabilized in PBS containing 1% bovine serum albumin (BSA) and 0.3% Triton X-100 overnight (ON) at 4 °C, followed by incubation with primary antibodies (PTEN (Abcam; 1:75), pSer240/244-S6 (1:100), Erg (1:200), desmin (1:200), Hes1 (1:50) and Ki67 (1:50) in permeabilization buffer ON at 4 °C. The following day, the eyes were washed three times with PBS containing 0.1% Tween (PBT), one time in Pblec buffer (1% Triton X-100, 1 mM CaCl<sub>2</sub>, 1 mM MgCl<sub>2</sub> and 1 mM MnCl<sub>2</sub> in PBS, pH 6.8) for 30 min and then incubated for 2 h at RT or ON at 4 °C in Pblec buffer containing Alexa-conjugated secondary antibodies (1:200) and IB4 (1:300), washed three times further with PBT and flat-mounted on microscope glass slides with Mowiol. For fixed confocal laser scanning microscopy, we use a Leica SP5. Images were analysed with Image J Software and Adobe Photoshop CS5.

**Embryoid bodies.** ES cells were cultured and EBs were generated, as previously described<sup>27</sup>. Briefly, ES cells were regularly cultured on a layer of irradiated DR4 mouse embryonic fibroblast in DMEM glutamax (Life Technologies, #61965-026) in the presence of 20% fetal bovine serum, HEPES (30 mM), sodium pyruvate (1.5 mM), monothioglycerol (1.5%) and leukaemia inhibitory factor (Chemicon#ESG1107, 123 units ml<sup>-1</sup>). For vascular sprouting assays, cells were cultured for two passages without feeders, depleted of leukaemia inhibitory factor and left in suspension as hanging drops. Four days after, the formed EBs were transferred to a polymerized collagen I gel with the addition of 60 ng ml<sup>-1</sup> VEGF (Peprotech). The medium was changed on day 6 and every day thereafter. Overall, 70,000 WT ES cells and 10,000 PTEN<sup>-/-</sup> ES cells were plated to generate EB. PTEN<sup>-/-</sup> ES cells were provided in ref. 53.

**Isolation and stimulation of mECs.** Mouse lungs were digested with Dispase (Life Technologies, #17105-041; 4 units ml<sup>-1</sup>) for 1 h at 37 °C, followed by positive selection with antimouse vascular endothelial-cadherin (Pharmingen, #555289) antibody coated with magnetic beads (DynaL Biotech, #110-35). Cells were seeded on a 12-well plate, and were coated with gelatin (0.5%) in DMEM/F12 supplemented with 20% fetal calf serum and EC growth factor (PromoCell, #C30140). After the first passage, the cells were re-purified with vascular endothelial-cadherin antibody-coated magnetic beads. Cells were cultured until passage 6. To induce gene deletion, 4-OHT (5  $\mu$ M) or vehicle (ethanol) was added to the cultured medium at P4 for 96 h and the medium was replaced every other day. For Dll4 stimulation, mouse Dll4 (500  $\mu$ g ml<sup>-1</sup>) was immobilized by coating culture dishes for 1 h at RT, followed by seeding mECs for 6, 8 or 24 h. Mouse and human Dll4 were used accordingly.

**In vitro measurement of mEC cell proliferation.** Overall, 10<sup>4</sup> mECs were plated in a 24-well plate for 48 h; 2 h before the termination of the experiment, BrdU (10  $\mu$ M) was added to the medium. For Ki67 staining, cells were plated for 24 h in Dll4-coated dishes. Cells were fixed in 4% PFA for 10 min at RT, permeabilized for 10 min with TBS-T (25 mM Tris HCl pH 7.4, 150 mM NaCl, 0.5% Triton X-100), blocked with TBS-T containing 2% BSA and incubated with primary antibodies BrdU (1:100) or Ki67 (1:50) at 4 °C ON. The following day, cells were washed three times with TBS-T and incubated with Alexa-conjugated secondary antibodies for 2 h at RT. DAPI was added in the final wash. Specimens were mounted in Mowiol. Cells were visualized in a Nikon-80I microscope. For pharmacological inhibition of class I PI3K and Aurora kinase, GDC-0941 (1  $\mu$ M) and VX680 (0.5  $\mu$ M) were added, respectively, on plating.

**Plasmids and transfections.** pRK5-Myc-PTEN, C124S pEGFP-PTEN-wt and pEGFP-PTEN-K13,289E expressing human WT, lipid phosphatase-inactive and nuclear-excluded PTEN mutants, respectively, were provided in ref. 22. All three PTEN mutants were subcloned with an N-terminal yellow fluorescent protein into a modified lentiviral vector TRIPZ. Lentiviral particles were prepared by transfecting HEK293FT cells with the TRIPZ vector of interest and the packaging vectors pSPAX, VSV-G and pTAT. Viral particles in the supernatant were concentrated with Lenti-X-concentrator (Clontech). mECs of P2 or P3 from *Pdgfb*CreER<sup>T2</sup>; PTEN<sup>fllox/fllox</sup> were infected with lentivirus expressing WT PTEN, PTEN (C124S) or PTEN (K13,289E) in the presence of viralplus transduction enhancer (Applied Biological Material #G698). For infection, mECs were plated at

a density of  $4 \times 10^4$  per well of 12-well plate and infected with virus from 293FT cells 48 h after transfection. After 48 h post infection, mECs were re-plated and treated with 4-OHT ( $5 \mu\text{M}$ ) to induce gene deletion for 72 h. Next,  $10^4$  mECs were plated in 24-well plate for 48 h in the presence of doxycycline ( $4 \mu\text{M}$ ); 2 h before the termination of the experiment, BrdU ( $10 \mu\text{M}$ ) was added to the medium. Cells were then fixed in 4% PFA for 10 min at RT, permeabilized for 10 min with TBS-T ( $25 \text{ mM}$  Tris HCl pH 7.4,  $150 \text{ mM}$  NaCl,  $0.5\%$  Triton X-100), blocked with TBS-T containing 2% BSA and incubated with primary antibodies BrdU (1:100) at  $4^\circ\text{C}$  ON. The following day, cells were washed three times with TBS-T and incubated with Alexa-conjugated secondary antibodies for 2 h at RT. DAPI was added in the final wash. Specimens were mounted in Mowiol. Cells were visualized in a Nikon-80I microscope.

**MTS viability assay.** mECs were cultured in 96-well plate (2,000 cells per 100  $\mu\text{l}$  culture medium per well) in the presence of the test compounds (GDC-0941 ( $1 \mu\text{M}$ ) and VX680 ( $0.5 \mu\text{M}$ )) or the respective controls for 48 h, followed by MTS assay (Promega, #G5421).

**Protein extraction and immunoblotting.** mECs, human umbilical vascular ECs (HUVECs (Lonza #CC-2519)) and lungs were lysed in  $50 \text{ mM}$  Tris HCl pH 7.4,  $5 \text{ mM}$  EDTA,  $150 \text{ mM}$  NaCl,  $50 \text{ mM}$  NaF and  $1\%$  Triton X-100 supplemented with  $2 \text{ mg ml}^{-1}$  aprotinin,  $1 \text{ mM}$  pepstatin,  $1 \text{ ng ml}^{-1}$  leupeptin,  $1 \text{ mM}$  phenylmethylsulfonylfluoride and  $1 \text{ mM}$  sodium orthovanadate, followed by clearance of lysates using microcentrifugation. Supernatants were resolved on a 10% SDS-PAGE gel, transferred on nitrocellulose membranes and probed with the indicated antibodies. Detection was performed by enhanced chemiluminescence. Uncropped immunoblots and larger blot areas are presented in Supplementary Fig. 8.

**qPCR analysis.** qPCR was performed using the following proprietary TaqMan Gene Expression assay FAM/TAMRA primers (Applied Biosystems): Dll4 (Mm00446968\_m1), Hes1 (Mm01342805\_m1), Hey1 (Mm00468865\_m), Nrarp (Mm00482529\_m1), Ephb4 (Mm00438750\_m1), Efnb2 (Mm01215897\_m1), Nr2f2 (Mm00772789\_m1) and Hprt (Mm00446968\_m1). The levels of PTEN mRNA were measured using SYBR Green I Master (Roche, #04.887.352.001) in the LightCycler480 system. Primers used are as follow: forward ( $5'$ -GTTTACCGCGCA GCATCAAAAT- $3'$ ) and reverse ( $5'$ -CCCCACTTTAGTGAC- $3'$ ).

**Luciferase assays.** Reporter assays in HUVECs were performed with the Dual Luciferase Assay System (Promega, #E1910) and a LUMAT LB 9507 luminometer (BERTHOLD Technologies). HUVECs were grown to 60–70% confluence in endothelial basal medium (EGM; Lonza #CC-3124) and co-transfected (Trans Pass V Reagents (New England Biolabs, # M2558S)) with V5-NICD (ref. 54), PTEN-luciferase reporter (pGL3 PTEN HindIII-NotI) construct<sup>37</sup> and the constitutive Renilla luciferase reporter pGL4.74hRluc/TK (Promega). Twenty-four hours after, HUVECs were lysed and reporter assays performed according to the manufacturers' protocol. To induce Notch activity with Dll4, transfected HUVECs were re-plated on Dll4-coated dishes 6 h after plasmid infection. Luciferase activity was measured after an additional 24 h. To inhibit Notch signalling, cells were pretreated for at least 1 h before stimulating with Dll4 with  $0.08 \mu\text{M}$  DBZ ((S,S)-2-[2-(3,5-Difluorophenyl)acetylamino]-N-(5-methyl-6-oxo-6,7-dihydro-5H-dibenzo[b,d]azepin-7-yl)propionamide).

**ChIP assay.** To analyse the binding sites for RBPJ located in the PTEN proximal promoter, we used the Genomatix software. For analysis, the gene bank sequence used was NG\_007466.2, which contains the promoter sequence AF406618.1. Three putative RBPJ-binding sites located at  $-1,914$ ,  $-1,492$  and  $-1,132$  positions relative to transcription initiation site<sup>37</sup> were identified. ChIP assay was performed as previously described<sup>55</sup>. Briefly, chromatin was isolated from HUVECs stimulated for 2 h with vehicle or Dll4 ( $500 \text{ ng ml}^{-1}$ ). Crosslinked chromatin was sonicated for 10 min, to medium-sized powder particles, at 0.5-min intervals, with a Bioruptor (Diagenode) and precipitated with anti-NICD or control IgG. After crosslinkage reversal, DNA was used as a template for PCR. qPCR was performed with SYBR Green I Master (Roche, #04.887.352.001) in the LightCycler480 system. Primers used are described in Supplementary Table 1.

## References

- Adams, R. H. & Alitalo, K. Molecular regulation of angiogenesis and lymphangiogenesis. *Nat. Rev. Mol. Cell Biol.* **8**, 464–478 (2007).
- Potente, M., Gerhardt, H. & Carmeliet, P. Basic and therapeutic aspects of angiogenesis. *Cell* **146**, 873–887 (2011).
- Ruhrberg, C. *et al.* Spatially restricted patterning cues provided by heparin-binding VEGF-A control blood vessel branching morphogenesis. *Genes Dev.* **16**, 2684–2698 (2002).
- Gerhardt, H. *et al.* VEGF guides angiogenic sprouting utilizing endothelial tip cell filopodia. *J. Cell Biol.* **161**, 1163–1177 (2003).
- Blanco, R. & Gerhardt, H. VEGF and Notch in tip and stalk cell selection. *Cold Spring Harb. Perspect. Med.* **3**, a006569 (2012).
- Roca, C. & Adams, R. H. Regulation of vascular morphogenesis by Notch signaling. *Genes Dev.* **21**, 2511–2524 (2007).
- Phng, L. K. & Gerhardt, H. Angiogenesis: a team effort coordinated by notch. *Dev. Cell* **16**, 196–208 (2009).
- Noseda, M. *et al.* Notch activation induces endothelial cell cycle arrest and participates in contact inhibition: role of p21Cip1 repression. *Mol. Cell Biol.* **24**, 8813–8822 (2004).
- Hellstrom, M. *et al.* Dll4 signalling through Notch1 regulates formation of tip cells during angiogenesis. *Nature* **445**, 776–780 (2007).
- Phng, L. K. *et al.* Nrarp coordinates endothelial Notch and Wnt signaling to control vessel density in angiogenesis. *Dev. Cell* **16**, 70–82 (2009).
- Benedito, R. *et al.* The notch ligands Dll4 and Jagged1 have opposing effects on angiogenesis. *Cell* **137**, 1124–1135 (2009).
- Benedito, R. & Hellstrom, M. Notch as a hub for signaling in angiogenesis. *Exp. Cell Res.* **319**, 1281–1288 (2013).
- Song, M. S., Salmena, L. & Pandolfi, P. P. The functions and regulation of the PTEN tumour suppressor. *Nat. Rev. Mol. Cell Biol.* **13**, 283–296 (2013).
- Leslie, N. R., Maccario, H., Spinelli, L. & Davidson, L. The significance of PTEN's protein phosphatase activity. *Adv. Enzyme Regul.* **49**, 190–196 (2009).
- Hopkins, B. D., Hodakoski, C., Barrows, D., Mense, S. M. & Parsons, R. E. PTEN function: the long and the short of it. *Trends Biochem. Sci.* **39**, 183–190 (2014).
- Cantley, L. C. The phosphoinositide 3-kinase pathway. *Science* **296**, 1655–1657 (2002).
- Vanhaesebroeck, B., Guillermet-Guibert, J., Graupera, M. & Bilanges, B. The emerging mechanisms of isoform-specific PI3K signalling. *Nat. Rev. Mol. Cell Biol.* **11**, 329–341 (2010).
- Hawkins, P. T., Anderson, K. E., Davidson, K. & Stephens, L. R. Signalling through Class I PI3Ks in mammalian cells. *Biochem. Soc. Trans.* **34**, 647–662 (2006).
- Hamada, K. *et al.* The PTEN/PI3K pathway governs normal vascular development and tumor angiogenesis. *Genes Dev.* **19**, 2054–2065 (2005).
- Choorapokayil, S., Weijts, B., Kers, R., de Bruin, A. & den Hertog, J. Loss of Pten promotes angiogenesis and enhanced vegfaa expression in zebrafish. *Dis. Model Mech.* **6**, 1159–1166 (2013).
- Lindsay, Y. *et al.* Localization of agonist-sensitive PtdIns(3,4,5)P3 reveals a nuclear pool that is insensitive to PTEN expression. *J. Cell Sci.* **119**, 5160–5168 (2006).
- Song, M. S. *et al.* Nuclear PTEN regulates the APC-CDH1 tumor-suppressive complex in a phosphatase-independent manner. *Cell* **144**, 187–199 (2011).
- Whiteman, D. C. *et al.* Nuclear PTEN expression and clinicopathologic features in a population-based series of primary cutaneous melanoma. *Int. J. Cancer* **99**, 63–67 (2002).
- Ginn-Pease, M. E. & Eng, C. Increased nuclear phosphatase and tensin homologue deleted on chromosome 10 is associated with G0-G1 in MCF-7 cells. *Cancer Res.* **63**, 282–286 (2003).
- Manchado, E., Eguren, M. & Malumbres, M. The anaphase-promoting complex/cyclosome (APC/C): cell-cycle-dependent and -independent functions. *Biochem. Soc. Trans.* **38**, 65–71 (2010).
- Claxton, S. *et al.* Efficient, inducible Cre-recombinase activation in vascular endothelium. *Genesis* **46**, 74–80 (2008).
- Jakobsson, L. *et al.* Heparan sulfate in trans potentiates VEGFR-mediated angiogenesis. *Dev. Cell* **10**, 625–634 (2006).
- Ortega-Molina, A. *et al.* Pten positively regulates brown adipose function, energy expenditure, and longevity. *Cell Metab.* **15**, 382–394 (2012).
- Graupera, M. *et al.* Angiogenesis selectively requires the p110alpha isoform of PI3K to control endothelial cell migration. *Nature* **453**, 662–666 (2008).
- Armulik, A., Genove, G. & Betsholtz, C. Pericytes: developmental, physiological, and pathological perspectives, problems, and promises. *Dev. Cell* **21**, 193–215 (2010).
- Edgar, K. A. *et al.* Isoform-specific phosphoinositide 3-kinase inhibitors exert distinct effects in solid tumors. *Cancer Res.* **70**, 1164–1172 (2010).
- Nelen, M. R. *et al.* Germline mutations in the PTEN/MMAC1 gene in patients with Cowden disease. *Hum. Mol. Genet.* **6**, 1383–1387 (1997).
- Wang, H. *et al.* Allele-specific tumor spectrum in pten knockin mice. *Proc. Natl Acad. Sci. USA* **107**, 5142–5147 (2010).
- Siekman, A. F. & Lawson, N. D. Notch signalling limits angiogenic cell behaviour in developing zebrafish arteries. *Nature* **445**, 781–784 (2007).
- Moya, I. M. *et al.* Stalk cell phenotype depends on integration of Notch and Smad1/5 signaling cascades. *Dev. Cell* **22**, 501–514 (2012).
- Bertrand, F. E., McCubrey, J. A., Angus, C. W., Nutter, J. M. & Sigounas, G. NOTCH and PTEN in prostate cancer. *Adv. Biol. Regul.* **56**, 51–65 (2014).
- Palomero, T. *et al.* Mutational loss of PTEN induces resistance to NOTCH1 inhibition in T-cell leukemia. *Nat. Med.* **13**, 1203–1210 (2007).
- Wong, G. W., Knowles, G. C., Mak, T. W., Ferrando, A. A. & Zuniga-Pflucker, J. C. HES1 opposes a PTEN-dependent check on survival, differentiation, and proliferation of TCRbeta-selected mouse thymocytes. *Blood* **120**, 1439–1448 (2012).
- Benedito, R. *et al.* Notch-dependent VEGFR3 upregulation allows angiogenesis without VEGF-VEGFR2 signalling. *Nature* **484**, 110–114 (2012).

40. Shen, W. H. *et al.* Essential role for nuclear PTEN in maintaining chromosomal integrity. *Cell* **128**, 157–170 (2007).
41. Trotman, L. C. *et al.* Ubiquitination regulates PTEN nuclear import and tumor suppression. *Cell* **128**, 141–156 (2007).
42. Howitt, J. *et al.* Ndfip1 regulates nuclear Pten import *in vivo* to promote neuronal survival following cerebral ischemia. *J. Cell Biol.* **196**, 29–36 (2012).
43. Freeman, D. J. *et al.* PTEN tumor suppressor regulates p53 protein levels and activity through phosphatase-dependent and -independent mechanisms. *Cancer Cell* **3**, 117–130 (2003).
44. Herbert, S. P. *et al.* Arterial-venous segregation by selective cell sprouting: an alternative mode of blood vessel formation. *Science* **326**, 294–298 (2009).
45. Nicoli, S., Knyphausen, C. P., Zhu, L. J., Lakshmanan, A. & Lawson, N. D. wmiR-221 is required for endothelial tip cell behaviors during vascular development. *Dev. Cell* **22**, 418–429 (2012).
46. Graupera, M. & Potente, M. Regulation of angiogenesis by PI3K signaling networks. *Exp. Cell Res.* **319**, 1348–1355 (2013).
47. Soler, A. *et al.* Inhibition of the p110alpha isoform of PI 3-kinase stimulates nonfunctional tumor angiogenesis. *J. Exp. Med.* **210**, 1937–1945 (2013).
48. Wusthube, J. *et al.* Cerebral cavernous malformation protein CCM1 inhibits sprouting angiogenesis by activating DELTA-NOTCH signaling. *Proc. Natl Acad. Sci. USA* **107**, 12640–12645 (2010).
49. Carmeliet, P. & Jain, R. K. Principles and mechanisms of vessel normalization for cancer and other angiogenic diseases. *Nat. Rev. Drug Discov.* **10**, 417–427 (2011).
50. Suzuki, A. *et al.* T cell-specific loss of Pten leads to defects in central and peripheral tolerance. *Immunity* **14**, 523–534 (2001).
51. Garcia-Higuera, I. *et al.* Genomic stability and tumour suppression by the APC/C cofactor Cdh1. *Nat. Cell Biol.* **10**, 802–811 (2008).
52. Brooker, R., Hozumi, K. & Lewis, J. Notch ligands with contrasting functions: Jagged1 and Delta1 in the mouse inner ear. *Development* **133**, 1277–1286 (2006).
53. Di Cristofano, A., Pesce, B., Cordon-Cardo, C. & Pandolfi, P. P. Pten is essential for embryonic development and tumour suppression. *Nat. Genet.* **19**, 348–355 (1998).
54. Guarani, V. *et al.* Acetylation-dependent regulation of endothelial Notch signalling by the SIRT1 deacetylase. *Nature* **473**, 234–238 (2011).
55. Guiu, J. *et al.* Hes repressors are essential regulators of hematopoietic stem cell development downstream of Notch signaling. *J. Exp. Med.* **210**, 71–84 (2013).

## Acknowledgements

We thank Ramon Parsons (The Mount Sinai Hospital, NY, US) for pGL3 PTEN HindIII-NotI construct and Lluís Espinosa (IMIM, Barcelona), Alba Martínez (Research

Laboratory, Catalan Institute of Oncology, IDIBELL, Barcelona) and Magali Castells (Vascular Signalling laboratory, IDIBELL) for support with experiments. This work was supported by research grants SAF2010-15661 and SAF2013-46542-P from MICINN (Spain), 2014-SGR-725 from the Catalan Government, from the People Programme (Marie Curie Actions) of the European Union's Seventh Framework Programme FP7/2007-2013/ (REA grant agreement 317250) and Ajuts Joves Investigadors from IDIBELL to M.G., and SAF2013-40922 and RD12/0036/0054 to A.B. Personal support was from FPI of the Spanish Ministry of Education (A.S.), IDIBELL (H.S.) and Ramon y Cajal fellow of the Spanish Ministry of Education (M.G. and O.C.). The work of A.C. is supported by the Ramón y Cajal award, the Basque Department of Industry, Tourism and Trade (Etortek), health (2012111086) and education (PI2012-03), Marie Curie (277043), Movember, ISCIII (PI10/01484, PI13/00031) and ERC (336343). The work of M.P. is supported by the Max Planck Society, the Deutsche Forschungsgemeinschaft (SFB 834) and an ERC Starting Grant (ANGIOMET). H.G. is supported by Cancer Research UK, the Lister Institute of Preventive Medicine, the Leducq Network Grant ARTEMIS, BIRAX and an ERC starting grant Reshape 311719.

## Author contributions

H.S., I.C., A.A.-U., J.D.S., A.S., A.A.-A., A.R., R.L. and A.F. performed experiments, H.S., I.C., A.C., M.G. and H.G. designed research, analysed data and wrote the paper; R.L., A.F., F.V., M.P., A.B. and O.C. analysed data, M.M., M.F., M.S., P.P.P. and A.B. provided reagents.

## Additional information

**Supplementary Information** accompanies this paper at <http://www.nature.com/naturecommunications>

**Competing financial interests:** The authors declare no competing financial interests.

**Reprints and permission** information is available online at <http://npg.nature.com/reprintsandpermissions/>

**How to cite this article:** Serra, H. *et al.* PTEN mediates Notch-dependent stalk cell arrest in angiogenesis. *Nat. Commun.* **6**:7935 doi: 10.1038/ncomms8935 (2015).



This work is licensed under a Creative Commons Attribution 4.0 International License. The images or other third party material in this article are included in the article's Creative Commons license, unless indicated otherwise in the credit line; if the material is not included under the Creative Commons license, users will need to obtain permission from the license holder to reproduce the material. To view a copy of this license, visit <http://creativecommons.org/licenses/by/4.0/>

## Transcriptomic profiling of urine extracellular vesicles reveals alterations of CDH3 in prostate cancer

Felix Royo<sup>1,2,\*</sup>, Patricia Zuñiga-Garcia<sup>1,\*</sup>, Verónica Torrano<sup>1,\*</sup>, Ana Loizaga<sup>3,\*</sup>, Pilar Sanchez-Mosquera<sup>1</sup>, Aitziber Ugalde-Olano<sup>4</sup>, Esperanza González<sup>1</sup>, Ana R. Cortazar<sup>1</sup>, Laura Palomo<sup>1</sup>, Sonia Fernández-Ruiz<sup>1</sup>, Isabel Lacasa-Viscasillas<sup>3</sup>, Maria Berdasco<sup>5</sup>, James D. Sutherland<sup>1</sup>, Rosa Barrio<sup>1</sup>, Amaia Zabala-Letona<sup>1</sup>, Natalia Martín-Martín<sup>1</sup>, Amaia Arruabarrena-Aristorena<sup>1</sup>, Lorea Valcarcel-Jimenez<sup>1</sup>, Alfredo Caro-Maldonado<sup>1</sup>, Jorge Gonzalez-Tampan<sup>3</sup>, Guido Cachi-Fuentes<sup>3</sup>, Manel Esteller<sup>5</sup>, Ana M. Aransay<sup>1,2</sup>, Miguel Unda<sup>3</sup>, Juan M. Falcón-Pérez<sup>1,2,6,Ω</sup>, Arkaitz Carracedo<sup>1,6,7,Ω</sup>

<sup>1</sup>CIC bioGUNE, Bizkaia Technology Park, Biscay, Spain

<sup>2</sup>Centro de Investigación Biomédica en Red de Enfermedades Hepáticas y Digestivas (Ciberehd), Spain

<sup>3</sup>Department of Urology, Basurto University Hospital, Bilbao, Spain

<sup>4</sup>Department of Pathology, Basurto University Hospital, Bilbao, Spain

<sup>5</sup>Cancer Epigenetics and Biology Program, Bellvitge Biomedical Research Institute (IDIBELL), Barcelona, Spain

<sup>6</sup>Ikerbasque, Basque Foundation for Science, Bizkaia, Spain

<sup>7</sup>Biochemistry and Molecular Biology Department, University of the Basque Country (UPV/EHU), Bizkaia, Spain

\*These authors contributed equally to this work

ΩThese authors contributed equally to this work

**Correspondence to:** Arkaitz Carracedo, **e-mail:** acarracedo@cicbiogune.es  
Juan M. Falcón-Pérez, **e-mail:** jfalcon@cicbiogune.es

**Keywords:** *extracellular vesicles, exosomes, prostate cancer, urine biomarkers*

**Received:** August 18, 2015      **Accepted:** November 26, 2015      **Published:** January 12, 2016

### ABSTRACT

**Extracellular vesicles (EV) are emerging structures with promising properties for intercellular communication. In addition, the characterization of EV in biofluids is an attractive source of non-invasive diagnostic, prognostic and predictive biomarkers. Here we show that urinary EV (uEV) from prostate cancer (PCa) patients exhibit genuine and differential physical and biological properties compared to benign prostate hyperplasia (BPH). Importantly, transcriptomics characterization of uEVs led us to define the decreased abundance of Cadherin 3, type 1 (CDH3) transcript in uEV from PCa patients. Tissue and cell line analysis strongly suggested that the status of CDH3 in uEVs is a distal reflection of changes in the expression of this cadherin in the prostate tumor. CDH3 was negatively regulated at the genomic, transcriptional, and epigenetic level in PCa. Our results reveal that uEVs could represent a non-invasive tool to inform about the molecular alterations in PCa.**

### INTRODUCTION

In the recent years, the search of biomarkers in urine has focused on the characterization of urinary extracellular vesicles (uEVs), trying to overcome the complexity and variation of this biofluid [1, 2]. Under the denomination of uEVs, there is a complex mixture of vesicles, including exosomes, microvesicles and apoptotic bodies [3, 4]. Although there are no clear markers to distinguish them, exosomes are defined as small membrane vesicles with a

diameter of 40–150 nm formed by inward budding of the membrane of late endosomes resulting in the formation of multivesicular bodies (MVB) fulfilled of intraluminal vesicles. Then, some of these (MVB) fuse to the plasma membrane releasing in this manner the exosomes to the extracellular milieu [5]. Microvesicles or ectosomes refer to plasma membrane shedding vesicles of 0.1–1 μm [6]. Apoptotic bodies are assumed to be of bigger size [7]. uEVs are released by several tissues along the urinary tract and their cargo varies depending on their origin [8].

Evidence of the presence of uEVs belonging to prostate has been already reported [9, 10] and the cargo includes proteins of prostate origin such as prostate-specific membrane antigen (PSMA) [11]. Proteomic analysis of uEVs in PCa patients has been recently carried out with promising results as a source of biomarkers [12] and the use of microRNAs as markers for this disease have been also extensively reported and reviewed [13]. Most of the studies to date focus on the comparative analysis of healthy and PCa patients. This raises the question of the existence of biomarkers that can discriminate PCa from BPH [14], a pathology that has been shown to interfere with well established biomarkers such as prostate-specific antigen (PSA) [15]. In the present work, we aimed at identifying PCa biomarkers within uEVs through the analysis of the uEV transcriptome. We selected transcripts with a presence-absence pattern in BPH and PCa, and we extensively validated the candidate transcript encoded by the *Cadherin 3, type 1* gene (CDH3). Importantly, we corroborated this observation in a miniaturized assay that could facilitate the translation of the results into the clinic. Finally, the analysis of mRNA in prostate tumor tissue from patients revealed alterations in this gene, coherent with genomic transcriptional and epigenetic changes, all pointing at the inhibition of CDH3 in PCa. Overall, our results support that analysis of uEVs could represent a non-invasive method to evaluate and monitor PCa alterations.

## RESULTS

### Characterization of uEVs from BPH and PCa patients

As a first approach, we analyzed the physical characteristics of uEVs from patients with BPH and PCa by comparing more than 23–30 independent preparations from each group (Supplementary Table S1). In order to validate the ultracentrifugation procedure [16] for isolation of uEVs, the presence of double membrane vesicles by cryo-electron microscopy (Figure 1A) and EV markers by western blot [28] was confirmed (Supplementary Figure S1). We next analyzed uEV size and number in urine of BPH and PCa patients. Nanoparticle-tracking analysis (NTA) was performed in samples before and after urine ultracentrifugation. NTA-estimated particle number was comparable before ( $8.9e^{10} \pm 1.47e^{10}$  particles/ml in BPH, and  $9.3e^{10} \pm 1.29e^{10}$  particles/ml in PCa; mean  $\pm$  s.e.m.;  $n = 5$ ;  $p > 0.05$ ) and was reduced in PCa after ultracentrifugation ( $2.49e^8 \pm 2.46e^7$  particles/ml in BPH, and  $1.56e^8 \pm 1.69e^7$  particles/ml in PCa; mean  $\pm$  s.e.m.;  $p = 0.04$ ) (Figure 1B). However, no significant changes were observed in particle size before ( $217 \pm 13.2$  nm in BPH, and  $215.8 \pm 6.9$  nm in PCa; mean  $\pm$  s.e.m.;  $n = 5$ ;  $p > 0.05$ ) or after ultracentrifugation ( $176.6 \pm 6.7$  nm in BPH, and  $182.4 \pm 6.9$  nm in PCa; mean  $\pm$  s.e.m.;  $n = 5$ ;  $p > 0.05$ ) (Figure 1C). It is worth noting that NTA analysis in

samples before ultracentrifugation could detect non-uEV particles and contaminants as positive events (and hence explain the larger number and average size) while after filtration and ultracentrifugation the values obtained are more representative of an uEV-enriched preparation. Although no statistically significant differences were found, NTA analysis revealed a trend to a different size distribution of the uEVs, with a lower abundance of small vesicles (0–100 nm) and a greater abundance of large (150–200 nm) and very large (250–350 nm) vesicles in PCa when compared with BPH (Figure 1D). Of note, we observed a size discrepancy between TEM and NTA analysis of uEVs. Although it warrants further investigation, this fact is probably due to two main factors: the technology employed by NTA to determine particle size and the potential effect of the TEM sample preparation protocol on this parameter.

Further to this characterization, we analyzed the changes in cargo in BPH and PCa. RNA concentration per vesicle was comparable in BPH and PCa uEVs ( $0.017 \pm 0.006$  ng RNA per million uEVs in BPH and  $0.0046 \pm 0.0005$  ng RNA per million uEVs in PCa; mean  $\pm$  s.e.m.;  $n = 9–10$ ; Mann Whitney U  $p = 0.13$ ). Similarly, we did not observe significant differences in protein concentration ( $0.041 \pm 0.01$   $\mu$ g protein per million uEVs in BPH and  $0.019 \pm 0.003$   $\mu$ g protein per million uEVs in PCa; mean  $\pm$  s.e.m.;  $n = 9–10$ ; Mann Whitney U  $p = 0.18$ ).

### Transcriptomic analysis of PCa and BPH uEVs

We next aimed at identifying molecular alterations in uEV cargo from PCa patients. It has been recently reported that these particles present a genuinely differential proteome in patients harboring PCa [12]. However, little is known about the transcript content of uEVs and the potential of these molecules to inform about the biological characteristics of PCa, especially when comparing to patients with BPH. To address this question, we extracted RNA of uEVs from BPH and PCa patient samples. First, we observed lack of overt changes in overall RNA size distribution (Figure 2A). Next, we labeled and hybridized BPH and PCa uEV-derived RNA into whole genome Illumina gene expression microarrays. The results showed the detection (detection  $p$ -value  $< 0.01$ ) of 1336 unique transcripts in the two groups analyzed (presence in 50% of the cases in either group was defined as positive, Supplementary Table S3), 1010 in BPH and 956 in PCa (Figure 2B). Venn analysis revealed an overlap of 47.1% from total unique transcripts in BPH and PCa (Figure 2B). We performed a further step in candidate transcript selection by identifying genes that were selectively detected in one of the two biological settings (BPH or PCa, in at least 75% of the cases). Illumina platform provides information about the probability of a probe to present a signal that is different to background noise, for which purpose we established a confidence interval of

99% ( $p < 0.01$ ). The list of differentially detected probes is shown in Figure 2C. In addition, we took advantage of the microarray analysis in order to define housekeeping genes that would have similar abundance in uEVs from BPH and PCa patients. To this end, starting from normalized signal values, we defined genes with no differential abundance ( $p$ -value  $> 0.95$  and fold change no greater than  $\pm 5\%$ ; Supplementary Table S4). From this analysis, we selected two transcripts, Eukaryotic Elongation Factor 1A1 (EEF1A1) and Ribosomal Protein L6 (RPL6), that we monitored in subsequent studies. In addition, we also included Glyceraldehyde Phosphate Dehydrogenase (GAPDH) as a housekeeping gene supported by prior studies of our group [16].

## Validation of uEV biomarkers of PCa

To ascertain the potential of candidate uEV transcripts, we performed qRT-PCR from an independent set of ultracentrifuge-purified uEV retrotranscribed RNA (using an average of  $1.5 \times 10^7$  uEVs per reaction). Firstly, the abundance of housekeeping transcripts (RPL6, EEF1A1, GAPDH) was strongly correlated (Supplementary Figure S2A), reinforcing the notion of their value as housekeeping transcripts. The use of these controls allowed us to identify 4 cases with lack of amplification in all three transcripts, which was considered an exclusion criterion for the analysis. Secondly, the evaluation of 10 transcripts of interest (From Figure 2C) revealed that two candidates, Cadherin 3, type 1 (CDH3) and CKLF-Like MARVEL Transmembrane Domain

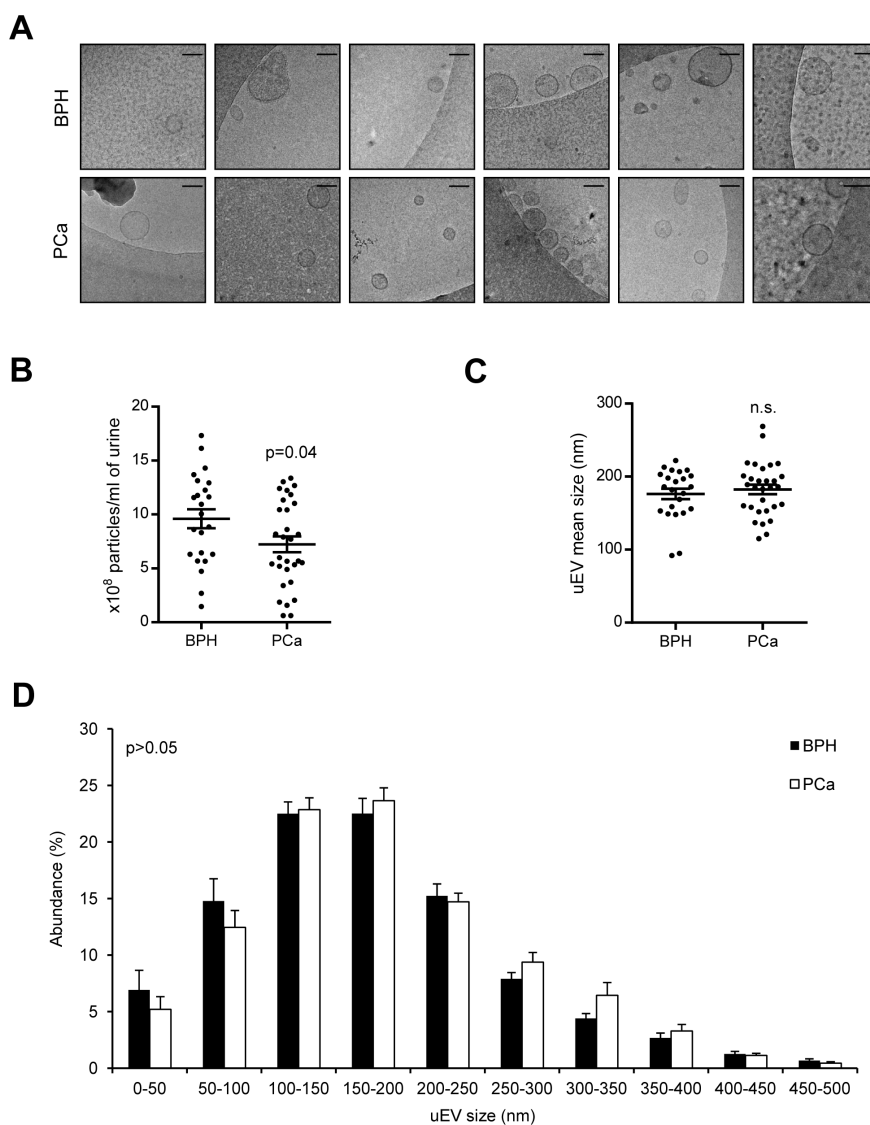


**Figure 1: Physical characterization of uEVs from PCa and BPH samples.** (A) Representatives cryo-TEM micrographs of uEVs isolated from BPH and PCa urine samples. Bar, 100 nm.  $n = 3$ . (B and C) Box-plots showing number (B) or size (C) of particles isolated from each group, indicating the mean and s.e.m. ( $n = 23$  fo BPH and 30 for PCa). (D) Size distribution of the particles isolated from each preparation (Mean  $\pm$  s.e.m. is depicted,  $n = 23$  fo BPH and 30 for PCa). Statistic test: Student  $t$  test.

Containing 3 (CMTM3), exhibited the predicted behavior in the validation dataset (Figure 2D). These two transcripts were predominantly detected in BPH uEVs, whereas the detection rate was below 30% in PCa uEVs. Of note, we confirmed that these transcripts were contained in uEVs, since they exhibited resistance to RNase treatment (Supplementary Figure S2B).

Our results demonstrate that we can identify transcripts with differential abundance in PCa uEVs, employing 50 mL of urine and using an ultracentrifugation-based method for uEV isolation [16]. However, biomarker identification requires miniaturization of the assay with the consequent scaling down of the starting material. To refine our detection method, we employed a commercial exosomal RNA purification procedure (Norgen Biotek) in an independent set of samples that allowed us to reduce urine volume to 10 mL. We then performed qRT-PCR from Norgen-purified retrotranscribed RNA. We evaluated the expression level of the two best candidates, CMTM3 and CDH3. As shown before, the two housekeeping transcripts employed (GAPDH and RPL6) exhibited a strong and significant correlation (Supplementary Figure S2C). Interestingly, this purification method precluded detection of CMTM3, while recapitulated the reduction in CDH3 with higher sensitivity using normalization against RPL6 ( $0.69 \pm 0.1$ ; mean  $\pm$  s.e.m.;  $p = 0.055$ ) and GAPDH ( $0.65 \pm 0.08$ ; mean  $\pm$  s.e.m.;  $p = 0.01$ ) (Figure 2E).

Taken together, our transcriptomic analysis reveals that CDH3 abundance is reduced in PCa uEVs and sets the basis for PCa biomarker search based on uEV transcript analysis.

### uEVs are indicators of PCa alterations

Our results convincingly show that CDH3 abundance is reduced in uEVs from PCa patients. On the basis of these results, we hypothesized that the alteration observed in uEVs might be a reflection of transcriptomic changes in the prostate tumor.

In order to confirm our hypothesis, we studied the expression of CDH3, in a set of BPH and PCa tissue specimens. The results of CDH3 expression analysis demonstrated that it was significantly decreased in tissue from patients with PCa compared to BPH ( $0.52 \pm 0.12$ ; mean  $\pm$  s.e.m.;  $p = 0.018$ ), in full coherence with our observation in uEVs (Figure 3A). Of note, these results could lead to the notion that the association between transcriptomic tumor cell landscape and exosome RNA cargo correlate at high frequency. However, prior studies from our lab showed that known cancer genes, such as PTEN, do not exhibit a direct correlation between uEVs mRNA abundance and PTEN tumor alterations [16], suggesting a selective process in cargo loading into uEVs.

Next, we ascertained the potential extrapolation of this observation to other biological contexts, such as a panel of benign prostate cells and metastatic

prostate cancer cell lines and large human PCa datasets. Interestingly, the expression of CDH3 in prostate cell lines revealed a down-regulation of the transcript in metastatic cancer cell lines (black), compared to benign-immortalized cells (grey) ( $0.17 \pm 0.07$ ; mean  $\pm$  s.e.m.) (Figure 3B). Importantly, this observation was confirmed in two datasets where the expression of PCa specimens was compared to biopsies from healthy patients [24, 25] (Figure 3C) and was in full agreement with a previous report [29].

We also monitored the expression levels of other transcripts identified in uEVs. On the one hand, CMTM3 expression, which was shown to be down-regulated in the ultracentrifugation uEVs (but not detected with Norgen extraction method), showed a significant reduction in PCa compared with BPH tissues, but this result was not reproduced in publicly available PCa datasets and exhibited only a modest trend in PCa cell lines (Supplementary Figure S3A–S3C). On the other hand, our housekeeping genes RPL6 and EEF1A1 showed no consistent alterations throughout the same analytical layout (Supplementary Figure S3A–S3C).

We next ask whether the reduction of CDH3 expression observed in PCa could be extrapolated to other urogenital cancers. Data mining analysis was performed in bladder and renal cancer datasets (www.oncomine.org, [30]). Although there was certain consistency in the alteration of CDH3 expression within the same tumor type, the directionality of the alterations was not preserved among the different tumor types (Supplementary Figure S3D).

In order to address whether gene expression alterations in CDH3 could be translated in a decrease in the protein expression, we took advantage on publicly available initiatives for immunoreactivity analysis. ProteinAtlas (www.proteinatlas.org, [31–35]) allows the visualization of immunohistochemistry (IHC) staining in a wide array of tissues. There was data available for CDH3 staining with high quality IHC-specific antibodies. Importantly, the staining in normal prostate epithelia corroborated the staining of basal prostate epithelial cells, in agreement with reports in this and other epithelial tissues [29, 36, 37] (Figure 3E, middle panel and Supplementary Figure S3F). As predicted, CDH3 expression was decreased in PCa specimens. This result was particularly evident in tumor samples with adjacent non-neoplastic tissue (Figure 3D). Interestingly, CDH3 sub-cellular distribution was altered in tumor cells, with a predominant loss of membrane immunoreactivity (Figure 3D).

We next asked the molecular cues leading to the down-regulation of CDH3 in PCa. On the one hand, we studied the genomic and epigenetic changes occurring in *CDH3* locus. The genomic analysis showed frequent shallow deletions of *CDH3* in four independent PCa datasets (Figure 4A, [24, 25, 38, 39]). Moreover, epigenetic analysis of *CDH3* promoter indicated increased methylation in PCa and a correlation between the methylation status of the locus and the transcript abundance

(Figure 4B, 4C; [38, 39]), in line with a previous report [29]). On the other hand, we evaluated the association of CDH3 expression with well-known upstream regulators. Tp63 is a basal prostate epithelial marker which is down-regulated in PCa specimens [40–42], and that has been reported to regulate CDH3 expression [43]. We found a strong correlation between the mRNA expression of Tp63 and CDH3 in prostate specimens, which suggests that transcriptional regulation of this cadherin downstream p63 is at play in PCa (Figure 4D). Altogether, our results indicate that genomic loss,

transcriptional regulation and promoter methylation contribute to the down-regulation of CDH3 in PCa.

## DISCUSSION

Extracellular vesicles including exosomes have been detected and characterized in urine [2, 44, 45]. These vesicles vary in composition and are associated with different diseases [12, 46]. Importantly, recent evidence suggests that PCa might exhibit alterations in the composition of uEVs [12, 47, 48]. The majority of

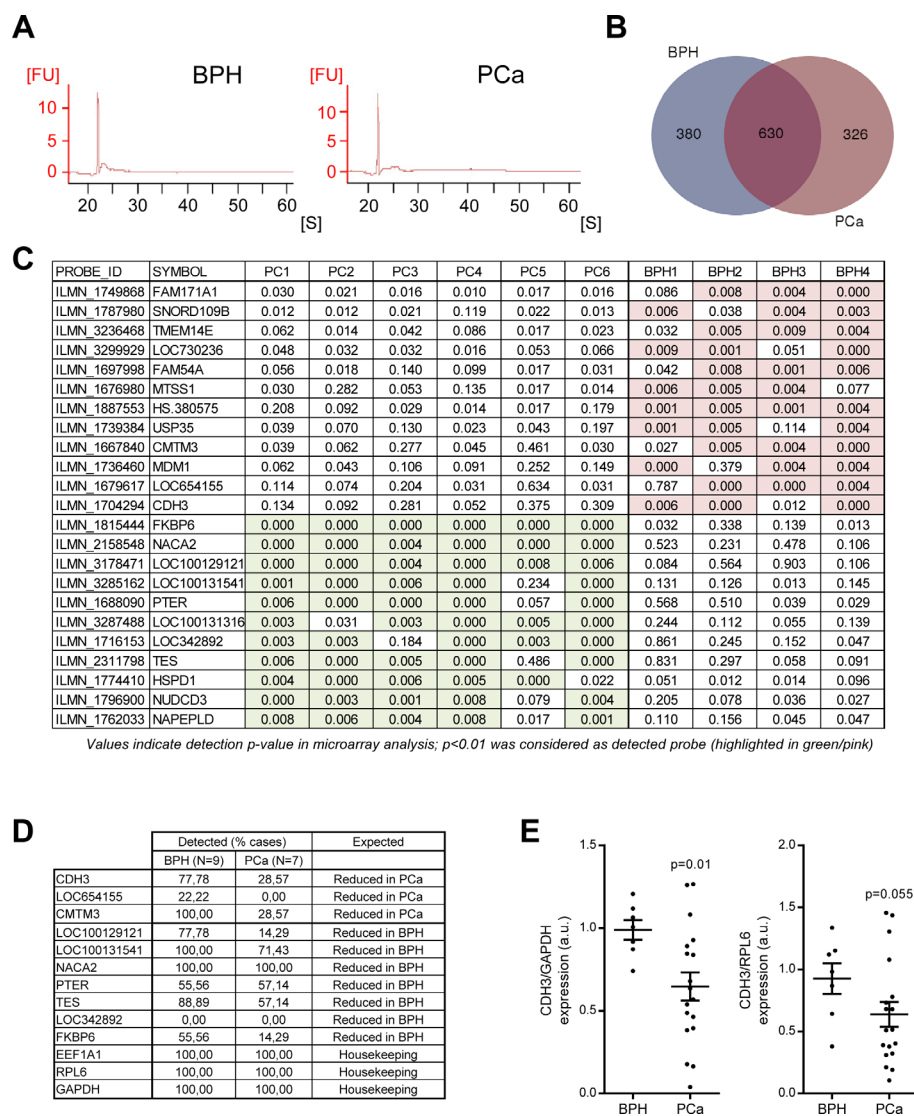


**Figure 2: Transcriptomic analysis of uEVs reveals transcripts with differential abundance in BPH and PCa.** (A) Representative analysis of RNA size distribution obtained from the Bioanalyzer analysis of uEV preparations.  $n = 4-6$ . (B) Venn diagram depicting the number of unique transcripts identified in each experimental condition ( $n = 4$  for BPH and  $n = 6$  for PCa). (C) Transcripts exhibiting a presence-absence pattern in BPH and PCa. The transcripts shown complied with the requirements of being absent in one condition and with a minimum presence of 75% of cases in the other. Detection  $p$ -value is presented, where a limit was established in  $p < 0.01$  in the microarray analysis (significant conditions are highlighted in pink or green in BPH and PCa, respectively). (D) Detection of ultracentrifugation-purified candidate uEV transcripts by qRTPCR. Detection was established as consistent amplification in the technical settings employed in the assay.  $n = 7$  for BPH and  $n = 9$  for PCa. (E) Transcript abundance of CDH3 relative to GAPDH (*left*) and RPL6 (*right*) in Norgen-purified uEVs-associated RNA samples.  $n = 6-7$  for BPH and  $n = 18$  for PCa. FU: fluorescence units. S: seconds. Error bar represents s.e.m. a.u. = Arbitrary units. Statistic test: Mann Whitney  $U$  test (E).



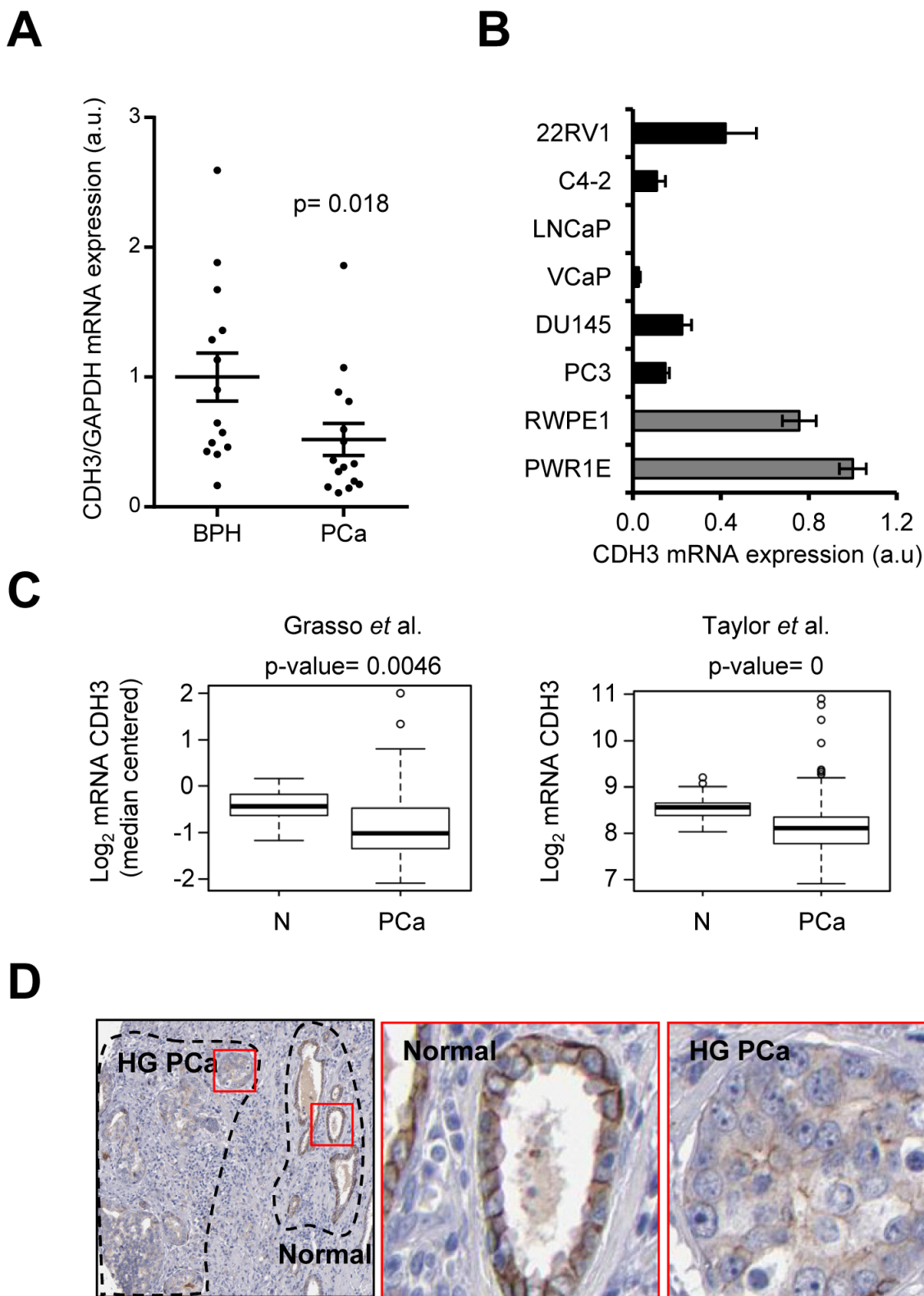


**Figure 3: CDH3 expression is reduced in PCa specimens.** (A) CDH3 expression in tissue biopsies from BPH and PCa. CDH3 expression relative to GAPDH is shown.  $n = 14$  for BPH and  $n = 15$  for PCa. (B) CDH3 expression in a panel of metastatic prostate cancer cell lines (black bars) and benign immortalized prostate cell lines (grey bars) relative to beta-Actin.  $n = 3$ . (C) CDH3 expression in two PCa datasets (Taylor PCa  $n = 150$ , normal  $n = 29$ ; Grasso PCa  $n = 76$ , normal  $n = 12$ ). (D) Representative images of immunohistochemical detection of CDH3 protein in PCa. Middle panel corresponds to a normal area and right panel to high grade PCa (HG PCa). Data source: Human Protein Atlas. Statistic test: Mann Whitney  $U$  test (A), Student  $t$  test (C).

the studies are carried out comparing healthy individuals with PCa patients. It is worth noting that there is an increasing incidence of BPH in association with age [14], and the interference that this might introduce to biomarker identification is poorly understood. To address this question, we have performed a transcriptomics analysis comparing the mRNA content of uEVs from patients with BPH or PCa. The results reveal that urine from these two groups have significant alterations in vesicle number. Little is known about alterations in EV production in different pathologies as compared to the nature of its cargo and this aspect warrants further investigation. Importantly, we found a markedly different transcriptomics profile in uEVs from BPH and PCa. We were able to reduce a whole genome analysis (which revealed 1336 transcripts detected in uEV preparations) to two candidate transcripts (CMTM3 and CDH3) with decreased abundance in PCa. Interestingly, the miniaturization of the assay employing

an alternative purification method revealed that CMTM3 detection is sensitive to the approach used. This suggests that the detection of uEV transcripts might be affected by the uEV purification protocol and calls for further refinement and characterization of the selectivity and specificity of the uEV isolation methods.

Placental cadherin (P-Cad or CDH3) has been widely studied in cancer [37, 49–59]. This protein regulates cell-cell adhesion processes and cellular differentiation. Interestingly, both oncogenic and tumor suppressive activities of this gene have been described in tissue-specific manner [37, 49–59]. We observe that CDH3 mRNA levels are down-regulated in PCa. This is coherent with preliminary observations at the protein level. It has been suggested that CDH3 is down-regulated and exerts tumor suppressive functions in hepatocellular carcinoma [50] and a prior study reported changes of CDH3 in PCa [29]. Our data suggest that CDH3 may be exerting tumor suppressive activities in PCa.

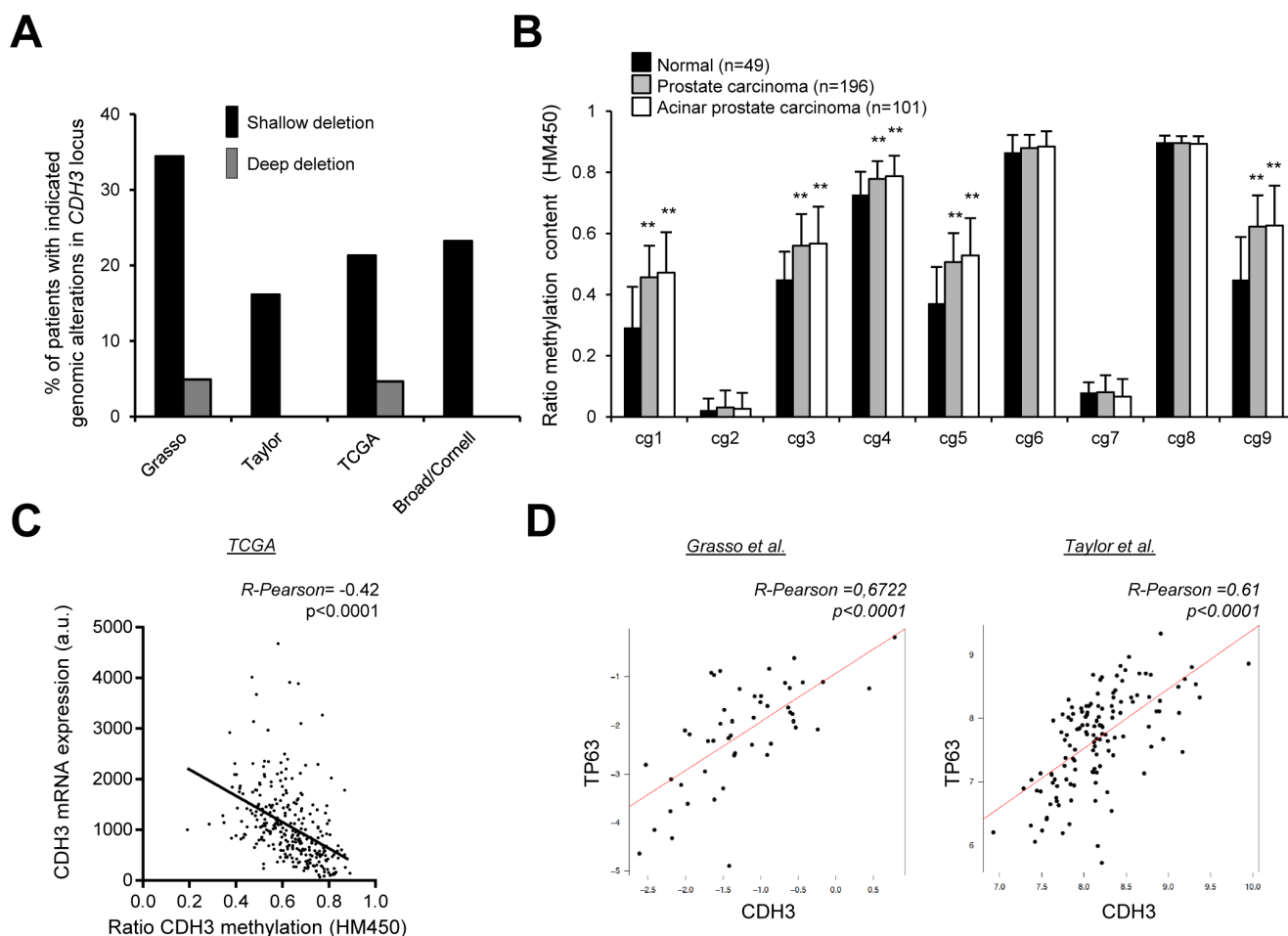


**Figure 4: Evaluation of the molecular events accounting for CDH3 down-regulation in PCa.** (A) Analysis of the genomic alterations in *CDH3* locus in four PCa databases (Taylor  $n = 93$ , Grasso  $n = 61$ , TCGA  $n = 258$ , Broad  $n = 56$ ). (B and C) Promoter methylation analysis from TCGA database evaluating methylation in *CDH3* locus (B)  $n = 49$  for normal tissue,  $n = 101$  acinar PCa and  $n = 196$  for PCa) and the correlation between methylation status and CDH3 mRNA expression (C)  $n = 294$ ). (D) Correlation analysis between CDH3 and TP63 expression in two independent datasets. (Grasso,  $n = 49$ ; Taylor,  $n = 131$ ; primary tumors). Statistic test: Student *t* Test (B); Pearson's coefficient (*R*) (C, D).

We show that the regulation of CDH3 expression in PCa occurs at multiple levels. On the one hand, genomic and epigenetic analysis strongly suggests that deletion and methylation of the locus accounts for changes in expression. On the other hand, we find potential regulations at the level of upstream transcriptional regulators. Prior studies showed that CDH3 is a basal epithelial cell marker [29, 37]. Interestingly, Tp63, an upstream regulator of CDH3 [36], presents similar behavior to our gene of interest. Tp63 localizes to basal epithelial cells and is down-regulated in PCa [40–42, 60]. Our correlation analysis in public PCa supports the notion that p63 is a transcriptional upstream regulator of CDH3.

Of note, immunoreactivity analysis has provided preliminary evidence of mis-localization of CDH3 in PCa cells compared to non-tumoral counterparts, Interestingly, this alteration is also observed in other cancers and is associated to poor prognosis [59].

Altogether, our data show multiple means of regulation (genomic loss, DNA methylation, transcriptional regulation, and protein mis-localization) that could potentially lead to the alteration of CDH3 function in PCa.

The function of EVs in cell communication and cancer aggressiveness has emerged in the past years [61, 62]. While their use as source of biomarkers is under intense investigation, there is limited evidence about their potential role as readouts of the tumoral genetic alterations [9]. This study informs about the properties of uEVs to reflect genetic alterations in the tumor of origin. We find that the decrease in abundance of CDH3 in uEVs is coherent with mRNA changes in the prostate tumor cells. This data opens new avenues in the non-invasive characterization of genetic alterations in PCa using uEVs, with the consequent potential for patient stratification.

## MATERIALS AND METHODS

### Patient samples and cell lines analysis

All urine samples were obtained from the Basque Biobank for research (BIOEF, <http://www.biobancovasco.org>, Basurto University Hospital) upon informed consent and with evaluation and approval from the corresponding ethics committee (CEIC code OHEUN11-12 and OHEUN14-14). Inclusion criteria: For BPH patients, samples were obtained from cases with normal PSA, with symptomatic alterations (polyuria, distress), and that were scheduled for surgery. For PCa cases, samples were obtained from patients with primary localized cancer diagnosed *de novo* and that were scheduled for radical prostatectomy. Urine (40–100 ml) was collected by spontaneous urination between 8–10 AM, in fasting conditions. Patient information, tumor characteristics and urine volume is described in Supplementary Table S1. For prostate tissue specimens, samples were prepared and

diagnosed as described in [16]. Cell lines were cultured as described in [17] and RNA was harvested in conditions of exponential growth.

### Urine extracellular vesicle purification

uEV isolation by ultracentrifugation was performed as described in [16]. Briefly, urine was centrifuged at  $2000 \times g$  for 5 min to remove cell debris and filtered through 0.22  $\mu\text{m}$  pore-filter before frozen at  $-80^\circ\text{C}$ . For uEV isolation sample was thawed and subjected to two sequential centrifugations of  $11500 \times g$  for 30 min and second  $118000 \times g$  for 90 minutes. The pellet containing uEVs was resuspended in 150  $\mu\text{l}$  of cold PBS and frozen for later processing. RNase treatment was not performed unless otherwise specified.

### Western blot

Western blot was performed as described [18], using CD26 (Abcam, Cambridge, UK), CD63 (clone H5C6; from Developmental Studies Hybridoma Bank, Iowa, US), CD13 (clone 3D8; from Santa Cruz Biotechnology Inc.), FLT1 (clone 18; from BD Biosciences) and AQP2 (Sigma-Aldrich) antibodies.

### Transmission electron microscopy (TEM) analysis

For cryo-electron microscopy, uEV preparations were directly adsorbed onto glow-discharged holey carbon grids (100 Holey carbon film of Cu with mesh 200; Quantifoil®, Germany). Grids were blotted at 95% humidity and rapidly plunged into liquid ethane with the aid of VITROBOT (Maastricht Instruments BV, The Netherlands). Vitrified samples were imaged at liquid nitrogen temperature using a JEM-2200FS/CR transmission cryo-electron microscope (JEOL, Japan) equipped with a field emission gun and operated at an acceleration voltage of 200 kV.

### Size analysis and size distribution

Size distribution within uEV preparations was analyzed by nanoparticle-tracking analysis (NTA) by measuring the rate of Brownian motion using a NanoSight LM10 system (Malvern, U.K.), which is equipped with a fast video capture and particle-tracking software. NTA post-acquisition settings were kept constant for all samples, and each video was analyzed to give the mean, mode, and median vesicle size, as well as an estimation of the concentration [19]. For each preparation, two videos of 30 seconds each were taken. For each video, at least 200 tracks were completed in post-capture tracking analysis.

## Transcriptomic analysis

Total RNA isolation from uEV was achieved by RNeasy columns (Qiagen, Inc). The integrity, size and quantification were evaluated in RNA Pico Chips (Bioanalyzer; Agilent Technologies). For transcriptomic analysis of mRNA-associated uEVs, Illumina whole genome (HumanHT-12\_V4.0; DirHyb, nt) method was used as reported [20]. cRNA synthesis was obtained out of 2–25 ng of Total RNA, with TargetAmp™ Nano-g™ Biotin-aRNA Labeling Kit for the Illumina® System (Epicentre, Cat# TAN07924) and subsequent amplification, labelling and hybridization were performed according to “Whole-Genome Gene Expression Direct Hybridization” Illumina Inc.’s protocol, except the hybridization cRNA concentration, which was 285 ng instead of the standard 750 ng. Raw expression data were background-corrected, log<sub>2</sub>-transformed and quantile-normalized using the lumi R package [21], available through the Bioconductor repository. Probes with a “detection *p*-value” lower than 0.01 in at least one sample were regarded as detected.

## Retrotranscription and quantitative real time PCR analysis

To extract RNA from uEVs isolated by ultracentrifugation, we employed miRCURY™ RNA Isolation Kit Cell & Plant (Exiqon). In average, 1.5e<sup>7</sup> vesicles were used per retrotranscription reaction. In addition, a set of samples was extracted by Norgen Biotek Exosomal RNA purification kit, following the manufacturers’ instructions. For cell lines, RNA was extracted using NucleoSpin® RNA isolation kit from Macherey-Nagel (ref: 740955.240C). cDNA was synthesized from 0.1–1 µg of RNA using Superscript III (Life Technologies) following the manufacturer’s recommendations. For prostate tissue samples, RNA was extracted as reported in [16]. Quantitative Real Time PCR (Taqman qRT-PCR) was performed as previously described [18]. Universal Probe Library (Roche) primers and probes employed are detailed in Supplementary Table S2. β-ACTIN (Hs99999903\_m1) and GAPDH (Hs02758991\_g1) housekeeping assays were from Applied Biosystems and showed similar results.

## DNA methylation

Raw intensity *CDH3* DNA methylation was extracted from The Cancer Genome Atlas dataset (<https://tcga-data.nci.nih.gov/tcga/>) based on Illumina’s 450K methylation array. Data analysis from normal tissues (*n* = 49), prostate carcinoma (*n* = 196) and acinar prostate carcinoma (*n* = 101) were included. A three step-based normalization procedure was performed using the lumi

[21] package available for Bioconductor [22], under the R statistical environment [23], consisting in color bias adjustment, background level adjustment and quantile normalization across arrays, as specified in [21]. Methylation level (β-value) for each of the 485, 577 CpG sites was calculated as the ratio of methylated signal divided by the sum of methylated and unmethylated signals plus 100. After normalization step, probes related to X and Y chromosomes were removed as well as those containing a SNPs with a frequency > 1% (1000 Genome project) in the probe sequence or interrogated CpG site.

## Bioinformatics analysis and statistics

The following statistical analysis were employed:

Database normalization: all the datasets used for the data mining analysis were downloaded from GEO and subjected to background correction, log<sub>2</sub> transformation and quartile normalization. In the case of using a pre-processed dataset, this normalization was reviewed and corrected if required.

For *CDH3* genomic analysis, data from PCa patients with copy number alteration information in Taylor [24], Grasso [25], Broad/Cornell [26] and Robinson [27] et al. datasets was extracted from *cbiportal.org*.

## Correlation analysis

Pearson correlation test was applied to analyze the relation between paired genes. From this analysis, Pearson’s coefficient (R) indicates the existing linear correlation (dependence) between two variables *X* and *Y*, giving a value between +1 and -1 (both included), where 1 is total positive correlation, 0 is no correlation, and -1 is total negative correlation. The *p*-value indicates the significance of this R coefficient.

## Statistical analysis

Data represent mean ± s.e.m. of pooled experiments unless otherwise stated. For data mining analysis, ANOVA test was used for multi-component comparisons. Student T test or Mann Whitney *U* test for two-group parametric or non-parametric comparisons, respectively. The confidence level used for all the statistical analyses was of 0.95 (alpha value = 0.05). Two-tail statistical analysis was applied for experimental design without predicted result and one-tail for validation experiments.

## ACKNOWLEDGMENTS AND FUNDING

Apologies to those whose related publications were not cited due to space limitations. We thank David Gil and Sandra Delgado from electron microscopy CIC bioGUNE platform for their technical assistance in the cryo-TEM analysis of EVs. We are thankful to the Basque Biobank

for research (BIOEF), for the acquisition, maintenance and distribution of urine samples. The work of AC is supported by the Ramón y Cajal award, the Basque Department of Industry, Tourism and Trade (Etortek), Health (2012111086) and Education (PI2012–03), Marie Curie (277043), Movember Foundation (GAP1), ISCIII (PI10/01484, PI13/00031) and ERC (336343). The work of JF-P is supported by ISCIII (PI12/01604). RB is supported by MINECO (BFU2014-52282-P, BFU2011-25986) and Basque Government (PI2012/42). N.M-M. is supported by the Spanish Association Against Cancer (AECC). A.A-A and L.V-J are supported by the Basque Government of education.

## CONFLICTS OF INTEREST

The authors declare no conflicts of interest.

## REFERENCES

- Pisitkun T, Johnstone R, Knepper MA. Discovery of urinary biomarkers. *Mol Cell Proteomics*. 2006; 5:1760–1771.
- Pisitkun T, Shen RF, Knepper MA. Identification and proteomic profiling of exosomes in human urine. *Proc Natl Acad Sci U S A*. 2004; 101:13368–13373.
- Kalra H, Simpson RJ, Ji H, Aikawa E, Altevogt P, Askenase P, Bond VC, Borrás FE, Breakefield X, Budnik V, Buzas E, Camussi G, Clayton A, et al. Vesiclepedia: a compendium for extracellular vesicles with continuous community annotation. *PLoS Biol*. 2012; 10:e1001450.
- Raposo G, Stoorvogel W. Extracellular vesicles: exosomes, microvesicles, friends. *J Cell Biol*. 2013; 200:373–383.
- Mathivanan S, Ji H, Simpson RJ. Exosomes: extracellular organelles important in intercellular communication. *Journal of proteomics*. 2010; 73:1907–1920.
- Cocucci E, Racchetti G, Meldolesi J. Shedding microvesicles: artefacts no more. *Trends Cell Biol*. 2009; 19:43–51.
- Crescitelli R, Lasser C, Szabo TG, Kittel A, Eldh M, Dianzani I, Buzas EI, Lotvall J. Distinct RNA profiles in subpopulations of extracellular vesicles: apoptotic bodies, microvesicles and exosomes. *Journal of extracellular vesicles*. 2013; 2.
- Miranda KC, Bond DT, McKee M, Skog J, Paunescu TG, Da Silva N, Brown D, Russo LM. Nucleic acids within urinary exosomes/microvesicles are potential biomarkers for renal disease. *Kidney Int*. 2010; 78:191–199.
- Nilsson J, Skog J, Nordstrand A, Baranov V, Mincheva-Nilsson L, Breakefield XO, Widmark A. Prostate cancer-derived urine exosomes: a novel approach to biomarkers for prostate cancer. *Br J Cancer*. 2009; 100:1603–1607.
- Duijvesz D, Luider T, Bangma CH, Jenster G. Exosomes as biomarker treasure chests for prostate cancer. *Eur Urol*. 2011; 59:823–831.
- Mitchell PJ, Welton J, Staffurth J, Court J, Mason MD, Tabi Z, Clayton A. Can urinary exosomes act as treatment response markers in prostate cancer? *J Transl Med*. 2009; 7:4.
- Overbye A, Skotland T, Koehler CJ, Thiede B, Seierstad T, Berge V, Sandvig K, Llorente A. Identification of prostate cancer biomarkers in urinary exosomes. *Oncotarget*. 2015; 6:30357–76. doi: 10.18632/oncotarget.4851.
- Hessvik NP, Sandvig K, Llorente A. Exosomal miRNAs as Biomarkers for Prostate Cancer. *Frontiers in genetics*. 2013; 4:36.
- Priest R, Garzotto M, Kaufman J. Benign prostatic hyperplasia: a brief overview of pathogenesis, diagnosis, and therapy. *Techniques in vascular and interventional radiology*. 2012; 15:261–264.
- Pienta KJ. Critical appraisal of prostate-specific antigen in prostate cancer screening: 20 years later. *Urology*. 2009; 73:S11–20.
- Ugalde-Olano A, Egia A, Fernandez-Ruiz S, Loizaga-Iriarte A, Zuniga-Garcia P, Garcia S, Royo F, Lacasa-Viscasillas I, Castro E, Cortazar AR, Zabala-Letona A, Martin-Martin N, Arruabarrena-Aristorena A, et al. Methodological aspects of the molecular and histological study of prostate cancer: focus on PTEN. *Methods*. 2015; 77–78:25–30.
- Kim DK, Lee J, Kim SR, Choi DS, Yoon YJ, Kim JH, Go G, Nhung D, Hong K, Jang SC, Kim SH, Park KS, Kim OY, et al. EVpedia: a community web portal for extracellular vesicles research. *Bioinformatics*. 2015; 31:933–939.
- Taylor BS, Schultz N, Hieronymus H, Gopalan A, Xiao Y, Carver BS, Arora VK, Kaushik P, Cerami E, Reva B, Antipin Y, Mitsiades N, Landers T, et al. Integrative genomic profiling of human prostate cancer. *Cancer Cell*. 2010; 18:11–22.
- Grasso CS, Wu YM, Robinson DR, Cao X, Dhanasekaran SM, Khan AP, Quist MJ, Jing X, Lonigro RJ, Brenner JC, Asangani IA, Ateeq B, Chun SY, et al. The mutational landscape of lethal castration-resistant prostate cancer. *Nature*. 2012; 487:239–243.
- Jarrard DF, Paul R, van Bokhoven A, Nguyen SH, Bova GS, Wheelock MJ, Johnson KR, Schalken J, Bussemakers M, Isaacs WB. P-Cadherin is a basal cell-specific epithelial marker that is not expressed in prostate cancer. *Clin Cancer Res*. 1997; 3:2121–2128.
- Rhodes DR, Yu J, Shanker K, Deshpande N, Varambally R, Ghosh D, Barrette T, Pandey A, Chinnaiyan AM. ONCOMINE: a cancer microarray database and integrated data-mining platform. *Neoplasia*. 2004; 6:1–6.
- Berglund L, Bjorling E, Oksvold P, Fagerberg L, Asplund A, Szigartyo CA, Persson A, Ottosson J, Wernerus H, Nilsson P, Lundberg E, Sivertsson A, Navani S, et al. A gene-centric Human Protein Atlas for expression profiles based on antibodies. *Mol Cell Proteomics*. 2008; 7:2019–2027.
- Ponten F, Jirstrom K, Uhlen M. The Human Protein Atlas—a tool for pathology. *J Pathol*. 2008; 216:387–393.

24. Uhlen M, Bjorling E, Agaton C, Szigyarto CA, Amini B, Andersen E, Andersson AC, Angelidou P, Asplund A, Asplund C, Berglund L, Bergstrom K, Brumer H, et al. A human protein atlas for normal and cancer tissues based on antibody proteomics. *Mol Cell Proteomics*. 2005; 4:1920–1932.
25. Uhlen M, Fagerberg L, Hallstrom BM, Lindskog C, Oksvold P, Mardinoglu A, Sivertsson A, Kampf C, Sjostedt E, Asplund A, Olsson I, Edlund K, Lundberg E, et al. Proteomics. Tissue-based map of the human proteome. *Science*. 2015; 347:1260419.
26. Uhlen M, Oksvold P, Fagerberg L, Lundberg E, Jonasson K, Forsberg M, Zwahlen M, Kampf C, Wester K, Hober S, Wernerus H, Bjorling L, Ponten F. Towards a knowledge-based Human Protein Atlas. *Nat Biotechnol*. 2010; 28:1248–1250.
27. Paredes J, Figueiredo J, Albergaria A, Oliveira P, Carvalho J, Ribeiro AS, Caldeira J, Costa AM, Simoes-Correia J, Oliveira MJ, Pinheiro H, Pinho SS, Mateus R, et al. Epithelial E- and P-cadherins: role and clinical significance in cancer. *Biochim Biophys Acta*. 2012; 1826:297–311.
28. Vieira AF, Ricardo S, Ablett MP, Dionisio MR, Mendes N, Albergaria A, Farnie G, Gerhard R, Cameselle-Teijeiro JF, Seruca R, Schmitt F, Clarke RB, Paredes J. P-cadherin is coexpressed with CD44 and CD49f and mediates stem cell properties in basal-like breast cancer. *Stem Cells*. 2012; 30:854–864.
29. Cerami E, Gao J, Dogrusoz U, Gross BE, Sumer SO, Aksoy BA, Jacobsen A, Byrne CJ, Heuer ML, Larsson E, Antipin Y, Reva B, Goldberg AP, et al. The cBio cancer genomics portal: an open platform for exploring multidimensional cancer genomics data. *Cancer Discov*. 2012; 2:401–404.
30. Gao J, Aksoy BA, Dogrusoz U, Dresdner G, Gross B, Sumer SO, Sun Y, Jacobsen A, Sinha R, Larsson E, Cerami E, Sander C, Schultz N. Integrative analysis of complex cancer genomics and clinical profiles using the cBioPortal. *Sci Signal*. 2013; 6:p11.
31. Grisanzio C, Signoretti S. p63 in prostate biology, pathology. *J Cell Biochem*. 2008; 103:1354–1368.
32. Signoretti S, Waltregny D, Dilks J, Isaac B, Lin D, Garraway L, Yang A, Montironi R, McKeon F, Loda M. p63 is a prostate basal cell marker and is required for prostate development. *Am J Pathol*. 2000; 157:1769–1775.
33. Weinstein MH, Signoretti S, Loda M. Diagnostic utility of immunohistochemical staining for p63, a sensitive marker of prostatic basal cells. *Mod Pathol*. 2002; 15:1302–1308.
34. Shimomura Y, Wajid M, Shapiro L, Christiano AM. P-cadherin is a p63 target gene with a crucial role in the developing human limb bud and hair follicle. *Development*. 2008; 135:743–753.
35. Gonzales PA, Pisitkun T, Hoffert JD, Tchapyjnikov D, Star RA, Kleta R, Wang NS, Knepper MA. Large-scale proteomics and phosphoproteomics of urinary exosomes. *J Am Soc Nephrol*. 2009; 20:363–379.
36. Hoorn EJ, Pisitkun T, Zietse R, Gross P, Frokiaer J, Wang NS, Gonzales PA, Star RA, Knepper MA. Prospects for urinary proteomics: exosomes as a source of urinary biomarkers. *Nephrology*. 2005; 10:283–290.
37. Perez A, Loizaga A, Arceo R, Lacasa I, Rabade A, Zorroza K, Mosen-Ansorena D, Gonzalez E, Aransay AM, Falcon-Perez JM, Unda-Urzaiz M, Royo F. A Pilot Study on the Potential of RNA-Associated to Urinary Vesicles as a Suitable Non-Invasive Source for Diagnostic Purposes in Bladder Cancer. *Cancers*. 2014; 6:179–192.
38. Duijvesz D, Burnum-Johnson KE, Gritsenko MA, Hoogland AM, Vredendregt-van den Berg MS, Willemsen R, Luider T, Pasatolic L, Jenster G. Proteomic profiling of exosomes leads to the identification of novel biomarkers for prostate cancer. *PLoS One*. 2013; 8:e82589.
39. Duijvesz D, Versluis CY, van der Fels CA, Vredendregt-van den Berg MS, Leivo J, Peltola MT, Bangma CH, Pettersson KS, Jenster G. Immuno-based detection of extracellular vesicles in urine as diagnostic marker for prostate cancer. *Int J Cancer*. 2015.
40. Baek S, Lee YW, Yoon S, Baek SY, Kim BS, Oh SO. CDH3/P-Cadherin regulates migration of HuCCT1 cholangiocarcinoma cells. *Anat Cell Biol*. 2010; 43:110–117.
41. Bauer R, Valletta D, Bauer K, Thasler WE, Hartmann A, Muller M, Reichert TE, Hellerbrand C. Downregulation of P-cadherin expression in hepatocellular carcinoma induces tumorigenicity. *Int J Clin Exp Pathol*. 2014; 7:6125–6132.
42. Hibi K, Goto T, Mizukami H, Kitamura YH, Sakuraba K, Sakata M, Saito M, Ishibashi K, Kigawa G, Nemoto H, Sanada Y. Demethylation of the CDH3 gene is frequently detected in advanced colorectal cancer. *Anticancer Res*. 2009; 29:2215–2217.
43. Hibi K, Kitamura YH, Mizukami H, Goto T, Sakuraba K, Sakata M, Saito M, Ishibashi K, Kigawa G, Nemoto H, Sanada Y. Frequent CDH3 demethylation in advanced gastric carcinoma. *Anticancer Res*. 2009; 29:3945–3947.
44. Lysne D, Johns J, Walker A, Ecker R, Fowler C, Lawson KR. P-cadherin potentiates ligand-dependent EGFR and IGF-1R signaling in dysplastic and malignant oral keratinocytes. *Oncol Rep*. 2014; 32:2541–2548.
45. Milicic A, Harrison LA, Goodlad RA, Hardy RG, Nicholson AM, Presz M, Sieber O, Santander S, Pringle JH, Mandir N, East P, Obszynska J, Sanders S, et al. Ectopic expression of P-cadherin correlates with promoter hypomethylation early in colorectal carcinogenesis and enhanced intestinal crypt fission *in vivo*. *Cancer Res*. 2008; 68:7760–7768.
46. Paredes J, Albergaria A, Oliveira JT, Jeronimo C, Milanezi F, Schmitt FC. P-cadherin overexpression is an indicator of clinical outcome in invasive breast carcinomas and is associated with CDH3 promoter hypomethylation. *Clin Cancer Res*. 2005; 11:5869–5877.
47. Sousa B, Ribeiro AS, Nobre AR, Lopes N, Martins D, Pinheiro C, Vieira AF, Albergaria A, Gerhard R, Schmitt F,

- Baltazar F, Paredes J. The basal epithelial marker P-cadherin associates with breast cancer cell populations harboring a glycolytic and acid-resistant phenotype. *BMC Cancer*. 2014; 14:734.
48. Taniuchi K, Nakagawa H, Hosokawa M, Nakamura T, Eguchi H, Ohigashi H, Ishikawa O, Katagiri T, Nakamura Y. Overexpressed P-cadherin/CDH3 promotes motility of pancreatic cancer cells by interacting with p120ctn and activating rho-family GTPases. *Cancer Res*. 2005; 65: 3092–3099.
  49. Yi S, Yang ZL, Miao X, Zou Q, Li J, Liang L, Zeng G, Chen S. N-cadherin and P-cadherin are biomarkers for invasion, metastasis, and poor prognosis of gallbladder carcinomas. *Pathol Res Pract*. 2014; 210:363–368.
  50. Mandeville JA, Silva Neto B, Vanni AJ, Smith GL, Rieger-Christ KM, Zeheb R, Loda M, Libertino JA, Summerhayes IC. P-cadherin as a prognostic indicator and a modulator of migratory behaviour in bladder carcinoma cells. *BJU Int*. 2008; 102:1707–1714.
  51. Signoretti S, Pires MM, Lindauer M, Horner JW, Grisanzio C, Dhar S, Majumder P, McKeon F, Kantoff PW, Sellers WR, Loda M. p63 regulates commitment to the prostate cell lineage. *Proc Natl Acad Sci U S A*. 2005; 102:11355–11360.
  52. Costa-Silva B, Aiello NM, Ocean AJ, Singh S, Zhang H, Thakur BK, Becker A, Hoshino A, Mark MT, Molina H, Xiang J, Zhang T, Theilen TM, et al. Pancreatic cancer exosomes initiate pre-metastatic niche formation in the liver. *Nat Cell Biol*. 2015; 17:816–826.
  53. Peinado H, Aleckovic M, Lavotshkin S, Matei I, Costa-Silva B, Moreno-Bueno G, Hergueta-Redondo M, Williams C, Garcia-Santos G, Ghajar C, Nitadori-Hoshino A, Hoffman C, Badal K, et al. Melanoma exosomes educate bone marrow progenitor cells toward a pro-metastatic phenotype through MET. *Nat Med*. 2012; 18:883–891.
  54. Nardella C, Chen Z, Salmena L, Carracedo A, Alimonti A, Egia A, Carver B, Gerald W, Cordon-Cardo C, Pandolfi PP. Aberrant Rheb-mediated mTORC1 activation and Pten haploinsufficiency are cooperative oncogenic events. *Genes Dev*. 2008; 22:2172–2177.
  55. Carracedo A, Weiss D, Leliaert AK, Bhasin M, de Boer VC, Laurent G, Adams AC, Sundvall M, Song SJ, Ito K, Finley LS, Egia A, Libermann T, et al. A metabolic prosurvival role for PML in breast cancer. *The Journal of clinical investigation*. 2012; 122:3088–3100.
  56. Dragovic RA, Gardiner C, Brooks AS, Tannetta DS, Ferguson DJ, Hole P, Carr B, Redman CW, Harris AL, Dobson PJ, Harrison P, Sargent IL. Sizing and phenotyping of cellular vesicles using Nanoparticle Tracking Analysis. *Nanomedicine: nanotechnology, biology, and medicine*. 2011; 7:780–788.
  57. Ruiz de Eguino G, Infante A, Schlangen K, Aransay AM, Fullaondo A, Soriano M, Garcia-Verdugo JM, Martin AG, Rodriguez CI. Sp1 transcription factor interaction with accumulated prelamin a impairs adipose lineage differentiation in human mesenchymal stem cells: essential role of sp1 in the integrity of lipid vesicles. *Stem Cells Transl Med*. 2012; 1:309–321.
  58. Du P, Kibbe WA, Lin SM. lumi: a pipeline for processing Illumina microarray. *Bioinformatics*. 2008; 24:1547–1548.
  59. Gentleman RC, Carey VJ, Bates DM, Bolstad B, Dettling M, Dudoit S, Ellis B, Gautier L, Ge Y, Gentry J, Hornik K, Hothorn T, Huber W, et al. Bioconductor: open software development for computational biology and bioinformatics. *Genome Biol*. 2004; 5:R80.
  60. Team RDC. R: A Language and Environment for Statistical Computing. (Vienna, Austria Vienna, Austria). 2011.
  61. Baca SC, Prandi D, Lawrence MS, Mosquera JM, Romanel A, Drier Y, Park K, Kitabayashi N, MacDonald TY, Ghandi M, Van Allen E, Kryukov GV, Sboner A, et al. Punctuated evolution of prostate cancer genomes. *Cell*. 2013; 153:666–677.
  62. Robinson D, Van Allen EM, Wu YM, Schultz N, Lonigro RJ, Mosquera JM, Montgomery B, Taplin ME, Pritchard CC, Attard G, Beltran H, Abida W, Bradley RK, et al. Integrative clinical genomics of advanced prostate cancer. *Cell*. 2015; 161:1215–1228.

# The metabolic co-regulator PGC1 $\alpha$ suppresses prostate cancer metastasis

Veronica Torrano<sup>1,18</sup>, Lorea Valcarcel-Jimenez<sup>1,18</sup>, Ana Rosa Cortazar<sup>1</sup>, Xiaojing Liu<sup>2</sup>, Jelena Urosevic<sup>3</sup>, Mireia Castillo-Martin<sup>4,5</sup>, Sonia Fernández-Ruiz<sup>1</sup>, Giampaolo Morciano<sup>6</sup>, Alfredo Caro-Maldonado<sup>1</sup>, Marc Guiu<sup>3</sup>, Patricia Zúñiga-García<sup>1</sup>, Mariona Graupera<sup>7</sup>, Anna Bellmunt<sup>3</sup>, Pahini Pandya<sup>8</sup>, Mar Lorente<sup>9</sup>, Natalia Martín-Martín<sup>1</sup>, James David Sutherland<sup>1</sup>, Pilar Sanchez-Mosquera<sup>1</sup>, Laura Bozal-Basterra<sup>1</sup>, Amaia Zabala-Letona<sup>1</sup>, Amaia Arruabarrena-Aristorena<sup>1</sup>, Antonio Berenguer<sup>10</sup>, Nieves Embade<sup>1</sup>, Aitziber Ugalde-Olano<sup>11</sup>, Isabel Lacasa-Viscasillas<sup>12</sup>, Ana Loizaga-Iriarte<sup>12</sup>, Miguel Unda-Urzaiz<sup>12</sup>, Nikolaus Schultz<sup>13</sup>, Ana Maria Aransay<sup>1,14</sup>, Victoria Sanz-Moreno<sup>8</sup>, Rosa Barrio<sup>1</sup>, Guillermo Velasco<sup>9</sup>, Paolo Pinton<sup>6</sup>, Carlos Cordon-Cardo<sup>4</sup>, Jason W. Locasale<sup>2,19</sup>, Roger R. Gomis<sup>3,15,19</sup> and Arkaitz Carracedo<sup>1,16,17,20</sup>

Cellular transformation and cancer progression is accompanied by changes in the metabolic landscape. Master co-regulators of metabolism orchestrate the modulation of multiple metabolic pathways through transcriptional programs, and hence constitute a probabilistically parsimonious mechanism for general metabolic rewiring. Here we show that the transcriptional co-activator peroxisome proliferator-activated receptor gamma co-activator 1 $\alpha$  (PGC1 $\alpha$ ) suppresses prostate cancer progression and metastasis. A metabolic co-regulator data mining analysis unveiled that PGC1 $\alpha$  is downregulated in prostate cancer and associated with disease progression. Using genetically engineered mouse models and xenografts, we demonstrated that PGC1 $\alpha$  opposes prostate cancer progression and metastasis. Mechanistically, the use of integrative metabolomics and transcriptomics revealed that PGC1 $\alpha$  activates an oestrogen-related receptor alpha (ERR $\alpha$ )-dependent transcriptional program to elicit a catabolic state and metastasis suppression. Importantly, a signature based on the PGC1 $\alpha$ -ERR $\alpha$  pathway exhibited prognostic potential in prostate cancer, thus uncovering the relevance of monitoring and manipulating this pathway for prostate cancer stratification and treatment.

The metabolic switch in cancer encompasses a plethora of discrete enzymatic activities that must be coordinately altered to ensure the generation of biomass, reductive power and the remodelling of the microenvironment<sup>1–4</sup>. Despite the existence of mutations in metabolic enzymes<sup>5</sup>, it is widely accepted that the main trigger for metabolic reprogramming is the alteration in cancer genes that remodel the signalling landscape<sup>2</sup>. Numerous reports provide evidence of the

pathways regulating one or a few enzymes within a metabolic pathway in cancer. However, the means of coordinated regulation of complex metabolic networks remain poorly documented.

Master transcriptional co-regulators of metabolism control a variety of genes that are in charge of remodelling the metabolic landscape, and their impact in cellular and systemic physiology has been studied for decades. It is worth noting that these co-regulators,

<sup>1</sup>CIC bioGUNE, Bizkaia Technology Park, Building 801A, 48160 Derio, Bizkaia, Spain. <sup>2</sup>Department of Pharmacology and Cancer Biology, Duke Cancer Institute, Duke Molecular Physiology Institute, Duke University School of Medicine, Durham, North Carolina 27710, USA. <sup>3</sup>Oncology Programme, Institute for Research in Biomedicine (IRB Barcelona), The Barcelona Institute of Science and Technology, Barcelona 08028, Catalonia, Spain. <sup>4</sup>Department of Pathology, Icahn School of Medicine at Mount Sinai, New York, New York 10029, USA. <sup>5</sup>Department of Pathology, Fundação Champalimaud, 1400-038 Lisboa, Portugal. <sup>6</sup>Department of Morphology, Surgery and Experimental Medicine, Section of Pathology, Oncology and Experimental Biology, University of Ferrara, 44100, Italy. <sup>7</sup>Vascular Signalling Laboratory, Institut d'Investigació Biomèdica de Bellvitge (IDIBELL), Gran Via de l'Hospitalet 199-203, 08907 L'Hospitalet de Llobregat, Barcelona, Spain. <sup>8</sup>Tumour Plasticity Team, Randall Division of Cell and Molecular Biophysics, King's College London, New Hunt's House, Guy's Campus, London SE1 1UL, UK. <sup>9</sup>Department of Biochemistry and Molecular Biology I, School of Biology, Complutense University and Instituto de Investigaciones Sanitarias San Carlos (IdiSSC), 28040 Madrid, Spain. <sup>10</sup>Biostatistics/Bioinformatics Uni, IRB Barcelona, Parc Científic de Barcelona, 08028 Barcelona, Spain. <sup>11</sup>Department of Pathology, Basurto University Hospital, 48013 Bilbao, Spain. <sup>12</sup>Department of Urology, Basurto University Hospital, 48013 Bilbao, Spain. <sup>13</sup>Computational Biology, Memorial Sloan-Kettering Cancer Center, New York 10065, USA. <sup>14</sup>Centro de Investigación Biomédica en Red de Enfermedades Hepáticas y Digestivas (CIBERehd). <sup>15</sup>Institució Catalana de Recerca i Estudis Avançats (ICREA), 08010 Barcelona, Spain. <sup>16</sup>Ikerbasque, Basque Foundation for Science, 48011 Bilbao, Spain. <sup>17</sup>Biochemistry and Molecular Biology Department, University of the Basque Country (UPV/EHU), PO Box 644, E-48080 Bilbao, Spain. <sup>18</sup>These authors contributed equally to this work. <sup>19</sup>These authors jointly supervised this work.

<sup>20</sup>Correspondence should be addressed to A.C. (e-mail: [acarracedo@cicbiogune.es](mailto:acarracedo@cicbiogune.es))



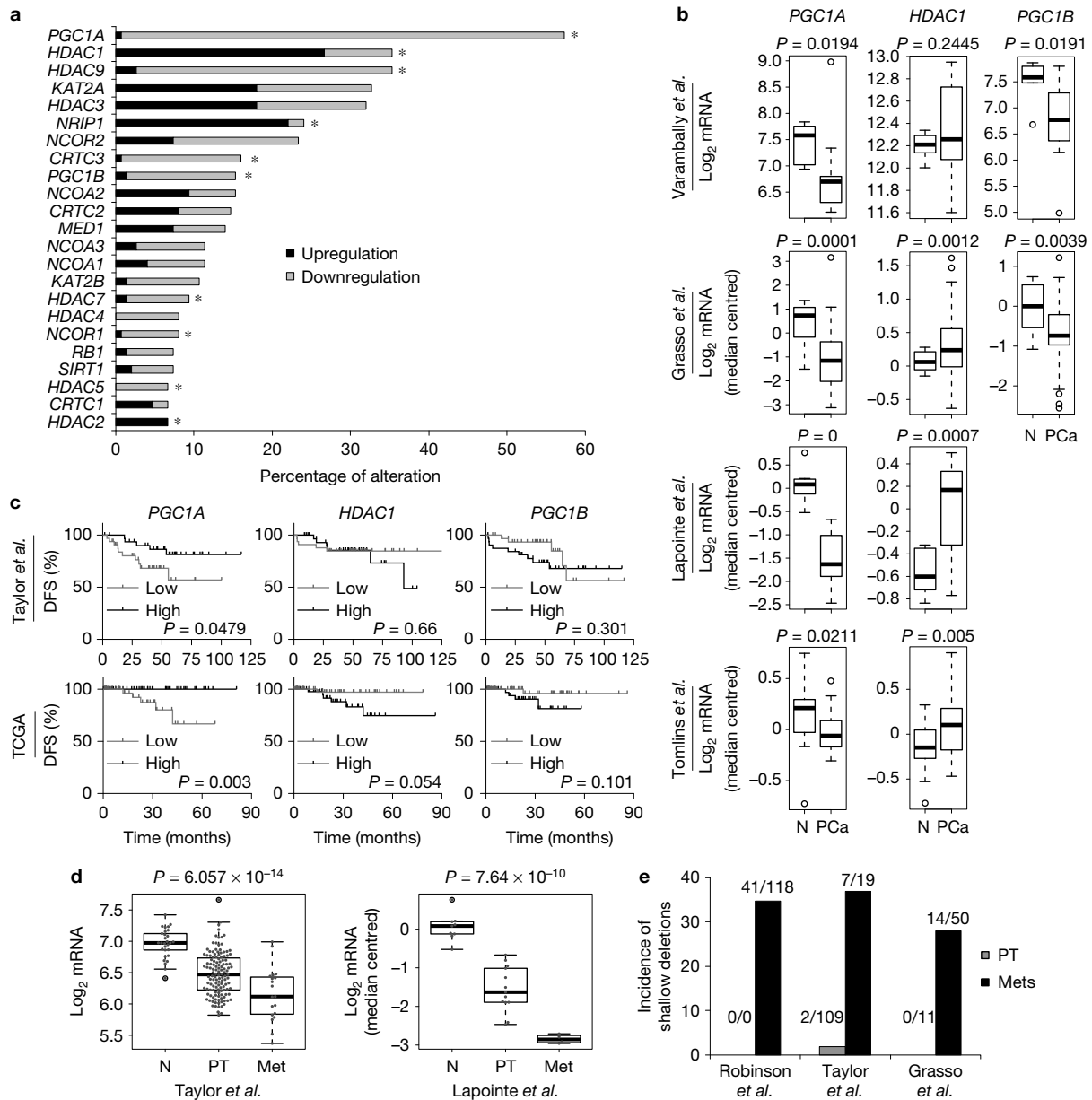


**Figure 1** *PGC1A* is downregulated in prostate cancer. **(a)** Frequency of alterations (differences greater than twofold versus mean expression of non-tumoral biopsies) in the expression of 23 master co-regulators of metabolism in a cohort of 150 PCa patients<sup>22</sup>. \* $P < 0.05$ , statistically different expression of the indicated gene in PCa ( $n = 150$ ) versus normal ( $n = 29$ ) patient specimens (according to Supplementary Fig. 1A). **(b)** Gene expression levels of *PGC1A*, *PGC1B* and *HDAC1* in up to four additional PCa data sets (N, normal; PCa, prostate cancer). Sample sizes: Tomlins *et al.*<sup>23</sup> (N, 23; PCa, 52); Grasso *et al.*<sup>21</sup> (N, 12; PCa, 76); Lapointe *et al.*<sup>18</sup> (N, 9; PCa, 17); and Varambally *et al.*<sup>24</sup> (N, 6; PCa, 13). **(c)** Association of the indicated genes with disease-free survival (DFS) in two PCa data sets

(low: first quartile distribution; high: fourth quartile distribution. Sample sizes: TCGA provisional data<sup>19,20</sup>, primary tumours  $n = 240$ ; Taylor *et al.*<sup>22</sup>, primary tumours  $n = 131$ ). **(d)** *PGC1A* expression in normal prostate (N), primary tumour (PT) and metastatic (Met) specimens in the Taylor and Lapointe data sets<sup>18,22</sup>. Sample sizes: Taylor (N, 29; PT, 131; Met, 19) and Lapointe (N, 9; PT, 13; Met, 4). **(e)** Incidence of *PGC1A* shallow deletions in three independent data sets (Robinson *et al.*<sup>25</sup>, Taylor *et al.* and Grasso *et al.*). Points outlined by circles indicate statistical outliers **(d)**. Error bars represent minimum and maximum values **(b,d)**.  $P$ ,  $P$  value. Statistical tests: two-tailed Student's  $t$ -test **(a,b)**, Kaplan-Meier estimator **(c)** and ANOVA **(d)**.

through their capacity to interact and regulate diverse transcription factors, exhibit a unique capacity to control complex and extensive transcriptional networks, making them ideal candidates to promote or oppose oncogenic metabolic programs.

The tumour suppressor PTEN is a negative regulator of cell growth, transformation and metabolism<sup>6–9</sup>. PTEN and its main downstream

pathway, PI(3)K, have been extensively implicated in prostate cancer (PCa) pathogenesis and progression<sup>10–12</sup>. This tumour suppressor is progressively lost through the progression of PCa, and complete loss of PTEN is predominant in advanced disease and metastasis<sup>8</sup>. Genetically engineered mouse models (GEMMs) recapitulate many of the features of PCa progression. However, the molecular and

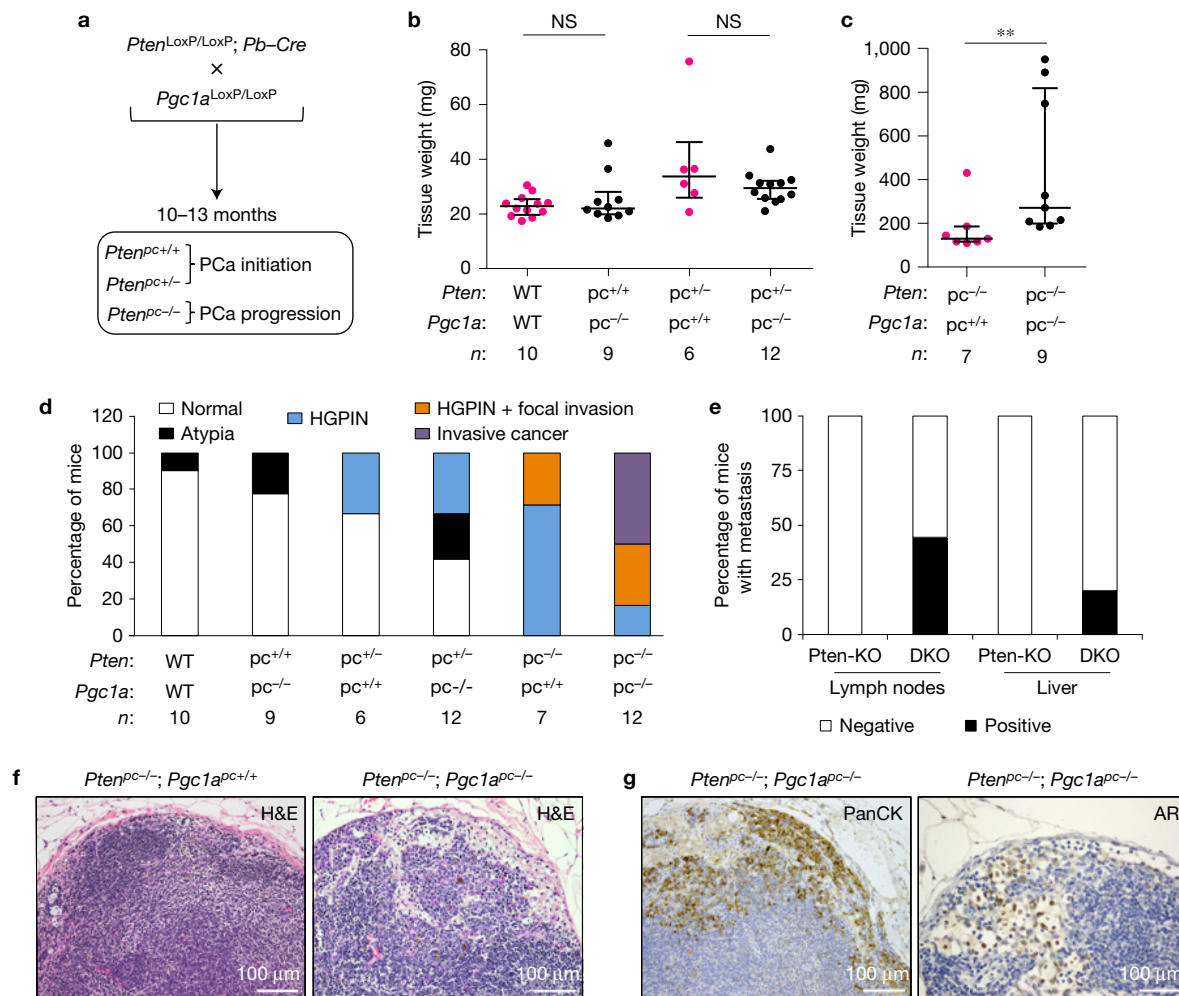


**Figure 2** Combined deletion of *Pgc1a* and *Pten* in the murine prostate epithelia results in prostate cancer progression and dissemination. (a) Schematic representation of the genetic cross and the time of analysis. (b,c) Comparison of anterior prostate lobe weights (when both anterior lobes were analysed, the average weight was calculated and represented) between genotypes.  $n$  = number of mice; pc, prostate-specific allelic changes; +, wild-type allele; -, deleted allele; WT, any given genotype resulting in the lack of deletion of *Pgc1a* or *Pten* alleles. (d) Histopathological characterization of the prostate (HGPIN, high-grade prostatic intraepithelial neoplasia) in the indicated genotypes.

(e) Quantification of the frequency of metastatic lesions in lymph nodes and liver of *Pten*-KO (5) and DKO (9) mice. (f) Representative histological images ( $\times 200$  magnification) of lymph nodes with (right) and without (left) metastasis in the indicated genotypes. (g) Representative immunohistochemical detection ( $\times 200$  magnification) of Pan-cytokeratin (panCK)- and androgen receptor (AR)-positive cells in metastatic lymph nodes of DKO mice. *Pten*-KO, *Pten*<sup>pc<sup>-/-</sup></sup> *Pgc1a*<sup>pc<sup>+/+</sup></sup>; DKO, *Pten*<sup>pc<sup>-/-</sup></sup> *Pgc1a*<sup>pc<sup>-/-</sup></sup>. NS, not significant; \*\* $P < 0.01$ . H&E, haematoxylin–eosin. Error bars indicate interquartile range (b,c). Statistical test: two-tailed Mann–Whitney *U*-test (b,c).

metabolic bases for PCa metastasis remain poorly understood<sup>13–16</sup>. Indeed, complete loss of PTEN in the mouse prostate does not result in metastasis<sup>11</sup>, in turn suggesting that additional critical events are required in this process.

In this study, we designed a bioinformatics analysis to interrogate multiple PCa data sets encompassing hundreds of well-annotated specimens. This approach allowed us to define a master regulator of PCa metabolism that is crucial for the progression of the disease. Our results identify the peroxisome proliferator-activated receptor gamma co-activator 1 alpha (PGC1 $\alpha$ ) as a suppressor of PCa metastasis. This transcriptional co-activator exerts its function through the regulation of oestrogen-related receptor alpha (ERR $\alpha$ ) activity, in concordance with the activation of a catabolic program and the inhibition of PCa metastasis.

## RESULTS

### A bioinformatics screen identifies *PGC1A* as a metabolic co-regulator associated with prostate cancer progression

We approached the study of PCa metabolism applying criteria to ensure the selection of relevant master regulators that contribute to the metabolic switch. We focused on transcriptional co-regulators of metabolism<sup>17</sup> that were consistently altered in several publicly available PCa data sets<sup>18–24</sup>, and were associated with reduced time to recurrence and disease aggressiveness. We first evaluated the expression levels of the metabolic co-regulators in a study comprising 150 PCa specimens and 29 non-pathological prostate tissues (or controls)<sup>22</sup>. The analysis revealed 10 co-regulators in the set of study with significant differential expression in PCa compared with non-neoplastic prostate tissue (Fig. 1a and Supplementary Fig. 1A).

We next extended this observation to four additional data sets<sup>18,21,23,24</sup> in which there were available data for non-tumoral and PCa tissues. Only the alteration in *PPARGC1A* (*PGC1A*), *PPARGC1B* (*PGC1B*) and *HDAC1* expression was further confirmed in most or all sets (Fig. 1b and Supplementary Fig. 1B). Among these, *PGC1A* was the sole co-regulator with altered expression associated with Gleason score (Supplementary Fig. 1C,D) and disease-free survival (Fig. 1c).

To rule out the possibility that cellular proliferation could contribute to the alteration of metabolic regulators, we carried out an additional analysis in which we compared the expression of *PGC1A* in PCa versus a benign hyper-proliferative condition (benign prostate hyperplasia or BPH). The results corroborated that the decrease in *PGC1A* expression is associated with a cancerous state rather than with a proliferative condition (Supplementary Fig. 1E).

We observed that the expression of *PGC1A* was progressively decreased from primary tumours to metastasis (Fig. 1d and Supplementary Fig. 1F). Strikingly, genomic analysis revealed shallow deletions of *PGC1A* exquisitely restricted to metastatic PCa specimens<sup>19–22,25</sup> (Fig. 1e), in full agreement with the notion that there is a selective pressure to reduce the expression of this transcriptional co-activator as the disease progresses.

From our analysis, *PGC1α* emerges as the main master metabolic co-regulator altered in PCa, with an expression pattern reminiscent of a tumour suppressor.

### ***Pgc1a* deletion in the murine prostate epithelium promotes prostate cancer metastasis**

*PGC1α* has been widely studied in the context of systemic metabolism<sup>26</sup>, whereas its activity in cancer is just beginning to be understood<sup>27–33</sup>. To ascertain the role of *PGC1α* in PCa *in vivo*, we conditionally deleted this metabolic co-regulator in the prostate epithelium<sup>34</sup>, alone or in combination with loss of the tumour suppressor *Pten*<sup>11</sup> (Fig. 2a–d and Supplementary Fig. 2A,B). *Pgc1a* deletion alone or in the context of *Pten* heterozygosity did not result in any differential tissue mass or histological alteration, which led us to conclude that it is not an initiating event (Fig. 2b,d). However, compound loss of both *Pten* and *Pgc1a* resulted in significantly larger prostate mass (Fig. 2c), together with a remarkable increase in the rate of invasive cancer (Fig. 2d). Histological analysis of the prostate revealed the existence of vascular invasion in double-mutant mice (DKO), but not in *Pten*-deleted (*Pten*-KO) prostates (Supplementary Fig. 2C). *PGC1α* regulates the inflammatory response, which could influence and contribute to the phenotype observed<sup>35</sup>. However, we did not observe significant differences in the infiltration of polymorphonuclear neutrophils and lympho-plasmacytic infiltrates in our experimental settings (Supplementary Fig. 2D). *PGC1α* has been also shown to induce angiogenesis in coherence with the induction of vascular endothelial growth factor (VEGF)-A expression<sup>36</sup>. *Pgc1a* status in our GEMMs did not alter VEGF-A expression and microvessel density (Supplementary Fig. 2E,F). We therefore excluded the possibility that regulation of angiogenesis or inflammation downstream of *PGC1α* could drive the phenotype characterized in this study.

PCa GEMMs faithfully recapitulate many of the features of the human disease<sup>37</sup>. A reduced number of mouse models with clinically relevant mutations show increased metastatic potential<sup>13–16</sup>. Strikingly,

histopathological analysis of our mouse model in the context of *Pten* loss revealed that DKO mice—but not *Pten*-KO counterparts—presented evidence of metastasis, which was estimated in 44% to lymph nodes and 20% to liver (Fig. 2e,f and Supplementary Fig. 2G). Metastatic dissemination was in agreement with the observation of pan-cytokeratin (panCK)- and androgen receptor (AR)-positive PCa cell deposits in the lymph nodes of DKO mice (Fig. 2g). Of note, 33% of *Pten*-KO mice presented small groups of panCK-positive cells in lymph nodes (without metastatic lesions; Supplementary Fig. 2H), suggesting that even if these cells are able to reach the lymph nodes, they lack capacity to establish clinical metastasis. Interestingly, bone analysis revealed disseminated groups (but not clinical metastasis) of panCK-positive cells in DKO but not in *Pten*-KO mice (Supplementary Fig. 2I–K). Analysis of a small cohort of *Pten*<sup>pc-/-</sup>; *Pgc1a*<sup>pc+/-</sup> mice demonstrated that heterozygous loss of *Pgc1a* is sufficient to promote aggressiveness, vascular invasion and metastasis (Supplementary Fig. 2L–N). This observation supports the notion that single-copy loss of *PGC1A* (as observed in metastatic human PCa specimens, Fig. 1e) could be a key contributing factor to the metastatic phenotype.

The cooperative effect observed in our mouse model between loss of *Pten* and *Pgc1a* was supported by the direct correlation of the two transcripts in patient specimens and the association of *PGC1A* downregulation with *PTEN* genomic loss (TCGA provisional data<sup>19,20</sup>, Supplementary Fig. 2O).

In summary, our results in GEMMs and patient data sets formally demonstrate that the downregulation of *PGC1α* in PCa is an unprecedented causal event for the progression of the disease and its metastatic dissemination.

### ***PGC1α* suppresses prostate cancer growth and metastasis**

To characterize the prostate tumour suppressive activity of *PGC1α*, we first evaluated its expression level in well-established PCa cell lines<sup>38</sup>. Using previously reported *PGC1α*-positive and -negative melanoma cells<sup>28</sup>, we could demonstrate that PCa cell lines lack detectable expression of the transcriptional co-activator at the protein level (Fig. 3a). In agreement with this notion, *PGC1α* silencing in these cells failed to impact on the expression of its well-established targets<sup>39</sup> (Supplementary Fig. 3A). Importantly, through the analysis of publicly available data sets<sup>22</sup>, we could demonstrate that the transcript levels of *PGC1A* in metastatic cell lines are comparable to those observed in human metastatic PCa specimens and vastly reduced compared with *PGC1α*-positive melanoma cells (Fig. 3a and Supplementary Fig. 3B). Despite our efforts to optimize the detection of the protein with different commercial antibodies, we could not identify an immunoreactive band that would correspond to *PGC1α*, in contrast with other reports<sup>40,41</sup>. Yet, we cannot rule out that in non-basal conditions, stimulation of other factors such as AR<sup>41</sup> or 5' AMP-activated protein kinase (AMPK)<sup>40</sup> could lead to the upregulation and allow detection of *PGC1α* in PCa cells.

Owing to the lack of *PGC1α* detection in PCa cellular systems, we aimed at reconstituting the expression of this gene to levels achievable in the cancer cell lines previously reported<sup>28</sup>. By means of lentiviral delivery of inducible *Pgc1a* and doxycycline titration, we reached expression levels of this protein in three PCa cell lines (AR-dependent—LnCaP—and independent—PC3 and DU145)

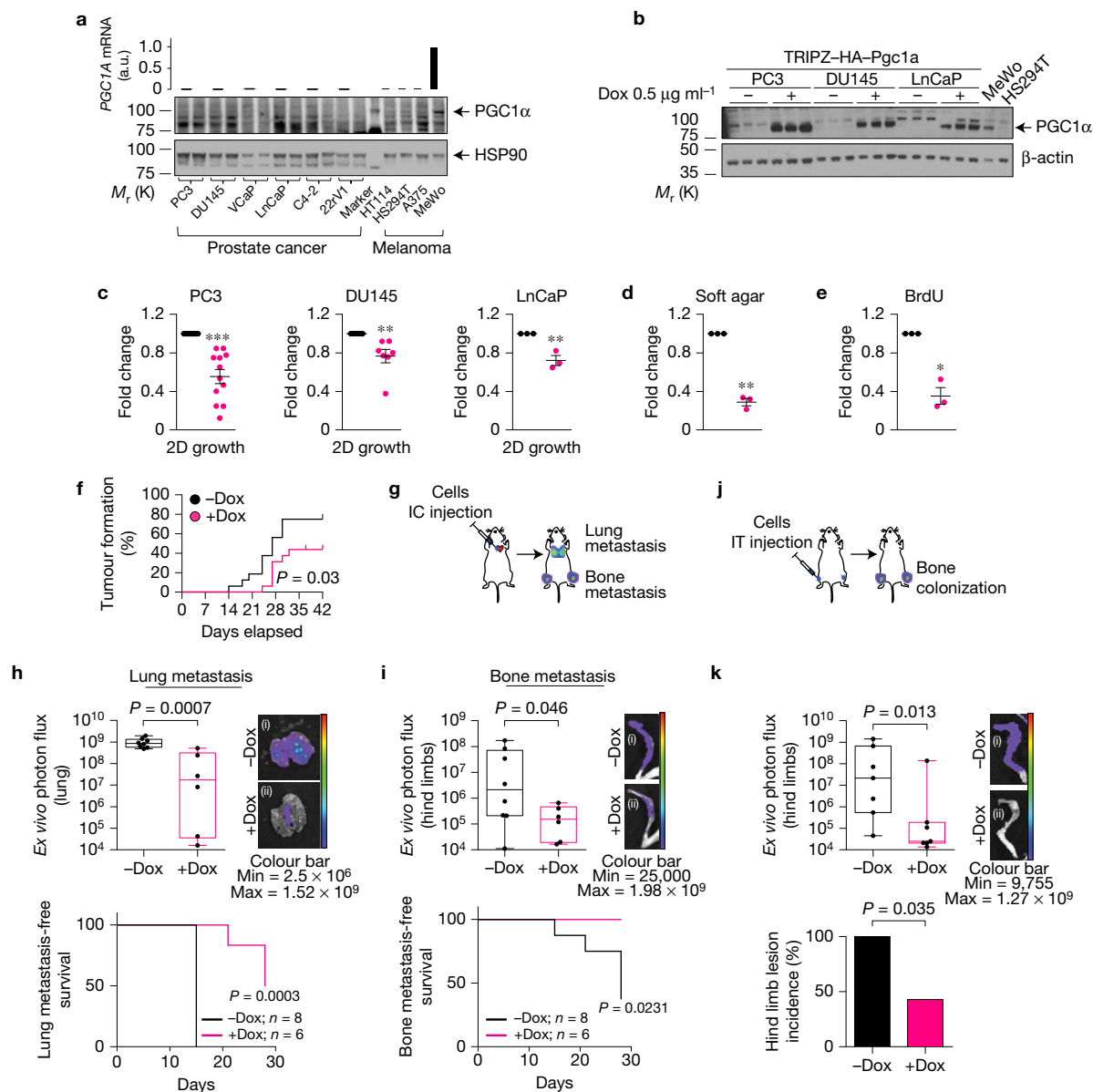


**Figure 3** PGC1 $\alpha$  exhibits tumour and metastasis suppressive activity in PCA cell lines. **(a)** Analysis of PGC1 $\alpha$  expression by quantitative rtPCR (top histogram) and western blot in a panel of prostate cancer cell lines (technical duplicates are shown), using melanoma cell lines as positive (MeWo) and negative (HT114, HS294T and A375) controls ( $n=3$ , independent experiments). **(b)** Representative experiment of PGC1 $\alpha$  expression in PC3, DU145 and LnCaP cell lines after treatment with 0.5  $\mu\text{g ml}^{-1}$  doxycycline (Dox) (similar results were obtained in three independent experiments). **(c)** Relative cell number quantification in Pgc1 $\alpha$ -expressing (+Dox, pink) and -non-expressing (-Dox, black) cells. Data are represented as cell number at day 6 relative to -Dox cells ( $n=12$  in PC3;  $n=7$  in DU145;  $n=3$  in LnCaP, independent experiments). **(d,e)** Effect of Pgc1 $\alpha$  expression on anchorage-independent growth **(d)**;  $n=3$ , independent experiments) and BrdU incorporation **(e)**;  $n=3$ , independent experiments) in PC3 cells. **(f)** Evaluation of tumour formation capacity in xenotransplantation experiments ( $n=7$  mice; two injections per mouse). **(g)** Schematic representation of metastasis assay through intra-cardiac (IC) injection. **(h,i)** Evaluation of metastatic capacity of Pgc1 $\alpha$ -expressing PC3 cells using IC xenotransplant assays ( $n=8$  mice for -Dox and  $n=6$  for +Dox). Luciferase-dependent signal intensity (upper panels) and metastasis-free survival curves (lower panels) of PCA cells in lungs **(h)** and limbs **(i)** were monitored for up to 28 days. Representative luciferase images are presented, referring to the quantification plots. In

hind limb photon flux analysis, the average signal from two limbs per mouse is presented. Images (i) and (ii) depict tibia or lung photon flux images from specimens that are proximal to the median signal in -Dox and +Dox, respectively. **(j)** Schematic representation of bone metastasis assay through intra-tibial (IT) injection. **(k)** Evaluation of the metastatic capacity of Pgc1 $\alpha$ -expressing PC3 cells using IT xenotransplant assays ( $n=7$  mice). Photon flux quantification at 20 days (upper panel) and incidence of metastatic lesions at the end point (lower panel). Representative luciferase images are presented, referring to the quantification plots. For photon flux analysis, the average signal from two limbs per mouse is presented. For incidence analysis, mice with at least one limb yielding luciferase signal  $>50,000$  units were considered metastasis-positive. Images (i) and (ii) depict tibia photon flux images from specimens that are proximal to the median signal in -Dox and +Dox, respectively. +Dox, Pgc1 $\alpha$ -induced conditions; -Dox, Pgc1 $\alpha$ -non-expressing conditions; BrdU, bromo deoxyuridine; a.u., arbitrary units. Error bars represent s.e.m. **(c-e)** or minimum and maximum values **(h,i,k)** (upper panels), log-rank test **(f,h,i)** (lower panels) and Fisher's exact test **(k)** (lower panels). \* $P < 0.05$ , \*\* $P < 0.01$ , \*\*\* $P < 0.001$ . Statistics source data for Fig. 3k are provided in Supplementary Table 9. Unprocessed original scans of blots are shown in Supplementary Fig. 8.

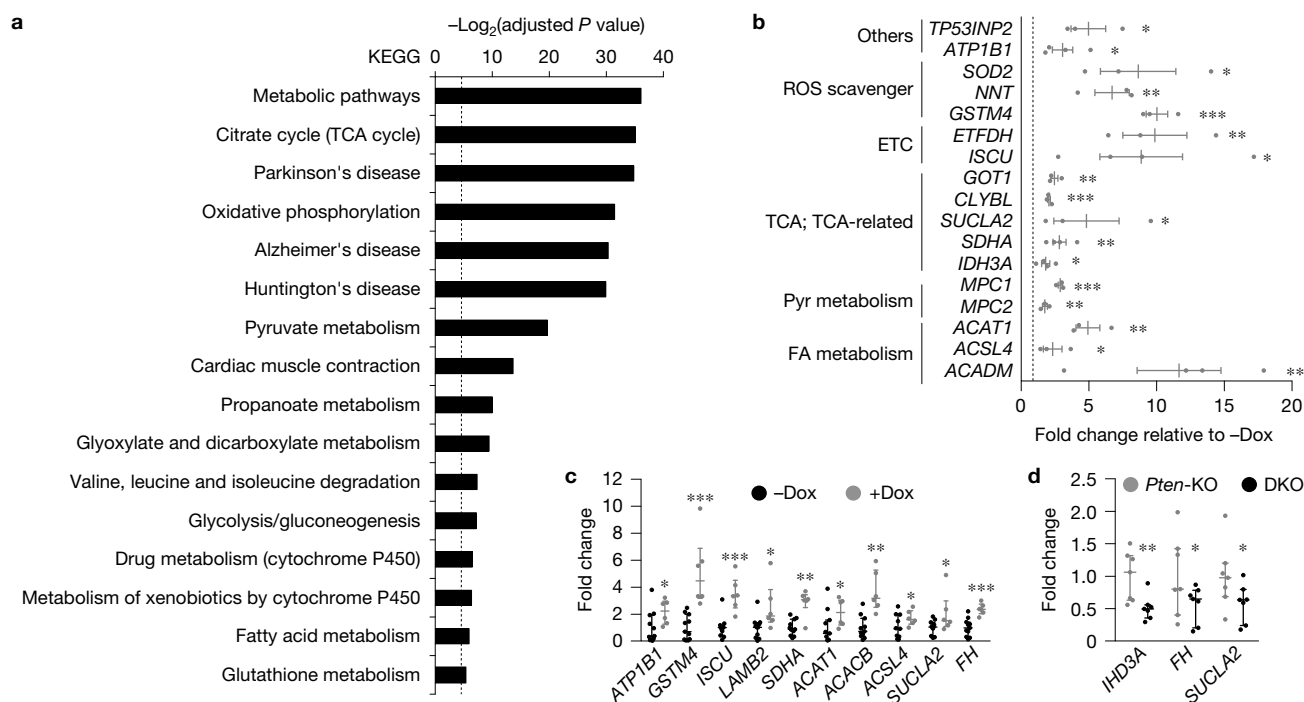


**Figure 4** PGC1 $\alpha$  induces a metabolic transcriptional program. (a) KEGG (Kyoto Encyclopaedia of Genes and Genomes) analysis of the transcriptional program regulated by PGC1 $\alpha$ . The dotted line indicates  $P=0.05$ . (b–d) Validation of microarray by quantitative rtPCR in PC3 TRIPZ-HA-Pgc1 $\alpha$  cells (b,  $n=3$  for *TP53INP2*, *SOD2*, *NNT*, *GSTM4*, *ETFDH*, *GOT1*, *CLYBL*, *SUCLA2*, *MPC1*, *MPC2*, *ACAT1* and *ACSL4*;  $n=4$  for *ATP1B1*, *ISCU*, *SDHA*, *IDH3A* and *ACADM*; independent experiments; data are normalized to the -Dox condition, represented by a black dotted line), xenograft

samples (c, -Dox  $n=11$  tumours; +Dox  $n=6$  tumours) and prostate tissue samples from *Pten*-KO and DKO mice (d,  $n=7$  mice). +Dox, Pgc1 $\alpha$ -induced conditions; -Dox, Pgc1 $\alpha$ -non-expressing conditions; *Pten*-KO, *Pten*<sup>pc-/-</sup>; *Pgc1a*<sup>pc+/+</sup>; DKO, *Pten*<sup>pc-/-</sup>, *Pgc1a*<sup>pc-/-</sup>. ROS, reactive oxygen species; ETC, electron transport chain; TCA, tricarboxylic acid cycle; Pyr, pyruvate; FA, fatty acid. Error bars indicate s.e.m. (b) or interquartile range (c,d). Statistical tests: one-tail Student's *t*-test (b); one-tail Mann-Whitney *U*-test (c,d). \* $P<0.05$ , \*\* $P<0.01$ , \*\*\* $P<0.001$ .

equivalent to that observed in the PGC1 $\alpha$ -expressing melanoma cell line MeWo (Fig. 3b and Supplementary Fig. 3C,D). Next, we evaluated the cellular outcome of expressing PGC1 $\alpha$  in PCa cell lines. Interestingly, expression of Pgc1 $\alpha$  in this context resulted in a reduction in bi-dimensional and three-dimensional growth (Fig. 3c,d and Supplementary Fig. 3E), cellular proliferation (Fig. 3e and Supplementary Fig. 3F) and cell cycle progression (Supplementary Fig. 3G). Of note, we excluded the possibility that doxycycline treatment could influence the result of the growth analysis (Supplementary Fig. 3H). The Pgc1 $\alpha$  phenotype was recapitulated *in vivo*, where ectopic expression of this gene decreased tumour formation and growth (Fig. 3f and Supplementary Fig. 3I–K). In agreement with the GEMM data, we did not observe a contribution of angiogenesis to the phenotype (Supplementary Fig. 3L–N).

We observed in GEMMs that *Pgc1a* loss resulted in metastatic dissemination (Fig. 2). We next sought to study whether Pgc1 $\alpha$  expression could oppose a pre-existing metastatic phenotype. To this end, we carried out xenotransplant assays in immunocompromised mice using luciferase-expressing Pgc1 $\alpha$ -inducible PC3 cells. Intra-cardiac injection of these cells (Fig. 3g) revealed that Pgc1 $\alpha$  expression blunted metastatic growth in the lung, and led to a remarkable decrease in bone colonization (Fig. 3h,i). As an additional approach, we sought to analyse metastatic tumour re-initiation capacity by means of local injection of PCa cells at the metastatic site. As PCa exhibits an osteotropic nature<sup>42</sup>, we carried out intra-tibial injection

of cells and the appearance of tumour masses in the bone was monitored<sup>43</sup> (Fig. 3j). The results demonstrated that PGC1 $\alpha$  exerts a potent anti-metastatic activity both in bone tumour mass and metastatic lesions (Fig. 3k). These data provide evidence of the anti-metastatic potential of PGC1 $\alpha$ .

### PGC1 $\alpha$ determines the oncogenic metabolic wiring in prostate cancer

PGC1 $\alpha$  regulates gene expression through the interaction with diverse transcription factors<sup>26</sup>. To define the transcriptional program associated with the tumour suppressive activity of PGC1 $\alpha$ , we performed gene expression profiling from Pgc1 $\alpha$ -expressing versus -non-expressing PC3 cells. We identified 174 probes with significantly altered signal encoding genes predominantly related to functions such as mitochondrial catabolic programs and energy-producing processes<sup>26,44</sup> (Supplementary Table 1 and Fig. 4a), which we validated by quantitative real-time PCR (rtPCR) (Fig. 4b–d and Supplementary Fig. 4).

To demonstrate that the tumour suppressive activity of PGC1 $\alpha$  was indeed accompanied by a global metabolic rewiring, we carried out integrative metabolomics. We analysed cell line, xenograft and GEMM tissue extracts using liquid-chromatography high-resolution mass spectrometry (LC–HRMS). LC–HRMS metabolomics and subsequent biochemical assays confirmed that oxidative processes such as fatty acid  $\beta$ -oxidation (Fig. 5a–d and Supplementary Fig. 5A–C and

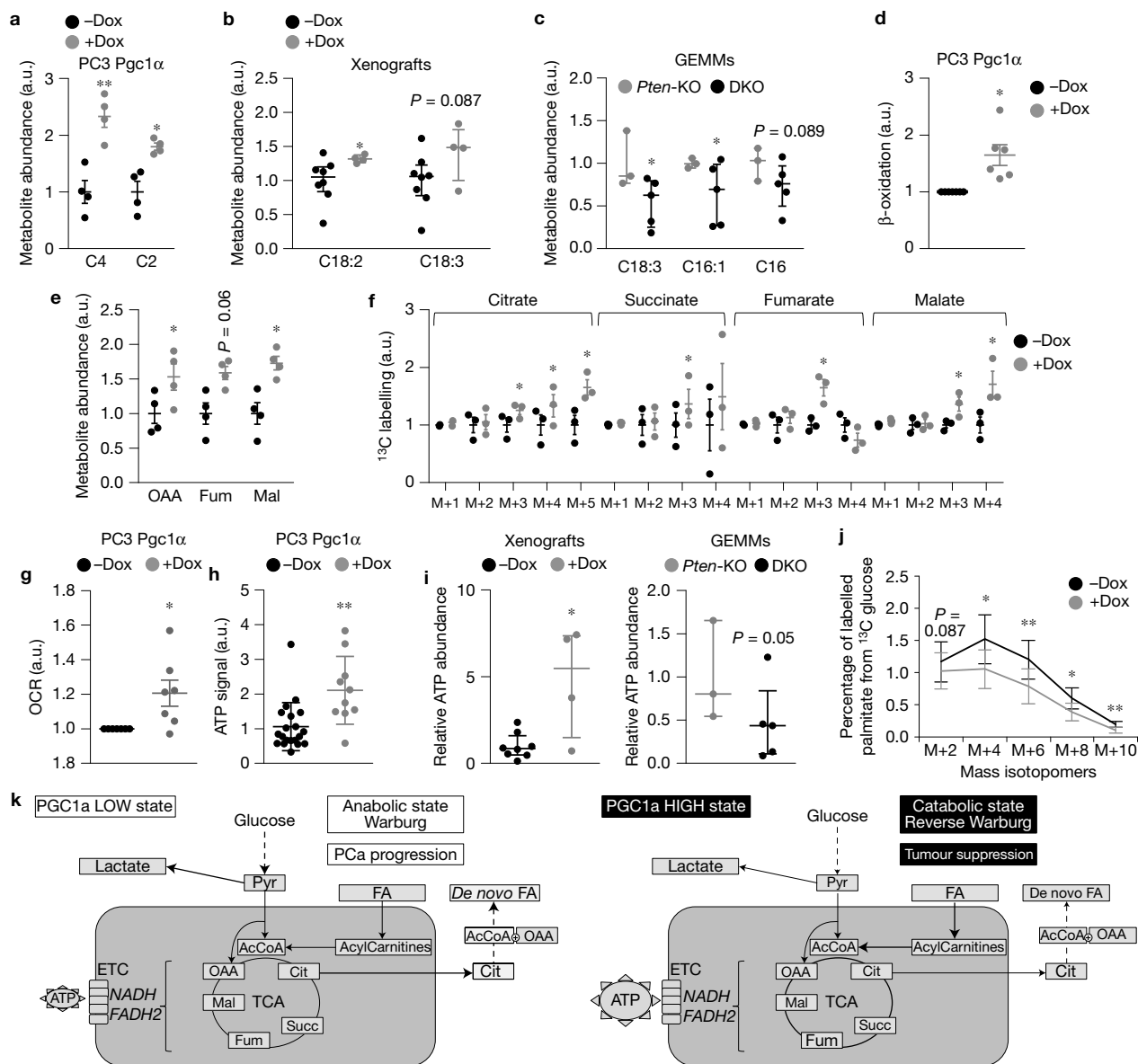


**Figure 5** PGC1 $\alpha$  induces a catabolic metabolic program. (**a–c**) Untargeted LC–HRMS analysis of differential abundance in metabolites involved in fatty acid catabolism in Pgc1 $\alpha$ -expressing PC3 cells (**a**,  $n = 4$ , independent experiments), xenografts (**b**, –Dox  $n = 8$  tumours; +Dox  $n = 4$  tumours) and GEMMs (**c**, *Pten* KO  $n = 3$  mice; DKO  $n = 5$  mice). (**d**) Evaluation of the dehydrogenation of tritiated palmitate (readout of fatty acid  $\beta$ -oxidation) in Pgc1 $\alpha$ -expressing PC3 cells ( $n = 6$ , independent experiments). (**e**) Effect of Pgc1 $\alpha$  expression on the abundance of tricarboxylic acid cycle (TCA) intermediates measured by LC–HRMS in PC3 cells ( $n = 4$ , independent experiments). (**f**) Effect of Pgc1 $\alpha$  expression on TCA intermediates (mass isotopomer abundance) after stable  $^{13}\text{C}$ -U $_6$ -glucose labelling in PC3 cells ( $n = 3$ , independent experiments). (**g**) Oxygen consumption rate (OCR) in PC3 Pgc1 $\alpha$ -expressing cells ( $n = 7$ , independent experiments). (**h**) Basal

mitochondrial ATP production in PC3 cells following Pgc1 $\alpha$  expression ( $n = 20$  for –Dox and  $n = 10$  for +Dox conditions, independent experiments). (**i**) LC–HRMS quantification of ATP abundance in xenografts (left panel, –Dox  $n = 8$  tumours; +Dox  $n = 4$  tumours) and GEMMs (right panel, *Pten*-KO  $n = 3$  mice; DKO  $n = 5$  mice). (**j**) Effect of Pgc1 $\alpha$  expression on palmitate paired mass isotopomer abundance after stable  $^{13}\text{C}$ -U $_6$ -glucose labelling in PC3 cells ( $n = 3$ , independent experiments). (**k**) Schematic representation of the main findings of the study. Pyr, pyruvate; AcCoA, acetyl CoA; OAA, oxaloacetate; Mal, malate; Fum, fumarate; Succ, succinate; Cit, citrate; ETC, electron transport chain; FA, fatty acids. a.u., arbitrary unit. Error bars indicate s.e.m. (**a, d–h, j**) or interquartile range (**b, c, i**). Statistical tests: two-tailed Student's *t*-test (**a, d–h, j**); one-tail Mann–Whitney *U*-test (**b, c, i**). \* $P < 0.05$ , \*\* $P < 0.01$ , \*\*\* $P < 0.001$ .

Supplementary Tables 2–5) and tricarboxylic acid cycle (TCA, Fig. 5e and Supplementary Fig. 5D) were increased in response to Pgc1 $\alpha$  expression. To quantitatively define the use of glucose in the TCA cycle, we carried out stable  $^{13}\text{C}$ -U $_6$ -glucose isotope labelling. This experimental approach provided definitive evidence of the increased oxidation of glucose in the mitochondria in Pgc1 $\alpha$ -expressing cells

(Fig. 5f). This metabolic wiring was consistent with elevated oxygen consumption (basal and ATP-producing) and ATP levels following Pgc1 $\alpha$  expression (Fig. 5g–i and Supplementary Fig. 5E–I and Supplementary Tables 2–5).

We next reasoned that over-activation of mitochondrial oxidative processes would lead to decreased anabolic routes. On the one hand,

we monitored the incorporation of carbons from  $^{13}\text{C}$ -U<sub>6</sub>-glucose into fatty acids (through the export of citrate from TCA to the cytoplasm<sup>45</sup> and conversion to acetyl CoA that is used for *de novo* lipid synthesis). Interestingly, we found a significant decrease in  $^{13}\text{C}$  incorporation into palmitate (reflected as  $^{13}\text{C}$  carbon pairs) when Pgc1 $\alpha$  was expressed (Fig. 5j and Supplementary Fig. 5J). On the other hand, we monitored lactate production as a readout of aerobic glycolysis or ‘the Warburg effect’<sup>2</sup>, which has been associated with the anabolic switch. As predicted, Pgc1 $\alpha$ -expressing cells exhibited reduced extracellular lactate levels (Supplementary Fig. 5K). Of note, lactate production and respiration were unaltered by doxycycline challenge in non-transduced PC3 cells (Supplementary Fig. 5L,M). Taken together, our data provide a metabolic basis for the tumour suppressive potential of PGC1 $\alpha$  in PCa, according to which this metabolic co-regulator controls the balance between catabolic and anabolic processes (Fig. 5k).

### An ERR $\alpha$ -dependent transcriptional program mediates the prostate tumour suppressive activity of PGC1 $\alpha$

We next aimed to identify the transcription factor that mediated the activity of PGC1 $\alpha$ , and hence we performed a promoter enrichment analysis. The results revealed a predominant abundance in genes regulated by ERR $\alpha$  (Fig. 6a). We corroborated these results with Gene Set Enrichment Analysis (GSEA; normalized enrichment score = 2.02; nominal *P* value = 0.0109)<sup>46</sup>. This transcription factor controls a wide array of metabolic functions, from oxidative processes to mitochondrial biogenesis<sup>44</sup>. We have shown that PGC1 $\alpha$  is indeed capable of regulating functions attributed to ERR $\alpha$ , such as mitochondrial oxidative metabolism (Figs 4 and 5 and Supplementary Figs 4 and 5). In addition, we observed that Pgc1 $\alpha$  expression led to increased mitochondrial volume (Supplementary Fig. 6A). To ascertain the extent to which the growth inhibitory and anti-metastatic activity of PGC1 $\alpha$  required its ability to interact with ERR $\alpha$ , we took advantage of a mutant variant of the co-activator (PGC1 $\alpha$ <sup>L2L3M</sup>) that is unable to interact with this and other nuclear receptors<sup>46,47</sup>. The expression of PGC1 $\alpha$ <sup>L2L3M</sup> in PC3 cells (Supplementary Fig. 6B) failed to upregulate target genes, to reprogram oxidative metabolism, to inhibit cell growth, and, importantly, to suppress bone metastasis in intra-tibial xenografts (Fig. 6b–f and Supplementary Fig. 6C). To further discriminate between PGC1 $\alpha$  functions that depend on ERR $\alpha$  or other nuclear receptors, we undertook a targeted silencing approach, and we transduced Pgc1 $\alpha$ -inducible PC3 cells with an ERR $\alpha$ -targeting or a scramble short hairpin RNA (shRNA; Supplementary Fig. 6D). In coherence with the L2L3M mutant data, ERR $\alpha$  silencing partially blunted the effects of Pgc1 $\alpha$  on gene expression and cell growth (Fig. 6g and Supplementary Fig. 6H). *In vivo*, silencing of ERR $\alpha$  in the presence of the ectopically expressed transcriptional co-activator resulted in a significant increase in bone metastasis incidence from 40% (in Pgc1 $\alpha$ -expressing cells transduced with scramble shRNA) to full penetrance (Fig. 6h). Of note, the requirement of ERR $\alpha$  for the effect of PGC1 $\alpha$  was recapitulated *in vitro* with a reverse agonist of the transcription factor, namely XCT790<sup>48</sup> (Supplementary Fig. 6F–I).

It is worth noting that other metabolic pathways have been suggested to sustain the metastatic phenotype. Oxidative stress has been shown to limit metastatic potential in breast cancer

and melanoma<sup>29,49</sup>. PGC1 $\alpha$  regulates the expression of antioxidant genes, and the enhancement of mitochondrial metabolism can lead to the production of reactive oxygen species<sup>28,29,49</sup> (ROS; Fig. 4b and Supplementary Table 1). We therefore tested whether ROS production was modified in our experimental settings and if it could contribute to the phenotype observed. Mitochondrial and cellular ROS production were not consistently altered by Pgc1 $\alpha$  expression *in vitro* (Supplementary Fig. 6J). In addition, lipid peroxidation (which serves as a readout of ROS production) was unaffected in our xenograft study (Supplementary Fig. 6K). These results are coherent with the inability of antioxidants to rescue the proliferative defect elicited by Pgc1 $\alpha$  (Supplementary Fig. 6L).

Our data provide a molecular mechanism by which ERR $\alpha$  activation downstream of PGC1 $\alpha$  promotes a metabolic rewiring that suppresses PCa proliferation and metastasis.

### A PGC1 $\alpha$ –ERR $\alpha$ transcriptional signature harbours prognostic potential

We have shown that reduced PGC1 $\alpha$  expression in PCa exhibits prognostic potential (Fig. 1c). As our data demonstrate that transcriptional regulation downstream of ERR $\alpha$  is key for the tumour suppressive activity of this co-activator, we reasoned that the association of PGC1 $\alpha$  with aggressiveness and disease-free survival should be recapitulated when monitoring ERR $\alpha$  target genes (Fig. 7a). We started the analysis from the list of genes positively regulated by PGC1 $\alpha$  in our cellular system (153 genes, Fig. 7b). As predicted, the analysis in two independent patient data sets confirmed that the average signal of the PGC1 $\alpha$  gene list was positively correlated with time to PCa recurrence (Fig. 7c). In addition, we observed a decrease in the expression of the aforementioned gene list associated with disease initiation and progression (Supplementary Fig. 7A). Importantly, comparable results were obtained when we performed the analysis with the subset of ERR $\alpha$ -target genes within the PGC1 $\alpha$  gene set (73 genes, Supplementary Table 6 and Fig. 7b,d and Supplementary Fig. 7B). We next sought to curate the gene list to consolidate a prognostic PGC1 $\alpha$ –ERR $\alpha$  gene set. We therefore focused on genes that exhibited a strong correlation with PGC1 $\alpha$  in patient data sets. We selected genes that were significantly correlated with the co-activator ( $R > 0.2$ ;  $p < 0.05$ ) in at least three out of five studies. The results unveiled a PGC1 $\alpha$  transcriptional signature in patients consisting of 17 genes, most of which exhibited decreased expression in PCa versus BPH, and were further downregulated in metastatic disease (Supplementary Table 7 and Supplementary Fig. 7C,D). Nearly 60% of these genes were regulated by ERR $\alpha$  (10 genes out of 17) and were selected for further analysis as a PGC1 $\alpha$ –ERR $\alpha$  curated gene set (Supplementary Table 7). The results revealed reduced PGC1 $\alpha$ –ERR $\alpha$  curated gene set expression as the disease progressed (Fig. 7e). We next analysed the association of the PGC1 $\alpha$ –ERR $\alpha$  curated gene set with disease recurrence. To this end, we compared patients harbouring primary tumours with ERR $\alpha$  curated gene set average signal values in the first quartile (Q1, termed signature-positive) versus the rest (Q2–Q4). Patients with signature-positive tumours exhibited reduced disease-free survival in two independent data sets (Fig. 7f). A hazard ratio of 4.2 (Taylor) and 17.8 (TCGA) was defined for signature-positive patients, whereas signature-negative individuals presented reduced risk of recurrence, with a hazard ratio

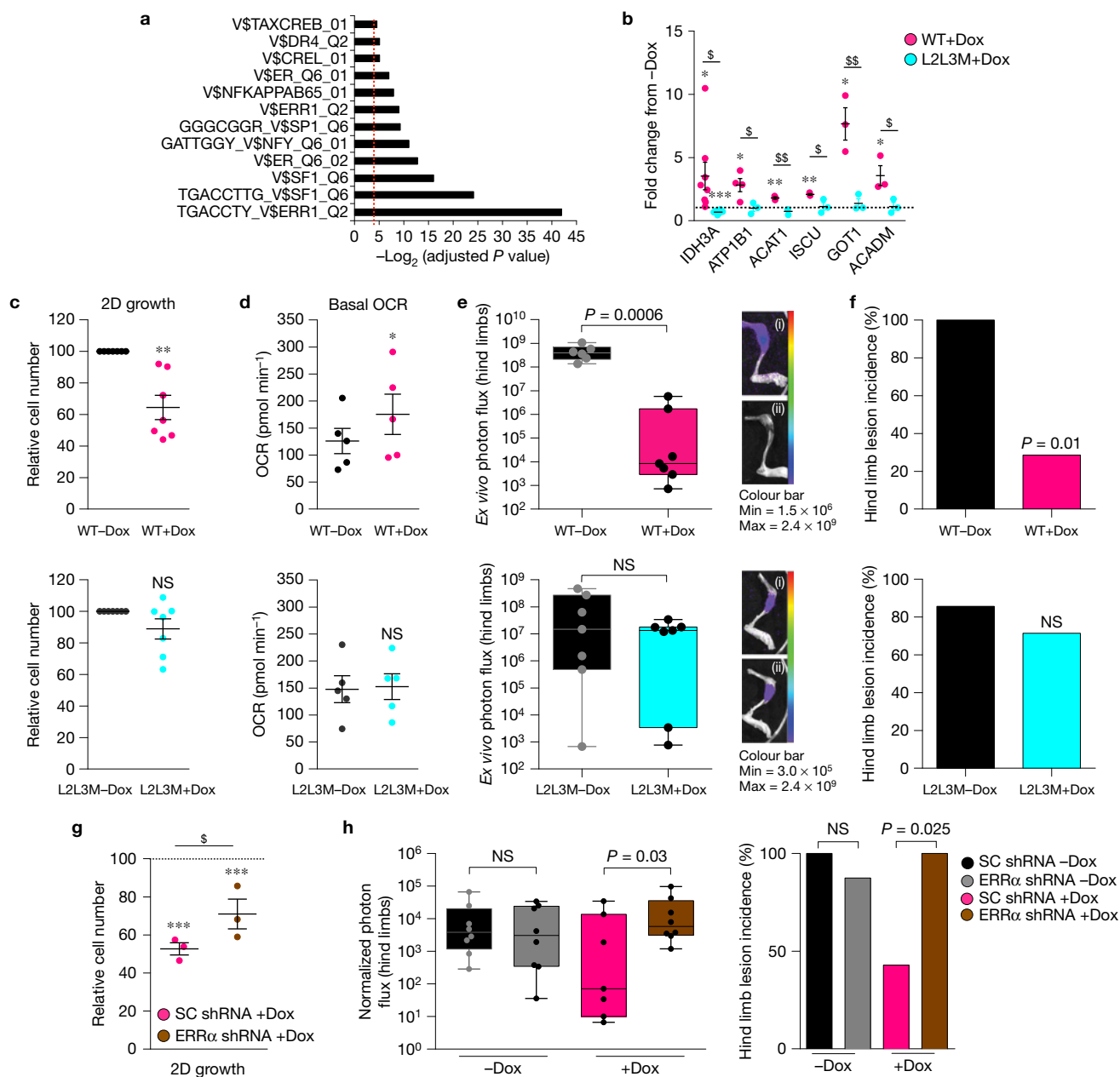


**Figure 6** An  $ERR\alpha$ -dependent transcriptional program mediates the tumour suppressive activity of  $PGC1\alpha$ . **(a)** Promoter enrichment analysis of the  $PGC1\alpha$  transcriptional program. The red dotted line indicates  $P=0.05$ . **(b–d)** Effect of  $Pgc1\alpha^{WT}$  (WT) or  $Pgc1\alpha^{L2L3M}$  ( $L2L3M$ ) induction on the expression of the indicated genes (**b**, quantitative rtPCR;  $n=8$  for  $IDH3A$ ;  $n=4$  for  $ATP1B1$ ;  $n=3$  for  $ACAT1$ ,  $ISCU$ ,  $GOT1$  and  $ACADM$  genes, independent experiments; data are normalized to each  $-Dox$  condition, represented by a black dotted line), relative cell number by crystal violet (**c**,  $n=7$ , independent experiments) and oxygen consumption rate (**d**, OCR,  $n=5$ , independent experiments). **(e,f)** Evaluation of the metastatic capacity of  $PC3$   $Pgc1\alpha^{WT}$  (WT)-expressing (upper panels) or  $PC3$   $Pgc1\alpha^{L2L3M}$  ( $L2L3M$ )-expressing (lower panels) cells using intra-tibial xenotransplant assays (**e**, photon flux quantification; WT,  $n=6$  mice;  $L2L3M$ ,  $n=7$  mice, two hind limbs per mouse; **f**, incidence of metastatic lesions presented as histograms). Representative luciferase images are presented referring to the quantification plots. For photon flux analysis, average signal from two limbs per mouse is presented. For incidence analysis, mice with at least one limb yielding luciferase signal  $>50,000$  units were considered metastasis-positive. Images (i) and (ii) depict tibia photon flux images from specimens

that are proximal to the median signal in  $-Dox$  and  $+Dox$ , respectively. **(g)** Relative cell number quantification following  $ERR\alpha$  silencing in  $Pgc1\alpha$ -expressing  $PC3$  cells. Data are represented as cell number at day 4 relative to  $-Dox$  cells ( $n=3$ , independent experiments). **(h)** Evaluation of metastatic capacity of  $Pgc1\alpha$ -expressing  $PC3$  cells transduced with SC shRNA or  $ERR\alpha$  shRNA using intra-tibial implantation for 14 days ( $n=8$  mice; two injections per mouse; incidence of metastatic lesions presented as histograms). For photon flux analysis (left panel), average signal from two limbs per mouse is presented. For incidence analysis (right panel), mice with at least one limb yielding luciferase signal  $>50,000$  units were considered metastasis-positive.  $+Dox$ ,  $Pgc1\alpha$ -induced conditions;  $-Dox$ ,  $Pgc1\alpha$ -non-expressing conditions. NS, not significant; SC, Scramble; OCR, oxygen consumption rate. Error bars represent s.e.m. **(b–d,g)** or minimum and maximum values **(e,h)**. Statistical tests: one-tailed Student's  $t$ -test **(b–d,g)**; one-tailed Mann-Whitney  $U$ -test **(e,h)** (left panel)); Fisher's exact test **(f,h)** (right panel)). \* or  $\$P < 0.05$ , \*\* or  $\$\$P < 0.01$ , \*\*\*  $P < 0.001$ . Asterisks indicate statistical difference between  $-Dox$  and  $+Dox$  conditions and dollar symbols between  $Pgc1\alpha^{WT}$  and  $Pgc1\alpha^{L2L3M}$  or SC shRNA and  $ERR\alpha$  shRNA. Statistics source data for Fig. 6e,h are provided in Supplementary Table 9.



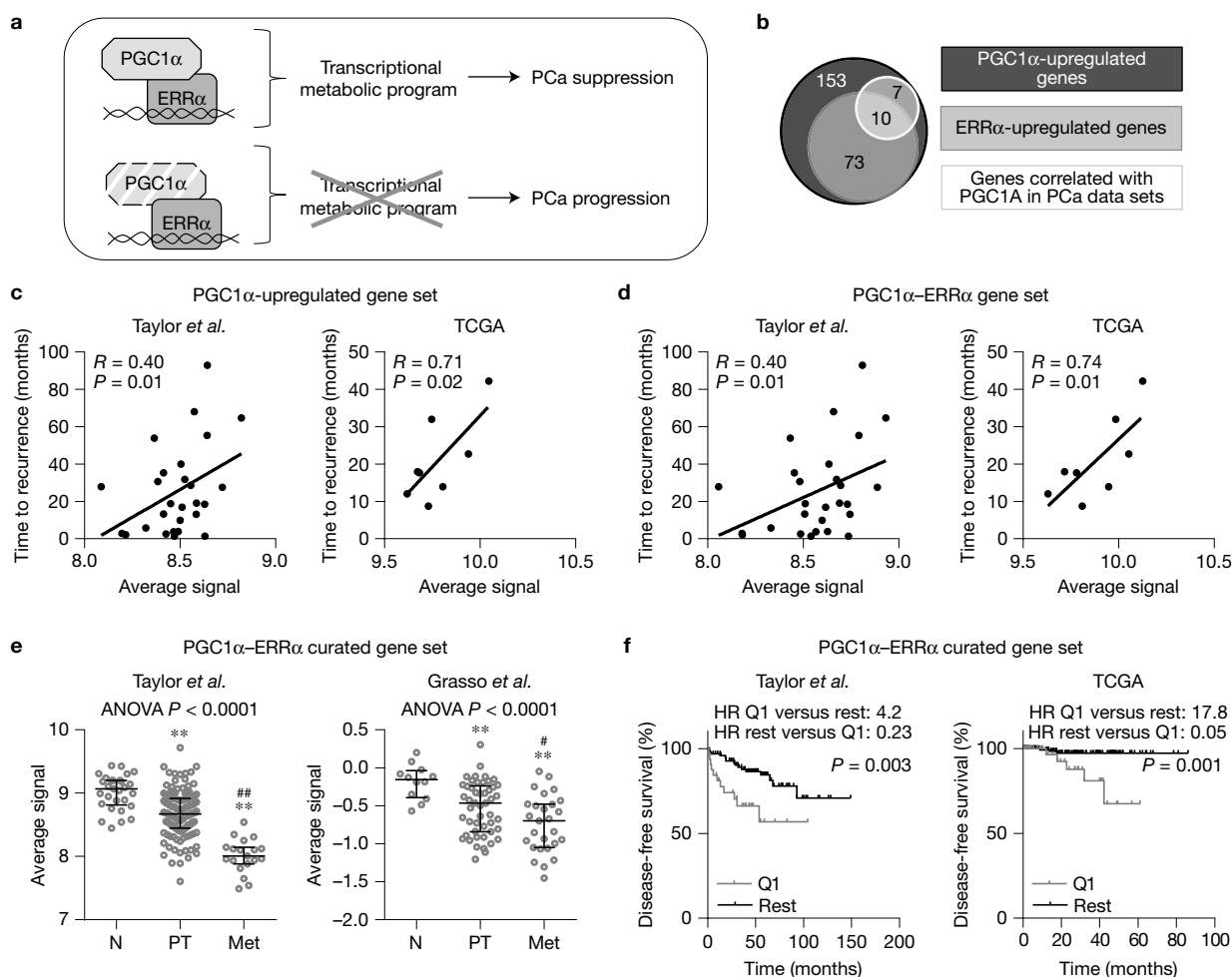


**Figure 7** The  $PGC1\alpha$  transcriptional program is associated with prostate cancer recurrence. **(a)** Schematic summary of the  $ERR\alpha$ -dependent regulation of the  $PGC1\alpha$  transcriptional metabolic program and its association with PCa progression. Dashed  $PGC1\alpha$  outline represents a decrease in abundance. **(b)** Venn diagram showing the distribution of  $PGC1\alpha$  target genes,  $ERR\alpha$  target genes (from Supplementary Table 6) and genes correlated with  $PGC1A$  expression in PCa patient specimens (from Supplementary Table 7). **(c,d)** Correlation between time to recurrence and the average signal of the genes within the  $PGC1\alpha$ -upregulated gene set **(c)** or the  $PGC1\alpha$ -dependent  $ERR\alpha$ -upregulated gene set **(d)** in the indicated data sets (Taylor<sup>22</sup>  $n=27$ ; TCGA provisional data set<sup>19,20</sup>  $n=8$ ). Each dot corresponds to an individual patient specimen. **(e)** Representation of the average signal of the genes within

the  $PGC1\alpha$ - $ERR\alpha$  curated gene set (Supplementary Table 7) in normal tissue (N; Taylor  $n=29$  and Grasso<sup>21</sup>  $n=12$ ), primary tumour (PT; Taylor  $n=131$  and Grasso  $n=49$ ) and metastasis specimens (Met; Taylor  $n=19$  and Grasso  $n=27$ ), in two independent data sets. Each dot corresponds to an individual patient specimen. **(f)** Association of the  $PGC1\alpha$ - $ERR\alpha$  signature with disease-free survival in the indicated patient data sets (Taylor  $n=131$ ; TCGA provisional data set  $n=240$ ). Q1 indicates patients with signature signal within the first quartile of primary tumours (Q1) in the corresponding data set. HR, hazard ratio. Error bars indicate interquartile range. Statistical tests: Pearson's coefficient ( $R$ ) **(c,d)**, ANOVA **(e)**, Student's  $t$ -test **(e)** and Kaplan-Meier estimator **(f)**. \*\* $P < 0.01$ ; # $P > 0.05$ . Asterisk indicates statistical difference versus N; hash indicates statistical difference versus PT.

of 0.23 (Taylor) and 0.05 (TCGA). Furthermore, the frequency of patients with signature-positive signal values was absent or low in the normal prostate group and further increased in metastasis compared with primary tumours (Supplementary Fig. 7E). Taken together,  $ERR\alpha$ -regulated metabolic transcriptional program is associated with the activity of  $PGC1\alpha$  in PCa. This interplay is conserved in patient specimens and defines a gene signature that harbours prognostic potential.

## DISCUSSION

In this study we provide a comprehensive analysis of master transcriptional co-regulators of metabolism in PCa. Through the use of human data mining analysis, GEMMs and cellular systems, our

study presents evidence demonstrating that  $PGC1\alpha$  exerts a tumour suppressive activity opposing PCa metastasis. Interestingly, three out of ten significantly altered co-regulators ( $PGC1A$ ,  $PGC1B$  and  $NR1P1$ , Fig. 1a) in the Taylor<sup>22</sup> PCa data set (two out of three consistently altered throughout databases, Fig. 1b) converge in the regulation of a common transcriptional metabolic program, led by  $ERR\alpha$  (ref. 44), and that is associated with the phenotype observed in this study. These data strongly suggest that such pathway is of critical importance for the control of aggressiveness properties in PCa. Indeed, our results demonstrate that a gene set composed of  $ERR\alpha$  target genes that are under the control of  $PGC1\alpha$  expression is progressively downregulated in PCa and metastatic disease, and presents prognostic potential for the identification of patients at risk of early recurrence.

The study of the tumour suppressive potential of *Pgc1 $\alpha$*  in mouse models allowed us to characterize a clinically relevant PCa GEMM presenting enhanced metastatic dissemination. *PGC1 $\alpha$*  is added to the shortlist of genetic events that drive metastasis in this model<sup>13–16</sup>, and the first to be explicitly linked to the regulation of the metabolic switch. Overall, our finding is of importance for the future study of the requirements for PCa metastasis and therefore for therapeutic purposes.

The sole alteration of *PGC1 $\alpha$*  expression in PCa has a profound impact on the oncogenic metabolic switch<sup>50</sup>. These data are in line with the reported activities of this protein in metabolism and mitochondrial biogenesis<sup>26</sup>. Of note, despite the widely accepted fact that the reported metabolic switch<sup>50</sup> has comparable consequences in all cancer scenarios, the study of *PGC1 $\alpha$*  in other tumour types has also revealed a selective pressure towards oxidative processes<sup>27–29</sup>. Previous work from others and us defined *PGC1 $\alpha$*  signalling as a selective advantage for breast cancer and melanoma cells<sup>4,27–29,51</sup>. The contribution of this co-activator to cellular proliferation differs between tumour types and experimental systems, promoting growth in melanoma<sup>28</sup> but irrelevant to breast cancer cells<sup>29</sup>. Interestingly, in breast circulating tumour cells, *PGC1 $\alpha$*  expression supports metastatic capacity<sup>29</sup>. The molecular pathways regulating these diverse biological features converge in the activation of *ERR $\alpha$*  and peroxisome proliferator-activated receptors (*PPAR*). Whereas *PPAR* activation mediates the increase in fatty acid  $\beta$ -oxidation<sup>4</sup>, *ERR $\alpha$*  is responsible for the overall increase in oxidative metabolism and mitochondrial biogenesis<sup>44</sup>. Similarly, the activation of an antioxidant transcriptional program has been suggested to contribute to anoikis and cancer cell dissemination in a *PGC1 $\alpha$* -dependent and independent manner<sup>27,28,49,52</sup>. In PCa, however, we demonstrate that the oxidative metabolic program elicited by *PGC1 $\alpha$*  prevents tumour growth and metastatic dissemination, in the absence of overt changes in ROS production, inflammatory response or angiogenic signals. These findings support the notion that the optimal metabolic wiring for tumour growth and metastasis might differ depending on the tumour type, the mutational landscape of the tumour and, potentially, the microenvironment. This would lead to opposite activities of *PGC1 $\alpha$*  depending on the cancer setting, from metastatic promoter<sup>29</sup> to metastasis suppressor (as we demonstrate in the present work).

In summary, our study identifies *PGC1 $\alpha$*  as a master regulator of PCa metabolism that opposes the dissemination of the disease. Therefore, a *PGC1 $\alpha$* -regulated *ERR $\alpha$* -dependent transcriptional program might open new avenues in the identification of metabolic transcriptional signatures that can be exploited for patient stratification and the use of metabolism-modulatory therapies. □

## METHODS

Methods and any associated references are available in the [online version of the paper](#).

Note: Supplementary Information is available in the [online version of the paper](#)

## ACKNOWLEDGEMENTS

Apologies to those whose related publications were not cited owing to space limitations. We would like to thank the following researchers: B. Spiegelman (Dana-Farber Cancer Institute, Harvard Medical School, Boston, Massachusetts, USA; Department of Cell Biology, Harvard Medical School, Boston, Massachusetts, USA) for providing the *Pgc1 $\alpha$ <sup>loxP</sup>* mice; D. Santamaría and M. Barbacid (Experimental

Oncology, Molecular Oncology Programme, Centro Nacional de Investigaciones Oncológicas (CNIO), Madrid, Spain) for technical help and advice with doxycycline-enriched diets in xenograft experiments; P. Puigserver (Department of Cell Biology, Harvard Medical School, and in the Department of Cancer Biology, Dana-Farber Cancer Institute, Boston, Massachusetts, USA) for providing *Pgc1 $\alpha$* -expressing constructs; B. Carver (Department of Surgery, Division of Urology, Human Oncology and Pathogenesis Program, Memorial Sloan Kettering Cancer Center, New York, USA) for help and advice with data set analysis, D. McDonnell (Department of Pharmacology and Cancer Biology, Duke University Medical Center, Durham, North Carolina, USA) for providing mutant *Pgc1 $\alpha$ <sup>1213M</sup>*-expressing constructs and M. D. Boyano (Department of Cell Biology and Histology, School of Medicine and Dentistry, University of the Basque Country (UPV/EHU), Leioa, Bizkaia, Spain) and A. Buqué (Medical Oncology Research Laboratory, Cruces University Hospital, Bizkaia, Spain) for providing melanoma cell lines. The work of A.C. is supported by the Ramón y Cajal award, the Basque Department of Industry, Tourism and Trade (Etorrek), health (2012111086) and education (PI2012-03), Marie Curie (277043), Movember, ISCIII (PI10/01484, PI13/00031), FER0 VIII Fellowship and the European Research Council Starting Grant (336343). N.M.-M. is supported by the Spanish Association Against Cancer (AECC). A.C.-M. is supported by the MINECO postdoctoral program and the CIG program from the European commission (660191). A.A.-A. and L.V.-J. are supported by the Basque Government of Education. P.Pinton is grateful to C. degli Scroveni for continuous support and the work in his laboratory was supported by the Italian Association for Cancer Research (AIRC: IG-14442), the Italian Ministry of Education, University and Research (COFIN no. 20129JLHSY\_002, FIRB no. RBAP11FXBC\_002, and Futuro in Ricerca no. RBF10EGVP\_001) and the Italian Ministry of Health. R.B. is supported by MINECO (BFU2014-52282-P, BFU2011-25986) and the Basque Government (PI2012/42). The work of V.S.-M. was supported by Cancer Research UK C33043/A12065; Royal Society RG110591. P.Pandya was supported by King's Overseas Scholarship. Work by the group of G.V. was supported by grants from the Spanish Ministry of Economy and Competitiveness/Instituto de Salud Carlos III (MINECO/ISCIII) together with the European Regional Development Fund (ERDF/FEDER): PS09/01401; PI12/02248 and PI15/00339, Fundación Mutua Madrileña and Fundació la Marató de TV3. C.C.-C. and M.C.-M. were financially supported by NIH P01CA087497. J.W.L. is supported by R00CA168997, R01CA193256 and R21CA201963 from the National Institutes of Health. Work in the M.Graupera laboratory was supported by SAF2014-59950-P from MINECO (Spain), 2014-SGR-725 from the Catalan Government, from the People Programme (Marie Curie Actions) of the European Union's Seventh Framework Programme FP7/2007-2013/ (REA grant agreement 317250), and the Institute of Health Carlos III (ISC III) and the European Regional Development Fund (ERDF) under the integrated Project of Excellence no. PIE13/00022 (ONCOPROFILE). J.U. is a Juan de la Cierva Researcher (MINECO). A.Bellmunt is a FPI-Severo Ochoa fellowship grantee (MINECO). R.R.G. research support was provided by the Spanish Government (MINECO) and FEDER grant SAF2013-46196, as well as the Generalitat de Catalunya AGAUR 2014-SGR grant 535.

## AUTHOR CONTRIBUTIONS

V.T. and L.V.-J. performed all *in vitro* and *in vivo* experiments, unless specified otherwise. A.R.C. carried out the bioinformatic and biostatistical analysis. A.Berenguer and N.S. provided support and advice in data set retrieval and normalization. S.F.-R. performed the histochemical stainings. P.S.-M. and S.F.-R. performed genotyping analyses. X.L. and J.W.L. contributed to the experimental design and executed the metabolomic analyses. G.M. and P.Pinton performed the biochemical ATP measurement *in vitro* and mitochondria analysis. G.V., P.Z.-G. and M.L. performed or coordinated (G.V.) subcutaneous xenograft experiments. J.U., A.Bellmunt, M.Guiu and R.R.G. performed or coordinated (R.R.G.) the intra-cardiac and intra-tibial metastasis assays. R.R.G. contributed to the design of the patient gene signature analysis. M.Graupera carried out microvessel staining and quantifications. P.Pandya and V.S.-M. provided technical advice and contributed to *in vitro* analysis. N.M.-M., A.A.-A. and A.Z.-L. contributed to the experimental design and discussion. A.C.-M. and N.E. performed Seahorse assays. J.D.S. and R.B. performed or coordinated (R.B.) the cloning of *Pgc1 $\alpha$*  in lentiviral vectors. C.C.-C. and M.C.-M. carried out the pathological analysis and scoring of the xenografts and GEMMs. A.U.-O., I.L.-V., A.L.-I. and M.U.-U. provided BPH and PCa samples for gene expression analysis from Basurto University Hospital. A.M.A. contributed to the discussion of the results. A.C. directed the project, contributed to data analysis and wrote the manuscript.

## COMPETING FINANCIAL INTERESTS

The authors declare no competing financial interests.

Published online at <http://dx.doi.org/10.1038/ncb3357>

Reprints and permissions information is available online at [www.nature.com/reprints](http://www.nature.com/reprints)

1. Loo, J. M. *et al.* Extracellular metabolic energetics can promote cancer progression. *Cell* **160**, 393–406 (2015).
2. Vander Heiden, M. G., Cantley, L. C. & Thompson, C. B. Understanding the Warburg effect: the metabolic requirements of cell proliferation. *Science* **324**, 1029–1033 (2009).
3. Vander Heiden, M. G. *et al.* Evidence for an alternative glycolytic pathway in rapidly proliferating cells. *Science* **329**, 1492–1499 (2010).
4. Carracedo, A., Cantley, L. C. & Pandolfi, P. P. Cancer metabolism: fatty acid oxidation in the limelight. *Nat. Rev. Cancer* **13**, 227–232 (2013).
5. Yang, M., Soga, T. & Pollard, P. J. Oncometabolites: linking altered metabolism with cancer. *J. Clin. Invest.* **123**, 3652–3658 (2013).
6. Ortega-Molina, A. *et al.* Pten positively regulates brown adipose function, energy expenditure, and longevity. *Cell Metab.* **15**, 382–394 (2012).
7. Garcia-Cao, I. *et al.* Systemic elevation of PTEN induces a tumor-suppressive metabolic state. *Cell* **149**, 49–62 (2012).
8. Salmena, L., Carracedo, A. & Pandolfi, P. P. Tenets of PTEN tumor suppression. *Cell* **133**, 403–414 (2008).
9. Song, M. S., Salmena, L. & Pandolfi, P. P. The functions and regulation of the PTEN tumour suppressor. *Nat. Rev. Mol. Cell Biol.* **13**, 283–296 (2012).
10. Di Cristofano, A., Pesce, B., Cordon-Cardo, C. & Pandolfi, P. P. Pten is essential for embryonic development and tumour suppression. *Nat. Genet.* **19**, 348–355 (1998).
11. Chen, Z. *et al.* Crucial role of p53-dependent cellular senescence in suppression of Pten-deficient tumorigenesis. *Nature* **436**, 725–730 (2005).
12. Majumder, P. K. *et al.* Prostate intraepithelial neoplasia induced by prostate restricted Akt activation: the MPAKT model. *Proc. Natl Acad. Sci. USA* **100**, 7841–7846 (2003).
13. Magnon, C. *et al.* Autonomic nerve development contributes to prostate cancer progression. *Science* **341**, 1236361 (2013).
14. Ding, Z. *et al.* SMAD4-dependent barrier constrains prostate cancer growth and metastatic progression. *Nature* **470**, 269–273 (2011).
15. Nandana, S. & Chung, L. W. Prostate cancer progression and metastasis: potential regulatory pathways for therapeutic targeting. *Am. J. Clin. Exp. Urol.* **2**, 92–101 (2014).
16. Cho, H. *et al.* RapidCaP, a novel GEM model for metastatic prostate cancer analysis and therapy, reveals myc as a driver of Pten-mutant metastasis. *Cancer Discov.* **4**, 318–333 (2014).
17. Mouchiroud, L., Eichner, L. J., Shaw, R. J. & Auwerx, J. Transcriptional coregulators: fine-tuning metabolism. *Cell Metab.* **20**, 26–40 (2014).
18. Lapointe, J. *et al.* Gene expression profiling identifies clinically relevant subtypes of prostate cancer. *Proc. Natl Acad. Sci. USA* **101**, 811–816 (2004).
19. Cerami, E. *et al.* The cBio cancer genomics portal: an open platform for exploring multidimensional cancer genomics data. *Cancer Discov.* **2**, 401–404 (2012).
20. Gao, J. *et al.* Integrative analysis of complex cancer genomics and clinical profiles using the cBioPortal. *Sci. Signal* **6**, pl1 (2013).
21. Grasso, C. S. *et al.* The mutational landscape of lethal castration-resistant prostate cancer. *Nature* **487**, 239–243 (2012).
22. Taylor, B. S. *et al.* Integrative genomic profiling of human prostate cancer. *Cancer Cell* **18**, 11–22 (2010).
23. Tomlins, S. A. *et al.* Integrative molecular concept modeling of prostate cancer progression. *Nat. Genet.* **39**, 41–51 (2007).
24. Varambally, S. *et al.* Integrative genomic and proteomic analysis of prostate cancer reveals signatures of metastatic progression. *Cancer Cell* **8**, 393–406 (2005).
25. Robinson, D. *et al.* Integrative clinical genomics of advanced prostate cancer. *Cell* **161**, 1215–1228 (2015).
26. Lin, J., Handschin, C. & Spiegelman, B. M. Metabolic control through the PGC-1 family of transcription coactivators. *Cell Metab.* **1**, 361–370 (2005).
27. Haq, R. *et al.* Oncogenic BRAF regulates oxidative metabolism via PGC1 $\alpha$  and MITF. *Cancer Cell* **23**, 302–315 (2013).
28. Vazquez, F. *et al.* PGC1 $\alpha$  expression defines a subset of human melanoma tumors with increased mitochondrial capacity and resistance to oxidative stress. *Cancer Cell* **23**, 287–301 (2013).
29. LeBleu, V. S. *et al.* PGC-1 $\alpha$  mediates mitochondrial biogenesis and oxidative phosphorylation in cancer cells to promote metastasis. *Nat. Cell Biol.* **16**, 992–1003 (2014).
30. LaGory, E. L. *et al.* Suppression of PGC-1 $\alpha$  is critical for reprogramming oxidative metabolism in renal cell carcinoma. *Cell Rep.* **12**, 116–127 (2015).
31. D'Errico, I. *et al.* Peroxisome proliferator-activated receptor-gamma coactivator 1- $\alpha$  (PGC1 $\alpha$ ) is a metabolic regulator of intestinal epithelial cell fate. *Proc. Natl Acad. Sci. USA* **108**, 6603–6608 (2011).
32. Sancho, P. *et al.* MYC/PGC-1 $\alpha$  balance determines the metabolic phenotype and plasticity of pancreatic cancer stem cells. *Cell Metab.* **22**, 590–605 (2015).
33. Audet-Walsh, E. *et al.* The PGC-1 $\alpha$ /ERR $\alpha$  axis represses one-carbon metabolism and promotes sensitivity to anti-folate therapy in breast cancer. *Cell Rep.* **14**, 920–931 (2016).
34. Lin, J. *et al.* Defects in adaptive energy metabolism with CNS-linked hyperactivity in PGC-1 $\alpha$  null mice. *Cell* **119**, 121–135 (2004).
35. Eisele, P. S. & Handschin, C. Functional crosstalk of PGC-1 coactivators and inflammation in skeletal muscle pathophysiology. *Semin. Immunopathol.* **36**, 27–53 (2014).
36. Saint-Geniez, M. *et al.* PGC-1 $\alpha$  regulates normal and pathological angiogenesis in the retina. *Am. J. Pathol.* **182**, 255–265 (2013).
37. Nardella, C., Carracedo, A., Salmena, L. & Pandolfi, P. P. Faithful modeling of PTEN loss driven diseases in the mouse. *Curr. Top. Microbiol. Immunol.* **347**, 135–168 (2011).
38. Nardella, C. *et al.* Aberrant Rheb-mediated mTORC1 activation and Pten haploinsufficiency are cooperative oncogenic events. *Genes Dev.* **22**, 2172–2177 (2008).
39. Li, S. *et al.* Genome-wide coactivation analysis of PGC-1 $\alpha$  identifies BAF60a as a regulator of hepatic lipid metabolism. *Cell Metab.* **8**, 105–117 (2008).
40. Tennakoon, J. B. *et al.* Androgens regulate prostate cancer cell growth via an AMPK-PGC-1 $\alpha$ -mediated metabolic switch. *Oncogene* **33**, 5251–5261 (2014).
41. Shiota, M. *et al.* Peroxisome proliferator-activated receptor gamma coactivator-1 $\alpha$  interacts with the androgen receptor (AR) and promotes prostate cancer cell growth by activating the AR. *Mol. Endocrinol.* **24**, 114–127 (2010).
42. Buijs, J. T. & van der Pluijm, G. Osteotropic cancers: from primary tumor to bone. *Cancer Lett.* **273**, 177–193 (2009).
43. Garcia, M. *et al.* Cyclooxygenase-2 inhibitor suppresses tumour progression of prostate cancer bone metastases in nude mice. *BJU Int.* **113**, E164–E177 (2014).
44. Feige, J. N. & Auwerx, J. Transcriptional coregulators in the control of energy homeostasis. *Trends Cell Biol.* **17**, 292–301 (2007).
45. Finley, L. W., Zhang, J., Ye, J., Ward, P. S. & Thompson, C. B. SnapShot: cancer metabolism pathways. *Cell Metab.* **17**, e462–466 (2013).
46. Stein, R. A. *et al.* Estrogen-related receptor alpha is critical for the growth of estrogen receptor-negative breast cancer. *Cancer Res.* **68**, 8805–8812 (2008).
47. Gaillard, S. *et al.* Receptor-selective coactivators as tools to define the biology of specific receptor-coactivator pairs. *Mol. Cell* **24**, 797–803 (2006).
48. Chang, C. Y. *et al.* The metabolic regulator ERR $\alpha$ , a downstream target of HER2/IGF-1R, as a therapeutic target in breast cancer. *Cancer Cell* **20**, 500–510 (2011).
49. Piskounova, E. *et al.* Oxidative stress inhibits distant metastasis by human melanoma cells. *Nature* **527**, 186–191 (2015).
50. Lunt, S. Y. & Vander Heiden, M. G. Aerobic glycolysis: meeting the metabolic requirements of cell proliferation. *Annu. Rev. Cell Dev. Biol.* **27**, 441–464 (2011).
51. Carracedo, A. *et al.* A metabolic prosurvival role for PML in breast cancer. *J. Clin. Invest.* **122**, 3088–3100 (2012).
52. Schafer, Z. T. *et al.* Antioxidant and oncogene rescue of metabolic defects caused by loss of matrix attachment. *Nature* **461**, 109–113 (2009).

## METHODS

**Reagents.** 3-[4-(2,4-Bis-trifluoromethylbenzyloxy)-3-methoxyphenyl]-2-cyano-N-(5-trifluoromethyl-1,3,4-thiadiazol-2-yl)acrylamide (XCT 790), etomoxir (ETO), doxycycline hyclate (Dox), oligomycin, N-acetyl-cysteine (NAC) and manganese (III) tetrakis (4-benzoic acid)porphyrin chloride (MnTBAP) were purchased from Sigma.

**Cell culture.** Human prostate carcinoma cell lines LnCaP, DU145 and PC3 were purchased from Leibniz-Institut DSMZ - Deutsche Sammlung von Mikroorganismen und Zellkulturen GmbH, who provided an authentication certificate. None of the cell lines used in this study were found in the database of commonly misidentified cell lines maintained by ICLAC and NCBI Biosample. Cells were transduced with a modified TRIPZ (Dharmacon) doxycycline-inducible lentiviral construct in which the RFP and miR30 region was replaced by *HA-Flag-Pgc1a* (ref. 51) or *HA-Flag-Pgc1a<sup>L2L3M</sup>* (ref. 47). Lentiviral shRNA constructs targeting *PGC1A* (TRCN000001166) and *ESRRA* (TRCN0000022180) were purchased from Sigma and a scramble shRNA (hairpin sequence: 5'-CCGGCAACAAGATGAAGAGCACCAACTCGAGTTGGTGCTCTTCATCTTGTG-3') was used as the control. For *ESRRA* shRNAs, the puromycin resistance cassette was replaced by the hygromycin cassette from pLKO.1 Hygro (Addgene Ref. 24150) using BamHI and KpnI sites. Melanoma lines were provided by M. D. Boyano<sup>53</sup> and A. Buqué and purchased from ATCC. Cell lines were routinely monitored for mycoplasma contamination and quarantined while treated if positive.

**Animals.** All mouse experiments were carried out following the ethical guidelines established by the Biosafety and Welfare Committee at CIC bioGUNE and The Institutional Animal Care and Use Committee of IRB Barcelona. The procedures employed were carried out following the recommendations from AAALAC. Xenograft experiments were performed as previously described<sup>54</sup>, injecting 10<sup>6</sup> cells per condition in two flanks per mouse. PC3 TRIPZ-HA-Pgc1a cells were injected in each flank of nude mice and 24 h post-injections mice were fed with chow or doxycycline diet (Research diets, D12100402). GEMM experiments were carried out as reported in a mixed background<sup>11,14,55,56</sup> (where the founder colony was cross-bred for at least three generations before the expansion of experimental cohorts to ensure a homogenous mixed background). The *Pten<sup>loxP</sup>* and *Pgc1a<sup>loxP</sup>* conditional knockout alleles have been described elsewhere<sup>11,34</sup>. Prostate epithelium-specific deletion was effected by the *Pb-Cre41*. Mice were fasted for 6 h before tissue collection (9:00–15:00) to prevent metabolic alterations due to immediate food intake.

For intra-tibial and intra-cardiac injections BALB/c nude male mice (Harlan) of 9–11 weeks of age were used. Before the injections, PC3 Tripz-HA-Pgc1a (WT, L2L3M, SC shRNA, ESRRA shRNA) cell lines were pre-treated for 48 h with PBS or doxycycline (0.5 µg ml<sup>-1</sup>). Mice injected with cells treated with doxycycline were also pre-treated for 48 h with 1 mg ml<sup>-1</sup> of doxycycline in drinking water. After the injections this group of mice was left on continuous doxycycline treatment (1 mg ml<sup>-1</sup> in drinking water). Before the injections mice were anaesthetized with a mixture of ketamine (80 mg kg<sup>-1</sup>) and xylazine (8 mg kg<sup>-1</sup>). For intra-tibial injections, 1 × 10<sup>4</sup> cells were resuspended in a final volume of 5 µl of cold PBS and injected as described previously<sup>57</sup>. For intra-cardiac injections 2 × 10<sup>5</sup> cells were resuspended in a final volume of 100 µl of cold PBS and injected as described previously<sup>57</sup>. After the injections, tumour development was followed on a weekly basis by BLI using the IVIS-200 imaging system from Xenogen. Quantification of bioluminescent images was done with Living Image 2.60.1 software. The development of metastasis was confirmed by examining *in vivo* or *ex vivo* (following necropsy) bioluminescent images of organs of interest (metastasis positivity in lesion incidence analysis was defined as tibias with luciferase signals greater than 50,000 units). When comparing cell lines independently transduced with the luciferase-expressing vector (Fig. 6h), photon flux values per limb were presented as normalized signal (corrected by basal signal, obtained within 24 h after injection): Normalized photon flux = (day 14 signal/day 0 signal) × 1,000. For metastasis-free survival curves, a metastatic event was scored when the measured value of bioluminescence bypassed 1/10 of the day 0 value.

**Patient samples.** All samples were obtained from the Basque Biobank for research (BIOEF, Basurto University hospital) on informed consent and with evaluation and approval from the corresponding ethics committee (CEIC code OHEUN11-12 and OHEUN14-14).

**Cellular, molecular and metabolic assays.** Cell number quantification with crystal violet<sup>58</sup> was performed as referenced. Soft agar assays were performed as previously described (INSERT REF 60) seeding 5,000 cells per well in 6-well plates.

Western blot was performed as previously described<sup>51</sup>. Antibodies used: PGC1α (H300; Santa Cruz Biotechnology sc-13067; dilution 1:1,000); ESRRA (E1G1; Cell Signaling no. 13826; dilution 1:1,000); β-actin (clone AC-74; Sigma no. A 5316;

dilution 1:2,000); GAPDH (clone 14C10; Cell Signaling no. 2218; dilution 1:1,000); HSP90 (Cell Signaling; no. 4874; dilution 1:1,000).

RNA was extracted using the NucleoSpin RNA isolation kit from Macherey-Nagel (ref: 740955.240C). For patients and animal tissues a Trizol-based implementation of the NucleoSpin RNA isolation kit protocol was used as reported previously<sup>59</sup>. For all cases, 1 µg of total RNA was used for cDNA synthesis using qScript cDNA Supermix from Quanta (ref. 95048). Quantitative real-time PCR (rtPCR) was performed as previously described<sup>51</sup>. Universal Probe Library (Roche) primers and probes employed are detailed in Supplementary Table 8. β-ACTIN (Hs99999903\_m1; Mm0607939\_s1) and GAPDH (Hs02758991\_g1, Mm99999915\_g1) housekeeping assays from Applied Biosystems showed similar results (all quantitative rtPCR data presented were normalized using GAPDH/Gapdh).

Fatty acid oxidation was performed as previously described<sup>51</sup>. Lactate production was measured as referenced<sup>60</sup> using the Trinity Biotech lactate measurement kit.

Oxygen consumption rate (OCR) was measured with an XF24 extracellular flux analyser (Seahorse Bioscience)<sup>61</sup>. Briefly, 50,000 cells per well were seeded in an XF24 plate, and OCR measurements were normalized to cell number analysed by crystal violet. Cells were initially plated in 10% FBS DMEM media for 24 h, and 1 h before measurements, the medium was changed to serum- and bicarbonate-free DMEM, with glutamine and glucose (10 mM). Mitochondrial stress test was carried out using the following concentration of injected compound: oligomycin (1 µM).

For mitochondrial ATP assays, 50,000 PC3 and DU145 cells were plated onto 13-mm coverslips and transfected with a mitochondrial-targeted luciferase chimera (mtLuc). Cells were perfused in the luminometer at 37 °C with KRB solution containing 25 µM luciferin and 1 mM CaCl<sub>2</sub> and supplemented with 5.5 mM glucose. Under these conditions, the light output of a coverslip of transfected cells was in the range of 5,000–20,000 c.p.s. for the luciferase construct versus a background lower than 100 c.p.s. Luminescence was entirely dependent on the presence of luciferin and was proportional to the perfused luciferin concentration between 20 and 200 µM.

Mitochondrial morphology was assessed by using a cDNA encoding mitochondrial matrix-targeted DsRed (mtDsRed). Cells were seeded onto 24-mm-diameter coverslips (thickness between 0.16–0.19 mm) (Thermo Scientific) and 24 h later cells were transfected with 2 µg mtDsRed (Lipofectamine LTX reagent; Invitrogen). mtDsRed expression was assessed 36 h later. All of the acquisitions were performed with a confocal Nikon Eclipse Ti<sub>2</sub> system and fluorescent images were captured by using NisElements 3.2.

Lipid peroxidation based on MDA detection was assayed in xenograft samples following the manufacturer's instructions (MAK085 Sigma-Aldrich).

ROS production was determined by Mitosox and DCF staining as previously described<sup>62</sup>.

**Histopathological analysis.** After euthanasia, histological evaluation of a haematoxylin and eosin (H&E)-stained section from formalin-fixed paraffin-embedded tissues of the following organs was performed: prostate gland, lymph nodes, long bones from lower limbs and other solid organs such as lungs and liver.

Following the consensus reported previously<sup>63</sup>, prostate gland alterations were classified into four categories: gland within normal limits; high-grade prostatic intraepithelial neoplasia (HGPIN); HGPIN with focal micro-invasion; and invasive carcinoma. Lymphovascular invasion was assessed in all cases where micro-invasion foci or invasive carcinoma were observed.

Lymph node metastasis and the presence of groups of PCa cells in bone marrow were determined after haematoxylin-eosin (H&E) staining (lymph nodes) and immunohistochemical identification of cytokeratin (CK) and androgen receptor (AR)-expressing cells using a panCK rabbit polyclonal antibody (Dako) and AR rabbit polyclonal antibody (Santa Cruz Biotechnology, sc-816) (lymph nodes and bone marrow). In the case of bone marrow, cases were classified as 'dissemination negative' when none or few scattered (fewer than five) CK-expressing cells were identified and 'dissemination positive' when more than five or small groups of these cells were observed.

To assess the inflammatory component in the prostate tissues we performed a semiquantitative analysis in the glandular and the stromal areas separately for each of the specimens. We first determined the type of inflammatory cell present in each tissue compartment: polymorphonuclear neutrophils versus lympho-plasmacytic infiltrates. Then we performed a quantification of these cells using the following score system: 0—no inflammatory cells, 1—few cells, 2—moderate amount of cells and 3—high amount of cells. Scores in between were also determined as 0.5, 1.5 and 2.5. If both types of cell were present in one compartment, we chose the highest as the final score.

Proliferation was assessed in paraffin-embedded xenografts samples by using Ki67 antibody (MA5-14520, Thermo Scientific). Microvessel density was determined and quantified in GEMMs and xenograft samples by the immunodetection of CD31 (rabbit anti-CD31; Ref. ab28364 Abcam).

**Metabolomics.** Liquid-chromatography high-resolution mass spectrometry (LC–HRMS) metabolomics and stable isotope  $^{13}\text{C}$ – $\text{U}_6$ –glucose labelling was performed as reported previously<sup>64–66</sup>. Briefly, for LC–HRMS metabolomics, PC3 TRIPZ–HA–Flag–Pgc1a cells treated or untreated for 72 h with  $0.5\ \mu\text{g ml}^{-1}$  doxycycline were plated at 500,000 cells per well in 6-well plates, and grown maintaining the doxycycline regime for 42 h before collection. For stable isotope  $^{13}\text{C}$ – $\text{U}_6$ –glucose labelling experiments, 24 h after seeding cells were washed and exposed to media with serum, without glucose and pyruvate and supplemented 2 mM  $^{13}\text{C}$ – $\text{U}_6$ –glucose. After a further 16 h, cells were washed and another  $^{13}\text{C}$ – $\text{U}_6$ –glucose pulse was performed for 2 h before collection.

**Transcriptomic analysis.** For transcriptomic analysis in PC3 TRIPZ–HA–Flag–Pgc1a cells, the Illumina whole-genome -HumanHT-12\_V4.0 (DirHyb, nt) method was used as reported previously<sup>67</sup>.

Promoter enrichment analysis was assessed with the Transcription Factors (TFs) data set from MSigDB (The Molecular Signature Database; <http://www.broadinstitute.org/gsea/msigdb/collections.jsp>). The TFs data set contains genes that share a transcription factor-binding site defined in the TRANSFAC (version 7.4, <http://www.gene-regulation.com>) database. Each of these gene sets was annotated by a TRANSFAC record. A hypergeometric test was used to detect enriched data set categories.

The GSEA was performed using the GenePattern web tool from the Broad Institute (<http://genepattern.broadinstitute.org>). The list of PGC1 $\alpha$ -upregulated genes ranked by their fold change was uploaded and analysed against a list of ERR $\alpha$  target genes<sup>46</sup>. The number of permutations carried out was 1,000 and the threshold was 0.05.

**Bioinformatic analysis.** For database normalization, all of the data sets used for the data mining analysis were downloaded from GEO, and subjected to background correction,  $\log_2$  transformation and quartile normalization. In the case of using a pre-processed data set, this normalization was reviewed and corrected if required.

Frequency of alteration of metabolic co-regulators (Fig. 1 and Supplementary Fig. 1A): expression levels of the selected co-regulators were obtained from the data set reported by Taylor *et al.*<sup>22</sup>. A matrix containing signal values and clinical information was prepared to ascertain the up- or downregulation. We computed the relative expression of an individual gene and tumour to the expression distribution in a reference population (patients without prostate tumour or metastasis). The returned value indicates the number of standard deviations away from the mean of expression in the reference population ( $Z$ -score). Using a fold change of +2 and –2 as a threshold, we determined the number of samples from the cancer data set that were up- or downregulated.  $P$  values were calculated by comparing the means of normal of cancerous biopsies.

For quartile analysis in disease-free survival, patients' biopsies from primary tumours were organized into four quartiles according to the expression of the gene of interest in two data sets. The recurrence of the disease was selected as the event of interest. The Kaplan–Meier estimator was used to perform the test as it takes into account right-censoring, which occurs if a patient withdraws from a study. On the plot, small vertical tick marks indicate losses, where a patient's survival time has been right-censored. With this estimator we obtained a survival curve, a graphical representation of the occurrence of the event in the different groups, and a  $P$  value that estimates the statistical power of the differences observed.

For PGC1 $\alpha$  genomic analysis, data from prostate cancer patients with copy number alteration information in Taylor<sup>22</sup>, Grasso<sup>21</sup> and Robinson<sup>25</sup> *et al.* data sets were extracted from [cbiportal.org](http://cbiportal.org). Percentage of shallow deletions of primary tumours and metastatic patients was calculated separately.

For correlation analysis, the Pearson correlation test was applied to analyse the relationship between paired genes. From this analysis, Pearson's coefficient ( $R$ ) indicates the existing linear correlation (dependence) between two variables  $X$  and  $Y$ , giving a value between +1 and –1 (both included), where 1 is total positive correlation, 0 is no correlation, and –1 is total negative correlation. The  $P$  value indicates the significance of this  $R$  coefficient.

**Statistics and reproducibility.** No statistical method was used to predetermine sample size. The experiments were not randomized. The investigators were not blinded to allocation during experiments and outcome assessment. Unless otherwise stated, data analysed by parametric tests are represented by the mean  $\pm$  s.e.m. of pooled experiments and median  $\pm$  interquartile range for experiments

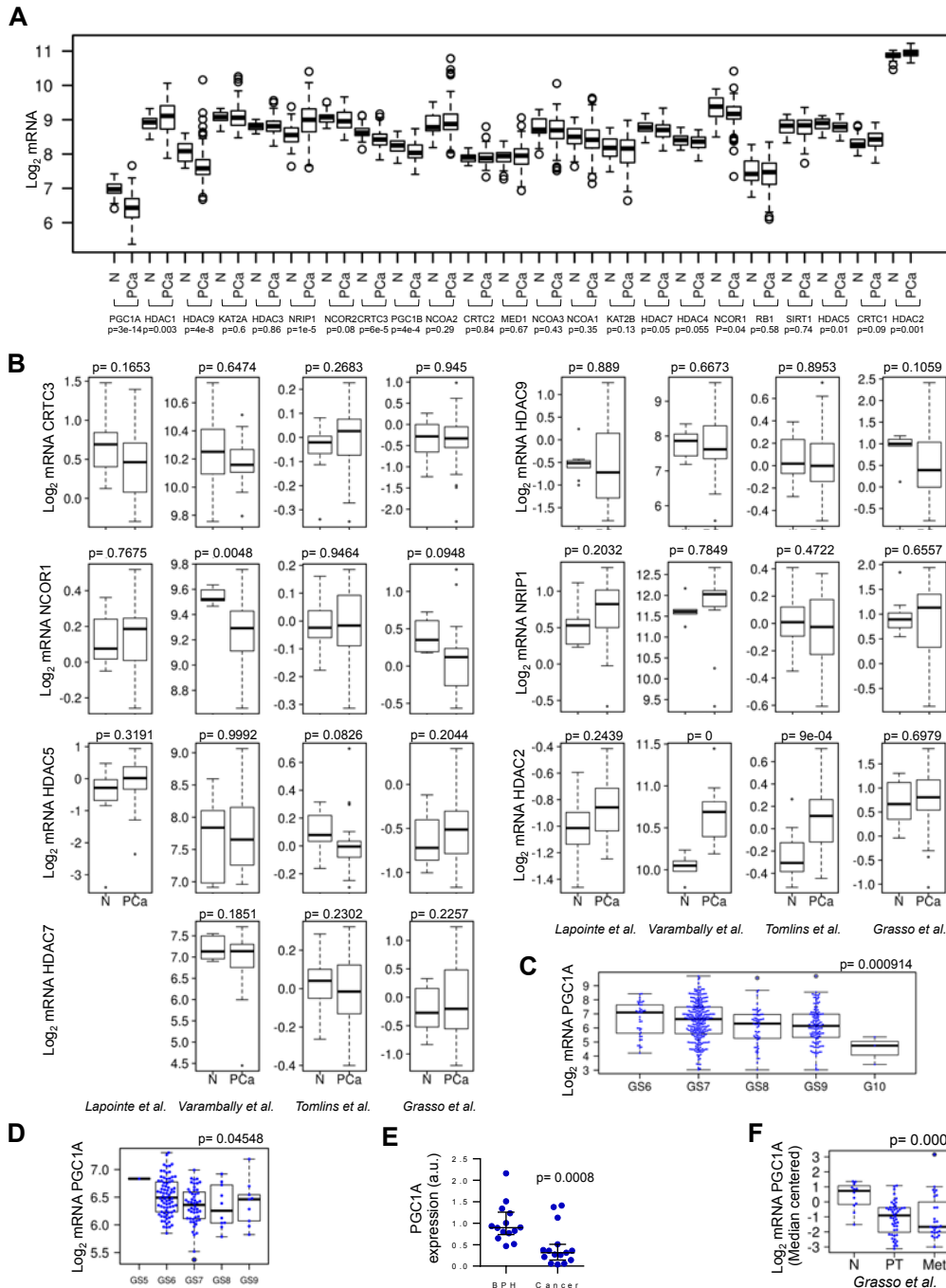
analysed by non-parametric tests.  $n$  values represent the number of independent experiments performed, the number of individual mice or patient specimens. For each independent *in vitro* experiment, at least three technical replicates were used (exceptions: in western blot analysis technical replicates are presented, in untargeted metabolomics two technical replicates were used and for  $^{13}\text{C}$ – $\text{U}_6$ –glucose isotope labelling one technical replicate was used) and a minimum number of three experiments were performed to ensure adequate statistical power. For data mining analysis, ANOVA test was used for multi-component comparisons and Student's  $t$ -test for two component comparisons. In the *in vitro* experiments, normal distribution was confirmed or assumed (for  $n < 5$ ) and Student's  $t$ -test was applied for two-component comparisons. For *in vivo* experiments, as well as for experimental analysis of human biopsies (from Basurto University Hospital) a non-parametric Mann–Whitney exact test was used, without using approximate algorithms to avoid different outcomes of statistics packages<sup>68</sup>. To this end, we applied the formulae described<sup>69</sup> for small-sized groups and Graphpad Prism for large-sized groups. In the statistical analyses involving fold changes, unequal variances were assumed. For contingency analysis, Fisher's exact test was used for two-group comparison (metastasis incidence) and Chi Square when analysing more than two groups (analysis of PGC1 $\alpha$ –ERR $\alpha$  signature frequency in PCa human specimens). The confidence level used for all the statistical analyses was of 95% (alpha value = 0.05). Two-tailed statistical analysis was applied for experimental design without predicted result, and one-tail for validation or hypothesis-driven experiments.

**Accession numbers and data sets.** Primary accessions: the transcriptomic data generated in this publication have been deposited in NCBI's Gene Expression Omnibus and are accessible through GEO Series accession number GSE75193.

Referenced accessions: Grasso *et al.*<sup>21</sup>, GEO: GSE35988; Lapointe *et al.*<sup>18</sup>, GEO: GSE3933; Taylor *et al.*<sup>22</sup>, GEO: GSE21032; Tomlins *et al.*<sup>23</sup>, GEO: GSE6099; Varambally *et al.*<sup>25</sup>, GEO: GSE3325.

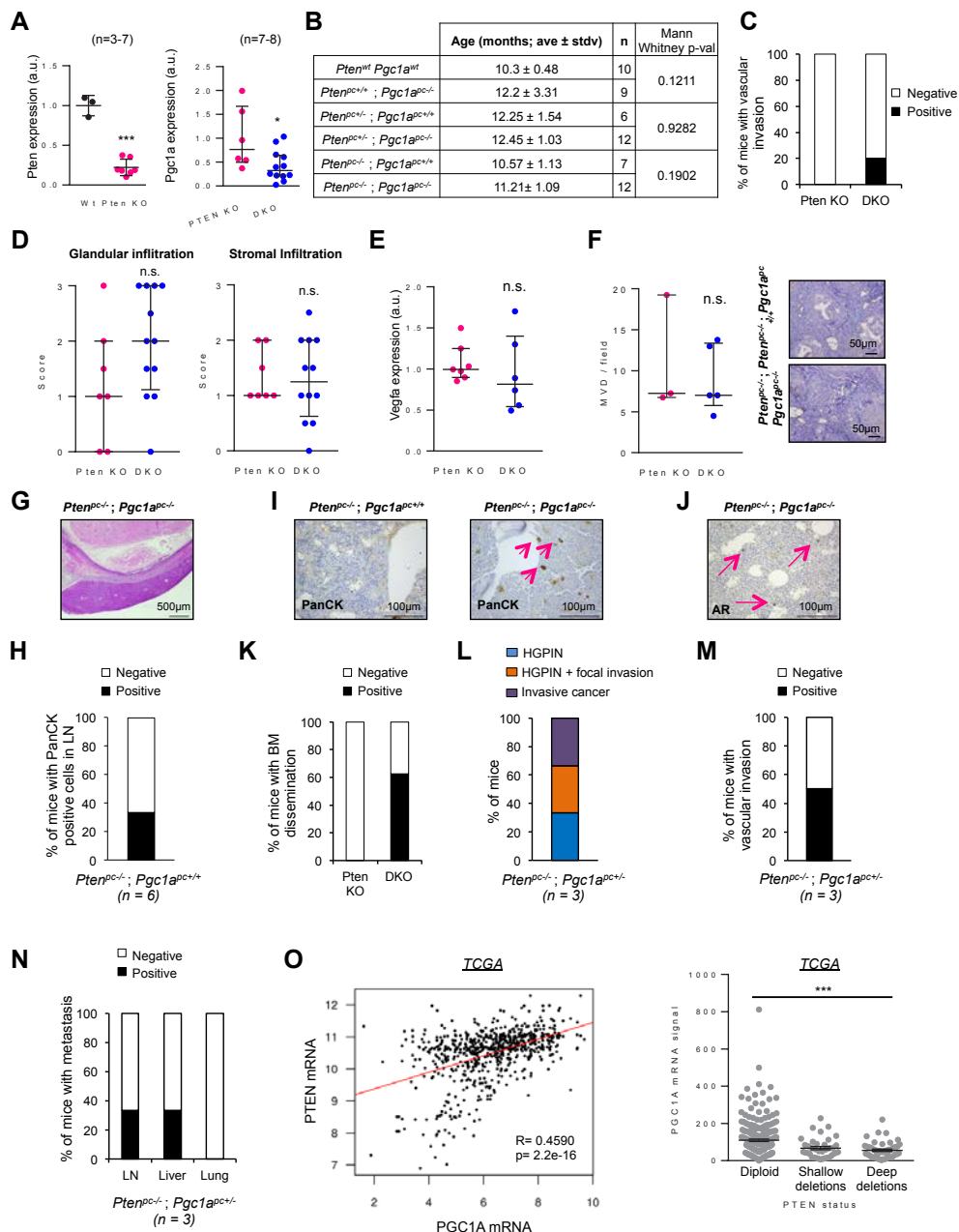
53. Arroyo-Berdugo, Y. *et al.* Involvement of ANXA5 and ILKAP in susceptibility to malignant melanoma. *PLoS ONE* **9**, e95522 (2014).
54. Song, M. S. *et al.* Nuclear PTEN regulates the APC-CDH1 tumor-suppressive complex in a phosphatase-independent manner. *Cell* **144**, 187–199 (2011).
55. Chen, Z. *et al.* Differential p53-independent outcomes of p19(Arf) loss in oncogenesis. *Sci. Signal* **2**, ra44 (2009).
56. Nardella, C. *et al.* Differential requirement of mTOR in postmitotic tissues and tumorigenesis. *Sci. Signal* **2**, ra2 (2009).
57. Guiu, M., Arenas, E. J., Gawrzak, S., Pavlovic, M. & Gomis, R. R. Mammary cancer stem cells reinitiation assessment at the metastatic niche: the lung and bone. *Methods Mol. Biol.* **1293**, 221–229 (2015).
58. Carracedo, A. *et al.* Inhibition of mTORC1 leads to MAPK pathway activation through a PI3K-dependent feedback loop in human cancer. *J. Clin. Invest.* **118**, 3065–3074 (2008).
59. Ugalde-Olano, A. *et al.* Methodological aspects of the molecular and histological study of prostate cancer: focus on PTEN. *Methods* **77–78**, 25–30 (2015).
60. Finley, L. W. *et al.* SIRT3 opposes reprogramming of cancer cell metabolism through HIF1 $\alpha$  destabilization. *Cancer Cell* **19**, 416–428 (2011).
61. Caro-Maldonado, A. *et al.* Metabolic reprogramming is required for antibody production that is suppressed in anergic but exaggerated in chronically BAFF-exposed B cells. *J. Immunol.* **192**, 3626–3636 (2014).
62. Wojtala, A. *et al.* Methods to monitor ROS production by fluorescence microscopy and fluorometry. *Methods Enzymol.* **542**, 243–262 (2014).
63. Ittmann, M. *et al.* Animal models of human prostate cancer: the consensus report of the New York meeting of the Mouse Models of Human Cancers Consortium Prostate Pathology Committee. *Cancer Res.* **73**, 2718–2736 (2013).
64. Liu, X. *et al.* High resolution metabolomics with acyl-CoA profiling reveals widespread remodeling in response to diet. *Mol. Cell. Proteomics* **14**, 1489–1500 (2015).
65. Liu, X., Ser, Z. & Locasale, J. W. Development and quantitative evaluation of a high-resolution metabolomics technology. *Anal. Chem.* **86**, 2175–2184 (2014).
66. Shestov, A. A. *et al.* Quantitative determinants of aerobic glycolysis identify flux through the enzyme GAPDH as a limiting step. *eLife* **3**, e03342 (2014).
67. Rodriguez, R. M. *et al.* Regulation of the transcriptional program by DNA methylation during human alphabeta T-cell development. *Nucleic Acids Res.* **43**, 760–774 (2015).
68. Bergmann, R., Ludbrook, J. & Spooren, W. P. J. M. Statistical computing and graphics: different outcomes of the Wilcoxon–Mann–Whitney test from different statistics packages. *Am. Statistician* **54**, 72–77 (2000).
69. Quinn, G. & Keough, M. *Experimental Design and Data Analysis for Biologists* (Cambridge Univ. Press, 2002).

DOI: 10.1038/ncb3357



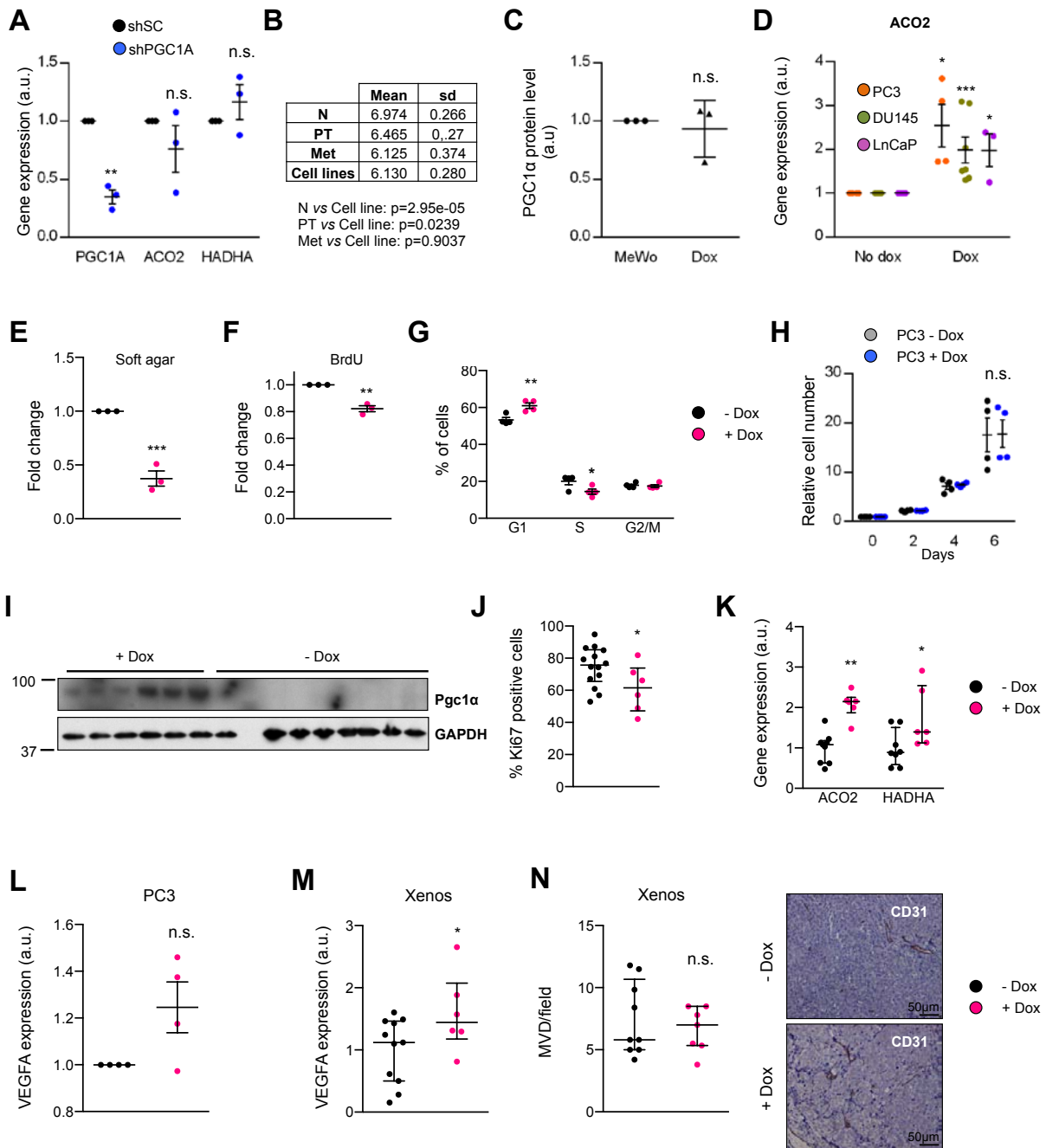
**Supplementary Figure 1 A**, Expression of 23 metabolic co-regulators in Taylor<sup>1</sup> dataset (N: normal; PCa: prostate cancer). **B**, Expression of 7 metabolic co-regulators from figure 1a in four additional prostate cancer datasets (N: normal; PCa: prostate cancer). In Varambally<sup>2</sup> dataset gene expression levels are presented in Log<sub>2</sub>. In Tomlins<sup>3</sup>, Grasso<sup>4</sup> and Lapointe<sup>5</sup> datasets gene expression levels are presented in median centred Log<sub>2</sub>. **C-D**, Association of *PGC1A* expression with Gleason score in TCGA provisional data<sup>6,7</sup> (C) and Taylor<sup>1</sup> datasets (D). **E**, Analysis of *PGC1A* expression

in benign prostatic hyperplasia (BPH) and PCa specimens from Basurto University Hospital cohort (qRT-PCR, BPH n= 14 patient specimens and Cancer n=16 patient specimens). **F**, *PGC1A* expression in normal prostate (N), primary tumour (PT) and metastatic (Met) specimens in Grasso dataset<sup>4</sup>. Points outlined by circles indicate statistical outliers (A, C, D and F). Error bars represent minimum and maximum values (A, B, C, D and F) or median with interquartile range (E). Statistic test: two-tailed Student T test (A, B), two-tailed Mann Whitney U test (E) and ANOVA (C, D and F).



**Supplementary Figure 2 A**, Analysis of *Pten* and *Pgc1a* gene expression in GEMMs of the indicated genotype (*Pten*<sup>wt</sup> *Pgc1a*<sup>wt</sup> n=3 mice; *Pten*<sup>pc/-</sup> *Pgc1a*<sup>pc/+</sup> n=7 mice; *Pten*<sup>pc/+</sup> *Pgc1a*<sup>pc/-</sup> n=6 mice; *Pten*<sup>pc/-</sup> *Pgc1a*<sup>pc/-</sup> n=12 mice; data is normalized to *Gapdh* expression). **B**, Age comparison between experimental cohorts (n as in Figure 2d). **C**, Quantification of prostate tissue with histological vascular invasion signs in *Pten* KO (2 mice) and DKO mice (9 mice) (limited to mice with invasive signs). **D**, Histological analysis of inflammatory signs (stromal and glandular infiltration) in *Pten* KO and DKO mice (*Pten* KO, n=7 mice; DKO, n=12 mice). **E** Quantification of *Vefga* mRNA expression in *Pten* KO and DKO mice (*Pten* KO, n=7 mice; DKO, n=6 mice; data is normalized to *Gapdh* expression). **F**, Quantification of microvessel density (MVD) (dot plot, left panels) and representative images of CD31 immunodetection (right panels) in *Pten* KO and DKO mice (*Pten* KO, n=3 mice; DKO, n=5 mice). **G**, Representative haematoxylin and eosin staining depicting liver metastasis in DKO (bar=500µm). **H**, Incidence of small groups of Pan-CK positive cells in the lymph nodes of *Pten* KO mice (6 mice). **I-J**, representative immunohistochemical detection (200X) of Pan-CK positive

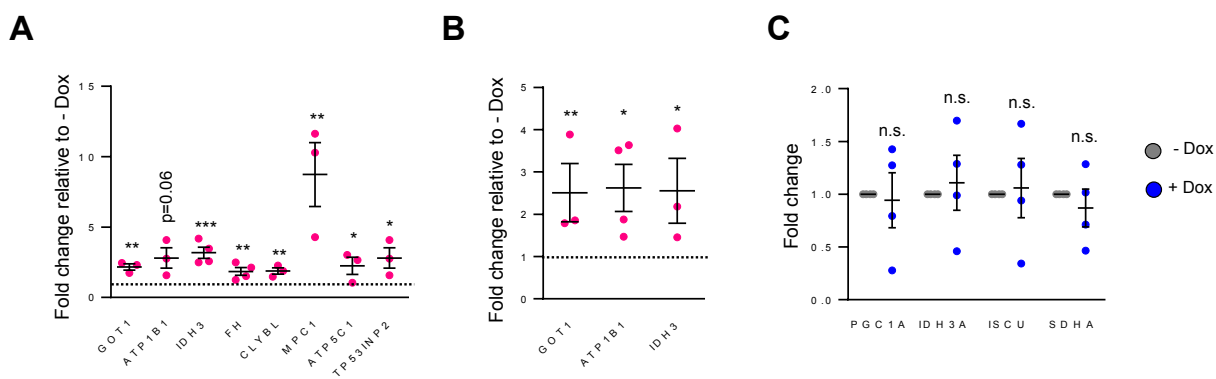
cells in the bone marrow (BM) of *Pten* KO and DKO (I) and androgen receptor (AR) in the bone marrow of DKO (J) (bar=100µm). Pink arrows indicate immunoreactive cells. **K**, Quantification of BM dissemination frequency (*Pten* KO, 6 mice; DKO, 8 mice). **L-M**, Histopathological characterization of the prostate tissue (L) and frequency of vascular invasion signs (M, only in mice with invasion signs) in *Pten*<sup>pc/-</sup> ; *Pgc1a*<sup>pc/+</sup> mice (3 mice). **N**, Frequency of metastatic lesions in lymph nodes (LN), liver and lung of *Pten*<sup>pc/-</sup> ; *Pgc1a*<sup>pc/+</sup> mice (3 mice). **O**, Correlation between *PGC1A* and *PTEN* gene expression in prostate cancer specimens (left panel) and the association of *PTEN* genomic loss to *PGC1A* gene expression (right panel) in TCGA provisional dataset. pc, prostate-specific allelic changes; +, Wildtype allele; -, deleted allele; wt: any given genotype resulting in the lack of deletion of *Pgc1a* and *Pten* alleles. *Pten* KO = *Pten*<sup>pc/-</sup> ; *Pgc1a*<sup>pc/+</sup> ; DKO = *Pten*<sup>pc/-</sup> ; *Pgc1a*<sup>pc/-</sup>. Stdv: standard deviation of the mean. All error bars represent median with interquartile range. p = p-value. a.u.: arbitrary units. Statistic tests: one-tailed Mann-Whitney U test (A, B), two-tailed Mann-Whitney U test (D, E and F); ANOVA (O, right panel); Pearson's coefficient (O, left panel). \*p < 0.05, \*\*\*p < 0.001.



**Supplementary Figure 3 A**, mRNA expression of *PGC1A*, *ACO2* and *HADHA* by qRT-PCR in PC3 cells transfected with scramble shRNA (shSC) or *PGC1A*-targeting shRNA (shPGC1A) (n=3). **B**, *PGC1A* expression in normal (N, n=29), primary tumour (PT, n=131), metastasis (Met, n=19) specimens and metastatic cell lines. Data is shown as Log<sub>2</sub> mRNA expression. **C**, Densitometry of PGC1α protein expression in MeWo (endogenous) and PC3 TRIPZ-HA-Pgc1α (ectopic) cell lines, relative to β-Actin (n=3, independent experiments). **D**, Effect of Pgc1α induction (+Dox) on *ACO2* mRNA expression in PC3 (n=4, independent experiments), DU145 (n=7, independent experiments) and LnCaP cells (n=3, independent experiments). **E-F**, Effect of Pgc1α expression on anchorage-independent growth (E, n=3, independent experiments) and BrdU incorporation (F, n=3, independent experiments) in DU145 cells. **G**, Effect of Pgc1α expression on cell cycle progression in PC3 cells (n=4, independent experiments). **H**, Effect of

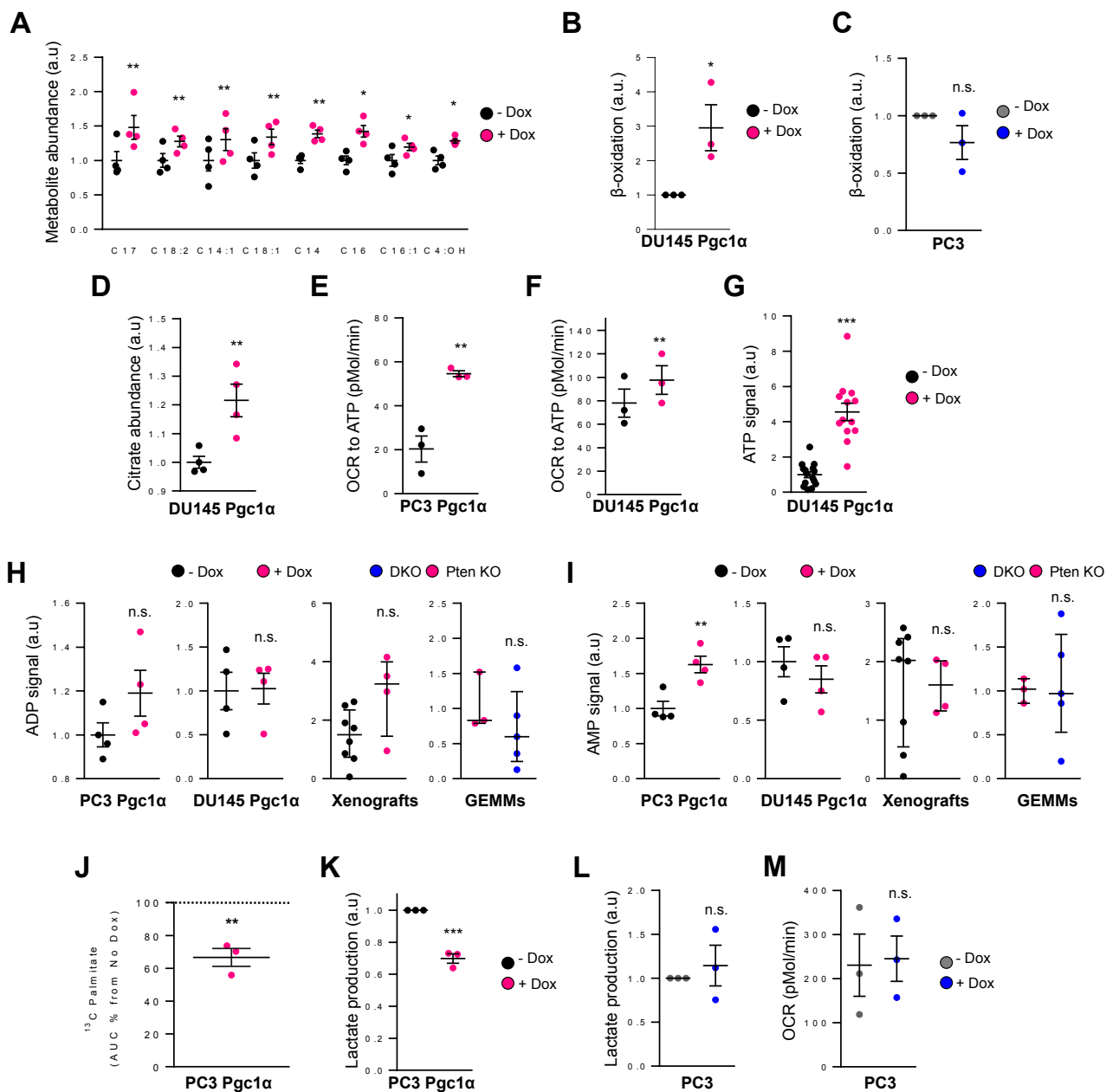
doxycycline treatment (0.5μg/ml) on cell growth of non-transduced PC3 cells (n=3, independent experiments). **I-J**, Pgc1α protein expression and cell proliferation by Ki67 immunoreactivity in xenograft samples from Fig. 3f (- Dox n=14 tumours, + Dox n=6 tumours). **K**, mRNA expression of *ACO2* and *HADHA* in xenograft samples from Fig. 3f. (- Dox n=9 tumours, + Dox n=6 tumours). **L-M**, Analysis of VEGFA mRNA expression upon Pgc1α induction in PC3 cells (L, n=4, independent experiments) and xenograft samples (M, - Dox n=9 tumours and + Dox n=6 tumours). **N**, Quantification of microvessel density (MVD) in xenograft samples (- Dox n=9 tumours and + Dox n=7 tumours). Right panels show representative CD31 staining micrographs. Error bars indicate s.e.m (A, C, D, E, F, G, H, L) and median with interquartile range (J, K, M, N). Statistic tests: two-tailed Student T test (A, B, C, D, E, F, G, H, L) and one-tailed Mann-Whitney U test (J, K, M, N). \* $p < 0.05$ , \*\* $p < 0.01$ , \*\*\* $p < 0.001$ .





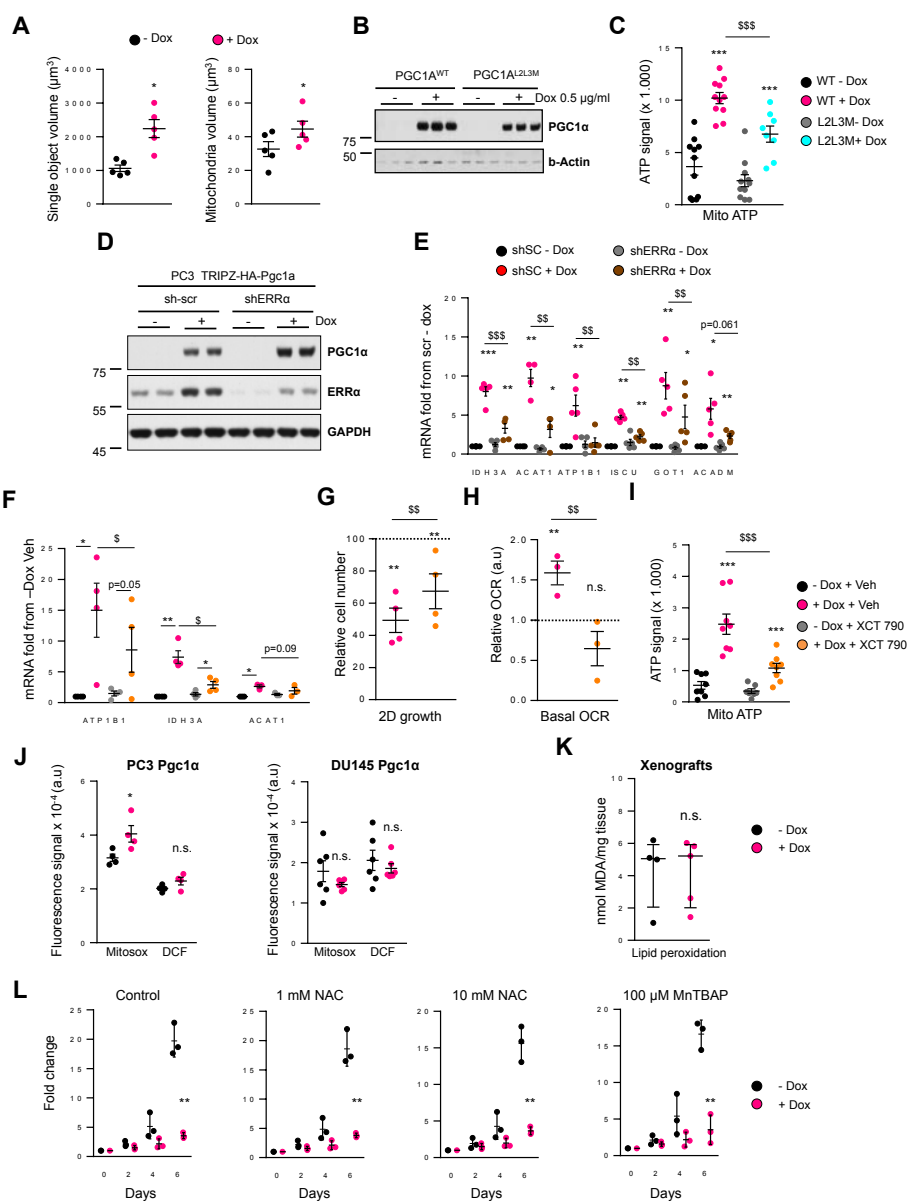
**Supplementary Figure 4 A-B**, Validation of the microarray by qRT-PCR in DU145 (n=4, independent experiments) and LnCaP (n=3, independent experiments) TRIPZ-HA-Pgc1a cells. Gene expression values relative to - Dox cells are represented (reference - Dox gene expression values are

indicated with a dotted line) **C**, mRNA expression of PGC1 $\alpha$  target genes in doxycycline-treated (0.5 $\mu$ g/ml) non-transduced PC3 cells (n=3, independent experiments). Error bars represent s.e.m. Statistic test: One tail Student T test. \*p < 0.05, \*\*p < 0.01, \*\*\*p < 0.001.



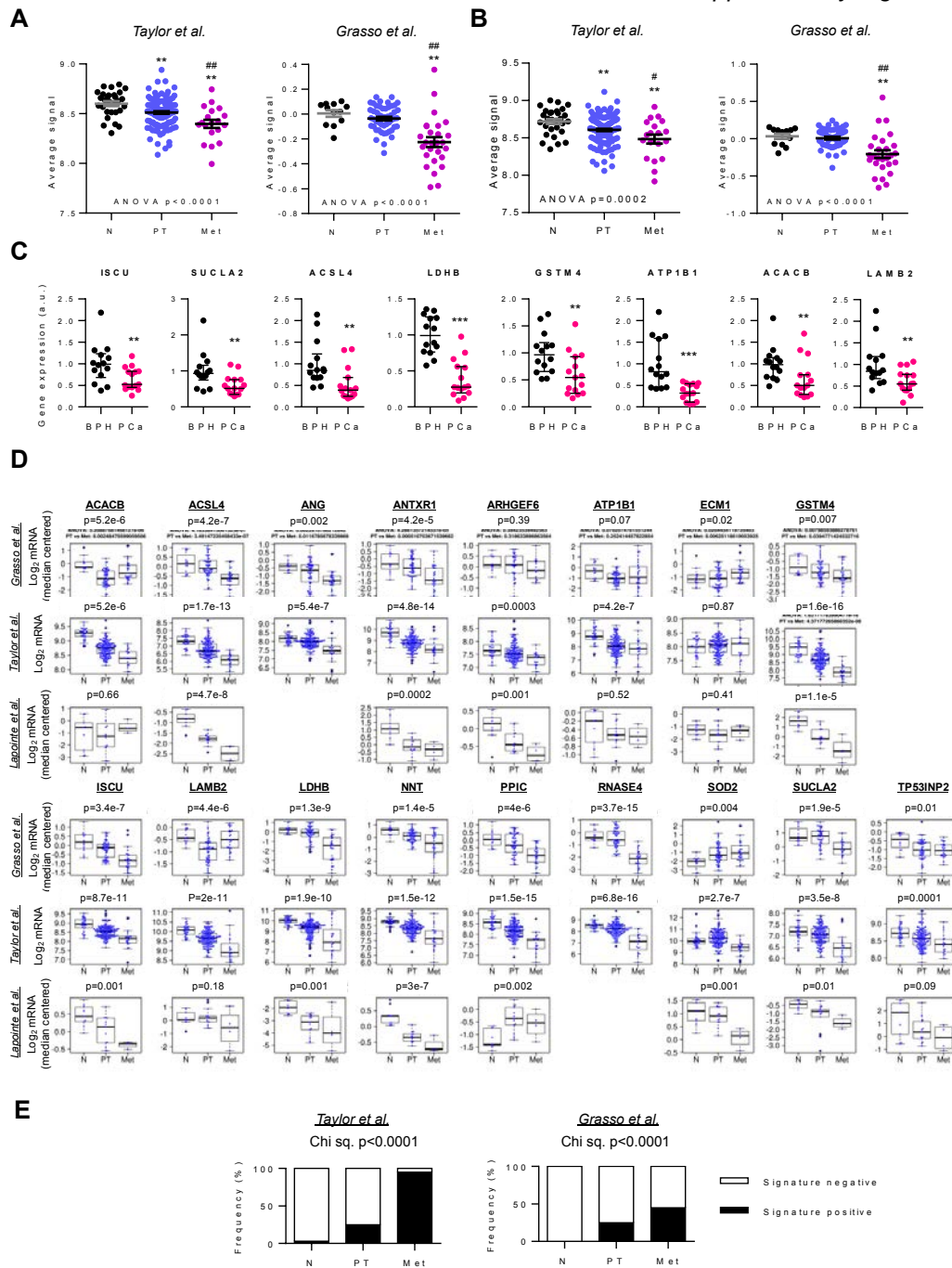
**Supplementary Figure 5 A**, Analysis of differential abundance in metabolites involved in fatty acid catabolism by untargeted LC-HRMS in DU145 TRIPZ-HA-Pgc1 $\alpha$  cells (n=4, independent experiments). **B-C** Evaluation of the dehydrogenation of  $^3\text{H}$ -palmitate (readout of  $\beta$ -oxidation) in DU145 cells upon Pgc1 $\alpha$  expression (B, n=3, independent experiments) and, in doxycycline-treated (0.5 $\mu\text{g}/\text{ml}$ ) non-transduced PC3 cells (C, n=3, independent experiments). Values relative to - Dox cells are presented. **D**, Effect of Pgc1 $\alpha$  expression on citrate abundance measured by LC-HRMS metabolomics in DU145 cells (n=4, independent experiments). **E-F**, ATP-producing OCR (upon complex V inhibition by oligomycin injection) in PC3 (E, n=3, independent experiments) and DU145 (F, n=3, independent experiments) cells upon Pgc1 $\alpha$  expression. **G**, Basal mitochondrial ATP production in DU145 cells upon Pgc1 $\alpha$  expression (n=10, independent experiments). **H-I**, LC-HRMS quantification of ADP (H) and AMP (I)

abundance in PC3 Pgc1 $\alpha$  (n=4, independent experiments), DU145 Pgc1 $\alpha$  (n=4, independent experiments), xenografts (- Dox n=8 tumours; + Dox n=4 tumours) and GEMMs (*Pten* KO n=3 mice; DKO n=5 mice). **J**, Quantification of area under the curve (AUC, relative to - Dox) of Palmitate labelling from  $^{13}\text{C}$ -U $_6$ -Glucose in PC3 TRIPZ-HA-Pgc1 $\alpha$  cells (data related to Fig. 5j, n=3, independent experiments). **K**, Determination of extracellular lactate in PC3 TRIPZ-HA-Pgc1 $\alpha$  cells (n=3, independent experiments). **L-M**, Lactate production (L) and OCR (M) in doxycycline-treated (0.5 $\mu\text{g}/\text{ml}$ ) non-transduced PC3 cells (n=3, independent experiments). Error bars represent s.e.m., except xenograft and GEMM data in H-I, that represent median with interquartile range. Statistic tests: two tailed Student T test (A, B, C, D, E, F, G, H (PC3 and DU145), I (PC3 and DU145), J, K, L, M) and one tailed Mann Whitney U test (H (Xenografts and GEMMs), I (Xenografts and GEMMs)). \*p < 0.05, \*\*p < 0.01, \*\*\*p < 0.001.



**Supplementary Figure 6** A, Analysis of mitochondrial morphology (mitochondrial volume) in PC3 cells upon *Pgc1α* expression (n=5, independent experiments). B, Expression of *PGC1α*<sup>WT</sup> and *PGC1α*<sup>L2L3M</sup> in PC3 cells after treatment with 0.5 µg/ml doxycycline (Dox) (a representative experiment with technical replicates is presented, similar results were obtained in three independent experiments). C, Basal mitochondrial ATP production in *PGC1α*<sup>WT</sup> and *PGC1α*<sup>L2L3M</sup> PC3 cells (n=11, independent experiments). D, Expression of *Pgc1α* and *ERRα* in doxycycline-treated PC3 TRIPZ-HA-*Pgc1α* cells transduced with sh-scramble (shSC) or shERRα (a representative experiment with technical replicates is presented, similar results were obtained in three independent experiments). E, mRNA expression of *PGC1α* target genes in doxycycline-treated PC3 TRIPZ-HA-*Pgc1α* cells transduced with shSC or shERRα (n=4 for ACAT1 and n=5 for IDH3A, ATP1B1, ISCU, GOT1 and ACADM; independent experiments). F-I, mRNA expression of *PGC1α* target genes (F, n=3 for ACAT1 and n=4 for ATP1B1 and IDH3A; independent experiments), cell number (G, n=4, independent experiments), basal oxygen consumption (H, n=3, independent experiments) and basal mitochondrial ATP production

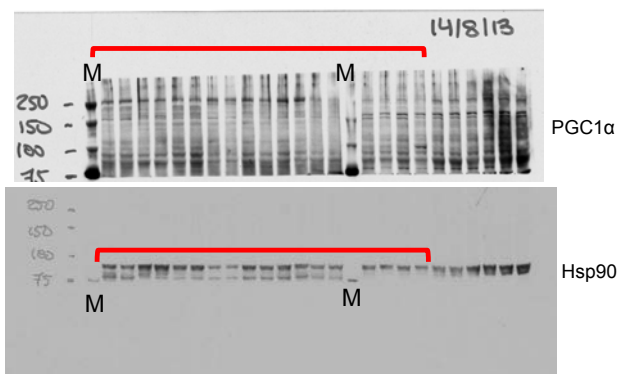
(I, n= 7 for - Dox + XCT790; n=8 the rest; independent experiments) in vehicle (Veh) or XCT790-treated *Pgc1α*-inducible PC3 cells. J, Evaluation of cellular (DCF) and mitochondrial-specific (Mitosox) ROS production in *Pgc1α*-expressing PC3 (left panel; n=4, independent experiments) and DU145 (right panel; n=6, independent experiments) cells. K, Evaluation of lipid peroxidation in xenograft tissues from Fig. 3f (- Dox n=4 tumours; + Dox n=5 tumours). L, Effect of the indicated antioxidant treatments on cell number (relative to day 0) of *Pgc1α*-expressing PC3 cells (n=3, independent experiments). DCF: 2',7'-dichlorodihydrofluorescein. n.s.: not significant. Error bars represent s.e.m. (A, C, E, F, G, H, I, J, L) or median with interquartile range (K). Statistic tests: two tailed Student T test (A, C, E, F, G, H, I, J, L) or one tailed Student T test (comparison between + Dox conditions in C, E, F, G, H, I) and two tailed Mann-Whitney U test (K). \*/\$ p < 0.05, \*\*/\$\$ p < 0.01, \*\*\*/\$\$\$ p < 0.001. Asterisks indicate statistic between - Dox and + Dox conditions (unless represented otherwise) and dollar symbol between either, vehicle (Veh) and XCT790-treated *Pgc1α*-expressing cells, shSC and shERRα-transduced *Pgc1α*-expressing cells or *Pgc1α*<sup>WT</sup> and *Pgc1α*<sup>L2L3M</sup>.



**Supplementary Figure 7 A-B**, Representation of the average signal of genes within the PGC1 $\alpha$ -upregulated gene set (A) (Fig. 7b, blue circle) and within the PGC1 $\alpha$ -dependent ERR $\alpha$ -upregulated gene set (B) (Fig. 7b, yellow circle, Table S6) in the indicated datasets<sup>1,4,6,7</sup>, in normal (N; Taylor n=29 and Grasso n=12), primary tumours (PT; Taylor n=131 and Grasso n=49) and metastasis (Mets; Taylor n=19 and Grasso n=27). **C**, qRT-PCR mRNA expression analysis of PGC1 $\alpha$  target genes from C, in benign prostatic hyperplasia (BPH) and PCa specimens from Basurto University Hospital cohort (BPH n=14 patient specimens; Prostate cancer n=16 patient specimens). **D**, Expression of the indicated genes (from Supplementary Table 7) in different disease states (N: normal, Lapointe n=9, Taylor n=29 and

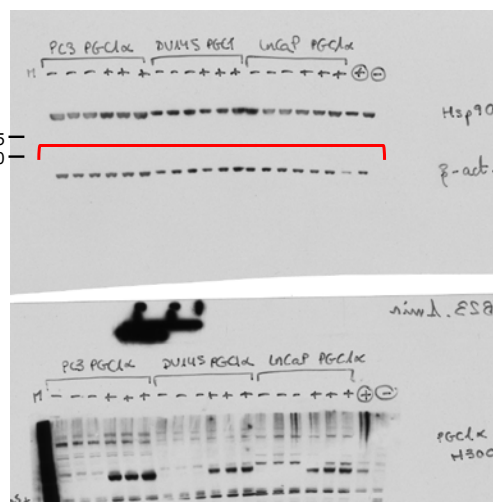
Grasso n=12; PT: primary tumour, Lapointe n= 13, Taylor n=131 and Grasso n=49; Met: metastasis, Lapointe n=4, Taylor n=19 and Grasso n=27) in three PCA datasets<sup>1,4,5</sup>. **E**, Representation of “PGC1 $\alpha$ -ERR $\alpha$  Q1 signature” frequency within different tumour types (N: normal; PT: primary tumour; Met: metastasis) in two datasets<sup>1,4</sup> (Taylor: N, n=29; PT, n= 131; Met, n=19; Grasso: N, n=12; PT, n=49; Met, n=27). Error bars represent s.e.m. (A, B), median with interquartile range (C) and maximum and minimum (D). Statistic tests: Statistic tests: ANOVA (A, B, D); two tailed Student T test (A, B), one tailed Mann Whitney U test (C), Chi Square (E). Asterisks in A, B indicates statistics between normal and metastasis and hash between primary tumours and metastasis. p: p-value. \*/#  $p < 0.05$ , \*\*/#  $p < 0.01$ , \*\*\*  $p < 0.001$ .

**A**

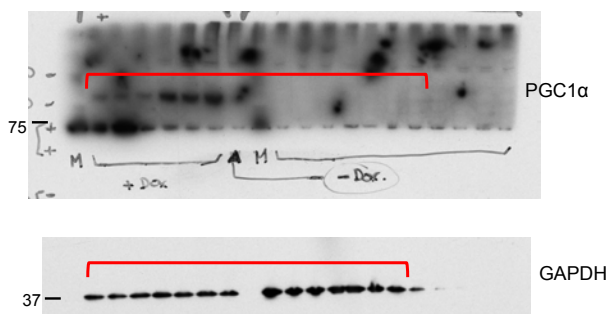


M: Marker (Precision Plus Protein™ Dual Color Standards, Ref #1610374)

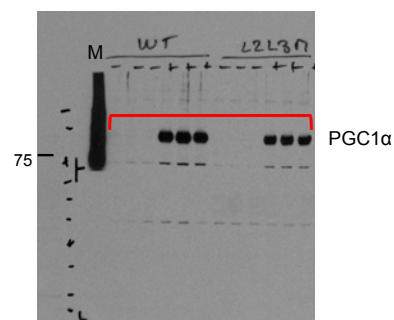
**B**



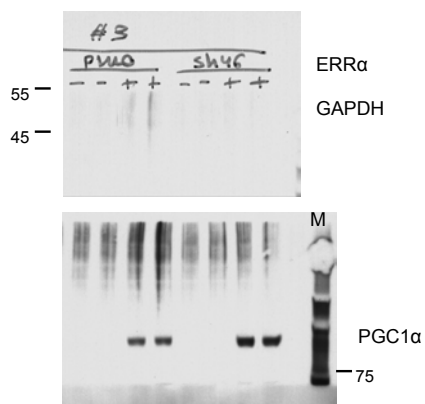
**C**



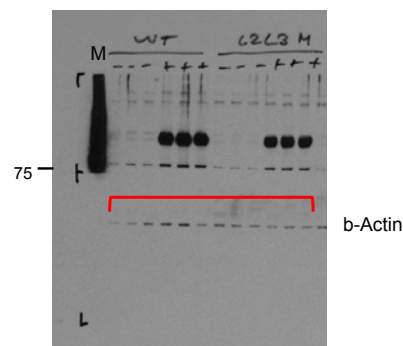
**D**



**E**



M: Marker (Pink Prestained protein ladder, Nippon Genetics, Cat.No. MWP02)



**Supplementary Figure 8** Unprocessed blots. **A**, Western blot corresponding to Figure 3a. **B**, Western blot corresponding to Figure 3b. **C**, Western blot corresponding to Supplementary Figure 3I. **D**, Western blot corresponding to Supplementary Figure 6B. **E**, Western blot

corresponding to Supplementary Figure 6D. Precision Plus Protein™ Dual Color Standards (Ref #1610374) markers was used in A-D. Pink Pre-stained protein ladder, Nippon Genetics, Cat.No. MWP02, was used in E.

## Table titles and legends

**Supplementary Table 1** Gene expression profiling in PC3 TRIPZ-HA-Pgc1 $\alpha$  cells (Doxycycline vs. No Doxycycline, (0.5 $\mu$ g/ml).

**Supplementary Table 2** Untargeted LC-HRMS metabolomic profiling in PC3 TRIPZ-HA-Pgc1 $\alpha$  cells (Doxycycline vs. No Doxycycline, (0.5 $\mu$ g/ml).

**Supplementary Table 3** Untargeted LC-HRMS metabolomic profiling in DU145 TRIPZ-HA-Pgc1 $\alpha$  cells (Doxycycline vs. No Doxycycline, (0.5 $\mu$ g/ml).

**Supplementary Table 4** Untargeted LC-HRMS metabolomic profiling in xenograft-derived tissues (from PC3 TRIPZ-HA-Pgc1 $\alpha$  cells) upon induction of Pgc1 $\alpha$  expression (Doxycycline diet vs. chow).

**Supplementary Table 5** Untargeted LC-HRMS metabolomic profiling in GEMM-derived prostate tissues (Pten<sup>PC-/-</sup>, Pgc1a<sup>PC-/-</sup> vs. Pten<sup>PC-/-</sup>, Pgc1a<sup>PC+/+</sup>).

**Supplementary Table 6** Definition of ERR $\alpha$  signature within the PGC1 $\alpha$  gene list. Genes included in the TGACCTY\_V\$ERR1\_Q2 dataset or identified in the study by Stein et al (STEIN\_ESRRA\_TARGETS<sup>8</sup>) were considered as ERR $\alpha$  targets.

**Supplementary Table 7** List of Pgc1 $\alpha$ -regulated genes in PC3 (Supplementary Table 1) that show significant and consistent correlation with *PGC1A* in human prostate cancer datasets ( $R > 0.2$ ;  $p < 0.05$ ) in at least three out five datasets.

**Supplementary Table 8** List of primers and probes (Universal Probe Library, Roche) used in qRTPCR.

**Supplementary Table 9** Statistics source data for animal experiments reported in Fig. 3k, and Fig. 6e, h. All data are organized into different sheets and named based on the corresponding figure/panel numbers.

## References:

- 1 Taylor, B. S. *et al.* Integrative genomic profiling of human prostate cancer. *Cancer Cell* **18**, 11-22, doi:10.1016/j.ccr.2010.05.026 (2010).
- 2 Varambally, S. *et al.* Integrative genomic and proteomic analysis of prostate cancer reveals signatures of metastatic progression. *Cancer Cell* **8**, 393-406, doi:10.1016/j.ccr.2005.10.001 (2005).
- 3 Tomlins, S. A. *et al.* Integrative molecular concept modeling of prostate cancer progression. *Nat Genet* **39**, 41-51, doi:10.1038/ng1935 (2007).
- 4 Grasso, C. S. *et al.* The mutational landscape of lethal castration-resistant prostate cancer. *Nature* **487**, 239-243, doi:10.1038/nature11125 (2012).
- 5 Lapointe, J. *et al.* Gene expression profiling identifies clinically relevant subtypes of prostate cancer. *Proc Natl Acad Sci U S A* **101**, 811-816, doi:10.1073/pnas.0304146101 (2004).
- 6 Cerami, E. *et al.* The cBio cancer genomics portal: an open platform for exploring multidimensional cancer genomics data. *Cancer Discov* **2**, 401-404, doi:10.1158/2159-8290.CD-12-0095 (2012).
- 7 Gao, J. *et al.* Integrative analysis of complex cancer genomics and clinical profiles using the cBioPortal. *Sci Signal* **6**, pl1, doi:10.1126/scisignal.2004088 (2013).
- 8 Stein, R. A. *et al.* Estrogen-related receptor alpha is critical for the growth of estrogen receptor-negative breast cancer. *Cancer Res* **68**, 8805-8812, doi:10.1158/0008-5472.CAN-08-1594 (2008).